Universität Hamburg
DER FORSCHUNG | DER LEHRE | DER BILDUNG

Fachbereich
Chemie

Dissertation

Materials for Future: Thermoreversible Networks and Functional Composite Materials through Recyclability by Design

submitted by

Florian C. Klein

Hamburg 2025

Faculty of Mathematics, Informatics, and Natural Science
Department of Chemistry

in conformity with the requirements for the degree of
Doctor rerum naturalium (Dr. rer. nat.)
submitted to the Universität Hamburg

„Die Wissenschaft fängt eigentlich erst da an,
recht interessant zu werden, wo sie aufhört.“

Justus von Liebig

Supervisor: Prof. Dr. Volker Abetz
1st Referee: Prof. Dr. Volker Abetz
2nd Referee: PD Dr. Christoph Wutz

Defense Committee:
Prof. Dr. Volker Abetz
Prof. Dr.-Ing. Jakob Albert
Prof. Dr. Ralph Holl

Date of Submission: 18.12.2025
Date of Oral Defense: 13.02.2026

The submitted dissertation was written under the supervision of Prof. Dr. Volker Abetz at the Institute of Physical Chemistry of the University of Hamburg. The practical work for the dissertation was conducted from April 2022 to August 2025. The dissertation was submitted in December 2025 and represents a cumulative dissertation that the audit committee has approved. The dissertation contains three first-author publications, which were published with the help of cooperation partners and co-workers mentioned in the publications. Contributions for the presented unpublished results are acknowledged in this dissertation in the particular subchapter as well.

Publications

This cumulative thesis includes three first-author contributions that were published prior to this work. The publications are cited as reprints in Chapter 5.

Publication 1:
Reprocessable Vanillin-based Polyschiff Vitrimer Networks: Tuning Mechanical and Thermomechanical Properties by Network Design

Florian C. Klein, Malte Vogt, and Volker Abetz
Macromol. Mater. Eng., **2024**, *309*, 2300187.
doi.org/10.1002/mame.202300187

Publication 2:
Bio-Based Vinylogous Urethane Vitrimers from Waste-Wood Lignosulfonate and Enzymatic Lignin: Explorations in Stress Relaxation Behavior and Mechanical Strength

Florian C. Klein, Nils Sobania, and Volker Abetz
J. Mater. Chem. A, **2025**, *13*, 29120–29137.
doi.org/10.1039/D5TA02533H

Publication 3:
Transparent Boronic Acid Acrylate Vitrimers Through One-Pot Click Reaction with Superior Strength as Matrix Material for Titania Nanoplates

Florian C. Klein, Jana Struck, Tobias Vossmeyer, and Volker Abetz
Macromol. Chem. Phys., **2025**, *226*, e00276.
doi.org/10.1002/macp.202500276

Table of Contents

Index of Symbols

$\dot{\gamma}$	shear rate
$<\tau>$	characteristic stress-relaxation time
^{13}C	carbon nucleus
^{1}H	hydrogen nucleus
^{31}P	phosphor nucleus
B-N	boron-nitrogen bond
C=C	carbon-carbon double bond
C=N	imine
C=O	carbon-oxygen double bond
E	Young´s modulus
E_a	activation energy
f	functionality
G	shear modulus
$G(t)$	stress-relaxation modulus
G'	(shear) storage modulus
G''	(shear) loss modulus
m	mass
n	molar amount
pK_a	acid dissociation constant
T	temperature
t	time
T_g	glass transition temperature
T_m	melting temperature
$T_{5\%}$	degradation temperature
T_v	vitrimer freezing temperature
X	molar fraction
β	stretch parameter
γ	strain, deformation
ΔG	free energy
ε	strain
η	viscosity
λ	wavelength
σ	stress
τ	characteristic relaxation time
τ	shear stress
τ_{cross}	characteristic timescale for rearrangement

Index of Abbreviations

2-MeTHF	2-methyltetrahydrofuran
AFM	atomic force microscopy
AFM-IR	atomic force microscopy infrared spectroscopy
AFT	addition fragmentation chain transfer
AIE	aggregation-induced-emission
ATR-FT-IR	attenuated total reflection Fourier transform infrared spectroscopy
BADGE	bisphenol A diglycidylether
BPAAC	propane-2,2-diylbis(4,1-phenylene) bis(3-oxobutanoate)
BVS	boronic acid acrylate vitrimer sample
CA	cycloaddition
CAN	covalent adaptable network
CGT	critical gelation temperature
DA	Diels-Alder
DADOX	1,8-diamino-3,6-dioxaoctan
DB	dioxaborolane
DBEDT	2,2-(1,4-phenylene)-bis[4-mercaptan-1,3,2-dioxaborolane]
DCC	dynamic covalent chemistry
DIN EN	Deutsches Institut für Normung, European Norm
DMA	dynamic mechanical analysis
DMSO	dimethyl sulfoxide
DSC	differential scanning calorimetry
DMTA	dynamic mechanical thermal analysis
e.g.	*Latin*: *exempli gratia*, *English*: for example
EP	epoxy polymer
eq	equivalent
ESI	electron spray ionization
et al.	*Latin*: *et alii*, *English*: and others
FDPA	10-(furan-2-carboxamido)decyl)phosphonic acid
FTIR	Fourier-transform infrared spectroscopy
GLYAAC	propane-1,2,3-triyl tris(3-oxobutanoate)
GVP	glycerol vitrimer polymer
i.e.	*Latin*: *id est*, *English*: that is
IPCAN	interpenetrating covalent adaptable network
IPN	interpenetrating polymer network
JT	Jeffamine T403
KWW	Kohlrausch-Williams-Watts
LVE	linear viscoelastic regime
M	molecular weight
MDPA	maleimide dodecyl phosphonic acid
MNR	molecular network rearrangement
NMP	nitroxide-mediated polymerizations
NMR	nuclear magnetic resonance spectroscopy
OA	oleic acid
PETAC	2,2-bis([(1-oxoallyl)oxy]methyl)1,3-propandiyldiacrylat
pH	*Latin*: *pondus hydrogenii*

Ph.D.	philosopher's degree
PS	precursor solution
R	ratio
R'	adjusted VIPOXY ratio
RILN	reversible interlocked polymer network
SEM	scanning electron microscopy
SFB	Sonderforschungsbereich (*English:* collaborative research center)
SFCF	solvent-free and catalyst-free
S_N1	monomolecular nucleophilic substitution reaction
S_N2	bimolecular nucleophilic substitution reaction
SPION	superparamagnetic iron oxide nanoparticle
TBAA	*tert*-butyl acetoacetate
TEC	thiol-ene click
THF	tetrahydrofuran
TM	thiol-Michael
TMDO	2,2,6-trimethyl-1,3-dioxin-4-one
TREN	triethyl amine
VIPOXY	vitrimer epoxy co-network
VU	vinylogous urethane
WLF	Williams-Landel-Ferry

1 Abstract

Polymers are a key component of modern society's lifestyle. They offer a wide range of properties, serve special applications, and being mass materials makes it nearly impossible to imagine human life without plastics. The staggering amount of plastics produced each year makes it a multibillion-dollar industry and a vital part of the global chemical industry. During times of political tension, fossil fuels play a crucial role, as they serve as the feedstock, and refinery industries are capable of producing fuels, monomers, and specialized chemicals for today's chemical industry needs. Modern technologies would be impossible without relying on polymer materials.

The vast amount of plastics produced results in a huge amount of plastic waste. The durability of most plastic materials is a major drawback because it contributes to pollution, fragmentation into microplastics, and negative impacts on societal and environmental systems. Recently, microplastics have been found in every ecosystem on our planet, including the Arctic and the deep sea.

Recycling of plastics has become a rapidly growing field in polymer research, covering waste recycling, thermal use by incineration, and landfilling, which are influenced by the properties of the polymer itself. Instead of focusing only on recycling products at the end of their life, an important task is to design materials with recyclability in mind from the start. In addition to reducing consumption, integrating a closed-loop carbon cycle into plastic materials is one of the most promising solutions to achieve sustainability. This is especially crucial given the connection between the “plastic crisis” and the “climate crisis.” With plastics' high versatility and advantageous properties, it is time to develop new sustainable solutions for end-of-life management to prevent the “plastic age” from becoming the dinosaur story of future generations, reflecting on our scientific and political progress. Potential solutions include using bio-based feedstocks, designing for recyclability, and conducting end-of-life analyses for produced materials. The use of covalent adaptable chemistry can enable the reprocessing and recyclability of high-performance materials like polymers and composites.

The main part of this work consists of the design, synthesis, and characterization of new polymeric materials with dynamic covalent bonds. In three publications and the following chapters of unpublished results, the influences of the building blocks, chemical reactivity, and network design are discussed. The developed covalent adaptable networks exhibit a thermoreversible group of cross-linked materials, which can be reshaped, reprocessed, and thus have the ability to enable recyclability by design. By using bio-based feedstocks, environmentally friendly synthetic methods, and following the principles of green chemistry, the presented work paves the way toward more sustainable polymer networks and composite materials.

In the first study, vanillin was used as a bio-based precursor derived from lignin, a component of lignocellulosic biomass that contains functional groups suitable for chemical modification.

By designing difunctional aldehyde building blocks, Schiff base vitrimers were created using less toxic amines as crosslinkers. Besides their thermomechanical properties, the exchange chemistry was a primary focus of this work. By carefully adjusting the number of free amines within the network, the rate of network rearrangement can be controlled. If excess amines are present, transimination can occur, whereas imine metathesis is the dominant exchange mechanism in a Schiff base network without excess amines. Since imine bonds are susceptible to hydrolysis, effective acidic hydrolysis was demonstrated as a method to chemically recycle the starting molecules. Therefore, these vitrimers can perform both associative exchange reactions and dissociative exchange mechanisms *via* small-molecule mediation, functioning as a dissociative covalent adaptable network.

The second publication focuses on developing vinylogous urethane vitrimers from lignocellulosic biomass. Lignin is one of the most abundant biopolymers and has a high density of functional groups. Currently, lignin is produced as a byproduct of the pulp and paper industry and is treated as a low-value waste material. Typically, this resource is incinerated. By simply modifying the hydroxy groups of lignin molecules, they can be converted into vinylogous urethane vitrimers when reacted with (bio-based) amines. Lignosulfonate is a somewhat impure lignin source obtained from sulfite pulping. However, the high polarity of the particles makes it water-soluble, enabling a greener synthesis route. Additionally, enzymatic lignin was characterized and transformed into lignin vitrimers. Their mechanical properties were analyzed with particular attention to the glass transition and the transamination reaction at elevated temperatures. It was observed that the segmental movability can significantly affect activation energy calculations and must be considered for industrial applications. This was demonstrated through injection molding with powder precursors, which were transformed into vitrimer test specimens. The resulting materials exhibit high mechanical strength and reprocessability.

The third publication features a more industrial-ready vitrimer concept that includes dioxaborolane metathesis chemistry, which is activated with low energy and allows reprocessability of tetrafunctional acrylates for at least 20 times. The mechanical properties are examined and compared after various reprocessing stages, showing minimal impact on performance. Interestingly, the thermal history was found to significantly influence stress-relaxation behavior, and this effect can be assessed using applied stretched exponential fits. The internal stress remaining can be relieved by thermal annealing, emphasizing the importance to consider thermal history before interpreting stress-relaxation data. This is especially crucial when comparing different materials. As a potential application, the incorporation of titanium dioxide nanoplates was demonstrated. Within the scope of the collaborative research center SFB986 – multiscale materials, a new strategy for producing highly filled nanocomposites was shown, enabling the formation of homogeneous hierarchical nanocomposites.

The findings from the publications were also further explored in the unpublished results. An interpenetrating covalent adaptable network was formed through a reactive simultaneous process using vinylogous urethanes and dioxaborolane chemistry. Additionally, vitrimer-epoxy co-networks were created to improve the performance of vinylogous urethane vitrimers by adding permanent covalent bonds.

Overall, this work advances the state-of-the-art of functional thermoreversible networks, offering new insights into stress-relaxation and network design. The materials and their properties improve recyclability by design and lay the foundation for future materials.

2 Kurzfassung

Polymere sind ein wesentlicher Bestandteil des Lebens der modernen Gesellschaft. Sie bieten eine Vielzahl von Eigenschaften und erfüllen spezielle Anforderungen. Ein menschliches Leben ohne Kunststoffe scheint aufgrund deren Massenproduktion und Verbreitung kaum vorstellbar. Die beeindruckende Menge an jährlich produzierten Kunststoffen macht daraus eine milliardenschwere Branche und einen wichtigen Teil der globalen chemischen Industrie. In Zeiten politischer Spannungen spielen auch fossile Brennstoffe eine entscheidende Rolle, da sie als Rohstoff der Raffinerieindustrien dienen, die daraus Kraftstoffe, Monomere und spezialisierte Chemikalien für die Anforderungen der heutigen chemischen Industrie produzieren. Viele moderne Technologien wären ohne den Einsatz neuer Polymermaterialien kaum vorstellbar.

Die enorme Menge an produzierten Kunststoffen führt zu einer riesigen Menge an Abfällen. Die Langlebigkeit der meisten Kunststoffmaterialien ist ein wesentlicher Nachteil, da sie zur Verschmutzung, Fragmentierung in Mikroplastik und negativen Auswirkungen auf gesellschaftliche und ökologische Systeme beiträgt. Kürzlich wurden Mikroplastikpartikel in jedem Ökosystem unseres Planeten gefunden, einschließlich der Arktis und der Tiefsee.

Das Recycling von Kunststoffen ist daher zu einem schnell wachsenden Forschungsfeld in der Polymerwissenschaft geworden und umfasst die Wiederverwertung von Abfällen, thermische Nutzung durch Verbrennung sowie Deponierung, wobei die Eigenschaften des Polymers selbst eine Rolle spielen. Statt sich nur auf das Recycling am Ende der Lebensdauer zu fokussieren, ist es eine wichtige Aufgabe, Materialien von Anfang an so zu gestalten, dass sie recycelbar sind. Neben der Reduktion des Verbrauchs an Ausgangsmaterialien ist die Integration eines geschlossenen Kohlenstoffkreislaufs in Kunststoffmaterialien eine der vielversprechendsten Lösungen, um Nachhaltigkeit zu erreichen. Dies ist besonders wichtig im Zusammenhang mit der Verbindung zwischen der „Kunststoff-“ und der „Klimakrise“. Aufgrund der hohen Vielseitigkeit und vorteilhaften Eigenschaften von Kunststoffen ist es an der Zeit, neue nachhaltige Lösungen für das *end-of-life*-Management zu entwickeln, um zu verhindern, dass das „Zeitalter des Plastiks“ zur Dinosauriergeschichte zukünftiger Generationen wird; als eine Reflexion unseres wissenschaftlichen und politischen Fortschritts. Mögliche Ansätze umfassen die Nutzung biobasierter Rohstoffe, die Gestaltung für Recyclingfähigkeit sowie die Durchführung von *end-of-life*-Analysen für hergestellte Materialien. Der Einsatz kovalent adaptiver Chemie kann die Wiederaufarbeitung und Recyclingfähigkeit von Hochleistungsmaterialien wie Polymeren und Verbundwerkstoffen ermöglichen.

Der Hauptteil dieser Arbeit besteht aus dem Entwurf, der Synthese und der Charakterisierung neuer Polymermaterialien mit dynamischen kovalenten Bindungen. In drei Veröffentlichungen und den unveröffentlichten Ergebnissen werden Einflüsse der Bausteine, der chemischen Reaktivität und des Netzwerksdesigns diskutiert.

Die entwickelten kovalent adaptiven Netzwerke zeigen eine Gruppe von thermoreversibel vernetzten Materialien, die umgeformt, neu verarbeitet werden können und somit die Fähigkeit besitzen, recyclebar zu sein aufgrund ihres Designs. Durch die Verwendung biobasierter Rohstoffe, umweltfreundlicher synthetischer Verfahren und die Beachtung der Prinzipien der Grünen Chemie ebnet die vorliegende Arbeit den Weg zu nachhaltigeren Netzwerken und Verbundwerkstoffen.

In der ersten Publikation wurde Vanillin als biobasierter Vorläufer verwendet, der aus Lignin gewonnen wird – einem Bestandteil lignocelluloser Biomasse, der viele funktionelle Gruppen enthält, die für chemische Modifikationen geeignet sind. Durch die Gestaltung bifunktioneller Aldehydbausteine wurden Schiff Basen Vitrimere hergestellt, wobei weniger toxische Amine als Vernetzungsmittel eingesetzt wurden. Neben ihren thermomechanischen Eigenschaften stand die Untersuchung der Austauschchemie im Mittelpunkt dieser Arbeit. Durch die sorgfältige Anpassung der Anzahl freier Amine im Netzwerk kann die Rate der Netzwerkumstrukturierung gesteuert werden. Bei Überschuss an Aminen kann Transiminierung auftreten, während bei keinen freien Aminen die Iminmetathese der vorherrschende Austauschmechanismus ist. Da Imine anfällig für Hydrolyse sind, wurde eine saure Hydrolyse als effektive Methode zur chemischen Wiederverwertung der Ausgangsmoleküle genutzt. Daher können diese Vitrimere sowohl assoziative als auch dissoziative Austauschmechanismen über die Vermittlung kleiner Moleküle durchführen und fungieren somit auch als dissoziatives kovalent adaptives Netzwerk.

Die zweite Publikation behandelt die Entwicklung von vinylogen Urethanvitrimeren aus lignocelluloser Biomasse. Lignin ist eines der am häufigsten vorkommenden Biopolymere und weist eine hohe Menge an funktionellen Gruppen auf. Lignin wird als Nebenprodukt der Zellstoffindustrie produziert und zumeist als minderwertiger Abfall betrachtet. Typischerweise wird diese Ressource thermisch durch Verbrennung genutzt. Durch einfache Modifikation der freien Hydroxygruppen der Ligninmolekülen können sie in Vitrimere umgewandelt werden, wenn sie z.B. mit (biobasierten) Aminen reagieren. Lignosulfonat ist eine unreine Ligninquelle, die als Abfallprodukt aus dem Sulfit-Prozess gewonnen wird. Die hohe Polarität der Partikel macht sie wasserlöslich, was einen umweltfreundlicheren Syntheseweg ermöglicht. Zusätzlich wurde enzymatisch gewonnenes Lignin charakterisiert und in Ligninvitrimere umgewandelt. Die mechanischen Eigenschaften wurden untersucht, wobei besonderes Augenmerk auf den Glasübergang und die Transaminierungsreaktion bei erhöhten Temperaturen gelegt wurde. Es wurde beobachtet, dass die Beweglichkeit der Segmente die Berechnung der Aktivierungsenergie erheblich beeinflussen kann und daher für industrielle Anwendungen berücksichtigt werden muss. Dies wurde durch Spritzgießen mit Vitrimerpulver nachgewiesen, bei dem die Materialfilme in Prüfkörper umgewandelt wurden. Die resultierenden Werkstoffe zeigen hohe mechanische Festigkeit und Reprozessierbarkeit.

Die dritte Veröffentlichung präsentiert ein noch industrietauglicheres Vitrimerkonzept, dass auf der Dioxaborolanmetathesechemie basiert. Diese kann mit geringem Energieaufwand aktiviert werden und ermöglicht die Wiederverarbeitbarkeit vernetzter tetrafunktionaler Acrylate mindestens 20 Mal.

Die mechanischen Eigenschaften wurden nach verschiedenen Reprozessierungsschritten untersucht und verglichen, wobei nur minimale Auswirkungen auf die mechanische Leistung festgestellt wurden. Interessanterweise wurde festgestellt, dass die thermische Vorgeschichte das Spannungsrelaxationsverhalten erheblich beeinflusst, was mittels gestreckter exponentieller Fits bewertet werden konnte. Die verbleibenden inneren Spannungen können durch eine thermische Behandlung abgebaut werden, was die Bedeutung der Berücksichtigung der thermischen Vorgeschichte vor der Interpretation der Spannungsrelaxationsdaten unterstreicht. Dies ist besonders wichtig beim Vergleich verschiedener Materialien. Als potenzielle Anwendung wurde die Einbindung von Titandioxid-Nanoplättchen demonstriert. Im Rahmen des Sonderforschungsbereichs SFB986 – Multiskalenmaterialien, wurde so eine neue Strategie zur Herstellung hochgefüllter Nanokomposite vorgestellt, die die Bildung homogener hierarchischer Nanokomposite ermöglicht.

Die Ergebnisse aus den Veröffentlichungen wurden auch in den unveröffentlichten Ergebnissen weiter untersucht. Es wurde ein interpenetrierendes kovalentes adaptives Netzwerk durch einen reaktiven, gleichzeitigen Prozess unter Verwendung von vinylogen Urethanen und Dioxaborolanen gebildet. Zusätzlich wurden Vitrimer-Epoxid-Co-Netzwerke hergestellt, um die Leistungsfähigkeit von vinylogen Urethanvitrimeren durch die Hinzufügung permanenter kovalenter Bindungen zu verbessern.

Insgesamt erweitert diese Arbeit den Stand der Technik bei funktionalen thermoreversiblen Netzwerken, bietet neue Einblicke in die Spannungsrelaxation und das Netzwerkdesign. Die Materialien und ihre Eigenschaften verbessern die Recycelbarkeit von vornherein und legen die Grundlage für zukünftige Materialien.

3 Introduction

The extensive use of synthetic polymers has led to a significant increase in production and research in macromolecular chemistry.[1] These materials can be tailored to suit their desired field of application and possess a variety of special features, for example, design versatility, low cost, formability, light weight, and bio-inertness, which have made them the material of choice in a broad range of applications.[2] Polymers are used everywhere in the modern world. For example, they are utilized in industrial machinery, building and construction, medicine, transportation, electronics, commodity items, textiles, packaging, adhesives, and many other applications.[3] With petroleum as a fossil-based resource, the production of low-cost plastics has rapidly grown since the 1950s, when production was at two million tons. Each year, the production of plastic increases, reaching a value of over 413 million tons in 2023, and is expected to further rise to 1.480 million tons by 2050.[4,5] Polymers are now used more than metals, both in terms of volume and weight. The high level of specialization means that, unfortunately, there are no practical natural alternatives for many synthetic polymers used in today's society. When total energy costs are compared covering raw materials, manufacturing, and shipping, polymeric items often outperform traditional options, such as glass versus plastic beverage bottles. However, their end-of-life remains difficult because they usually do not align with natural material life cycles. As a result, one of the challenges in polymer and materials science is developing suitable methods for recycling or finding effective strategies to improve the degradation of disposable artificial materials.[6,7]

Plastic consumption has led to greater convenience worldwide, but its rapid growth and misuse have caused significant societal, ecological, and waste problems, turning our era into the age of the "plastic crisis".[8] In 2019, 353 million tons of plastic waste were generated worldwide, with approximately half of it being single-use plastics.[9,10] Until 2017, only 7% of the plastic produced since the 1950s has been recycled. Most plastic waste ends up in landfills or incinerators, causing environmental issues and exacerbating the climate change crisis.[4] Figure 1 shows the life cycles of plastics made since the 1950s.

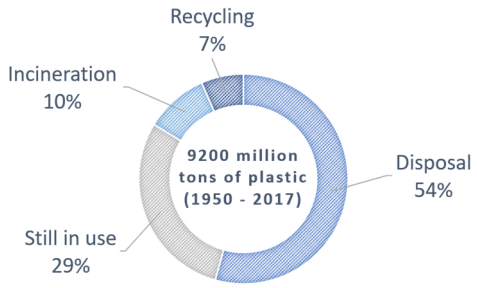

Figure 1: A glance at the waste management of plastics made since the 1950s shows that more than half of the waste disposal takes place in open dumps and landfills (54%). This is followed by incineration (10%) and recycling (7%). Approximately one-third are still in use (29%). It is essential to note that the production of recycled plastics also generates a waste stream.[4]

A significant amount of research focuses on the issues of plastic pollution.[11] To manage plastic waste effectively, closing the carbon loop is essential. This can be achieved through plastic reuse, mechanical and molecular recycling, carbon capture, and the adoption of bio-based building materials blocks.[12,13] The integration of reuse and recycling and their potential for waste prevention and eco-efficiency into building blocks needs to be exploited.[14] Thermosetting materials, in particular, pose a challenge to the circular economy due to their fixed molecular structural makeup.[15]

Dynamic covalent chemistry enables the development of thermally (re)processable and recyclable polymer networks, offering great potential for future generations of thermosetting materials.[16] The combination of dynamic covalent polymer networks with reprocessing technologies, along with a focus on sustainable chemical processes that follow green chemistry principles and utilize new bio-based building blocks, has significant potential to become a central focus in future plastics research.[17-19]

3.1 Introducing Recyclability by Design

The concept of inherent recyclability led to a rethinking of product and material design, shifting from a top-down approach to a bottom-up strategy where the potential for recycling is already integrated into the design of the building blocks used to create a product.[20] In polymer chemistry, a polymer can be engineered to achieve the optimal solution for a particular application. Nowadays, researchers, manufacturers, and waste managers are looking for ways to enhance the value of the materials, in addition to achieving the desired properties.[21] Therefore, when designing a specific building block, its end-of-life should be considered, and options for recycling or reprocessing should be included (recyclability by design). The combination of polymer networks with dynamic covalent chemistry (DCC) enables molecular network rearrangement reactions "on demand," allowing for precise control over material properties and their end-of-life management.[22,23]

3.1.1 Classical Polymer Chemistry and Dynamic Polymer Chemistry

The classical theory of polymers involves distinguishable classes of polymers, based on their response to temperature or solvent.[24] A thermoplastic polymer consists of linear or branched polymer chains. These thermoplastics can undergo melting upon an energy stimulus, such as heat, during which the chains can diffuse. Their melting behavior enables viscoelastic flow above their melting temperature T_m (in the case of semi-crystalline polymers) or glass transition temperature T_g (in the case of amorphous polymers), which solidifies again, allowing for polymeric manufacturing techniques such as injection molding or extrusion. Typical commercial examples include polyethylene, polypropylene, poly(vinyl chloride), and poly(ethylene terephthalate). Although most commercial thermoplastics consist of linear chains, there are many other topological possibilities, such as branched, bottle-brush, dendritic, and cyclic structures.[16]

Thermosetting polymers, on the other hand, are unable to flow when heated. Nevertheless, their inner structure softens if the T_g is reached. They offer deformation resistance without segmental motions, and chain diffusion is hindered due to the interconnection of the cross-linked structure throughout the whole sample. Above their T_g, they behave like viscoelastic solids, show no terminal flow, and exhibit elastic responses to deformations. In good solvents, only a limited fraction (sol) of the material can eventually dissolve, while the interconnected structure (gel) will swell in a good solvent. Therefore, a thermoset can be better defined as a polymer network cross-linked by chemical bonds that permeates the entire mass.[15]

An expansive research effort over the past 20 years has challenged the reprocessing of cross-linked materials while retaining the compelling features of conventional thermosets.[25] The core idea of most strategies is to utilize reversible bonds to form a cross-linked network, resulting in a dynamic polymer network.[16] Dynamic polymer networks can be divided into two subgroups, namely non-covalent and covalent reversible cross-links, depending on the nature of the bonds, as shown in Figure 2.

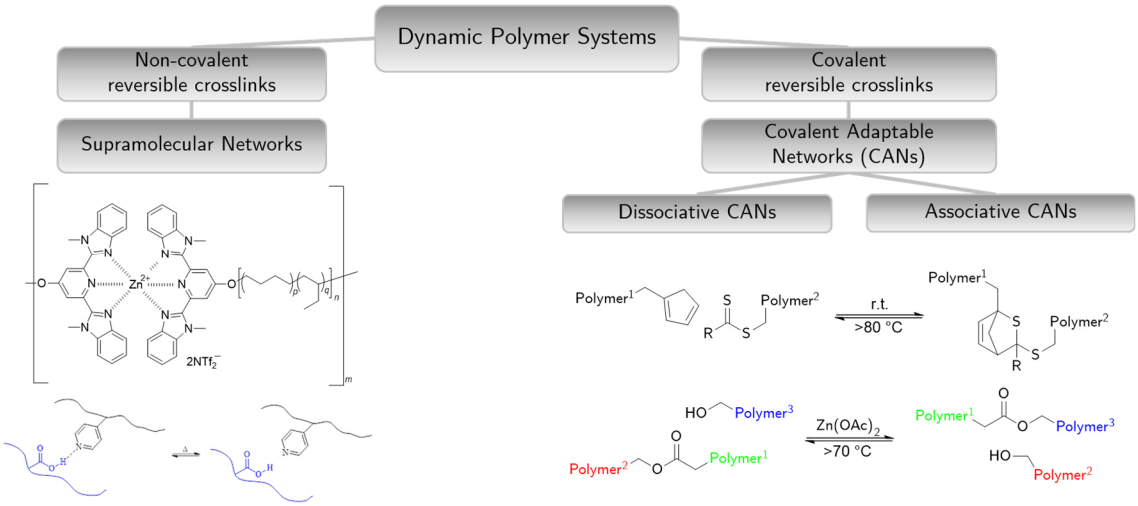

Figure 2: Diagram showing the classification of dynamic polymer systems into two main groups: non-covalent bond-based dynamic networks and covalent bond-based dynamic polymer networks, based on the nature of their reversible bonds.[26-29]

On the one hand, non-covalent dynamic crosslinks open up the subgroup of so-called supramolecular networks. Numerous non-covalent cross-linked materials based on hydrogen-bonding, metal coordination, and π-π stacking have been reported.[30-32] These interactions typically display strongly temperature-dependent association constants and high exchange rates, which are not resistant to creep above their critical gelation temperature (CGT).[33-35] On the other hand, polymer networks that feature reversible covalent bonds are defined as dynamic covalent polymers. Owing to the increased lifetime of the covalent bonds, these materials exhibit improved physical properties. Dynamic covalent polymers are macromolecules that are held together by dynamic covalent bonds that reversibly form and break under thermodynamic control.[36,37]

These reversible reactions of covalent adaptable networks (CANs) can proceed *via* different molecular network rearrangement (MNR) pathways, namely dissociative with a loss of network integrity during the rearrangement and associative with maintained network integrity also during the MNR.[38]

In 2004, Lehn *et al*. noted that dynamic covalent polymers and non-covalent polymers are closely linked, as in both types, polymerized units can interchange with one another.[39] Hence, he introduced the term “dynamers”, meaning both the polymers that are dynamic by nature (supramolecular) and by design (molecular). Dynamers are adaptive because they react to external stimuli that alter the equilibria of the bonds holding their components together. As a result, these materials can rearrange their constitutional structures.[40] The use of the word "dynamic" in the context of a dynamic covalent bond, therefore, indicates that a bond is reversible, and under appropriate conditions (*e.g.*, within a specific temperature range or with the addition of a catalyst), has sufficiently fast kinetics to reach thermodynamic equilibrium on a short timescale.[41] However, there is no exact cutoff for how fast the kinetics must be for a reversible bond to qualify as dynamic. This designation not only depends on the surrounding system of interest, but also on the targeted applications and the processing and usage conditions.

The distinction between thermoplastics and thermosets was challenged by dynamic polymer networks, designed as vitrimers, by Leibler *et al*.[29] These polymers, behaving like *vitreous* glass, can interchange bonds above a temperature T_v (vitrimer freezing temperature, located above their T_g). Below T_v, vitrimers are considered as covalently cross-linked networks without dynamics. Above T_v, vitrimers offer a dynamic covalent chemistry, which allows creeping and the relaxation of internal stress. This behavior enables them to be recycled, self-healed, or reshaped, bringing exciting opportunities in the field of recyclability by design.[15,42]

In Figure 3, the benefits of combining the desired properties of classic thermosets and thermoplastics, including mechanical strength, chemical resistance, thermomechanical resistance, recyclability, and stimuli responsiveness, are displayed for CANs.[38,43]

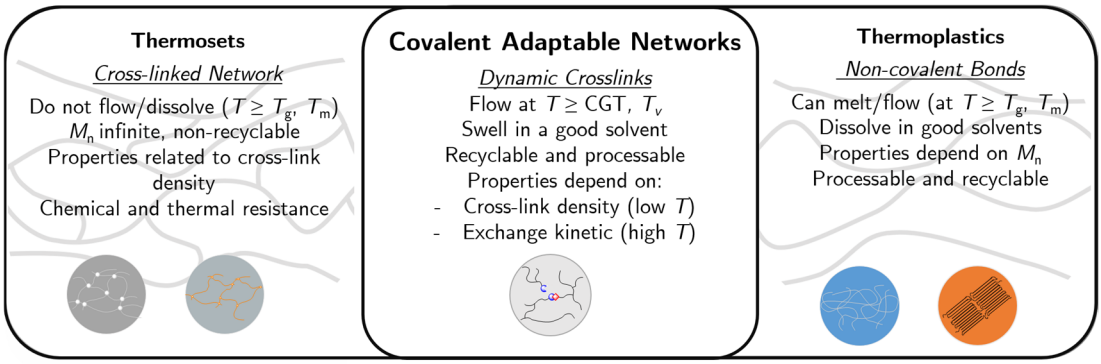

Figure 3: Representative schematic illustration of key properties in dynamic polymer networks. This class combines the mechanical strength, chemical and thermomechanical resistance characteristic of traditional thermosets with the recyclability and stimuli-responsive behavior typical of thermoplastics.[38,43]

3.2 Covalent Adaptable Networks

The combination of the desirable attributes of conventional thermosets with the dynamics of controllably reversible bond structures can be achieved in the form of CANs.[44] Although more widely adopted recently, CANs with dynamically bonded structures have historically been used for decades.[45,46] In the 1940s, Green and Tobolsky found that disulfides, existing in rubbers with disulfide bridges, are in fact at equilibrium, breaking and reforming, enabling non-degradative bond rearrangement or "permanent set" and have a relaxing nature.[47] More broadly, all bimolecular reactions are inherently reversible to some degree, as governed by the temperature dependence of the equilibrium constant. However, most reactions are effectively irreversible due to temperature limits that prevent them from serving as building blocks for CANs. These limits encompass a practical temperature range, potential side reactions at high temperatures, and the temperatures at which chemicals decompose. High-temperature stability is crucial for many thermosetting applications, ensuring the overall material performs optimally. Furthermore, the kinetics of the forward and reverse reactions (the reaction rates) must allow for MNR on an application-appropriate timescale, such that the network can adapt to an environmental stimulus without ruptures in the network structure. Therefore, both thermodynamic and kinetic elements of a given thermoreversible reaction must be considered, along with the application and time scale of the MNR.[41,48] The combination of networks with DCC is broadly enabling dimensional stability during use, self-healing, shape-recovery, stress-reduction, and recycling or reprocessing of polymer networks.[44,49]

3.2.1 Dissociative Covalent Adaptable Networks

A dissociative CAN relies on an equilibrium-governed dissociative stepwise MNR pathway, where an existing bond is broken before a new bond is formed (Figure 4). This resembles an S_N1 reaction with a high-energy intermediate of unbound, reactive chain fragments and topological changes, resulting in fluctuations in overall connectivity. The network connectivity of a dissociative material is instantaneously reduced in the unbound transition state. Under the application of a trigger (*e.g.*, through the application of thermal energy), the material can undergo a gel-sol transition, as the equilibrium shifts to the unbound state. For a dissociative stepwise MNR, no association of two polymer chain segments is required, as a polymer chain can undergo fragmentation independently. Dissociative networks exhibit similar traits to networks formed by supramolecular interactions. Specifically, the free energy (ΔG) of exchange balances the opposing entropic and enthalpic driving forces, with the entropic factor favoring debonding, and the enthalpic factor benefits of bonding overcoming this entropic penalty.[48] Heat can cause a reversible dissociative dynamic network to lose connectivity and promote viscoelastic flow. Similarly, adding solvent can cause a loss of connectivity and may lead to complete dissolution after significant bond loss in the network.[50]

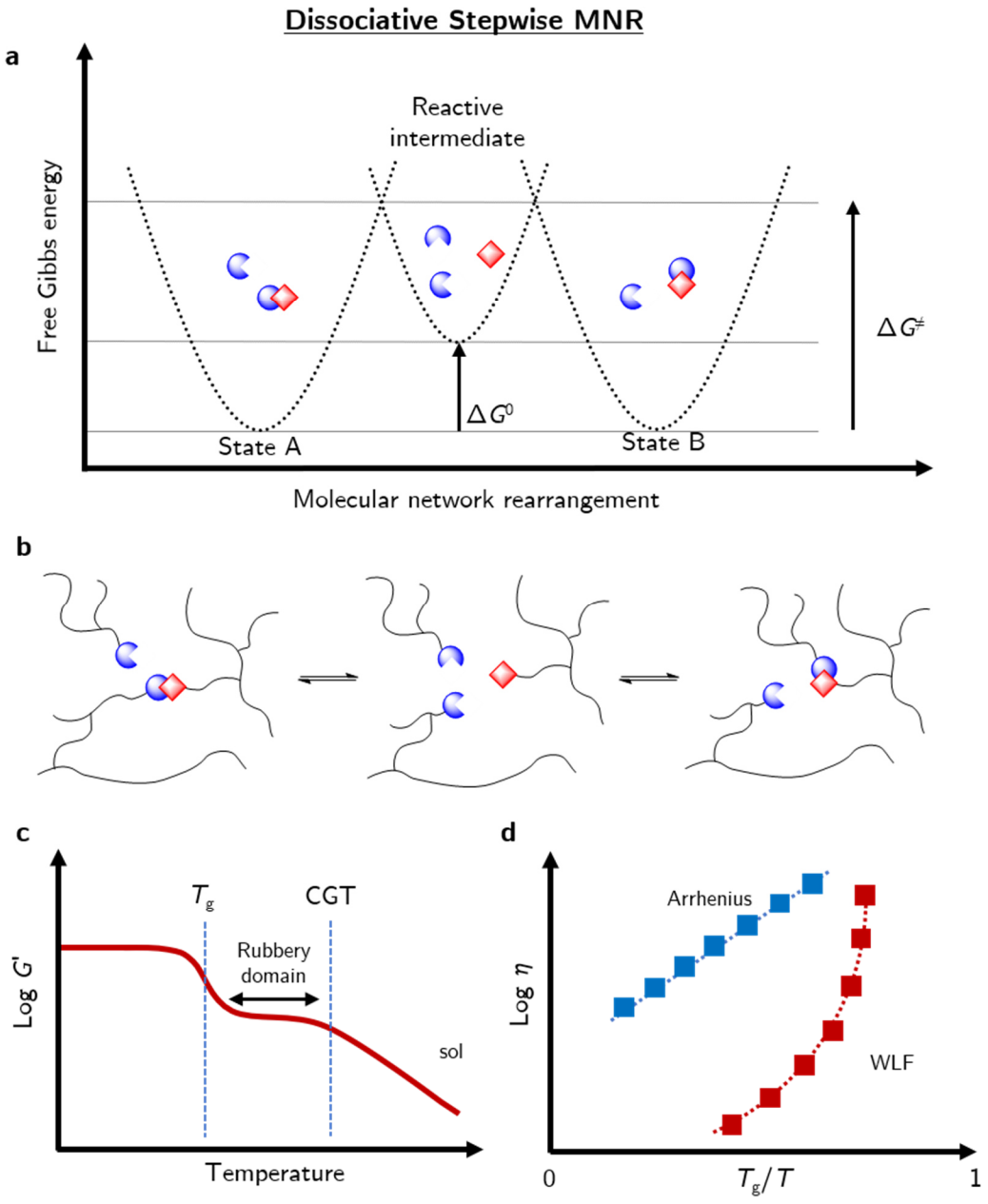

Figure 4: Overview of the characteristics of a dissociative stepwise MNR. (a) Energy profile showing a dissociative, stepwise MNR. (b) Illustration of a dissociative CAN through a less cross-linked intermediate state. (c) Exemplary temperature behavior of a dissociative CAN, showing a rubbery plateau above its T_g during standard operating temperatures before reaching a critical gelation temperature (CTG), which causes a sol-gel transition. (d) The viscosity of a dissociative CAN can show Arrhenius behavior. Still, it has also been reported that some dissociative CANs show sudden changes consistent with the Williams-Landel-Ferry (WLF) law.[48,50]

Reforming a cross-link can occur in a second step that involves another polymer chain, leading to the overall dissociative, stepwise MNR reaction. In dynamic mechanical thermal analysis (DMTA), dissociative networks can exhibit behavior similar to a rubbery plateau at standard operating temperatures that exceed their T_g, before eventually reaching the CGT, which leads to a gel-sol transition.

The viscosity of a dissociative CAN can follow Arrhenius behavior. However, it has also been suggested that specific dissociative networks may undergo sudden changes in their temperature-dependent viscosity once a critical temperature for bond formation or scission is reached, aligning with the WLF law.[48] In Figure 5, selected examples of dissociative CANs are shown.

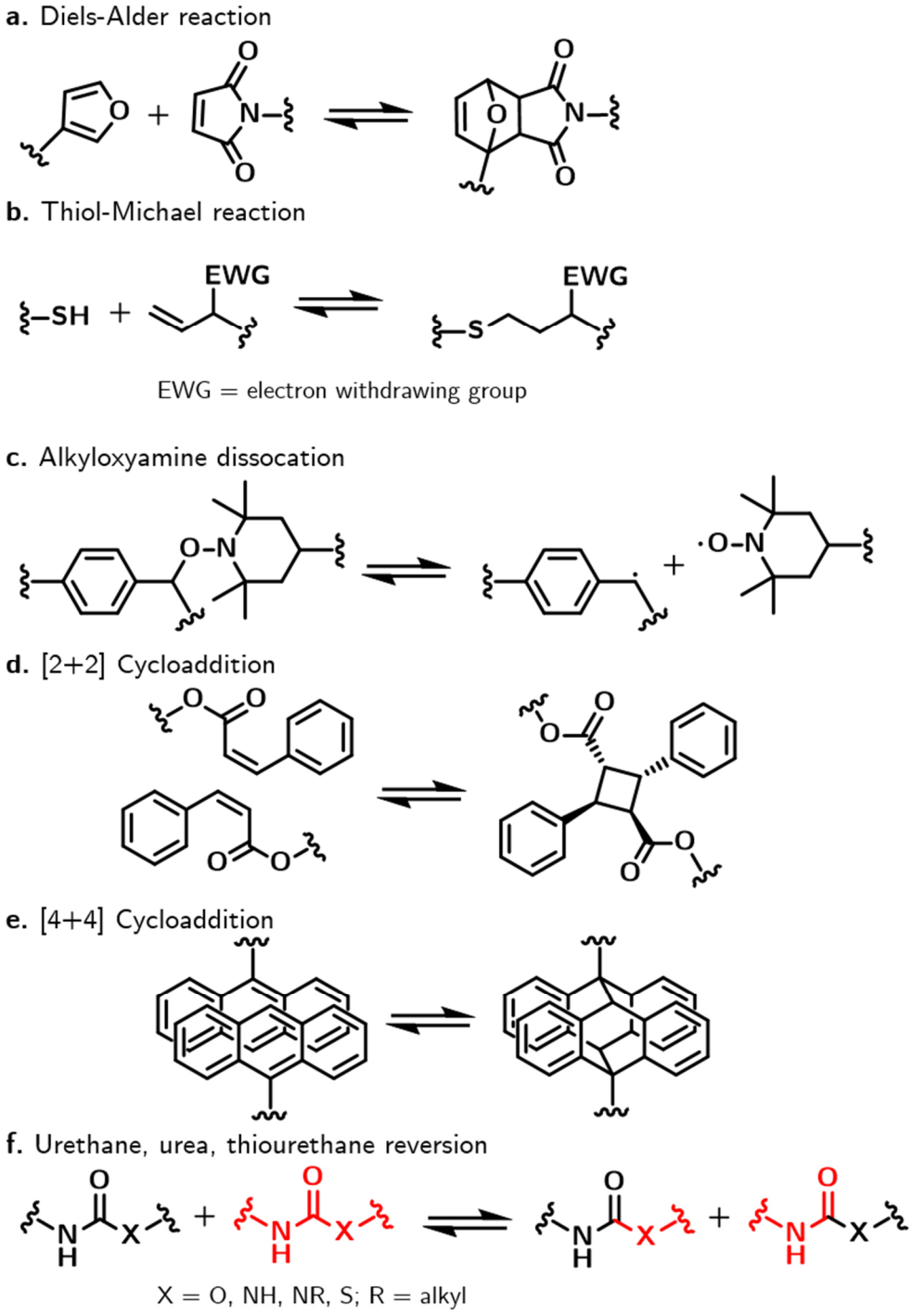

Figure 5: Reaction schemes of dissociative CAN exchange mechanisms. (a) Diels-Alder, (b) thiol-Michael reaction, (c) alkyloxyamine dissociation, (d) [2+2] CA, (e) [4+4] CA, (f) urethane, urea, and thiourethane reversion.[51-61]

The most common reaction associated with dissociative CANs is the catalyst-free thermoreversible Diels-Alder (DA) reaction, in which a diene and an ene compound form a DA adduct, often realized by using furan and maleimide groups.[51,52] A typical formation is achieved at 60 °C, whereas the retro-DA reaction becomes significant at temperatures of 110 – 150 °C.[53,54] In Thiol-Michael (TM) reaction systems, a Michael reaction is employed to form the network, which can subsequently be dissociated *via* a retro-Michael reaction above 90 °C.[55] However, the TM requires catalysts such as bases and nucleophiles, making it susceptible to rearrangement through temperature changes or alterations in the pH value.[56,57] Alkyloxy-amine-based materials have long been known in nitroxide-mediated polymerizations (NMPs) and are employed in dynamic vinyl polymers. The homolytic cleavage of the C-N bond results in reactive transient carbon-centered radicals and stable nitroxide radicals, which reversibly recombine to alkoxyamines by lowering the threshold dissociation temperature.[58] These systems are typically stable below 60 °C and become reversible at 100 °C. However, this thermoreversible reaction is relatively slow, taking up to 24 hours for self-healing.[59] Typical examples for light-driven reversible dissociative mechanisms are cycloadditions (CAs). The [2+2] CA of coumarin derivatives proceeds at room temperature and can be precisely triggered by UV-light using wavelength-gated DCC. A wavelength $\lambda > 260$ nm triggers the bond formation of cinnamate and coumarin derivatives, whereas irradiation with $\lambda < 260$ nm triggers the reverse reaction.[60] The [4+4] CA system of anthracene derivatives can be activated with $\lambda > 300$ nm for bond formation and $\lambda < 300$ nm for dissociation, and can also be initiated by temperature.[62] Due to their thermodynamic characteristics, urethane thermosets were initially perceived as impractical for applications in CANs. However, Brutman *et al*. demonstrated that the stress-relaxation of urethane networks occurs through urethane reversion, facilitated by the rapid formation of highly reactive isocyanates, which are readily consumed at 100 – 190 °C with stannous octoate as a catalyst.[61]

Another specific dissociative stepwise MNR pathway occurs through the mediation of a reactive small molecule. For example, polymer chains are reversibly cross-linked *via* a condensation reaction, joining two chain fragments by releasing a small molecule (*e.g.*, water). As long as this molecule remains within the polymer matrix, the cross-links stay reversible through a dissociated intermediate state. All bond cleavage events depend strictly on the presence of a small molecule polymer additive. An association of the polymer chains is not necessary; instead, a crosslink and a (more mobile) small molecule additive must first associate before a chain can split into two new reactive ends. If only a catalytic amount of the transfer group is present, the network cannot undergo extensive depolymerization. It will mostly stay intact, although it can rearrange its structure through the intermediacy of decross-linked chain ends. It is important to note that this process is inherent to nearly all associative MNR systems, as a low-molecular-weight, monofunctional additive exhibits the same reactivity as a dynamic link, creating potential pathways for side reactions and network defects.[50] The small molecule-mediated dissociative stepwise MNR is illustrated in Figure 6.

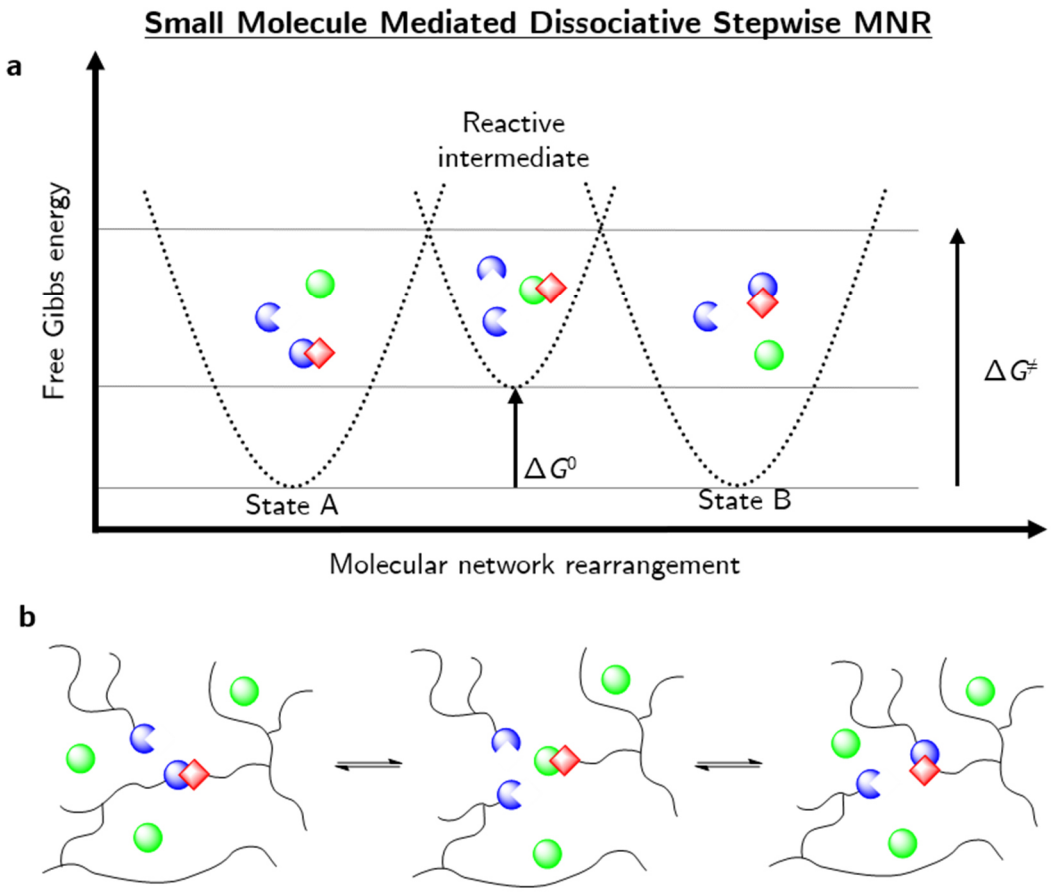

Figure 6: Overview of the features of a small molecule-mediated dissociative stepwise MNR. (a) Energy profile illustrating a small molecule-mediated dissociative stepwise MNR. (b) Illustration of a dissociative CAN that undergoes exchanges facilitated by small molecules (green) through a less cross-linked intermediate state.[50]

In Figure 7, small molecule-mediated dissociative stepwise MNRs are shown, with selected examples of these processes. Hydrogels, cross-linked by borax-derived boric esters, exhibit self-healing properties at room temperature and facilitate rapid MNR reactions.[63,64] However, these hydrogels can be susceptible to hydrolysis at higher temperatures. The amount of vicinal *cis*-diols, temperature, and pH value determine the rate of MNR.[65,66] Polyimine and poly(acyl)hydrazine networks have been extensively studied to demonstrate a dissociative, reversible condensation, as they are formed by the condensation of aldehydes or ketones with amines or hydrazides.[39,67] An endothermic hydrolysis can be facilitated by applying thermal energy or by increasing the concentration of water. Polyimine networks can undergo associative exchange reactions under dry conditions, and can be switched to a prevalent dissociative MNR by the addition of water.[68] Transalkylation reactions of amines can be achieved by temporarily de-cross-linking bromine ions, which serve as good nucleophiles. Here, the polyionic networks undergo an S_N2 cleavage at the benzylic position, releasing a highly reactive benzyl bromide intermediate chain end. This can, in turn, react again *via* an S_N2 process with other free amines.[69]

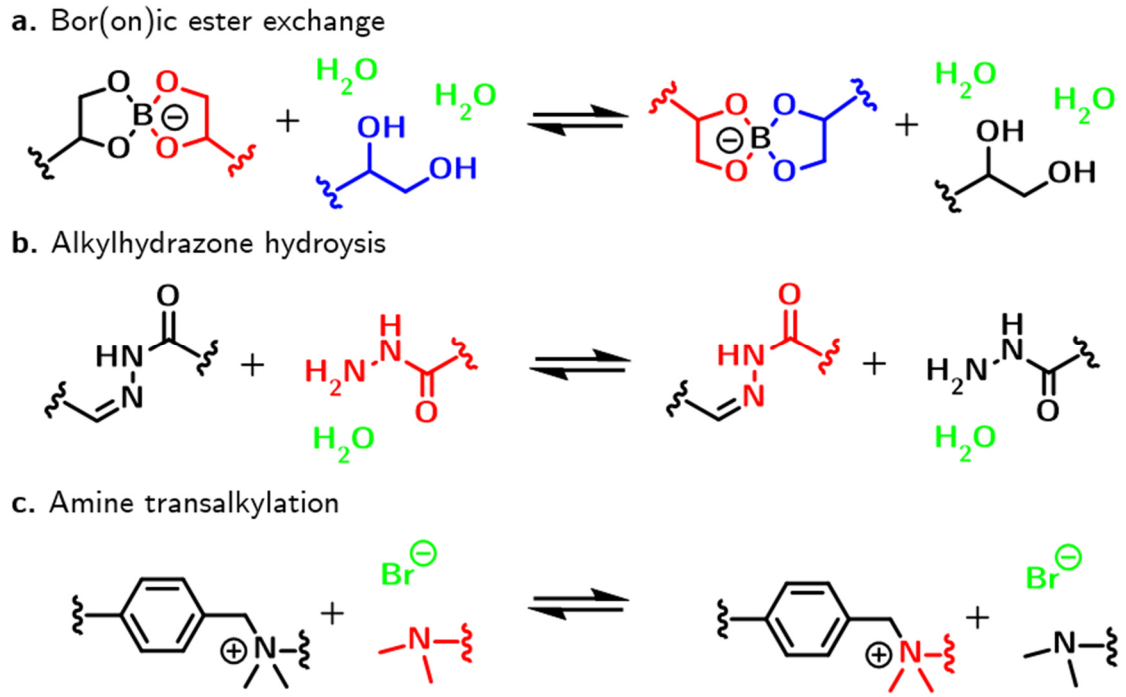

Figure 7: Reaction schemes of small molecule-mediated dissociative CAN exchange mechanisms. (a) Bor(on)ic ester exchange, (b) alkylhydrazone hydrolysis, (c) amine transalkylation.[63-69]

3.2.2 Associative Covalent Adaptable Networks

An associative CAN rearranges *via* a kinetically controlled associative stepwise mechanism, characterized by the formation of the new bond before bond rupture, similar to an S_N2 reaction (Figure 8). This mechanism enables the network topology to rearrange without decreasing network connectivity, except for an instantaneous increase in connectivity during the intermediate (higher energy) state.

In principle, the associative networks could dissolve in a non-reactive solvent through the formation of loops that disrupt network connectivity. The rearrangement pathway includes the prior association of two polymer chains, resulting in a new covalent bond, followed by an elimination step that fragments another network bond. This situation does not meet the ideal requirements for the topology and connectivity fluctuations of vitrimer materials, as the overall connectivity can increase upon a thermal stimulus, allowing the equilibrium to shift to the endothermic side. In practice, however, this effect is often negligible, resulting in a practically constant cross-link density under a wide range of conditions.[50] Significantly, bond exchange in an associative network conditionally depends on the availability of a nearby reactive group, in contrast to dissociative networks, and can be activated by thermal energy, pH value, or light. The mechanical properties of associative CANs are temperature-dependent, as measured in DMTA. Above the T_g, associative networks exhibit a rubbery plateau, as observed for elastomeric materials. In contrast, the viscosity exhibits an Arrhenius behavior as a function of inverse temperature.[48]

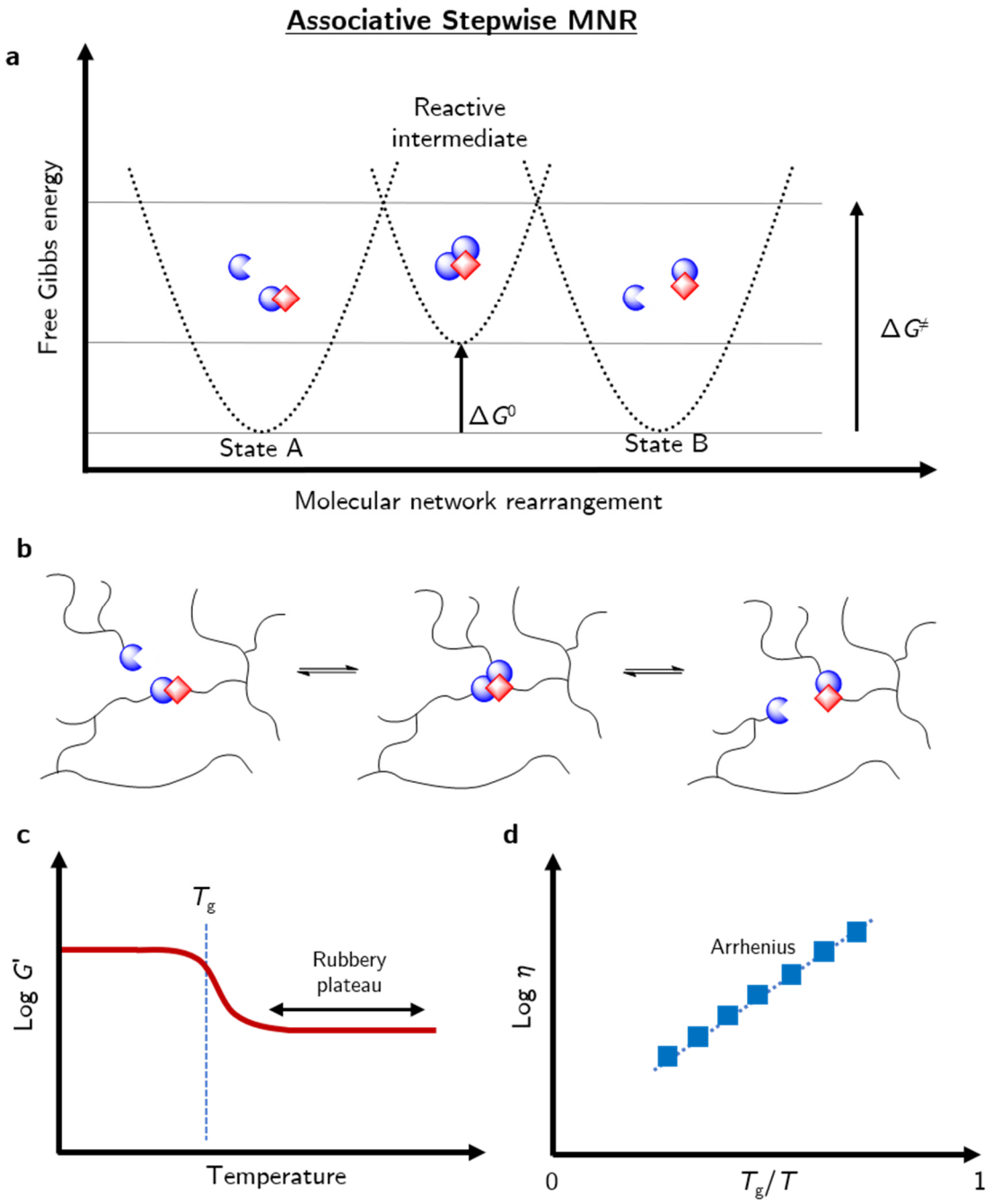

Figure 8: Overview of the characteristics of an associative stepwise MNR. (a) Energy profile showing an associative stepwise MNR. (b) Illustration of an associative CAN through a higher cross-linked intermediate state. (c) Exemplary temperature behavior of an associative CAN, showing a rubbery plateau above its T_g during standard operating temperatures. (d) The viscosity of an associative CAN shows Arrhenius behavior, analogous to that of vitreous glasses.[48,50]

In 2011, Leibler *et al.* introduced an associative bond exchange reaction into a polymer network. The first so-called "vitrimer" material was designed using an epoxy-based polyester resin that includes free hydroxy groups in the polymer backbone (Figure 9).[29]

Together with a suitable Lewis acid or base catalyst, the dynamic interaction between the ester and hydroxyl linkages occurs in an efficient addition-elimination pathway.[70] The polymer network is swellable but completely insoluble in good solvents even at high temperatures. Moreover, the material exhibits complete stress-relaxation and remoldability mediated by the DCC.[71] Without undergoing side reactions, the material cannot show a sol-gel transition in the DMTA, as the overall cross-link density is constant at every temperature. The temperature dependence of the viscosity and the chemical reaction rate is in good agreement, showing a connection between the dynamics of viscoelastic flow and chemical dynamics.[50]

Analogous to transesterification, thiol-thioester exchange was observed in elastomeric thiol-ene networks at ambient temperatures under the use of light-generated catalyst bases. The transition between a viscoelastic solid and a viscoelastic fluid state can be enabled by light irradiation, leading to the generation or consumption of the catalyst and, consequently, a rapid associative bond rearrangement even below the T_g.[72] Thermoreversible urea-amine exchange can occur as low as 37 °C and is typically used above 100 °C. Catalysts are bases or free amines.[73] Both transcarbomylation and transcarbonation normally proceed at 150 – 180 °C in minutes to hours, accompanied by stannous organo-catalysts. The rate is dependent on hydroxyl group concentration, and the associative MNR can be initiated by temperature.[74,75] Enamine-ones derived from amines and β-ketoesters were introduced in 2015 as a catalyst-free platform.[76,77] The formed vinylogous urethane (VU) exhibits a vinylic bond inserted between the electron-donating nitrogen and the electron-withdrawing ester moiety. Based on this electronic effect, the VU is a thermodynamically stable bond, similar to classical isocyanate-derived urethane cross-links. However, in contrast to urethanes, they do not undergo (catalyzed) addition-fragmentation reactions due to their weak electrophilic properties. Although VUs are more reactive due to their Michael-type reactivity of the α,β-unsaturated carbonyl moiety, they are resistant against hydrolysis, as amines and β-ketoesters spontaneously undergo a condensation reaction to form the enaminone, even in aqueous media.[78] Another classical associative stepwise MNR pathway is observed in siloxanes with hydroxyl groups. These high T_g networks undergo rapid addition-elimination reactions of the silyloxy groups to the silyl ether linkages. Catalysts include acids or bases, *e.g.*, sodium octanoate, to produce silanols.[79,80]

Photochemically activated bond exchange can also be employed for associative stepwise MNRs, using photoinduced radical addition fragmentation chain transfer (AFT) reactions resulting in plasticity and a certain stress-relaxation.[81] As they are chain mechanisms, their overall rate depends on the concentration of free radicals and on the relative rates of many competing processes (*e.g.*, initiation and termination rates).[82] These radical addition and fragmentation reactions often proceed without barriers, operating at the diffusion limit with no real activation energy.[83] Since they do not require thermal triggers, they offer an interesting, yet different chemical platform in the class of associative CANs.[84]

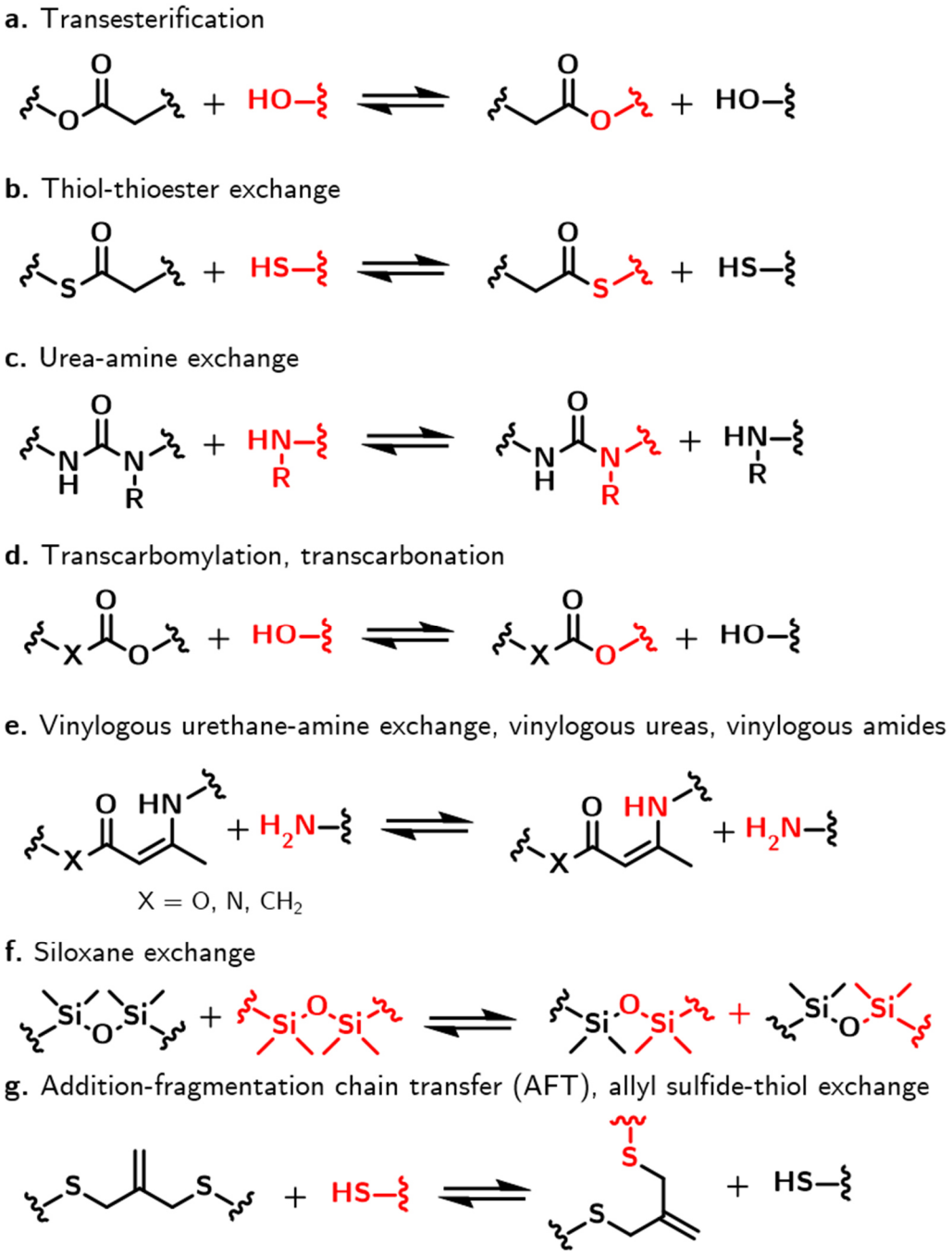

Figure 9: Reaction schemes of associative CAN exchange mechanisms. (a) Transesterification, (b) thiol-thioester exchange, (c) urea-amine exchange, (d) transcarbomylation, transcarbonation, (e) vinylogous urethane-amine exchange, vinylogous urea, vinylogous amides, (f) siloxane exchange, (g) allyl sulfide-thiol exchange.[72-84]

3.2.3 Viscoelastic Properties of Vitrimers

The viscoelastic properties of an amorphous vitrimer are described by two essential transition temperatures: the T_g and the topology freezing temperature T_v. The T_g can be observed in a DMTA measurement, analogous to that of conventional polymers, and describes the transition from a glassy state to a rubbery state due to the onset of segmental motion. Leibler and coworkers introduced the T_v to describe the macroscopic result of topological reshuffling.[29] During the heating of a vitrimer , the kinetics of the associative rearrangement reaction increases, resulting in a decrease in the lifetime of the dynamic bonds and, consequently, macroscopic flow above this crossover temperature. When the timescale of the bond exchange reactions becomes shorter than the timescale of material deformation, the network can rearrange its topology, resulting in flow.[85]

The T_v defines the upper operational temperature and the lower threshold for reprocessing and recycling, thus being an essential factor of consideration for the susceptibility of creep of a particular material.[86,87] Initially, it was determined as the temperature at which the viscosity of the vitrimer reaches 10^{12} Pa s, since it was assumed that above this viscosity, chemical exchanges become negligible. However, since the introduction of vitrimers as a class of polymer materials, the characterization of T_v is a complex and debated issue in neat vitrimers.[88] The current determination standards are based on viscoelastic measurements, such as stress-relaxation measurements, which are biased toward frictional contributions but overlook the dynamic contributions of chemical bond exchange.[89] New analysis techniques include aggregation-induced-emission (AIE) luminogens, atomic force microscope-infrared spectroscopy (AFM-IR), and nuclear magnetic resonance spectroscopy (NMR), providing a more precise understanding of the onset of molecular motion in associative CANs.[86,90]

The T_v is a temperature associated with a specific exchange mechanism and polymer topology, and should not be taken as a comparison for different materials.[85] However, it can be considered a conceptual value, and it is interesting to compare its value to the T_g of a material, to quickly determine which factor will be more critical for polymer chain dynamics: exchange chemistry or intermolecular forces.[85]

The relative arrangement of the T_g and T_v has essential implications for the mechanical behavior of vitrimer materials. Two distinct cases can be distinguished: In the first case, the T_g is lower than T_v (Figure 10).[22] Suppose the vitrimer is heated from a temperature below T_g. In that case, the material undergoes a transition from the glassy state into a rubbery state, since the MNR reaction is so slow that the network structure is essentially fixed. On further heating, the rate of the exchange reaction increases and becomes relevant at temperatures above T_v, transforming the viscoelastic solid into a viscoelastic liquid. As stated above, the flow is primarily controlled by the dynamic network rearrangement kinetics, resulting in the typical Arrhenian viscosity decrease. This behavior, where $T_g < T_v$, is observed in most vitrimer materials. Another behavior is observed when an intrinsically fast exchange reaction is embedded in a rigid polymer matrix with a T_v that is lower than the T_g.[80] Since segmental motion is restricted at temperatures below T_g, no significant exchange reactions can occur, and the network is fixed.

Upon heating above the glass transition temperature, segmental motion is gradually initiated, whereas the exchange reactions are already happening at a rapid rate. In this initial situation, the exchange reaction kinetics are diffusion-controlled, leading to MNRs dominated by segmental motion, resulting in a WLF behavior. Heating further, the exchange kinetics change from a diffusion-controlled regime to one controlled by exchange reactions, which follow the Arrhenius law.[80]

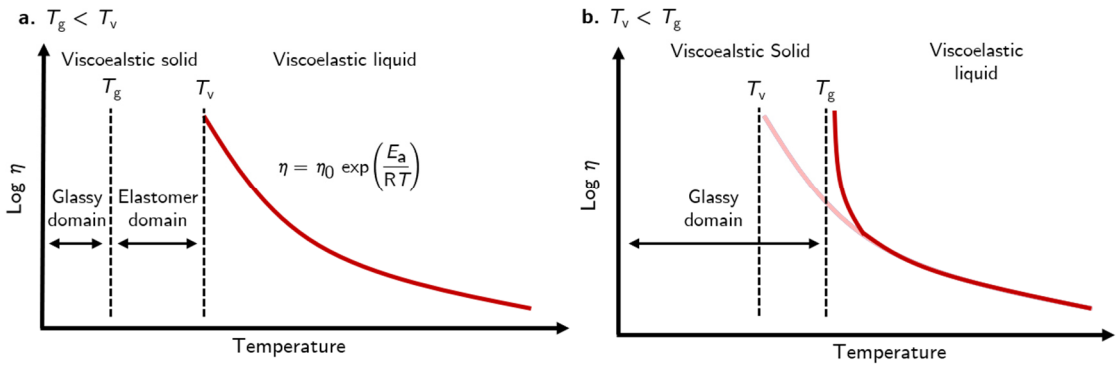

Figure 10: (a) Plot of the viscosity of an amorphous vitrimer in which the T_v is greater than the T_g. (b) Plot of the viscosity of an amorphous vitrimer in which the T_g is greater than the T_v.[16,80]

3.2.4 Stress-Relaxation Theory

Vitrimers relax stress due to their cross-links based on DCC. At temperatures below T_g, the restricted segmental motion of the polymer chains reduces stress-relaxation or can completely prevent it. At temperatures above T_g and T_v, vitrimers relax stress depending on the kinetics of the MNR reaction. Hence, the stress-relaxation times follow the Arrhenius law.

Stress-relaxation can be measured by static rheological measurements, *i.e.*, rheology at a constant strain.[16] In this experimental setup, the dissipation of energy is measured over time in the form of the relaxation modulus $G(t)$. Relaxation times have been estimated by applying the single Maxwell model (Equation 1), which models viscoelastic materials as a combination of an elastic spring and a viscous dashpot in series.[91]

$$\tau(t) = \tau_0 \cdot e^{\frac{E_a}{R \cdot T}} \qquad \text{Equation 1}$$

A single exponential decay then fits the normalized stress-relaxation data. Normalization is performed by the value at $t = 0.1$ s, the first recorded data point at each temperature. The time when the normalized moduli decays to a value of $1/e$ is frequently taken to be the characteristic relaxation time τ. In many cases, this estimation has been found to correspond to values recorded in small molecule studies.[43,78]

However, the manner in which stress is relaxed in dynamic polymer networks is complex, as not only MNR can lead to the relaxation of stress, but also, for example, the reorganization of physical interactions (such as hydrogen bonding and π-π stacking) and ordering (*e.g.*, crystallization and liquid crystallinity) can influence the stress-relaxation behavior.[92] Thus, it was found that the distribution of relaxation times is higher than in systems where stress-relaxation is driven by molecular flow.[93] The stretched-exponential or Kohlrausch-Williams-Watts (KWW) function (Equation 2) is a widely used model for stress or dielectric relaxation in disordered systems.[94-96]

$$G(t) = G_0\, e^{\left(\frac{-t}{\tau_r}\right)^{\beta}} \qquad \text{Equation 2}$$

The parameter β can take values of $0 < \beta \leq 1$, with a single-mode Maxwell model that exhibits exponential decay if $\beta = 1$. For $0 < \beta < 1$, the relaxation modulus G(t) is stretched out with lower values corresponding to a broader distribution of relaxation times. The stretched exponential decay function is superior to fitting a single Maxwell mode and inferring the relaxation time using the $1/e$ criterion.[97] Nevertheless, for small values of β, the terminal relaxation can extend several orders of magnitude beyond the timescale τ, which can lead to incorrectly projecting observations at short timescales onto longer timescales.[98] Equation 3 can calculate the characteristic stress-relaxation time for the KWW function.

$$\langle \tau_r \rangle = \frac{\tau_r\, \Gamma\left(\frac{1}{\beta}\right)}{\beta} \qquad \text{Equation 3}$$

The terminal relaxation of CANs may be challenging to observe due to their sluggish relaxation behavior. Another method to determine the network flow and thus the stress-relaxation of the network is small-amplitude oscillatory shear rheology, which yields shear storage and loss moduli that describe the material's ability to store and dissipate energy, respectively. Unlike permanent networks, CANs display frequency-dependent moduli at temperatures that allow bond exchange. Hence, in a frequency sweep, the crossover frequency τ_{cross} represents the characteristic timescale at which a material transitions from solid-like (oscillations faster than the characteristic timescale for rearrangement) to liquid-like (oscillations slower than that timescale). The temperature dependence of τ_{cross} provides insight into the molecular rearrangements that control viscosity, leading to an Arrhenius relationship and potentially allowing for the determination of the activation energy. However, the timescale of vitrimer systems can be too slow to reveal crossover within an experimentally accessible frequency range.[99]

3.3 Bio-based Vitrimers

Integrating DCC into material design enables reprocessing and reshaping beyond a specific temperature while maintaining the strength and stability characteristics of thermosets below this temperature.[100] These features account for their ease of recycling at the end of their life, enabling recyclability by design. Closed-loop circularity provided by DCC in vitrimers is illustrated in Figure 11.[100,101] To combine the beneficial feature of recyclability, one of the main goals of using similar polymer overall compositions is to enable the recycling of the material through specific chemical reactions. This ability enhances the materials' lifespan and opens new innovative applications in fields ranging from automotive to biomedical engineering. By enabling efficient recycling processes and adaptability, vitrimers are closely related to the principles of green chemistry, sustainability, and the circular economy.[102,103]

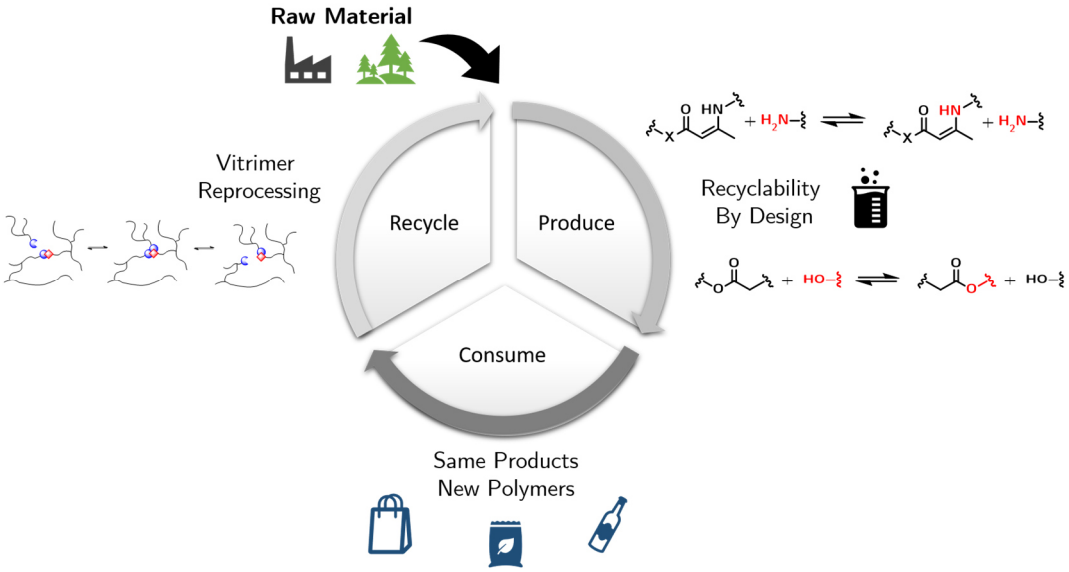

Figure 11: Illustration of closed-loop circularity provided by recyclability by design and vitrimer reprocessing, which leads to the increased retention of plastics in the production and consumption cycle.[100,101]

The combination of the concept of vitrimers with bio-based monomers and resources in the form of bio-based vitrimers aligns with the current needs for sustainability, as described in the demanding Sustainable Development Goals.[104] In this context, 'bio-based' refers to the origin of the monomers and materials used to produce vitrimers with the same functionalities as those used in non-renewable petroleum-based networks.[105,106] Renewable resources include, for instance, starch[107,108], cellulose[109,110], lignin[111,112], vegetable oils[113,114], sugars[115,116], and agricultural waste[117,118]. By utilizing these resources, the dependence on fossil fuels can be reduced, thereby lowering the carbon footprint through decreased greenhouse gas emissions during production and end-of-life management, and offering the potential for biodegradability and compostability.

This includes applying the principles of green chemistry, such as utilizing less harmful monomers and minimizing the use of toxic chemicals in production.[119] However, there are also challenges regarding bio-based materials, such as optimizing potential for scalability, developing bio-based catalysts and solvents, and the need for new equipment for processing and adjusting process parameters.[19] While the cost of fossil-based materials is normally relatively low and mainly depends on the price of crude oil, the cost of biomass can vary significantly depending on the specific biomass source, production process (*e.g.*, pre-treatment, purification, monomer synthesis), and desired performance. One of the biggest challenges is producing green materials that can compete both in price and performance with comparable, already established systems. In a broader context, these materials should also offer solutions that are easily usable for a wide range of customers without requiring special equipment or knowledge.[17] Bio-based vitrimers combine the adaptable properties of CANs with the sustainability of bio-derived building blocks. Potential applications include sustainable adhesives, self-healing coatings, recyclable packaging, composite materials, and advanced biomedical applications.[101]

3.3.1 Future Prospects of Green Vitrimers

To assess the potential and limitations of bio-based vitrimers, a techno-economic analysis includes an examination of their practical viability and market potential. Here, production cost, performance parameters, life-cycle impacts, and the environmental advantages are discussed in comparison with their fossil-based alternatives. To gain market competitiveness, economic feasibility is necessary for production and scale-up.[18]

This is mainly due to the variation in the cost of biomass, which is influenced by factors such as availability, seasonal shifts, location, extraction, and processing. In some cases, the higher initial price can be tackled by the later decrease in greenhouse gas emissions during the product's life cycle. Furthermore, bio-based raw materials must not compete with the food supply, highlighting the importance of utilizing agricultural waste or purpose-grown non-food crops.[120]

Production costs can be kept low by utilizing well-established reactions, electrification, and implementing optimized bio-based catalysts, green solvents, or performing reactions in bulk or water.[121,122] More efficient, less energy-intensive processes can significantly lower the cost of synthesis and production.[123] However, to justify increased costs, the materials must provide benefits such as enhanced durability, mechanical strength, or additional specific features, such as self-healing abilities.[124]

One of the most significant advantages of bio-based vitrimers is their potential for waste management and end-of-life strategies, including biodegradability, composting, chemical recycling, and reuse.[125] These strategies can significantly reduce greenhouse gas emissions and lower environmental pollution, aiding in the fight against climate change and the plastic crisis.[126,127]

3.4 Schiff Base Vitrimers

Schiff bases, or imines, are formed by a nucleophilic addition reaction between an aldehyde or ketone and a primary amine to obtain a dynamic C=N bond. The reaction is displayed in Figure 12. In the first step, the amine attacks the aldehyde, forming a hemiaminal as an intermediate. Dehydration of the hemiaminal gives the imine; the reverse reaction is known as imine hydrolysis. Imines are readily hydrolyzed back to a carbonyl compound and an amine by aqueous acids. However, imines can be stabilized by using electronegative substituents, which can participate in the delocalization of the imine bond.[128]

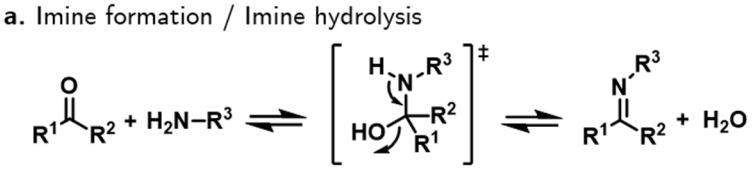

Figure 12: Formation of an imine by condensation between an aldehyde and an amine. The reverse reaction follows a hydrolysis reaction.[128]

Imines have been investigated in biochemical enzymatic reactions. They are gaining interest in material chemistry, due to their straightforward synthesis, catalyst-free exchange, and thermoreversible network rearrangements, which hold potential for utilizing bio-based aldehyde molecules such as vanillin or lignin.[129-132]

Three exchange reactions are known for imine-based vitrimers: A small-molecule-mediated dissociative exchange reaction can be initiated by hydrolysis and subsequent reaction with another amine.[133,134] The associative exchange between an imine bond and a free amine moiety is called transimination, and a direct imine-imine associative exchange is termed imine metathesis.[130] Both associative exchange reactions are displayed in Figure 13.[135]

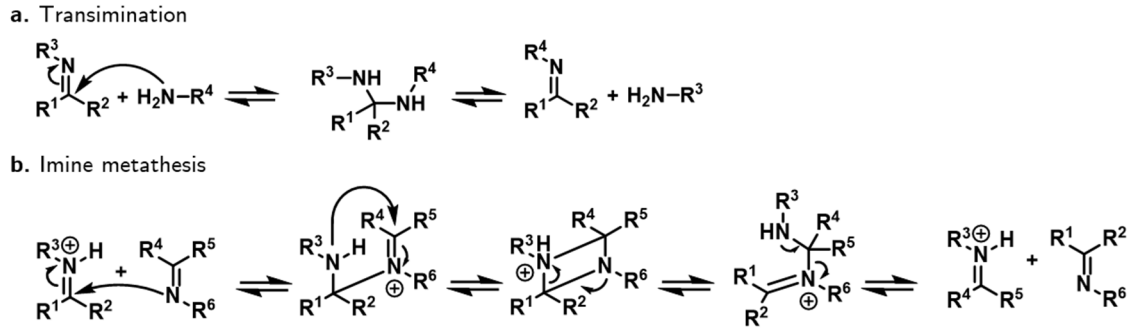

Figure 13: (a) Schematic illustration of the associative transimination MNR of imines, if an excess of amines is present. (b) The imine metathesis is an associative mechanism undergoing a direct imine-imine exchange.[135]

Besides the ability for chemical recycling by the dissociative hydrolysis, only the transimination and the imine metathesis are of interest for associative CAN design.[136] In case of transimination, residual amines are required for the exchange to proceed. The *R*-value describes the ratio of aldehyde groups to amine groups, which needs to be $R < 1$ for transimination. The first and rate-determining step consists of the attack of a free primary amine on the imine carbon atom to form a geminal tetrahedral intermediate. Then, two hydrogen protons transfer from the nitrogen atom of the formerly attacking amino moiety to the nitrogen atom of the former imine group. Finally, the exchanged amino moiety dissociates, leading to fragmentation and the formation of a new imine. The imine metathesis proceeds if $R = 1$ by nucleophilic addition of a neutral imine to a protonated imine. The intermediate state is described by a 1,3-diazetidinium intermediate, resulting in exchanged imines or the initial reactants.[137]

3.5 Vinylogous Urethane Vitrimers

The exchange of amine moieties on enamine-ones was reported in the late 1970s.[138] However, the first implementation of this exchange chemistry was performed in 2014 by Sanchez-Sanchez *et al.* in the form of single-chain polymer nanoparticles.[139] In 2015, Denissen *et al.* reported the first vinylogous urethane (VU) vitrimer, which displayed outstanding exchange kinetics without the need for external catalysts.[77] Enamine-ones are commonly termed vinylogous urethanes and can be easily prepared by acetoacetylation of hydroxy groups followed by a condensation reaction with a primary amine.[135]

Acetoacetates can be synthesized by using alcohols and an acetoacetylation reagent. Here, *tert*-butyl acetoacetate (TBAA) is commonly employed to functionalize alcohols (acetoacetates), resulting in vinylogous urethanes, or other nucleophiles such as amines (acetoacetamides), resulting in vinylogous ureas.[76] At elevated temperatures, TBBA undergoes a fragmentation reaction, forming *tert*-butanol and acetylketene. The highly reactive acetylketene undergoes fast addition reactions.[140] Alternatively, 2,2,6-trimethyl-1,3-dioxin-4-one (TMDO) can be used to generate acetylketene, undergoing a retro-DA reaction with the byproduct acetone.[141] It was found that, depending on the structure of the polyols, TMDO is a more reactive acetoacetylation reagent, resulting in faster acetoacetylation of aromatic alcohols compared to TBAA.[142] The acetoacetylation of alcohols with both TBAA and TMDO, with the respective byproducts, and the formation reaction between a primary amine and an acetoacetate are displayed in Figure 14.

Depending on the conditions of the surrounding environment, different exchange pathways can be distinguished depending on whether the medium is acidic, neutral, or basic (Figure 15).[78] In acidic and neutral conditions, free primary amines are protonated, resulting in the formation of an ammonium ion. This ammonium-enamine pair is in equilibrium with the amine-iminium couple, which can react with the nitrogen atom of the amine to form an iminium, resulting in a geminal amine-ammonium tetrahedral adduct, similar to the previously described transimination reaction.

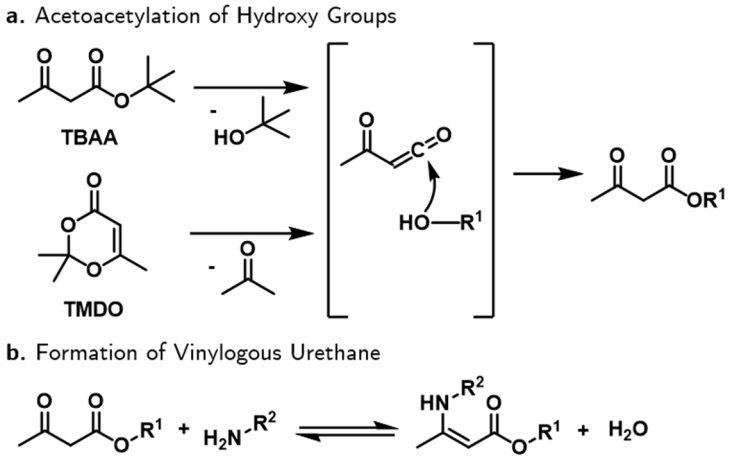

Figure 14: (a) Acetoacetylation process of (alcohol) nucleophiles by the fragmentation of TBAA or the retro-DA of TMDO, forming reactive acetylketene to give the respective acetoacetylated species. (b) A condensation reaction between an acetoacetate and an amine to form a vinylogous urethane bond.[142]

Then, dissociation of the adduct occurs, yielding the exchanged products or reactants with an activation energy (E_a) of the exchange reaction of $E_a = 70 – 76$ kJ mol^{-1}. The reaction can not only proceed *via* an amine-iminium pathway for Brønsted-acids, but can also be catalyzed by Lewis acids, then through a zwitterionic intermediate. In a basic environment, a slower exchange reaction pathway involves a direct Michael addition pathway of a neutral amine on a neutral VU with $E_a = 99 – 141$ kJ mol^{-1}.[143] It is known that some VU vitrimers exhibit a dual temperature response. Different pH conditions did not explain the dual behavior; however, the iminium pathway was preferred at lower temperatures, while the neutral Michael-type pathway prevailed at higher temperatures, likely due to the varying activation energies of the MNR pathways.[144]

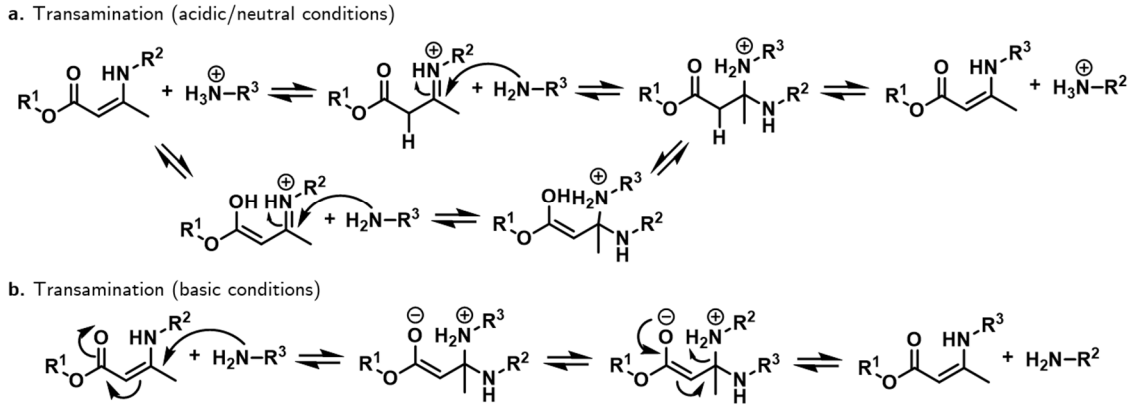

Figure 15: Exchange mechanisms of vinylogous urethanes. (a) The transamination mechanism involves the formation of a reactive iminium ion intermediate, which is subsequently substituted by a free amine. (b) A direct attack of an amine on the carbon double bond forms a zwitterionic intermediate state, which can then fragment into reshuffled products.[143]

In VUs, the dynamicity is closely related to the *R*-value, which is determined by the ratio between the number of acetoacetates and amines. Due to the requirement of free amines for both rearrangement reaction pathways, the *R*-value is usually $R < 1$, with a lower *R*-value enabling a higher rate due to a higher number of exchanging associative VU groups.[142] The rate of exchange can be further manipulated using organic catalysts such as *p*-toluene sulfonic acid or acidic alumina.[145,146]

3.6 Dioxaborolane Vitrimers

Cyclic boronic esters, also known as dioxaborolanes (DBs), are characterized by the presence of a boron atom that is linked to both an alkoxy group and a carbon atom.[147] They are synthesized through a condensation reaction under ambient conditions, involving a boronic acid compound with 1,2- or 1,3-diols, which leads to stable five- or six-membered rings, respectively.[148] The reversible formation reaction is displayed in Figure 16. Ring formation is entropically favored by the expulsion of two molecules of water. In biological media, this reactivity results in a dissociative behavior, since boronic esters are prone to hydrolysis in aqueous media.[149] The formation of a boronic ester must be performed at a pH higher than the pK_a of the acid. The pK_a is highly dependent on the chemical modification; for instance, the pK_a of phenylboronic acids is 8.8, compared to that of methylboronic acid, which is 10.4.[150,151]

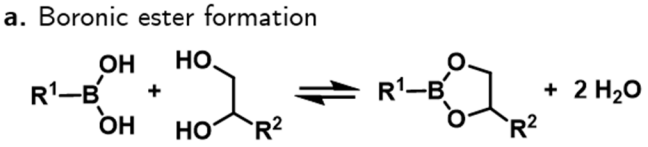

Figure 16: Formation of a boronic ester through a condensation reaction.[147]

The reversible properties of DBs rely on their ability to form reversible bonds, making them suitable for applications such as self-healing hydrogels or environmentally responsive materials.[64,152-155] This reversibility is most attributable to the electron-deficient boron atom, which facilitates the dynamic interaction with nucleophiles, including alcohols and water. Various parameters, including pH and temperature, influence the reactivity of DBs.[156] The boron-oxygen bonds are powerful due to their significant π-bonding character between the oxygen lone pair and the unoccupied *p*-orbital on boron, reminiscent of a classical carbonyl bond. At the same time, the boron center remains highly electrophilic and readily forms tetrahedral adducts with a broad range of nucleophiles.[150]

Three different bond exchange mechanisms are known and applied in boronic ester CANs.[157,158] Classical boronic ester dissociation and reesterification can occur in the presence of water under acidic conditions, whereas in an arid environment, an associative mechanism similar to transesterification was proposed.[159]

Moreover, under neutral and basic conditions, the boronic esters may exhibit stability, facilitating controlled release and reformation of the covalent linkage. A third kind of exchange reaction was reported for systems in which no free diol groups are present.[160] The DB metathesis reaction occurs directly between two boronic ester moieties and requires no additional catalyst or other functionality except the DB. However, the exact mechanism of this reaction has not been proven. It is hypothesized that the transition state involves an intermediate with a higher connectivity, as shown in Figure 17.[135] In the formed zwitterionic adduct, the alkoxide residues can be readily exchanged between the two boron centers, ultimately enabling a complete crossover of bonding partners.[50]

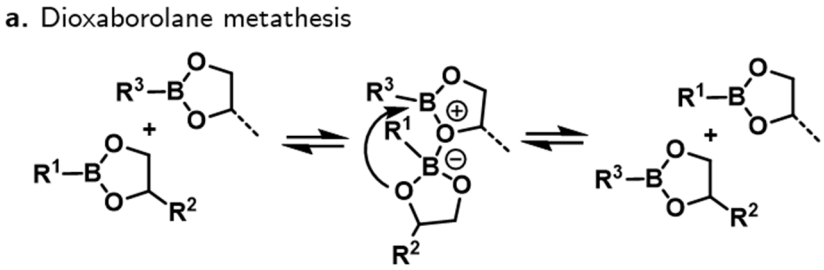

Figure 17: Exchange mechanism of a DB *via* the formation of a zwitterionic intermediate through a metathesis reaction.[135]

3.7 (Nano-)composites

Natural polymers and minerals often show weak mechanical properties on a large scale. Therefore, nature excels at synthesizing and utilizing strong nanocomposites.[161,162] Strong composites such as bone, tooth, shell, and wood are created by combining two or more phases, with at least one phase at the nanometer scale range.[163-165] Biological materials composed of ordered, complex, hierarchical materials can achieve orders-of-magnitude improvements in strength and toughness that artificial composites cannot reach.[166,167] Also, the mechanical-property amplification often occurs in a nonadditive manner that goes beyond a simple rule of mixing.[168]

The exceptional lightweight mechanical properties of biological materials have been a focus of extensive studies over the last few decades, leading to a new research field that connects biology, chemistry, and materials science, guided by the principles of biological nanocomposites.[169-171] These materials display multiple levels of so-called hierarchical structures, ranging from microscopic to macroscopic scales. For example, seashells have two to three orders of lamellar structures, and bone has up to seven orders of magnitude. The small building blocks are composed of nanometer-sized rigid inclusions embedded in a soft protein matrix in a staggered “brick-and-mortar” pattern. Tooth enamel is composed of long, needle-like mineral crystals, embedded in a soft matrix.

Bone has a nanostructure consisting of mineralized fibrils, arranged in a staggered pattern within a collagen matrix. Wood contains nanocrystals, composed of a polymer-polymer organo-composite structure with hard crystalline cellulose fibrils dispersed in an amorphous hemicellulose-lignin matrix.[168]

The complex structure of natural nanocomposites presents significant challenges in their fabrication. The deficiency of man-made nanocomposites is mainly related to the difficulty of obtaining well-dispersed large-volume fractions of nanoparticles and a lack of geometrical and structural control in hierarchical structures. The two primary features of natural materials, namely, nanostructure and complex hierarchy, are widely recognized as the foundations of their superior mechanical strength. Six mechanical principles have been proposed in the structural design of nanocomposites. The first principle involves staggering the arrangement of complex phases within soft matrices, which, together with a high modulus ratio between the hard and soft phases, facilitates a unique load transfer mechanism. The second principle emphasizes flaw-tolerant design in the hard phase and across higher hierarchical levels. The third principle pertains to the shape and geometry of the hard phase, such as aspect ratio and characteristic length. The fourth principle focuses on achieving large deformation and energy dissipation within the soft phase. The fifth principle highlights the importance of hybrid interfaces between soft and hard phases. The six principles include hierarchical structuring, enhancing fracture toughness, robustness, and adaptability to complex loading conditions and environments.[172]

The combination of nanocomposite materials with DCC and CANs can improve the recyclability and processability of the materials. Vitrimers have been established as functional soft matrix attributed to their beneficial structural features and flexibility in exchanging chemistries. By using specific nanoparticles, special features of these particles can be integrated into the material, for example, for magnetic separation during recycling or light-induced heating for self-healing applications.[173,174]

The natural design of the hierarchical assembly of nacre, a composite comprised of micron-sized aragonite platelets and proteins with polysaccharides, is typically structured in a "brick-and-mortar" pattern.[175] This synergistic structure provides stiffness and toughness, resists crack propagation, and leads to a toughness 3000 times higher than that of the individual constituent. The recycling of highly reinforced nacre-mimetic nanocomposites is enabled by vitrimer chemistry, which allows sustainability for bio-inspired nanocomposites and sets the pace for a nano-cyclic economy.[176]

To fabricate nacre-mimetics, several approaches have been employed, including layer-by-layer techniques, freeze casting, colloidal self-assembly, and evaporative self-assembly.[177-179] The approach presented in this work avoids the use of solvents and follows the principles of green chemistry by introduction of nanoparticles into a vitrimer matrix and then processing them by heat compression into nanocomposites with a high proportion of inorganic nanofillers.

4 Objectives of the Work

In this Ph.D. thesis, new prospects in the field of dynamic polymer networks are explored, with a focus on bio-based green chemistry routes, novel building blocks, and methods for forming (nano-)composites. As part of the collaborative research center SFB-986 of the German Research Foundation, the aim was to combine these new polymer networks into hierarchical nanocomposite materials. This approach is inspired by ultra-tough natural materials such as tooth enamel or nacre, which combine beneficial features of both inorganic particles and sophisticated natural polymers. Regarding the need for more sustainable starting materials, manufacturing methods, and end-of-life assessments of more complex materials, the aim was to develop reprocessable matrix systems with inherent recyclability by design, as well as reprocessability and fabrication methods that align with the principles of green chemistry. The combination of inorganic nanoparticles with special magnetic and optical features with covalent adaptable networks in the form of vitrimers offers ways towards sustainable hierarchical nanocomposites.

This work investigated three associative covalent adaptable network chemistries as potential matrix materials, focusing on their exchange reaction mechanisms and unique features such as chemical recycling, malleability, and optical transparency. Moreover, interpenetrating polymer networks were synthesized using orthogonal exchange mechanisms, providing new insights into the complex properties of vitrimer mixtures. Using different building blocks, ranging from small linker molecules to lignin particles, while maintaining a sustainable manufacturing process, enables recyclability by design when combined with nanoparticles. These nanocomposites and methods were developed for different levels of hierarchy, opening up possibilities for synthesizing artificial nanocomposites with high loading of inorganic particles.

Small bio-based molecules derived from lignin can be produced sustainably, offering the potential for bio-based vitrimers. Vanillin offers an aldehyde group and can be functionalized as a cross-linker in Schiff base vitrimers. By alternation of the building blocks, network effects on mechanical properties, stress-relaxation, and recycling behavior can be manipulated. Variation in the amount of free amine groups can accelerate the exchange rate of associative imine bonds by mixing both imine metathesis and transimination as potential exchange mechanisms. Due to their susceptibility to hydrolysis, mild acidic conditions can be used to cleave the network. This work highlights the most critical design aspects for vitrimers and emphasizes recyclability by design through the synthesis and selection of monomer molecules.

Sustainable networks were then prepared using lignin, one of the most abundant biomolecules, as a component for vinylogous urethane networks. Lignosulfonates are by far the biggest class of industrial waste products of the pulping industry. By transforming their highly functionalized particle surface into associatively exchangeable moieties, the material becomes an organo-composite comprising organic lignin structures in combination with soft amine linkers.

It was proven that the materials are composed of VUs that form a homogeneous network. By processing *via* injection molding, industrial manufacturing methods could be used to fabricate test specimens. These methods prove an extensive understanding of this new class of organo-composite materials.

Optical properties, especially optical transparency, are a necessary criterion for optically active nanocomposites. By using DB chemistry, acrylate composites were fabricated, and the properties of the vitrimer material were investigated. Interestingly, the stress-relaxation behavior was found to be highly dependent on the timescale of thermal (re-)processing and could be restored by thermal annealing. Due to its transparent material properties, the material was further processed into fiber composites, demonstrating the feasibility of additive manufacturing. In combination with titanium dioxide nanoplates, nanocomposite materials were produced with a loading of 50 wt.% nanoparticles, which is a step in the direction of natural materials.

Furthermore, in the section of unpublished results, supporting evidence was investigated in the fields of new thermoreversible networks, hierarchical nanocomposites, and the organic synthesis of dynamic phosphonic acids. By combining vinylogous urethanes and DB chemistry, interpenetrating vitrimer networks were formed, allowing for reprocessing. Using co-networks of thermoreversible covalent adaptable bonds and static network cross-links, the creep performance of composite matrices could be improved. Moreover, ligands with ene- and diene motifs were synthesized and characterized to facilitate the formation of a thermoreversible first hierarchical layer in the nacre-inspired nanocomposites.

In summary, this work brings new prospects in the field of networked polymers, combining these with DCC in the form of thermoreversible CANs. By specifically implementing recyclability by design, sustainable, recyclable, and reprocessable materials were synthesized and characterized, providing new insights into design strategies for future materials.

5 Results and Discussion – Published Works

This chapter contains the reprints of three published peer-reviewed first-author articles that represent the central part of this dissertation. The author acknowledges the support of co-authors, collaborators, students, and colleagues. The following section introduces each work with a synopsis that summarizes the main research goals and the most significant findings.

5.1 Publication 1: Schiff Base Vanillin Vitrimers

This work was partially created with the assistance of Malte Vogt (Universität Hamburg) within the scope of his bachelor's thesis. Maltes' help is gratefully acknowledged.

This publication focuses on the synthesis and characterization of bio-based covalent adaptable networks derived from lignin-based vanillin. The combination of sustainable feedstock with excellent properties and closed-loop recycling meets the need for transforming materials developed in both academia and industry. Vanillin can be produced from lignin and acts as a small, aromatic, and versatile building block with both a hydroxy and aldehyde group, making it a platform for various modifications. The dimerization yields dialdehydes with different alkyl spacer lengths to explore how the backbones affect the mechanical properties of Schiff base imine-based CANs. To reduce the use of toxic amines, alternative commercial and bio-based amine building blocks were tested. The developed vitrimers are high-performance materials characterized by reprocessability, recyclability, self-healing, and shape-memory properties, all of which are attributed to reversible imine bonds.

Homogeneous vitrimer films were produced by carefully adjusting the pre-curing of the networks through storage under reduced pressure at elevated temperature. By combining different building blocks, various mechanical properties were achieved, and a structure-property relationship was established. The effects of network composition, backbone chain length, and the stoichiometry of amine and aldehyde groups on properties such as thermal stability, recyclability, and stress-relaxation were systematically examined. Moreover, these findings highlight the importance of network design, as described in the unpublished results, where more complex dynamic network architectures are discussed (chapter 6.1 and chapter 6.2)

Key findings highlight how the availability of free amine groups influences the process, as they are essential for transamination to occur. When the amounts of aldehydes and amines are equal, the network can still rearrange because imine metathesis remains the primary exchange pathway that reshuffles the network. Adding an excess of free amine groups enables transimination, allowing the network to exchange at a faster rate.

Consequently, the recycling features of imine networks can be adjusted based on the amount of free amines, and the topology can be accelerated without the need for external catalysts. Additionally, the materials can be reprocessed through heat compression. Due to the properties of imine bonds, hydrolysis under mild acidic conditions enables the chemical recycling and recovery of used monomers. In this process, small molecule-mediated exchange is observed, while the thermal reshuffling of the network involves associative transimination and imine metathesis.

The network design was found to influence the material properties significantly and can be tailored to create materials with specific mechanical, reprocessable, or stress-relaxing features. The results demonstrate the potential of vanillin-based Schiff base vitrimers as sustainable alternatives to commercial thermosets, offering recyclable, custom-made polymers that present promising concepts for bio-based CANs.

Reproduced from “Reprocessable Vanillin-Based Schiff Base Vitrimers: Tuning Mechanical and Thermomechanical Properties by Network Design,” *Macromol. Mater. Eng.*, **2024**, *309*, 2300187 (doi.org/10.1002/mame.202300187) with permission from Wiley VCH Verlag GmbH & Co. The related supporting information is available in Section 9.2.

RESEARCH ARTICLE

Macromolecular Materials and Engineering
Open Access
www.mame-journal.de

Reprocessable Vanillin-Based Schiff Base Vitrimers: Tuning Mechanical and Thermomechanical Properties by Network Design

*Florian C. Klein, Malte Vogt, and Volker Abetz**

Bio-based polymer building blocks derived from abundant biomass represent a promising class of monomers for the synthesis of sustainable high-performance polymers. Lignin-derived vanillin is used as a bio-based, aromatic molecular platform for chemical modifications. The use of vanillin aldehyde derivatives as monomers with different alkyl chain length, cured with bio-based and less-toxic di- and triamines, leads to covalent adaptable Schiff base networks and thus enables sustainable and thermally reprocessable high-performance materials without using highly toxic amines. A process is presented to prepare homogeneous films of crosslinked materials that are thermally reprocessable while maintaining their mechanical performance. The network structures, mechanical properties, and thermal stability of the obtained polymeric sheets are characterized in detail. By systematically adjusting the composition of the network building blocks, the mechanical properties could be varied from tough materials with a high elastic modulus of 1.6 GPa to materials with high flexibility and elastomeric behavior with an elongation at break of 400%. Furthermore, the stress–relaxation behavior of stoichiometric and nonstoichiometric Schiff base vitrimers is investigated. The combination of bio-based building blocks and the degradability of Schiff base networks under acidic conditions resulted in sustainable, environmentally friendly, chemically and thermomechanically recyclable vitrimers with self-healing and shape-memory properties.

1. Introduction

The use of bio-based feedstocks in combination with covalent adaptable chemistry for crosslinked polymeric materials has attracted increasing attention from both academia and industry in recent years, as this powerful combination enables sustainable materials with outstanding properties and closed-loop recycling.[1–4] Renewable raw materials represent a promising opportunity to replace commonly used fossil-based monomers and will make an important contribution to solve the environmental and societal problems caused by the extensive use of most of the presently established synthetic polymers in modern society.[5,6] In general, polymeric materials can be divided into two different big groups, namely thermoplastics and thermoplastic elastomers on the one hand, and thermosets and chemically crosslinked elastic networks on the other, which differ in their morphologies and temperature dependent mechanical properties. Thermoplastic polymers have linear or branched polymer chains, they can be semicrystalline or be composed of chemically different blocks with different melting or glass transition temperatures. Depending on their composition, they exhibit hard and brittle, tough or elastomeric properties. They also undergo chain diffusion, and behave like a viscoelastic liquid above glass transition or melting temperature. This enables melting and processing as well as recycling.[7] However, they are limited in terms of thermomechanical stability and quality of the recycled material in many cases, e.g. if additives are used.[8] Thermosetting polymers, on the other hand, are macromolecular networks with a high crosslinking density that exhibit extensive resistance to deformation, are insoluble and have increased dimensional stability.[9] Compared with thermosets, less dense crosslinked elastomers can be deformed and swollen by suitable solvents, but they retain their dimensional stability and, like the thermosets, are considered solid materials that cannot melt. Despite their good mechanical properties, they have the major disadvantage that they can no longer be processed once the material is chemically fixed by covalent bonds, as they cannot be dissociated under sufficiently mild conditions that do not degrade the other parts of the material. The situation changes dramatically when

F. C. Klein, M. Vogt, V. Abetz
Universität Hamburg
Institute of Physical Chemistry
Grindelallee 117, 20146 Hamburg, Germany
E-mail: volker.abetz@uni-hamburg.de
V. Abetz
Helmholtz-Zentrum Hereon
Institute of Membrane Research
Max-Planck-Straße 1, 21502 Geesthacht, Germany

The ORCID identification number(s) for the author(s) of this article can be found under https://doi.org/10.1002/mame.202300187

DOI: 10.1002/mame.202300187

chemical crosslinks are present that can exchange under a particular trigger without degradation of the whole material. This trigger can be, for example, a moderately elevated temperature, at which crosslinks in so-called associative covalent adaptable networks (CANs) defined as vitrimers change without changing the number of crosslinks. Therefore, vitrimers represent a class of CAN materials characterized by a permanent network with thermally induced associative exchange mechanisms without depolymerization upon heating. They combine both classes of polymeric materials with new unique properties.[10] Since covalent bonds are broken only when new ones are formed at the same time, these networks can be considered both permanent and dynamic. The characteristic properties of vitrimers can be controlled by parameters such as the crosslink density, the intrinsic stiffness of the monomers, the exchange reaction kinetics, the density of exchangeable bonds and groups, and thus by the network design.[11] In addition, this class of polymer materials exhibits self-healing, shape-programming, shape-memory, and reprocessing.[9] The use of vitrimers as mechanically and chemically recyclable materials in combination with renewable bio-based feedstocks is highly desirable to reduce carbon emissions and avoid the lack of recyclability and reuse of classical crosslinked polymer materials.[12–14] Several vitrimers were synthesized using different bond exchange mechanisms, e.g., transesterification, vinylogous urethane exchange, boronic esters-based exchange, urethane-based exchange, and hydroxyurethane-based exchange.[15–19] Schiff base vitrimers based on imine bonds are promising candidates for applications such as self-healing coatings, adhesives, composites, and renewable materials due to their monomer recovery properties.[20] They combine the advantages of being degradable by hydrolysis of imine bonds while allowing associative bond exchange by imine metathesis and transimination reaction.[21]

Vanillin, derived from lignocellulosic biomass, provides a sustainable platform for a variety of vitrimer materials and is available on an industrial scale.[20,22,23] The molecule was used for the design of bio-based vitrimers based on vinylogous urethane chemistry with high renewable carbon content, fast reprocessability and recyclability.[24] Several studies focused on the combination of epoxidized vanillin as an aldehyde building block cured with amines to produce materials with exchangeable imine bonds.[25–30] It has also been used to prepare reprocessable light-curing resins by transesterification reactions.[31]

The modification of vanillin as a dialdehyde monomer for Schiff base vitrimers has recently gained attention as it has been used to produce materials of high mechanical strength and a variety of thermomechanical and chemical reprocessing as well as recycling options. A fully bio-based Schiff base vitrimer with self-healing ability at room temperature was synthesized by Jiang et al. using vanillin, 2,5-furandicarboxylic acid, succinic acid, and bio-based Priamines.[32] It displayed a tensile strength of 2.45 MPa and a glass transition temperature (T_g) of 25.1 °C. In 2020, Hajj et al. presented bio-based polyimine elastomeric vitrimers prepared by reactions between di- and trifunctional polyetheramines and a furan-based dialdehyde, focusing on the crosslink density, which affects the physical properties of the material, especially the relaxation behavior.[33] It was found that the crosslink density has a large influence on the relaxation properties, which control the physical properties of the networks. Jiang et al. prepared dialdehyde building blocks with an aromatic linker and used polyetheramine resulting in a degradable, recyclable material with a tensile strength of 50 MPa and a T_g of 42.6 °C.[34] Vanillin-based polyimine vitrimers were prepared by Tao et al. using a vanillin dialdehyde in combination with a trifunctional building block synthesized from phosphorous oxychloride and vanillin with diethylenetriamine (DETA) for the vanillin-based polyimine vitrimers to obtain materials that can be recycled and self-healed by gel-sol transition in good solvents. Furthermore, they investigated the influence of vanillin building block structure on the network properties.[35] These highly crosslinked materials achieved a tensile strength of 84.1 MPa and an elastic modulus (*E*-modulus) of up to 2.55 GPa. Using similar di- and trifunctional vanillin building blocks, Zhou et al. combined them with bio-based Priamines to form elastomeric polyimine vitrimers with an *E*-modulus of 4.90 MPa and a high elongation at break ϵ_b of up to 394%, which degrade rapidly in 0.1 M aqueous hydrochloric acid (HCl) solution.[36] By synthesizing a dialdehyde monomer from 1,4-dibromobutane and vanillin in combination with DETA and tris(2-aminoethyl)amine (TREN), three films with different degrees of crosslinking and tensile strengths between 47.4 MPa and 57.1 MPa were prepared by the group of Geng et al.[37] In 2022, Wang et al. used the same vanillin building block to form carbon fiber reinforced composites based on TREN and commercially available diamines such as 4,4′-diamino diphenylmethane, which displayed an elastic modulus of 2.89 GPa and tensile strength of 80.3 MPa, as well as good recyclability.[38] However, despite the recyclability and self-healing, the stress relaxation and characteristic vitrimer properties were not investigated.

An important factor for the thermal and mechanical behavior as well as the stress relaxation of Schiff base vitrimers is the chemical structure of the building blocks, which influences the physical properties of the networks. Herein, dialdehyde building blocks were synthesized from vanillin using two different chain spacers with varying lengths between the aromatic rings. In addition, the commonly used highly toxic di- and triamines DETA and TREN were compared with more environmentally friendly and less-toxic alternatives such as the potentially bio-based C5-diamine 1,5-diaminopentane, cadaverine (CAD), and the commercially available polyetheramines Jeffamine D-400 (JD) and T-403 (JT).[39–44] This study provides a detailed analysis of the mechanical, thermomechanical, and stress–relaxation properties of these Schiff base vitrimers.

2. Results and Discussion

2.1. Synthesis, Preparation, and Characterization of Schiff Base Vitrimer Films

Vanillin-derived difunctional aldehydes (DAV-1 and DAV-2) with different alkyl chain lengths were obtained in high yield from 1,4-dibromobutane, 1,10-dibromodecane, and vanillin, respectively (**Figure 1**a), following a synthesis procedure previously described by Geng et al.[37]

The successful synthesis of the ether functions is reflected in the ATR-FT-IR (Figure S1, Supporting Information), ^{1}H NMR, and ^{13}C NMR spectra of both molecules (Figures S2–S5, Supporting Information). In addition, mass spectrometry (ESI) showed

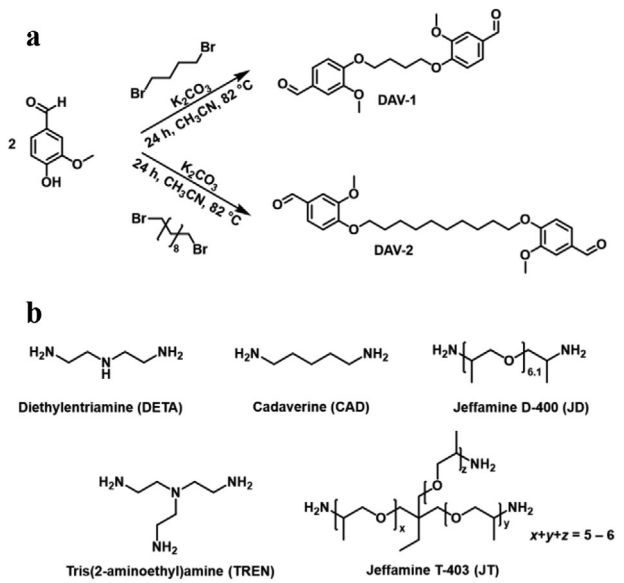

Figure 1. a) Reaction scheme of the synthesis of the vanillin-based dialdehyde building blocks DAV-1 and DAV-2 with different alkyl chain length between the aromatic centers. b) Chemical structures of the difunctional amines DETA, JD, CAD, and the triamines TREN and JT.

the correct *m/z* value for the DAV-1 and the DAV-2 monomer (Figures S6 and S7, Supporting Information). The analytical data is consistent with the literature.[37]

To obtain homogeneous Schiff base vitrimer films from the two prepared DAV monomers, the dialdehyde molecules were reacted with different di- and trifunctional amine building blocks to prepare Schiff base vitrimers with a wide range of properties, ranging from rigid networks to elastomeric films. The various network precursors are shown in Figure 1b, and the formulations of the vitrimers with the respective molar ratios of the amines are listed in Table S1 (Supporting Information). The Schiff base vitrimer films were abbreviated according to the following nomenclature: first, the DAV building block is introduced, followed by the di- and trifunctional amines. The relative number of amino groups with respect to the aldehyde groups is given as subscripts (Equation (S1), Supporting Information). An example of this is DAV-1/$DETA_{0.3}TREN_{0.7}$ with an *R*-value of 1.0 (*R* is the ratio of aldehyde groups/amino groups). The DAV-1/$DETA_{0.3}TREN_{0.7}$ material was investigated in a previous study of Geng et al. and also studied in this work for comparison and an improvement in mechanical properties was observed by preparing it according to the preparation protocol in this work.[37] In case of DAV-1.2, an equimolar amount of both aldehyde compounds (related to the amount of aldehyde functions) was used in a combined material. The amine precursors had different chain lengths and ranged from short amine building blocks, such as the bio-based CAD, to the commercially available less-toxic and larger Jeffamines JT and JD, which are commonly used for epoxy curing while providing high impact strength to these materials by their longer chain structures.[45,46] The mechanical and thermomechanical properties, such as stress–relaxation and shape-memory behavior of the networks therefore depend on the flexibility or rigidity of the combined molecules, resulting in films with a wide variety of properties.[33,47]

After mixing the solutions of the DAV-monomer and the corresponding amines in dichloromethane, the stirred solution turned slightly yellow and became more viscous within 10 min at 50 °C. The mixture was then poured into a polytetrafluoroethylene (PTFE) mold, forming an opaque precursor film after the solvent evaporated. To ensure complete conversion of the functional groups in the Schiff base vitrimer films, the by-product water was evaporated under vacuum at 100 °C for 24 h, resulting in yellowish to brown polymeric sheets. Subsequently, these sheets were cut by scissors and processed in heat compression at 150 °C under a pressure of 10 kN for 30 min resulting in homogeneous, defect-free polymeric films with a thickness of 1 mm. Without the storage under vacuum at 100 °C for 24 h of the polymeric sheets, bubbles appeared, indicating incomplete prepolymerization and the release of water during heat compression. The thermal treatment thus ensured the complete integrity of the network and the comparability for all Schiff base vitrimer films.

Schiff base vitrimer formation was confirmed by ATR-FT-IR measurements of the films (Figure S8, Supporting Information). The absorption bands of the monomers at 1674 and 1681 cm^{-1} decreased in intensity whereas a characteristic imine stretching vibration band appeared at around 1641 cm^{-1} confirming the condensation reaction between amine and aldehyde groups. A small broad band around 1680 cm^{-1} indicated few unreacted aldehyde functions in the materials DAV-2/$DETA_{0.3}TREN_{0.7}$, DAV-1/$JD_{0.3}JT_{0.7}$, and DAV-1/$CAD_{0.3}JT_{0.7}$. Varying the *R*-value from 1.0 to 0.71 results in the complete disappearance of the aldehyde peaks because of the excess of amine building blocks. To further characterize the formation of polymeric networks, solubility tests were carried out in tetrahydrofuran (THF), methanol (MeOH), dimethylformamide (DMF), and water for 24 h. The corresponding fractions are reported in Table S2 (Supporting Information). The results display a low soluble fraction for the highly crosslinked material DAV-1/$DETA_{0.3}TREN_{0.7}$ with short chain length of the amine building blocks. All other materials show high soluble fractions or even complete dissolution in THF, which can be considered to be due to the cleavage and hydrolyzation of imine bonds. When the solvent was removed from the materials with a soluble fraction of 100% in THF, yellow films could be obtained again. In MeOH and H_2O, low soluble fractions were detected for all materials. In DMF, the synthesized films, except DAV-2/$DETA_{0.3}TREN_{0.7}$ and DAV-1/$CAD_{0.3}JT_{0.7}$, which also completely dissolved, showed low soluble fractions. This demonstrates their network integrity even if the respective materials dissolve in THF. The solvation behavior of Schiff base vitrimers in good solvents like THF and DMF has been reported already before for Schiff base vitrimers.[34–36] However, since the definition of vitrimers requires a crosslinked material, other methods such as dynamic mechanical analysis, non-normalized stress–relaxation curves, and frequency sweeps were performed in the following to characterize the network structure of all Schiff base vitrimers.

2.1.1. Thermal Properties of Schiff Base Vitrimer Films

The Schiff base vitrimer films exhibited T_gs (as determined by differential scanning calorimetry (DSC) (Figure S9, Supporting Information)), which differed significantly by the choice of the

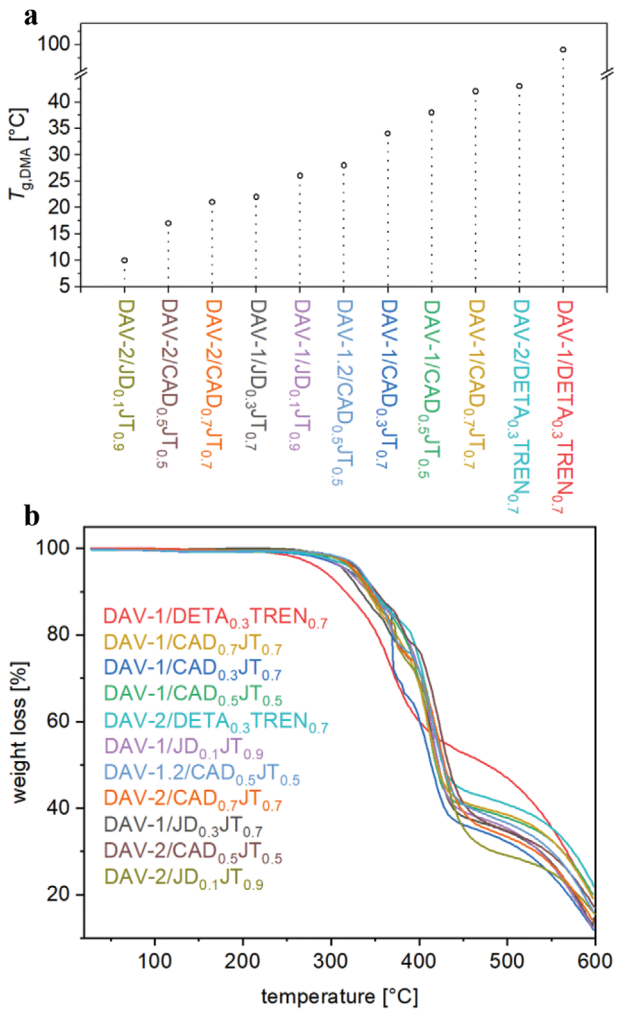

Figure 2. a) $T_{g,DMA}$ values for the Schiff base vitrimer films measured via temperature-dependent DMA measurements (ω = 62.8 rad s^{-1}, γ = 0.1%, T = 0–150 °C). Thermogravimetric analysis measurements b) of the Schiff base vitrimer films with different DAV and di- and triamine building blocks carried out in the range of 25 to 600 °C (10 K min^{-1}) under ambient atmosphere, showing thermal degradation temperatures $T_{5\%}$ of 290 to 332 °C.

dialdehyde monomer, crosslink density, and backbone of the amines. With this, elastomeric and thermosetting vitrimers with $T_{g,DSC}$ values between 7 and 91 °C could be prepared (Table S3, Supporting Information). T_gs, displayed in **Figure 2**a, obtained by temperature-dependent DMA measurements (Figure S10, Supporting Information) supported the results of the T_gs from the DSC, obtaining similar values (Table S3, Supporting Information). Differences of the T_gs from the DSC and DMA are due to the different determination procedure of both techniques.

In particular, a longer alkyl chain in DAV is expected to increase the flexibility of the network as it allows rotation and torsion between the aromatic rings.[48,49] The similar formulations of di- and triamines resulted in vitrimer films with different crosslink density and chain structure for DAV-1 and DAV-2, which affected the thermal properties of the films. Thus, the polymer films with DAV-2 exhibited lower T_gs than the formulations with DAV-1, while maintaining the same amine composition, which is therefore a way to tune the thermal properties of the films. By variation between film DAV-1/DETA$_{0.3}$TREN$_{0.7}$ to DAV-2/DETA$_{0.3}$TREN$_{0.7}$ the T_g could be influenced significantly from 99 to 43 °C. Furthermore, the combination of DAV-1 and DAV-2 with cadaverine and Jeffamine-T (DAV-1.2/CAD$_{0.5}$JT$_{0.5}$) proved to be a homogeneous mixture resulting in a Schiff base vitrimer film without phase separation and therefore statistical crosslink distribution throughout the material, since the $T_{g,DMA}$ of DAV-1.2/CAD$_{0.5}$JT$_{0.5}$ at 28 °C lies in between the materials DAV-1/CAD$_{0.5}$JT$_{0.5}$ with 38 °C and DAV-2/CAD$_{0.5}$JT$_{0.5}$ with 17 °C. Interestingly, the variation of the *R*-value between the aldehyde and amino groups from 1.0 to 0.71 (DAV-1/CAD$_{0.5}$JT$_{0.5}$, DAV-1/CAD$_{0.7}$JT$_{0.7}$ and DAV-2/CAD$_{0.5}$JT$_{0.5}$, DAV-2/CAD$_{0.7}$JT$_{0.7}$) increased the T_g slightly, indicating a higher crosslink density for the systems with R = 0.71, which agrees well with the absence of aldehyde functions in these systems discussed before. Via the preparation procedure, including storage at elevated temperatures and subsequent hot pressing, the thermal properties of the previously synthesized DAV-1/DETA$_{0.3}$TREN$_{0.7}$ could be improved to a high $T_{g,DMA}$ of 99 °C in this work.[37] Thermogravimetric analysis of the materials showed thermal degradation temperatures (temperature at 5% mass loss, $T_{5\%}$) of 290–332 °C at ambient atmosphere (Table S3 and Figure 2b, Supporting Information). Short building blocks in DAV-1/DETA$_{0.3}$TREN$_{0.7}$ feature a lower $T_{5\%}$ of 290 °C than in the materials with higher molecular weight between the crosslinks. The residual weight fractions of the polyimine films range between 12% to 22% at 600 °C. In addition, isothermal TGA measurements at 150 °C under oxygen and nitrogen atmosphere for 2 h displayed no significant weight loss of all synthesized materials. (Figures S11 and S12, Supporting Information). These results show the thermal stability of the Schiff base vitrimers in the observed temperature range of DMA and DSC.

2.1.2. Mechanical Properties of Schiff Base Vitrimer Films

Temperature-dependent DMA measurements were performed at a frequency of ω = 62.8 rad s^{-1} and strain amplitude in the linear viscoelastic regime of γ = 0.1% (Figure S13, Supporting Information). The maximum storage moduli G' ranged between 0.012 to 0.87 GPa at 10 °C, with a low value of 0.012 GPa and 0.014 GPa the materials containing the ether-based triamine building blocks of higher molecular weight in the materials DAV-1/JD$_{0.3}$JT$_{0.7}$ and DAV-2/JD$_{0.1}$JT$_{0.9}$, respectively (Table S3 and Figure S14, Supporting Information). The modulus reached a value of 0.30 GPa for DAV-1/JD$_{0.1}$JT$_{0.9}$, indicating an influence of introducing more network crosslinking points into the material. The sample DAV-1/DETA$_{0.3}$TREN$_{0.7}$ and DAV-2/DETA$_{0.3}$TREN$_{0.7}$ did not reach a rubbery plateau within the observed temperature range but rather display a broad glass transition region which can also be observed in the tan δ curve (Figure S10, Supporting Information). The rubbery plateaus of the other vitrimers could be determined in the range of 0.18 MPa to 1.71 MPa at 110 °C, which are associated to the type and amount of amine and aldehyde building blocks (Table S3 and Figure S15, Supporting Information). Decreasing values of storage modulus for vitrimers are observed for the materials containing CAD$_{0.5}$,

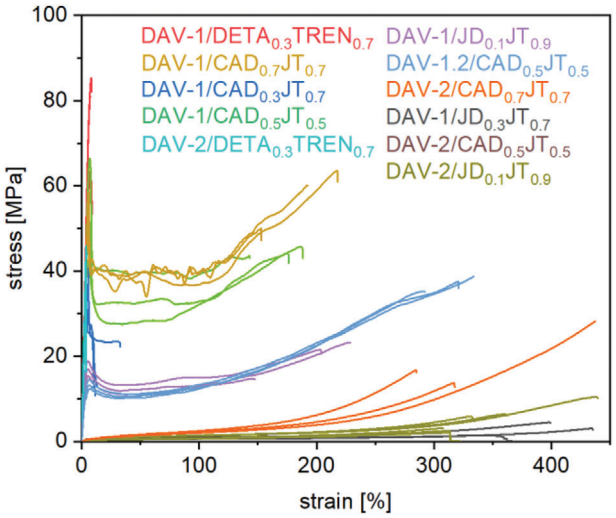

Figure 3. Stress–strain measurement curves of the prepared Schiff base vitrimer films with different DAV and di- and triamine building blocks (T = 23 °C). Overall, four different areas of material behavior can be distinguished ranging from thermoplastic to thermosetting vitrimers depending on the building blocks.

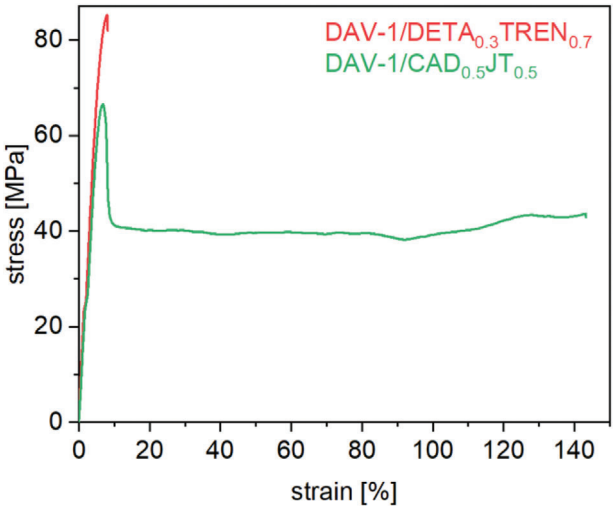

Figure 4. Representative stress–strain measurement curves of the materials DAV-1/DETA$_{0.3}$TREN$_{0.7}$ and DAV-1/CAD$_{0.5}$JT$_{0.5}$, which show a superior elongation behavior of the latter, while both samples have similar stiffness (E-modulus).

where the rubbery plateau decreased from a value of 1.01 MPa (DAV-1/CAD$_{0.5}$JT$_{0.5}$ to 0.35 MPa for DAV-2/CAD$_{0.5}$JT$_{0.5}$, if DAV-2 is used. The glass transition regions follow the thermal properties of the Schiff base vitrimer films observed by DSC and show a narrow glass transition regime between the high modulus glassy state and the rubbery plateau, except for the material containing DETA and TREN. Sorting the glass transition temperatures $T_{g,DMA}$ in an ascending order, it can be concluded, that shorter amine building blocks, such as CAD, DETA, and TREN, increase the $T_{g,DMA}$ due to their shorter distance between crosslinking points (Figure 2a). A similar trend can be observed by using DAV-1 instead of DAV-2. No terminal flow was observed during the temperature-sweeps, which is consistent with the associative network properties of these vitrimers.[50,51]

2.1.3. Stress–Strain Measurements of Schiff Base Vitrimer Films

Stress–strain measurements were performed to evaluate the mechanical properties of the Schiff base vitrimer films at room temperature. From the stress-strain curves for each vitrimer in **Figure 3**, it can be concluded that the prepared networks can be tailored for desired properties in a wide range.

In particular, DAV-1/DETA$_{0.3}$TREN$_{0.7}$ exhibited the highest yield stress (σ_y) of 76.6 ± 11.6 MPa, stress at break (σ_b) of 73.2 ± 17.4 MPa, and an E-modulus of 1574 ± 138 MPa. Substitution of DAV-1 with DAV-2 decreased the maximum tensile stress ($\sigma_m = \sigma_b$) to 41.6 ± 6 MPa while the E-modulus was within the same range of 1412 ± 178 MPa. This indicated that the short chain length of the amines DETA and TREN dominates the elastic behavior of these thermosets with strain at break (ϵ_b) of 3.73 ± 0.2% and 7.44 ± 0.5%, respectively. In terms of replacing DETA and TREN in the sample formulations, as expected, a combination of the difunctional JD and the trifunctional JT led to elastomeric materials with a high ϵ_b of 400 ± 34% in case of DAV-1/JD$_{0.3}$JT$_{0.7}$. Comparable elongations ϵ_b were recorded for vitrimers containing higher amounts of JT with values of 193 ± 42% (DAV-1/JD$_{0.1}$JT$_{0.9}$) and 311 ± 3.2% (DAV-2/JD$_{0.1}$JT$_{0.9}$). The difference is due to the higher number of crosslinks within the material and the more flexible building block DAV-2. The E-moduli increased from 1.55 ± 1.03 MPa (DAV-1/JD$_{0.3}$JT$_{0.7}$) to 580 ± 137 MPa (DAV-1/JD$_{0.1}$JT$_{0.9}$) and prove that a flexible material can be generated by simple network modification, which displays a higher E-modulus and an increased yield stress σ_y of 17.0 ± 1.74 MPa compared to 0.46 ± 0.17 MPa at lower crosslinking degree. An improved material could be prepared by replacing DETA and TREN in the formulation by diamine CAD and triamine JT (DAV-1/CAD$_{0.5}$JT$_{0.5}$), which showed a high E-modulus of 1364 ± 158 MPa and a yield stress σ_y of 50.5 ± 7.42 MPa. However, due to the flexible nature of the alkyl ether chains of JT, the strain at break of the material is 169 ± 22%, resulting in a higher mechanical resilience (**Figure 4**) and ductility of the material.

The possibility to tune the materials properties in a simple way is demonstrated on the example of vitrimers with a dialdehyde component ranging from pure DAV-1 via the blend DAV-1.2 to pure DAV-2, while keeping the amine composition constant (DAV-1/JD$_{0.5}$JT$_{0.5}$, DAV-1.2/CAD$_{0.5}$JT$_{0.5}$, and DAV-2/JD$_{0.5}$JT$_{0.5}$) (**Figure 5**).

The formulations show systematic trends in the stress-strain measurements, demonstrating the influence of the alkyl chain spacer. Simple blending of components in various ratios allows the production of materials ranging from elastomers to thermosets. Also, a series with lower R-value of 0.71 displayed comparable results, indicating no mechanical effect of pendant amines within these formulations.

2.1.4. Stress-Relaxation of Schiff Base Vitrimer Films

Stress-relaxation experiments were performed to determine the activation energies for the molecular network rearrangement reactions occurring in the Schiff base vitrimer films and to compare

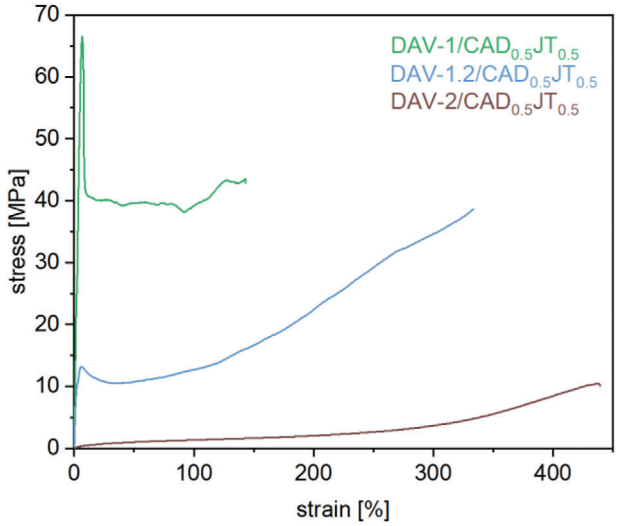

Figure 5. Representative stress–strain curves of the materials DAV-1/$CAD_{0.5}JT_{0.5}$, DAV-1.2/$CAD_{0.5}JT_{0.5}$, and DAV-2/$CAD_{0.5}JT_{0.5}$ with three different elongation behaviors, depending on the amount and the chain length of the dialdehyde building block.

the reprocessing abilities of the different formulations. Therefore, stress–relaxation curves at different temperatures in the range of 90–150 °C were measured by a torsional deformation of 1% and normalized. This temperature range was chosen to ensure only small variability in the initial relaxation modulus G_0 and sufficient relaxation in the time window studied. For example, for vitrimer DAV-1.2/$CAD_{0.5}JT_{0.5}$, the non-normalized stress–relaxation curve displays a nearly constant initial relaxation modulus G_0 with one exponential decay in every curve (**Figure 6**a). The normalized stress–relaxation curves of DAV-1.2/$CAD_{0.5}JT_{0.5}$ show full stress–relaxation in the observed time frame (Figure 6b).

The activation energies for the molecular network rearrangement reactions were calculated by using a single Maxwell element for viscoelastic fluids and an Arrhenius law (Equation S2, Supporting Information).[36,52,53] The logarithm of the stress–relaxation time at 37% of the normalized stress–relaxation was plotted versus $1000/T$ (Figure 6c) and an activation energy of 80.8 ± 0.64 kJ mol^{-1} was calculated from the slope. Fitting the experimental data to a single Maxwell element is valid only if the initial modulus G_0 is similar over the observed temperature range and show one exponential decay. This was demonstrated for the materials by plotting the G_0 values versus the temperature and versus time (Figures S16–S26, Supporting Information).[54] All films showed full stress–relaxation in the observed temperature range (Figures S27–S36, Supporting Information). It should be noted that not all samples could be measured in the entire temperature range of 150–90 °C due to high T_g values (DAV-1/$DETA_{0.3}TREN_{0.7}$) and metrological limitations of the instrument (DAV-2/$JD_{0.1}JT_{0.9}$). The stress–relaxation times of the vitrimers ranged from 0.58 to 214 s at 130 °C (Table S3, Supporting Information). Using amines with longer chain length in combination with DAV-2 led to the vitrimer with the longest stress–relaxation time of 214 s (DAV-2/$JD_{0.1}JT_{0.9}$), indicating a possible impact of the segmental motions of the polymer chains. The stress–relaxation is caused by exchange reactions, but the viscoelastic flow of the chain segments could hinder the segmental movement of the exchanging groups. Except from the material DAV-2/$JD_{0.1}JT_{0.9}$ all Schiff base vitrimers exhibited stress–relaxation times below 13 s at 130 °C in a narrow range for all materials, except for the materials with an *R*-value of 0.71 that showed faster stress–relaxation below 0.7 s. The respective activation energies of each material were calculated from the slope of the linear regression of at least four points in the temperature range of 150–90 °C (Figures S37–S46, Supporting Information). The activation energies ranged between 47.6 to 126 kJ mol^{-1}. These values are within the range of typical activation energies of Schiff base vitrimers which range from 12 to 157 kJ mol^{-1}.[36,55,56] The rate of a vitrimer exchange reaction can be manipulated via different strategies. On the one hand, the reaction rate constant k can be increased by using an external or internal catalyst.[57] Schiff base vitrimers require no additional catalyst for reprocessing, which is also advantageous for producing more sustainable materials, as an additional catalyst could leach out of the material. On the other hand, the concentration of amino groups can be increased, while maintaining the network, to increase the rate of the bond exchanges. In case of formulations with an *R*-value of 1.0, imine metathesis is most likely to occur as associative network rearrangement reaction. However, pendant amino groups cannot be excluded and might lead to deviations by accelerating stress–relaxation via the reaction pathway of a transimination reaction. This is supported by the fact, that both formulations with an *R*-value of 0.71 (DAV-1/$CAD_{0.7}JT_{0.7}$, DAV-2/$CAD_{0.7}JT_{0.7}$) with an excess of free amino groups showed significantly shorter stress relaxation times of 0.65 s and 0.58 s at 130 °C, respectively, compared to the formulations with an *R*-value of 1.0 (DAV-1/$CAD_{0.5}JT_{0.5}$, DAV-2/$CAD_{0.5}JT_{0.5}$) with times of 6.0 s and 13 s, respectively (**Figure 7**).

This effect can be attributed to a higher concentration of exchange functions, increasing the overall rate of dynamic network rearrangement reactions. It also indicates internal catalysis of transimination reaction in these Schiff base vitrimers caused by the free amine functions. To further characterize the associative behavior of the bond exchange reactions, frequency sweep measurements were carried out between 120 to 150 °C for all materials (Figures S47–S56, Supporting Information). At high frequencies, the storage modulus G' is nearly constant and even increases slightly with increasing temperature. This indicates that the total number of bonds remains constant during the exchange process, which is consistent with an associative pathway.[58] The crossover of G' and G'' reflects the transition from a viscoelastic solid to a liquid and can be interpreted as the onset of flow in vitrimers.[60] The crossover time $\tau_{crossover}$ was determined as $1/\omega_{crossover}$ and compared with the stress–relaxation time τ at 130°C. For the highly crosslinked DAV-1/$DETA_{0.3}TREN_{0.7}$ vitrimer, there is a large discrepancy: $\tau_{crossover,130°C}$ of 100 s instead of $\tau_{130°C} = 6.2$ s. It was found, that a higher crosslink density can lead to a less ideal network and larger deviations between frequency and stress–relaxation data.[59] This is also the case for the materials based on long polyether chains DAV-1/$JD_{0.1}JT_{0.9}$, DAV-1/$JD_{0.3}JT_{0.7}$ and DAV-2/$JD_{0.1}JT_{0.9}$, since no $\tau_{crossover}$ could be detected in the observed frequency range. However, for the DAV-1/$CAD_{0.5}JT_{0.5}$, DAV-1.2/$CAD_{0.5}JT_{0.5}$, DAV-2/$CAD_{0.5}JT_{0.5}$ materials, $\tau_{crossover,130°C}$ was 2.7 s, 11.9 s, and 17.8 s, respectively, which

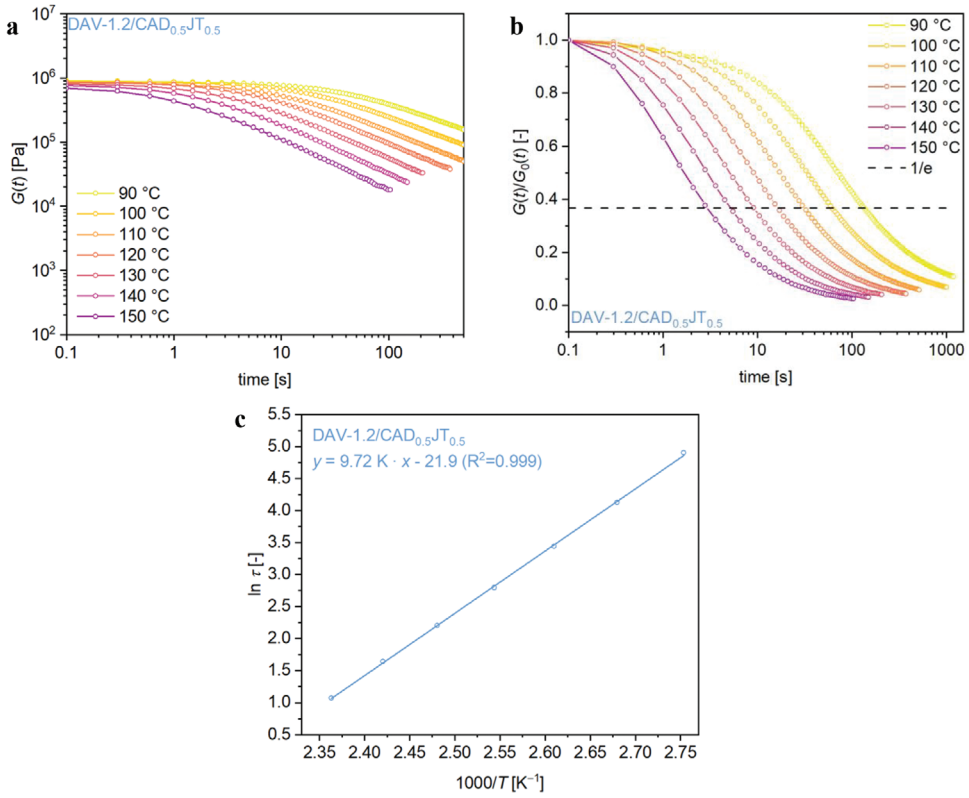

Figure 6. Non-normalized a) and normalized b) stress–relaxation measurement between 90 and 150 °C of the material DAV-1.2/$CAD_{0.5}JT_{0.5}$. c) Arrhenius plot of ln τ versus 1000/T to calculate the activation energy of 80.8 ± 0.64 kJ mol^{-1} from the linear fit of the measured τ values.

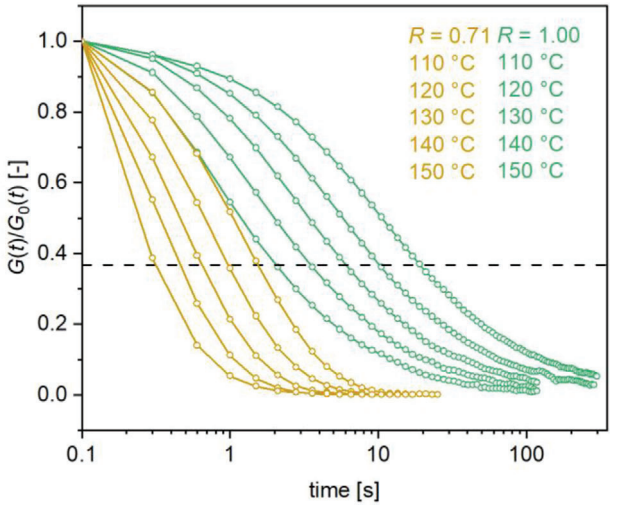

Figure 7. Comparison of representative stress–relaxation measurements at 110, 120, 130, 140, and 150 °C for the formulations DAV-1/$CAD_{0.5}JT_{0.5}$ and DAV-1/$CAD_{0.7}JT_{0.7}$ of DAV-1 with diamine CAD and triamine JT with R-values of 1.0 and 0.71 displaying shorter stress–relaxation times with an Arrhenius dependence by increasing the amount of amine functions within the material. The dashed line is 1/e and localizes the relaxation time.

follows the trend that higher molecular weight of the building blocks leads to slower stress–relaxation. These values are in the same range as the stress–relaxation data at 130°C. For DAV-2/$DETA_{0.3}TREN_{0.7}$ and DAV-1/$CAD_{0.3}JT_{0.7}$, the $\tau_{crossover,130°C}$ showed good agreement with the stress–relaxation data as well. The sample obtained from the mixture of the two dialdehydes (DAV-1.2) showed a value in between the values of the two materials based only on one dialdehyde compound. Varying the R-value from 1.00 to 0.71 shifted the crossover to higher frequencies and thus to lower $\tau_{crossover,130°C}$ values of 0.50 s for DAV-1/$CAD_{0.7}JT_{0.7}$ and 0.41 s for DAV-2/$CAD_{0.7}JT_{0.7}$, which also supports the trend of faster stress–relaxation due to a higher concentration of exchange functions.

2.1.5. Reprocessing, Reshaping, and Self-Healing

DAV-1.2/$CAD_{0.5}JT_{0.5}$ and DAV-1.2/$CAD_{0.5}JT_{0.5}$ were used as examples to demonstrate the reprocessing and reshaping properties of the produced Schiff base vitrimers. Two consecutive cycles of successive grinding and heat compression molding were performed (**Figure 8**a), for DAV-1.2/$CAD_{0.5}JT_{0.5}$ proving the reprocessability of the material.

ATR-FT-IR spectra confirmed the identity of the recycled material and the pristine material (Figures S57, Supporting Information). The stress–strain data remain similar after three reprocessing cycles (Figure S58, Supporting Information). The results display the opportunity for recycling and remolding of the material. In addition, the stress–relaxation behavior of a recycled material was measured after two consecutive recycling cycles with only a slight increase in stress–relaxation time from 7.1 s to 10 s, showing comparable stress–relaxation performance (Figures S59–S62, Supporting Information).

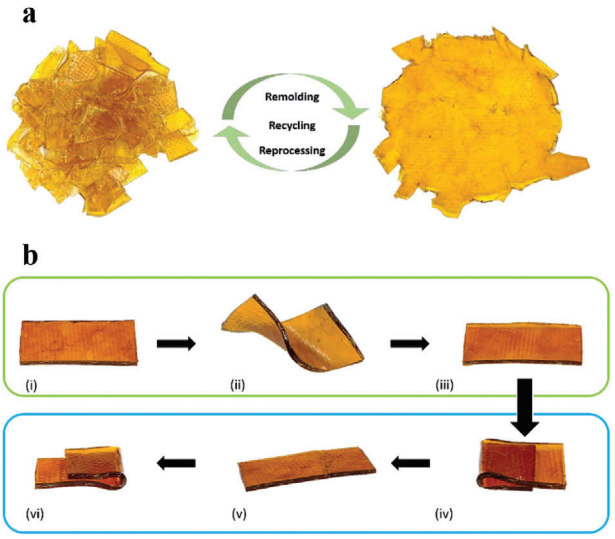

Figure 8. Demonstration of reprocessing of the Schiff base vitrimer film a) by consecutive grinding and heat compression molding (150 °C, 30 min, 10 kN), generating homogeneous, bubble-free recycled film DAV-1.2/$CAD_{0.5}JT_{0.5}$. b) Exemplary shape-memory properties of the Schiff base vitrimer DAV-1/$CAD_{0.5}JT_{0.5}$ examined by thermo-shape adaptation of a flat sheet i) which was heated at 80 °C for 10 s, then freezing the polymer below the T_g at room temperature ii) and heating to 80 °C led to relaxation to the original shape (80 °C, 10 s, iii). Programming a new shape was possible by heating the material to 150 °C for 10 min and subsequent cooling to room temperature led to new solid-state plasticity iv). Again, a heating cycle to 80 °C for 10 s the formation of a flat sheet again showed the thermoadaptive properties after cooling to room temperature v). The new permanent shape could be recovered after heating to 80 °C for 30 s vi).

The solubility tests after the 2nd recycling step showed comparable results to the original material (Table S4, Supporting Information). For THF, complete solvation was again observed. However, after removal of the solvent, the ATR-FT-IR spectrum showed the new formation of the Schiff base network (Figure S63, Supporting Information).

Materials with the capability of changing and recovering shape according to an environmental stimulus, which they are exposed to, are well-known as shape-memory materials.[60] The ability to recover an original shape from a significant and seemingly plastic deformation upon a particular stimulus is known as shape-memory effect.[61] By applying different temperature protocols to vitrimers, they present shape-memory properties and allow for the programming of different shapes (Figure 8b).[62,63] Storing the sample of DAV-1/$CAD_{0.5}JT_{0.5}$ for a short time above its T_g (10 s, 80 °C) enables for thermo-shape adaption and forming of a twisted shape from a formerly flat Schiff base vitrimer film. Cooling to room temperature led to freezing of the polymer and subsequent shape-memory of the permanent flat shape when heating again above the T_g (10 s, 80 °C). Heating up to high temperature for a longer time (150 °C, 10 min) enables for thermally induced associative exchange mechanisms within the network transforming the material into a new permanent shape with solid state plasticity. This shape can be transformed above T_g into a flat shape which reforms the newly programmed permanent shape after a successive cooling and heating cycle (10 s, 80 °C; 25 °C; 30 s, 80 °C) showing actuation properties. This enables self-healing and engineering applications. Self-healing was demonstrated by storing a scratched polymer film DAV-1/$CAD_{0.5}JT_{0.5}$ at 120 °C for 1 h (Figure S64, Supporting Information). The scratch healed completely after 1 hour by molecular network rearrangement, successfully demonstrating the rapid self-healing of the surface.

2.1.6. Chemical Recycling

Considering the circularity of polymeric materials, in 2021 less than 10% of plastics were recycled world-wide with less than 1% being recycled more than once. Circularity in polymer life cycles remains challenging because of heterogeneity in waste streams and thermodynamics. This challenge can be approached by applying circularity by chemical recycling as a part of the macromolecular design.[64] Schiff base vitrimers not only offer reprocessability by thermal treatment, but also feature hydrolysis of the C=N bond, which can be converted into the aldehyde building blocks and amines by acid catalysis.[65–67] The Schiff base vitrimers presented in this work can be hydrolyzed under mild acidic conditions (0.1 M aqueous HCl) and recovered to the original DAV monomer and di- and triamines offering potential for degradation and recycling.[36] The degradation experiment was conducted for all investigated vitrimer films and showed successful decrosslinking with free aldehyde and amine peaks in the ^{1}H NMR spectra (Figure S65, Supporting Information) of the dried white residues and visual fragmentation (Figure S66, Supporting Information) of the film fragments after exposing them for 16 h to 0.1 M aqueous HCl at room temperature.

3. Conclusion

Schiff base vitrimers were synthesized from two vanillin-based dialdehydes and different di- and triamines. The film preparation procedure enabled homogeneous, defect-free films. By using bio-based 1,5-diaminopentane and commercially available Jeffamine polyetheramines, the highly toxic and environmentally harmful chemicals DETA and TREN were substituted. Yet, the good mechanical properties of the short building blocks could not be reproduced. By careful tailoring the network design, materials with a wide range of thermomechanical, mechanical and reprocessing properties were obtained. Using polyetheramines with the dialdehyde building blocks yielded vitrimer elastomers with high elongation at break. The influence of the length of the alkyl chain spacer in the dialdehydes was demonstrated by comparing both building blocks in the same formulation of amines. Further experiments demonstrated the possibility of tuning the material properties by blending two dialdehyde components while keeping the amine composition constant. The vitrimers DAV-1.2/$CAD_{0.5}JT_{0.5}$ and DAV-1/$CAD_{0.5}JT_{0.5}$ exhibited good mechanical stability and proved excellent reprocessing as well as shape-memory properties. Full stress–relaxation was successfully demonstrated for all Schiff base vitrimers and the rate of the exchange reaction could be accelerated without adding an external catalyst by varying the *R*-value of the formulations from 1.0 to 0.71, while maintaining the mechanical performance. Molecular network rearrangement activation energies were calculated exhibiting typical values for Schiff base vitrimers in a broad temperature range of 90 to 150 °C. Chemical recycling of the films

was possible by treatment in mild acidic solution. This work expands the knowledge of bio-based Schiff base vanillin vitrimers, their thermomechanical performance, and the influence of the network design on the properties of the materials. The results offer new perspectives for more sustainable and environmentally friendly recyclable materials with a broad range of thermomechanical properties as well as self-healing and shape-memory properties.

4. Experimental Section

Materials: Vanillin (≥99%, Sigma-Aldrich), tris(2-aminoethyl)amine (97%, Thermo Scientific), diethylenetriamine (>98%, TCI), 1,5-pentanediamine (>98%, TCI), 1,4-dibromobutane (≥98% Apollo Scientific), 1,10-dibromodecane (97%, Alfa Aesar), potassium carbonate (99%, Merck), acetonitrile (anhydrous, ACS, VWR), hydrochloric acid (AR, 37%, VWR), sodium hydroxide (99%, Grüssing), magnesium sulfate (99%, Grüssing), tetrahydrofurane (99.5%, Thermo Scientific), methanol (≥99%, Fisher Scientific), dimethylformamide (99.5%, VWR), deuterated chloroform (99.5%, Eurisotop), deuterated dimethyl sulfoxide (99.8%, Euroisotop), and dichloromethane (VMP) were purchased and used as received without purification. Jeffamine D-400 and Jeffamine T-430 were provided by Huntsman.

Synthesis of Dialdehyde Monomer (DAV-1): Vanillin (11.0 g, 72.3 mmol, 1.00 eq.), anhydrous potassium carbonate (10.0 g, 72.4 mmol, 1.00 eq.), and acetonitrile (180 mL) were added to a 500 mL three-neck flask under magnetic stirring to give a green suspension. The mixture was then degassed with nitrogen for 30 min and 1,4-dibromobutane (6.48 g, 0.41 eq.) was slowly added using a dropping funnel. After complete addition of the dibromide compound, the reaction was heated to 82 °C and was stirred under reflux for 24 h. Finally, the colorless reaction mixture was poured into demineralized water (3 L) and the precipitate was collected by filtration, which was dried at 60 °C under reduced pressure. Then, it was dissolved in DCM (180 mL), washed three times with 400 mL of aqueous sodium hydroxide solution (NaOH, 1 M) and three times with 400 mL of demineralized water. The organic phase was dried over anhydrous magnesium sulfate. The solvent was removed in vacuo and the remaining solid was dried in vacuo at 60 °C (0.001 mbar). DAV-1 was obtained as a colorless solid powder in 84% yield.

^{1}H NMR (500 MHz, $CDCl_3$, δ): 9.84 (s, 2H, CHO), 7.43 (dd, ^3J = 8.2 Hz, ^4J = 1.9 Hz, 2H; Ar H), 7.40 (d, ^3J = 8.2 Hz, ^4J = 1.9 Hz, 2H; Ar H), 6.98 (d, ^3J = 8.1 Hz, 2H; Ar H), 4.21 (t, ^3J = 5.8 Hz, 4H; CH_2), 3.90 (s, 6H; CH_3), 2.15–2.06 (m, 4H; CH_2); ^{13}C NMR (126 MHz, $CDCl_3$, δ): 191.1 (C = O), 154.0 (C4), 149.9 (C4), 130.1 (C4), 126.9 (Ar), 111.5 (Ar), 109.3 (Ar), 68.8 (CH_2), 56.1 (CH_3), 25.9 (CH_2); FT-IR (ATR): ν = 3083 (vw), 2956 (w), 2935 (w), 2919 (w), 2881 (m), 2874 (m), 2839 (m), 2831 (m), 2764 (m), 2737 (m), 2703 (m), 1695 (m), 1673 (s), 1595 (m), 1583 (s), 1506 (s), 1464 (s), 1423 (s), 1398 (s), 1352 (w), 1317 (vw), 1275 (s), 1263 (s), 1238 (s), 1198 (m), 1159 (m), 1132 (vs), 1055 (m), 1028 (m), 999 (s), 960 (m), 948 (b), 926 (w), 868 (m), 810 (s), 754 (m), 729 (s), 660 (m), 588 (m), 571 (m), 486 (w), 467 (w) cm^{-1}; HRMS (ESI) m/z: $[M + Na]^+$ calcd for $C_{20}H_{22}O_6$, 381.130; found, 381.130.

Synthesis of Dialdehyde Monomer (DAV-2): Vanillin (11.0 g, 72.3 mmol, 1.00 eq.), anhydrous potassium carbonate (9.95 g, 72.0 mmol, 1.00 eq.), and acetonitrile (180 mL) were added to a 500 mL three-necked round bottom flask under magnetic stirring, producing a green suspension. The mixture was then degassed with nitrogen for 30 min. Afterward, 1,10-dibromobutane (9.03 g, 30.1 mmol, 0.42 eq.) was dissolved in 20 mL acetonitrile and was slowly added using a dropping funnel. After complete addition of the dibromide solution, the reaction was heated to 82 °C and stirred under reflux for 24 h. Finally, the colorless suspension was poured into demineralized water (3 L), the precipitate was collected by filtration and it was dried at 60 °C under reduced pressure. Then, it was dissolved in DCM (180 mL), washed three times with 400 mL of aqueous sodium hydroxide solution (NaOH, 1 M) and three times with 400 mL of demineralized water. The organic phase was dried over anhydrous magnesium sulfate. The solvent was removed in vacuo and the remaining solid was dried in vacuo at 60 °C (0.001 mbar). DAV-2 was obtained as a colorless solid powder in 90% yield.

^{1}H NMR (600 MHz, $CDCl_3$, δ): 9.84 (s, 2H, CHO), 7.44 (dd, ^3J = 8.1 Hz, ^4J = 1.9 Hz, 2H; Ar H), 7.41 (d, ^4J = 1.9 Hz, 2H; Ar H), 6.96 (d, ^3J = 8.2 Hz, 1H; Ar H), 4.09 (t, ^3J = 6.8 Hz, 2H; CH_2), 3.92 (s, 6H; CH_3), 1.88 (m, 4H; CH2), 1.47 (m, 4H; CH_2), 1.34 (m, 8H; CH_2); ^{13}C NMR (151 MHz, $CDCl_3$, δ): 191.0 (C═O), 154.0 (C4), 150.0 (C4), 130.0 (C4), 126.9 (Ar), 111.5 (Ar), 109.4 (Ar), 69.3 (CH_2), 56.2 (CH_3), 29.52 (CH_2), 29.42 (CH_2), 29.02 (CH_2), 25.99 (CH_2); FT-IR (ATR): ν = 3072 (vw), 2941 (m), 2935 (m), 2919 (w), 2871 (w), 2854 (m), 2833 (w), 2758 (vw), 2725 (vw), 1720 (vw), 1681 (vs), 1583 (s), 1511 (s), 1466 (s), 1423 (m), 1398 (m), 1387 (m), 1338 (m), 1321 (b), 1290 (w), 1275 (vs), 1263 (vs), 1242 (vs), 1199 (m), 1169 (m), 1159 (m), 1134 (s), 1119 (vs), 1032 (m), 1013 (s), 981 (m), 960 (b), 933 (w), 922 (w), 881 (m), 862 (m), 815 (b), 794 (s), 781 (s), 750 (w), 729 (s), 665 (m), 635 (w), 588 (m), 575 (m), 543 (w), 503 (w), 461 (w), 441 (w) cm^{-1}; HRMS (ESI) m/z: $[M + Na]^+$ calcd for $C_{26}H_{34}O_6$, 465.229; found, 465.227.

Schiff Base Vitrimer Preparation: All vitrimer films were prepared according to the following procedure: DAV-1 or DAV-2 or a combination of both was dissolved in 10 mL of DCM and an exact amount of di- and triamines was added with magnetic stirring at 50 °C for 10 min. Then, the mixtures were poured into a PTFE mold and stored at room temperature for 24 h yielding a yellowish polymer sheet. Afterwards, the sheets were stored for 24 h in vacuum and pressed in a heat compression press at 150 °C and 10 kN for 30 min to obtain defect-free amber to brown polymer sheets for all formulations with a thickness of 1 mm. Different test specimens were cut from these and processed.

Reprocessing was performed by consecutive grinding and remolding, cutting the films in small pieces and pressing for 30 min at 150 °C with a pressure of 10 kN into a 1 mm thick film. ATR-FT-IR and tensile test measurements were carried out after reprocessing.

Self-healing was performed by scratching a polymer film with a blade and successive storage at 120 °C in an oven. Optical images were taken with a camera connected to an optical microscope after 0, 5, 30, and 60 min of storage.

Chemical Recycling: Tests were performed using a 0.1 M aqueous hydrochloric acid solution dissolving 10 mg mL^{-1} of a polymeric film. After 16 h, the solution was dried and the white residues were measured via ^{1}H NMR.

Solubility tests were performed by adding samples of 3–5 mm diameter, 1 mm of thickness, and around 50 mg (m_0) to a vial and then immersing them in 1 mL of THF, MeOH, DMF, and deionized water for 24 h at 25 °C. Afterward, the samples were taken out of the solution and then dried under vacuum for 48 h and weighted (m_1). The soluble fraction (SF) was calculated via: $100\% \cdot (m_0 - m_1)/m_0$.

Instrumentation: Nuclear magnetic resonance spectra (^{1}H NMR and ^{13}C NMR) were recorded on a Bruker Avance III HD (600 MHz) and a Bruker Avance I (500 MHz) spectrometer (Bruker Corporation, Billerica, United States) with $CDCl_3$ or DMSO-D_6 as solvent and internal standard. Sample concentrations were between 10 and 40 mg mL^{-1}, and measurements were recorded at 298 K. Data processing was carried out with MestReNova (14.1.0, Mestrelab Relearch S.L., Santiago de Compostela, Spain).

Electrospray ionization (ESI) was measured by an Agilent 6224 ESI-TOF device coupled with an Agilent HPLC 1200 Series (Agilent, Santa Clara, United States) and direct injection (110–3200 m/z). Data processing was carried out with MestReNova (14.1.0, Mestrelab Relearch S.L., Santiago de Compostela, Spain).

Attenuated Total Reflection-Fourier Transformation-Infrared (ATR-FT-IR) spectra were measured in the range of 4000 – 400 cm^{-1} with a resolution of 4 cm^{-1} and 64 scans using a Bruker FT-IR Vertex 70 spectrometer (Bruker Optics GmbH & Co. KG, Ettlingen, Germany). Measurements and data processing were carried out with Opus (8.7, Bruker Optics GmbH & Co. KG, Ettlingen, Germany).

Thermogravimetric analysis (TGA) was carried out on a TG 209 F1 Libra (NETZSCH-Gerätebau GmbH, Selb, Germany) to determine the mass loss during heat treatment. A temperature range of 25–600 °C

with a heating rate of 10 K min^{-1} under ambient atmosphere (oxygen) was used in a flow rate of 20 mL min^{-1}. Isothermal measurements were carried out at 150 °C for 2 h with ambient (oxygen) and nitrogen atmosphere in a flow rate of 20 mL min^{-1}. An amount of 5–10 mg of polymer was weighed into an aluminum crucible. Data processing was performed with Proteus Analysis (8.0.3, NETZSCH-Gerätebau GmbH, Selb, Germany).

Thermal properties of the Schiff base films were determined on a differential scanning calorimeter DSC 204 F1 Phoenix (NETZSCH-Gerätebau GmbH, Selb, Germany). An amount of 5–10 mg polymer was weighed into an aluminum crucible. The heating and cooling rate was set to 10 K min^{-1}. The measurements were carried out in a nitrogen atmosphere with a flow rate of 20 ml min^{-1} in the temperature range between −50 and 150 °C and the thermal properties were analyzed using the DSC data of the second heating curve by determining the mid-point of the DSC-curve step as the glass transition temperature T_g. Data processing was performed with Proteus Analysis (8.0.3, NETZSCH-Gerätebau GmbH, Selb, Germany).

Rheological measurements by dynamic-mechanical analysis (DMA) were carried out using an Anton Paar MCR 502 rheometer (Anton Paar Graz, Austria) using a plate-plate geometry with a diameter of 8 mm. A heat chamber with flooded nitrogen atmosphere was used. The temperature was controlled by a Peltier plate. The gap between the upper and the lower plate was usually set to 1 mm. Prior to all rheological measurements, amplitude-sweeps in oscillatory mode were performed at 110°C between 0.05% and 10% shear strain γ at a constant angular frequency of 62.8 rad s^{-1}. This should ensure that the chosen strain amplitude γ_0 was within the linear viscoelastic regime, so that the storage modulus G' and the loss modulus G'' were independent of strain. Temperature-sweep measurements were carried out in oscillatory mode with a constant angular frequency of 62.8 rad s^{-1} at a constant shear strain of 0.1% in the temperature range of 150–90 °C. Stress relaxation measurements were carried out with a shear strain of 1%, and the relaxation modulus was recorded as a function of time in temperature ranges of 150 –90 °C. Frequency-sweep measurements were carried out at a constant shear strain of 0.1% at the temperatures 120, 130, 140, and 150 °C in the frequency range of 0.01–100 rad s^{-1}. Data processing was performed with RheoCompass (1.30, Anton Paar GmbH, Graz, Austria). Specimens for the DMA were pushed out with an 8 mm punch.

Stress–strain curves were recorded at room temperature (23 °C) on a universal testing machine zwickiLine Z 5.0 TH (Zwick Roell GmbH & Co. KG, Ulm, Germany) using a 5 kN load cell. The measurements were carried out in accordance with the test standard DIN EN ISO 527-1. The initial force was 0.1 MPa, and the clamping length was 13.24 mm. The elastic modulus was determined at a speed of 1 mm min^{-1} between 0.05% and 0.25% elongation and the rest of the test was carried out at 10 mm min^{-1}. Data was processed using TestXpert II (V3.71, Zwick Roell GmbH & Co. KG, Ulm, Germany). The test specimens for the tensile test were punched out with a cutting press type ZCP020 (Zwick Roell GmbH & Co. KG, Ulm, Germany) with the attachment for test specimens of type 5B (according to DIN EN ISO 527-2).

Optical microscopy images were taken by a 5.6 M pixels Microscope Digital USB-camera attached to a Hengtech Zoomstereomikroskop XTL (Hengtech, optische Instrumente, Mannheim, Germany).

Supporting Information

Supporting Information is available from the Wiley Online Library or from the author.

Acknowledgements

The authors gratefully acknowledge financial support from the German Research Foundation (DFG) via SFB986 "M3," subproject A2. The authors would like to address special thanks to Martin Kehden who conducted all DSC and TGA measurements. The authors acknowledge the nuclear magnetic resonance division, and the mass spectrometry division of the chemistry department at Universität Hamburg and acknowledge financial support from the Open Access Publication Fund of Universität Hamburg.

Open access funding enabled and organized by Projekt DEAL.

Conflict of Interest

The authors declare no conflict of interest.

Author Contributions

F.C.K., V.A.: conceptualization; F.C.K.: methodology, investigation, data curation, formal analysis, validation, and performing the experiments together with M.V.; V.A.: supervision and resources; F.C.K.: writing – the original draft; F.C.K., V.A.: writing – review and editing.

Data Availability Statement

The data that support the findings of this study are available from the corresponding author upon reasonable request.

Keywords

bio-based, covalent adaptable networks, Schiff bases, stress–relaxation, vanillin, vitrimers

Received: August 23, 2023
Published online: September 7, 2023

[1] M. J. Webber, M. W. Tibbitt, *Nat. Rev. Mater.* **2022**, *7*, 541.
[2] Y. Liu, Z. Yu, B. Wang, P. Li, J. Zhu, S. Ma, *Green Chem.* **2022**, *24*, 5691.
[3] X.-L. Zhao, P.-X. Tian, Y. I.-D. Li, J.-B. Zeng, *Green Chem.* **2022**, *24*, 4363.
[4] P. Chakma, D. Konkolewicz, *Angew. Chem., Int. Ed. Engl.* **2019**, *58*, 9682.
[5] F. Pei, L. Liu, H. Zhu, H. Guo, *Polymers* **2023**, *15*, 829.
[6] C. G. Schirmeister, R. Mülhaupt, *Macromol. Rapid Commun.* **2022**, *43*, e2200247.
[7] J. M. Winne, L. Leibler, F. E. Du Prez, *Polym. Chem.* **2019**, *10*, 6091.
[8] P. Jagadeesh, S. Mavinkere Rangappa, S. Siengchin, M. Puttegowda, S. M. K. Thiagamani, R. G. Arpitha, M. Hemath Kumar, O. P. Oladijo, V. Fiore, M. M. Moure Cuadrado, *Polym. Compos.* **2022**, *43*, 5831.
[9] W. Denissen, J. M. Winne, F. E. Du Prez, *Chem. Sci.* **2016**, *7*, 30.
[10] W. Alabiso, S. Schlögl, *Polymers* **2020**, *12*, 1660.
[11] C. Taplan, M. Guerre, J. M. Winne, F. E. Du Prez, *Mater. Horiz.* **2020**, *7*, 104.
[12] B. Krishnakumar, A. Pucci, P. P. Wadgaonkar, I. Kumar, W. H. Binder, S. Rana, *Chem. Eng. J.* **2022**, *433*, 133261.
[13] M. A. Lucherelli, A. Duval, L. Avérous, *Prog. Polym. Sci.* **2022**, *127*, 101515.
[14] T. Vidil, A. Llevot, *Macromol. Chem. Phys.* **2022**, *223*, 2100494.
[15] R. Tang, B. Xue, J. Tan, Y. Guan, J. Wen, X. Li, W. Zhao, *ACS Appl. Polym. Mater.* **2022**, *4*, 1117.
[16] P. Haida, G. Signorato, V. Abetz, *Polym. Chem.* **2022**, *13*, 946.
[17] M. O. Saed, A. Gablier, E. M. Terentejv, *Adv. Funct. Mater.* **2019**, *30*, 1906458.
[18] N. Zheng, Z. Fang, W. Zou, Q. Zhao, T. Xie, *Angew. Chem., Int. Ed. Engl.* **2016**, *55*, 11421.

[19] X. Liu, X. Yang, S. Wang, S. Wang, Z. Wang, S. Liu, X. Xu, H. Liu, Z. Song, *ACS Sustainable Chem. Eng.* **2021**, *9*, 4175.
[20] M. A. Rashid, M. d. N. Hasan, M. d. A. R. Dayan, M. S. Ibna Jamal, M. K. Patoary, *Reactions* **2023**, *4*, 66.
[21] F. Cuminet, S. Caillol, É. Dantras, É. Leclerc, V. Ladmiral, *Macromolecules* **2021**, *54*, 3927.
[22] Y. Zhu, J. Liu, W. Lv, L. Ma, C. Wang, *Nature* **2017**.
[23] Y. Wang, S. Sun, F. Li, X. Cao, R. Sun, *Ind. Crops Prod.* **2018**, *116*, 116.
[24] S. Engelen, A. A. Wróblewska, K. De Bruycker, R. Aksakal, V. Ladmiral, S. Caillol, F. E. Du Prez, *Polym. Chem.* **2022**, *13*, 2665.
[25] Q. Yu, X. Peng, Y. Wang, H. Geng, A. Xu, X. Zhang, W. Xu, D. Ye, *Eur. Polym. J.* **2019**, *117*, 55.
[26] S. Wang, S. Ma, Q. Li, X. Xu, B. Wang, W. Yuan, S. Zhou, S. You, J. Zhu, *Green Chem.* **2019**, *21*, 1484.
[27] H. Memon, H. Liu, M. A. Rashid, L. Chen, Q. Jiang, L. Zhang, Y. Wei, W. Liu, Y. Qiu, *Macromolecules* **2020**, *53*, 621.
[28] X.-L. Zhao, Y.-D. Li, J.-B. Zeng, *Polym. Chem.* **2022**, *13*, 6573.
[29] D. Zhang, Z. Cheng, S. Gao, H. Shi, *Mater. Chem. Phys.* **2022**, *279*, 125730.
[30] A. Roig, P. Hidalgo, X. Ramis, S. De la Flor, À. Serra, *ACS Appl. Polym. Mater.* **2022**, *4*, 9341.
[31] S. Grauzeliene, M. Kastanauskas, V. Talacka, J. Ostrauskaite, *ACS Appl. Polym. Mater.* **2022**, *4*, 6103.
[32] L. Jiang, Y. Tian, X. Wang, J. Zhang, J. Cheng, F. Gao, *Polym. Chem.* **2023**, *14*, 862.
[33] R. Hajj, A. Duval, S. Dhers, L. Avérous, *Macromolecules* **2020**, *53*, 3796.
[34] L. Jiang, Y. Tian, J. Cheng, J. Zhang, *Polym. Chem.* **2021**, *12*, 6527.
[35] Y. Tao, L. Fang, J. Zhou, C. Wang, J. Sun, Q. Fang, *ACS Appl. Polym. Mater.* **2019**, *2*, 295.
[36] Z. Zhou, X. Su, J. Liu, R. Liu, *ACS Appl. Polym. Mater.* **2020**, *2*, 5716.
[37] H. Geng, Y. Wang, Q. Yu, S. Gu, Y. Zhou, W. Xu, X. Zhang, D. Ye, *ACS Sustainable Chem. Eng.* **2018**, *6*, 15463.
[38] Y. Wang, A. Xu, L. Zhang, Z. Chen, R. Qin, Y. Liu, X. Jiang, D. Ye, Z. Liu, *Macromol. Mater. Eng.* **2022**, *307*, 2100893.
[39] X. Wang, S. Gao, J. Wang, S. Xu, H. Li, K. Chen, P. Ouyang, *Chin. J. Chem. Eng.* **2021**, *30*, 4.
[40] K. P. Cortés-Guzmán, A. R. Parikh, M. L. Sparacin, A. K. Remy, L. Adegoke, C. Chitrakar, M. Ecker, W. E. Voit, R. A. Smaldone, *ACS Sustainable Chem. Eng.* **2022**, *10*, 13091.
[41] S. Wang, S. Ma, Q. Li, X. Xu, B. Wang, K. Huang, Y. Liu, J. Zhu, *Macromolecules* **2020**, *53*, 2919.
[42] H. Wang, S. Guo, X. Zhang, Y. Liu, T. Liu, H. Yu, *Mater. Des.* **2022**, *221*, 110924.
[43] L. Yu, Z. Lei, X. Sun, P. Ding, A. Wesche, Y. Jin, W. Zhang, R. Long, *ACS Appl. Polym. Mater.* **2021**, *3*, 5808.
[44] B. B. Roy, C. Myers, *Toxic Subst. Mech.* **2015**, *16*, 151.
[45] L. Shan, K. N. E. Verghese, C. G. Robertson, K. L. Reifsnider, *J. Polym. Sci., Part B: Polym. Phys.* **1999**, *37*, 2815.
[46] S. Subramaniyan, M. Bergoglio, M. Sangermano, M. Hakkarainen, *Glob Chall* **2023**, *7*, 2200234.
[47] A. Breuillac, A. Kassalias, R. Nicolaÿ, *Macromolecules* **2019**, *52*, 7102.
[48] H. Memon, Y. Wei, C. Zhu, *Mater. Today Commun.* **2021**, *29*, 102814.
[49] I. Azcune, A. Huegun, A. Ruiz De Luzuriaga, E. Saiz, A. Rekondo, *Eur. Polym. J.* **2021**, *148*, 110362.
[50] M. Hayashi, *Nihon Reoroji Gakkaishi* **2022**, *50*, 15.
[51] C. J. Kloxin, C. N. Bowman, *Chem. Soc. Rev.* **2013**, *42*, 7161.
[52] W. Denissen, G. Rivero, R. Nicolaÿ, L. Leibler, J. M. Winne, F. E. Du Prez, *Adv. Funct. Mater.* **2015**, *25*, 2451.
[53] A. Liguori, M. Hakkarainen, *Macromol. Rapid Commun.* **2022**, *43*, e2100816.
[54] F. Van Lijsebetten, Y. Spiesschaert, J. M. Winne, F. E. Du Prez, *J. Am. Chem. Soc.* **2021**, *143*, 15834.
[55] S. Dhers, G. Vantomme, L. Avérous, *Green Chem.* **2019**, *21*, 1596.
[56] H. Zheng, Q. Liu, X. Lei, Y. Chen, B. Zhang, Q. Zhang, *J. Polym. Sci., Part A: Polym. Chem.* **2018**, *56*, 2531.
[57] N. J. Van Zee, R. Nicolaÿ, *Macromolar EngInerring: From Precise Synthesis to Macroscopic Materials and Applications*, Wiley, New York **2022**.
[58] T. Debsharma, V. Amfilochiou, A. A. Wróblewska, I. De Baere, W. Van Paepegem, F. E. Du Prez, *J. Am. Chem. Soc.* **2022**, *144*, 12280.
[59] L. E. Porath, C. M. Evans, *Macromolecules* **2021**, *54*, 4782.
[60] H. Lu, S. Du, *Polym. Chem.* **2014**, *5*, 1155.
[61] W. M. Huang, Z. Ding, C. C. Wang, J. Wei, Y. Zhao, H. Purnawali, *Mater. Today* **2010**, *13*, 54.
[62] A. Liguori, S. Subramaniyan, J. G. Yao, M. Hakkarainen, *Eur. Polym. J.* **2022**, *178*, 111489.
[63] T. X. Wang, H. M. Chen, A. V. Salvekar, J. Lim, Y. Chen, R. Xiao, W. M. Huang, *Polymers* **2020**, *12*, 2330.
[64] L. T. J. Korley, T. H. Epps, B. A. Helms, A. J. Ryan, *Science* **2021**, *373*, 66.
[65] X. Xu, S. Ma, J. Wu, J. Yang, B. Wang, S. Wang, Q. Li, J. Feng, S. You, J. Zhu, *J. Mater. Chem. A* **2019**, *7*, 15420.
[66] S. Wang, S. Ma, Q. Li, W. Yuan, B. Wang, J. Zhu, *Macromolecules* **2018**, *51*, 8001.
[67] K. Hong, Q. Sun, X. Zhang, L. Fan, T. Wu, J. Du, Y. Zhu, *ACS Sustainable Chem. Eng.* **2022**, *10*, 1036.

5.2 Publication 2: Lignin-based Vinylogous Urethane Vitrimers

This work was carried out in collaboration with Nils Sobania. The project began as Nils' master's thesis and was later continued to synthesize the prepared materials and carry out the characterizations.

Recyclability by design involves a preliminary assessment of the feedstock materials to facilitate more sustainable solutions. Instead of using preprocessed small molecules of high purity and a distinct knowledge about their functional groups and reactivity, this work highlights the use of a crude feedstock material derived from lignocellulosic biomass. Lignin is one of the most abundant biopolymers globally and offers significant potential as a renewable feedstock for high-performance polymers. However, it remains underutilized in industry, primarily due to its irregular macromolecular structure, residues from the production process, and challenges in closed-loop recycling without degradation during the recycling steps.

In this work, catalyst-free vinylogous urethane vitrimers are synthesized from lignosulfonate and enzymatic lignin sources using environmentally friendly processes, thereby aligning with the principles of green chemistry. Especially, waste-wood lignosulfonate offers promising potential since it is otherwise mostly used thermally *via* incineration. The comparison between lignosulfonates and enzymatically purified lignin for vitrimers presents the possibility to utilize the described synthetic routes and material compositions for other lignin sources. The study includes an in-depth investigation of the morphology of the lignin precursors and the resulting materials, thereby enhancing the understanding of vitrimers based on organo-composites comprising lignin particles and smaller amine linkers.

The production of lignin-based vitrimers starts with a direct acetoacetylation process, which uses a water/acetone mixture instead of toxic solvent combinations. This goes along with the principles of green chemistry. Bio-based amines are then used in the condensation reaction to form neat networks, which can be processed *via* heat compression into lignin-based vitrimer films. The ratio between the amines and the formed vinylogous urethanes was found to influence the thermal and mechanical properties, as well as the lignin source and the use of a small molecule linker.

Notably, the glass transition of the lignin molecules themselves significantly influences the stress-relaxation behavior, underscoring the importance of carefully analyzing the materials and the assumption of exchange reactions above the T_g. The study revealed that the activation energies are strongly influenced by the T_g, lignin source, and microstructure. The relaxation processes involve complex segmental motions and are based on transamination reactions, influenced by the amount of free amines. The lignin vitrimers can be reprocessed through thermomechanical grinding and heat compression cycles.

This recycling method improves the evaluation of vitrimer recyclability, as grinding affects the entire material, not just select parts. As anticipated, the mechanical performance exhibits structural changes and degradation, affecting properties such as mechanical moduli and elongation.

A new processing technique for lignin-based vinylogous urethane vitrimers is introduced, utilizing injection molding at elevated temperatures and pressures, with mechanical performance comparable to that of the neat material. This conventional thermoplastic technique paves the way for potential large-scale manufacturing and integration into industrial production processes. Possible applications, such as protective coatings, damping materials, and recyclable containers, are also demonstrated through measurements of UV-light blocking, Shore D hardness, and resistance to fatigue under cyclic loading. The industrial applicability of VU-systems is further investigated in the unpublished results, as presented in Chapter 6.2.4.

All in all, this research presents new advances in sustainable polymer engineering, including a closed carbon cycle achieved by using eco-friendly lignin vitrimers with reprocessability, as well as desirable mechanical and optical properties. The integration of simple, scalable processes and the detailed understanding of the materials' microstructure contributes to the growing research field of greener polymer alternatives by waste valorization and the development of green production processes.

Reproduced from “Bio-based vinylogous urethane vitrimers from waste-wood lignosulfonate and enzymatic lignin: explorations in stress relaxation behavior and mechanical strength,” *J. Mater. Chem. A*, **2025**, *13*, 29120–29137, (doi.org/10.1039/d5ta02533h) with permission from the Royal Society of Chemistry. The related supporting information is available in Section 9.3.

Journal of Materials Chemistry A

ROYAL SOCIETY OF CHEMISTRY

PAPER

View Article Online
View Journal | View Issue

Cite this: J. Mater. Chem. A, 2025, 13, 29120

Bio-based vinylogous urethane vitrimers from waste-wood lignosulfonate and enzymatic lignin: explorations in stress relaxation behavior and mechanical strength†

Florian C. Klein, [a] Nils Sobania [a] and Volker Abetz *[ab]

Lignin is one of the most promising materials for a biocircular economy. It is not only the most abundant biomaterial, but it has also gathered significant interest in both academia and industry as a new feedstock for plastics. Lignin is primarily produced as a byproduct in the pulping industry, but it can also be extracted from lignocellulosic biomass contributing to waste-wood valorization. The combination with thermomechanical reprocessable polymers, such as vitrimers, enables the synthesis of thermosetting materials with high mechanical strength that can be reused. Herein, we present catalyst-free vinylogous urethane vitrimers based on lignosulfonate and enzymatic lignin, using a commercial bio-based diamine and a bio-based diol linker. Materials are synthesized following green chemistry principles using a direct acetoacetylation process of lignin in non-toxic solvents, which can subsequently be used to produce homogeneous materials. The thermomechanical properties and recyclability over five cycles demonstrate that the materials represent a promising class of tougher, greener, and sustainable vitrimers. The stress-relaxation properties of the materials are characterized through a detailed study focusing on the influence of the glass transition temperature of the materials. Mechanical testing yielded elastic moduli of up to 0.83 GPa and tensile strengths of up to 30 MPa. Additionally, processing through injection molding was demonstrated, producing homogeneous samples for tensile testing.

Received 30th March 2025
Accepted 17th July 2025

DOI: 10.1039/d5ta02533h

rsc.li/materials-a

Introduction

New polymeric materials must possess a lot of characteristics to meet the societal demand for more sustainable options.[1] Recyclable bioplastics can enhance the sustainability of the commercial plastic life cycle as part of a circular economy, particularly when they adhere to green chemistry principles.[2,3] Macromolecules derived from biomass, such as starch, cellulose, mycelium, and lignin from lignocellulosic biomass, are favorable feedstocks for the design of new, more sustainable multifunctional polymers.[4–8] Lignin is derived as a primary component of plant biomass and, along with cellulose and hemicellulose, forms lignocellulosic biomass, which is the most abundant type of biomass on the planet.[9,10] Technical lignin is produced as a byproduct of different pretreatments or separation processes that use lignocellulosic biomasses as raw material, such as in pulp or second-generation ethanol production. The pulp mill remains the main commercial source of lignin.[11] While polysaccharides such as cellulose and hemicellulose are utilized in the production of bio-based compounds, lignin remains underutilized, despite its high potential as a substitute for the high demand of fossil-based raw materials.[2,3,12–14] Only 5% of the produced lignin is used in low-value applications, such as fillers, or is burned for energy and electricity.[15] The remaining lignin is either incinerated as a low-grade fuel or landfilled.[16] However, recent focus in academia and industry on the structure and valorization of lignin and its derivatives highlights their significant potential and interest for advanced applications.[15,17–19] In particular, lignin is used in composite materials, energy storage materials, as a starting material for small aromatic molecules such as vanillin, in lignin-based nanoparticles, and in active food packaging.[16,20–28] Currently, lignosulfonates account for 90% of the total commercial lignin market and approximately 1.8 million metric tons are produced annually.[29] Due to the presence of sulfonate groups, lignosulfonates are anionically charged and therefore water soluble.[30] This allows for the use of water-based solvent systems throughout the formation of lignosulfonate-based materials as potential alternatives for fossil-based products. For instance,

[a]Institute of Physical Chemistry, University of Hamburg, Grindelallee 117, 20146 Hamburg, Germany

[b]Institute of Membrane Research, Helmholtz-Zentrum Hereon, 21502 Geesthacht, Germany. E-mail: volker.abetz@hereon.de

† Electronic supplementary information (ESI) available. See DOI: https://doi.org/10.1039/d5ta02533h

these are used in applications such as animal feed, pesticides, surfactants, and plasticizers in concrete admixtures.[31–33]

Integrating the concepts or recyclability, renewability, and green chemical processes into the formation of polymer networks provides a framework for designing sustainable materials. The combination of natural bioresources, such as lignin, with the concept of dynamic covalent chemistry imparts mechanical reprocessing and recycling properties to the polymeric materials.[34] The concept of vitrimers was first introduced in 2011 by the group of Leibler, demonstrating materials with transesterification exchange reactions which were reprocessable *via* injection molding.[35] In most cases of vitrimers, the reprocessing is limited to compression molding. The group of Du Prez demonstrated extrusion and injection molding for vinylogous urethane (VU) vitrimers with low-viscosity.[36] Vitrimers become malleable and show a thermoplastic flow behaviour when exhibited to a certain stimulus, as they are dynamic associative networks which can rearrange their crosslinks at a constant crosslink density.[37] This phenomenon occurs through stimulus-activated exchange reactions (*e.g.*, temperature, solvent, light), in which inter-polymer bonds are simultaneously cleaved and reformed, thus combining the beneficial features of both thermosets and thermoplastics.[38] When the rate of exchange reactions becomes sufficiently fast, the viscosity of vitrimers is primarily controlled by these reactions, resulting in a decrease in viscosity. These characteristics enable for self-healing, recycling, injection molding, and an overall increased lifecylcle.[34] The valorization and utilization of lignin in vitrimer materials were investigated based through various associative dynamic covalent adaptable chemistries, including transesterification, transacetalization, transcarbomylation, imine bond exchange, transalkylation, and disulfide exchange.[39–44]

VU vitrimers are based on transamination dynamic covalent chemistry and do not require an external catalyst. Here, acetoacetylated monomers are crosslinked with an excess of amine linker molecules, allowing for molecular network rearrangements at elevated temperatures.[45] Krall *et al.* highlighted the potential of the multi-hydroxy building block of Kraft lignin monomers as precursors for vinylogous urethane vitrimers, as they can be easily acetoacetylated using *tert*-butyl acetoacetate (TBAA).[46] However, the first work incorporating lignin into the design of VU vitrimers was published in 2023 by Sougrati *et al.*, utilizing organosolv lignin. The organosolv lignin was modified in a mixture of poly(ethylene glycol) (PEG) using ethylene carbonate. After acetoacetylation, the mixtures were vitrified in chloroform ($CDCl_3$) through condensation with hexamethylenediamine, achieving a lignin content of 30–40 wt%. The different network structures exhibited glass transition temperatures (T_gs) from −28 to 18 °C.[47] Liu *et al.* focused on acetoacetylated purified alkali wheat straw lignin (Protobind 1000 by LignoPure), obtained through soda pulping, and utilized a bio-based fatty acid amine (Priamine™ 1075) to form fully bio-based vitrimer materials with a lignin content of 40–50 wt% for adhesive applications. The acetoacetylation was carried out in 1,4-dioxane (DOX) with TBAA, forming the vitrimers in 2-methyl tetrahydrofuran, with a T_g range of 87–134 °C and an *E* modulus of 184 MPa. The materials showed fast stress-relaxation (9 s at 180 °C) using a single Maxwell model to fit the stress-relaxation.[48] Recently, Sougrati *et al.* prepared VU lignin vitrimers from organosolv lignin with 20–50 wt% lignin, synthesizing the acetoacetylated lignin with 2,2,6-trimethyl-4*H*-1,3-dioxin-4-on (TMDO). The vitrimers were formed in $CDCl_3$ and could be chemically recycled in an acidic solution. They obtained *E* moduli of up to 71 MPa and stresses at break of up to 3.8 MPa.[49]

In this work, we present the synthesis and characterization of bio-based recyclable vinylogous urethane lignin vitrimers synthesized *via* direct acetoacetylation with TBAA, utilizing lignosulfonate (Ls) from native biomass without further purification. Additionally, to compare the influence of impurities and structure of large-scale technical Ls to the material, Lignova™ Crude (LnC) and Lignova™ Pure (LnC) from Fibenol OÜ derived from a mild enzymatic hydrolysis process were used to prepare materials. The acetoacetylated lignin molecules are combined with bio-based Priamine™ 1073 linkers. An acetoacetylated bio-based poly(oxy-1,3-propanediyl) (PPD) was used as a linear linker. We present synthetic procedures without the use of toxic solvents such as DOX, enabling the formation of lignin-based vitrimers in a non-toxic mixture of water/acetone. To the best of our knowledge, this is the first study on acetoacetylated technical lignin derived from the sulfite process and enzymatic lignin sources, conducted with the substitution of toxic solvents. The content of lignin was between 40–62 wt% and the VU chemistry enables fast processing *via* heat compression at 180 °C for 30 min with a pressure of 1.9–2.5 MPa. Furthermore, we present an in-depth characterization of the stress-relaxation behavior of the materials *via* a stretched exponential fit using the Kohlrausch–Williams–Watts (KWW) function for lignin-based VU vitrimers, demonstrating the influence of the chemical microstructure of the vitrimers and the T_g influence of both the linkers and the lignin molecules.[50] The described processes and materials will be useful as recyclable damping materials, coatings, or containers that provide protection against environmental stress while offering a closed carbon-cycle and industrial processing methods, such as injection molding.

Experimental

Materials

Acetone (technical grade, BCD Chemie GmbH), *tert*-butyl acetoacetate (TBAA, TCI, 98%), calcium chloride ($CaCl_2$, anhydrous, Merck KGaA, 100%), calcium hydride (Merck KGaA, 100%), chloroform-d_1 ($CDCl_3$, Deutero GmbH, 99.8%), dimethyl sulfoxide (DMSO, Merck, 99%), dimethyl sulfoxide-d_6 (DMSO-d_6, Deutero GmbH, 99.8%), *N*,*N*-dimethylformamide (DMF, VWR, 99.5%), *N*,*N*-dimethylformamide-d_7 (DMF-d_7, Deutero GmbH, 99.5%), *endo*-*N*-hydroxy-5-norbonene-2,3-dicarboxylic acid imide (NHND, Alfa Aesar, 97%), lignosulfonate (Ls, dealkaline sodium lignosulfonate L0045, prepared from needle-leaved trees and broad-leaved trees through treatment of sodium sulfite, TCI), Lignova™ Crude (LnC, prepared from hard-wood by mild thermo-mechanical pre-treatment process with enzymatic hydrolysis, Fibenol OÜ), Lignova™ Pure (LnP,

prepared from hard-wood by mild thermo-mechanical pre-treatment process with enzymatic hydrolysis, Fibenol OÜ), phosphorus trichloride (Fisher Scientific, 99%), pinacol (TCI, >98%), bio-based poly(oxy-1,3-propanediyl) (M_n = 400–600 g mol^{-1}, PPD, Sigma-Aldrich), Priamine™ 1073 (Priamine, M = 534.59 g mol^{-1}, Croda), tetrahydrofuran (THF, Fisher Scientific, 99.5%), tris(acetylacetonato)chromium(III) ($Cr(acac)_3$, Fisher Scientific) were purchased and used as received. The crude, brownish 2,2,6-trimethyl-4*H*-1,3-dioxin-4-one (TMDO, Sigma-Aldrich, >93%) was purified by vacuum distillation prior to use to obtain a pure colorless liquid. Triethylamine (Grüssing) was pre-dried over molecular sieves (4 Å) for 4 days. Then, calcium hydride was added and the white suspension was refluxed for 24 h. Anhydrous triethylamine was obtained by distillation and stored under inert gas over molecular sieves. *N*,*N*-dimethylformamide (anhydrous, DMF, Fisher Scientific, 99.8%), pyridine (anhydrous, Fischer Scientific, 99.8%), and *n*-pentane (anhydrous, Thermo Scientific, >99.5%) were stored over molecular sieves (4 Å) and under inert gas atmosphere. The NMR solvent mixtures DMF/DMF-d_7 and $CDCl_3$/pyridine were stored over molecular sieves (4 Å) to remove residual moisture.

Instrumentation

Nuclear magnetic resonance spectroscopy (^{1}H NMR, ^{13}C NMR, heteronuclear single quantum correlation spectroscopy (HSQC), and heteronuclear multiple bond correlation spectroscopy (HMBC)). Nuclear magnetic resonance spectroscopy (^{1}H NMR, ^{13}C NMR, heteronuclear single quantum correlation spectroscopy (HSQC), and heteronuclear multiple bond correlation spectroscopy (HMBC)) were performed on a Bruker Avance III HD (600 MHz or 400 MHz) and a Bruker Avance I (500 MHz) spectrometer (Bruker Corporation, Billerica, United States) with $CDCl_3$ or DMSO-d_6 as solvent. Sample concentrations were between 10–60 mg mL^{-1}, and measurements were recorded at 298 K. When needed for quantification, DMF was added as internal standard. Data processing was carried out with MestReNova (14.1.0, Mestrelab Research S.L, Santiago de Compostela, Spain).

^{31}P NMR spectra. ^{31}P NMR spectra were recorded according to a quantitative ^{31}P NMR protocol with a frequency of 243 MHz, 256 scans, an inverse gated decoupling pulse (zigig), a spectral width of 100 ppm, an acquisition time of 2.6913 s, a relaxation delay D1 of 10 s, and the center of spectrum at 140 ppm. As the solubility of the different lignin types varied, two different anhydrous solvent systems, DMF-d_7/DMF/pyridine or $CDCl_3$/pyridine were used as solvent.[51,52] Lignova™ Crude and Lignova™ Pure were dissolved in $CDCl_3$/pyridine and lignosulfonate was dissolved in DMF-d_7/DMF/pyridine. Prior to each measurement, all samples were stored at 50 °C under vacuum for at least 24 h and subsequently in a glass desiccator over anhydrous calcium chloride. For measurements in DMF-d_7/DMF/pyridine, 30 mg of lignin were dissolved in 338 μL of a mixture of DMF-d_7 and DMF (1 : 1, v/v). An amount of 75 μL of an internal standard solution of NHND in anhydrous DMF (18 mg mL^{-1}) and 75 μL of a relaxation agent solution of $Cr(acac)_3$ in anhydrous pyridine (5.7 mg mL^{-1}) were added under stirring. Afterwards the solution was stirred for 12 h. The reactive compound 2-chloro-4,4,5,5-tetramethyl-1,3,2-dioxaphospholane (ClTMDP, 75 μL) was added 15 min before analysis and left to react for 5 min while stirring.[53] For analysis, the mixture was transferred into an NMR-tube. The signal of phosphitylated NHND at 152.78 ppm was used as internal standard. For measurements in $CDCl_3$/pyridine, an amount of 30 mg lignin was dissolved in 500 μL of a mixture of anhydrous pyridine and $CDCl_3$ (1.6 : 1, v/v) under stirring. An amount of 100 μL of an internal standard solution (anhydrous pyridine and $CDCl_3$ (1.6 : 1, v/v)) containing 18 mg mL^{-1} NHND and 5 mg mL^{-1} $Cr(acac)_3$ was added and the obtained mixture was stirred for 12 h. The reactive compound ClTMDP (75 μL) was added 15 min before analysis and left to react for 5 min while stirring. For analysis, the mixture was transferred into an NMR-tube. The signal of TMDP + H_2O at 132.20 ppm was used as internal standard. Data processing was carried out with MestReNova (14.1.0, Mestrelab Research S.L, Santiago de Compostela, Spain).

Electrospray ionization (ESI). Electrospray ionization (ESI) was measured by a Bruker maXis ESI-Q-TOF device (Bruker Corporation, Billerica, United States) coupled with Dionex Ultimate 3000 UPCL (Dionex Corporation, Sunnyvale, United States) and direct injection. Data processing was carried out with MestReNova (14.1.0, Mestrelab Research S.L, Santiago de Compostela, Spain).

Attenuated total reflection-Fourier transformation-infrared (ATR FT-IR). Attenuated Total Reflection-Fourier Transformation-Infrared (ATR FT-IR) were measured in the range of 4400–600 cm^{-1} with a resolution of 4 cm^{-1} and 64 scans using a Bruker FT-IR Vertex 70 spectrometer (Bruker Optics GmbH & Co. KG, Ettlingen, Germany). Measurements and data processing were carried out with Opus (8.7, Bruker Optics GmbH & Co. KG, Ettlingen, Germany).

Elemental analysis (CHNSO). Elemental analysis (CHNSO) was performed on a Unicube analyzer (Elementar Analysensysteme GmbH, Langenselbold, Germany). Each analysis was carried out twice.

Grinding. Grinding of materials was performed using a Mixer Mill MM 400 (RETSCH GmbH, Haan, Germany) with steel screw-top jars and a steel grinding ball under horizontal oscillation. For cryogenic grinding, the loaded steel jar was cooled in liquid nitrogen for 15 min with subsequent grinding. Exact parameters are listed in Table S1, ESI.†

Heat compression. Heat compression was carried out with a 2-column lab press PW 10 with a heating plate system HKP 500 160 × 160 mm and a TRG 3 temperature control unit (Paul-Otto Weber GmbH, Remshalden, Germany). The lignin-based vitrimers were filled into a custom-built stainless-steel compression mold (circular geometry, d = 5 cm, Fig. S1, ESI†). The samples were heated for 5 min before pressing. Heat compression was performed to produce homogeneous bubble-free black polymer sheets. Exact parameters are listed in Table S1, ESI.†

Solubility and swelling tests. Solubility and swelling tests were performed by addition of 1 mL of solvent (deionized water, acetone) to approximately 50 mg of the respective sample in

a glass vial. The vials were subsequently sealed for 24 h and stored at 25 °C. Afterwards, the supernatant was decanted, and the sample was weighed and stored at 80 °C under reduced pressure for at least 24 h until a constant mass was measured.

Thermogravimetric analysis (TGA). Thermogravimetric analysis (TGA) was carried out on a TG 209 F1 Libra (NETZSCH Gerätebau GmbH, Selb, Germany) to determine the mass loss during heat treatment. A temperature range of 25–700 °C with a heating rate of 10 K min^{-1} under ambient atmosphere (oxygen) was used in a flow rate of 20 mL min^{-1}. Isothermal measurements were carried out at 180 °C for 3 h with ambient (oxygen) atmosphere in a flow rate of 20 mL min^{-1}. An amount of 10–15 mg was weighed into an aluminum crucible. Data processing was performed with Proteus Analysis (8.0.3, NETZSCH-Gerätebau GmbH, Selb, Germany).

Differential scanning calorimetry (DSC). Differential scanning calorimetry (DSC) was carried out on a 204 F1 Phoenix (NETZSCH Gerätebau GmbH, Selb, Germany) to determine the thermal properties of the lignins and lignin-based materials. An amount of 5–10 mg was weighed into an aluminum crucible. The heating rate was set to 10 K min^{-1} or 20 K min^{-1} using a nitrogen atmosphere with a flow rate of 20 mL min^{-1}. A temperature range between −50–200 °C or −80–250 °C was used in three heating cycles. The thermal properties were analyzed determining using the DSC data of the second heating curve. Data processing was performed with Proteus Analysis (8.0.3, NETZSCH-Gerätebau GmbH, Selb, Germany).

Optical microscopy (OM). Optical microscopy (OM) images were taken with a Keyence VHX-6000 digital microscope with a VH-Z20UR lens (Keyence Deutschland GmbH, Neu-Isenburg, Germany).

Scanning electron microscopy (SEM). Scanning electron microscopy (SEM) images were recorded on a LEO Gemini 1550 (Carl Zeiss, Oberkochen, Germany). Secondary electrons were detected with an Everhart-Thornley detector, operating with 1–5 kV and 50–100 pA.

Dynamic light scattering (DLS). Dynamic light scattering (DLS) analysis was carried out using an ALV/LSE-5003 multi-tau digital correlator and a He–Ne laser (633 nm, 35 mW) using a measurement angle of 90° and a duration of 30 s. Three measurements were performed for each sample and the mean value was calculated. The temperature was set to 30 °C with a toluene bath. The data was analyzed using a MATLAB R2021a script written by B. Hankiewicz. The hydrodynamic radius R_h was calculated assuming spherical particle geometry starting at a minimum radius of 5 nm. The solutions for the measurement were prepared dissolving the analyte with a concentration of 3 mg mL^{-1} in a mixture of acetone/water (9 : 1, v/v) or DMSO.

Atomic force microscopy (AFM). Atomic force microscopy (AFM) investigations of the vitrimer films were performed in intermittent contact mode using a JPK Nanowizard (Bruker Corporation, Billerica, United States of America) microscope with a Si-tip ($f = 280$ kHz, $r = 10$ nm).

Energy-dispersive X-ray spectroscopy (EDX). Energy-dispersive X-ray spectroscopy (EDX) was carried out using the SEM LEO Gemini 1550 (Carl Zeiss, Oberkochen, Germany) with its adjunct EDX analyzer Ultim Max 100 Silizium Drift Detector (Oxford Instruments, High Wycombe, United Kingdom).

Stress–strain measurements. Stress–strain measurements were performed at room temperature ($T = 23$ °C) on a universal testing machine zwickiLine Z 5.0 TH (ZwickRoell GmbH & Co. KG, Ulm, Germany) using a 5 kN load cell. The measurements were carried out in accordance with the test standard DIN EN ISO 527-1. The initial force was set to 0.1 MPa, and the clamping length was 13.24 mm. The elastic modulus was determined at a speed of 1 mm min^{-1} and the rest of the test was carried out at 10 mm min^{-1}. Data was processed using TestXpert II (3.71, ZwickRoell GmbH & Co. KG, Ulm, Germany). Test specimens were punched out with a cutting press type ZCP020 (ZwickRoell GmbH & Co. KG, Ulm, Germany) with the attachment for test specimens of type 5 B (according to DIN EN ISO 527-2-5B). Durability tests were performed in an oscillating procedure, with a speed of 1 mm min^{-1} until a force of 50 N was reached. The initial force was set to 0.05 N, and the clamping length was 5 mm. Afterwards, the stress was released until a force of 0.1 N was reached. 1000 consecutive cycles were performed on a test specimen with the dimensions 10 × 10 × 1 mm.

Dynamic-mechanical analysis (DMA). Dynamic-mechanical analysis (DMA) was carried out with an Anton Paar MCR 502 rheometer (Anton Paar GmbH, Graz, Austria) using a plate–plate geometry with a diameter of 8 mm. The measurements were carried out using a heat chamber (Anton Paar CTD180) with a nitrogen atmosphere, a Peltier plate temperature control and a normal force of 1 N. The gap between the upper and the lower plate was usually set to 1 mm and each sample was annealed for at least 3 min before starting the respective measurement. Prior to all rheological measurements, amplitude sweeps between 0.001% and 10% shear strain γ were performed at a constant angular frequency of 6.28 rad s^{-1} at 110 °C. This should ensure that the chosen strain amplitude γ_0 is located within the linear viscoelastic regime of the material, so that the storage modulus G' and the loss modulus G'' were independent of strain. Temperature-sweep measurements were carried out in oscillatory mode with a constant angular frequency of 6.28 rad s^{-1} at a constant shear strain of 0.01% in the temperature range of 150–0 °C at a rate of 2 K min^{-1}. Stress relaxation measurements were carried out with a shear strain of 1% at temperatures in the range of 180–110 °C. Data processing was performed with RheoCompass (1.32, Anton Paar GmbH, Graz, Austria). Specimens for the DMA were punched out with an 8 mm tool.

UV-light irradiation testing. UV-light irradiation testing was performed using an OmniCure® AC 450 UV lamp (Polytec GmbH, Waldbronn, Germany) with a wavelength of 365 nm and an optical power of 45 W. A GTC 400 C Professional thermal imaging camera (Robert Bosch Power Tools GmbH, Leinfelden-Echterdingen, Germany) with a 19 200-pixel infrared sensor was used to capture images after 10 s, 60 s, and 300 s of irradiation.

Injection molding. Injection molding was carried out using a MiniJet Pro (Thermo Fisher Scientific, Waltham, United States) with a melt temperature of 250 °C, a mold temperature of 220 °C, and an injection pressure of 1000 bar. A typical injection molding protocol was carried out as follows: the

ground sample was heated for 5 min. Then, the injection pressure was applied for 45 s with a subsequent rest time of 20 s at 100 bar using a mold for tensile test specimens DIN EN ISO 527-2-5B or a rectangular mold of the size 10 × 10 × 4 mm.

Shore hardness. Shore hardness was measured using a Manual Shore test stand TI-AC with an analogue Shore hardness tester HBA 100-0 (Kern & Sohn GmbH, Baldingen-Frommern, Germany) and a Manual Shore test stand TI-D with an analogue Shore hardness tester HBD 100-0 (Kern & Sohn GmbH, Baldingen-Frommern, Germany). The Shore-Hardness was determined according to DIN ISO 7619-1 using a material block formed by injection molding of a size of 10 × 10 × 4 mm and a time of 15 s, before the hardness was measured. An average of five measurements was used to calculate the hardness according to the Shore D scale.

Synthetic procedures

Acetoacetylation of lignosulfonate (Ls). Lignosulfonate (30.45 g) was dissolved in DMSO (90 mL) at 80 °C under stirring until a homogeneous dark brown mixture was obtained. Afterwards, TBAA (58 mL) was added and the mixture was heated to 135 °C for 6 h, while the byproduct *tert*-butanol was removed by distillation during the reaction. The solvent was removed under reduced pressure at 135 °C until a black solid was obtained. Subsequently, the obtained solid was ground into a brown powder and further dried under vacuum at 60 °C for at least 15 h. The dried product was stored in a glass desiccator over $CaCl_2$.

Acetoacetylation of Lignova™ Crude (LnC). Lignova™ Crude (20.08 g) was dissolved in DMSO (120 mL) at 120 °C under stirring until a homogeneous dark brown mixture was obtained. Afterwards, TBAA (33 mL) was added and the mixture was heated to 135 °C for 6 h, while the byproduct *tert*-butanol was removed by distillation during the reaction. The solvent was removed under reduced pressure at 135 °C until a black solid was obtained. Subsequently, the obtained solid was ground into a brown powder and dried under vacuum at 60 °C for at least 15 h. The dried product was stored in a glass desiccator over $CaCl_2$.

Acetoacetylation of Lignova™ Pure (LnP). Lignova™ Pure (20.13 g) was dissolved in DMSO (70 mL) at 80 °C under stirring until a homogeneous dark brown mixture was obtained. Afterwards, TBAA (43 mL) was added and the mixture was heated to 135 °C for 6 h, while the byproduct *tert*-butanol was removed by distillation during the reaction. The solvent was removed under reduced pressure at 135 °C until a black solid was obtained. Subsequently, the obtained solid was ground into a brown powder and dried under vacuum at 60 °C for at least 15 h. The dried product was stored in a glass desiccator over $CaCl_2$.

Acetoacetylation of bio-based poly(oxy-1,3-propanediyl) (PPD). The synthesis was performed according to a standard procedure for the acetoacetylation of hydroxy groups.[54] TMDO (38 mL) and PPD (50.11 g) were mixed *via* stirring at room temperature. After a homogeneous solution was obtained, the mixture was heated to 135 °C under stirring. The byproduct acetone, dehydroacetic acid and residual TMDO were removed by distillation. The mixture was dried in vacuum at 135 °C to give acetoacetylated PPD (APPD) as a dark red liquid (6.90 g, 97%).

Vitrimer formation in water/acetone. The formation of vitrimers was performed in a mixture of water and acetone (1 : 4, v/v) to ensure a sustainable and environmentally friendly route. Exact parameters are listed in Table S1, ESI.† An exemplary synthesis was conducted as follows: Acetoacetylated lignin was dissolved in 10 mL of the solvent mixture at ambient temperature (23 °C) under stirring until a homogeneous black mixture was obtained, which usually took 60 min. If APPD was used, it was added together with the lignin. Subsequently, the amine linker Priamine™ 1073 was added while vigorously stirring. The mixture was left to react for 30 min without stirring. Then, the black gel-like mixture was carefully heated step-wise up to 120 °C while stirring. The black solid was dried under reduced pressure at 100 °C for at least 13 h and subsequently at 150 °C for 1 h. The obtained black material was ground with a ball mill into a brownish powder. A film of 1 mm thickness was pressed using heat compression in a custom-made stainless-steel mold with a diameter of 5 cm (Fig. S1, ESI†).

Results and discussion

Acetoacetylation of lignosulfonates and enzymatic lignin

The variety and complexity of lignin's structure and functional groups are advantageous for many applications. However, underlying limitations such as poor solubility and barriers to traditional analytics have been addressed, thereby increasing the suitability of lignin in many chemical processes. Different lignin resources with different degrees of purity were tested to determine the applicability of the hereby developed procedure, with lignosulfonate (Ls) as an example of a large-scale industrial grade lignin containing impurities and sulfonate, and Lignova™ Crude (LnC) as well as Lignova™ Pure (LnP) as sulfur-free lignin alternatives with higher purity. Further information on the lignins can be found in Table 1.

To achieve a reliable and reproducible acetoacetylation, the hydroxy content of the raw lignins was first determined *via* quantitative ^{31}P NMR spectroscopy to calculate the necessary amount of acetoacetylation agent, *tert*-butyl acetoacetate (TBAA). This analytical protocol involves the phosphitylation of the hydroxy (OH) groups of a lignin sample followed by ^{31}P NMR spectroscopy.[51,52,55] Depending on the solubility of the different lignins, two different solvent systems were used, consisting either of $CDCl_3$ for LnP and LnC or DMF/DMF-d_7 for Ls. For the latter, phosphitylated aliphatic hydroxy groups appear in the range of 152.0–145.5 ppm, phosphitylated phenolic hydroxy groups between 145.5–137.5 ppm, and phosphitylated carboxylic groups between 137.5–135.0 ppm, respectively (Fig. S2–S4, ESI†).[52] The amount of hydroxy groups was determined using eqn (S1) (ESI†) and are listed Table 2. Since the acetoacetylation of carboxylic groups can produce reactive and easily hydrolysable carboxylic anhydrides, these groups were not considered in the following. For Ls, LnC, and LnP, total amounts of 2.69 mmol g^{-1}, 3.68 mmol g^{-1}, and 3.50 mmol g^{-1} of non-carboxylic OH groups were determined, respectively. These

Table 1 Comparison of the different lignin sources used in this work. Structures are just examples that represent common substructures and functional groups for the respective lignin-type

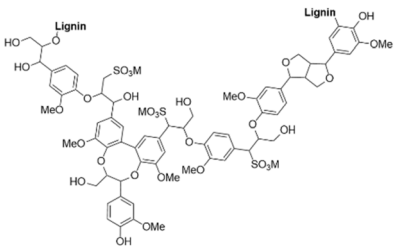

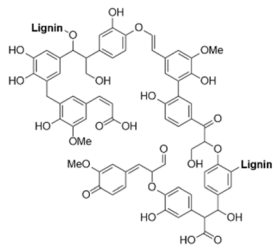

	Lignosulfonate (Ls)	Lignova™ Crude (LnC)[a]	Lignova™ Pure (LnP)[a]
Molar mass [Da]	1000–400 000 (ref. 56)	16 000 (average)	10 000 (average)
Sulfur content [%]	4.4[b]	<0.2	<0.2
Saccharide content [%]	—	<3	—
Solubility	Water/DMSO	Organic solvent	Organic solvent
Ash and ionic content [%]	18[c]	0.3	1.7

[a] Information was provided by Fibenol OÜ. [b] Determined by elemental analysis. [c] Determined by TGA displaying the amount of substance left after complete decomposition.

Table 2 Calculated amount of OH moieties from quantitative analysis of different lignins (Ls, LnC, and LnP), as well as of respective acetoacetylated species (ALs, ALnC, ALnP) by ^{31}P NMR and ^{1}H NMR spectroscopy. Conversion rates of acetoacetylated species are calculated based on the OH content determined by ^{31}P NMR for respective lignin resource

		OH content [mmol g^{-1}]		
Lignin		Aliphatic OH [mmol g^{-1}]	Phenolic OH [mmol g^{-1}]	Total non-carboxylic OH [mmol g^{-1}]
Ls		1.37	1.32	2.69
ALs		0.08	0.81	0.89
Conversion	^{31}P	94%	39%	67%
	^{1}H	—	—	61%
LnC		2.06	1.62	3.68
ALnC		0.04	1.01	1.05
Conversion	^{31}P	98%	38%	71%
	^{1}H	—	—	70%
LnP		1.51	1.99	3.50
ALnP		0.03	1.33	1.36
Conversion	^{31}P	98%	33%	61%
	^{1}H	—	—	65%

values may also include impurities, such as low molecular weight carbohydrates, which are included into the VU network, since the lignin sources were not further purified.

Especially LnC contains still remaining saccharides after the hydrolysis process which are responsible for the higher amount of aliphatic OH observed as sharp peaks in the aliphatic region of ^{31}P NMR spectroscopy.[57] The acetoacetylation of OH groups with TBAA is well known and involves the intermediate formation of reactive acetyl ketene by cleavage of TBAA under the release of *tert*-butanol, which can be removed by distillation throughout the reaction.[54] In this work, DMSO was used as an alternative solvent replacing carcinogenic DOX and DMF, which have been used for the direct acetoacetylation of lignin.[46,48] DMSO acts as a solvent and also prevents precipitation of the acetoacetylated products during the reaction.

In FT-IR, the acetoacetylated lignins present the characteristic peaks of acetoacetate bonds at around 1712 cm^{-1} and 1741 cm^{-1} (Fig. 1a). For ALs, the latter appears as a broad shoulder. The ^{1}H and ^{13}C NMR spectra are provided in the ESI, Fig. S5–S10.† A broad peak between 2.4 ppm and 1.8 ppm can be assigned to the terminal methyl group of acetoacetates (Fig. 1b).[46,49] 2D NMR techniques (HSQC and HMBC) were used to verify the signals from ^{1}H NMR (Fig. S11–S16, ESI†). The methylene group of acetoacetates can be assigned to a broad signal at 3.6 ppm, that undergoes ^{1}J coupling with the carbon atom of the methylene group at 50 ppm. Also, further characteristic ^{2}J couplings for acetoacetates can be observed *via* HMBC. Interestingly, ^{2}J coupling between the methylene group and carbonylic carbon atoms of acetoacetylated lignins can only be observed when measuring with 600 MHz, as seen in the 2D spectra of ALs, probably as a result of the low intensity of ^{13}C NMR. Quantification of acetoacetylation of ALs, ALnC, and ALnP was examined by ^{31}P NMR and ^{1}H NMR. As a result of the acetoacetylation of hydroxy moieties, the number of hydroxy groups decreases. The decreased amount of OH moieties observed in the ^{31}P NMR spectra can thus be assigned to acetoacetylated groups. Notable, this analytical procedure can distinguish the different conversions of aliphatic and phenolic hydroxy groups of lignins. A conversion of over 90% for aliphatic hydroxy groups and of 33–39% for aromatic hydroxy groups was calculated (Table 2), as it was also observed in the literature for similar model compounds.[46] The difference in conversions can be attributed to the accessibility of the aliphatic hydroxy groups and the slower rate of conversion for aromatic hydroxy groups. Additional broadened peaks between 135.0 ppm and 134.0 ppm can be assigned to the phosphitylated enol form of acetoacetates.[47] To simplify the analysis of

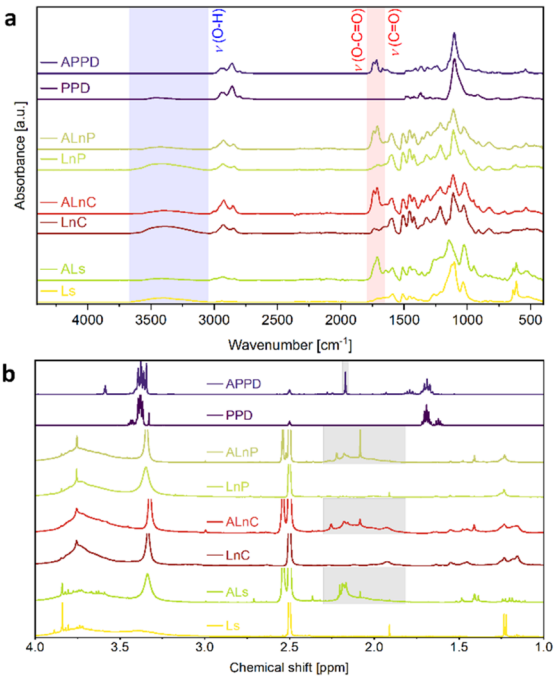

Fig. 1 (a) ATR-FT-IR spectra of the different lignin sources (Ls, LnC, and LnP), as well as of poly(oxy-1,3-propanediyl) (PPD) and the respective acetoacetylated species (ALs, ALnC, ALnP, and APPD) showing the characteristic bands of the acetoacetate group with the C=O ester (1735–1741 cm^{-1}) and C=O ketone (1712–1716 cm^{-1}) stretching vibration bands. The lignin backbone represents the C–O (995–1148 cm^{-1}), C–C (2850–3050 cm^{-1}), C=C (1148–1650 cm^{-1}), and O–H (3050–3650 cm^{-1}) stretching vibration bands. (b) ^{1}H NMR spectra of PPD, LnP, LnC, and Ls, as well as the acetoacetylated APPD, ALnP, ALnC, and ALs, showing the characteristic chemical shift of the acetoacetate groups (grey) (400 MHz, 298 K, DMSO-d_6).

acetoacetylated lignin sources, a ^{1}H NMR protocol was employed, using a known amount of DMF as an internal standard, allowing for direct calculation of acetoacetate moieties from the ^{1}H NMR (Fig. S17–S19, ESI†). Here, integrals of the proton of DMF appearing at 7.95 ppm and the broad peak between 2.4–1.8 ppm of the methylene group of the acetoacetate moieties was used to calculate the amount of acetoacetate moieties. Comparison between the results in Table 2 show the values from both NMR techniques in good agreement and only a maximum deviation of 6%. For this procedure, the highest amount of acetoacetate moieties was achieved with LnC because of the higher content of aliphatic hydroxy groups. Thus, the choice of lignin influences the acetoacetylation process and conversions can be calculated by quantitative NMR spectroscopy methods. For increasing the processability of the Ls-based vitrimers (*vide infra*), smaller molecules were added to the formulation of the materials. Therefore, bio-based poly(oxy-1,3-propanediyl) (PPD) (^{1}H NMR, ^{13}C NMR and ESI-MS spectra, Fig. S20–S22, ESI†) was used in an acetoacetylation protocol using TMDO. The successful acetoacetylation of acetoacetylated PPD (APPD) is proven by FT-IR, ^{1}H NMR, ^{13}C NMR, and 2D NMR spectroscopy (Fig. 1, H NMR, ^{13}C NMR, HSQC, and HMBC spectra are displayed in more detail in Fig. S23–S29, ESI†).

Synthesis and network formation of VU-based lignin vitrimers

Vitrimers from ALs, ALnC, and ALnP were synthesized in a mixture of acetone and water (4 : 1, v/v) by performing a condensation reaction with the amine functions of Priamine™ 1073 (Priamine), displayed in Scheme 1. A higher concentration of acetone reduces the solubility of acetoacetylated lignins, while an increased amount of water decreases solubility of Priamine. Therefore, a 4 : 1 (v/v) ratio of acetone to water was found as optimal for the formation of vinylogous urethanes, ensuring adequate solubility of all reactants. In the case of VU-(ALs/APPD$_x$-Pri)$_{0.6}$-Vitrimers, APPD was added to the mixture to ensure homogeneous materials. Especially for ALs-based systems, it was found that a higher content of lignin (>55 wt%) resulted in brittle materials, which were too brittle to be processed (Fig. S30, ESI†). By adding APPD as a plasticizer, homogeneous films can be produced and samples with three different weight percentages of APPD (5, 10, 15 wt%) were investigated. To minimize the factors of the amine-linker contributing to changes in material behavior and properties, the amount of amines was kept constant. This results in changing both the amount of lignin and APPD in the sample series. All vitrimer formulations are listed in Table S1, ESI† with the mass fractions of lignin, APPD, and amine building block listed in Table 3.

After a homogeneous mixture was obtained, Priamine was added, leading to gelation, which indicated a crosslinking reaction. Subsequently, the solvent and byproducts were removed, and the black residue was ground into a powder. This procedure ensures a homogeneous distribution of acetoacetylated lignin across the entire material. By using an excess of amine, the transamination reaction can be triggered by a thermal stimulus, which is the required dynamic exchange reaction for the vitrimer.[58] The excess of amines can be expressed by the *R*-value, which is the ratio of amine to acetoacetate functions. Here, *R*-values between 0.4–0.9 were chosen to ensure processability. The Ls-based vitrimers required a higher number of amines (*R*-values of 0.4–0.6) to produce processable materials, which may be attributed to the sulfonate moieties potentially deactivating amine groups. The formation of lignin-based VU vitrimers can be characterized by FT-IR spectroscopy with new absorption bands between 3000 cm^{-1} and 2850 cm^{-1}. Moreover, the characteristic acetoacetate bands at 1741 cm^{-1} and 1711 cm^{-1} are absent, indicating full conversion of the acetoacetate functions (Fig. S31–S34, ESI†).

To ensure that the grinding process before the vitrimer film formation has no influence on the backbone structure of the lignin vitrimer materials, FT-IR spectra were measured for all materials after the ball milling process and before sample formation, displayed in Fig. S35–S46.† The results indicate no change in the backbone structure with observable unreacted acetoacetate groups before heat compression. The heat compression process results in homogeneous films with all acetoacetates reacted after film formation due to the applied pressure and temperature. This behaviour is particularly evident for the materials VU-(ALnC-Pri)$_{0.7}$, Fig. S41,† VU-(ALnC-Pri)$_{0.9}$, Fig. S43,† and VU-(ALnP-Pri)$_{0.8}$, Fig. S45.†

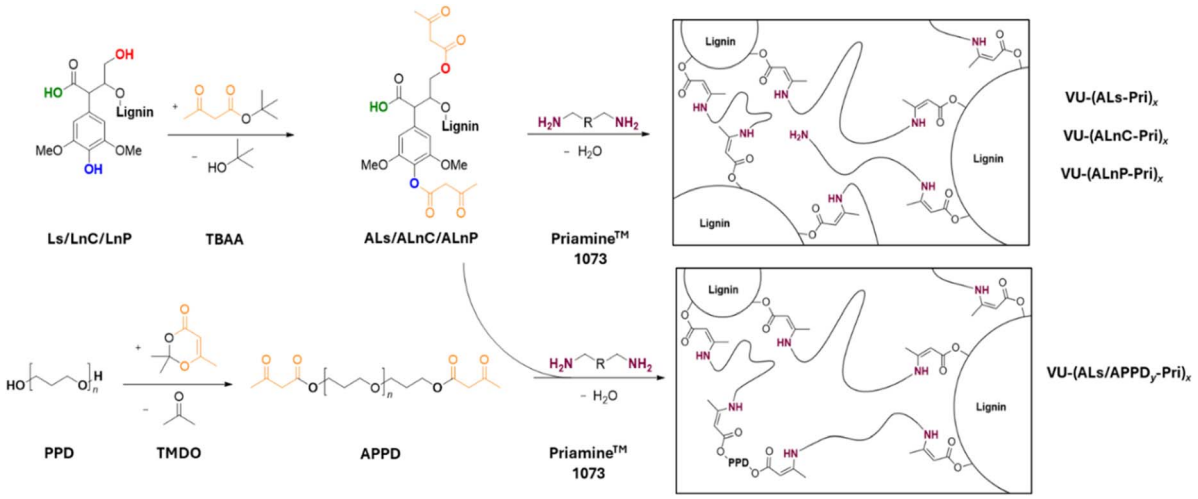

Scheme 1 Synthesis of acetoacetylated lignins (ALs, ALnC, and ALnP) from the different lignin sources (Ls, LnC, and LnP) with *tert*-butyl acetoacetate (TBAA) and acetoacetylated APPD from PPD using 2,2,6-trimethyl-1-3-dioxin-4-one (TMDO). Subsequently, the formation of vinylogous urethane vitrimers through a condensation reaction with Priamine™ 1073 gives the polymer materials VU-(ALs-Pri)$_x$, VU-(ALnC-Pri)$_x$, VU-(ALnP-Pri)$_x$, and VU-(ALs/APPD$_y$-Pri)$_x$, with x abbreviating the R-value and y abbreviating the amount [wt%] of APPD in the formulations.

Swelling tests were performed to confirm the network structure by exposing the polymeric materials to water and acetone. The swelling ratio (S) and the soluble fraction (SF) were calculated with eqn (S2) and (S3),† results are listed in Table S2, ESI.† Maximum values of S at 41% indicate network formation, while SF-values of less than 10% demonstrate the integrity during the swelling and confirm the reaction of acetoacetates and amines to form vinylogous urethanes. Interestingly, LnC- and LnP-based vitrimers exhibited almost no swelling (1.6–5.1%) and negligible soluble fraction values (≤0.3%) in water. The sulfonate groups and their corresponding ionic structures in the LS vitrimers results in higher values for S and SF, reaching up to 39% and 4.4%, respectively, in water. In acetone, higher values for S of up to 36% and for SF of up to 9.6% were observed. Notably, technical lignin sources can contain impurities such as ash, inorganic salts and compounds of low molecular weight compounds, which can lead to an increase in SF. All in all, the vitrimers from Ls, LnC, and LnP demonstrate intact network structures. Furthermore, the results indicate that impurities can influence the swelling properties.

Analysis of the morphology

Optical microscopy (OM) was performed on the raw lignin samples and the acetoacetylated lignins to evaluate the morphology of the vitrimer materials. The lignin precursors were ground in a ball mill to achieve a homogeneous structure and to break down aggregates. The OM images indicate that there are no significant visible differences in the lignins before and after the modification (Fig. S47, ESI†).

In SEM, the lignin sources display a particle-like structure with aggregated lignin fragments (Fig. S48–S50, ESI†). The structures of the agglomerated fragments appear smaller for

Table 3 Overview of the composition of the different vitrimer materials with details of the respective lignin source, the lignin content, the APPD content, the Priamine™ 1073 content and the R-value

Sample	Lignin content [wt%]			APPD [wt%]	Priamine [wt%]	R-value [—]
VU-(Lignin/APPD-Pri)$_x$	ALs	ALnC	ALnP	APPD	Pri	x
VU-(ALs-Pri)$_{0.4}$	46	—	—	—	54	0.4
VU-(ALs-Pri)$_{0.5}$	50	—	—	—	50	0.5
VU-(ALs-Pri)$_{0.6}$	54	—	—	—	46	0.6
VU-(ALs/APPD$_5$-Pri)$_{0.6}$	51	—	—	5	44	0.6
VU-(ALs/APPD$_{10}$-Pri)$_{0.6}$	46	—	—	10	44	0.6
VU-(ALs/APPD$_{15}$-Pri)$_{0.6}$	41	—	—	15	44	0.6
VU-(ALnC-Pri)$_{0.7}$	—	50	—	—	50	0.7
VU-(ALnC-Pri)$_{0.8}$	—	53	—	—	47	0.8
VU-(ALnC-Pri)$_{0.9}$	—	57	—	—	43	0.9
VU-(ALnP-Pri)$_{0.7}$	—	—	55	—	45	0.7
VU-(ALnP-Pri)$_{0.8}$	—	—	59	—	41	0.8
VU-(ALnP-Pri)$_{0.9}$	—	—	62	—	38	0.9

LnC and LnP than for Ls, which can also be assumed by comparison of the molecular mass distribution in Table 1. These aggregates could result from intrinsic self-assembly of lignin organic moieties and their amphiphilic properties, especially found in lignosulfonates.[27] To verify the existence of particles, acetoacetylated lignin species ALs and ALnP were dissolved in acetone/water (9 : 1, v/v) or DMSO and dynamic light scattering (DLS) was performed on the solutions. ALnC was not examined *via* DLS because the samples did not fully dissolve in the solvent systems. For ALs and ALnP, hydrodynamic radii of approximately 90 nm and 50 nm were found, respectively with a narrower distribution for ALnP (Fig. S51, ESI†). These hydrodynamic radii are in a similar range found for lignin nanoparticles, ranging between 50–176 nm.[27,59,60] It is important to note that the observed small reduction in the correlation curve at 10^{-3} ms of ALnP could indicate the presence of smaller species which could not be resolved in the size distribution.

In order to investigate the morphology of the lignin vitrimer films, they were also examined using the SEM. Fiber-like structures appear in the cross-section for ALs-based vitrimers VU-(ALs-Pri)$_{0.5}$ (Fig. S52, ESI†) and VU-(ALs/APPD$_{10}$-Pri)$_{0.6}$ (Fig. S53, ESI†). These fragments were further characterized using energy-dispersive X-ray spectroscopy (EDX), measuring a high amount of sodium, oxygen, and sulfur in these structures. An EDX spectrum next to the fragments only obtained carbon and oxygen (Tables S3 and S4, ESI†). In contrast, the vitrimer films based on enzymatic lignin exhibit a homogeneous internal structure with no visible lignin fragments in the SEM images (Fig. S54 and S55†). This is similar to what has been observed in other homogeneous lignin systems based on Kraft lignin or organosolv lignin.[61] The higher homogeneity of the material could also be caused by the smaller particle size distribution of ALnP compared to ALs, as can be seen in DLS. This can then lead to a better distribution of lignin moieties and therefore, a more homogeneous material. Additional EDX measurements for ALnC and ALnP based materials VU-(ALnC-Pri)$_{0.8}$ and VU-(ALnP-Pri)$_{0.8}$ are presented in Tables S5 and S6, ESI.† The results show that no sulfur or sodium is present, which is in good agreement with the purity of the enzymatic lignins.

A difference in the morphology can be observed in AFM height images of the vitrimer films. AFM images showing both height and phase information are displayed in Fig. S56–S59, ESI.† The surface plot of VU-(ALs-Pri)$_{0.5}$ shows a rough surface with a homogeneous distribution of lignin fragments. For VU-(ALs/APPD$_{10}$-Pri)$_{0.6}$, a more regular surface is observed, indicating an influence of APPD and a lower mass fraction of lignin. Both AFM images of VU-(ALnC-Pri)$_{0.8}$ and VU-(ALnP-Pri)$_{0.8}$ display surface morphologies with smaller granules and less irregularities. The surface structure is most likely caused by the polytetrafluorethylene (PTFE) sheets used for heat compression.

Despite the existence of particles observed by DLS, no particle-like structure could be detected in the material by SEM and AFM, confirming a homogeneous formation of lignin-based vitrimers.

Thermomechanical properties

To determine the thermomechanical stability of the lignin vitrimers, thermogravimetric analysis (TGA) was conducted on each prepared material under ambient (oxygen) atmosphere (Fig. S60, ESI†). The decomposition temperature $T_{5\%}$, defined as the temperature at which 5% mass loss of the initial sample occurs, ranged from 272–307 °C, indicating that all samples exhibited good thermal stability. This $T_{5\%}$ range was also observed for VU vitrimers produced from oxyalkylated acetoacetylated organosolv lignin (OOSL, 266 °C), organosolv lignin (OSL, 270 °C), and for soda pulped wheat straw lignin (WSL) (309 °C).[47–49] The residual weight of the Ls-based films of 15–23% is attributed to carbonized material (char) and ionic residues. To ensure thermal stability during heat compression, isothermal TGA was conducted for 3 hours at 180 °C under ambient (oxygen) atmosphere (Fig. S61, ESI†). All samples exhibited an isothermal mass loss of 1–3%, indicating stability under the processing conditions during dynamic mechanical analysis, heat compression, recycling, and stress relaxation measurements.

Thermal properties were further analyzed using dynamic differential scanning calorimetry (DSC). The measured heat flow was represented by a flat curve without significant transitions (Fig. S62, ESI†). A clear glass transition could not be detected in the samples; instead a broad glass transition region was observed between −50–250 °C, with a slight shift to higher temperatures when using ALnC and ALnP as a monomer. These glass transition regions can be attributed to the distribution of acetoacetylated lignin within the polymeric APPD and Priamine chains, which broadens the glass transition range.[56] This observation can also be verified by DMA, which found a tan(δ) with a broad distribution for ALs-based materials and distinguishable glass transitions for ALnC- and ALnP-based materials.

Mechanical properties

The mechanical properties of the lignin vitrimers were determined through uniaxial tensile testing at room temperature (23 °C). Stress–strain curves of the materials are presented in Fig. 2. The strength and strain behavior of the materials are influenced by the type of lignin used in the formulation, the lignin content, the APPD content, and the *R*-value. The materials range from softer films to more rigid structures, exhibiting averaged elastic moduli (E) from 108 MPa to 837 MPa, tensile strengths (σ_m) from 6.0 MPa to 30.3 MPa, and elongations at strain at break (ε_m) ranging from 2.1% to 20.1%. The results indicate that as the *R*-value increases, the values of E also increase, resulting in more rigid materials, as demonstrated by the decreasing values of ε_m. On one hand, this is attributed to the decreasing number of dangling amine groups in the materials. On the other hand, the relative amount of lignin crosslinker increases with higher *R*-values, highlighting the influence of the rigid lignin molecules. The mixtures and results are displayed in Fig. 3 and listed in Table S7.† In case of the lignosulfonate materials, σ_m increases from 13.5 ± 0.2 MPa for VU-(ALs-Pri)$_{0.4}$ to 17.5 ± 1.3 MPa for VU-(ALs-Pri)$_{0.5}$. However, this trend is not continued

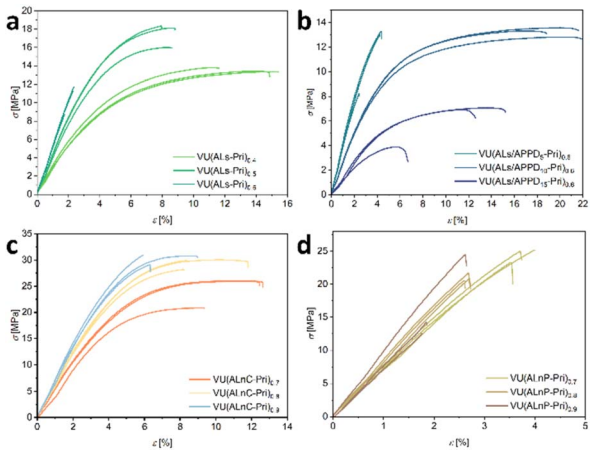

Fig. 2 Stress–strain curves (T = 23 °C) of the lignin vitrimer materials derived from ALs (a and b), ALnC (c), and ALnP (d). The materials range from softer films to more rigid ones, showing averaged elastic moduli (E) in the range of 108 MPa up to 837 MPa, tensile strengths (σ_m) of 6.0 MPa up to 30.3 MPa, and elongations at an ultimate stress (ε_m) of 2.1% to 20.1%.

for VU-(ALs-Pri)$_{0.6}$, as the material becomes brittle, as displayed by the low value of ε_m (2.1% ± 0.3%). To ensure good processability and reduce brittleness, a linear APPD crosslinker was introduced at concentrations of 5 wt%, 10 wt%, and 15 wt% while maintaining a constant R-value (Fig. 2b and 3b, c). As expected, with increasing amounts of APPD, ε_m increases, with material VU-(ALs/APPD$_{10}$-Pri)$_{0.6}$ exhibiting the best compromise between strength and toughness, showing σ_m values of 13.0 ± 0.3 MPa and ε_m values of 20.1% ± 1.7% for an R-value of 0.6. This demonstrates the potential to modify the materials not only by varying the amount of free amines, but also by compounding with shorter, flexible molecules in a straightforward manner to prepare materials with desired properties. Overall, the vitrimers prepared from enzymatic lignin exhibit higher values of E and σ_m compared to those based on lignosulfonate, highlighting the influence of the morphology and fewer impurities in the crosslinking compound. Additionally, there are increasing values of E and σ_m associated with higher R-values (Fig. 3b and c). The highest value of σ_m was observed for VU-(ALnC-Pri)$_{0.9}$, which had a value of 30.3 ± 1.0 MPa probably as a result of the higher crosslink density due to the higher amount of saccharides found in ALnC. Materials using ALnP exhibit more brittle behavior, showing decreasing values of σ_m for higher R values, with the highest value of E recorded for VU-(ALnP-Pri)$_{0.9}$ at 837 ± 114 MPa. Since E in these samples is proportional to the mass fraction of respective acetoacetylated lignins, this is attributed to the fact that ALnP-based vitrimers have the highest amount of lignin content. Here, all mixtures display a narrow range of properties, attributed to the influence of the regular crosslinkers. These findings highlight the influence of the lignin source on the material's properties, which can be modified by adjusting the weight proportions of the different lignins, linkers, and amines. This influence of the amount of lignin crosslinkers was also found for materials synthesized from OSL and acetoacetylated poly(ethylene glycol) forming a vinylogous urethane with hexamethylene diamine linkers (lignin content varied from 30–50 wt%). Here, the E modulus increased from 0.2 ± 0.1 MPa with σ_m of 0.2 ± 0.1 MPa and ε_m values of 98% ± 10% with 30 wt% of lignin in the matrix up to 420 ± 30 MPa and with σ_m of 17.2 ± 0.7 MPa and ε_m values of 22 ± 3%, when using 50 wt% of lignin.[49] A detailed comparison of three vinylogous urethane vitrimer materials from OOSL, OSL and WSL is presented in Table S8,† including mechanical, rheological, and thermal properties of the samples. An excellent review on different lignin sources reviewing various dynamic covalent chemistries is provided by Karoki *et al.*, which lists values for E ranging from 0.2–85 MPa.[39]

Dynamic mechanical properties

Dynamic mechanical properties were further analyzed using dynamic mechanical analysis (DMA) and static stress relaxation experiments. Prior to all oscillatory experiments, amplitude sweep measurements were conducted at 110 °C to determine the linear viscoelastic regime (LVE) of the materials (Fig. 4a and S63, ESI†). An increase in the R-value reduces the number of dangling chains, as the amount of free amine functions decreases. This effect can be observed by higher values of the storage modulus in VU-(ALs-Pri)$_{0.6}$ and VU-(ALs-Pri)$_{0.5}$ compared to VU-(ALs-Pri)$_{0.4}$ in the LVE (Fig. S63a–c, ESI†). Maintaining the R-value at 0.6 and compounding with the linear chains of APPD enhances the elastic properties of VU-(ALs/APPD$_5$-Pri)$_{0.6}$. This process expands the LVE to higher values of shear strain γ for VU-(ALs/APPD$_{15}$-Pri)$_{0.6}$, while preserving the values of the storage modulus G' in the LVE. This is an initial indication of the powerful potential to precisely tune the properties of lignin vitrimers. The LVE range was observed between 0.001% and 1% for all lignosulfonate-based vitrimers. This range expands to higher values for higher APPD content and lower R-values. For the vitrimers produced from ALnC and ALnP, the LVE range is between 0.001% and 0.5%, following the same trend in the R-value as discussed before. VU-(ALnP-Pri)$_{0.8}$ and VU-(ALnP-Pri)$_{0.9}$ display a more rigid structure in the amplitude sweeps, showing breaking events after reaching the non-linear regions at 1% and 0.3%, respectively. This may be due to the more regular morphology (as seen in SEM), fewer impurities (as seen in EDX), and higher content of lignin in ALnP, which enhance the interactions between lignin moieties and therefore the arrangement of lignin fragments in the material, thereby increasing stiffness. Moreover, impurities such as saccharides in ALnC may enhance the toughness of these materials. Therefore, to prevent damage to the structure, all subsequent oscillatory measurements were performed within the LVE, using a deformation of 0.01%. Temperature-sweep measurements are displayed in Fig. 4b and S64, ESI.† The examined samples did not show a rubbery plateau in the examined temperature range of 150 °C to 0 °C but displayed a broad glass transition region. This suggests that the distribution of lignin moieties within the material is heterogeneous in size, leading to a broadening of the chain movement resolution in the tan(δ). This was also observed in the work of Liu *et al.* for alkali lignin, where Priamine™ 1075 was used as soft

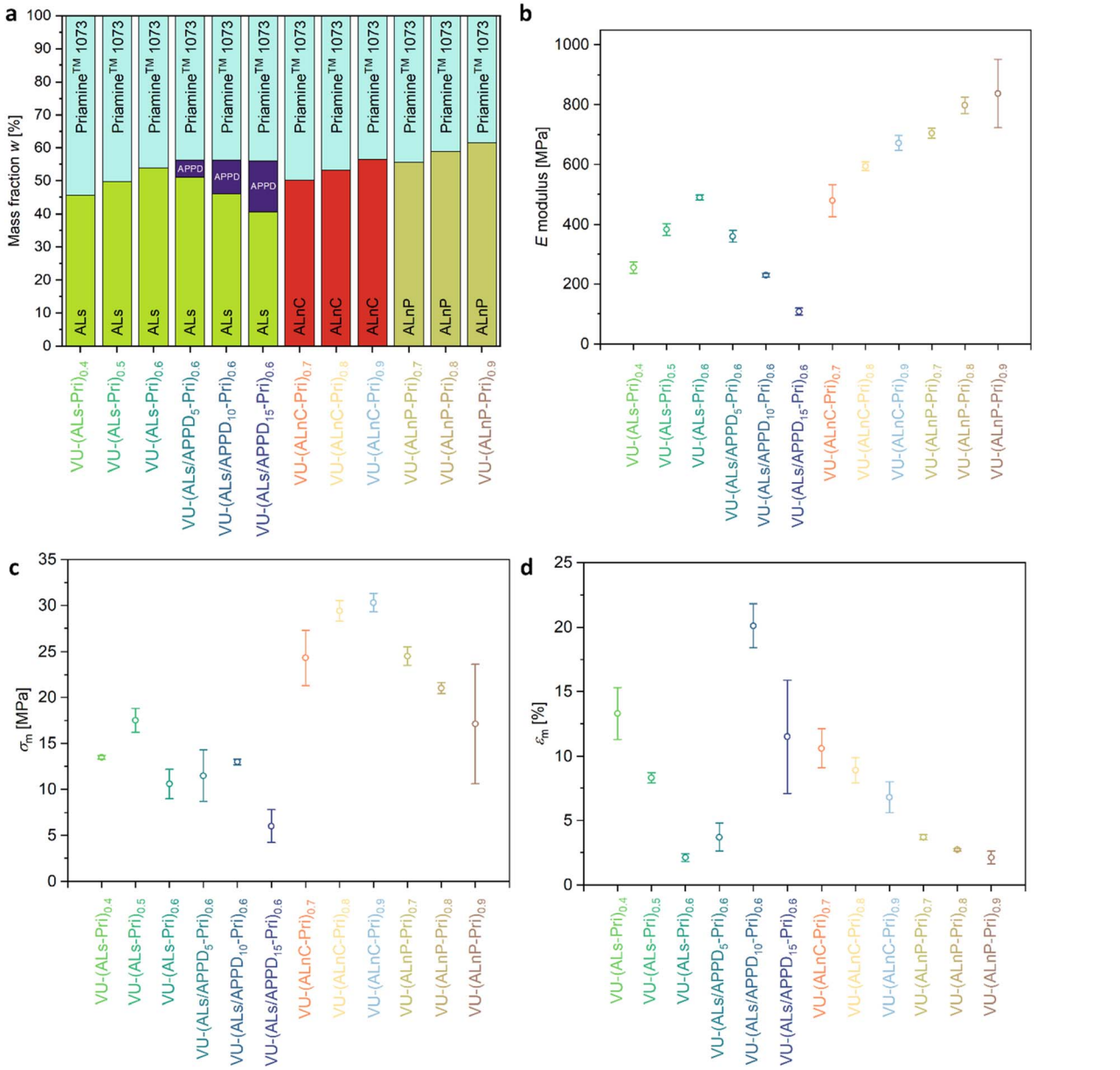

Fig. 3 (a) Mass fractions of the used building blocks of the lignin vitrimers with the acetoacetylated lignin species ALs, ALnC, and ALnP, respectively, the linear difunctional APPD, and the amount of Priamine™ 1073. (b–d) Tensile test data of the lignin vitrimers ($T = 23$ °C), (b) tensile modulus (E), (c) tensile strengths (σ_m), (d) elongation at ultimate stress (ε_m).

segment in a material crosslinked by hard and rigid lignin segments.[48] An interesting influence of the morphology of the used lignin type on the glass transition, displayed in Fig. 4c and S65,† can be found by comparing the temperature-sweep measurements of the lignosulfonates VU-(ALs-Pri) and VU-(ALs/APPD-Pri) with the materials VU-(ALnC-Pri) and VU-(ALnP-Pri). The ALs crosslinker results in a broad glass transition region, with a T_g at 30 °C for VU-(ALs-Pri)$_{0.4}$, which flattens and shifts to higher temperatures with increasing R-values. At 20 °C, the samples are in the glassy region, with storage moduli ranging from 85 MPa to 487 MPa. For the enzymatic lignin sources, ALnC and ALnP, a glass transition can be identified as a peak in tan(δ). The T_g shifts from 85 °C (VU-(ALnC-Pri)$_{0.7}$) to higher values with increasing R-values, resulting in a T_g of 110 °C for VU-(ALnC-Pri)$_{0.9}$. The purified enzymatic lignin exhibits even higher T_g values, demonstrating the same dependence on pending free amines within the material, with the T_g ranging from 115 °C for VU-(ALnP-Pri)$_{0.7}$ to 135 °C for VU-(ALnP-Pri)$_{0.9}$. This highlights the influence of the morphology of different lignin sources, as materials exhibit higher T_g values when they have a higher lignin content and fewer impurities like sulfonate groups in ALs-based materials, as discussed before. Interestingly, these materials, with broad T_gs, show stress-relaxation behavior even at temperatures as low as 120 °C. However, the T_g of the lignin particles can superimpose the stress-relaxation

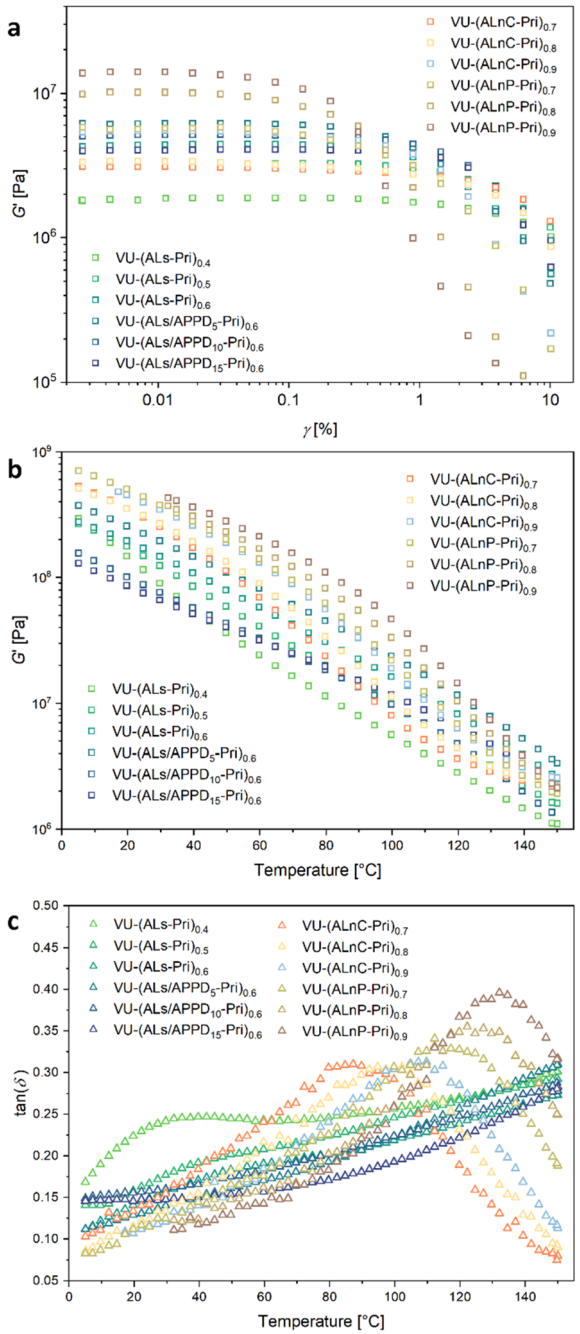

Fig. 4 DMA results of the lignin vitrimers based on lignosulfonate and enzymatic lignins (ω = 6.28 rad s^{-1}, F_N = 1 N). (a) Amplitude-sweep measurement results of the tested lignin vitrimers (T = 110 °C). (b and c) Temperature-sweep measurements of the lignin vitrimers (T = 150–0 °C, γ = 0.01%), (b) storage modulus G', (c) loss factor tan(δ).

behavior, potentially leading to inaccurate activation energy calculations.

Stress-relaxation properties

Stress-relaxation measurements were conducted on all lignin vitrimer materials to determine molecular network rearrangement. Vinylogous urethane bonds can exchange with free amines under thermal activation *via* a transamination reaction. As thermal energy increases, the rate of the bond exchanges also increases. Additionally, the structural and conformational properties of the material influence the dynamics of the free chains undergoing a molecular network rearrangement reaction. Commonly, the dependence of the stress-relaxation on the kinetics of dynamic exchange reactions in lignin-based vitrimers was proven by testing for the Arrhenius behavior using a single Maxwell model.[42,48,62] However, polymers, vitrimers, and organic composites like acetoacetylated lignin fragments should not be considered to be materials showing only a single relaxation, as they can display inhomogeneities and structural defects as well as show dependence from the T_g of the lignin, particularly if the thermal activation is close to the T_g.[63,64] A more realistic model that fits the data is the Kohlrausch–Williams–Watts (KWW) stretched exponential decay (ESI, eqn (S4)†).[7,47,50] A non-normalized version of the KWW model was used to calculate all parameters of the fit for the stress relaxation modulus $G(t)$. The stretching variable β is a measure for the uniformity of the exponential decay. A value of $\beta = 1$ indicates that the relaxation is described with a single relaxation time. The smaller the value, the broader is the distribution of relaxation times.[65] As a constrained condition, $G(t)$ is expected to be zero within experimental error at infinite time. In a first series of single-step deformation experiments of 1% deformation, the stress-relaxation modulus was measured as a function of time over a temperature range of 110 °C to 180 °C for all materials. The first criterion for stress-relaxation measurements is verifying if the initial relaxation modulus, G_0, remains nearly constant at different temperatures to confirm the assumption of an associative network rearrangement path. The values of G_0 in the range of 110–180 °C are shown in Fig. S66† and fulfill this criterion for the materials VU-(ALs-Pri)$_x$, VU-(ALs/APPD$_y$-Pri)$_x$. The materials VU-(ALnC-Pri)$_x$ and VU-(ALnP-Pri)$_x$ (Fig. S66b†) exhibit two different slopes in the straight lines connecting the values above and below 160 °C, suggesting a first indication of deviation from the expected stress-relaxation behavior, caused by T_g. Non-normalized stress-relaxation curves are presented alongside with the KWW function applied to the non-normalized stress relaxation data of the vitrimers VU-(ALs-Pri)$_x$, VU-(ALs/APPD$_y$-Pri)$_x$ VU-(ALnC-Pri)$_x$, and VU-(ALnP-Pri)$_x$ in Fig. S67.† The average relaxation times were calculated using eqn (S5).†[50,65] As listed in Table S9,† the stress relaxation results were well fit to stretched exponential decays for the materials VU-(ALs-Pri)$_x$, VU-(ALs/APPD$_y$-Pri)$_x$, and VU-(ALnC-Pri)$_{0.7}$, but result in high values for the averaged stress relaxation times for the respective materials VU-(ALnC-Pri)$_x$ and VU-(ALnP-Pri)$_x$. This demonstrates the influence of the high T_g values of ALnC and ALnP, also indicated by β values below 0.1. Therefore, these materials were excluded from the calculations of activation energies (E_a) for the transamination of the vinylogous urethane functions. In VU-(ALs-Pri)-based materials, the influence of the T_g appears less pronounced, as the softer matrix has a greater impact on the molecular network rearrangement, allowing for the calculation of E_as. Values of E_a for VU-(ALs-Pri)$_x$, VU-(ALs/APPD$_y$-Pri)$_x$, and VU-(ALnC-Pri)$_{0.7}$ were calculated by linear regression of the values of $\ln\langle\tau_r\rangle$ as a function of 1000/T in the

linear range of points between 110–180 °C (Fig. S68, ESI†). Calculated activation energies between 61.4–123 kJ mol^{-1} are typical values for transamination reactions.[58] Activation energies between 38–114 kJ mol^{-1} were calculated for OSL and OOSL and 134 kJ mol^{-1} for WSL, assuming a single relaxation.[47–49]

It has to be mentioned, that at temperatures of 170 °C and 180 °C slower stress relaxation was observed and also some measurements at 120 °C showed faster relaxation than the respective measurement at 130 °C, indicating measurement errors. The greater the influence of the harder lignin crosslinker segments and thus of the higher T_g, the greater becomes the influence of the limited segmental motion of the materials. This results in the spike in the Arrhenius plots for VU-(ALnC-Pri)$_{0.8}$, VU-(ALnC-Pri)$_{0.9}$, and all ALnP-based materials. The plot of the values of $\ln\langle\tau_r\rangle$ as a function of $1000/T$ displays a local maximum in the average stress-relaxation time in the region of the T_g. The KWW-fits calculate β values below 0.1, indicating a very broad distribution of relaxation times (ESI, Fig. S68(h–l) and ESI, Table S9†).

However, for these materials, the stress relaxations at 170 °C and 180 °C are particularly interesting for further investigations within this temperature range, as they appear to exhibit a linear relationship, suggesting that these materials could be processed at 180 °C. To investigate the potential stress-relaxation behavior of the material VU-(ALnC-Pri)$_x$ and VU-(ALnP-Pri)$_x$, additional stress relaxation measurements were conducted in the temperature range of 170–180 °C. In this temperature range, G_0 remains nearly constant across all materials, as displayed in Fig. S69.† A comparison of the different stress-relaxation behaviors of the materials VU-(ALs-Pri)$_{0.5}$ and VU-(ALnP-Pri)$_{0.7}$ is displayed in Fig. 5. The non-normalized stress-relaxation curves for VU-(ALnC-Pri)$_x$, and VU-(ALnP-Pri)$_x$ are shown together with the KWW function applied to the non-normalized stress relaxation data in Fig. S70.† The calculated values of β and $\langle\tau_r\rangle$ are listed in Table S10.† Next, the values of $\ln\langle\tau_r\rangle$ were plotted as a function of $1000/T$ in the linear range of points between 170–180 °C in Fig. S71, ESI,† showing linearity for VU-(ALnC-Pri)$_x$, and VU-(ALnP-Pri)$_{0.7}$. An increasing R-value for the materials VU-(ALnP-Pri)$_{0.8}$ and VU-(ALnP-Pri)$_{0.9}$ leads to the observation of increasing stress relaxation times at lower temperatures, deviating from linearity. As discussed before, the broad range of the T_g of the different materials influences the stress-relaxation behavior, leading to false assumptions of the activation energies and time-scales of the reprocessing. The calculated activation energies between 220–773 kJ mol^{-1} do not show values of stress-relaxation energies caused by transamination reactions, but are influenced by other relaxations in the materials. This is also highlighted by the deviation of the activation energy calculated for VU-(ALnC-Pri)$_{0.7}$, which shows an activation energy of 79.3 kJ mol^{-1} for the calculation between 120–180 °C and 220 kJ mol^{-1} for the calculation between 170–180 °C. These findings highlight the importance of using a KWW stretched exponential fit for stress-relaxation data of complex materials such as lignin vitrimers and to take the thermal properties such as the T_g of the monomers into account.

Recycling

The recycling of new sustainable materials is a key feature for a circular carbon economy. By recycling of lignin vitrimers, an industrial waste product can be used even after the first lifecycle by reprocessing and remolding, implementing green chemistry

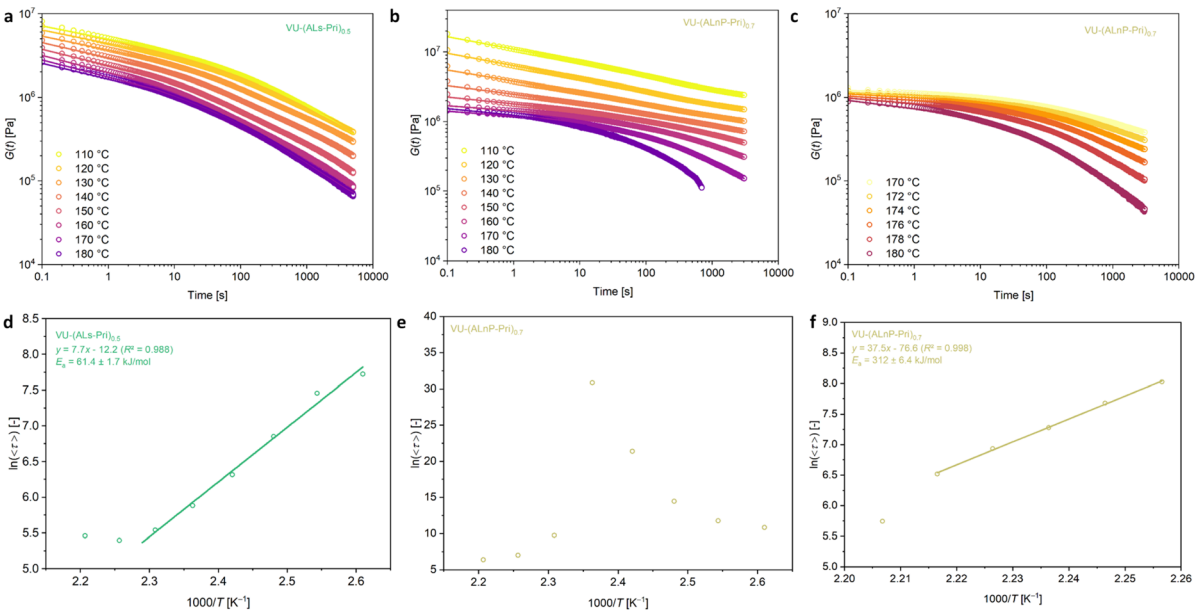

Fig. 5 Non-normalized stress-relaxation measurement ($\gamma = 1\%$, $F_N = 1$ N) between 110 °C and 180 °C of the material (a) VU-(ALs-Pri)$_{0.5}$ and (b) VU-(ALnP-Pri)$_{0.7}$. (c) Non-normalized stress-relaxation measurement ($\gamma = 1\%$, $F_N = 1$ N) between 170 °C and 180 °C of the material VU-(ALnP-Pri)$_{0.7}$. (d and e) Arrhenius plot of $\ln\langle\tau_r\rangle$ *versus* $1000/T$. For VU-(ALnP-Pri)$_{0.7}$, a non-linear plot (e) was found due to the high T_g of the lignin particles in the range of 110–180 °C. A linear stress-relaxation relation could be found for VU-(ALnP-Pri)$_{0.7}$ in the range of 170–180 °C (f).

principles towards a sustainable circular economy.[66,67] For this, exemplary samples of all materials were ground into a powder using a ball mill (1 min, 30 Hz, 23 °C) and remolded by heat compression (30 min, 20 kN, 180 °C) in five successive cycles. The results of the recycling experiments are displayed in Fig. 6. The integrity of the network properties after the recycling were reanalyzed after the fifth recycling step. Tensile testing results are listed in Table S11.† The properties of the reprocessed Ls-based material VU-$(ALs\text{-}Pri)_{0.5}$ were similar to the neat material with values of $E = 415 \pm 26.3$ MPa and $\sigma_m = 18.3 \pm 1.0$ MPa.

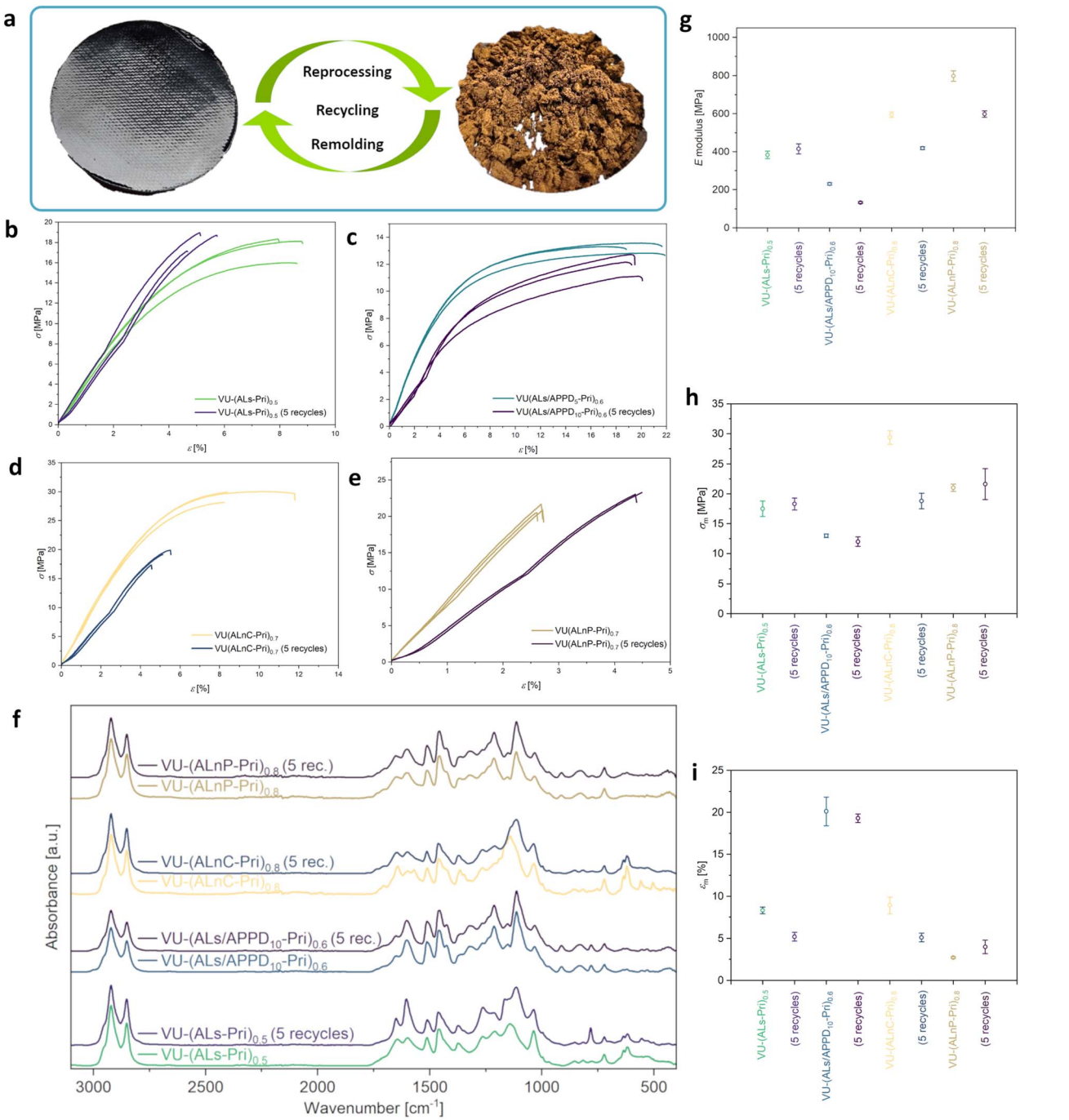

Fig. 6 (a) Illustration of the repetitive ball milling (1 min, $f = 30$ Hz, $T = 23$ °C) and reprocessing cycle through heat compression (30 min, 20 kN, 180 °C), showing a ground lignin vitrimer powder and a reprocessed vitrimer film. Stress–strain curves ($T = 23$ °C) of selected vitrimers VU-$(ALs\text{-}Pri)_{0.5}$ (b), VU-$(ALs/APPD_{10}\text{-}Pri)_{0.6}$ (c), VU-$(ALnC\text{-}Pri)_{0.8}$ (d) and VU-$(ALnP\text{-}Pri)_{0.8}$ (e) in comparison of the pristine and five times reprocessed specimens, showing different curves with overall similar material properties. (f) Repetitively measured ATR-FT-IR spectra show rather similar curve shapes of the pristine materials and after five times recycling procedure, measuring the characteristic stretching vibrations of the vinylogous urethane bond. (g–i) Tensile test data of the pristine and five times reprocessed lignin vitrimers ($T = 23$ °C), (g) E modulus, (h) tensile strengths (σ_m), (i) elongations at ultimate stress (ε_m).

The value of ε_m decreased from 8.3 ± 0.4% to 5.2 ± 0.5%, indicating an influence of the grinding process on the samples. In SEM and EDX measurements, displayed in Fig. S72–S75, ESI,† the structure of the cross-sections of the recycled vitrimers was analyzed. For VU-(ALs-Pri)$_{0.5}$ and VU-(ALs/APPD$_{10}$-Pri)$_{0.6}$, the distribution of sulfur-containing fragments appears homogeneous throughout the observed area. For VU-(ALs/APPD$_{10}$-Pri)$_{0.6}$, sulfur and sodium were also found in regions which only contained carbon and oxygen before the recycling, indicating an influence of the mechanical recycling on the structure by grinding and mixing. For the samples containing enzymatic lignin, SEM and EDX (Fig. S72–S75 and Tables S12–S15, ESI†) confirmed again a homogeneous structure. However, no influence of the recycling could be determined by these characterizations. As for the neat materials, again AFM measurements were carried out for the recycled materials, displayed in Fig. S76–S79, ESI.† After recycling, the films display a smoother surface, which could be due to a better mixture after consecutive grinding and remolding steps.

For tensile testing, the E modulus of the VU-(ALs/APPD$_{10}$-Pri)$_{0.6}$ decreased from 230 ± 6.0 MPa to 133 ± 5.9 MPa, indicating a degradation of the APPD linker molecules. However, the values of σ_m and ε_m were restored, which also shows the reprocessing potential of these compounds. Enzymatic lignin-based materials VU-(ALnC-Pri)$_{0.8}$ and VU-(ALnP-Pri)$_{0.8}$ displayed lower E moduli than the initial materials (797 MPa to 598 MPa and 594 MPa to 418 MPa), with VU-(ALnC-Pri)$_{0.8}$ also displaying ε_m decreased from 29.4 ± 1.1% to 18.8 ± 1.3%, also showing internal effects of low molecular weight compounds, which can also degrade during the milling and remolding steps.[68]

In comparison, for OSL, reprocessing was demonstrated by Sougrati *et al.* using a material with 40 wt% lignin, VU-40-400, which was cryo-ground in a coffee grinder. After three consecutive recycling cycles, the materials displayed a recovery of 71% of the initial stress at break, which was attributed to the alternation of the vitrimers structure. It was hypothesized, that not only dynamic bonds, but also bonds forming the network from lignin's bulky structure could be affected by the recycling process.[49] When recycling WSL Vitrimer-1 by Liu *et al.* by cutting the sample into pieces and recovering by hot pressing, after 4 consecutive cycles, the material properties were maintained, highlighting the influence of the mechanical process to recycle the lignin vitrimer and the amount of the linkers used.[48] This also becomes evident for a more recent work of Sougrati *et al.* on OOSL, where they obtained recycled materials without significant changes in chemical structure and mechanical properties for the vitrimer Ph-VU-600 with a lignin content of 46 wt% and a long PEG linker with a molar mass of 600 g mol^{-1}. This highlights the influence of a soft linker, resulting in an overall softer material (E = 2.4 ± 0.1 MPa), which facilitates preserving mechanical integrity after three reprocessing steps.[49]

DMA results of amplitude sweeps show a decrease in the LVE range for VU-(ALs-Pri)$_{0.5}$, VU-(ALs/APPD$_{10}$-Pri)$_{0.6}$, and VU-(ALnC-Pri)$_{0.8}$, whereas for VU-(ALnP-Pri)$_{0.8}$ it remained nearly the same, only the values of G' and G'' were lower (Fig. S80, ESI†). This may be explained by grinding of larger lignin fragments, resulting in samples with smoother surfaces, as seen in the AFM images. This can be observed in the temperature sweep data, showing overall decreased mechanical strength (Fig. S81, ESI†). As a result of better mixing and grinding of the polymer, a more homogeneous matrix could be achieved and the T_gs of VU-(ALs-Pri)$_{0.5}$ and VU-(ALs/APPD$_{10}$-Pri)$_{0.6}$ can be clearly determined in contrast to the pristine samples. For VU-(ALnC-Pri)$_{0.8}$ and VU-(ALnP-Pri)$_{0.8}$, the T_gs were shifted to higher temperatures (Fig. S82, ESI†). These results show that the internal morphology of the materials is affected by the reprocessing as shown by tensile testing. Stress-relaxation was investigated at four different temperatures, aligned with the previously determined temperature range for ALs, ALnC, and ALnP-based materials (Fig. S83, S84, Tables S16 and S17, ESI†). Except for VU-(ALs-Pri)$_{0.5}$, the materials show vitrimer-like stress-relaxation with increased characteristic relaxation times. Integrating APPD into the matrix of ALs-based vitrimers appears to enhance recyclability, as these materials continue to exhibit the characteristic relaxation behaviour of vitrimers even after recycling. The high activation energies do not display only the energy of transamination molecular network rearrangement but can be assigned to various relaxing effects, such as segmental motions.

UV-light absorbance

The suitability of materials for use as containers depends on their ability to absorb UV-light without heating or degradation.[69,70] When the vitrimer films were irradiated with UV-light (365 nm), no significant thermal effect was observed, other than an increase in the surface temperatures of both the sample and the PTFE sheet holding the sample. Three different time intervals (10 s, 60 s, and 300 s) were tested with an irradiation intensity of 69 mW cm^{-2}, showing no thermal heating effect of the neat vitrimer film (Fig. S85, ESI†).

Processing by injection molding

To demonstrate the suitability of lignin-based VU vitrimers for injection molding, the material VU-(ALnC-Pri)$_{0.7}$ was ground to a powder using a ball mill (25 °C, 30 Hz, 1 min) and subsequently filled into the injection molding cylinder at 250 °C, the mold was heated to 220 °C. Then, the specimens (Fig. 7a) were produced applying a pressure of 1000 bar for 45 s and a pressure of 100 bar for 20 s. After cooling, the specimens were extracted from the mold and tested by tensile testing (Fig. 7b), showing similar stress–strain curves and only slightly lower elastic moduli (406 MPa ± 16.2 MPa) as the heat compressed materials (479 MPa ± 53.2 MPa). This demonstrates the potential of processability of lignin-based VU-vitrimers not only by heat compression but also by injection molding, which could simplify the production of lignin-based materials by utilizing already existing large-scale production methods.

Durability tests and damping properties

To assess, if the vitrimer materials will be useful as recyclable damping materials, coatings, or containers that provide protection against environmental stress while offering a closed

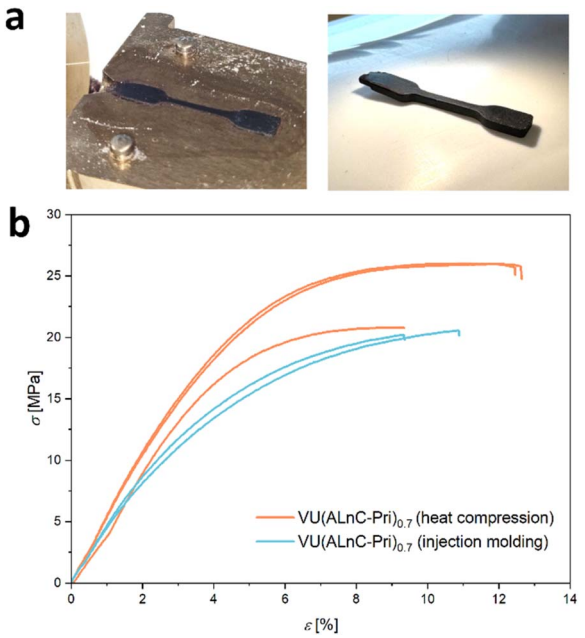

Fig. 7 (a) Pictures of the injection mold and the produced test specimen. (b) Comparison of the stress–strain curves specimens produced through heat compression and through injection molding.

carbon-cycle and industrial processing methods, durability tests were carried out.[71,72] The Shore-hardness of the injection molded VU-(ALnC-Pri)$_{0.7}$ was measured using a durometer device and an averaged value of 62D was measured in five measurement cycles. This proves the potential applicability as a protection against environmental mechanical stress and indicates durability.[73–75] The values are similar to lignin biocomposites, displaying values of 60D–80D, and display the influence of the mass loading of lignin.[76] Damping materials can effectively dissipate mechanical energy such as vibrations and absorb this energy while maintaining their structure.[77,78] As displayed in the previous chapter, the materials show a broad T_g due to a broad morphological size distribution allowing them to dissipate energy. A durability test was carried out with a square-shaped sample of VU-(ALnP-Pri)$_{0.7}$, applying a tensile-force of 50 N in an oscillating experiment with 1000 repetitive cycles of force and relaxation. The consecutive cycles are displayed in Fig. S86, ESI.† Fatigue can occur due to dynamic loading at stress amplitudes below the fracture strength. The material displayed no permanent deformation, cracks or material fatigue, indicating resistance against frequent vibrations. However, the elongation increased in the first 700 cycles by 33%, reaching a plateau value, indicating a quasi-stationary state.

Conclusions

A series of vinylogous urethane vitrimers derived under mild conditions from new lignin sources using lignosulfonate and enzymatic lignin (Lignova Crude™ and Lignova Pure™) is studied. These materials represent a promising class of tougher, greener, and sustainable vitrimers, characterized by strong mechanical properties, such as an elastic modulus of up to 0.83 GPa. Acetoacetylation using TBAA was performed in DMSO as a one-step bulk reaction. Subsequently, polymerization of lignin-based acetoacetates with a bio-based amine and an acetoacetylated polyol was carried out in a non-toxic water/acetone mixture. This process yielded vitrimer films after consecutive ball milling and remolding in a heat compression mold. The materials demonstrate stability against solvents, such as water and acetone, as indicated by swelling tests. Additionally, they exhibit high thermal stability, with a $T_{5\%}$ ranging from 272–307 °C, enhancing the thermal properties of the raw lignins. Twelve lignin vitrimers have been synthesized and compared regarding their morphology and mechanical properties, showing elastic moduli of 108–837 MPa, tensile strengths of 6.0–30.3 MPa, and elongations at ultimate stress of 2.1–20.1%. In general, vitrimers based on lignosulfonate were less homogeneous as observed by optical and scanning electron microscopy. They showed less tensile strength than vitrimers based on LnC and LnP. This results from the higher degree of impurities, heterogeneity, and dispersity of lignosulfonate. Stress-relaxation was investigated in two different temperature regimes, depending on the lignin resource used. The measurements were fitted using the Kohlrausch–Williams–Watts stretched exponential decay function, highlighting the importance of taking several relaxation phenomena (segmental motion and transamination reaction) into account for stress relaxation and calculation of activation energies. Furthermore, the materials allow for thermomechanical reprocessing through grinding and remolding, displaying the potential for closed-loop recycling of a waste product resource. The material properties were measured and compared after five successive grinding and remolding steps, highlighting the reprocessability, which is affected by the alteration of the inner structure of the materials. In addition, the materials display interesting optical properties such as blocking of UV-light, good Shore D hardness, and resistance against fatigue. Since mainly soft, elastomeric lignin-based vitrimers were reported before, focusing on organosolv lignin and Kraft lignin, this work contributes to the development of tough lignin vitrimers from waste-wood lignosulfonate lignin and enzymatic lignin with a high lignin content, and gives an in-depth investigation of mechanical and stress-relaxation properties, and introducing new processing methods such as injection molding for vinylogous urethane lignin vitrimers.

Data availability

Data is available upon reasonable request from the authors.

Author contributions

F. C. K. and N. S. contributed equally to this work. F. C. K., N. S., and V. A.: conceptualization; F. C. K. and N. S.: methodology, investigation, data curation, formal analysis, validation, visualization, and experiments; V. A.: supervision and resources; F.

C. K. and N. S.: writing – the original draft; F. C. K., N. S., and V. A.: writing – review and editing.

Conflicts of interest

There are no conflicts to declare.

Acknowledgements

The authors gratefully acknowledge financial support from the German Research Foundation (DFG) *via* SFB986 "M3," subproject A2. The authors would like to thank Fibenol OÜ, especially Kait Kaarel Puss, for providing the lignin samples and the friendly correspondence. The authors acknowledge the NMR division of the chemistry department at Universität Hamburg (UHH) with a special thanks to Claudia Wontorra for conducting the ^{31}P NMR measurements. We thank Robert Schön of the EM division for capturing the SEM images. The authors would like to address special thanks to Martin Kehden who conducted all DSC and TGA measurements. We thank Marvin Groß (OM), the MS division, Andreas Meyer (AFM), and Birgit Hankiewicz (DLS). This open access publication was funded by the University of Hamburg as part of the TIB-RSC-Platinum agreement with the Royal Society of Chemistry.

References

1 M. Calisto Friant, W. J. V. Vermeulen and R. Salomone, *Circ. Econ. Sustainability*, 2023, **4**, 23–42.
2 J. G. Rosenboom, R. Langer and G. Traverso, *Nat. Rev. Mater.*, 2022, **7**, 117–137.
3 M. Tschulkow, M. Pizzol, T. Compernolle, S. Van den Bosch, B. Sels and S. Van Passel, *Resour., Conserv. Recycl.*, 2024, **204**, 107466.
4 R. Shorey, A. Salaghi, P. Fatehi and T. H. Mekonnen, *RSC Sustainability*, 2024, **2**, 804–831.
5 P. Haida, S. Chirachanchai and V. Abetz, *ACS Sustainable Chem. Eng.*, 2023, **11**(22), 8350–8361.
6 C. Li, B. Ju and S. Zhang, *Cellulose*, 2021, **28**, 2879–2888.
7 L. Sougrati, A. Duval and L. Avérous, *J. Mater. Chem. A*, 2025, **13**, 4921–4939.
8 A. Duval, W. Benali and L. Averous, *ChemSusChem*, 2025, **18**, e202401480.
9 M. Bilal, S. A. Qamar, M. Qamar, V. Yadav, M. J. Taherzadeh, S. S. Lam and H. M. N. Iqbal, *Biomass Convers. Biorefin.*, 2022, **14**, 4457–4483.
10 J. Becker and C. Wittmann, *Biotechnol. Adv.*, 2019, **37**, 107360.
11 F. José Borges Gomes, R. E. de Souza, E. O. Brito and R. C. Costa Lelis, *J. Appl. Biotechnol. Bioeng.*, 2020, 100–105, DOI: **10.15406/jabb.2020.07.00222**.
12 L. Dessbesell, M. Paleologou, M. Leitch, R. Pulkki and C. Xu, *Renewable Sustainable Energy Rev.*, 2020, **123**, 109768.
13 D. D. S. Argyropoulos, C. Crestini, C. Dahlstrand, E. Furusjo, C. Gioia, K. Jedvert, G. Henriksson, C. Hulteberg, M. Lawoko, C. Pierrou, J. S. M. Samec, E. Subbotina, H. Wallmo and M. Wimby, *ChemSusChem*, 2023, **16**, e202300492.
14 M. Y. Balakshin, E. A. Capanema, I. Sulaeva, P. Schlee, Z. Huang, M. Feng, M. Borghei, O. J. Rojas, A. Potthast and T. Rosenau, *ChemSusChem*, 2021, **14**, 1016–1036.
15 J. J. Liao, N. H. A. Latif, D. Trache, N. Brosse and M. H. Hussin, *Int. J. Biol. Macromol.*, 2020, **162**, 985–1024.
16 Y. Yang, Y. Guan, C. Li, T. Xu, L. Dai, J. Xu and C. Si, *Adv. Compos. Hybrid Mater.*, 2024, **7**, 61.
17 C. Libretti, L. Santos Correa and M. A. R. Meier, *Green Chem.*, 2024, **26**, 4358–4386.
18 N. I. Jeffri, N. F. Mohammad Rawi, M. H. Mohamad Kassim and C. K. Abdullah, *Int. J. Biol. Macromol.*, 2024, **274**, 133506.
19 M. J. Getahun, B. B. Kassie and T. S. Alemu, *Process Biochem.*, 2024, **145**, 261–287.
20 M. T. Munir, M. Naqvi, B. Li, R. Raza, A. Khan, S. A. A. Taqvi and A.-S. Nizami, *J. Energy Storage*, 2024, **82**, 110477.
21 P. D'Arrigo, L. A. M. Rossato, A. Strini and S. Serra, *Molecules*, 2024, **29**, 442.
22 S. Behera, S. Mohapatra, B. C. Behera and H. Thatoi, *Crit. Rev. Biotechnol.*, 2024, **44**, 774–794.
23 R. Priyadarshi, T. Ghosh, S. D. Purohit, V. Prasannavenkadesan and J.-W. Rhim, *J. Cleaner Prod.*, 2024, **469**, 143151.
24 M. Mujtaba, L. Fernandes Fraceto, M. Fazeli, S. Mukherjee, S. M. Savassa, G. Araujo de Medeiros, A. do Espírito Santo Pereira, S. D. Mancini, J. Lipponen and F. Vilaplana, *J. Cleaner Prod.*, 2023, **402**, 136815.
25 L. Sougrati, A. Duval and L. Avérous, *Mater. Sci. Eng., R*, 2024, **161**, 100882.
26 G. F. Bass and T. H. Epps, *Polym. Chem.*, 2021, **12**, 4130–4158.
27 R. Grappa, V. Venezia, L. Basta, M. L. Alfieri, L. Panzella, M. Verrillo, B. Silvestri, M. Commodo, G. Luciani and A. Costantini, *ACS Sustainable Chem. Eng.*, 2024, **12**, 10653–10664.
28 L.-Y. Zhan, P. Li, Y.-D. Li, Y. Ran and J.-B. Zeng, *Eur. Polym. J.*, 2025, **227**, 113749.
29 T. Aro and P. Fatehi, *ChemSusChem*, 2017, **10**, 1861–1877.
30 T. Tang, J. Fei, Y. Zheng, J. Xu, H. He, M. Ma, Y. Shi, S. Chen and X. Wang, *ChemistrySelect*, 2023, **8**, e202204941.
31 A. Khajeh, Z. Nazari, M. Movahedrad and A. H. Vakili, *Sci. Total Environ.*, 2024, **943**, 173500.
32 J. Köhnke, N. Gerlinger, B. Prats-Mateu, C. Unterweger, P. Solt, A. Mahler, E. Schwaiger, F. Liebner and W. Gindl-Altmutter, *BioResources*, 2019, **14**, 1091–1109.
33 G. Unkelbach and T. Hirth, *EFB Bioeconomy J.*, 2022, **2**, 100036.
34 M. A. Lucherelli, A. Duval and L. Avérous, *Prog. Polym. Sci.*, 2022, **127**, 101515.
35 D. Montarnal, M. Capelot, F. Tournilhac and L. Leibler, *Science*, 2011, **334**, 965–968.
36 C. Taplan, M. Guerre, J. M. Winne and F. E. Du Prez, *Mater. Horiz.*, 2020, **7**, 104–110.
37 W. Denissen, J. M. Winne and F. E. Du Prez, *Chem. Sci.*, 2016, **7**, 30–38.
38 J. M. Winne, L. Leibler and F. E. Du Prez, *Polym. Chem.*, 2019, **10**, 6091–6108.

39 P. K. Karoki, S. Zhang, Y. Pu and A. J. Ragauskas, *Mater. Adv.*, 2024, **5**, 7075–7096.
40 Y. Du and D. Wang, *ACS Appl. Mater. Interfaces*, 2024, **16**, 41551–41561.
41 A. Moreno, M. Morsali and M. H. Sipponen, *ACS Appl. Mater. Interfaces*, 2021, **13**, 57952–57961.
42 J. Liu and K. V. Bernaerts, *J. Mater. Chem. A*, 2024, **12**, 2959–2973.
43 W. Zhao, Z. Liang, Z. Feng, B. Xue, C. Xiong, C. Duan and Y. Ni, *ACS Appl. Mater. Interfaces*, 2021, **13**, 28938–28948.
44 W. Zhuo, X. Luo, H. Yan, L. Shuai and Z. Wu, *Int. J. Biol. Macromol.*, 2025, 141550, DOI: **10.1016/j.ijbiomac.2025.141550**.
45 P. Haida and V. Abetz, *Macromol. Rapid Commun.*, 2020, **41**, e2000273.
46 E. M. Krall, E. M. Serum, M. P. Sibi and D. C. Webster, *Green Chem.*, 2018, **20**, 2959–2966.
47 L. Sougrati, A. Duval and L. Averous, *ChemSusChem*, 2023, **16**, e202300792.
48 J. Liu, A. Pich and K. V. Bernaerts, *Green Chem.*, 2024, **26**, 1414–1429.
49 L. Sougrati, A. Duval and L. Avérous, *Chem. Eng. J.*, 2025, **511**, 162201.
50 L. Li, X. Chen, K. Jin and J. M. Torkelson, *Macromolecules*, 2018, **51**, 5537–5546.
51 X. Meng, C. Crestini, H. Ben, N. Hao, Y. Pu, A. J. Ragauskas and D. S. Argyropoulos, *Nat. Protoc.*, 2019, **14**, 2627–2647.
52 A. Stücker, J. Podschun, B. Saake and R. Lehnen, *Anal. Methods*, 2018, **10**, 3481–3488.
53 A. Granata and D. S. Argyropoulos, *J. Agric. Food Chem.*, 1995, **43**, 1538–1544.
54 P. Haida, G. Signorato and V. Abetz, *Polym. Chem.*, 2022, **13**, 946–958.
55 Y. Archipov, D. S. Argyropoulos, H. I. Bolker and C. Heitner, *J. Wood Chem. Technol.*, 1991, **11**, 137–157.
56 J. Ruwoldt, *Surfaces*, 2020, **3**, 622–648.
57 M. Li, C. G. Yoo, Y. Pu and A. J. Ragauskas, *ACS Sustainable Chem. Eng.*, 2017, **6**, 1265–1270.
58 W. Denissen, G. Rivero, R. Nicolaÿ, L. Leibler, J. M. Winne and F. E. Du Prez, *Adv. Funct. Mater.*, 2015, **25**, 2451–2457.
59 J. D. Zwilling, X. Jiang, F. Zambrano, R. A. Venditti, H. Jameel, O. D. Velev, O. J. Rojas and R. Gonzalez, *Green Chem.*, 2021, **23**, 1001–1012.
60 B. Wang, D. Sun, H.-M. Wang, T.-Q. Yuan and R.-C. Sun, *ACS Sustainable Chem. Eng.*, 2018, **7**, 2658–2666.
61 C. Miao and W. Y. Hamad, *J. Appl. Polym. Sci.*, 2016, **134**, 44669.
62 G. Zhang, C. Tian, H. Chu, J. Liu, B. Guo and L. Zhang, *J. Mater. Chem. A*, 2023, **11**, 25356–25367.
63 T.-W. Lin, B. Mei, S. Dutta, K. S. Schweizer and C. E. Sing, *Macromolecules*, 2025, **58**, 1481–1497.
64 X. Cui, Y. Luo, Y. Yang and P. Tang, *Macromolecules*, 2025, **58**, 1898–1911.
65 A. Dhinojwala, J. C. Hooker and J. M. Torkelson, *J. Non-Cryst. Solids*, 1994, **172–174**, 286–296.
66 T. L. Chen, H. Kim, S. Y. Pan, P. C. Tseng, Y. P. Lin and P. C. Chiang, *Sci. Total Environ.*, 2020, **716**, 136998.
67 P. Anastas and N. Eghbali, *Chem. Soc. Rev.*, 2010, **39**, 301–312.
68 F. Gamardella, S. De la Flor, X. Ramis and A. Serra, *React. Funct. Polym.*, 2020, **151**, 104574.
69 A. I. Quilez-Molina, U. Chandra Paul, D. Merino and A. Athanassiou, *ACS Sustainable Chem. Eng.*, 2022, **10**, 15402–15413.
70 S. Shankar, J. P. Reddy and J. W. Rhim, *Int. J. Biol. Macromol.*, 2015, **81**, 267–273.
71 O. Yu and K. H. Kim, *Appl. Sci.*, 2020, **10**, 4626.
72 B. Krishnakumar, A. Pucci, P. P. Wadgaonkar, I. Kumar, W. H. Binder and S. Rana, *Chem. Eng. J.*, 2022, **433**, 133261.
73 N. L. Kapuge Dona, P. Y. Sauceda-Oloño and R. C. Smith, *J. Polym. Sci.*, 2024, **63**, 789–799.
74 J. M. Lang, U. M. Shrestha and M. Dadmun, *Front. Energy Res.*, 2018, **6**, 4.
75 C.-W. Chen, H.-I. Mao, H.-K. Lee, J.-Y. Chou and S.-P. Rwei, *J. Polym. Environ.*, 2023, **32**, 621–631.
76 M. Goliszek and B. Podkościelna, *Physicochem. Probl. Miner. Process.*, 2019, **55**, 1375–1381.
77 M. A. Shaid Sujon, A. Islam and V. K. Nadimpalli, *Polym. Test.*, 2021, **104**, 107388.
78 Y. Li, H. Feng, J. Xiong and L. Li, *Materials*, 2024, **17**, 5062.

5.3 Publication 3: Dioxaborolane Acrylate Vitrimers

This work was conducted in collaboration with Jana Struck, who synthesized and characterized the titania nanoplates and assisted with producing nanocomposites. The research was carried out in close cooperation with Tobias Vossmeyer's group, as part of the collaborative research center SFB 986 (subproject A1). We gratefully acknowledge the helpful supervision and advice of Tobias Vossmeyer and his team.

The concept of vitrimers enables a variety of different exchange chemistries, numerous building blocks, synthetic strategies, and recycling options. In this work, the focus was on identifying a material with outstanding features, enabling a concept for the industrial scalability of chemical reactions in accordance with green chemistry principles and providing a matrix for (nano)composites. The 'recyclability by design' thought is applied from typical lab experiments to real-world problems, and these use cases are elaborated in detail.

By using boronic ester metathesis in the form of DB in combination with a highly cross-linked network based on a tetrafunctional acrylate, excellent recyclability was demonstrated, with at least 20 consecutive recycling cycles. It was found that residual stress within the material influences its relaxation behavior and can be investigated through thermal annealing of the samples. The combination of a building block with an integrated dynamic exchange function enables the construction of industrial materials based on acrylates or ene-containing materials, facilitating the simple integration of the vitrimer concept into research fields where recyclability by design has not been a feature yet. The prepared network was further utilized to form interpenetrating covalent adaptable networks (IPCANs), described in the unpublished results in chapter 6.1.

Since the acrylate thiol coupling is not prone to side reactions, including oxidation, optically transparent materials can be produced from the chosen starting materials. The optical transparency was assessed, and potential protective shielding was demonstrated with digital images. Along with the optical features, the mechanical performance showed high mechanical strength, which is preserved for at least 10 recycling cycles. This recycling feature enables the grinding and heat compression of the material as a matrix in nanocomposites. The rapid curing process of the acrylate thiol coupling reaction enables the production of impregnated carbon fiber mesh composites with a thermoresponsive DB vitrimer matrix.

A solid-solid mixing process of titanium nanoplates and the DB vitrimer represents a novel approach to form nanocomposites. The heat compression process enables a homogeneous distribution of nanoplates within the matrix, which is reinforced by the particles acting as an inorganic filler. This approach allows for the formation of up to 50 wt.% of inorganic nanoparticles within the matrix, resulting in superior mixing compared to a solution-based mixing process, which avoids issues such as insolubility, agglomeration, and chemical inhomogeneity.

In short, rethinking commercial acrylate-based plastic formulations can be achieved in a recyclable manner if reconfigurable building blocks are utilized in the formulation. The resulting materials provide optical transparency and good mechanical properties, along with excellent reproducibility of at least 20 times. With these features, (nano)composites were made with a high content of inorganic fillers, which are evenly distributed within the vitrimer matrix.

Reproduced from "Transparent Dioxaborolane Acrylate Vitrimers Through One-Pot Reaction with Superior Strength as Matrix Material for Carbon Fibers and TiO_2 Nanoplates," *Macromol. Chem. Phys.*, **2025**, *226*, e00276 (doi.org/10.1002/macp.202500276) with permission from Wiley VCH Verlag GmbH & Co. The related supporting information is available in Section 9.4.

Macromolecular Chemistry and Physics

Macromolecular Chemistry and Physics
www.mcp-journal.de

RESEARCH ARTICLE OPEN ACCESS

Transparent Dioxaborolane Acrylate Vitrimers Through One-Pot Reaction With Superior Strength as Matrix Material for Carbon Fibers and TiO_2 Nanoplates

Florian C. Klein[1] | Jana Struck[1] | Tobias Vossmeyer[1] | Volker Abetz[1,2]

[1]Institute of Physical Chemistry, University of Hamburg, Hamburg, Germany | [2]Institute of Membrane Research, Helmholtz-Zentrum Hereon, Geesthacht, Germany

Correspondence: Volker Abetz (volker.abetz@uni-hamburg.de)

Received: 1 July 2025 | **Revised:** 29 August 2025 | **Accepted:** 3 September 2025

Funding: German Research Foundation (DFG), SFB986 "M3", funding number 192346071, subprojects A1 and A2; German Research Foundation (DFG), Cluster of Excellence CUI: Advanced Imaging of Matter, EXC2056, funding number 390715994; Open Access Publication Fund of Universität Hamburg, Project DEAL.

Keywords: acrylates | dioxaborolanes | fibers | nanocomposites | optical properties | titanium dioxide | vitrimers

ABSTRACT

This study presents an innovative approach to synthesizing multi-reprocessable materials by combining acrylates with dynamic dioxaborolane chemistry. The presented method enables a rapid, solvent-free, and cost-effective synthesis with a tetrafunctional linker to create highly crosslinked materials. The optically transparent vitrimers exhibit a glass transition temperature ($T_{g,DMA(6.28\ rad\ s^{-1})}$) of 58°C and a low activation energy of 33.4 kJ mol^{-1}, allowing for robust thermosetting polymers with exceptional thermal stability—demonstrated by a thermal degradation temperature of 305°C. The stress-relaxation dynamics show a rapid relaxation in 18 s at 110°C. Static stress-relaxation experiments are analyzed using a stretched exponential fit. Furthermore, frequency sweep measurements are used to determine the stress-relaxation properties and to discuss the applicability of two models to fit the stress-relaxation data after annealing. In the tensile test, the materials display an elastic modulus of 1.9 GPa and a tensile strength at maximum elongation of 58 MPa at room temperature after 20 recycling cycles. Finally, potential applications as matrix material for carbon fiber mesh composites or titanium dioxide nanoplates (50 wt.%) are presented.

1 | Introduction

Polymers with optical transparency and high mechanical stability have gained increasing interest in the field of dynamic covalent adaptable networks (CANs) [1, 2]. They allow to build lightweight and low-cost materials for applications requiring transparency, while maintaining a cross-linked polymer backbone [3–5]. Amorphous polymeric materials match these requirements and offer a broad variety of properties. However, these materials often lack thermal stability, recyclability, and resistance to solvents, which can limit their potential application in a closed-loop recycling [6].

The introduction of CANs into transparent and colorless materials allows for the application of transparency, robustness, flexibility, shape memory, and sustainability as well as thermo-programming of shapes [7–9]. This enables potential use-cases in smart electronic devices, packaging materials, transparent adhesives, decorative materials, and light management [10].

The incorporation of functional nanoparticles has great potential due to the variety of particle types and shapes and the filling degree [11–13]. Also, the addition of fibers such as carbon or cellulose nanofibers allows for the production of multifunctional composite materials [14–17].

The combination of the properties of two polymer classes, namely thermosets and thermoplastics, allows for materials that offer a permanent as well as dynamic network, which can be reconfigured via an associative molecular network rearrangement pathway by a stimulus, such as thermal energy, light, or pH [18, 19]. This class of associative CANs, the so-called vitrimers, broadens the field of traditional polymers using dynamic cross-links by taking advantage of the dimensional stability, higher thermomechanical properties of thermosetting materials, and plasticity, repairability, deformability, and recoverability of thermoplastic materials [20, 21]. Depending on the nature of the exchanging covalent bond, vitrimers offer different associative reaction pathways, including simultaneous bond formation and dissociation, for example, transesterification [22], disulfide exchange [23], imine metathesis [24], transimination [25], transamination [26], and siloxane exchange [27]. The chemical nature of the vitrimers determines the reaction kinetics as well as the temperature-dependence of the network rearrangement [28–31]. Moreover, self-healable soft hydrogels can be prepared using borax, which is used as a catalyst for a Michael-type thiol-ene polyaddition of poly(ethylene glycol) diacrylate and dithiothreitol [32]. Borate ions are capable of forming dynamic ester bonds with hydroxyl groups in bio-based materials such as starch, lignins, and cellulose [33].

However, to achieve stronger networks and to reduce the potential risk of contamination of biological systems when using borax, aliphatic or aromatic derivatives of boronic acids have become popular [34]. Dioxaborolanes represent esters of a trivalent organoboron compound, a boronic acid, linked with two vicinal hydroxy groups in a five-membered ring obtained through a condensation reaction [35]. These structures can rearrange through a metathesis reaction, leading to a reshuffling in the network, which allows for reprocessing with a low activation energy (E_a) between 7 and 52 kJ mol^{-1} for the exchange reaction [36–38]. Boronic esters can be introduced in different ways using trivalent organoboron compounds (boronic acids), forming five- and six-membered rings, named dioxaborolanes and dioxaborinanes, respectively [39]. A very interesting molecule is benzene-1,4-diboronic acid, which can be transferred into a variety of functionalized linkers by using vicinal 1,2-diols [37]. The use of boronates as monomers rather than direct condensation in the vitrimer formation is advantageous, since it excludes the need to remove water from the reaction system. The usage of boronates was first introduced by the group of Sumerlin et al., using divinyl compounds hardened via light-initiated thiol-ene addition [40, 41]. Thermal activation of thiol acrylate addition was utilized for the synthesis of soybean oil-based vitrimers with the linker 2,2'-(1,4-phenylene)-bis[4-mercaptan-1,3,2-dioxaborolane] (DBEDT) after curing the soybean acrylate at 120°C for 24 h. The material had a low E_a of 29 kJ mol^{-1} and a low T_g of 11°C [2]. The combination of the reactive thiol groups of DBEDT was performed with different electrophiles, such as epoxies, double bonds or acrylates [13, 15, 42–44]. Also, the linker has been used to prepare vitrimer materials from elastomers [45], polybenzoxazines [46], polyurethanes [47], plant oils [48], and commercial methylvinyl silicone rubber [49]. In these works, the mechanical and self-healing capabilities have been explored in detail. However, the stress-relaxation, recycling properties of more than five recycling cycles, and composite formation via fiber impregnation or loading with a large amount of nanoparticles have not been investigated in great detail.

In this work, the combination of a dithiol dioxaborolane monomer with a low molecular weight tetrafunctional acrylate allows for the formation of a highly crosslinked network with close proximity of the functional groups. This ensures fast exchange between the different network fragments and the formation of a material with a high elastic modulus (E), tensile strength, and low maximum elongation. The reaction follows the principles of green chemistry introduced by Anastas and Warner, using a bulk reaction, no by-products except water are formed in the reaction of the dioxaborolanes, and the reaction produces a functional material which can be reprocessed at least 20 times without any deterioration in its mechanical properties [50]. The concept of green chemistry was developed to prevent environmental pollution during the life-cycle of artificial materials, including waste prevention, less hazardous chemical synthesis, design for environmentally friendly degradation, atom economy, design for energy efficiency, and the use of renewable feedstock [51].

By using an acrylate monomer and the DBEDT crosslinker, an optically transparent material could be prepared. The production enables the casting and impregnation of materials such as carbon fiber mesh and the formation of nanocomposites with titanium dioxide (TiO_2) nanoplates with a high filling degree of 50 wt.%. The evaluation of 1, 5, 10, and 20 stages of remolding and reprocessing of the material enables an in-depth characterization of the closed-loop recycling for such materials. The employed synthetic route is promising for industrial applications of novel vitrimers using commercial acrylates, that can normally not be recycled due to their thermosetting nature.

2 | Experimental Section

2.1 | Materials

Benzene-1,4-diboronic acid (98.5%, Apollo Scientific), ethanol (anhydrous, ≥ 99.8%, VWR), 1-thioglycerol (> 95%, TCI), 2,2-bis([(1-oxoallyl)oxy]methyl)1,3-propandiyl diacrylate (Sigma Aldrich), tetrahydrofuran (99.5%, Thermo Scientific), toluene (99.5%, Fisher Scientific), acetone (99%, BCD Chemicals or VWR), oleic acid (technical grade, 90%, Sigma Aldrich), oleyl amine (>98% primary amine, Sigma Aldrich), 1-octadecene (technical grade 90%, Sigma Aldrich), titanium(IV) fluoride (98%, Sigma Aldrich or Fisher scientific), chloroform (99%, VWR), isopropyl alcohol (99.7%, VWR), and deuterated chloroform (99.5%, Eurisotop) were purchased and used as received without further purification. Plain weave carbon fiber mesh (3k, 200 g m^{-2}, EsportsMJJ) was purchased and used as received.

2.2 | Synthetic Procedures

2.2.1 | Environmentally Friendly Synthesis of 2,2-(1,4-phenylene)-bis(4-mercaptan-1,3,2-dioxaborolane) (DBEDT)

The synthesis was carried out according to the procedure following green chemistry principles described in the litera-

ture, using a solvent-free and catalyst-free process, without the generation of any waste or by-products, including recyclability-by-design [2, 46]. Benzene-1,4-diboronic acid (20.00 g, 120 mmol) and α-thioglycerol (25.96 g, 240 mmol) were dissolved in 400 mL degassed anhydrous ethanol (EtOH) and stirred for 24 h under nitrogen atmosphere at room temperature (24°C). Subsequently, EtOH and water were removed under reduced pressure, and the product was obtained as a white powder (36.8 g, 98%).

2.2.2 | Solvent-Free and Catalyst-Free Thiol-Acrylate Coupling Reaction to Produce Dioxaborolane Acrylate Vitrimer Films

DBEDT (6.20 g, 20 mmol) was filled into an aluminum mold and stored at 120°C on a heat plate (IKA RET Basic with a PT 1000.60 temperature sensor placed in an oil bath, IKA-Werke GmbH & Co. KG, Staufen, Germany) until the white powder was melted to a liquid. Then, 2,2-bis([(1-oxoallyl)oxy]methyl)1,3-propandiyl diacrylate (PETAC, 3.52 g, 10 mmol) was heated to 120°C in a glass vial on the same heat plate and added under manual stirring to the aluminum mold. After an optically homogeneous solution was achieved, gelation occurred after ≈60 s and the boronic acid acrylate vitrimer sample (BVS) was stored at 120°C for 24 h in an Heraeus VT6025 Vacutherm vacuum drying oven (Heraeus Holding GmbH, Hanau, Germany) at ambient pressure to achieve full crosslinking of the material. Afterward, the material was removed as a plate from the aluminum mold and processed using heat compression (150°C, 10 min, 10 kN) to obtain homogeneous transparent dioxaborolane acrylate vitrimer film BVS-1 with a thickness of approximately 0.5 or 1 mm. To prevent the films from sticking to the metal of the heat compression, poly(tetrafluoroethylene)-coated fiberglass fabric sheets (PTFE sheets), (PTFE permanent baking foil 0.13–570, Hightechflon GmbH & Co. KG, Konstanz, Germany) were used to obtain transparent vitrimer films. For the production of opaque surfaces, PTFE films were used (PTFE virgin film, 0.10–1200, Hightechflon GmbH & Co. KG, Konstanz, Germany.)

2.2.3 | Formation of a Dioxaborolane Acrylate Vitrimer Carbon Fiber Reinforced (BVCF) Composite

The formation of the BVCF composite was conducted using the solvent-free and catalyst-free thiol-acrylate coupling reaction to produce BVS with a modification. After the formation of the optically homogeneous solution by the addition of PETAC at 120°C, a carbon fiber mesh (3k, 200 g m^{-2}, plain weave) was embedded into the solution in the aluminum mold. Gelation occurred, and the BVCF composite was stored at 120°C for 24 h in an Heraeus VT6025 Vacutherm vacuum drying oven at ambient pressure to achieve full crosslinking of the material. Afterward, the material was removed from the aluminum mold and processed using heat compression and PTFE sheets (150°C, 10 min, 10 kN) to obtain homogeneous transparent dioxaborolane acrylate vitrimer film BVS-1 with a thickness of ≈1 mm. The formation process is displayed in Figure S1.

2.2.4 | Synthesis of the Titania Nanoplates

The titania nanoplates (TNPs) were synthesized according to the procedure by Gordon et al. [52]. with minor modifications. For details on the used synthesis parameters see Table S1. For purification, the TNP suspension was centrifuged at 4000 g at 15°C for 15 min. The blue residue was dispersed in chloroform and precipitated 1:1 (*V*:*V*) with a mixture of isopropyl alcohol and acetone with a ratio of 2:1 (*V*:*V*). This was followed by another centrifugation step as described above. The precipitation and centrifugation were repeated once. The obtained blue solid was dispersed in 8 mL of chloroform, resulting in a slightly turbid, blue solution. To remove the turbidity, the nanoparticle solution was filtrated with a syringe filter (PTFE, 0.45 µm). The filter was rinsed with 2 mL of chloroform, resulting in 10 mL of a clear, blue TNP solution.

Warning: During the TNP synthesis, hydrofluoric acid is formed in situ as a by-product in the reaction of TiF_4 and oleic acid.

2.2.5 | Formation of a Vitrimer Nanocomposite (BVS-TNP)

The BVS-TNP nanocomposite was formed by mixing 50 mg titanium dioxide nanoplates (TiO_2) with an edge length of ∼25 nm and a thickness of ∼6 nm to 50 mg of ground BVS-1 until a homogeneous compound of the two powders was achieved. The mixture was subsequently pressed in a hot press at 150°C for 10 min at a pressure of 10 kN using a custom-made stainless-steel mold (Figure S2) to give a circular test specimen with a diameter of 8 mm and a thickness of approximately 1 mm.

2.2.6 | Reprocessing

Reprocessing was performed by consecutive remolding, cutting the films in small pieces and pressing for 10 min at 150°C with a pressure of 10 kN into a 1 mm thick film. Attenuated total reflection-Fourier transformation-infrared (ATR-FT-IR), tensile test, and dynamic mechanical analysis (DMA) measurements were carried out after reprocessing.

2.2.7 | Self-Healing

Self-healing was performed by scratching a polymer film with a blade and successive holding at 150°C in an Heraeus VT6025 Vacutherm vacuum drying oven. Optical images were taken with a camera connected to an optical microscope after 0, 5, 30, 60, 120, and 180 min.

2.2.8 | Solubility Tests

Solubility tests were performed by adding samples of 4 mm diameter, 1 mm of thickness, and around 80 mg (m_0) to a vial and then immersing them in 1 mL of tetrahydrofuran (THF), toluene, acetone, and deionized water for 24 h at 23°C. Afterward,

the samples were taken out of the solution and then dried under vacuum for 24 h at 100°C and weighed (m_1).

2.3 | Instrumentation

Nuclear magnetic resonance spectra (^{1}H NMR and ^{13}C NMR) were recorded on a Bruker Avance III HD (600 MHz) and a Bruker Avance I (500 MHz) spectrometer (Bruker Corporation, Billerica, United States) with $CDCl_3$ as solvent and internal standard. Sample concentrations were between 10 and 40 mg mL^{-1}, and measurements were recorded at 298 K. Data processing was carried out with MestReNova (14.1.0, Mestrelab Research S.L., Santiago de Compostela, Spain).

Heat compression was carried out with a 2-column lab press PW (Presswerkzeug) 10 H (Hydraulik) with a heating plate system HKP (Heiz-/Kühlplattensystem) 500 160·160 mm and a TRG 3 (Temperaturregelgerät) temperature control unit (Paul-Otto Weber GmbH, Remshalden, Germany). The samples were heated for 2 min before pressing. PTFE sheets were used on top and underneath the sample to prevent the material from adhering to the metal surface of the heat compression.

ATR-FT-IR spectra were measured in the range of 4000–400 cm^{-1} with a resolution of 4 cm^{-1} and 64 scans using a Bruker FT-IR Vertex 70 spectrometer and a diamond ATR probe (Bruker Optics GmbH & Co. KG, Ettlingen, Germany) at room temperature (23°C). Measurements and data processing were carried out with Opus (8.7, Bruker Optics GmbH & Co. KG, Ettlingen, Germany).

Viscosity measurements were measured using an Anton Paar MCR 502 rheometer (Anton Paar Graz, Austria) with a cylindrical Peltier-temperature-controlled device (C-PTD 200) with a standard coaxial cylinder measuring system (Searle principle) consisting of a measurement bob B-CC27 and a cylinder C-CC27. The measurement system has a measuring gap of 1.133 mm. The viscosity was determined at 120°C while increasing the shear rate $\dot{\gamma}$ from 1 s^{-1} up to 1000 s^{-1}. Curing measurements were performed at a constant value of $\dot{\gamma} = 10$ s^{-1} at 120°C. Preheated PETAC (120°C) was added to the molten DBEDT after 88 s using a pipette. The measurement was stopped after the shear rate reached a value of 0 s^{-1}.

Thermogravimetric analysis (TGA) was carried out on a TG 209 F1 Libra (NETZSCH-Gerätebau GmbH, Selb, Germany) to determine the mass of a sample over time as the temperature changes. A temperature range of 25°C–600°C with a heating rate of 10 K min^{-1} under ambient atmosphere (oxygen) was used in a flow rate of 20 mL min^{-1}. Isothermal measurements were carried out at 150°C and 220°C for 2 h with ambient (oxygen) atmosphere in a flow rate of 20 mL min^{-1}. An amount of 5–10 mg of polymer or the dried TNPs was weighed into an aluminum crucible. For the determination of the organic content of the TNPs another heating program was utilized, while purging with nitrogen (40 mL min^{-1}). The samples were heated to 120°C at a rate of 10 K min^{-1} and kept for 10 min. Next, a temperature range of 120°C–800°C with a heating rate of 10 K min^{-1} was applied and kept at 800°C for 10 min. Lastly, the test chamber was exposed to ambient atmosphere (20 mL min^{-1}) for 10 min. Data processing was performed with Proteus Analysis (8.0.3, NETZSCH-Gerätebau GmbH, Selb, Germany).

Thermo-physical properties of the vitrimer films were determined on a differential scanning calorimeter DSC 204 F1 Phoenix (NETZSCH-Gerätebau GmbH, Selb, Germany). An amount of 5–10 mg polymer was weighed into an aluminum crucible. The heating and cooling rate was set to 10 K min^{-1}. The measurements were carried out in a nitrogen atmosphere with a flow rate of 20 mL min^{-1} in the temperature range between −50°C and 150°C and the thermal properties were analyzed using the DSC data of the second heating curve by determining the mid-point of the DSC-curve step as the glass transition temperature T_g. Data processing was performed with Proteus Analysis (8.0.3, NETZSCH-Gerätebau GmbH, Selb, Germany).

Rheological measurements by dynamic-mechanical analysis (DMA) were carried out using an Anton Paar MCR 502 rheometer (Anton Paar Graz, Austria) using a plate-plate geometry with a diameter of 8 mm. A CTD-180 heat chamber with flooded nitrogen atmosphere was used. The temperature was controlled by a Peltier system. The gap between the upper and the lower plate was usually set to 1 mm, a PP08 measurement tool with a diameter of 8 mm was used. Prior to all rheological measurements, amplitude-sweeps in oscillatory mode were performed at 110°C between 0.001% and 10% shear strain γ at a constant angular frequency of 6.28 rad s^{-1}. This should ensure that the chosen strain amplitude γ_0 was within the linear viscoelastic regime, so that the storage modulus G' and the loss modulus G'' were independent of strain. Temperature-sweep measurements were carried out in oscillatory mode with a constant angular frequency of 6.28 rad s^{-1} at a constant shear strain of 0.1% in the temperature range of 0°C–150°C. Stress-relaxation measurements were carried out with a shear strain amplitude of 1%, and the relaxation modulus was recorded as a function of time in the temperature range of 110°C–150°C. Frequency-sweep measurements were carried out at a constant shear strain of 0.1% in the temperature range of 120°C–180°C in the frequency range of 0.01–100 rad s^{-1}. Data processing was performed with RheoCompass (1.30, Anton Paar GmbH, Graz, Austria). Specimens for the DMA were pushed out with an 8 mm punch.

Stress-strain curves were recorded at room temperature (23°C) on a universal testing machine zwickiLine Z 5.0 TH (Zwick Roell GmbH & Co. KG, Ulm, Germany) using a 5 kN load cell. The measurements were carried out in accordance with the test standard DIN EN ISO 527-1. The initial force was 0.1 MPa, and the clamping length was 13.24 mm. The elastic modulus was determined at a speed of 1 mm min^{-1} between 0.05% and 0.25% elongation and the rest of the test was carried out at 10 mm min^{-1}. Data was processed using TestXpert II (V3.71, Zwick Roell GmbH & Co. KG, Ulm, Germany). The test specimens for the tensile test were punched out with a cutting press type ZCP020 (Zwick Roell GmbH & Co. KG, Ulm, Germany) with the attachment for test specimens of type 5B (according to DIN EN ISO 527-2).

UV–vis spectroscopy was performed on a UV5 spectrometer (Mettler Toledo, Gießen, Germany) in the spectral range of 230–900 nm with a sample holder for polymer films and a xenon light source. A film with a thickness of 0.5 mm was measured three

times and the absorption data was averaged and normalized. Data processing was performed with LabX (11.0.1, Mettler Toledo, Gießen, Germany).

Scanning electron microscopy (SEM) images were recorded on a LEO Gemini 1550 (Carl Zeiss, Oberkochen, Germany) using a carbon-coated copper transmission electron microscopy (TEM) grid. Secondary electrons were detected with an Everhart-Thornley detector, operating with 1–5 kV and 50–100 pA.

TEM images were recorded on a JEOL JEM-1011 (JEOL, Freising, Germany, LaB_6 cathode) with an acceleration voltage of 100 kV. For sample preparation, 7 µL of the TNP solution were added to 1 mL of toluene. Then, 10 µL of the diluted TNP solution were drop-casted onto a carbon-coated copper TEM grid (400 mesh).

X-ray diffraction (XRD) measurements were recorded with a Philips X'Pert PRO MPD (Philips, Amsterdam, Netherlands) from 20°–90°. The device was equipped with a copper K_α source ($\lambda = 0.154$ nm). For sample preparation, 60 µL of the TNP solution were drop-casted onto a silicon wafer and dried under ambient atmosphere. The diffractograms were referenced to the anatase crystal structure obtained from the ICSD database [53].

Grinding of materials was performed using a Mixer Mill MM 400 (RETSCH GmbH, Haan, Germany) with steel screw-top jars and a steel grinding ball under horizontal oscillation at 30 Hz for 1 min. For cryogenic grinding, the loaded steel jar was cooled in liquid nitrogen for 15 min before subsequent grinding.

Optical microscopy images were taken by a 5.6 M pixels Microscope Digital USB-camera attached to a Hengtech Zoom Stereomikroskop XTL (Hengtech, optische Instrumente, Mannheim, Germany).

3 | Results and Discussion

3.1 | Synthesis of Dioxaborolane Acrylate Vitrimers and Recycling Performance

The dioxaborolane linker DBEDT was synthesized in good yields according to the literature, starting from the corresponding boronic acid and diol [2]. The procedure employed an environmentally friendly protocol using non-toxic solvents at room temperature, as illustrated in Figure S3 [2, 46]. The product was obtained as a white powder. Its characterization by ATR-FT-IR, ^{1}H NMR, and ^{13}C NMR spectroscopy is presented in Figures S4–S6. By using a thiol compound and a commercially available acrylate, thiol-acrylate coupling chemistry is employed to form a covalent adaptable network without the need for an initiator, under thermal activation [2, 54]. This approach ensures the network formation in the absence of side products under atmospheric conditions, thus enabling easy processing and sample preparation. The formation of the dioxaborolane vitrimer is displayed in Figure 1a.

To ensure a homogeneous mixture, the dioxaborolane monomer was heated to 120°C. Once liquified, the preheated acrylate was added while stirring manually, and the mixture was homogenized. After approximately 60 s, gelation occurred.

The gelation process was investigated in detail by measuring the viscosity of the network formation in a Searle viscosity cell with an immovable vessel. Before the curing measurement, DBEDT was melted in the vessel at 120°C, and the viscosity was measured while increasing the shear rate from 1 s^{-1} up to 1000 s^{-1} (Figure S7). Next, the curing measurement was carried out at a constant speed of the measuring bob of 10 s^{-1} at 120°C. The time-dependent viscosity measurement is displayed in Figure 2. Preheated PETAC (120°C) was added to the molten DBEDT (1), which had a viscosity of 3.48 mPa·s, at 88 s using a pipette, followed by a mixing period (2). After 110 s, the reactive mixture reached a viscosity of 140 mPa·s, which can be assigned to the beginning of the pot life. The end of the pot life region (3) with a duration of approximately 60 s is reached after 153 s with a viscosity of 280 mPa s. Subsequently, the open time regime (2,3, and 4) spans out until 250 s. At this time, gelation occurs, which can be assigned to the increase of viscosity from $2.38 \cdot 10^5$ mPa·s to $4.37 \cdot 10^8$ mPa·s, leading to the hardening of the material (5). Based on the determined pot life of approximately 60 s, the stirring was kept to 60 s, and the prepared material was subsequently stored at 120°C for 24 h to ensure full conversion of thiol groups.

Subsequently, heat compression was used to process the material into homogeneous, transparent polymeric films, with network rearrangement facilitated by dioxaborolane metathesis reaction, as illustrated in Figure 1b [38, 55]. The complete consumption of the thiol groups of the films was confirmed by ATR-FT-IR spectroscopy in comparison with the acrylate PETAC and the dithiol building block DBEDT in Figure 3. In the spectrum of BVS-1, the characteristic thiol S–H vibration at 2563 cm^{-1} is no longer observable. Additionally, the vibrations associated with the acrylate groups disappear after complete reaction, as indicated by the vanishing signals at 1630 and 1611 cm^{-1}. Furthermore, the integrity of the dioxaborolane rings is preserved, as confirmed by the cyclic dioxaborolane ester, which is visible by a strong vibrational band at 652 cm^{-1}.

To evaluate reprocessability, the material underwent 5, 10, and 20 cycles of consecutive grinding and remolding, leading to the materials BVS-5, BVS-10, and BVS-20, respectively. To assess network formation, the samples were soaked in dry THF, toluene, and acetone for 24 h. The swelling ratio (S) and the soluble fraction (SF) were determined utilizing Equations S1 and S2, which are summarized in Table 1.

Subsequently, the samples remained intact, with values of SF ranging from 0% to 3%, indicating negligible solubility in the tested solvents. The swelling ratio S was found to depend on the solvent used, with the highest values observed in THF, followed by toluene, and the lowest in acetone. This indicates an influence of the polarity by aromatic building blocks of the polymer network, which enables higher swelling ratios for THF and toluene in the dioxaborolane network [36, 56]. When exposed to water, the samples exhibited slight hydrolysis, attributable to the reversibility of the dioxaborolane linkages. This behavior is advantageous for chemical recycling in aqueous environments. However, this reversibility may limit the material's suitability for outdoor applications or environments with high moisture levels. Moreover, this behavior is linked to the absorption of water molecules during the swelling process, leading to high values of

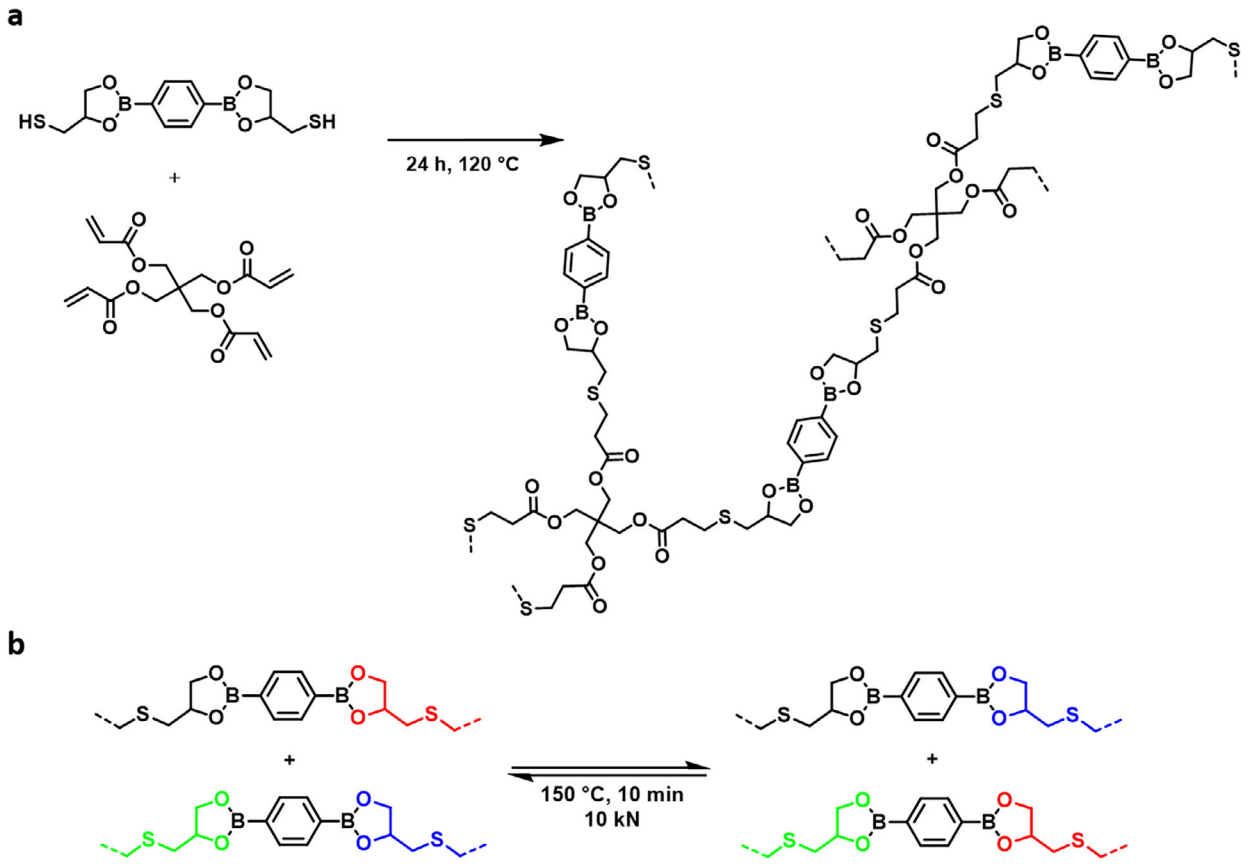

FIGURE 1 | (a) Monomers DBEDT and PETAC were reacted after mixing at 120°C until gelation occurred after approximately 60 s. To ensure complete network formation of the material BVS, the material was stored at 120°C for 24 h. (b) The macromolecular network rearrangement occurs through the dioxaborolane dithiol linker molecule, with reshuffling facilitated by the dioxaborolane metathesis reaction (150°C, 10 min, 10 kN).

S and dissociation, limiting the significance of the determined values for *S* and *SF* for water.

The described process enables the fabrication of transparent material films in specific shapes and allows for the reprocessing of the vitrimer using heat compression. The ATR-FT-IR spectra of the films after various reprocessing stages confirmed the preservation of the network structure (Figure S8). The subsequent discussion addresses the characterization results for all four reprocessed materials: BVS-1, BVS-5, BVS-10, and BVS-20.

3.2 | Thermal Performance

To assess the thermal performance of the formed dioxaborolane vitrimers, TGA was performed under ambient (oxygen) atmosphere, as shown in Figure 4. The decomposition temperature at 5% mass loss ($T_{5\%}$) ranged between 304°C and 307°C, confirming the high thermal stability of the reprocessed materials (Figure 4a). After reaching the degradation temperature, a steep decline in weight was observed, which can be determined at 328°C by the first derivative curves for the TGA measurement (Figure S9), resulting in a residual char content of 28%–30%. This residue can be attributed to the boronic remnants, indicating the flame-retardant potential of the material due to the high content of the dioxaborolane linker. To confirm thermal stability during heat compression, isothermal TGA was conducted for 2 h at 150°C under an ambient (oxygen) atmosphere. With a mass loss of less than 1%, the material demonstrates stability under (re)processing conditions, as well as during dynamic mechanical analysis, recycling, and stress-relaxation measurements (Figure 4b). To assess the short-term heat stability, isothermal TGA was also performed at 220°C for 2 h, indicating that the material remains thermally stable with only a 5% mass loss (Figure S10). These results show that the material exhibits minimal thermal degradation over short durations. Thermal properties were further examined using differential scanning calorimetry (DSC), which revealed no significant thermal alterations aside from an endothermal step corresponding to the $T_{g,DSC}$. It was determined as the midpoint of two tangents in the second DSC heating cycle, yielding a value of 45°C. Importantly, this $T_{g,DSC}$ remained unchanged even after 20 cycles of reprocessing (Figure 4c).

3.3 | Mechanical Properties

Uniaxial tensile testing was performed at room temperature (T = 23°C). Due to the high degree of crosslinking achieved with the tetrafunctional linker, the material exhibits a rigid behavior. Additionally, the materials provide a tough matrix suitable for composite applications, as a substantial tensile force is required to fracture the test specimens. Stress-strain curves illustrating the mechanical response after various stages of reprocessing are presented in Figure 5a. The excellent reprocessability is

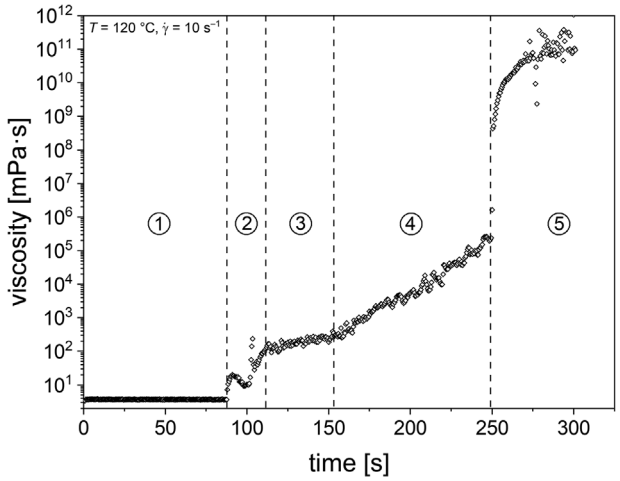

FIGURE 2 | Time-dependent viscosity measurement of the curing reaction between DBEDT and PETAC at 120°C applying a shear rate of 10 s^{-1}. In the initial phase (1), liquid DBEDT was in the measurement cylinder. Afterward, preheated PETAC (120°C) was added into the measuring gap using a pipette (2), leading to a mixture of both components (3) with a pot life until the viscosity begins to increase (4). After the end of the open time (2, 3, and 4), gelation occurs (5) indicating the curing of the vitrimer network with a step-like huge increase in the viscosity value.

demonstrated by the similar tensile test curves. The material's strength, characterized by the Young modulus E, is characterized by a value of 1.92 ± 0.13 GPa for BVS-1 and 1.79 ± 0.15 GPa for BVS-20. The data is summarized in Figure 5b. Welch's t-test with a significance level of $p = 0.05$ was performed to compare the means of E of the independent tensile test samples ($N = 3$) [57–59]. It was found that the means of the independent samples do not differ significantly. This confirms the preservation of the crosslinked network and the integrity of the covalent bonds, such as esters, thioethers, and dioxaborolanes. Because of the high density of dynamic covalent links, rupture events do not impair the overall mechanical performance of the materials. In fact, the mean of the tensile strength (σ_m) of BVS-20 with 68.0 ± 6.3 MPa differs significantly (Welch's t-test, $p = 0.05$, $N = 3$) from the mean of BVS-1 with 52.7 ± 2.3 MPa (Figure 5c). Since the means of BVS-1 and BVS-5, as well as BVS-1 and BVS-10 do not differ significantly, it can be assumed, that between 10 and 20 recycling steps, σ_m increases. The elongations at ultimate stress (ε_m) is 3.0% ± 0.3% for BVS-1 and 4.4% ± 0.5% for BVS-20 (Figure 5d). Again, the mean of ε_m of BVS-20 differs significantly (Welch's t-test, $p = 0.05$, $N = 3$) from the mean of BVS-1. Moreover, the means of BVS-1 and BVS-5, as well as BVS-1 and BVS-10 do not differ significantly. Thus, it can be assumed, that between 10 and 20 recycling steps, ε_m increases, indicating the scission of a small amount of non-reversible links in the backbone.

3.4 | Rheological Properties

To assess the thermomechanical performance of the synthesized dioxaborolane vitrimers, DMA was conducted. Before performing the oscillatory measurements, amplitude sweep tests were carried out at 110°C to establish the linear viscoelastic (LVE) regime and to ensure that the materials properties remained strain-independent (Figure S11). Within the tested amplitude range of 0.01% to 10%, the LVE was maintained up to approximately 4%–5%. Therefore, all subsequent oscillatory measurements were performed within this regime, using a deformation γ of 0.1% to avoid damaging the microstructure. Temperature sweep measurements were conducted over the range of 150°C–0°C and are presented in Figure S12. The curve exhibits two plateau regions separated by a transition step, corresponding to the glass transition. Below the $T_{g,DMA}$, indicated by the peak in the loss factor tan δ at approximately 55°C, the material is in the glassy state. Above 80°C, a rubbery plateau is observed, characterized by the absence of degradation and terminal flow, indicating the retention of the network structure in the rubbery state. Reprocessing influences the dynamic $T_{g,DMA}$, shifting it to 58°C after 10 recycling steps and further to 60°C after 20 recycling steps. This shift confirms the preservation of the network integrity and supports the earlier discussion of network reshuffling. Due to the low activation energy barrier of dioxaborolane vitrimers, the higher $T_{g,DMA}$ is beneficial, since it separates the material's properties at ambient temperature (23°C) from the reprocessing regime. Stress-relaxation measurements were conducted to investigate the dynamics of the molecular network rearrangement. Dioxaborolane linkages can undergo exchange via a metathesis reaction under thermal activation [53]. As the temperature increases, the rate of the dioxaborolane metathesis reaction also accelerates. Additionally, the network structure—specifically, the proximity of the functional groups—determines the exchange kinetics, influencing the overall relaxation behavior of the vitrimer. To determine the activation energy, a Kohlrausch-Williams-Watts (KWW) stretched exponential decay model was employed to determine the distribution of the relaxation times of the stress-relaxation [60]. This ensures a consideration of different relaxation modes contributing to the relaxation [61]. A non-normalized version of the KWW model (Equation S3) was used to calculate all parameters of the fit for the stress-relaxation modulus $G(t)$. The stretching parameter β is a measure of the uniformity of the exponential decay. A value of $\beta < 1$ indicates that the relaxation cannot be ascribed to a single relaxation time. Under ideal constrained conditions, $G(t)$ is expected to approach zero within experimental error at infinite time. To determine the relaxation dynamics, a single-step deformation of 1% was applied, and the stress-relaxation modulus was measured as a function of time over a temperature range of 110°C–150°C. The initial relaxation modulus G_0 remained constant across all examined temperatures and stages of recycling, confirming the presence of an associative network rearrangement (Figure S13). Non-normalized stress-relaxation curves are shown alongside the application of the KWW function to the data in Figure S14. The results, summarized in Table S2, demonstrate that the stress-relaxation behavior is well described by stretched exponential fits, with R^2 values exceeding 0.998. Overall, the distribution of characteristic relaxation times broadens with increasing temperature—for example, $\beta_{BVS\text{-}1,110°C}$ is 0.779, while at 150°C it decreases to 0.675-indicating an accelerated exchange rate. This is also reflected in the faster characteristic relaxation time $<\tau>$, calculated with Equation S4, which decreases from 18.0 to 5.7 s at 110°C and 150°C for BVS-1, respectively. The activation energy E_a for the dioxaborolane metathesis reaction was determined by linear regression of the experimentally derived $<\tau_r>$ values as a function of $1000/T$ in the linear range between 110°C–150°C (Figure S15). The calculated activation energy for BVS-1 was 34.4 ± 0.6 kJ mol^{-1}, a typical value for dioxaborolane

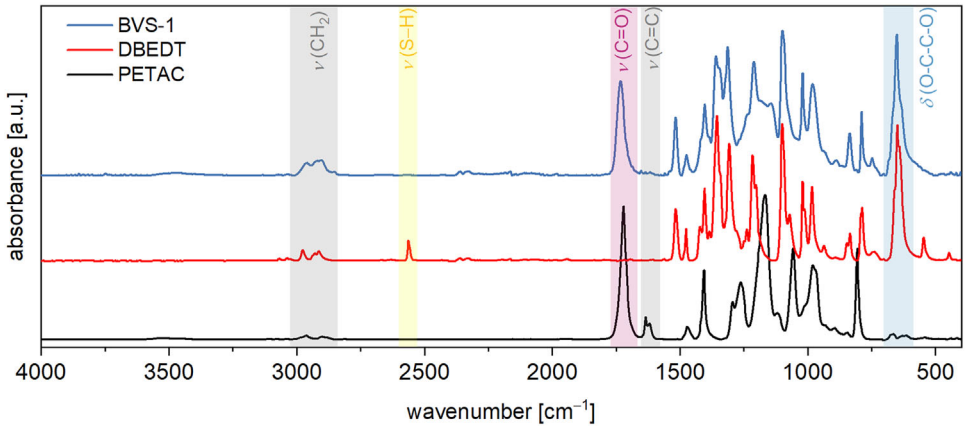

FIGURE 3 | ATR-FT-IR spectrum of BVS-1 and the monomers PETAC and DBEDT. The cyclic dioxaborolane ester appears as a strong band at 652 cm^{-1} (blue). Additionally, the vibrations of the CH_2 backbone are observed between 3100 and 2800 cm^{-1} (grey), while the ester bonds of the tetrafunctional acrylate linker appear at 1736 cm^{-1} (pink). The characteristic thiol S–H vibration at 2563 cm^{-1} is no longer observable in the vitrimer film BVS-1. Additionally, the vibrations associated with the acrylate groups of PETAC disappear after complete reaction, as indicated by the vanishing signals at 1630 and 1611 cm^{-1}.

TABLE 1 | Results of the swelling tests performed by addition of 1 mL of solvent (THF, toluene, acetone, and deionized water) to approximately 80 mg (m_0) of the respective sample. The vials were subsequently sealed and stored for 24 h at 23°C. Afterward, the supernatant was decanted, and the sample was weighed (m_1) and stored at 100°C under vacuum for at least 24 h until a constant mass was measured (m_2). The swelling ratio was calculated via $(m_1–m_0)/m_0$; the soluble fraction was calculated via $(m_0–m_2)/m_0$.

Sample	THF		Toluene		Acetone		Water	
	S **[wt.%]**	***SF*** **[wt.%]**	***S*** **[wt.%]**	***SF*** **[wt.%]**	***S*** **[wt.%]**	***SF*** **[wt.%]**	***S*** **[wt.%]**	***SF*** **[wt.%]**
BVS-1	188	0	133	0	88	2	279	48
BVS-5	168	1	104	3	79	2	343	54
BVS-10	187	0	134	6	110	2	228	51
BVS-20	201	3	143	1	115	1	372	48

metathesis. As expected, it did not increase significantly after 20 cycles of reprocessing with a value of 36.1 ± 0.4 kJ mol^{-1}. Significance was tested using a two-tailed *t*-test, using the slopes of the linear regressions of the experimentally derived $<\tau_r>$ values as a function of $1000/T$ of BVS-1 and BVS-20 with a significance level α of 0.05 [62]. The null hypothesis of the *t*-test is that there is a significant difference between the slopes of the linear regressions for the samples BVS-1 and BVS-20. A *p*-value of 0.0642 was calculated using Equation S5. Therefore, $p > 0.05$, and the null hypothesis is rejected. With increasing recycling cycles, the values of β decrease, and stress-relaxation occurs more rapidly at all tested temperatures (Table S2). This behavior may be attributed to the increasing number of broken non-dynamic bonds within the material, which would facilitate faster relaxation processes. Interestingly, this trend was not observed in the tensile-testing and DMA, suggesting that no significant degradation occurs during the recycling steps. Thus, it was hypothesized, that the reprocessing induced internal stress within the material that was not fully relaxed in the relevant timescales of reprocessing (10 min) and subsequent measurement. To investigate the influence of thermal treatment on stress-relaxation, the material BVS-20 was tempered at 120°C for 20 h. The results of the DMA and stress-relaxation are presented in Table S3 and Figures S16 and S17. The data suggest the presence of residual internal stress, as the distribution of relaxation times approaches the values observed in material BVS-1. Specifically, the relaxation time distribution for $\beta_{\text{BVS-20,annealed,110°C}}$ shows 0.759 and for $\beta_{\text{BVS-20,annealed,150°C}}$ it was 0.676, indicating a partial recovery toward the behavior of the initial material after one recycling step. The values of $<\tau>$ are comparable to those observed for BVS-1 and are significantly higher than for the non-annealed material BVS-20. This highlights the influence of thermal history—specifically, heat treatment—on stress-relaxation behavior. It underscores the importance of thermal timescales for the application range and the recycling processes of these materials. Following annealing, the activation energy remained similar to that of the non-annealed sample (36.5 ± 1.2 kJ mol^{-1}). The validity of the activation energy calculation and the vitrimer model was further supported by frequency sweep tests conducted at various temperatures in the range of 120°C and 180°C, with angular frequencies between 0.01 and 100 rad s^{-1} (Figure S18). These tests showed that, with increasing temperature, the storage modulus remained in the same order of magnitude across the frequency range of 10–100 rad s^{-1}, confirming the presence of an associative exchange mechanism of crosslinks. The crossover points at lower frequencies were used to extract a characteristic stress-relaxation time, τ. By performing a linear regression of τ values plotted against $1000/T$, an activation energy was determined

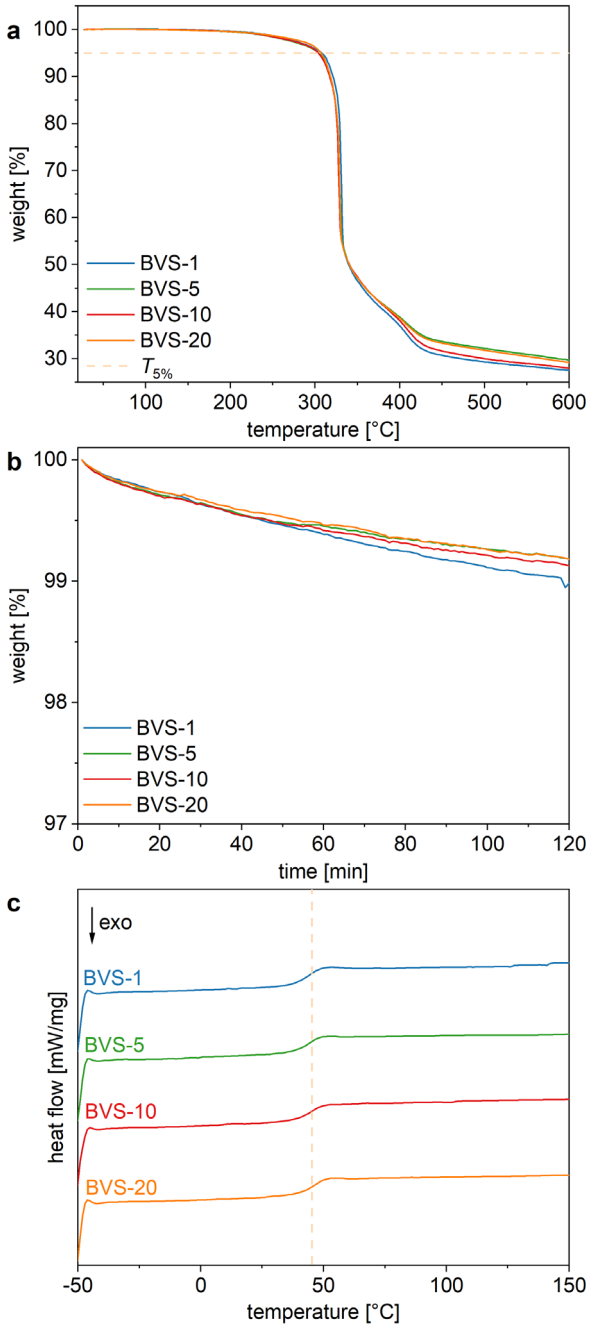

FIGURE 4 | (a) Thermogravimetric analysis (TGA) of the dioxaborolane vitrimer (BVS) materials over the temperature range of 25°C–600°C at a heating rate of 10 K min^{-1} under ambient (oxygen) atmosphere, revealing thermal degradation temperatures between 304°C and 307°C. (b) Isothermal TGA conducted at 150°C for 2 h under the same atmosphere showed no significant thermal degradation. (c) Differential scanning calorimetry (DSC) heating curves in the range of −50°C to 150°C at 10 K min^{-1} under nitrogen atmosphere, analysis of the second heating cycle indicated an unchanged $T_{g,DSC}$ of 45°C after all reprocessing cycles.

under the assumption of a single Maxwell element (Figure S19). The resulting activation energies ranged from 39.9 ± 2.8 to 32.8 ± 1.6 kJ mol^{-1}. For the annealed sample, the frequency sweep analysis yielded an activation energy of 32.1 ± 0.5 kJ mol^{-1} (Figure S20). However, this approach assumes that the entire stress-relaxation process can be accurately represented by a single, average stress-relaxation time, which is an oversimplification for a vitrimer material. Nonetheless, the consistency between the two activation energy values indicates that, for highly crosslinked vitrimer systems, approximating the relaxation time distribution can provide valuable insights into their stress-relaxation behavior.

3.5 | Optical Properties, Shape-Memory, Self-Healing

The optical transparency of the material was investigated using UV–vis spectroscopy, measuring the absorbance of BVS-1 across the spectral range of 230–900 nm (Figure 6). The results clearly show that the absorbance was at its maximum within the 230–300 nm wavelength range. Beyond this range, the absorbance gradually decreased, reaching values of 0.22 at 400 nm and 0.11 and 900 nm. These results indicate that the vitrimer exhibits a high degree of transparency, which is also evident from the corresponding digital images in Figure 6.

By using different PTFE sheets in the heat compression process, different surface morphologies can be achieved, resulting in either opaque or transparent films (Figure 7a). The processability was confirmed by ATR-FT-IR spectroscopy and tensile testing (see above), demonstrating that homogeneous films could be produced after 10 min of heat compression at a pressing force of 10 kN and a temperature of 150°C.

Smart shape-memory materials have the capacity to change, store, and recover shapes in response to environmental stimuli. The phenomenon where a material can revert to its original shape after a significant plastic deformation upon the application of a specific stimulus is known as the shape-memory effect. Different thermal stimuli can reveal multiple shape-memory abilities, as shown in Figure 7b,c. For instance, a 0.5 mm thick dioxaborolane vitrimer can be thermally programmed for shape adaption: twisting the material at an elevated temperature (80°C, 10 s) creates a deformed shape that can be "frozen" by cooling to room temperature. Subsequent heating above its T_g restores the material to its original linear shape (Figure 7b). Additionally, by heating to a higher temperature for a longer duration (150°C, 1 min), a new permanent shape—such as a helix—can be programmed through solid state plasticity. Cooling to room temperature preserves this new shape, which can then be reactivated and transformed through controlled heating, enabling applications in self-healing and engineering (Figure 7c). Self-healing was demonstrated by scratching a BVS-1 film, followed by storage at 150°C in an oven (Figure S21). After 180 min, healing was observed by molecular network rearrangement, effectively repairing the scratched surface.

3.6 | Formation and Chemical Recycling of Carbon Fiber Reinforced Composites

The current state-of-the-art production of carbon fiber (CF)-reinforced composites involves the use of thermosetting resins to create stable composite materials. By impregnating a CF mesh with the BVS material to form BVCF, a homogeneous matrix surrounding the fibers was obtained, illustrating the potential

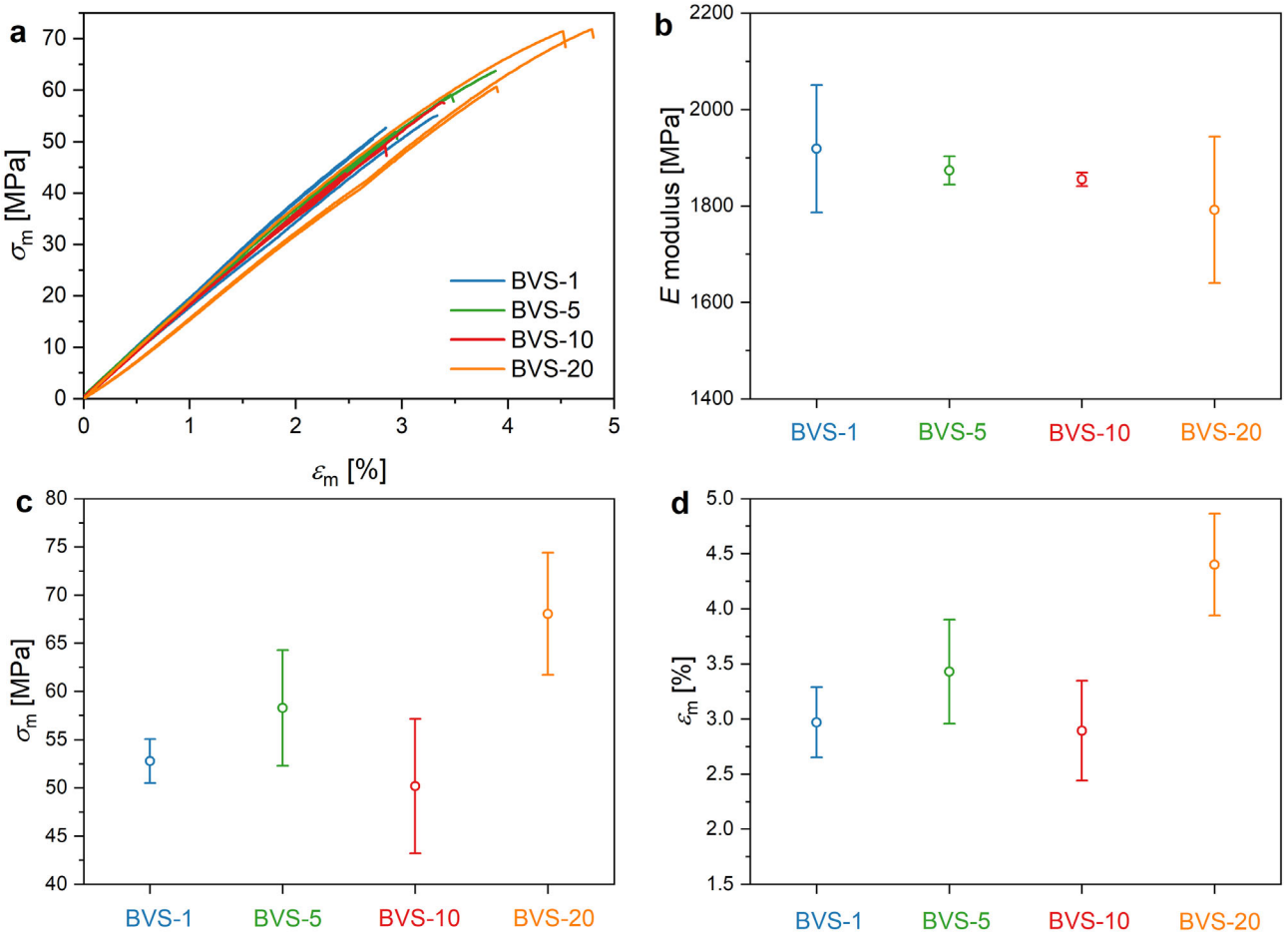

FIGURE 5 | (a) The stress-strain curves (at $T = 23°C$) of the BVS materials after various reprocessing stages display a rigid behavior with similar profiles. Upon reprocessing, the E modulus decreases slightly from 1.92 ± 0.13 GPa to 1.79 ± 0.15 GPa (b). Meanwhile, the tensile strength (σ_m) increases from 52.7 ± 2.3 MPa to 68.0 ± 6.3 MPa (c), and the elongations at ultimate stress (ε_m) rises from 3.0% ± 0.3% to 4.4% ± 0.5% (d), indicating consistent or lightly improved mechanical performance after multiple reprocessing cycles.

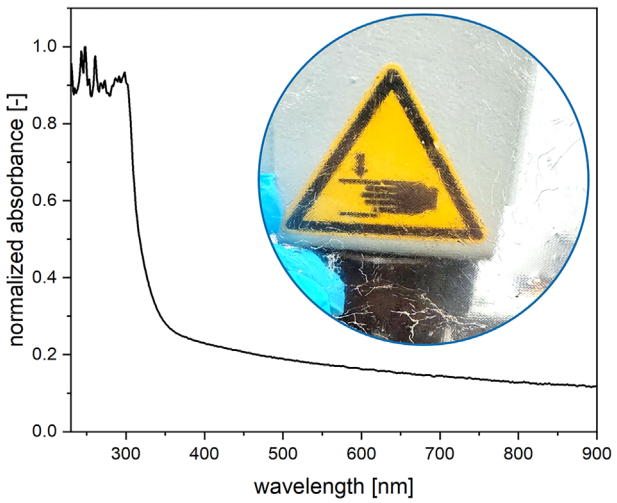

FIGURE 6 | UV–vis transmission spectrum of BVS-1 with a thickness of 0.5 mm and a digital image of the film BVS-1 (thickness 1 mm) with a symbol in the background.

application of BVS in coatings or surface modifications (Figure S1; Figure 8).

This composite leverages the advances of both components, resulting in increased tensile strength and enhanced flexibility (improved elongation performance). Overall, this combination improves the toughness of the BVS. However, the stiffness of the material remains unchanged, as evidenced by the consistent E modulus value, indicating that the reinforcement does not adversely affect the elastic properties (Table 2). Interestingly, the composite exhibits peaks in the gradual slope of the tensile test curve, indicating crack formation within the domains in between different CF strains.

Self-healing was investigated by scratching the surface of BVCF, followed by storage at 150°C in an oven (Figure S22). Again, after 180 min, healing was observed by molecular network rearrangement. Since these experiments are of a qualitative nature, no difference between the optical healing properties between BVS-1 and BVCF could be determined.

The fabrication of this CF-reinforced material demonstrates the simplicity of utilizing thiol-based linkers and readily available acrylates for rapid curing applications of composites, such as adhesives and other functional materials. The process requires no additional reactants, and the absence of by-products ensures bubble-free, homogeneous curing. By employing dioxaborolane

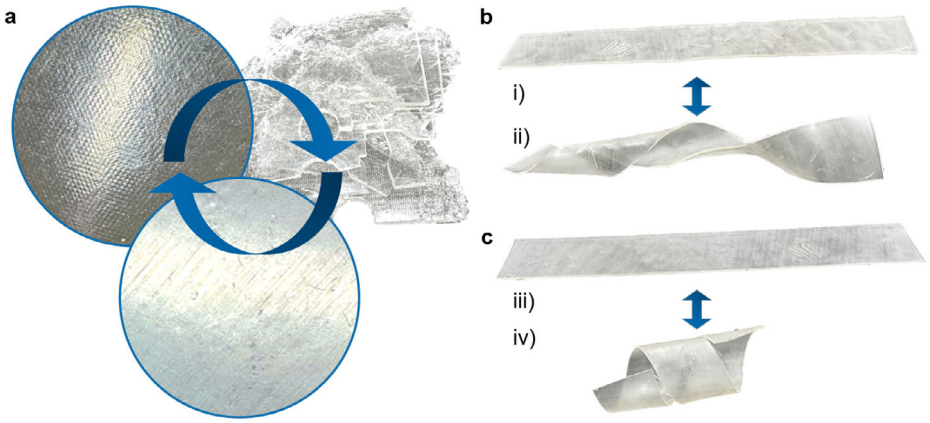

FIGURE 7 | (a) The reprocessing cycle of the dioxaborolane-based material BVS was demonstrated through consecutive grinding and heat compression molding (150°C, 30 min, 10 kN), resulting in the formation of homogeneous vitrimer films. The surface morphology of the films could be tailored by selecting different PTFE sheets during the compression process. (b) Exemplary shape-memory properties of the dioxaborolane vitrimer examined by thermo-shape adaptation of a flat sheet (i) which was heated at 80°C for 10 s, then freezing the film below T_g at room temperature into a twisted shape (ii) and heating to 80°C led to relaxation to the original shape. (c) Programming a new shape was possible by heating the material (iii) to 150°C for 30 s and subsequent cooling to room temperature led to new solid-state plasticity (iv). Again, a heating cycle to 80°C demonstrated the thermoadaptive properties after cooling to room temperature (iii). The newly programmed shape could be recovered after heating above the T_g for 30 s (iv).

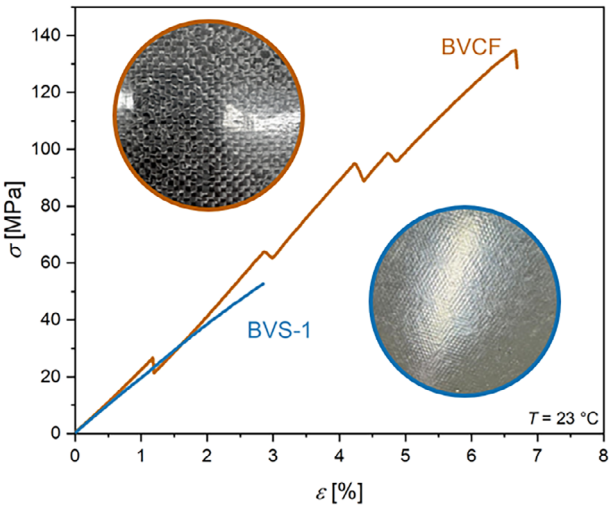

FIGURE 8 | Tensile testing of the BVCF material (digital image in the upper left corner) compared to the matrix BVS-1 without CF reinforcement (digital image in the lower right corner). A comparison of the tensile test results demonstrates similar *E* moduli, and an increase in tensile strength at maximum elongation and in the ductility of the material.

TABLE 2 | Results of the tensile testing of BVCF compared to BVS-1 without CF reinforcement with E, σ_m, and ε_m.

Sample	E [GPa]	σ_m [MPa]	ε_m [%]
BVS-1	1.9 ± 0.1	52.8 ± 2.2	3.0 ± 0.3
BVCF	2.7 ± 0.6	123.4 ± 16.1	6.0 ± 0.9

vitrimer chemistry, the recycling and reuse of carbon fibers becomes possible—since dioxaborolanes are hydrolysable, the vitrimer matrix can be removed from the CFs. However, for applications in wet environments with high humidity, it would be necessary to combine the composite with water-resistant materials to ensure durability.

3.7 | Vitrimer Nanocomposites With TiO_2 Nanoplates

A homogeneous matrix with excellent reprocessing capabilities is essential for the development of nanocomposites. By forming and subsequently cryo-grinding of BVS-1, a powder precursor suitable for inorganic-organic composites can be prepared (Figure 9a,b). In this approach, dried TiO_2 nanoplates (see Tables S1 and S4, and Figures S23–S26, for details on the synthesis parameters and the properties of the TNPs) were mixed with 50 wt.% of the ground BVS-1 and then processed via heat compression in a custom-made stainless-steel mold (Figure S2) to produce a nanocomposite pellet with a diameter of 8 mm. The resulting bluish material was further analyzed using scanning electron microscopy (SEM), which revealed a uniform distribution of nanoplates within the vitrimer matrix (Figure 9c,d).

The platelet shape was chosen because it is predestined in nature to form composite materials with good mechanical properties. One example for a natural composite material is nacre, which consists of hard calcium carbonate mineral platelets and a soft organic matrix (proteins, polysaccharides) [63]. The resulting microstructure is ordered on multiple hierarchical levels, providing exceptional mechanical properties, such as high strength, toughness, and ductility [64, 65]. A platelet shape results in a higher theoretical packing density (approximately 90 vol%) [66] compared to, for example spheres (approximately 75 vol%) [66, 67], and therefore in theoretically better mechanical properties.

To determine the influence of the nanoplates on the thermomechanical performance of the synthesized dioxaborolane vitrimers, dynamic mechanical analysis (DMA) was conducted

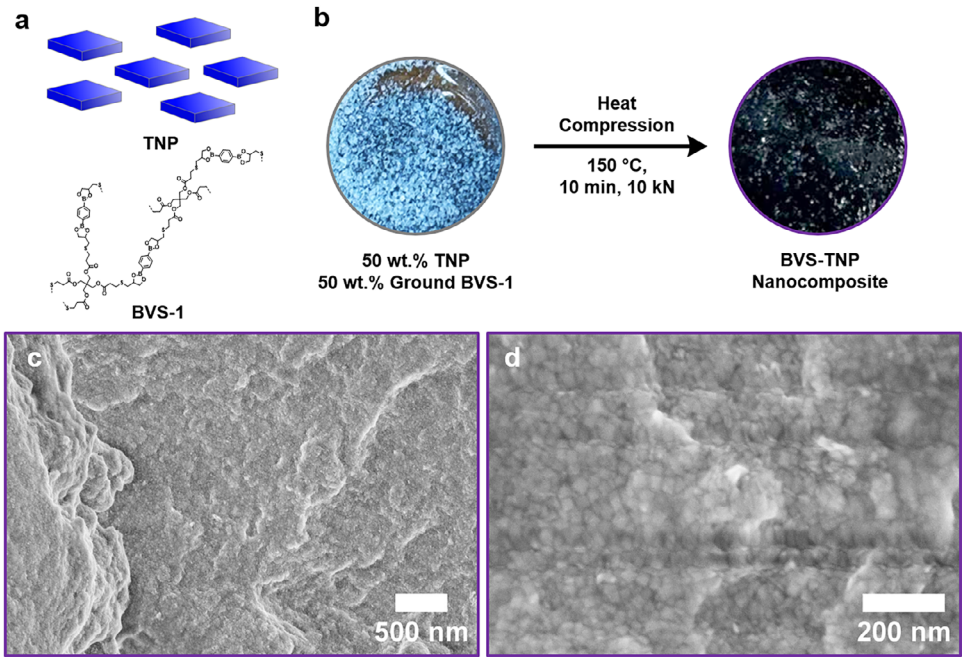

FIGURE 9 | (a) Illustration of TiO_2 nanoplates (TNPs) and BVS-1. (b) Schematic of the formation of TNP-filled dioxaborolane vitrimer nanocomposites (BVS-TNP). In this process, TNPs were mixed with ball-milled (60 s, 30 Hz, cryo) BVS-1 matrix powder, followed by blending and heat compression in a custom-made stainless-steel mold (150°C, 10 min, 10 kN) to produce a nanoparticle-filled composite material with an inorganic loading of 50 wt.%. (c,d) SEM images of the resulting BVS-TNP material at different magnitudes, revealing a homogeneous distribution of the TiO_2 nanoplates within the vitrimer matrix.

with the produced test specimen. Before performing the oscillatory measurements, an amplitude sweep test was carried out at 110°C to establish the LVE regime and to ensure that the materials properties remained strain-independent (Figure S27). Within the tested amplitude range of 0.01% to 10%, the LVE was maintained up to 2%. Due to a higher value of G'', the nanoplates seem to intensify the energy dissipation within the matrix. The temperature sweep curve, displayed in Figure S13, displays the glass transition at 60°C. In comparison with the neat material BVS-1, the storage modulus is characterized by higher values above the glass transition, which can be assigned to reinforcement by the inorganic filler (Figure S28). No influence on the self-healing performance could be determined, since the surface became non-uniform after storage at 150°C in an oven (Figure S29).

Again, stress-relaxation measurements were carried out, with the results displayed in Figure S30. The analysis of the non-normalized stress-relaxation data with a KWW-fit (Table S5) yields values of β in the range of 0.226–0.286 and very fast averaged stress-relaxation times (>1 s). This indicates a broadening of the relaxation time distribution, caused by the nanoplates. The influence of the inorganic filler also becomes evident in the activation energy, which showed a value of 58.7 kJ mol^{-1}, indicating that the network rearrangement is influenced by interactions between particles, matrix, and between matrix and particles. This method demonstrates the ability to create nanocomposites with high loadings of inorganic nanoparticles and introduces a novel approach to fabrication through solid-solid mixing and subsequent molecular network rearrangement of the vitrimer.

4 | Conclusions

The prepared dioxaborolane vitrimer demonstrates the potential of utilizing a dithiol linker with a tetrafunctional acrylate to produce fast-curing, homogeneous vitrimer. Its molecular network rearrangement operates via dioxaborolane metathesis reaction, and due to the high density of dynamic bonds and their spatial proximity, the materials exhibit exceptional reprocessing capability—allowing for at least 20 recycling cycles without degradation of mechanical properties. The vitrimer exhibits favorable mechanical and thermal properties with an elastic modulus of 1.9 GPa, a degradation temperature onset $T_{5\%}$ of 305°C, and glass transition temperatures of 45°C (DSC) and 58°C–65°C (DMA). The polymer network was formed through solvent-free bulk polymerization of the monomers, achieving complete curing after 24 h of hardening. The resulting vitrimer films could be readily reprocessed via heat compression at 150°C and 10 kN for 10 min, demonstrating their recyclability and structural stability. The material demonstrates stability against common organic solvents, including THF, toluene, and acetone. Stress-relaxation tests conducted after various reprocessing cycles reveal rapid relaxation behavior; with each cycle, the relaxation time distribution broadens and shifts toward lower values, indicating faster stress-relaxation. Due to its amorphous network structure, the materials exhibit high transparency to visible light, rendering them colorless and suitable for applications such as coatings, adhesives, and lacquers. Additionally, by impregnation of a carbon fiber mesh with the vitrimer and processing it accordingly, a CF-reinforced composite was produced, resulting in enhanced tensile strength and ductility, thereby improving the overall toughness of the material. An alternative approach

to produce composites involves forming nanoparticle reinforced vitrimer composites by mixing nanoparticles with ground vitrimer powder. This results in homogeneous nanocomposites with a high inorganic loading of 50 wt.% while maintaining uniform nanoparticle distribution. The nanoparticles reinforce the matrix and influence the stress-relaxation behavior, leading to stretched decays of the relaxation modulus. These findings emphasize the importance of testing numerous reprocessing cycles to ensure high reusability. Additionally, thermo-responsive shape-memory and shape-programming were successfully demonstrated. Due to its ability to be recycled many times without major changes to the highly cross-linked network structure, the dioxaborolane vitrimer produced may become useful in new manufacturing processes for nanocomposite materials with high inorganic content. Furthermore, it enables the system to be used as a dynamic network structure in commercial acrylate-based plastic formulations that should include recycling capabilities for more sustainable plastics.

Author Contributions

F.C.K.: writing – review and editing, writing – the original draft, conceptualization, methodology, investigation, data curation, formal analysis, validation, and performing the experiments; J.S.: writing – review and editing, writing – original draft, investigation, formal analysis, synthesis and characterization of the nanoparticles, T.V.: writing – review and editing, writing – original draft, supervision, resources, and funding acquisition; V.A.: writing – review and editing, writing – original draft, conceptualization, supervision, resources, and funding acquisition.

Acknowledgements

The authors gratefully acknowledge financial support from the German Research Foundation (DFG) via SFB986 "M3", funding number 192346071, subprojects A1 and A2. J.S. acknowledges financial support from the Cluster of Excellence CUI: Advanced Imaging of Matter of the DFG—EXC2056—project ID 390715994. Open Access Publication was enabled by Universität Hamburg by the Project DEAL. The authors would like to address special thanks to Martin Kehden who conducted the DSC and TGA measurements. The authors thank Nina Schober for measuring the XRD diffractograms. The authors acknowledge the nuclear magnetic resonance division and the electron microscopy division of the chemistry department at Universität Hamburg. The authors thank Robert Schön and Stefan Werner for the morphological investigations by SEM and TEM, respectively.

Open access funding enabled and organized by Projekt DEAL.

Conflicts of Interest

The authors declare no conflicts of interest.

Data Availability Statement

The data that support the findings of this study are available from the corresponding author upon reasonable request.

References

1. A. Mariani and G. Malucelli, "Biobased Vitrimers: toward Sustainability and Circularity," *Chemical Communications* 61 (2025): 2173–2189.

2. A. Zych, J. Tellers, L. Bertolacci, et al., "Biobased, Biodegradable, Self-Healing Boronic Ester Vitrimers from Epoxidized Soybean Oil Acrylate," *ACS Applied Polymer Materials* 3 (2020): 1135–1144.

3. J. Kang and C. Nam, "Next-generation Vitrimer Composites for Future Mobility: Balancing Sustainability and Functionality—A Perspective," *European Polymer Journal* 233 (2025): 113967.

4. S. Maes, N. Badi, J. M. Winne, and F. E. Du Prez, "Taking Dynamic Covalent Chemistry out of the Lab and into Reprocessable Industrial Thermosets," *Nature Reviews Chemistry* 9 (2025): 144–158.

5. V. Amfilochiou, T. Debsharma, I. De Baere, F. Du Prez, and W. Van Paepegem, "Thermomechanical Characterisation of Reprocessable, Siloxane-based, Glass-fibre-reinforced Vitrimers," *Composites Part B* 276 (2024): 111354.

6. S. Shekhar, M. E. Hoque, P. K. Bajpai, H. Islam, and B. Sharma, "Chemical Upcycling of Plastics as a Solution to the Plastic Trash Problem for an Ideal, Circular Polymer Economy and Energy Recovery," *Environment, Development and Sustainability* 26 (2023): 5629–5664.

7. M. Hayashi and A. Katayama, "Preparation of Colorless, Highly Transparent, Epoxy-Based Vitrimers by the Thiol-Epoxy Click Reaction and Evaluation of Their Shape-Memory Properties," *ACS Applied Polymer Materials* 2 (2020): 2452–2457.

8. J. Ma, L. E. Porath, Md. F. Haque, et al., "Ultra-thin Self-healing Vitrimer Coatings for Durable Hydrophobicity," *Nature Communications* 12 (2021): 5210.

9. X. Fan, L. Wang, S. Feng, and L. Li, "Bio-Based Vitrimeric Silicone Materials with High-Strength, Reprocessable, Healing, and Transparent Properties," *Macromolecular Rapid Communications* 44 (2023): 2300445.

10. X. Liu, J. Yang, C. Guan, and J. Wang, "Building a Circular Economy for Flexible Electronics: Design, Fabrication, Service, and Recycling," *Matter* 8 (2025), 1–23.

11. N. Lorenz, W. E. Dyer, and B. Kumru, "High-Performance Vitrimer Entailing Renewable Plasticizer Engineered for Processability and Reactivity toward Composite Applications," *ACS Applied Polymer Materials* 7 (2025): 1934–1946.

12. G. Signorato, L. R. Klauke, P. Haida, T. Vossmeyer, and V. Abetz, "Superparamagnetic Iron Oxide Nanoparticle—Vitrimer Nanocomposites: Reprocessable and Multi-responsive Materials," *Polymer* 318 (2025): 127968.

13. M. Cvek, J. Sevcik, J. Vilcakova, A. Athanassiou, and A. Zych, "Self-healing Recyclable Bio-based Magnetic Composites with Boronic Ester Vitrimer Matrix," *Applied Materials Today* 35 (2023): 101997.

14. A. Basu, S. Parasuram, S. H, A. S. Salvi, S. Kumar, and S. Bose, "Triple Dynamic Network-Enabled Vitrimer for Repairable and Recyclable Carbon Fiber-Reinforced Composites," *ACS Applied Polymer Materials* 7 (2025): 4931–4943.

15. D. Sangaletti, L. Ceseracciu, L. Marini, A. Athanassiou, and A. Zych, "Biobased Boronic Ester Vitrimer Resin from Epoxidized Linseed Oil for Recyclable Carbon fiber Composites," *Resources, Conservation & Recycling* 198 (2023): 107205.

16. T. Zhang, T. Yuan, X. Xiao, et al., "Transparent and Shape-memory Cellulose Paper Reinforced by Vitrimer Polymer for Efficient Light Management and Sustainability," *Cellulose* 29 (2022): 8781–8795.

17. V. Kumar, W. Kuang, and L. S. Fifield, "Carbon Fiber-Based Vitrimer Composites: A Path toward Current Research That Is High-Performing, Useful, and Sustainable," *Materials* 17 (2024):3265.

18. B. Krishnakumar, R. V. Sanka, W. H. Binder, V. Parthasarthy, S. Rana, and N. Karak, "Vitrimers: Associative Dynamic Covalent Adaptive Networks in Thermoset Polymers," *Chemical Engineering Journal* 385 (2020): 123820.

19. W. Denissen, J. M. Winne, and F. E. Du Prez, "Vitrimers: Permanent Organic Networks with Glass-Like Fluidity," *Chemical Science* 7 (2016): 30–38.

20. M. K. Mcbride, B. T. Worrell, T. Brown, et al., "Enabling Applications of Covalent Adaptable Networks," *Annual Review of Chemical and Biomolecular Engineering* 10 (2019): 175–198.

21. H. Zhang, J. Cui, G. Hu, and B. Zhang, "Recycling Strategies for Vitrimers," *International Journal of Smart and Nano Materials* 13 (2022): 367–390.

22. D. Berne, F. Cuminet, S. Lemouzy, et al., "Catalyst-Free Epoxy Vitrimers Based on Transesterification Internally Activated by an α–CF 3 Group," *Macromolecules* 55 (2022): 1669–1679.

23. Q. Zhang, M. Li, P. Feng, L. Meng, X. Jian, and J. Xu, "Rapid Stress Relaxation and Degradable Aromatic Disulfide Vitrimer for Recyclable Carbon fiber Reinforced Composite," *Journal of Polymer Research* 31 (2024): 1–12.

24. A. Liguori and M. Hakkarainen, "Designed from Biobased Materials for Recycling: Imine-Based Covalent Adaptable Networks," *Macromolecular Rapid Communications* 43 (2022): 2100816.

25. K. S. K. Reddy, Y.-C. Chen, R.-J. Jeng, M. M. Abu-Omar, and C.-H. Lin, "Upcycling Waste Polycarbonate to Poly(carbonate imine) Vitrimers with High Thermal Properties and Unprecedented Hydrolytic Stability," *ACS Sustainable Chemistry Engineering* 11 (2023): 8580–8591.

26. L. Sougrati, A. Duval, and L. Avérous, "From Lignins to Renewable Aromatic Vitrimers Based on Vinylogous Urethane," *Chemsuschem* 16 (2023): 202300792.

27. T. Debsharma, V. Amfilochiou, A. A. Wróblewska, I. De Baere, W. Van Paepegem, and F. E. Du Prez, "Fast Dynamic Siloxane Exchange Mechanism for Reshapable Vitrimer Composites," *Journal of the American Chemical Society* 144 (2022): 12280–12289.

28. F. Snijkers, R. Pasquino, and A. Maffezzoli, "Curing and Viscoelasticity of Vitrimers," *Soft Matter* 13 (2016): 258–268.

29. M. Guerre, C. Taplan, J. M. Winne, and F. E. Du Prez, "Vitrimers: Directing Chemical Reactivity to Control Material Properties," *Chemical Science* 11 (2020): 4855–4870.

30. C. Taplan, M. Guerre, J. M. Winne, and F. E. Du Prez, "Fast Processing of Highly Crosslinked, Low-viscosity Vitrimers," *Materials Horizons* 7 (2020): 104–110.

31. N. J. Van Zee and R. Nicolaÿ, "Vitrimers: Permanently Crosslinked Polymers with Dynamicnetwork Topology," *Progress in Polymer Science* 104 (2020): 101233.

32. L. He, D. Szopinski, Y. Wu, G. A. Luinstra, and P. Theato, "Toward Self-Healing Hydrogels Using One-Pot Thiol–Ene Click and Borax-Diol Chemistry," *ACS Macro Letters* 4 (2015): 673–678.

33. K. Lu, X. Lan, R. Folkersma, V. S. Voet, and K. Loos, "Borax Cross-Linked Acrylamide-Grafted Starch Self-Healing Hydrogels," *Biomacromolecules* 25 (2024): 8026–8037.

34. S. Van Hurne, S. K. Raut, and M. M. Smulders, "Recyclable Covalent Adaptable Polystyrene Networks Using Boronates and TetraAzaADamantanes," *ACS Applied Polymer Materials* 6 (2024): 7918–7925.

35. S. Wu, H. Yang, W.-S. Xu, and Q. Chen, "Thermodynamics and Reaction Kinetics of Symmetric Vitrimers Based on Dioxaborolane Metathesis," *Macromolecules* 54 (2021): 6799–6809.

36. A. Breuillac, A. Kassalias, and R. Nicolaÿ, "Polybutadiene Vitrimers Based on Dioxaborolane Chemistry and Dual Networks with Static and Dynamic Cross-links," *Macromolecules* 52 (2019): 7102–7113.

37. M. Gosecki and M. Gosecka, "Boronic Acid Esters and Anhydrates as Dynamic Cross-Links in Vitrimers," *Polymers* 14 (2022): 842.

38. M. Röttger, T. Domenech, R. van der Weegen, A. Breuillac, R. Nicolaÿ, and L. Leibler, "High-performance Vitrimers from Commodity Thermoplastics through Dioxaborolane Metathesis," *Science* 356 (2017): 62–65.

39. C. D. Roy and H. C. Brown, "Stability of Boronic Esters—Structural Effects on the Relative Rates of Transesterification of 2-(phenyl)-1,3,2-dioxaborolane," *Journal of Organometallic Chemistry* 692 (2007): 784–790.

40. J. J. Cash, T. Kubo, A. P. Bapat, and B. S. Sumerlin, "Room-Temperature Self-Healing Polymers Based on Dynamic-Covalent Boronic Esters," *Macromolecules* 48 (2015): 2098–2106.

41. J. J. Cash, T. Kubo, D. J. Dobbins, and B. S. Sumerlin, "Maximizing the Symbiosis of Static and Dynamic Bonds in Self-healing Boronic Ester Networks," *Polymer Chemistry* 9 (2018): 2011–2020.

42. F. Ferretti, G. Damonte, F. Cantamessa, et al., "On a Biobased Epoxy Vitrimer from a Cardanol Derivative Prepared by a Simple Thiol–Epoxy "Click" Reaction," *ACS Omega* 9 (2023): 1242–1250.

43. G. Damonte, A. Pellis, D. Battegazzore, et al., "On Sustainable Vitrimers Based on Polycaprolactones," *ACS Applied Polymer Materials* 6 (2024): 3875–3882.

44. M. Nardi, L. Ceseracciu, V. Scribano, M. Contardi, A. Athanassiou, and A. Zych, "Sustainable Adhesives: Exploring Boronic Ester Vitrimers Containing Lignin Microparticles," *Chemical Engineering Journal* 495 (2024): 153400.

45. L. Wang, Y. Liu, Y. Qiao, et al., "Molecularly Engineered Dual-crosslinked Elastomer Vitrimers with Superior Strength, Improved Creep Resistance, and Retained Malleability," *Polymer Chemistry* 13 (2022): 4144–4153.

46. X. Wang, S. Zhang, Y. He, W. Guo, and Z. Lu, "Reprocessable Polybenzoxazine Thermosets with High T_gs and Mechanical Strength Retentions Using Boronic Ester Bonds as Crosslinkages," *Polymers* 14 (2022): 2234.

47. X. Pan, J. Li, F. Liu, C. Hu, and Y. Zeng, "Self-Healable, Weldable, and Reprocessable castor Oil-Based Poly(thiourethane-urethane) Networks," *Journal of Applied Polymer Science* 140 (2023): 54539.

48. S. Ren, Z. Li, W. Zhou, et al., "Simultaneous Robustness, Reprocessing and Self-healing of castor Oil-based Polyurethane Vitrimers Enabled by Supramolecular Nitrogen-coordinated Dynamic Covalent Boronic Ester," *Industrial Crops & Products* 206 (2023): 117738.

49. Y. Zhao, T. Qin, C. Jiang, et al., "Boronic Ester-based Vitrimeric Methylvinyl Silicone Elastomer with "Solid-liquid" Feature and Rate-dependent Mechanical Performance," *Polymer* 265 (2023): 125545.

50. P. Anastas and N. Eghbali, "Green Chemistry: Principles and Practice," *Chemical Society Reviews* 39 (2010): 301–312.

51. T.-L. Chen, H. Kim, S.-Y. Pan, P.-C. Tseng, Y.-P. Lin, and P.-C. Chiang, "Implementation of Green Chemistry Principles in Circular Economy System toward Sustainable Development Goals: Challenges and Perspectives," *Science of the Total Environment* 716 (2020): 136998.

52. T. R. Gordon, M. Cargnello, T. Paik, et al., "Nonaqueous Synthesis of TiO2 Nanocrystals Using TiF_4 to Engineer Morphology, Oxygen Vacancy Concentration, and Photocatalytic Activity," *Journal of the American Chemical Society* 134 (2012): 6751–6761.

53. M. Horn, C. F. Schwerdtfeger, and E. P. Meagher, "Refinement of the Structure of Anatase at Several Temperatures*," *Zeitschrift Für Kristallographie* 136 (1972): 273–281.

54. A. Przybylska, A. Szymanska, and H. Maciejewski, "A Library of New Organofunctional Silanes Obtained by Thiol-(meth)acrylate Michael Addition Reaction," *RSC Advances* 13 (2023): 14010–14017.

55. J. M. Winne, L. Leibler, and F. E. Du Prez, "Dynamic Covalent Chemistry in Polymer Networks: a Mechanistic Perspective," *Polymer Chemistry* 10 (2019): 6091–6108.

56. Y. Spiesschaert, C. Taplan, L. Stricker, M. Guerre, J. M. Winne, and F. E. Du Prez, "Influence of the Polymer Matrix on the Viscoelastic Behaviour of Vitrimers," *Polymer Chemistry* 11 (2020): 5377–5385.

57. B. L. Welch, "The Generalization of 'Student's' Problem When Several Different Population Variances Are Involved," *Biometrika* 34 (1947): 28–35.

58. B. L. Welch, "On the Comparison of Several Mean Values: an Alternative Approach," *Biomimetrika* 38 (1951): 330–336.

59. M. H. Herzog, G. Francis, and A. Clarke, *Understanding Statistics and Experimental Design*, (Springer Nature, 2019) 1st ed., 52–57.

60. R. G. Ricarte and S. Shanbhag, "A Tutorial Review of Linear Rheology for Polymer Chemists: Basics and Best Practices for Covalent Adaptable Networks," *Polymer Chemistry* 15 (2024): 815–846.

61. L. Li, X. Chen, K. Jin, and J. M. Torkelson, "Vitrimers Designed both To Strongly Suppress Creep and To Recover Original Cross-Link Density after Reprocessing: Quantitative Theory and Experiments," *Macromolecules* 51 (2018): 5537–5546.

62. T. Mandal, U. Ozten, M. Ghanbarian, S. Rahavi, and M. Naraghi, "Identifying the Origin of Intrinsic Self-healing Gradual Decay in Vitrimer Carbon fiber Reinforced Polymer Composites," *Journal of Composite Materials* (2025): 1–12, https://doi.org/10.1177/00219983251362394.

63. A. P. Jackson, J. F. Vincent, and R. M. Turner, "The Mechanical Design of nacre," *Proceedings of the Royal Society of London* 234 (1988): 415–440.

64. U. G. K. Wegst, H. Bai, E. Saiz, A. P. Tomsia, and R. O. Ritchie, "Bioinspired Structural Materials," *Nature Materials* 14 (2015): 23–36.

65. J. Sun and B. Bhushan, "Hierarchical Structure and Mechanical Properties of Nacre: a Review," *RSC Advances* 2012, 2, 7617–7632.

66. V. Semeykina, C. Appiah, S. Rothberg, S. Heinrich, D. Giuntini, and G. A. Schneider, "Expectations vs. reality in nacre-Like Composites: Dominating Role of Particle Packing and Polymer Confinement in Mechanical Performance," *Advanced Composites and Hybrid Materials* 8 (2025): 1–14.

67. D. A. Weitz, "Packing in the Spheres," *Science* 303 (2004): 968–969.

Supporting Information

Additional supporting information can be found online in the Supporting Information section.

Supporting file: macp70123-sup-0001-SuppMat.docx

6 Unpublished Results

6.1 Interpenetrating Covalent Adaptable Networks

This chapter describes the design and characterization of an interpenetrating polymer network (IPN) based on two orthogonal (*i.e.*, orthogonal associative exchange mechanisms) vitrimer networks. IPNs display two physically percolating cross-linked networks that do not have chemical connections.[180,181] It is essential to highlight that the presented IPNs in this work comprise two associative CANs instead of one associative CAN, which is combined with a dissociative CAN. This more straightforward method has already been described in detail in literature and comprises, oftentimes, supramolecular networks based on hydrogen bonding or DA networks. One IPN concept based on vegetable oils was investigated under supervision in Hanh Pham's master's thesis in 2024, which involved combining an associative and dissociative network based on VU and DA utilizing vegetable castor oil. However, as outlined in the introduction, this strategy lacks the beneficial feature of a constant crosslinking degree throughout two percolating dynamic networks. The so-called reversible interlocked polymer networks (RILNs) are based on the topological rearrangement of two preformed cross-linked polymers containing reversible covalent bonds and can undergo interlocking-unlocking cycles. One example, by Liu *et al*., includes the use of DA and alkoxyamines to achieve molecular-level RILNs. However, this strategy leads to phase separations at higher temperatures, *e.g.*, during hot pressing.[182]

DBs were investigated as reversible crosslinks in semi-IPNs to strengthen PE thermoplastics through a dynamic covalent networking additive based on alkyl boron chemistry.[183] Interpenetrating covalent adaptable networks (IPCANs) are based on two percolating orthogonal covalent adaptable networks. One example, based on abundant imines and DBs, was prepared by Lin *et al*. and presented new ideas for developing recyclable IPNs with DCC.[184] These strategies include de-crosslinking and subsequent re-crosslinking, which are achieved through the reversibility of both bonds *via* hydrolysis and condensation, respectively, *via* solution mixing.

Herein, IPCANs are prepared in a simultaneous formation route using VU and DB reversible chemistry, offering orthogonal associative exchange reaction pathways. This should exclude phase separation at higher temperatures and present a new route towards IPCANs. The synthetic route and characterization of the single networks and the IPCAN are presented below.

6.1.1 Glycerol-based Vinylogous Urethane Network

As a byproduct of biodiesel production, glycerol presents a promising feedstock for various platform chemicals, including glycerol triglycidyl ether and epichlorohydrin.

From the transesterification reaction to produce biodiesel, more than 300000 m³ of glycerol were made in 2015.[185,186] Glycerol was found to undergo fast and efficient acetoacetylation using TMDO, providing a suitable starting molecule for VU networks.[107]

The system used in this work was described in Philipp Haida's dissertation, utilizing 1,8-diamino-3,6-dioxaoctane (DADOX) with an *R*-value of 0.75 and a gelation time of 3 – 4 minutes at room temperature.[187] In this work, an *R*-value of 0.7 was chosen to enhance recyclability in the IPCAN, due to the increased amount of free amine groups, and to achieve a similar T_g for both orthogonal networks. Furthermore, the formation of the VU network was performed at elevated temperatures to integrate with the IPCAN production process at 120 °C.

The synthesis of the acetoacetylated glycerol, propane-1,2,3-triyl tris(3-oxobutanoate) (GLYAAC), was carried out according to the literature, with the reaction scheme presented in Figure 18.[107] The characterization of GLYAAC with ATR-FT-IR, ^{1}H NMR, ^{13}C NMR, and ESI is presented in the Appendix, Figure A1 – Figure A4.

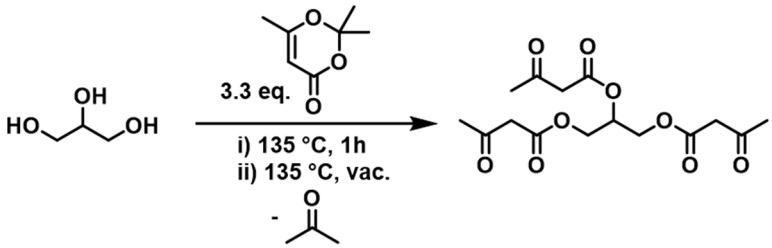

Figure 18: Acetoacetylation reaction of glycerol to yield propane-1,2,3-triyl tris(3-oxobutanoate) (GLYAAC), using TMDO at 135 °C in a bulk reaction.[107]

The glycerol vitrimer polymer (GVP) was synthesized through a condensation reaction of GLYAAC with DADOX, resulting in an *R*-value of 0.7. Unlike the method reported in Moritz Wolff's bachelor's thesis, which was performed at room temperature (23 °C), the temperature was maintained at 120 °C, significantly accelerating the reaction. The synthesis was conducted in bulk without the use of any solvent. Gelation occurred after a brief induction period of 20 – 30 seconds, during which mechanical stirring was perormed, and bubbling and foaming were observed as the reaction progressed. The network formation is shown in Figure 19.

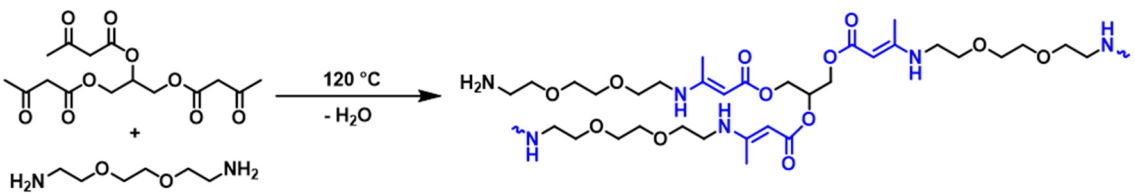

Figure 19: Condensation reaction between GLYAAC and DADOX to form the VU vitrimer GVP at 120 °C.

Then, the material was stored at 23 °C for 12 hours, followed by 23 hours under reduced pressure at 120 °C, and finally 1 hour at 150 °C under reduced pressure to eliminate any remaining water. The dried material was then processed with heat compression. A uniform, yellow, bubble-free vitrimer film was produced and characterized by ATR-FT-IR to confirm the formation of VU bonds and the integrity of the backbone, as shown in Figure 20.

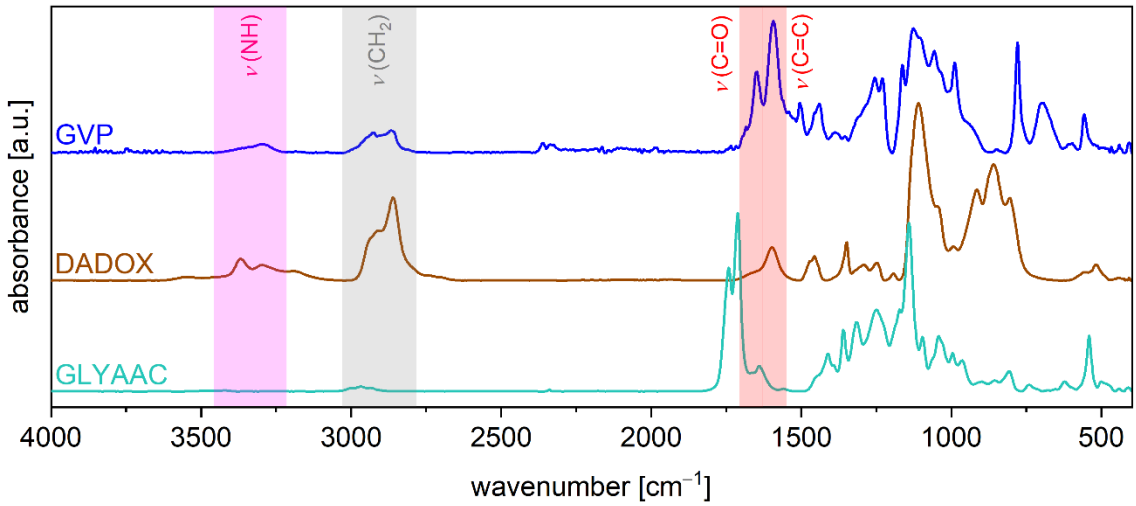

Figure 20: ATR-FT-IR of GVP after heat compression, DADOX, and GLYAAC. The characteristic NH (pink), CH_2 (grey), and VU (red) stretching vibrations are highlighted, indicating the successful formation of the VU material.

In ATR-FT-IR, the characteristic VU bands are present in the final material, as indicated by the C=C band (1594 cm^{-1}) and the C=O ester band (1649 cm^{-1}). To examine the effect of temperature on network structure, a GVP material was produced at 23 °C, followed by the same storage and heat compression process. The ATR-FT-IR in Figure A5 shows no difference between the materials.

6.1.2 Dioxaborolane Thiol-Acrylate Vitrimer Network

The second network of the IPCAN was created using the formulation of the material BVS, as described in Publication 3. Detailed information on the synthesis process and mechanical data can be found in the publication. The network formation is shown in Figure 21.

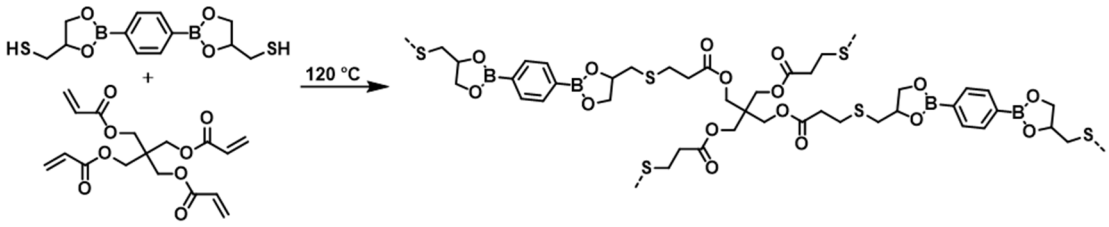

Figure 21: Monomers DBEDT and PETAC were reacted after mixing at 120 °C until gelation occurred. To ensure complete network formation of the BVS material, it was stored at 120 °C for 24 h.

The formation of BVS was carried out in bulk at 120 °C under mechanical stirring to ensure the melting of DBEDT and subsequent gelation after the addition of PETAC. The gelation time was found to be around 60 seconds. Since no base is present in the mixture, the reaction proceeds through a thermally activated solvent-free and catalyst-free (SFCF) thiol-ene click (TEC) pathway rather than a thia-Michael addition.[188,189] This is especially important to note because the mixture used to form GVP in the IPCAN contains an amine, a potential Michael donor. The reactivities of the monomers to form the IPCAN are discussed in greater detail in the following chapter.

6.1.3 Orthogonality of Monomers and Exchange Chemistries

The first step in investigating the IPCANs was to determine the optimal parameters for the network formation reaction, without altering the single networks and preserving the orthogonal associative exchange reactions. Orthogonal exchange mechanisms ensure the non-interference of the transamination and the dioxaborolane metathesis.[190,191] Boron-nitrogen (B-N) coordination can influence the material's mechanical performance due to supramolecular interactions.[192] However, as thiols, amines, and acetoacetates can undergo Michael additions with acrylates, the formation process requires the investigation of potential side reactions.[193]

6.1.4 Sequential Reaction Pathway

A first attempt to create the IPCAN involved a modified sequential reaction pathway. This method excludes potential Michael additions of monomer molecules because network formation occurs step by step. In sequential IPN formation, the primary network forms first, followed by impregnation with precursors of the second network. Then, the second network polymerizes within the first, resulting in a mixture of the two networks at the molecular level.[194] However, the fast reaction kinetics of both network-forming reactions at 120 °C, the water produced during VU formation, and slow diffusion due to gelation posed challenges, leading to inhomogeneous products. Therefore, both GVP and BVS were prepared as films and ground into powder by cryogenic grinding. The powders were then mixed and hot-pressed using heat compression with a 1 mm gap. The resulting product appeared non-homogeneous, with gaps and irregularities in the film material. As a result, the sequential pathway *via* powder mixing of two vitrimer networks was not further explored in this study.

6.1.5 Simultaneous Reaction Pathway

Next, the simultaneous formation of both the VU and DB networks was investigated. Since the melting of DBEDT into the liquid state and the TEC reaction required elevated temperatures, a reaction temperature of 120 °C was chosen.

The synthetic route was designed to separate the monomers into two precursor solutions (PS-1 and PS-2), which were then heated to 120 °C on a heat plate for 5 min. Each solution contains two monomers: thiol/amine (DBEDT/DADOX, PS-1) and acetoacetate/acrylate (GLYAAC/PETAC, PS-2), which appear as low-viscosity fluids without gelation during the observed heating period. The precursor mixtures and the structure of the IPCAN are presented in Figure 22.

Although the selection of exchanging bonds ensures the orthogonality of the dynamic bonds, the formation reaction of the networks and the precursor solutions also requires consideration of orthogonality. As stated above, DBEDT and DADOX do not undergo a reaction. In contrast, PS-2 contains the acrylate PETAC, which represents a Michael acceptor, since the activated double bond is capable of a conjugate addition.[128]

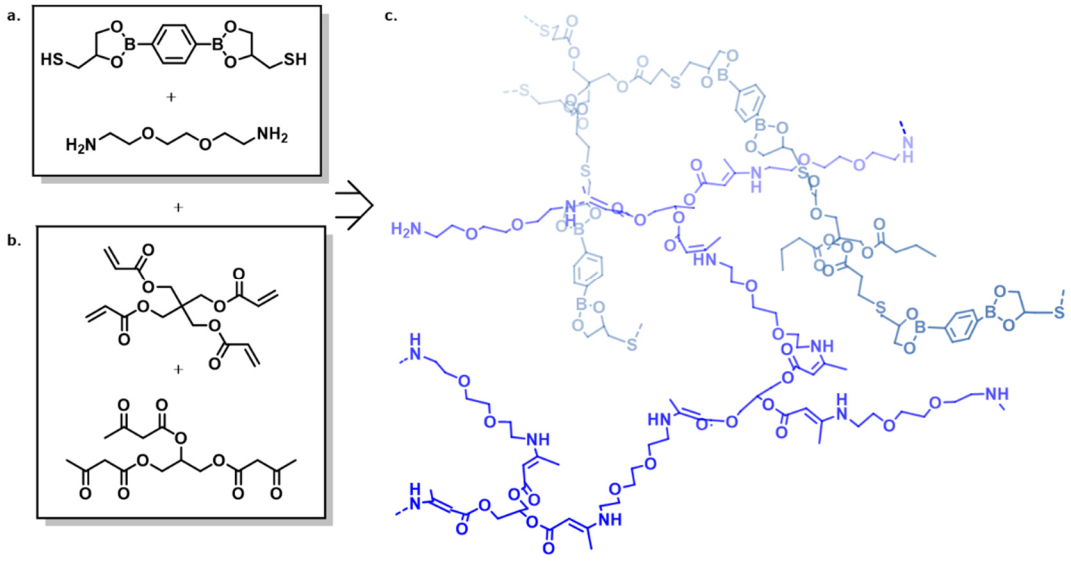

Figure 22: Overview of the simultaneous formation process for creating IPCAN from DB and VU. (a) Precursor solution 1 (PS-1) includes DBEDT and DADOX. (b) PS-2 contains PETAC and GLYAAC. (c) The IPCAN forms through two physically cross-linked networks of DB and VU.

The addition of a Michael donor, such as an acetoacetate, to an acrylate is a typical example of a Michel addition reaction.[195] Since the reaction proceeds through an enolate anion, a prior deprotonation of the activated methylene group is necessary.[193] A base catalyst typically facilitates this. Since no base is present, and the reaction kinetics are highly dependent on base strength, Michael addition of the acetoacetate on PETAC is unlikely and not observed. It should be noted that double curing reactions, e.g., when using a photo-base initiator, within vitrimer formulations hold potential for reinforcement or two-stage curing reactions to design multifunctional materials.[196-198]

To form the IPCAN, the curing reactions are initiated through a combination of both precursor formulations. The preferred reactions include the thermally activated thiol-ene reaction between the thiol and acrylate groups, as well as the condensation of the amine with the acetoacetate groups to form the VU.

The condensation reaction is observed by the formation of bubbles as soon as gelation occurs. Furthermore, the characteristic VU bands are observable in ATR-FT-IR (Figure 23). After storing for 23 hours at 23 °C, the sample was cured at 120 °C under reduced pressure for 23 hours and then for 1 hour under reduced pressure at 150 °C. Subsequently, the material was processed using heat compression (150 °C, 10 kN, 10 min) with a 1 mm gap. The material was prepared as a dense film with inhomogeneous color domains (brown and yellow). In ATR-FT-IR, the material exhibits the characteristic bands of both BVS and GVP, indicating a mixture of both network types. However, the material was sticky and soft, which can be attributed to an incomplete curing reaction. It was observed that the formation of the VU proceeded faster at 120 °C than at the DB, indicating an inhomogeneous mixture inside the IPCAN. However, this preliminary result showed that a mixture of both networks and the synthesis in a simultaneous route is possible when selecting both BVS and GVP as networks.

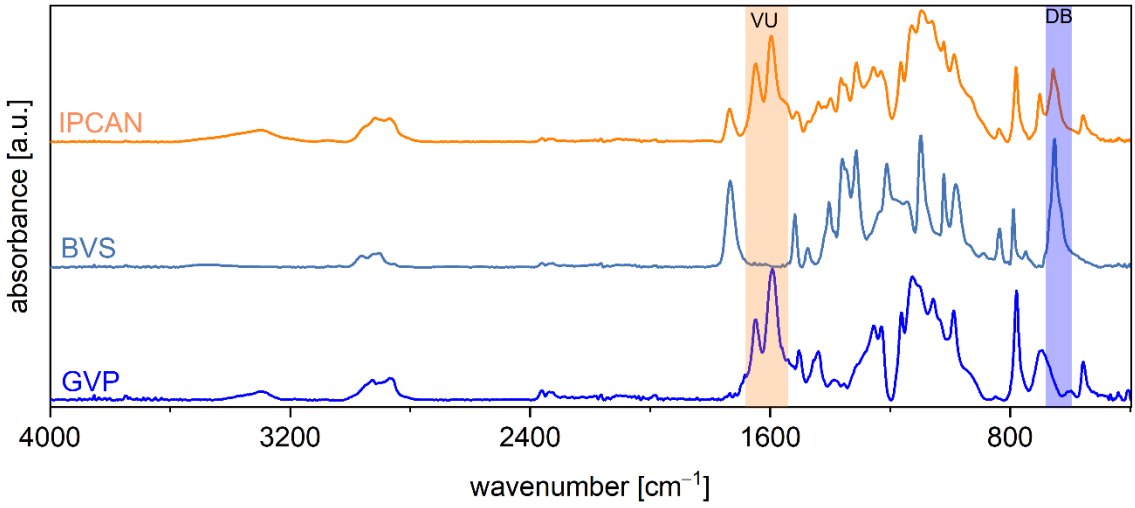

Figure 23: ATR-FT-IR image of the IPCAN, synthesized in a simultaneous route with the spectra of BVS and GVP. Highlighted are the characteristic bands of the VU group and the DB ring, indicating a material that contains both VU and DB.

6.1.6 Solvent-mediated Simultaneous Reaction Pathway IPCAN

Since the aim was to prepare an IPCAN that consists of both networks mixed at a molecular level with comparable mechanical properties, the preparation procedure for the IPCAN was adjusted accordingly. The condensation reaction of the VU proceeds very fast at 120 °C. Nonetheless, this temperature is required for the formation of the BVS, since DBEDT must be melted and the TEC reaction is thermally initiated. Interesting parameters could be the addition rate of PS-2 (slower, controlled), the stirring procedure (*e.g.*, using a high-speed mixer), or the reaction environment (use of solvent). It was found that the use of a non-reactive solvent increases the mixture of all reactants and drastically reduces the reaction rates of both VU and DB network formation. Dimethyl sulfoxide (DMSO) was chosen due to its high boiling point and solubility with all reactants.

To form the IPCAN in DMSO, both solutions, PS-1 and PS-2, were mixed with 10 mL of DMSO. After mixing with a stirring bar for 5 minutes, both mixtures were combined under stirring with a stirring bar at 120 °C and reacted for 12 hours. The transformation of the network formation process into a solution brings the advantage that the reaction rates are slowed down, as no gelation occurred during the first hour. Evolving water as a byproduct of the VU condensation appeared as steam and bubbles and was removed from the reactive mixture. After two hours, gel-like fragments began to appear in the solution. After 12 h, a black gel was obtained. The exact gelation point when stirring stopped was not determined. The gel was dried under reduced pressure at 120 °C for 24 h. Subsequently, it was removed from the beaker and processed *via* heat compression (150 °C, 10 min, 10 kN) with a 1 mm gap. The material was received as a homogeneous black film. In contrast to the product from the bulk process, the material appeared dimensionally stable, and it was possible to process it without the formation of bubbles or visible inhomogeneities. The ATR-FT-IR (Figure 24) confirmed the formation of a material that contains both characteristic DB and VU groups.

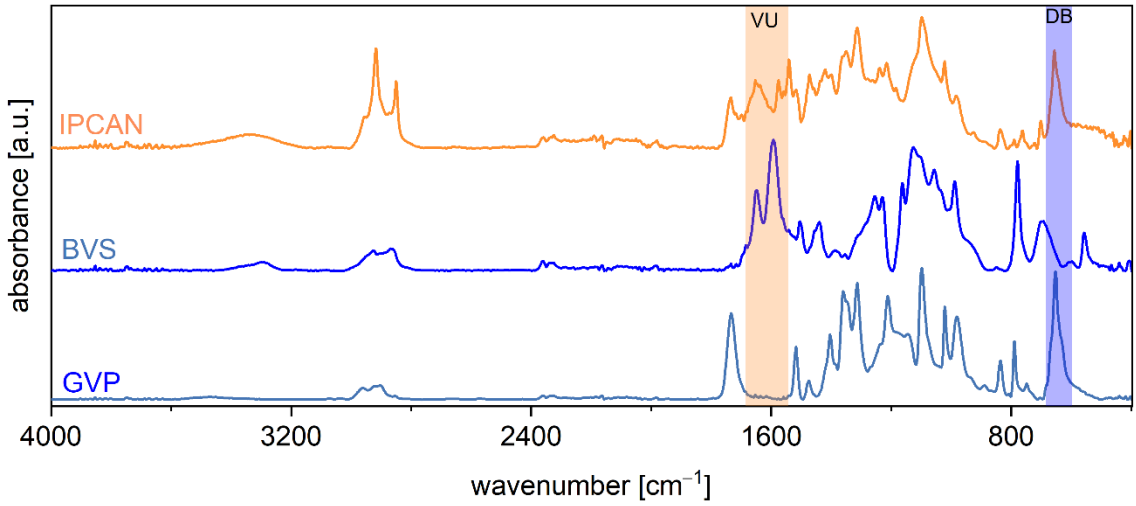

Figure 24: ATR-FT-IR image of the IPCAN, synthesized in a solvent-mediated simultaneous route with the spectra of BVS and GVP. Highlighted are the characteristic bands of the VU group and the DB ring, indicating a material that contains both VU and DB.

The strong band at 652 cm^{-1} confirms the preservation of the DB ring structure. The bands at 1649 cm^{-1} and 1594 cm^{-1} confirm the presence of the vinylogous urethane groups. Free amines are visible in the region of 3300 - 3050 cm^{-1}. A comparison of the ATR-FT-IR spectra (Figure A6) shows less pronounced VU bands in the solvent-mediated IPCAN$_{DMSO}$ than in the spectrum of bulk-formed IPCAN$_{bulk}$. This highlights the role of the solvent in forming the IPCAN, resulting in a more regular network structure and a homogeneous mixture. This method presents a valuable synthetic route towards IPCANs based on vinylogous urethanes and other orthogonal networks. In the following, IPCAN is referred to the material formed in the solvent process, IPCAN$_{DMSO}$.

6.1.7 Mechanical Properties of the IPCAN

To evaluate the mechanical and thermo-physical properties of the IPCAN, a comparison is carried out with the networks BVS and GVP. In Figure 25, the DSC results of the three materials are shown. For both BVS and GVP, the T_g can be determined at 44 °C. The IPCAN displays a shift in T_g to a higher value of 55 °C.

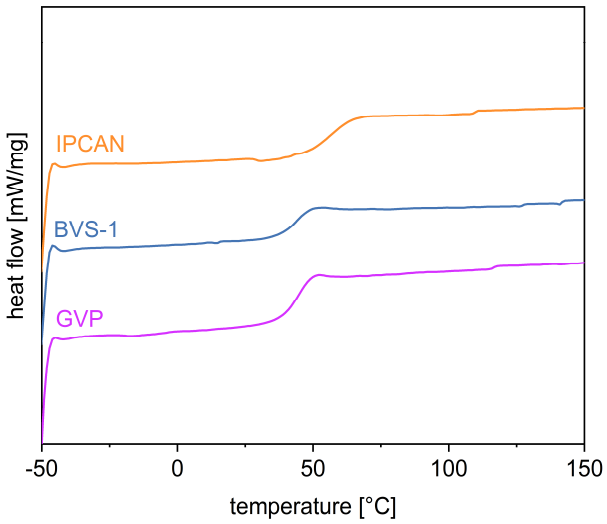

Figure 25: DSC measurement of the IPCAN compared to the measurements of GVP and BVS. The curves display the data from the second heating cycle under an ambient (oxygen) atmosphere.

Using TGA (Figure 26a), the flame-retardant properties of the boronic esters in BVS are demonstrated by the residual char content, which indicates the non-flammable remnants and a degradation temperature ($T_{5\%}$) of 308 °C.

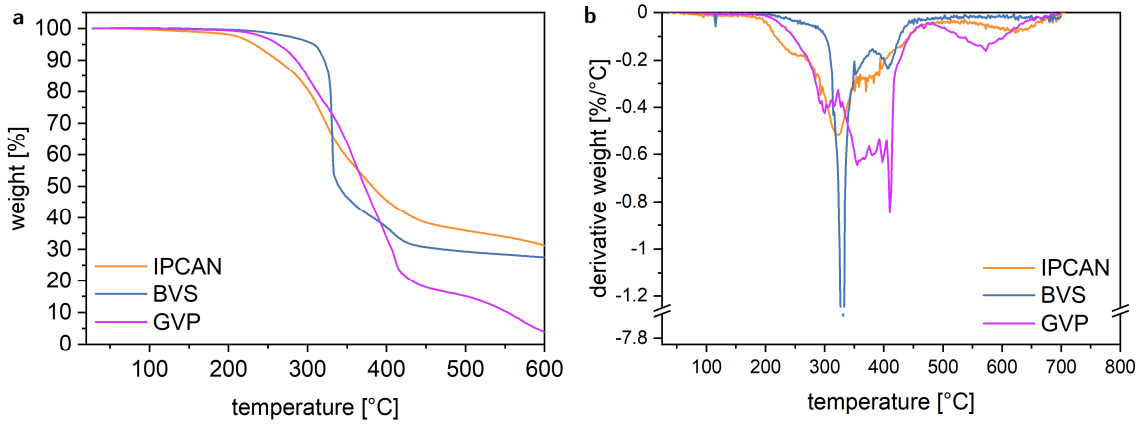

Figure 26: TGA curves (oxygen atmosphere) (a) of the IPCAN from the solvent-mediated process, BVS, and GVP, and the derivatives (b) of the curves.

In comparison, the GVP-based material can be fully burnt at 600 °C and has a lower T5% of 254 °C. The IPCAN exhibits lower thermal stability, with a T5% of 230 °C. The decrease is less steep than for BVS, but resembles elements from both BVS and GVP. Until the $T_{5\%}$ of BVS, the degradation follows the same behavior as for GVP; however, afterwards, the material exhibits the degradation behavior of BVS. This indicates again the simultaneous formation of both networks, which preserve their individual network properties, and the IPCAN properties are a combination of these two single networks. This behavior becomes further evident in the first derivative of the dynamic TGA curve, which shows a combination of the curves of BVS and GVP (Figure 26b).

Before the rheological investigation, an amplitude sweep measurement was performed to investigate the LVE. For all subsequent oscillatory measurements, a strain amplitude of 0.1% was chosen to prevent an influence of strain on the molecular structure. In Figure 27, the amplitude sweep measurements are shown. Both BVS and the IPCAN display an LVE expanding up to 10%. For GVP, the LVE reaches the yield point at a strain of 1%. Combined with the higher value of G″, the IPCAN thus shows good energy dissipation, as anticipated for an IPN structure.

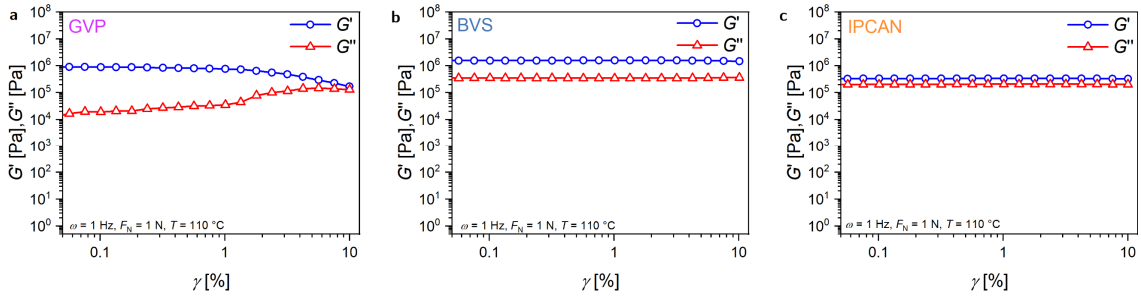

Figure 27: Amplitude-sweep measurements of GVP, BVS, and IPCAN at 110 °C, a frequency of 1 Hz, and a normal force of 1 N.

To expand the investigation of the thermomechanical properties, temperature sweep measurements were conducted between 5 and 150 °C (Figure 28).

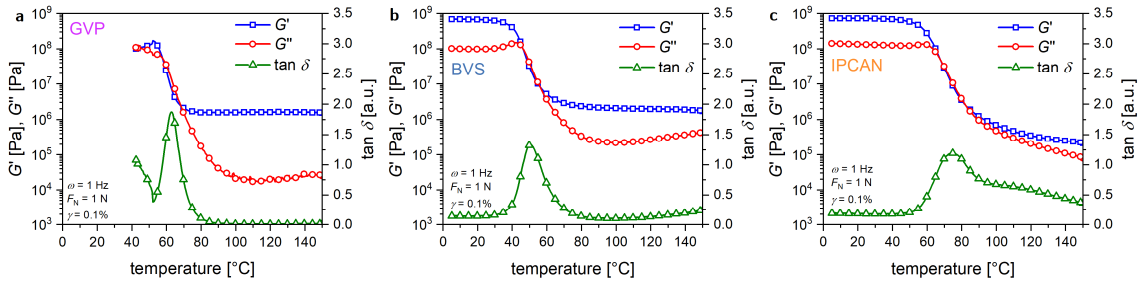

Figure 28: Temperature sweep measurements of the GVP, BVS, and IPCAN in the temperature range of 0 – 150 °C performed at a constant angular frequency of 6.28 rad s^{-1}, a constant shear strain of 0.1%, and a normal force F_N of 1 N.

The curves display two linear regimes separated by a step, indicating the T_g. In the case of BVS, the measurement was stopped at 40 °C because the sample lost contact with the measurement stamp. Interestingly, the T_g of the IPCAN of 75 °C follows the same trend as the values in DSC and lies above the T_gs of BVS (50 °C) and GVP (62 °C). One explanation could be the formation of additional chemical crosslinks between the networks, for example, through Michael additions. However, the rubbery plateau of the IPCAN yields lower values than those of BVS and GVP, which does not support the thesis of additional crosslinks.

The rearrangement of dynamic networks can be investigated using stress-relaxation measurements, which involve applying a single-step strain of 1% and measuring the stress-relaxation modulus. The stress-relaxation data in the range of 110 – 150 °C are displayed in Figure 29. The data was fitted using a KWW fit to determine the relaxation time distribution and the characteristic stress-relaxation times.

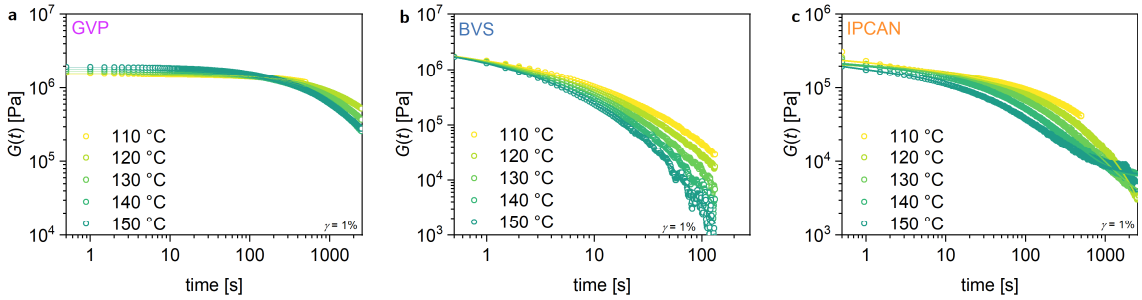

Figure 29: Stress-relaxation measurements of GVP, BVS, and IPCAN, plotting the stress-relaxation modulus $G(t)$ versus the stress-relaxation time measured at temperatures in the range of 110 – 150 °C while applying a shear strain of 1%. The lines display the stretched exponential fit functions for the respective temperatures, calculated from the stress-relaxation data.

The initial relaxation moduli G_0 of all three materials remained constant across all measured temperatures, which is characteristic of associative network rearrangement reactions. Especially for IPCAN, this behavior confirms the presence of network rearrangements mediated by dioxaborolane metathesis and transamination. The parameters of the stress-relaxation fit data and the characteristic stress-relaxation times are listed in Table 1.

Table 1: Summary of the values of the stretch factor β and the calculated average values of the characteristic stress-relaxation time $\langle\tau\rangle$ for the KWW fit of the stress-relaxation measurements (γ = 1%, F_N = 1 N) between 110 – 150 °C of the tested materials GVP, BVS, and IPCAN.

Sample	$\beta_{110°C}$ [-]	$\beta_{120°C}$ [-]	$\beta_{130°C}$ [-]	$\beta_{140°C}$ [-]	$\beta_{150°C}$ [-]	$\langle\tau\rangle_{110°C}$ [s]	$\langle\tau\rangle_{120°C}$ [s]	$\langle\tau\rangle_{130°C}$ [s]	$\langle\tau\rangle_{140°C}$ [s]	$\langle\tau\rangle_{150°C}$ [s]
GVP	0.625	0.656	0.711	0.720	0.752	166517[a)]	3561	1028	746	494
BVS	0.350	0.360	0.367	0.378	0.396	1.45	1.16	0.91	0.77	0.70
IPCAN	0.079	0.412	0.428	0.424	0.358	621189[a)]	87.5	50.6	28.9	12.5

a) The values are calculated mathematically and were excluded from the calculation of the activation energy, as they indicate restricted flow at 110 °C.

The data show that for GVP at 110°C, the stress-relaxation time is very high, indicating a thermal threshold. This behavior was observed for lignin-based vitrimers in Publication 2 and demonstrates the influence of T_g on stress-relaxation. At 120 °C, stress-relaxation proceeds at higher rates, which becomes evident by $<\tau>_{120°C}$ of 3561 s. This temperature restriction was also observed for IPCAN, indicating an influence of slow transamination reactions at 110 °C. The BVS stress-relaxation is comparably fast, with values < 1.5 s. Moreover, the stretch exponential β is below 0.4. As outlined in Publication 3, this behavior, characterized by fast stress-relaxation and stretched fits, can be attributed to the thermal history of the material, as it was measured directly after heat compression. It is also important to note that the values of β do not decline as the temperature rises. The interpretation should be carried out with care, as these findings highlight the importance of standardized test procedures (as examined in the Publications 1, 2, and 3), the influence of T_g (Publication 2), and thermal history (Publication 3). Nonetheless, the focus of the stress-relaxation measurements in this chapter was to evaluate the dynamicity of the formed IPCAN. This was achieved by calculating the activation energies (E_as) for the stress-relaxation data by plotting the values of $<\tau>$ against $1000/T$ in Figure 30 and determining the slope of the resulting regression line.

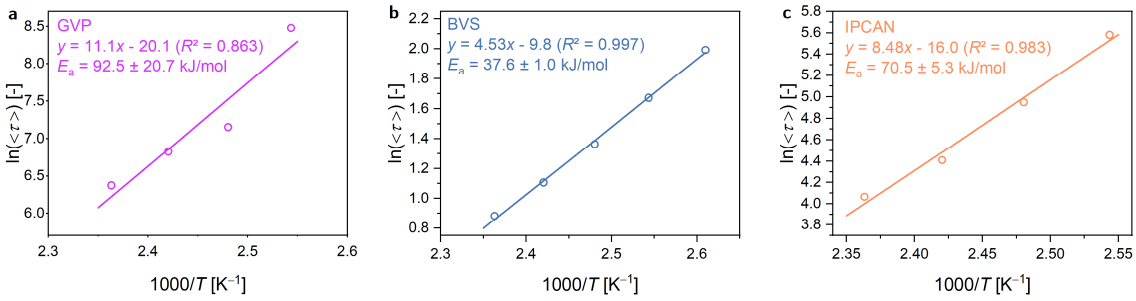

Figure 30: Plots of τ versus $1000/T$ of GVP, BVS, and IPCAN to calculate the activation energies from the slope of the linear fit of the calculated $<\tau>$ values from the stretched exponential fit in the temperature range of the stress-relaxation measurements (γ = 1%, F_N = 1 N) between 110 – 150 °C for BVS and 110 – 150 °C for GVP and IPCAN.

The E_a of GVP was calculated between 120 – 150 °C, since at 110 °C, the stress-relaxation was influenced by the T_g. The R^2 value of 0.863 indicates a higher deviation of the calculated E_a. However, the value of 92.5 ± 20.7 kJ mol^{-1} is in the reported range of typical VU materials. The documented material cured at room temperature had an E_a of 77.0 ± 0.8 kJ mol^{-1}.[187] It is worth noting that this value was determined assuming a single Maxwell element for the description of the stress-relaxation. For the DB-based network, the E_a for the dioxaborolane metathesis is in the same range as reported in Publication 3, with a value of 37.6 ± 1.0 kJ mol^{-1}. Interestingly, the IPCAN obtains an E_a of 70.5 ± 5.3 kJ mol^{-1}, which falls in between the values of the single networks. The stress-relaxation rate is slower than that of BVS but is drastically accelerated compared to GVP. This indicates an accelerating influence of a flexible and dynamic chemical environment on VU-based materials.

Moreover, this demonstrates the dynamicity of the formed IPCAN, which is assembled through transamination and dioxaborolane metathesis. It would be interesting if the E_as can be adjusted by the volume percentages of the two associative networks and if a two-temperature relaxation of the network is possible by using a DCC with a higher activation energy needed for the DCC to proceed. This could enable two-temperature shape memory programming, innovative materials, and intelligent robotics.

To investigate the mechanical response of the IPCAN, tensile tests were conducted to evaluate its strength and elasticity in comparison to the single networks. The stress-strain curves are displayed in Figure 31 and show a rigid behavior of BVS (as demonstrated in Publication 3) and a tougher VU-based GVP.

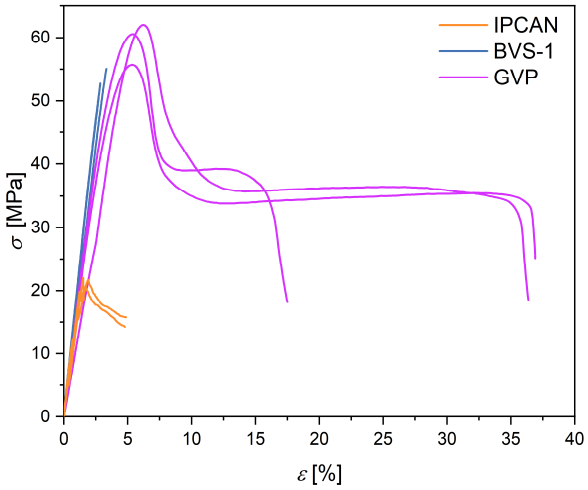

Figure 31: Stress-strain curves (at T = 23 °C) of GVP, BVS, and IPCAN.

In combination with the IPCAN, the material is less rigid and shows less strength compared to the single networks. The stress-strain data are summarized in Table 2.

Table 2: Comparison of the stress-strain data of GVP, BVS, and IPCAN, with the values of E, σ_m, and ε_b.

Sample	***E* [MPa]**	**σ_m [MPa]**	**ε_b [%]**
GVP	1454 ± 253	59.4 ± 3.3	30.3 ± 11.1
BVS	1852 ± 155	47.5 ± 13.5	2.9 ± 0.9
IPCAN	1713 ± 178	21.4 ± 0.73	1.7 ± 0.2

The values display similar mechanical strength, characterized by a decrease in Young's modulus, a reduction of tensile strength, and a less flexible response, indicating a rigid material response and reduced toughness. This could be attributed to the higher T_g, which could then lead to a more brittle material response. It would be interesting if a tougher IPCAN could be produced using other monomers.

In summary, a simultaneous IPCAN was prepared from two associative CANs using a solvent-mediated formation process. The IPCAN was compared to single-network materials and displayed a mixture of properties, as well as reprocessability during film formation. This suggests that this approach may be a suitable synthetic route for preparing future IPNs from two orthogonal associative chemistries, one of which is a vinylogous urethane.

6.2 Nacre-Inspired Thermoreversible Nanocomposites

In the following chapter, the synthesis and characterization, as well as the potential applications, of thermoreversible phosphonic acid ligands and thermoreversible matrices are presented, with a special focus on the functionalization of superparamagnetic iron oxide nanoparticles (SPIONs). The work was carried out in cooperation with Lea Klauke in SFB 986 (subproject A1) under the supervision of Tobias Vossmeyer. The help of Paul Körner and Jannik Winter with the ligand synthesis is gratefully acknowledged. The analysis of the nanocomposites was conducted in collaboration with the group of Gerold Schneider at the TUHH.

6.2.1 Concept of Hierarchical CAN-based Magnetic Nanocomposites

Biological materials, such as tooth enamel or nacre, exhibit an exceptional synergy of mechanical properties, including hardness, rigidity, strength, and toughness, compared to conventional artificial materials.[168] These properties are achieved by the self-assembly of hard mineral core structures combined with a soft organic shell in multi-level hierarchies.[199,200] The combination of soft and hard materials with a high loading (>50 wt.%) of inorganic material yields materials that superimpose the properties of the main constituents. Thus, bio-imitation has been a growing field in material science, and many reports on different hierarchical self-assembled materials have been published. Potential applications include sensors, the reinforcement of coatings, or stimuli-responsive self-healing materials.[173,174,201]

Nanoclusters of SPIONs can be prepared while maintaining the individual superparamagnetic properties of the single particles and increasing the magnetophoretic mobility of the assembled clusters.[202] In previous works, these SPIONs were cross-linked through the irreversible reaction of the oleic acid (OA) ligands, forming covalent bonds that mimic the ultra-strong properties of materials such as nacre.[177,178] These composite materials, however, have been fixed in their molecular networks due to the use of non-dynamic covalent bonds, meaning they lack reversibility. The preparation of SPIONs and the self-assembly of OA by Lea Klauke resulted in functionalized particles at the first hierarchical level.[202,203]

The integration of thermoreversible bonding in the first hierarchical level can provide a possible feature for recyclability by design for such nanocomposites. In the following approach, an artificial material consisting of SPIONs and a thermoreversibly crosslinked matrix material was prepared to combine the properties of the particles through self-assembly, resulting in a hierarchical multi-layer structure. For the first hierarchical level, spherical and cubic SPIONs, produced by Lea Klauke, should be cross-linked by a reversible DA reaction.[202] Since the DA reaction is of a dissociative nature at elevated temperatures, it can be utilized as a click approach to combine SPIONs into a thermoreversible nanocluster, which is subsequently coated with a polymer shell. This should enable excellent thermomechanical properties, chemical stability, and recyclability.

In a second step, the fixed molecular makeup of commonly used epoxy-based matrices should be optimized by a dynamic matrix based on a vitrimer-epoxy (VIPOXY) co-network approach, which combines dynamicity with the outstanding properties of classical epoxy-based materials. In Figure 32, the approach to form magnetic thermoreversible nanocomposites is displayed, showing the ligands for the first hierarchical level, the thermoreversible clustering, and the formation of core-shell supraparticles. Finally, the formed supraparticles were used as inorganic reinforcements of a thermoreversible, VIPOXY-based matrix.

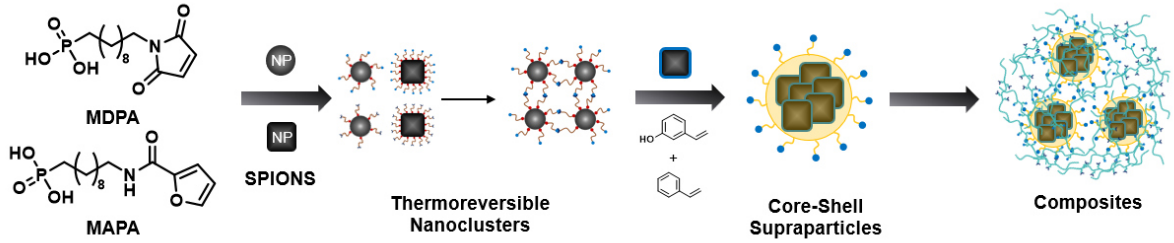

Figure 32: Illustration of the synthesized Diels-Alder Ligands MDPA and FDPA, which are then used in a ligand exchange procedure with spherical and cubical SPIONS. These Diels-Alder-functionalized SPIONS can then be clustered *via* the thermoreversible dissociative Diels-Alder reaction. In the next step, core-shell supraparticles are formed through the radical polymerization of styrene and 3-vinylphenol within micelles. In a final step, these core-shell supraparticles are incorporated into a vitrimer-based matrix, which can be recycled *via* an associative mechanism of vinylogous urethanes.

6.2.2 Investigation of a Maleimide Dodecyl Phosphonic Acid

The synthesis of (10-(2,5-dioxo-2,5-dihydro-1*H*-pyrrol-1-yl)decyl)phosphonic acid (maleimide dodecyl phosphonic acid, MDPA) is described in the literature.[204,205] In the cooperation, Lea Klauke functionalized SPION particles with the synthesized ligand and investigated the reversible DA-functionality.[202]

The results proved that an efficient ligand exchange is possible using cubic SPIONs with a size of 19 nm with a 4 to 5-fold excess of ligands about the particle's surface. The product MDPA@SPIONs was investigated by dynamic light scattering (DLS) experiments and proved efficient ligand exchange. It was discovered that the ligand exchange leads to a change in the solubility of the MDPA@SPION in chloroform compared to the OA@SPIONs, which is due to the polarity of the maleimide group. The cluster size increased to 80 – 900 nm. The possibility of reversible DA-reactions was tested using furan and difurfuryl sulfide. Both diene functionalities were capable of performing DA reactions, thereby verifying the availability of the maleimide groups on the SPION surface.

6.2.3 Synthesis of (10-(furan-2-carboxamido)decyl)phosphonic acid

As indicated in the prior chapter, the idea was to find a ligand that can form the diene compound for the ene-bearing MDPA ligand. Inspired by the synthesis route and the particle-ligand interaction results, the synthesis of a new diene-ligand was conducted. The first three steps of the synthesis of (10-(furan-2-carboxamido)decyl)phosphonic acid (FDPA) followed the protocol by Kickelbick *et al*. to give the primary amine *N*-(10-aminodecyl)diethyl phosphonate.[204-206] Initially, the *N*-(10-bromodecyl)phthalimide was prepared by reacting potassium phthalimide with 1,10-dibromodecane, followed by a Michaelis-Arbuzov reaction to introduce the phosphonate ester by the reaction with triethyl phosphite. Then, a hydrazinolysis was used *via* Gabriel synthesis to yield the primary amine *N*-(10-aminodecyl)diethyl phosphonate. In the next step, the ene functionality was introduced in the form of furan carboxylic acid through amide coupling using 1,1'-carbonyldiimidazole, which resulted in the formation of diethyl(10-(furan-2-ylamino)decyl)phosphonate.[207] In the final step, the ester groups were cleaved with bromotrimethylsilane, and subsequent hydrolysis with methanol gave (10-(furan-2-carboxamido)decyl)phosphonic acid. This approach enabled a long alkyl chain spacer to be placed between the anchoring group and the diene. The multistep approach to synthesizing FDPA is displayed in Figure 33. The successful synthesis of FDPA was confirmed by ^{1}H NMR, ^{31}P NMR, and ESI-MS, showing the characteristic peaks and intensities (Figure A7 - Figure A9). This approach demonstrates the possibility of functionalizing amine compounds with a furan group. The amide adds polarity to the DA group, which may be beneficial for the accessibility of the groups at the particle surface after ligand exchange.

Lea Klauke then investigated the FDPA ligand as a suitable DA anchoring group for SPIONs, and the overall results are summarized. A ligand exchange was performed using cubic SPIONs with a size of 19 nm with a 4 to 5-fold excess of the FDPA ligand on the particle's surface. DLS experiments investigated the product FDPA@SPIONs, and efficient ligand exchange was observed. The cluster size increased to 100 – 800 nm.
To investigate the reversible DA reaction of both MDPA@SPIONs and FDPA@SPIONs, the ligands MDPA and FDPA were reacted (1:1) in methanol at 60 °C to receive the DA adduct DA-X (Figure 34). Afterwards, DA-X was dried and dissolved in THF. Then it was mixed with OA@SPIONs (11 nm, cubes) in THF. The addition of DA-X led to the precipitation of the particles, which could be separated magnetically. Transmission FTIR was used to investigate the dried particles at different temperatures.[202]

The results demonstrated that the concept of cross-linked ene and diene particles holds potential towards thermoreversible reactions between nanoparticles. However, the results show only a small amount of inter-particle crosslinking. A higher amount of DA-X seems to undergo addition to the same SPIONs. A potential strategy could be the DA reaction between MDPA@SPIONs and FDPA@SPIONs in a solvent-based mixing reaction to reach a DA-X@SPIONs network. Another way could be the integration of the MDPA ligand into covalent adaptable polyamide networks through internal catalysis.[208]

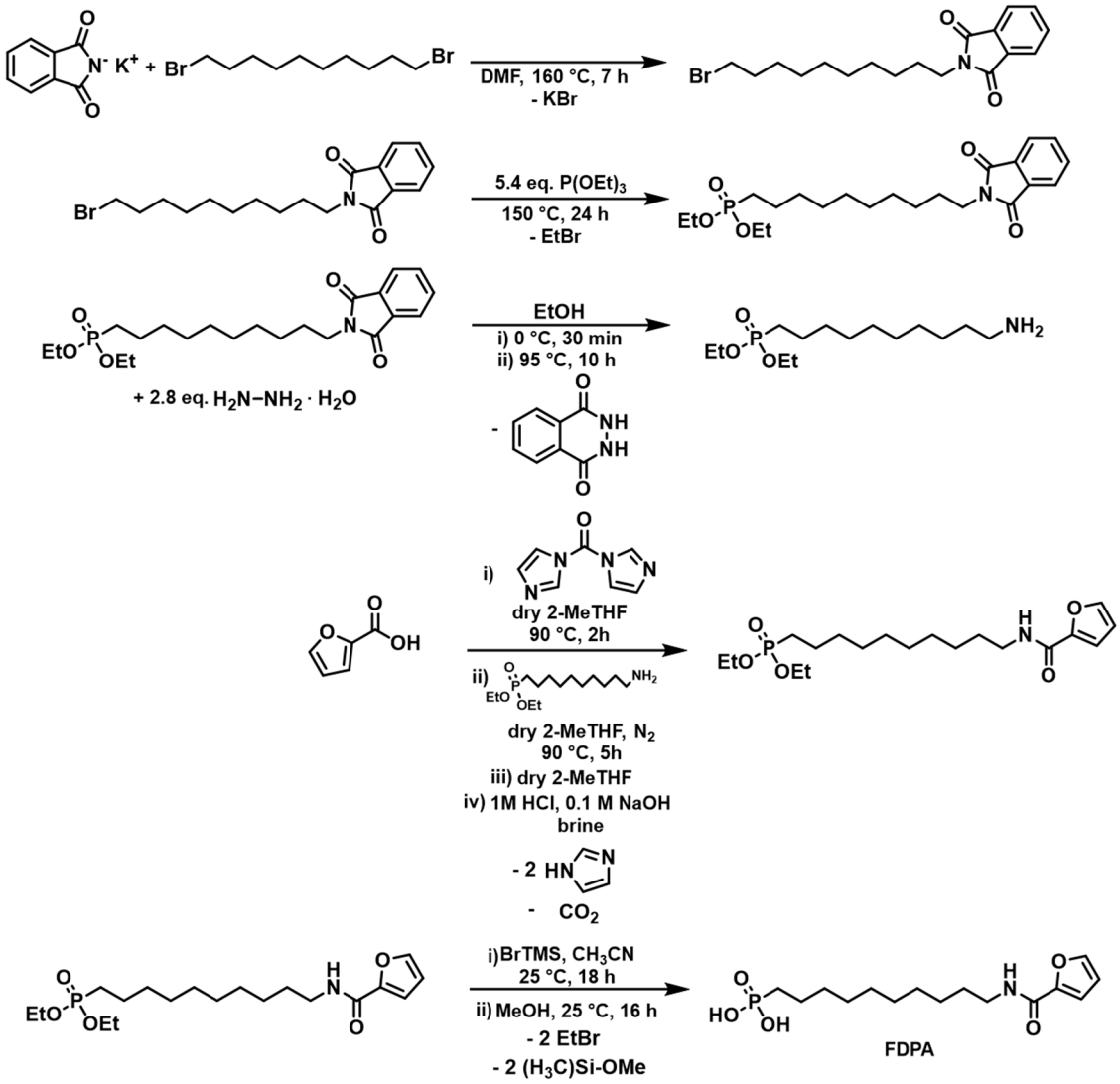

Figure 33: Synthesis of (10-(furan-2-carboxamido)decyl)phosphonic acid (FDPA) starting from 1,10-dibromodecane.

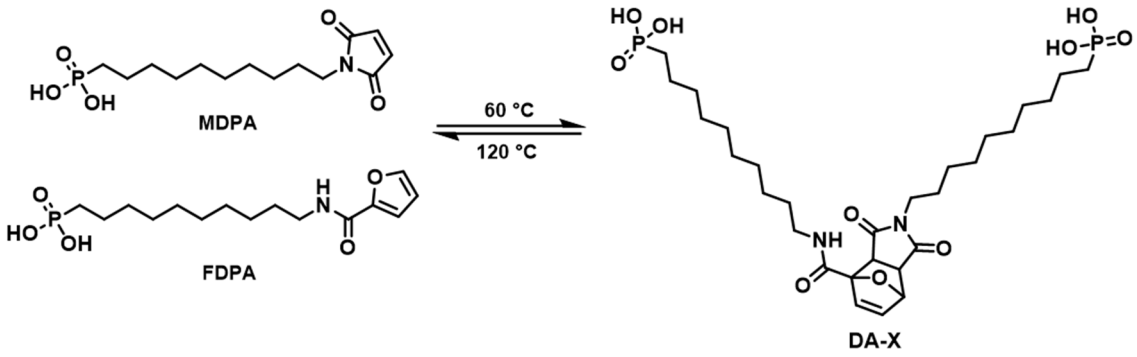

Figure 34: Crosslinking reaction *via* DA reaction of MDPA and FDPA at 60 °C and the reverse DA reaction at 120 °C.

6.2.4 Vinylogous-Urethane Epoxy Co-Networks

Thermosetting polymers prepared from epoxy resins are a widely used class of materials across various fields.[209] Their use in coatings, electronic materials, adhesives, and matrices for fiber-reinforced materials originates from their outstanding properties. For example, they display high adhesion strength, good heat resistance, high electrical resistance, and a broad range of epoxy resin types, curing agents, and curing processes.[210-212] As for all fields of polymer science, sustainability gained a growing importance also for epoxy resins, including vitrimers based on epoxy chemistry, bio-based building blocks, and alternative approaches.[213-217]

Another strategy involves the formation of co-networks from covalent and covalent adaptable crosslinks, which suppress creep while maintaining reprocessability. This strategy was introduced by Torkelson *et al*. in 2018, where they found the critical fraction of permanent cross-links in a transesterification vitrimer to be 40 mol%.[93] This approach ensured full reprocessability and a high reduction of creep. The critical point is reached when the permanent network allows a percolated network to form within the vitrimer. The approach follows a point of view that is the reverse of Flory and Stockmayer's, asking how high a permanent network cross-link density can be achieved in a vitrimer, just below the critical gelation point, which suppresses creep while still allowing for melt-state reprocessability. This amount was calculated theoretically to be 50 mol% of permanent links. Experimentally, a 40 mol% amount was found to be reprocessable without significant degradation of the mechanical properties.[93]

Moreover, the combination of acetoacetates used to form VUs with epoxy resins provides a facile approach to creating co-networks, as both epoxy resins and acetoacetates react readily with amines.[218] In 2022, Wu *et al*. reported VU-based epoxy vitrimers with a closed loop and multiple recycling routes, based on GLYAAC, bisphenol F, and *m*-xylylenediamine.[219] Here, they prepared the materials with an amine excess of 10 mol% based on the mechanical properties investigated in preliminary experiments. Since the condensation reaction of the VU network leads to the formation of water, this can result in the trapping of water inside the co-network, requiring an additional processing step (grinding/compression molding). Thus, Spiesschaert *et al*. developed a curing agent composed of TREN, acetoacetylated ethylene glycol, and 1,3-bis(aminomethyl)cyclohexane to prepare VU-containing epoxy vitrimers from BADGE.[220] They used a composition containing 42 mol% VU bonds and 5% excess of amines to provide processability, which displayed similar material properties to the commercial VU-free epoxy reference material. These co-network materials find applications, for example, in self-healing epoxy-based protection coatings.[221] Water-free VU-based materials can also be prepared by using CANs based on double Michael addition on alkynone precursors.[222] This approach was further investigated to prepare water-free VU networks by polyaddition using alkyne esters and the corresponding amines.[223] Covalent and covalent adaptable co-networks were also investigated, for example, for epoxy-imine co-networks and epoxy-acetal co-networks.[224,225]

The developments paved the way towards the newly formed class of bio-based epoxy vitrimers, which enable the integration of recyclability by design into industrial applications of epoxy-based chemistries.[226]

The following chapter is based on the preliminary work and results of Philipp Haida, who investigated vitrimer-epoxy co-networks (VIPOXY) from bisphenol A diglycidyl ether (BADGE), acetoacetylated bisphenol A (BPAAC), and Jeffamine T403 (JT). The prepared VIPOXY networks contained an epoxide-to-acetoacetate ratio of 70:30 mol% and an *R*-value of 0.7. It was demonstrated that the prepared network was reprocessable; however, the T_g was low (14 °C), and the mechanical properties of the network remained inferior to those of the fully epoxy-based network.[187]

In the following, an improved strategy for preparing these VIPOXY networks is presented, which considers the consumption of amine groups by the epoxy networks and maintains a new defined *R′*-value of 0.7 for all presented networks, ensuring the same amount of free amines for all co-networks. With this consideration, VIPOXY co-networks were prepared with high T_g and high mechanical properties, which were comparable to those of the neat epoxy-based material. Furthermore, the critical amount of permanent crosslinks was investigated when a constant *R′*-value of 0.7 was applied to the VIPOXY networks.

This concept enables a new platform for designing recyclable BADGE-based networks without altering a promising vitrimer formulation, which can be easily integrated into a commercially available curing formulation. The results show that, with the right combination of networks, material properties can be maintained, and easy processing is ensured through standardized heat compression procedures.

In a first synthesis, bisphenol A was acetoacetylated to yield propane-2,2-diylbis(4,1-phenylene) bis(3-oxobutanoate) (BPAAC) using TMDO. In contrast to the reported procedure, the acetoacetylation in this work was performed without the use of a solvent, thereby reducing the need for additional chemicals, in line with green chemistry principles, to obtain a product with the same properties.[142] The reaction is displayed in Figure 35. The resulting 1H NMR, 13C NMR, and ESI-MS spectra show the characteristic peaks and intensities and are displayed in Figure A10 – Figure A12. Since the BPAAC building block has a melting temperature above 90 °C, the formation reactions of the different networks were performed at 100 °C.

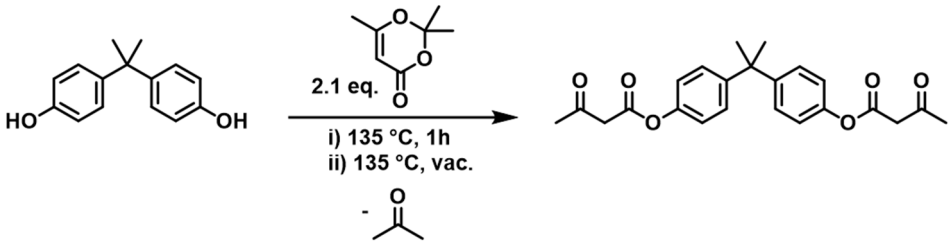

Figure 35: Synthesis of BPAAC in a bulk reaction with TMDO, starting from bisphenol A.[142]

The reactivity of epoxy and acetoacetate groups differs in the reaction with the amines present to cure the co-network. In Figure 36, the addition reaction of a primary amine and an epoxy group is displayed. In contrast to the addition, the condensation of amines with acetoacetates produces water as a byproduct. Regarding the chosen reaction conditions, this byproduct can be removed in situ, for example, by using elevated temperatures and reduced pressure. The formed VU bond and the *β*-hydroxy ether bond display a similar backbone structure.

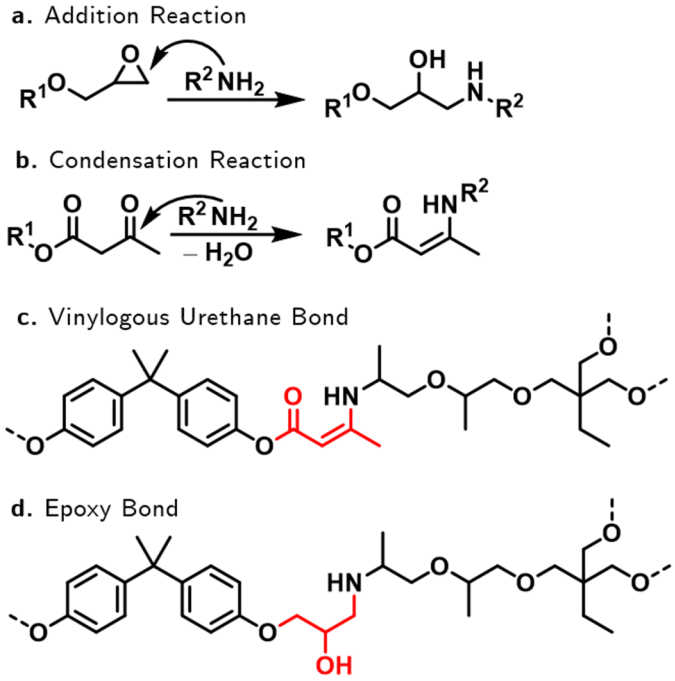

Figure 36: (a) Addition reaction of epoxy groups with primary amines. Secondary amines and hydroxy groups can likewise undergo addition reactions with epoxy groups. (b) Condensation reaction of acetoacetate groups with primary amines to prepare vinylogous urethanes. (c) Main product of the vinylogous urethane bond formation. d) The main product of the first addition reaction of the epoxy groups with the primary amine.

For network formation, the ratio between the reactive groups and the abundant amines is crucial for both the formation and reversibility of the VU vitrimer. To reduce the softening effect of free amines and chain fragments, an *R*-value of 1 was chosen for the network formed between BADGE and JT, meaning the same amount of epoxy groups and amine groups was reacted to form the network EP-1. To ensure good reprocessability, the VU formed by reacting BPAAC and JT was synthesized with an *R*-value of 0.7, resulting in the network VU-1. The *R*-value of a VU can generally be calculated by Equation 4, considering the functionality *f* of the different building blocks.

$$R = \frac{n_{AcAc} \cdot f_{AcAc}}{n_{Amine} \cdot f_{Amine}} \qquad \text{Equation 4}$$

If different molar amounts of the two networks are mixed, both the epoxy groups and the acetoacetates will react with the amine. The molar fraction of the epoxy compound in the VIPOXY networks can be calculated using Equation 5.

$$X_{EP} = \frac{n_{\mathrm{EP}}}{(n_{\mathrm{EP}} + n_{\mathrm{AcAc}})} \qquad \text{Equation 5}$$

Different amounts of the epoxy resin BADGE were used for the VIPOXY materials. The composition of the networks is indicated by the indices VU_xEP_y, where x represents the molar amount of acetoacetate and y represents the molar amount of epoxy.

Since the epoxy group consumes free amines until all free epoxies have reacted, the R-value can be modified by introducing the R'-value in Equation 6. This modification ensures that the amount of free amines is constant in all formulations.

$$R' = \frac{n_{\mathrm{AcAc}} \cdot f_{\mathrm{AcAc}}}{(n_{\mathrm{Amine}} \cdot f_{\mathrm{Amine}}) - (n_{\mathrm{EP}} \cdot f_{\mathrm{EP}})} \qquad \text{Equation 6}$$

Using this equation, the formulations could be prepared by calculating the amount of amines by using Equation 7.

$$n_{\mathrm{Amine}} = \frac{n_{\mathrm{AcAc}} \cdot f_{\mathrm{AcAc}} + R' \cdot \left(\cdot \left(\frac{X_{\mathrm{EP}} \cdot n_{\mathrm{AcAc}}}{1\text{-}X_{\mathrm{EP}}} \right) f_{\mathrm{EP}} \right)}{R' \cdot f_{\mathrm{Amine}}} \qquad \text{Equation 7}$$

The amount of epoxy can be calculated accordingly, using Equation 8.

$$n_{EP} = \frac{X_{\mathrm{EP}} \cdot n_{\mathrm{AcAc}}}{1\text{-}X_{\mathrm{EP}}} \qquad \text{Equation 8}$$

The formulations and the different network compositions are shown in Figure 37, including an exemplary fraction of a VIPOXY network.

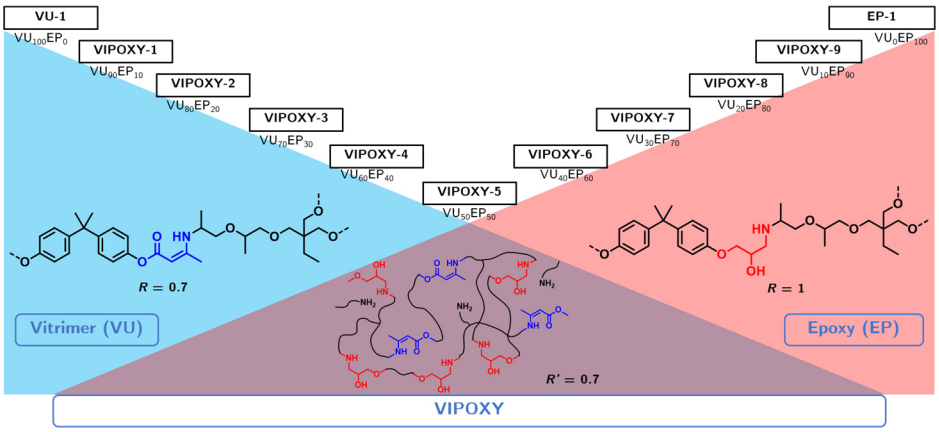

Figure 37: Illustration of the formulations of the VU-1 vitrimer network with an R-value of 0.7 and the epoxy network with an R-value of 1. The VIPOXY-co-networks are abbreviated according to their formulation, *e.g.*, VIPOXY-1 is a co-network composed of 90 mol% VU bonds and 10 mol% EP bonds, with an R'-value of 0.7.

It is worth noting that for VIPOXY-6, 7, 8, and 9, reprocessing was not possible during the preparation procedure. Therefore, they are excluded from the following characterizations and test methods. As mentioned before, this is due to the formation of a percolating permanent network, which restricts the dynamic bond exchange. During the formation of VU bonds, water is evolved as a byproduct, resulting in bubbles that are then trapped in a non-dynamic matrix. This reaction can be used to prepare a foamed epoxy material analogous to foamed urethanes, eliminating the need for additional foaming reagents.

The successful network formation was characterized using ATR-FT-IR. In comparison to the starting materials (Figure A13), the characteristic stretching vibration of the oxirane ring of BADGE is no longer present at 910 cm^{-1} for the material VIPOXY-3, and the vanishing of the characteristic acetoacetate bands can be observed (Figure A14). Furthermore, the N-H and O-H stretching vibrations appear in the region of 3100 – 3600 cm^{-1} as well as the characteristic VU bands of the C=C and the C=O bands (1594 and 1647 cm^{-1}). Interestingly, at 1720 cm^{-1}, a new band appears for all materials containing VU bonds. This band most likely belongs to an ester C=O vibration. In Figure 38, the ATR-FT-IR spectra of the VU-1 and EP-1 networks, as well as the spectra of the VIPOXY networks, are displayed, showing the characteristic bands of the formed co-networks.

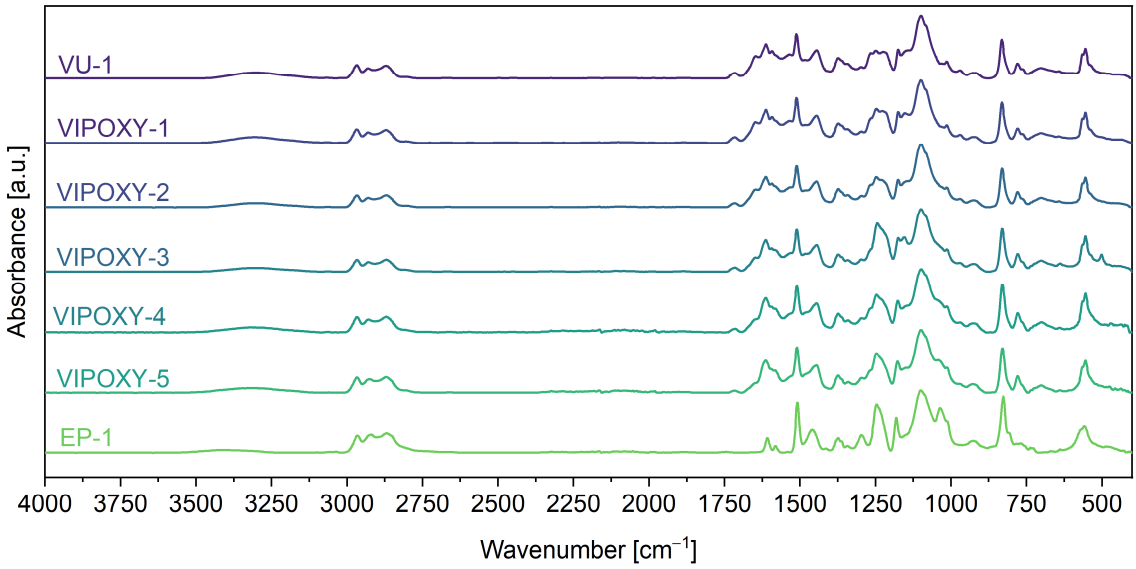

Figure 38: ATR-FT-IR spectra of the prepared materials VU-1 and EP-1, as well as the formed co-networks with increasing epoxy content.

Next, the thermophysical properties of the materials were determined using DSC (Figure 39), which revealed a T_g of 31 °C for VU-1 and 50 °C for EP-1. With increasing epoxy content, the T_g increases, showing values of 33 °C for VIPOXY-2 and 45 °C for VIPOXY-5. This trend shows a reinforcing effect of the co-network formation on the T_g. The ether bond displays higher thermal stability than VUs, which is also due to the non-dynamic covalent character of the ether.

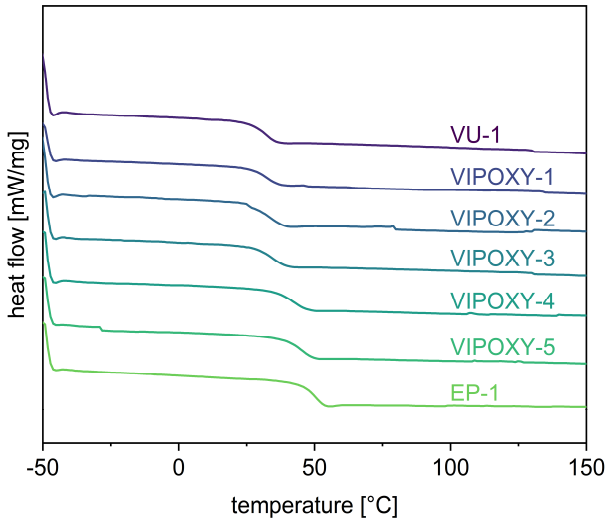

Figure 39: DSC measurement of the prepared materials VU-1 and EP-1, as well as the formed co-networks with increasing epoxy content. The curves display the data from the second heating cycle under an ambient (oxygen) atmosphere.

In the TGA (Figure 40), the free amines of the VU-network decrease the thermal stability, with materials of lower epoxy content displaying a lower $T_{5\%}$ of 248 °C (VIPOXY-1) and 267 °C (VIPOXY-5). EP-1 displays, as expected, the highest thermal stability with 328 °C, as no free amines are present. With the formation of co-networks, the thermal stability of vitrimers can be enhanced by reducing thermal decomposition and increasing rigidity through the introduction of permanent crosslinks.

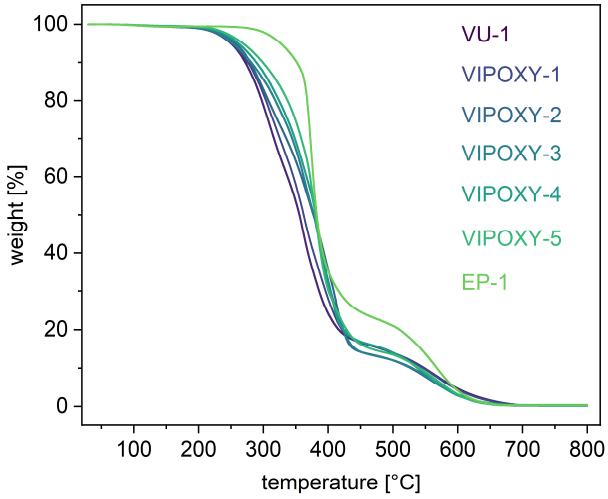

Figure 40: TGA measurement of the prepared materials VU-1 and EP-1, as well as the formed co-networks with increasing epoxy content under ambient (oxygen) atmosphere.

The influence of pendant amines also becomes evident by optical investigations of the materials. Digital images of VU-1, test specimens of VU-1, and EP-1 are displayed in Figure 41.

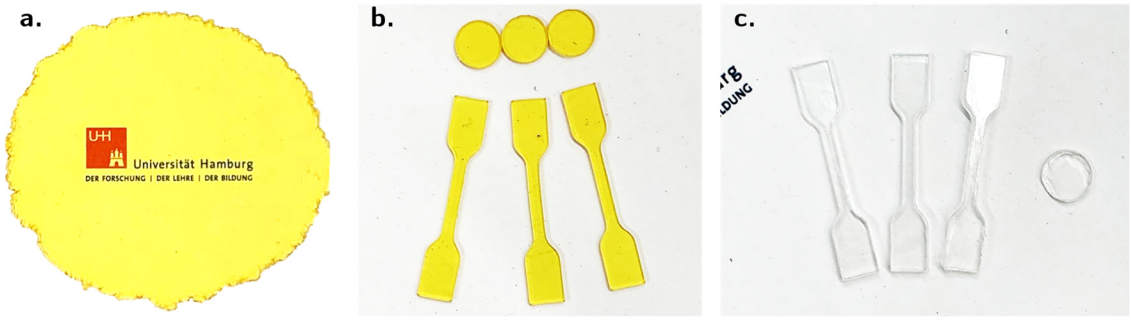

Figure 41: Digital images of VU-1 (a), test specimens of VU-1 (b), and EP-1 (c).

The yellowish color is a typical observation in VU-based materials compared to optically transparent DB vitrimers (Publication 3) and epoxy-based materials (EP-1). The color is influenced by the oxidation sensitivity of the used amine (VU or imines, Publication 1), the conjugated backbone structure, and also by the grade of the acetoacetylation agent, which affects the color of the acetoacetylated monomers. For the presented VIPOXY materials, TMDO from Sigma Aldrich was used after distillation. If a batch of TCI was used, the VIPOXY materials appeared brownish, and the produced BPAAC already obtained a darker color. This color behavior of different acetoacetates was also observed, *e.g.*, in GLYAAC. However, these observations were not further investigated within the scope of this work.

Next, tensile testing was performed on the networks and co-networks to demonstrate their mechanical behavior at 23 °C. In Figure 42, exemplary tensile-test curves are shown.

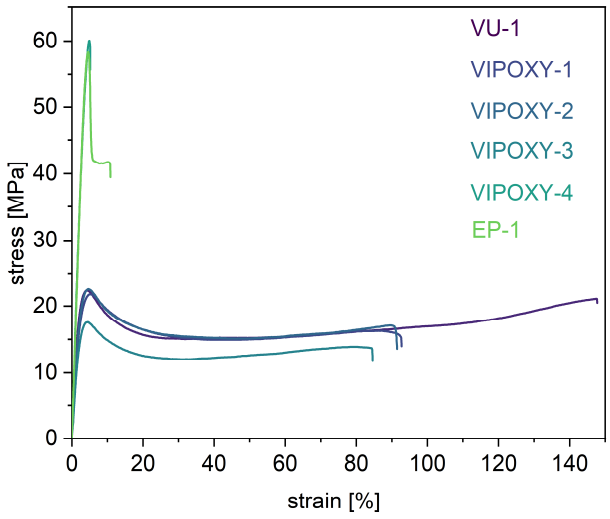

Figure 42: Exemplary stress-strain curve of the network materials VU-1 and EP-1, as well as the co-networks VIPOXY at 23 °C.

The mechanical behavior of the materials shifts from elastomeric (VU-1, VIPOXY-1) towards a more rigid behavior (EP-1, VIPOXY-4). Interestingly, VIPOXY-4 exhibits similar mechanical properties to the epoxy network, as listed in Table 3.

Table 3: Comparison of the stress-strain data of the network materials VU-1 and EP-1, as well as the co-networks VIPOXY at 23 °C, with the values of E, σ_m, σ_b, and ε_b determined from the mean of three measurements.

Sample	E [MPa]	σ_m [MPa]	σ_b [MPa]	ε_b [%]
VU-1	731 ± 231	21.4 ± 1.9	17.7 ± 5.4	139 ± 27
VIPOXY-1	410 ± 300	13.0 ± 7.7	8.3 ± 5.0	60.5 ± 32
VIPOXY-2	848 ± 300	25.0 ± 9.0	15.7 ± 5.4	73.1 ± 26
VIPOXY-3	807 ± 90	25.1 ± 3.5	10.3 ± 1.5	32.5 ± 13
VIPOXY-4	1568 ± 121	55.6 ± 7.5	47.7 ± 21	5.8 ± 1.5
EP-1	1454 ± 253	59.4 ± 3.3	20.6 ± 3.9	30.3 ± 11

A co-network with a BPA-based backbone, featuring VU and EP with 40 mol% of EP bonds and an R'-value of 0.7, yields a mechanically comparable co-network that exhibits recyclability and reprocessability. The E-moduli are in the same range, with 1.6 GPa and 1.5 GPa for VIPOXY-4 and EP-1, respectively. The maximum tensile strength is also comparable with 55.6 MPa and 59.4 MPa. However, the co-network loses toughness, as the elongation at break decreases from 30.3% for EP-1 to 5.8% for VIPOXY-4. The addition of epoxy bonds can reinforce the VU network; however, this leads to reduced toughness. Nevertheless, this highlights once again the reinforcing effect of the co-network structure, for example, in the case of repairable coatings. Before all oscillatory rheological measurements, amplitude sweep tests were performed to ensure that the amplitude of strain was within the LVE (Figure 43). All materials display an LVE in the range of 0.01% and 1%, with VIPOXY-4 showing a yield point at 10% amplitude. In comparison, EP-1 shows a more rigid structure in the amplitude sweep curve, similar to VIPOXY-1. The co-networks VIPOXY-3 and VIPOXY-4 display more energy dissipation with an increasing loss modulus.

Subsequently, temperature sweep measurements were performed at a constant frequency of 1 Hz, a normal force of 1 N, and a constant shear amplitude of 0.1% in the temperature range of 0 – 150 °C. The temperature sweep data in Figure 44 displays similar network structures for all co-networks and EP-1, as the rubbery plateau is located in the same order of magnitude. As the networks display a constant cross-link density, the storage moduli remain constant at elevated temperatures (>140 °C), a characteristic feature of thermosets and vitrimers in their rubbery state. Also, the co-networks resemble this behavior. In the case of EP-1, the typical value of G' in a glassy state (approx. 10^9 Pa) is not reached below T_g. This is most likely due to a measurement error. VIPOXY-4 shows both the highest rubbery plateau and T_g regime, validating the findings of the tensile testing. The temperature sweep test also underscores the reinforcing effect of the co-network structure with 40 mol% epoxy bonds.

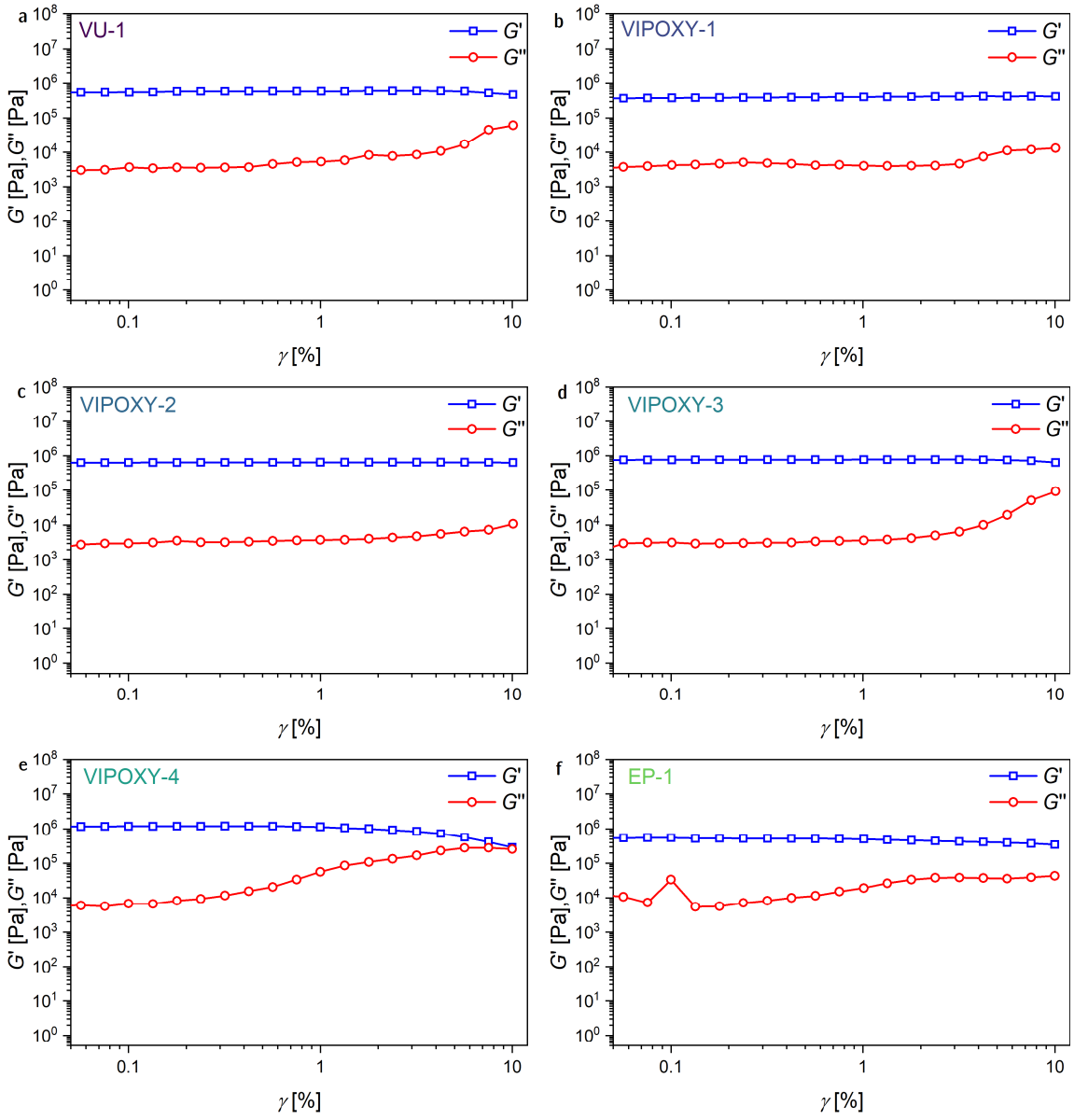

Figure 43: Amplitude-sweep measurements of the network materials VU-1 (a) and EP-1 (f), as well as the co-networks VIPOXY (b-e) at 110 °C, a frequency of 1 Hz, and a normal force of 1 N.

To investigate the reprocessing capability of the materials, stress-relaxation measurements were performed with a constant shear strain step of 1% and subsequent measurement of the stress-relaxation modulus for the vitrimer network VU-1 and the co-network VIPOXY-4. The results of the KWW fit for the non-normalized stress-relaxation data are listed in Table 4.

Table 4: Summary of the values of the stretch factor β and the calculated average values of the characteristic stress-relaxation time $\langle\tau\rangle$ for the KWW fit of the stress-relaxation measurements (γ = 1%, F_N = 1 N) between 110 – 150 °C of the tested materials VU-1 and VIPOXY-4.

Sample	$\beta_{110°C}$ [-]	$\beta_{120°C}$ [-]	$\beta_{130°C}$ [-]	$\beta_{140°C}$ [-]	$\beta_{150°C}$ [-]	$\langle\tau\rangle_{110°C}$ [s]	$\langle\tau\rangle_{120°C}$ [s]	$\langle\tau\rangle_{130°C}$ [s]	$\langle\tau\rangle_{140°C}$ [s]	$\langle\tau\rangle_{150°C}$ [s]
VU-1	0.830	0.745	0.740	0.558	0.667	2616	1403	701	44.4	20.6
VIPOXY-4	0.855	0.789	0.707	0.586	0.489	15144	7806	3739	1463	278

The stretch factors of both materials fall within the same range at the same temperatures, *e.g.*, 0.558 and 0.585 at 140 °C, respectively. Furthermore, the co-network structure results in longer characteristic stress-relaxation times (<τ>), indicating that the addition of non-dynamic bonds restricts the movement of chain fragments and hinders dynamic network rearrangement reactions.

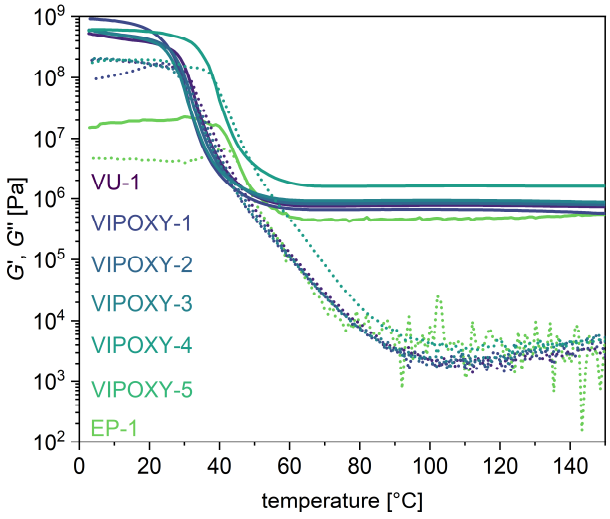

Figure 44: Temperature sweep measurements of the network materials VU-1 and EP-1, as well as the co-networks VIPOXY in the temperature range of 0 – 150 °C, performed at a constant angular frequency of 6.28 rad s^{-1}, an amplitude of 0.1%, and a normal force F_N of 1 N. A line represents the storage modulus, while the loss modulus is drawn as a dashed line.

The stress-relaxation measurements and the calculation of the activation energies are displayed in Figure 45. For both materials, the activation energies were calculated in the linear ranges of 110–130 °C and 110–140 °C, respectively, based on the computed ln <τ> over 1000/T. At 150 °C, the relaxation of both networks is faster; thus, 150 °C was chosen as the reprocessing temperature. At higher temperatures, the stretch factors are 0.667 and 0.489, indicating secondary relaxation effects that cannot be attributed to the transamination reaction. From the linear slope, the E_as were calculated to be 78.9 kJ mol^{-1} (VU-1) and 86.5 kJ mol^{-1} (VIPOXY-4). The E_as are in the same range, display typical values for transaminations, and show that the co-network is also reprocessable with 40 mol% of non-dynamic bonds.

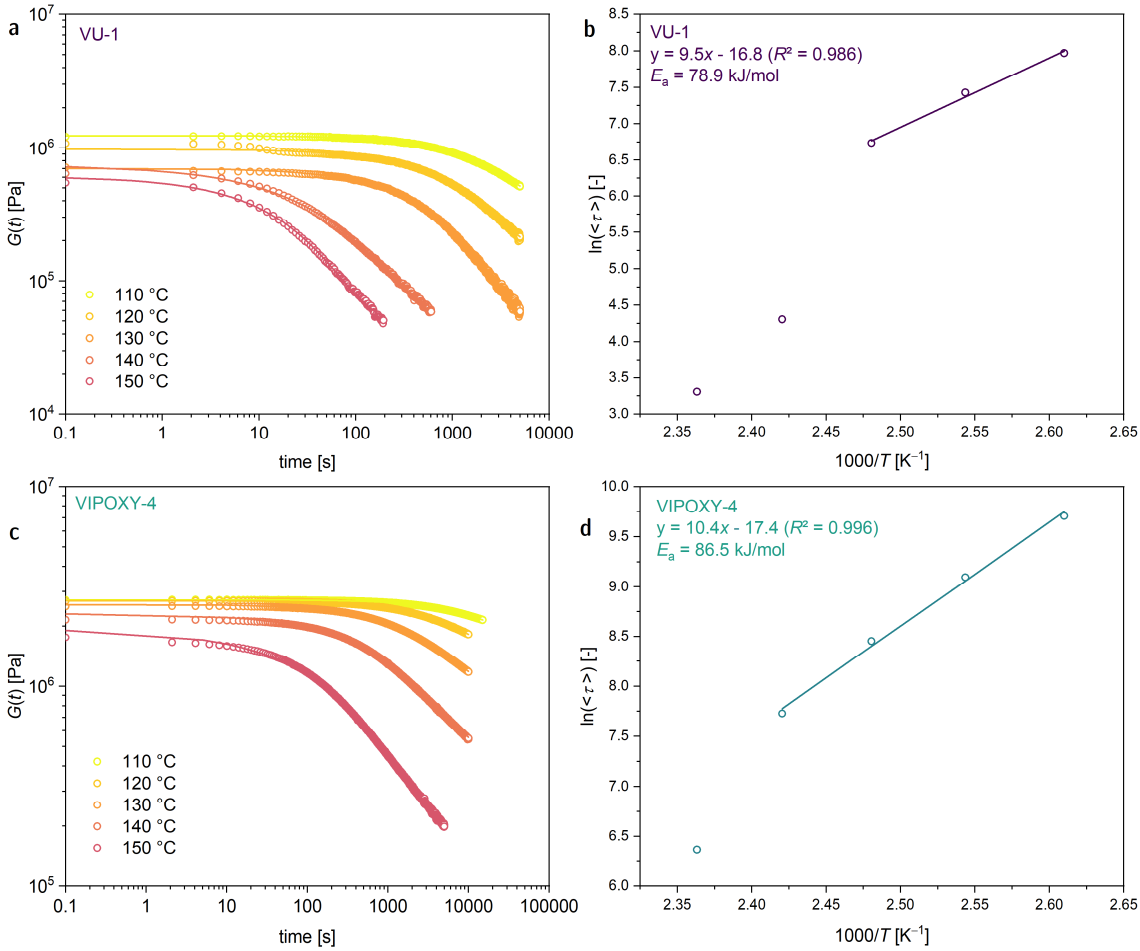

Figure 45: Stress-relaxation measurements of VU-1 (a) and VIPOXY-4 (c), plotting the stress-relaxation modulus $G(t)$ versus the stress-relaxation time measured at temperatures in the range of 110 – 150 °C while applying a shear strain of 1%. The lines display the stretched exponential fit functions for the respective temperatures, calculated from the stress-relaxation data. Plots of τ versus $1000/T$ of VU-1 (b) and VIPOXY-4 (d) to calculate the activation energies from the slope of the linear fit of the calculated $<\tau>$ values from the stretched exponential fit in the temperature range of the stress-relaxation measurements (γ = 1%, F_N = 1 N) between 110 – 130 °C for VU-1 and 110 – 140 °C for VIPOXY-4.

6.2.5 VIPOXY-Based Hierarchical Nanocomposites

Until now, (nano-)composites have been fixed in their molecular networks due to the use of non-dynamic covalent bonds. Vitrimers can bridge this gap, as they represent polymer networks that undergo thermally induced bond exchange reactions upon heating and exhibit self-healing, shape-programming, shape-memory, and reprocessability. The outstanding mechanical properties of the VIPOXY co-networks result from a combination of both permanent and dynamic polymer networks, enabling excellent thermomechanical properties and chemical stability while maintaining the reprocessability of the materials. The addition of self-assembled SPION nanoclusters, produced by Lea Klauke, was included in the VIPOXY-4 matrix to provide reinforcement and create an artificial hierarchical structure.

In this way, strong, sustainable, and magnetic nanocomposites were prepared without having to forego the outstanding properties of classical thermosetting matrices. The synthetic approach for producing multi-level hierarchical nanocomposites based on nanometer-sized superparamagnetic iron oxide nanocubes is illustrated in Figure 46.

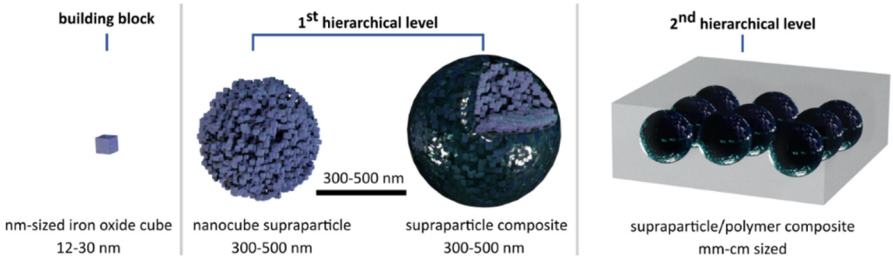

Figure 46: Schematic of the synthetic approach to fabricate multi-level hierarchical structured nanocomposites based on superparamagnetic nm-sized nanocubes, assembled into spherical supraparticles. Subsequently, the supraparticles are encapsulated. Finally, the encapsulated supraparticles are embedded into tailored vitrimer-derived matrices.

The production of the nanocomposites follows the solid-solid formation process of nanocomposites described in Publication 3. Here, VIPOXY-4 was ground into a powder using a cryo-ball mill. Next, 50 wt.% of ground matrix material was mixed with the supraparticles and pressed using the stainless-steel mold described in Publication 3. The formation process is illustrated in Figure 47. The mechanical performance of the produced nanocomposites is discussed in detail in the dissertation of Lea Klauke.[202] The formation process of the nanocomposites was successful, as dimensionally stable pellets were produced.

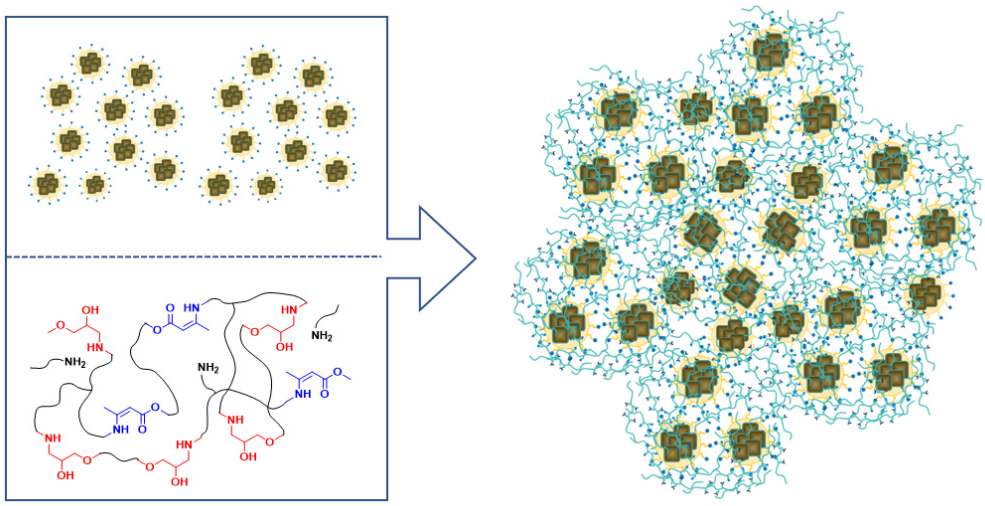

Figure 47: Illustration of the incorporation of core-shell supraparticles into a vitrimer-based matrix, which can be recycled *via* a thermoreversible associative mechanism of vinylogous urethanes, forming the second hierarchical level of the material.

A scanning electron microscopy (SEM) image, displayed in Figure 48, shows a homogeneous distribution of supraparticles, indicating the successful formation of composites consisting of high amounts of inorganic material, up to 70 wt.%. Nevertheless, due to heat compression, mechanical stress can lead to specific degradation of the supraparticles (SPs). Here, a matrix with a lower E_a could be beneficial in enhancing the integrity of the supraparticles, *e.g.*, the BVS material described in Publication 3. Moreover, the covalent integration of the SPs could improve the mechanical performance of the highly filled nanocomposites, as they currently appear brittle.

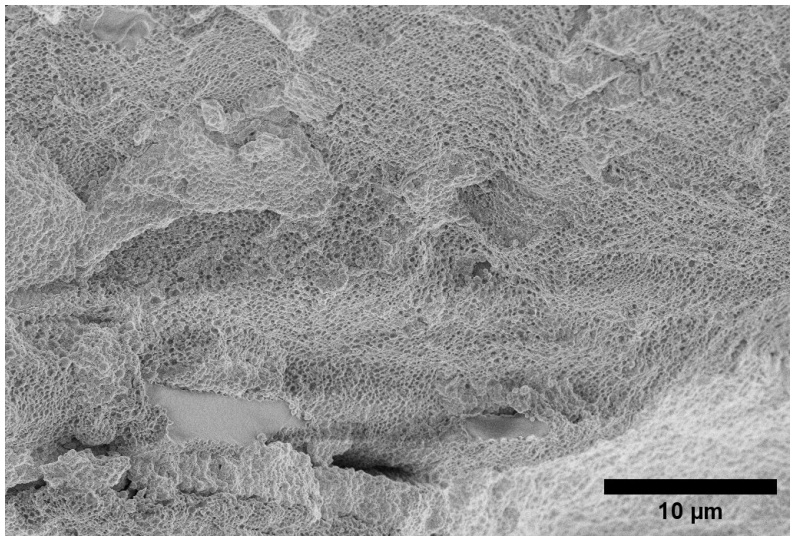

Figure 48: SEM image of the formed VIPOXY-based hierarchical nanocomposite showing a homogeneous distribution of supraparticles within the dynamic co-network structure.

In summary, highly filled nanocomposite materials can be produced using the bulk synthesis method. A multi-level hierarchy is achievable, starting with single nanocubes, which are then encapsulated in a first hierarchical level and finally in the dynamic co-network matrix. The final materials exhibit a homogeneous distribution of supraparticles. The mechanical performance can be enhanced by optimizing the heat compression process and improving the thermoreversible network structure.

6.3 Experimental Section

6.3.1 Materials

This chapter shows the raw materials used, their purities, and suppliers.

1,10-Dibromodecane (97%, Alfa Aesar), 1,1'-carbonyldiimidazole (100%, Sigma Aldrich), 1,4-dibromobutane (100%, VWR), 1-thioglycerol (Sigma Aldrich), 2,2,6-trimethyl-4*H*-1,3-dioxin-4-one (Sigma Aldrich, TCI), 2-methyltetrahydrofuran (VWR), acetone (99%, BCD), acetonitrile (99.9%, Fisher Scientific), benzene-1,4-diboronic acid (Apollo), bio-based poly(oxy-1,3-propanediyl) (Sigma Aldrich), bisphenol A diglycidyl ether (Sigma Aldrich), calcium chloride (Merck), calcium hydride (VWR), carbon fiber (100%, MJJSports), chloroform (99%, VWR), deuterated chloroform (99.8%, Deutero), deuterated dimethyl sulfoxide (99.8%, Deutero), dichloromethane (BCD), diethyl ether (99%, VWR), diethyl phosphonate (ABCR), diethylenetriamine (TCI), dimethylsulfoxide (99.5%, Grüssing), ethanol (99.8%, Roth), ethyl acetate (99.8%, VWR), 2-furoic acid (Sigma Aldrich), glycerol (98%, VWR), hydrazine monohydrate (Sigma Aldrich), hydrochloric acid (37%, Fisher Scientific), lignosulfonate (TCI), magnesium sulfate (99%, Grüssing), methanol (99.8%, Fisher Scientific), *N*,*N*-dimethylformamide (99.5%, VWR), deuterated *N*,*N*-dimethylformamide (Deutero), *n*-hexane (95%, Fisher Scientific), *n*-pentane (99.8%, Thermo Scientific), oleic acid (90%, Sigma Aldrich), oleyl amine (70%, ChemPUR), phosphorus trichloride (99%, Fisher Scientific), potassium carbonate (99%, Grüssing), potassium phthalimide (98%, Alfa Aesar), pyridine (99.5%, Fisher Scientific), sodium chloride (99%, Grüssing), sodium hydroxide (99%, Grüssing), *tert*-butyl acetoacetate (TCI), tetrahydrofuran (99.7%, Fisher Scientific), titanium dioxide (Sigma Aldrich), triethyl phosphite (98%, Sigma Aldrich), triethylamine (99%, Sigma Aldrich), trimethylsilyl bromide (Sigma Aldrich), tris(2-aminoethyl)amine (VWR), tris(acetylacetonato)chromium(III) (Fisher Scientific), vanillin (99%, VWR), xylene (99%, Grüssing), and toluene (99.5%, Fisher Scientific) were purchased. Fibenol OÜ provided Lignova™ Crude and Lignova™ Pure. Huntsman provided Jeffamine® D-400 and Jeffamine® T-430. Croda International provided Priamine™ 1073.

6.3.2 Synthesis

6.3.2.1 Synthesis of propane-1,2,3-triyl tris(3-oxobutanoate)

The crude, brownish 2,2,6-trimethyl-4H-1,3-dioxin-4-one (TMDO) was purified by vacuum distillation prior to use to obtain a pure colorless liquid. Glycerol (10.0 g, 109 mmol, 1 eq.) and 2,2,6-trimethyl-4*H*-1,3-dioxin-4-one (TMDO) (51.2 g, 360 mmol, 3.3 eq.) were stirred for 1 hour at 135 °C. The product was then dried under reduced pressure at 135 °C and received as a yellow liquid.

6.3.2.2 Synthesis of glycerol vitrimer polymer

1,8-Diamino-3,6-dioxaoctan (4.90 g, 33 mmol) and propane-1,2,3-triyl tris(3-oxobutanoate) (5.3 g, 15 mmol) were mixed with a spatula under constant stirring at 23 °C or at 120 °C. As soon as a gel was obtained, the vitrimer gel was filled onto a Teflon sheet and stored at ambient conditions (23 °C) for 12 hours. Afterwards, it was cured for 23 h at 120 °C under reduced pressure (oil pump). Afterward, the vitrimer was post-cured for 1 h at 150 °C in vacuo to ensure complete conversion and removal of the remaining reaction water. Next, the samples were pressed for 5 − 10 min at 150 °C with a pressure of 10 kN into a 1 mm thick yellow film. To prevent the films from sticking to the metal of the heat compression, poly(tetrafluoroethylene)-coated fiberglass fabric sheets (PTFE sheets) were used.

6.3.2.3 Synthesis of 2,2-(1,4-phenylene)-bis[4-mercaptan-1,3,2-dioxaborolane]

The synthesis was carried out according to the procedure, following the principles of green chemistry described in the literature, using a solvent-free and catalyst-free process, without generating any waste or by-products, and with recyclability by design. Benzene-1,4-diboronic acid (20.00 g, 120 mmol) and α-thioglycerol (25.96 g, 240 mmol) were dissolved in 400 mL of degassed, anhydrous ethanol (EtOH) and stirred for 24 hours under a nitrogen atmosphere at room temperature (24 °C). Subsequently, EtOH and water were removed under reduced pressure, and the product was obtained as a white powder (36.8 g, 98%).

6.3.2.4 Synthesis of dioxaborolane thiol-acrylate vitrimer network

DBEDT (6.20 g, 20 mmol) was filled into an aluminum mold and stored at 120 °C on a heat plate until the white powder was melted to a liquid. Then, 2,2-bis([(1-oxoallyl)oxy]methyl)1,3-propandiyl diacrylate (PETAC, 3.52 g, 10 mmol) was heated to 120 °C in a glass vial on the same heat plate and added under manual stirring to the aluminum mold. After an optically homogeneous solution was achieved, gelation occurred approximately 60 s later, and the boronic acid acrylate vitrimer sample (BVS) was stored at 120 °C for 24 hours in a drying oven at ambient pressure to achieve full cross-linking of the material. Afterwards, the material was removed as a plate from the aluminum mold and processed using heat compression (150 °C, 10 min, 10 kN) to obtain a homogeneous, transparent dioxaborolane acrylate vitrimer film, BVS-1, with a thickness of approximately 1 mm. To prevent the polymer films from sticking to the metal of the heat compression, PTFE sheets were used to obtain transparent vitrimer films.

6.3.2.5 Synthesis of interpenetrating covalent adaptable networks (sequential)

For the sequential reaction pathway, both GVP and BVS were prepared as indicated in subchapters 6.3.2.2 and 6.3.2.4. Subsequently, the films were milled using a steel screw-top jar and a steel grinding ball under horizontal oscillation at 30 Hz for 1 minute.

For cryogenic grinding, the loaded steel jar was cooled in liquid nitrogen for 15 min before subsequent grinding. Approximately 1 g of each powder was mixed and hot-pressed using heat compression (150 °C, 10 kN, 10 min) with a 1 mm gap. The product appeared non-homogeneous, displaying a film material with gaps and irregularities.

6.3.2.6 Synthesis of interpenetrating covalent adaptable networks (simultaneous)

Precursor solution 1 (PS-1) was formed by mixing 6.20 g DBEDT and 4.89 g DADOX at 120 °C on a heat plate. For PS-2, 5.30 g GLYAAC were mixed with 3.52 g PETAC at 120 °C in an aluminum mold on a heat plate. After the solutions appeared homogeneous, PS-1 was added to PS-2 under stirring in the aluminum mold. After approximately 10 s, bubble formation occurred, and the material formed an orange gel. The gel was stored for 20 hours at room temperature (23 °C). Then, it was stored in an oven (120 °C, 24 h) and subsequently pressed in a heat compression (150 °C, 10 kN, 10 min) with a 1 mm gap. The product appeared non-homogeneous, displaying a film material with gaps and irregularities.

6.3.2.7 Synthesis of interpenetrating covalent adaptable networks (solvent-mediated simultaneous)

Precursor solution 1 (PS-1) was formed by mixing 6.20 g DBEDT and 4.89 g DADOX at 120 °C on a heat plate in 10 mL DMSO in a beaker. For PS-2, 5.30 g GLYAAC were mixed with 3.52 g PETAC at 120 °C in 10 mL DMSO in a second beaker. After 5 min, the solutions appeared homogeneous, and the PS-1 solution was added under stirring to the beaker containing PS-2. The solution was heated to 120 °C and maintained for 12 hours. After 12 h, a black gel was obtained and stored at 120 °C for 24 h in a drying oven under reduced pressure. Subsequently, it was removed from the beaker and processed *via* heat compression (150 °C, 10 min, 10 kN) with a 1 mm gap to form a homogeneous black film.

6.3.2.8 Synthesis of *N*-(10-bromodecyl)phthalimide

The reaction was carried out in the absence of water and oxygen. To a suspension of 1,10-dibromodecane (25.00 g, 76.2 mmol, 4 eq.) in dry DMF (35 mL), potassium phthalimide (3.55 g, 19.2 mmol, 1 eq.) was added, and the solution was stirred under reflux at 160 °C for 7 hours. The solution was allowed to cool to room temperature, and 140 mL of an ether-diethyl ether mixture (v/v 1:1) was added. After the addition of 70 mL of a saturated sodium chloride solution, the organic phase was separated from the aqueous phase. The organic phase was dried over magnesium sulfate, and the solvents were removed under reduced pressure. The crude product was purified by column chromatography. Initially, hexane was used, followed by a solvent gradient of n-hexane and ethyl acetate starting at 9:1 (R_f = 0.3) and then transitioning from 7:3 to 1:1. The product was received as a yellow oil (5.9 g, 16.1 mmol, 84%).

6.3.2.9 Synthesis of *N*-(10-phthalimidoalkyl)diethyl phosphonate

3.00 g of *N*-(10-bromodecyl)phthalimide (8.2 mmol, 1 equiv.) was placed in a 50 mL three-necked flask, and then triethyl phosphite (44.3 mmol, 5.4 equiv., 7.36 g) was added dropwise at room temperature. The solution was refluxed for 24 hours at 150 °C. Subsequently, excess triethyl phosphite was removed at 60 °C under reduced pressure (4 mbar), and the byproduct diethyl phosphonate was separated *via* vacuum distillation. The product was received as a yellow oil (4.32 g, 7.8 mmol, 95%).

6.3.2.10 Synthesis of *N*-(10-aminodecyl)diethyl phosphonate

The reaction was carried out in the absence of water and oxygen. To a solution of absolute ethanol (200 mL) and *N*-(10-phthalimidodecyl)diethyl phosphonate (2.35 g, 5.6 mmol, 1 eq.), hydrazine monohydrate (2.82 eq.) was added while stirring at 0 °C. After stirring for 30 minutes at 0 °C, the reaction mixture was heated to 95 °C and stirred for 10 hours. Subsequently, the mixture was slowly cooled to room temperature, and the resulting precipitate was filtered. The solvent was then removed under reduced pressure. The crude product was dissolved in 10 mL of dichloromethane (absolute), and the precipitate was filtered. The solvent was removed under reduced pressure, yielding the product as a colorless oil.

6.3.2.11 Synthesis of diethyl(10-(furan-2-ylamino)decyl)phosphonate

In a dry three-necked flask, furancarboxylic acid (1.79 g, 16 mmol, 1.2 eq.), 2-methyltetrahydrofuran (25 mL, dry), and 1,1'-carbonyldiimidazole (2.60 g, 16 mmol, 1.2 eq.) were heated under a nitrogen atmosphere for 2 hours under reflux (90 °C) while stirring. Subsequently, *N*-(10-aminodecyl)diethyl phosphonate (3.90 g, 13.3 mmol, 1 eq.) was added, and the mixture was stirred for an additional 5 hours at 90 °C. The mixture was cooled to room temperature and diluted with 25 mL of 2-MTHF. The solution was washed with HCl solution (1 M, 74 mL), NaOH solution (0.1 M, 94 mL), and NaCl solution (15 mL). The organic phase was then concentrated, and the product was received as a yellow oil.

6.3.2.12 Synthesis of diethyl(10-(furan-2-ylamino)decyl)phosphonate

In a dry three-necked flask, *N*-(10-maleimido-decyl)diethyl phosphonate (1.88 g, 4.86 mmol, 1 eq.) was dissolved in 20 mL of absolute acetonitrile. Then, trimethylsilyl bromide (11.2 mmol, 1.71 g, 1.50 mL, 2.3 eq.) was added dropwise at 0 °C while stirring, and after warming to room temperature, the mixture was stirred for 18 hours at 25 °C. The intermediate was dried under reduced pressure at room temperature and then dissolved in 8 mL of degassed methanol. The mixture was stirred for an additional 16 hours at room temperature. The solution was then concentrated by half, and subsequently precipitated in cold *n*-hexane. The product was filtered as a precipitate and dried. The product was received as a white solid (1.10 g, 3.3 mmol, 68%).

6.3.2.13 Synthesis of propane-2,2-diylbis(4,1-phenylene) bis(3-oxobutanoate)

The crude, brownish TMDO was purified by vacuum distillation prior to use to obtain a pure colorless liquid. Bisphenol A (50.0 g, 220 mmol, 2 eq.) and TMDO (65.4 g, 460 mmol, 2.1 eq.) were stirred for 1 hour at 135 °C. The product was then dried under reduced pressure at 135 °C and received as a yellow solid.

6.3.2.14 Synthesis of VIPOXY-materials

Propane-2,2-diylbis(4,1-phenylene)bis(3-oxobutanoate) (BPAAcAc) was provided in a rolled rim glass and heated up in an oil bath at 100 °C. JT403 was added under constant stirring. As soon as a homogeneous, opaque gel was obtained, the vitrimer gel was filled onto a Teflon sheet, stored at room temperature for 24 hours, and then cured for 20 hours at 100 °C in a vacuum (oil pump). Afterward, the vitrimer was post-cured for 1 h at 150 °C in vacuo to ensure complete conversion and removal of the remaining reaction water. Next, the samples were pressed for 5 − 10 min at 150 °C with a pressure of 10 kN into a 1 mm thick film. The synthetic route follows the same protocol for the synthesis of the epoxy resins and the blended VIPOXY materials with the molar amounts and masses listed in Table S1. BPAAcAc and BADGE were mixed at 100 °C to a homogeneous mass. The amine was added according to the described synthetic procedure. The products were obtained as yellowish films.

Table S1: Overview of the synthesized vitrimer film VU, the VIPOXY co-networks VIPOXY-1 – 6 and the epoxy material EP-1 with the molar amounts listed for the monomers used.

Sample	R' [-]	n_{BPAAC} [mmol]	m_{BPAAC} [g]	X_{EP} [-]	n_{EP} [mmol]	m_{EP} [g]	n_{JA} [mmol]	m_{JT403} [g]	R [-]
VU-1	0.7	12.6	5.0	0.0	0.0	0.0	12.0	5.3	0.70
VIPOXY-1	0.7	11.4	4.5	0.1	1.3	0.4	11.7	5.1	0.65
VIPOXY-2	0.7	10.6	4.2	0.2	2.6	0.9	11.9	5.2	0.60
VIPOXY-3	0.7	10.1	4.0	0.3	4.3	1.5	12.5	5.5	0.54
VIPOXY-4	0.7	8.8	3.5	0.4	5.9	2.0	12.3	5.4	0.48
VIPOXY-5	0.7	7.6	3.0	0.5	7.6	2.6	12.3	4.3	0.41
VIPOXY-6	0.7	5.0	2.0	0.6	7.6	2.6	9.8	4.2	0.34
EP-1	1.0	0.0	0.0	1.0	12.6	4.3	8.4	3.7	1.00

6.3.2.15 Synthesis of VIPOXY-nanocomposite materials

The vitrimer-SP composites are formed by mixing a certain amount of SPs (30, 50, and 70 wt.%) with the respective amount of ground VIPOXY vitrimer-co-network until a homogeneous compound of the two powders is achieved. The mixture is subsequently pressed in a hot press at 150 °C for 10 min with a pressure of 78.5 MPa to give circular test specimens with a diameter of 8 mm.

6.3.3 Instrumentation

6.3.3.1 Nuclear magnetic resonance (NMR)

Nuclear magnetic resonance spectra (^{1}H NMR, ^{31}P, and ^{13}C NMR) were recorded on a Bruker Avance I (500 MHz) spectrometer (Bruker Corporation, Billerica, United States) with $CDCl_3$ or DMSO-d_6 as solvent and internal standard. Sample concentrations were between 10 – 40 mg mL^{-1}, and measurements were recorded at 298 K. Data processing was carried out with MestReNova (14.1.0, Mestrelab Research S.L., Santiago de Compostela, Spain).

6.3.3.2 Mass spectrometry (MS)

Electron spray ionization (ESI) was measured by an Angilent 6224 ESI-TOF device coupled with an Agilent HPLC 1200 Series (Agilent Technologies, Santa Clara, United States) and direct injection (110 – 3200 *m*/*z*). Data processing was carried out with MestReNova (14.1.0, Mestrelab Research S.L, Santiago de Compostela, Spain).

6.3.3.3 Atennuated total reflection Fourier transform infrared (ATR-FT-IR)

Attenuated Total Reflection Fourier Transformation Infrared (ATR FT IR) spectra were measured in the range of 4000 – 400 cm^{-1} with a resolution of 4 cm^{-1} and 64 scans using a Bruker FT-IR Vertex 70 spectrometer (Bruker Optics GmbH & Co. KG, Ettlingen, Germany). Measurements and data processing were carried out with Opus (8.7, Bruker Optics GmbH & Co. KG, Ettlingen, Germany).

6.3.3.4 Thermogravimetric Analysis (TGA)

Thermogravimetric analysis (TGA) was carried out on a TG 209 F1 Libra (NETZSCH-Gerätebau GmbH, Selb, Germany) to determine the mass of a sample over time as the temperature changes. A temperature range of 25 – 600 °C or 25 – 800 °C with a heating rate of 10 K min^{-1} under ambient atmosphere (oxygen) was used in a flow rate of 20 mL min^{-1}. An amount of 5 – 10 mg of polymer was weighed into an aluminum crucible. Data processing was performed with Proteus Analysis (8.0.3, NETZSCH-Gerätebau GmbH, Selb, Germany).

6.3.3.5 Differential Scanning calorimetry (DSC)

Thermo-physical properties of the vitrimer films were determined on a differential scanning calorimeter DSC 204 F1 Phoenix (NETZSCH-Gerätebau GmbH, Selb, Germany). An amount of 5 – 10 mg polymer was weighed into an aluminum crucible. The heating and cooling rate was set to 10 K min^{-1}. The measurements were carried out in a nitrogen atmosphere with a flow rate of 20 ml min^{-1} in the temperature range between −50 – 150 °C and the thermal properties were analyzed using the DSC data of the second heating curve by determining the midpoint of the DSC-curve step as the T_g. Data processing was performed with Proteus Analysis (8.0.3, NETZSCH-Gerätebau GmbH, Selb, Germany).

6.3.3.6 Dynamic mechanical analysis (DMA)

Rheological measurements by dynamic-mechanical analysis (DMA) were carried out using an MCR 502 rheometer (Anton Paar Graz, Austria) using a plate-plate geometry with a diameter of 8 mm. A CTD-180 heat chamber with flooded nitrogen atmosphere was used. The temperature was controlled by a Peltier system. The gap between the upper and the lower plate was usually set to 1 mm, a PP08 measurement tool with a diameter of 8 mm was used. Prior to all rheological measurements, amplitude sweeps in oscillatory mode were performed at 110 °C between 0.001% and 10% shear strain γ at a constant angular frequency of 6.28 rad s^{-1}. This should ensure that the chosen strain amplitude γ_0 was within the linear viscoelastic regime, so that the storage modulus G' and the loss modulus G'' were independent of strain. Temperature-sweep measurements were carried out in oscillatory mode with a constant angular frequency of 6.28 rad s^{-1} at a constant shear strain of 0.1% in the temperature range of 0 – 150 °C. Stress-relaxation measurements were carried out with a shear strain amplitude of 1%, and the relaxation modulus was recorded as a function of time in the temperature range of 110 – 150 °C. Data processing was performed with RheoCompass (1.34, Anton Paar GmbH, Graz, Austria). Specimens for the DMA were pushed out with an 8 mm punch.

6.3.3.7 Tensile testing

Stress strain curves were recorded at room temperature (23 °C) on a universal testing machine zwickiLine Z 5.0 TH (Zwick Roell GmbH & Co. KG, Ulm, Germany) using a 5 kN load cell. The measurements were carried out in accordance with the test standard DIN EN ISO 527 – 1. The initial force was 0.1 MPa, and the clamping length was 13.24 mm. The elastic modulus was determined at a speed of 1 mm min^{-1} between 0.05% and 0.25% elongation and the rest of the test was carried out at 10 mm min^{-1}. Data was processed using TestXpert II (V3.71, Zwick Roell GmbH & Co. KG, Ulm, Germany). The test specimens for the tensile test were punched out with a cutting press type ZCP020 (Zwick Roell GmbH & Co. KG, Ulm, Germany) with the attachment for test specimens of type 5B (according to DIN EN ISO 527 – 2).

6.3.3.8 Scanning electron microscopy (SEM)

Scanning electron microscopy (SEM) images were recorded on a LEO Gemini 1550 (Carl Zeiss, Oberkochen, Germany) using a carbon-coated copper transmission electron microscopy (TEM) grid. Secondary electrons were detected with an Everhart-Thornley detector, operating with 1 – 5 kV and 50 – 100 pA.

7 Discussion and Outlook

This work presents perspectives on the design, synthesis, and characterization of high-performance thermoreversible network materials. Various associative and dissociative exchange mechanisms were examined and utilized to deepen the understanding of these materials and to develop complex network structures such as interpenetrating covalent adaptable polymer networks and vitrimer-epoxy co-networks.

In the first part of this work, the concept of recyclability by design, the potential of thermoreversible covalent adaptable polymer networks, and an outlook on the sustainable production of vitrimers are provided. Mechanistic details are examined, and the various network rearrangement reactions are discussed in the context of creating network materials with unique mechanical and recycling properties. Finally, composites are explored, with a special emphasis on hierarchical artificial self-assembled nanocomposites. The field of materials science is expanding, and the focus on closed-loop recycling adds an important feature to these materials, promoting sustainability and end-of-life assessment.

The first publication, titled "Reprocessable Vanillin-Based Schiff Base Vitrimers: Tuning Mechanical and Thermomechanical Properties by Network Design," combines sustainable building blocks from vanillin with excellent mechanical properties and offers insights into the structure-property relationship of Schiff base vitrimers. Producing uniform vitrimer films required adjusted heat compression and storage procedures, which ensured the formation of defect-free polymer films that could be reprocessed, matching the mechanical properties of the original materials. The study focused on the effects of backbone length, composition, and the stoichiometry of aldehyde and aldehyde groups. It identified the availability of free amine groups and the mobility of these chain ends as key factors for predicting internal catalytic effects. Additionally, besides mechanical recycling, small-molecule-mediated dissociative hydrolysis enables chemical recycling, providing another end-of-life option for thermoreversible networks. Tailor-made recyclable materials can be created by leveraging beneficial structure-property relationships and carefully tuning the underlying network rearrangement reaction conditions.

In the second publication, titled "Bio-based vinylogous urethane vitrimers from waste-wood lignosulfonate and enzymatic lignin: explorations in stress relaxation behavior and mechanical strength," the focus shifts more toward the building blocks. Lignin is used in different grades. After functionalization, acetoacetylated lignin molecules are reacted with bio-based amines to produce lignin vitrimers. By adjusting the reaction parameters, toxic solvents are replaced with environmentally friendly solvent mixtures, and reprocessability opens the door to end-of-life solutions for this class of bio-based vitrimers. New reprocessing methods, such as injection molding for lignin vitrimers, demonstrate and expand the industrial applicability of this material class, offering potential alternatives to conventional polymers.

It also highlights the importance of analyzing how the material's microstructure influences macroscopic properties like mechanical strength or stress-relaxation. The use of stretched exponential fit functions is discussed and deemed crucial when materials exhibit complex viscosity behavior. Utilizing waste-wood components like lignosulfonate showcases potential for waste valorization in high-performance materials.

In the third publication, titled "Transparent Dioxaborolane Acrylate Vitrimers Through One-Pot Reaction with Superior Strength as Matrix Material for Carbon Fibers and TiO_2 Nanoplates," dioxaborolane metathesis chemistry is used to create multi-reprocessable materials suitable for bulk composite production. This work moves the recyclability by design concept from typical laboratory issues to real-world applications, addressing optical properties, processability over more than five recycling cycles, and employing a low-cost, scalable one-pot curing reaction with commercially available acrylate building blocks. The study examines stress-relaxation in relation to the thermal history of the materials, which significantly influences the evaluation of stretched exponential decays and can be controlled through thermal annealing. The fast-curing reaction, analyzed in detail *via* viscosity measurements, opens potential for impregnating carbon fibers. Additionally, a new method is developed by solid-solid mixing ground vitrimer powder with well-defined titanium dioxide nanoplatelets to form nanocomposites with a high inorganic filler content. These findings facilitate the straightforward integration of vitrimer chemistry into acrylate systems and offer insights into design-for-recyclability for multi-reprocessable materials.

The results of the publications were further examined through unpublished data. Firstly, the formation of interpenetrating covalent adaptable networks is discussed. These networks consist of two orthogonal vitrimers and are formed *via* a solvent-mediated, simultaneous network formation reaction. The use of a solvent controls the network formation kinetics, resulting in a well-defined formation of two percolating vitrimer networks. Potential side reactions, such as the presence of different Michael acceptors and donors, are also discussed, along with an in-depth characterization of how the network structure influences mechanical properties and stress-relaxation.

The last focus of this work was on producing nacre-inspired thermoreversible nanocomposites. These hierarchical nanocomposites enable reinforcement of coatings or stimuli-responsive self-healing materials. Dissociative Diels-Alder ligands were synthesized through a modified organic synthesis route. By forming an amide, a diene building block was introduced into a phosphonic acid. The modified nanoparticle clusters were examined; however, the thermoreversible behavior has not yet been fully characterized.

To expand knowledge of a potential thermoreversible matrix with mechanical properties similar to those of commonly used thermosetting bisphenol A-based matrices, a co-network of acetoacetylated bisphenol A, bisphenol A diglycidyl ether, and trifunctional amines, vitrimer-β-hydroxy ether co-networks, was developed. These networks were analyzed in detail and showed a reinforcing effect when 40 mol% of non-dynamic epoxy-based bonds were present. It was demonstrated that these networks are still reprocessable and can be used in a solid-solid mixing process to create hierarchical nanocomposites with an inorganic filler content of up to 70 wt.%.

Calculating the number of free amine groups is essential to maintaining defined material properties while increasing epoxy content, thereby producing materials with high glass transition temperatures, stress-relaxation, and tensile strength.

Overall, it becomes clear that selecting building blocks for thermoreversible networks starts with assessing chemical reactivity, potential thermoreversible reactions, and whether the dynamic network functionality is integrated into one of the building blocks or introduced after the network forms. Additionally, stress-relaxation behavior is more complex and requires more investigations than simple step-strain rheology experiments, which cannot be described by a Maxwell model. The thermal history of materials and their intrinsic properties, such as glass transition temperature, can influence results and lead to misinterpretations of stretch factors and their attribution to network properties, which are more likely due to thermal effects of residual stress. It is clear that stress-relaxation experiments should be performed in exactly the same way for different network compositions when comparing materials, and activation energies do not define the timeframe in which a material can be reprocessed on a full molecular scale. Also, systematic experiments in the non-linear viscoelastic region will be important in future studies. Using the unique thermoreversible (or simply reversible) properties of covalent adaptable networks allows for the formation of complex structures like interpenetrating polymer networks and co-networks. Furthermore, these properties can be utilized to create highly ordered hierarchical nanocomposites.

The discussed synthetic protocols, network analytics, and characterization methods highlight the potential of applying bio-based thermoreversible building blocks and networks in future materials. Recyclability by design can be achieved through a bottom-up approach, including an end-of-life assessment for new polymer materials. The beneficial features of polymers will continue to be useful in the future, but recycling should always be considered in the initial design to reduce energy use, environmental pollution, and persistent microplastics in our ecosystems.

8 References

[1] R. Porta, "Anthropocene, the plastic age and future perspectives", *FEBS Open Bio*, **2021**, *11*, 948-953.

[2] G. Odian, "*Principles of Polymerization*", 4th ed., Wiley-Interscience, Hoboken, **2004**.

[3] J. A. Brydson, "*Plastics Materials*", 7th ed., Butterworth Heinemann, Woburn, **1999**.

[4] J. E. Alegado, J. M. Aliño, S. Cheuk Fai Chow, Ma. B. L.Diola, P. Jagath D. Gamaralalage, L. Gurrero, V. Hernandez, Y. Ishimura, M. Kato, E. Kim, C. Liu, M. Moinuddin, D. Moon, M. Okuno, S. Hoiberg Olsen, G. Pelogio, P. Pey, N. B. Pham, T. Samson, S. Shekhar Swain, M. A. Tanchuling., "*Plastic Atlas Asia Edition*", 1st ed., Heinrich Boll Stiftung Hong Kong Office, **2021**.

[5] R. Teigland, M. Wiberg, J. Erik Borgen, M. de Freitas, J. Landberg, M. Rouhi, K. Teigland, W. Wiest, "*Circular Material Flows, the twin transition of manufacturing, and the future of labour*", in "*The Future of Labour - How AI, Technological Disruption and Practice Will Change the Way We Work*", Routledge, Oxon, **2025**, pp. 234-251.

[6] C. S. Brazel, S. L. Rosen, "*Fundamental Principles of Polymeric Materials*", 3rd ed., Wiley, **2012**.

[7] Jeannette M. Garcia, M. L. Robertson, "The future of plastics recycling", *Science* **2017**, *358*, 870-872.

[8] T. D. Nielsen, J. Hasselbalch, K. Holmberg, J. Stripple, "Politics and the plastic crisis: A review throughout the plastic life cycle", *WIREs Energy and Environment* **2019**, *9*, 2020;9:e360.

[9] D. Kwon, "Three ways to solve the plastics pollution crisis", *Nature* **2023**, *616*, 234-237.

[10] Y. Chen, A. K. Awasthi, F. Wei, Q. Tan, J. Li, "Single-use plastics: Production, usage, disposal, and adverse impacts", *Science of the Total Environment* **2021**, *752*, 141772.

[11] E. Jankowska, M. R. Gorman, C. J. Frischmann, "Transforming the Plastic Production System Presents Opportunities to Tackle the Climate Crisis" *Sustainability* **2022**, *14*, 6539.

[12] B. Johnson, "The closed carbon cycle in a managed, stable Anthropocene", *The Anthropocene Review* **2024**, *11*, 3-25.

[13] M. A. Hillmyer, "The promise of plastics from plants", *Science* **2017**, *358*, 868-870.

[14] C. G. Schirmeister, R. Mülhaupt, "Closing the Carbon Loop in the Circular Plastics Economy", *Macromolecular Rapid Communications* **2022**, *43*, e2200247.

[15] J. P. Pascault, R. J. J. Williams, "*Overview of thermosets: Present and future in Thermosets*", in "*Thermosets – Structure, Properties, and Applications*", 2nd ed., Elsevier, **2018**, pp. 3-34.

[16] N. J. Van Zee, R. Nicolaÿ, "*Vitrimer Chemistry and Applications*", in "*Macromolecular Engineering: From Precise Synthesis to Macroscopic Materials and Applications*", 2nd ed. ,WILEY-VCH, **2022**, pp. 1-38.

[17] S. Maes, N. Badi, J. M. Winne, F. E. Du Prez, “Taking dynamic covalent chemistry out of the lab and into reprocessable industrial thermosets”, *Nature Reviews Chemistry* **2025**, *9*, 144-158.

[18] M. A. Lucherelli, A. Duval, L. Avérous, “Bio-based vitrimers: Towards sustainable and adaptable performing polymer materials”, *Progress in Polymer Science* **2022**, *127*, 101515.

[19] T. Vidil, A. Llevot, “Fully Bio-based Vitrimers: Future Direction toward Sustainable Cross-Linked Polymers”, *Macromolecular Chemistry and Physics* **2022**, 2100494.

[20] R. Hatti-Kaul, L. J. Nilsson, B. Zhang, N. Rehnberg, S. Lundmark, “Designing Bio-based Recyclable Polymers for Plastics“, *Trends in Biotechnology* **2020**, *38*, 50-67.

[21] S. Z. Khairul Anuar, A. H. Nordin, S. M. Nur Husna, A. H. Yusoff, S. H. Paiman, S. F. Md Noor, M. L. Nordin, S. N. Ali, Y. M. Nazir Syah Ismail, “Recent advances in recycling and upcycling of hazardous plastic waste: A review”, *Journal of Environmental Management* **2025**, *380*, 124867.

[22] N. J. Van Zee, R. Nicolaÿ, “Vitrimers: Permanently cross-linked polymers with dynamic network topology”, *Progress in Polymer Science* **2020**, *104*, 101233.

[23] P. R. Christensen, A. M. Scheuermann, K. E. Loeffler, B. A. Helms, “Closed-loop recycling of plastics enabled by dynamic covalent diketoenamine bonds”, *Nature Chemistry* **2019**, *11*, 442-448.

[24] M. D. Lechner, K. Gehrke, E. Nordmeier, Lechner, Gehrke, Nordmeier, “*Makromolekulare Chemie*“, 6th ed., Springer, Berlin, Heidelberg, **2024**.

[25] R. J. Wojtecki, M. A. Meador, S. J. Rowan, “Using the dynamic bond to access macroscopically responsive structurally dynamic polymers”, *Nature Materials* **2011**, *10*, 14-27.

[26] M. Burnworth, L. Tang, J. R. Kumpfer, A. J. Duncan, F. L. Beyer, G. L. Fiore, S. J. Rowan, C. Weder, “Optically healable supramolecular polymers”, *Nature* **2011**, *472*, 334-337.

[27] A. J. Inglis, L. Nebhani, O. Altintas, F. G. Schmidt, C. Barner-Kowollik, “Rapid Bonding/Debonding on Demand: Reversibly Cross-Linked Functional Polymers via Diels-Alder Chemistry”, *Macromolecules* **2010**, *43*, 5515-5520.

[28] M. E. Lamm, L. Song, Z. Wang, M. A. Rahman, B. Lamm, L. Fu, C. Tang, “Tuning Mechanical Properties of Biobased Polymers by Supramolecular Chain Entanglement“, *Macromolecules* **2019**, 52, 8967-8975.

[29] D. Montarnal, M. Capelot, F. Tournilhac, L. Leibler, “Silica-Like Malleable Materials from Permanent Organic Networks”, *Science* **2011**, *334*, 965-968.

[30] E. Rahmstorf, V. Abetz, “Supramolecular Networks from Block Copolymers Based on Styrene and Isoprene Using Hydrogen Bonding Motifs — Part 1: Synthesis and Characterization”, *Materials* **2018**, *11*, 1608.

[31] D. M. L. Wayne C. Yount, and Stephen L. Craig, “Small-molecule dynamics and mechanisms underlying the macroscopic mechanical properties of coordinatively cross-linked polymer networks “, *Journal of the American Chemical Society* **2005**, *127*, 14488-14496.

[32] S. Burattini, B. W. Greenland, D. H. Merino, W. Weng, J. Seppala, H. M. Colquhoun, W. Hayes, M. E. Mackay, I. W. Hamley, S. J. Rowan, "A healable supramolecular polymer blend based on aromatic pi-pi stacking and hydrogen-bonding interactions", *Journal of the American Chemical Society* **2010**, *132*, 12051-12058.

[33] L. Voorhaar, R. Hoogenboom, "Supramolecular polymer networks: hydrogels and bulk materials", *Chemical Society Reviews* **2016**, *45*, 4013-4031.

[34] F. Herbst, D. Dohler, P. Michael, W. H. Binder, "Self-healing polymers via supramolecular forces", *Macromolecular Rapid Communications* **2013**, *34*, 203-220.

[35] B. Marco-Dufort, R. Iten, M. W. Tibbitt, "Linking Molecular Behavior to Macroscopic Properties in Ideal Dynamic Covalent Networks", *Journal of the American Chemical Society* **2020**, *142*, 15371-15385.

[36] P. T. Corbett, J. Leclaire, L. Vial, K. R. West, J.-L. Wietor, J. K. M. Sanders, S. Otto, "Dynamic combinatorial chemistry ", *Chemical Reviews* **2006**, *106*, 3652-3711.

[37] Y. Jin, C. Yu, R. J. Denman, W. Zhang, "Recent advances in dynamic covalent chemistry", *Chemical Society Reviews* **2013**, *42*, 6634-6654.

[38] W. Alabiso, S. Schlögl, "The Impact of Vitrimers on the Industry of the Future: Chemistry, Properties and Sustainable Forward-Looking Applications", *Polymers* **2020**, *12*, 1660.

[39] Williams G. Skene, J.-M. P. Lehn, "Dynamers: Polyacylhydrazone reversible covalent polymers, component exchange, and constitutional diversity", *Proceedings of the National Academy of Sciences* **2004**, *101*, 8270-8275.

[40] N. Roy, B. Bruchmann, J.-M. Lehn, "DYNAMERS: dynamic polymers as self-healing materials", *Chemical Society Reviews* **2015**, *44*, 3786-3807.

[41] C. J. Kloxin, T. F. Scott, B. J. Adzima, C. N. Bowman, "Covalent Adaptable Networks (CANs): A Unique Paradigm in Cross-Linked Polymers", *Macromolecules* **2010**, *43*, 2643-2653.

[42] W. Denissen, J. M. Winne, F. E. Du Prez, "Vitrimers: permanent organic networks with glass-like fluidity", *Chemical Science* **2016**, *7*, 30-38.

[43] D. Berne, S. Lavieville, E. Leclerc, S. Caillol, V. Ladmiral, C. Bakkali-Hassani, "How to Characterize Covalent Adaptable Networks: A User Guide", *ACS Polymers Au* **2025**, *5*, 214-240.

[44] C. N. Bowman, C. J. Kloxin, "Covalent Adaptable Networks: Reversible Bond Structures Incorporated in Polymer Networks", *Angewandte Chemie International Edition* **2012**, *51*, 4272-4274.

[45] L. P. Engle, K. B. Wagener, "A Review of Thermally Controlled Covalent Bond Formation in Polymer Chemistry", *Journal of Macromolecular Science, Part C: Polymer Reviews* **1993**, *33*, 239-257.

[46] American Chemical Society National Historic Chemical Landmarks. U.S. Synthetic Rubber Program.http://www.acs.org/content/acs/en/education/whatischemistry/landmarks/syntheticrubber.html (accessed 10 5, **2025**).

[47] M. S. Green, A. V. Tobolsky, "A New Approach to the Theory of Relaxing Polymeric Media", *The Journal of Chemical Physics* **1946**, *14*, 80-92.

[48] M. J. Webber, M. W. Tibbitt, "Dynamic and reconfigurable materials from reversible network interactions", *Nature Reviews Materials* **2022**, *7*, 541-556.

[49] F. Van Lijsebetten, T. Debsharma, J. M. Winne, F. E. Du Prez, "A Highly Dynamic Covalent Polymer Network without Creep: Mission Impossible?", *Angewandte Chemie International Edition* **2022**, *61*, e202210405.

[50] J. M. Winne, L. Leibler, F. E. Du Prez, "Dynamic covalent chemistry in polymer networks: a mechanistic perspective", *Polymer Chemistry* **2019**, *10*, 6091-6108.

[51] X. Chen, M. A. Dam, K. Ono, A. Mal, S. R. Nutt, H. Shen, K. Sheran, F. Wudl, "A Thermally Remendable Cross-Linked Polymeric Material", *Science* **2002**, *295*, 1698-1702.

[52] A. Gandini, "The furan/maleimide Diels–Alder reaction: A versatile click–unclick tool in macromolecular synthesis", *Progress in Polymer Science* **2013**, *38*, 1-29.

[53] S. Schäfer, G. Kickelbick, "Thermoreversible Reactions on Inorganic Nanoparticle Surfaces: Diels–Alder Reactions on Sterically Crowded Surfaces", *ACS Applied Nano Materials* **2018**, *1*, 2640-2652.

[54] D. N. Amato, G. A. Strange, J. P. Swanson, A. D. Chavez, S. E. Roy, K. L. Varney, C. A. Machado, D. V. Amato, P. J. Costanzo, "Synthesis and evaluation of thermally-responsive coatings based upon Diels–Alder chemistry and renewable materials", *Polymer Chemistry* **2014**, *5*, 69-76.

[55] B. Zhang, Z. A. Digby, J. A. Flum, P. Chakma, J. M. Saul, J. L. Sparks, D. Konkolewicz, "Dynamic Thiol–Michael Chemistry for Thermoresponsive Rehealable and Malleable Networks", *Macromolecules* **2016**, *49*, 6871-6878.

[56] P. Chakma, L. H. Rodrigues Possarle, Z. A. Digby, B. Zhang, J. L. Sparks, D. Konkolewicz, "Dual stimuli responsive self-healing and malleable materials based on dynamic thiol-Michael chemistry", *Polymer Chemistry* **2017**, *8*, 6534-6543.

[57] N. Kuhl, R. Geitner, J. Vitz, S. Bode, M. Schmitt, J. Popp, U. S. Schubert, M. D. Hager, "Increased stability in self-healing polymer networks based on reversible Michael addition reactions", *Journal of Applied Polymer Science* **2017**, *134*, 44805.

[58] H. Otsuka, "Reorganization of polymer structures based on dynamic covalent chemistry: polymer reactions by dynamic covalent exchanges of alkoxyamine units", *Polymer Journal* **2013**, *45*, 879-891.

[59] Q. An, I. D. Wessely, Y. Matt, Z. Hassan, S. Bräse, M. Tsotsalas, "Recycling and self-healing of dynamic covalent polymer networks with a precisely tuneable crosslinking degree", *Polymer Chemistry* **2019**, *10*, 672-678.

[60] H. Frisch, D. E. Marschner, A. S. Goldmann, C. Barner-Kowollik, "Wavelength-Gated Dynamic Covalent Chemistry", *Angewandte Chemie International Edition* **2018**, *57*, 2036-2045.

[61] J. P. Brutman, D. J. Fortman, G. X. De Hoe, W. R. Dichtel, M. A. Hillmyer, "Mechanistic Study of Stress Relaxation in Urethane-Containing Polymer Networks ", *The Journal of Physical Chemistry B* **2019**, *123*, 1432-1441.

[62] L. A. Connal, R. Vestberg, C. J. Hawker, G. G. Qiao, "Fabrication of Reversibly Crosslinkable, 3-Dimensionally Conformal Polymeric Microstructures", *Advanced Functional Materials* **2008**, *18*, 3315-3322.

[63] E. Pezron, A. Ricard, L. Leibler, "Rheology of Galactomannan-Borax Gels", *Journal of Polymer Science Part B: Polymer Physics* **1990**, *28*, 2445-2461.

[64] J. J. Cash, T. Kubo, A. P. Bapat, B. S. Sumerlin, "Room-Temperature Self-Healing Polymers Based on Dynamic-Covalent Boronic Esters", *Macromolecules* **2015**, *48*, 2098-2106.

[65] M. E. Smithmyer, C. C. Deng, S. E. Cassel, P. J. LeValley, B. S. Sumerlin, A. M. Kloxin, "Self-healing boronic acid-based hydrogels for 3D co-cultures", *ACS Macro Letters* **2018**, *7*, 1105-1110.

[66] W. Ge, S. Cao, F. Shen, Y. Wang, J. Ren, X. Wang, "Rapid self-healing, stretchable, moldable, antioxidant and antibacterial tannic acid-cellulose nanofibril composite hydrogels", *Carbohydrate Polymers* **2019**, *224*, 115147.

[67] M. E. Belowich, J. F. Stoddart, "Dynamic imine chemistry ", *Chemical Society Reviews* **2012**, *41*, 2003-2024.

[68] P. Taynton, K. Yu, R. K. Shoemaker, Y. Jin, H. J. Qi, W. Zhang, "Heat- or water-driven malleability in a highly recyclable covalent network polymer", *Advanced Materials* **2014**, *26*, 3938-3942.

[69] P. Chakma, Z. A. Digby, M. P. Shulman, L. R. Kuhn, C. N. Morley, J. L. Sparks, D. Konkolewicz, "Anilinium Salts in Polymer Networks for Materials with Mechanical Stability and Mild Thermally Induced Dynamic Properties", *ACS Macro Letters 2019*, *8*, 95-100.

[70] M. Capelot, D. Montarnal, F. Tournilhac, L. Leibler, "Metal-Catalyzed Transesterification for Healing and Assembling of Thermosets", *Journal of the American Chemical Society* **2012**, *134*, 7664-7667.

[71] Q. Shi, K. Yu, X. Kuang, X. Mu, C. K. Dunn, M. L. Dunn, T. Wang, H. Jerry Qi, "Recyclable 3D printing of vitrimer epoxy", *Materials Horizons* **2017**, *4*, 598-607.

[72] B. T. Worrell, M. K. McBride, G. B. Lyon, L. M. Cox, C. Wang, S. Mavila, C. H. Lim, H. M. Coley, C. B. Musgrave, Y. Ding, C. N. Bowman, "Bistable and photoswitchable states of matter ", *Nature Communications* **2018**, *9*, 2804.

[73] A. Erice, A. Ruiz de Luzuriaga, J. M. Matxain, F. Ruipérez, J. M. Asua, H.-J. Grande, A. Rekondo, "Reprocessable and recyclable cross-linked poly(urea-urethane)s based on dynamic amine/urea exchange", *Polymer* **2018**, *145*, 127-136.

[74] D. J. Fortman, J. P. Brutman, C. J. Cramer, M. A. Hillmyer, W. R. Dichtel, "Mechanically Activated, Catalyst-Free Polyhydroxyurethane Vitrimers", *Journal of the American Chemical Society* **2015**, *137*, 14019-14022.

[75] R. L. Snyder, D. J. Fortman, G. X. De Hoe, M. A. Hillmyer, W. R. Dichtel, "Reprocessable Acid-Degradable Polycarbonate Vitrimers", *Macromolecules* **2018**, *51*, 389-397.

[76] W. Denissen, I. De Baere, W. Van Paepegem, L. Leibler, J. Winne, F. E. Du Prez, "Vinylogous Urea Vitrimers and Their Application in Fiber Reinforced Composites", *Macromolecules* **2018**, *51*, 2054-2064.

[77] W. Denissen, G. Rivero, R. Nicolaÿ, L. Leibler, J. M. Winne, F. E. Du Prez, "Vinylogous Urethane Vitrimers", *Advanced Functional Materials* **2015**, *25*, 2451-2457.

[78] W. Denissen, M. Droesbeke, R. Nicolay, L. Leibler, J. M. Winne, F. E. Du Prez, "Chemical control of the viscoelastic properties of vinylogous urethane vitrimers", *Nature Communications* **2017**, *8*, 14857.

[79] P. Zheng, T. J. McCarthy, "A surprise from 1954: siloxane equilibration is a simple, robust, and obvious polymer self-healing mechanism", *Journal of the American Chemical Society* **2012**, *134*, 2024-2027.

[80] Y. Nishimura, J. Chung, H. Muradyan, Z. Guan, "Silyl Ether as a Robust and Thermally Stable Dynamic Covalent Motif for Malleable Polymer Design", *Journal of the American Chemical Society* **2017**, *139*, 14881-14884.

[81] Timothy F. Scott, Andrew D. Schneider, Wayne D. Cook, C. N. Bowman, "Photoinduced plasticity in cross-linked polymers", *Science* **2005**, *308*, 1615-1617.

[82] H. Y. Park, C. J. Kloxin, A. S. Abuelyaman, J. D. Oxman, C. N. Bowman, "Stress relaxation via addition-fragmentation chain transfer in high T(g), high conversion methacrylate-based systems", *Macromolecules* **2012**, *45*, 5640-5646.

[83] Y. Amamoto, J. Kamada, H. Otsuka, A. Takahara, K. Matyjaszewski, "Repeatable photoinduced self-healing of covalently cross-linked polymers through reshuffling of trithiocarbonate units", *Angewandte Chemie International Edition* **2011**, *50*, 1660-1663.

[84] N. Sowan, C. N. Bowman, L. M. Cox, P. K. Shah, H. B. Song, J. W. Stansbury, "Dynamic Covalent Chemistry at Interfaces: Development of Tougher, Healable Composites through Stress Relaxation at the Resin–Silica Nanoparticles Interface", *Advanced Materials Interfaces* **2018**, *5*, 1800511.

[85] M. Guerre, C. Taplan, J. M. Winne, F. E. Du Prez, "Vitrimers: directing chemical reactivity to control material properties", *Chemical Science* **2020**, *11*, 4855-4870.

[86] S. S. Rohewal, J. T. Damron, J. Seo, N. Kanbargi, S. Gupta, H. E. Humphrey, L. T. Kearney, J. Chang, L. Tetard, A. K. Naskar, "Hierarchically Structured Vitrimer Biocomposites for Sustainable Manufacturing", *Small* **2025**, e2500721.

[87] H. Fang, W. Ye, Y. Ding, H. H. Winter, "Rheology of the Critical Transition State of an Epoxy Vitrimer", *Macromolecules* **2020**, *53*, 4855-4862

[88] F. Meng, M. O. Saed, E. M. Terentjev, "Rheology of vitrimers", *Nature Communications* **2022**, *13*, 5753.

[89] R. G. Ricarte, S. Shanbhag, "Unentangled Vitrimer Melts: Interplay between Chain Relaxation and Cross-link Exchange Controls Linear Rheology", *Macromolecules* **2021**, *54*, 3304-3320.

[90] Y. Yang, S. Zhang, X. Zhang, L. Gao, Y. Wei, Y. Ji, "Detecting topology freezing transition temperature of vitrimers by AIE luminogens", *Nature Communications* **2019**, *10*, 3165.

[91] V. Zhang, B. Kang, J. V. Accardo, J. A. Kalow, "Structure-Reactivity-Property Relationships in Covalent Adaptable Networks", *Journal of the American Chemical Society* **2022**, *144*, 22358-22377.

[92] M. K. McBride, B. T. Worrell, T. Brown, L. M. Cox, N. Sowan, C. Wang, M. Podgorski, A. M. Martinez, C. N. Bowman, "Enabling Applications of Covalent Adaptable Networks", *Annual Review of Chemical and Biomolecular Engineering* **2019**, *10*, 175-198.

[93] L. Li, X. Chen, K. Jin, J. M. Torkelson, "Vitrimers Designed Both To Strongly Suppress Creep and To Recover Original Cross-Link Density after Reprocessing: Quantitative Theory and Experiments", *Macromolecules* **2018**, *51*, 5537-5546.

[94] R. G. Ricarte, S. Shanbhag, "A tutorial review of linear rheology for polymer chemists: basics and best practices for covalent adaptable networks", *Polymer Chemistry* **2024**, *15*, 815-846

[95] R. Kohlrausch, "Theorie des elektrischen Rückstandes in der Leidener Flasche", *Annalen der Physik* **1854**, *167*, 179-214.
[96] D. C. W. Graham Williams, "Non-symmetrical dielectric relaxation behaviour arising from a simple empirical decay function", *Transactions of the Faraday Society* **1970**, *66*, 80-85.
[97] M. L. Martins, X. Zhao, Z. Demchuk, J. Luo, G. P. Carden, G. Toleutay, A. P. Sokolov, "Viscoelasticity of Polymers with Dynamic Covalent Bonds: Concepts and Misconceptions", *Macromolecules* **2023**, *56*, 8688-8696.
[98] D. C. Johnston, "Stretched exponential relaxation arising from a continuous sum of exponential decays", *Physical Review B* **2006**, *74*, 179901.
[99] L. E. Porath, C. M. Evans, "Importance of Broad Temperature Windows and Multiple Rheological Approaches for Probing Viscoelasticity and Entropic Elasticity in Vitrimers", *Macromolecules* **2021**, *54*, 4782-4791.
[100] T. Yan, A. H. Balzer, K. M. Herbert, T. H. Epps III, L. T. J. Korley, "Circularity in polymers: addressing performance and sustainability challenges using dynamic covalent chemistries", *Chemical Science* **2023**, *14*, 5243-5265.
[101] A. Mariani, G. Malucelli, "Bio-based vitrimers: towards sustainability and circularity", *Chemical Communications* **2025**, *61*, 2173-2189.
[102] S. Sadashiv Rege, I. Dey, R. Sen Gupta, M. Ajnas N, R. Jose, A. Misra, K. Manna, K. Samanta, S. Bose, "Closed-loop circular economy in 'upcycled' acrylonitrile–butadiene–styrene vitrimer", *European Polymer Journal* **2024**, *220*, 113451.
[103] S. Kamarulzaman, Z. M. Png, E. Q. Lim, I. Z. S. Lim, Z. Li, S. S. Goh, "Covalent adaptable networks from renewable resources: Cross-linked polymers for a sustainable future", *Chem* **2023**, *9*, 2771-2816.
[104] C. Allen, G. Metternicht, T. Wiedmann, "Initial progress in implementing the Sustainable Development Goals (SDGs): a review of evidence from countries", *Sustainability Science* **2018**, *13*, 1453-1467.
[105] D. B. Tiz, F. A. Vicente, A. Kroflič, B. Likozar, "Lignin-Based Covalent Adaptable Network Polymers─When Bio-Based Thermosets Meet Recyclable by Design", *ACS Sustainable Chemistry & Engineering* **2023**, *11*, 13836-13867.
[106] X.-L. Zhao, P.-X. Tian, Y.-D. Li, J.-B. Zeng, "Bio-based covalent adaptable networks: towards better sustainability of thermosets", *Green Chemistry* **2022**, *24*, 4363-4387.
[107] P. Haida, S. Chirachanchai, V. Abetz, "Starch-Reinforced Vinylogous Urethane Vitrimer Composites: An Approach to Bio-based, Reprocessable, and Biodegradable Materials", *ACS Sustainable Chemistry & Engineering* **2023**, *11*, 8350-8361.
[108] K. Lu, X. Lan, R. Folkersma, V. S. D. Voet, K. Loos, "Borax Cross-Linked Acrylamide-Grafted Starch Self-Healing Hydrogels", *Biomacromolecules* **2024**, *25*, 8026-8037.
[109] T. Zhang, T. Yuan, X. Xiao, H. Peng, X. Fang, K. Wang, X. Liu, Y. Li, "Transparent and shape-memory cellulose paper reinforced by vitrimer polymer for efficient light management and sustainability", *Cellulose* **2022**, *29*, 8781-8795.
[110] C. Li, B. Ju, S. Zhang, "Construction of a new green vitrimer material: introducing dynamic covalent bond into carboxymethyl cellulose", *Cellulose* **2021**, *28*, 2879-2888.

[111] L. Sougrati, A. Duval, L. Avérous, "Introducing phenol-yne chemistry for the design of lignin-based vitrimers: towards sustainable and recyclable materials", *Journal of Materials Chemistry A* **2025**, *13*, 4921-4939.

[112] J. Liu, A. Pich, K. V. Bernaerts, "Preparation of lignin-based vinylogous urethane vitrimer materials and their potential use as on-demand removable adhesives", *Green Chemistry* **2024**, *26*, 1414-1429.

[113] M. Fei, T. Liu, B. Zhao, A. Otero, Y.-C. Chang, J. Zhang, "From Glassy Plastic to Ductile Elastomer: Vegetable Oil-Based UV-Curable Vitrimers and Their Potential Use in 3D Printing", *ACS Applied Polymer Materials* **2021**, *3*, 2470-2479.

[114] C. Di Mauro, S. Malburet, A. Genua, A. Graillot, A. Mija, "Sustainable Series of New Epoxidized Vegetable Oil-Based Thermosets with Chemical Recycling Properties", *Biomacromolecules* **2020**, *21*, 3923-3935.

[115] A. Adjaoud, L. Puchot, P. Verge, "High-T_g and Degradable Isosorbide-Based Polybenzoxazine Vitrimer", *ACS Sustainable Chemistry & Engineering* **2021**, *10*, 594-602.

[116] A. Rai, M. Pandey, S. Tripathi, A. S. Parmar, K. V. S. Ranganath, "Bio-based Polyimine Vitrimers: Promising Materials for Fluorescence Quenching, Anticounterfeiting, and Plastic Degradation", *ACS Omega* **2025**, *10*, 24756-24767.

[117] X. Zhang, L. Lin, H. Zhou, G. Zhou, X. Wang, "All-natural chitosan-based polyimine vitrimer with multiple advantages: A novel strategy to solve nondegradable plastic waste pollution", *Journal of Hazardous Materials* **2024**, *465*, 133030.

[118] Z. Feng, Y. Huang, J. Chen, H. Gao, J. Zhu, S. Mu, W. Li, W. Zhao, B. Xue, Y. Ni, "Green hybrid materials from biomass waste: Distiller's grains/epoxy vitrimer—Green synthesis, superior properties, and potential application in solar-thermal-electric generator", *Industrial Crops and Products* **2024**, *222*, 119732.

[119] C. J. Clarke, W. C. Tu, O. Levers, A. Brohl, J. P. Hallett, "Green and Sustainable Solvents in Chemical Processes", *Chemical Reviews* **2018**, *118*, 747-800.

[120] M. Kaltschmitt, M. Scherzinger, J. Gescher, "*Energie aus Biomasse*", 4th ed., Springer Vieweg, Wiesbaden, **2024**.

[121] A. Toktarova, L. Göransson, F. Johnsson, "Electrification of the energy-intensive basic materials industry – Implications for the European electricity system", *International Journal of Hydrogen Energy* **2025**, *107*, 279-295.

[122] A. U. Khan, M. Shahzad, A. Mushtaq, M. M. Naseer, "Green and sustainable synthesis of chiral alcohols: the role of *Daucus carota* as a biocatalyst in organic chemistry", *RSC Advances* **2025**, *15*, 11863-11880.

[123] A. A. Carmona-Martínez, A. Rueda, C. A. Jarauta-Córdoba, "Deep decarbonization of the energy intensive manufacturing industry through the bioconversion of its carbon emissions to fuels", *Fuel* **2024**, *371*, 131922.

[124] A. Enayati-Gerdroodbar, A. Khayati, A. Zolfagharian, M. Salami-Kalajahi, M. Bodaghi, "Vitrimers for sustainable electronics and control of e-waste", *Smart Materials & Methods* **2024**, *1*, 251-293.

[125] Iacopo Bianchi, Luciano Greco, Chiara Mignanelli, Michela Simoncini, A. Vita, "Environmental Sustainability of vitrimer-based composite materials", *Procedia CIRP* **2024**, *122*, 1059-1064.

[126] P. Zamani, O. Zabihi, M. Ahmadi, M. R. Zamani, M. J. Zohuriaan-Mehr, T. Kannangara, P. Joseph, M. Naebe, "Assessing sustainability and green chemistry in synthesis of a Vanillin-based vitrimer at scale: Enabling sustainable manufacturing of recyclable carbon fiber composites", *Composites Part A: Applied Science and Manufacturing* **2024**, *179*, 108016.

[127] J. J. Q. Mah, N. E. B. Surat'man, B. Li, S. Wang, Z. Li, "Recent Advances of Dynamic Covalent Chemistry Polymers Aligning with Principles of Green Chemistry", *ChemSusChem* **2025**, *18*, e202500480.

[128] J. Clayden, "*Organic chemistry*", 1st ed., Oxford University Press, Oxford, **2001**.

[129] N. M. Cerqueira, P. A. Fernandes, M. J. Ramos, "Computational Mechanistic Studies Addressed to the Transimination Reaction Present in All Pyridoxal 5′-Phosphate-Requiring Enzymes", *Journal of Chemical Theory and Computation* **2011**, *7*, 1356-1368.

[130] R. Hajj, A. Duval, S. Dhers, L. Avérous, "Network Design to Control Polyimine Vitrimer Properties: Physical Versus Chemical Approach", *Macromolecules* **2020**, *53*, 3796-3805.

[131] H. Geng, Y. Wang, Q. Yu, S. Gu, Y. Zhou, W. Xu, X. Zhang, D. Ye, "Vanillin-Based Polyschiff Vitrimers: Reprocessability and Chemical Recyclability", *ACS Sustainable Chemistry & Engineering* **2018**, *6*, 15463-15470.

[132] J. Liu, K. V. Bernaerts, "Preparation of lignin-based imine vitrimers and their potential application as repairable, self-cleaning, removable and degradable coatings", *Journal of Materials Chemistry A* **2024**, *12*, 2959-2973.

[133] P. Chakma, D. Konkolewicz, "Dynamic Covalent Bonds in Polymeric Materials", *Angewandte Chemie International Edition* **2019**, *58*, 9682-9695.

[134] M. Ciaccia, S. Di Stefano, "Mechanisms of imine exchange reactions in organic solvents ", *Organic & Biomolecular Chemistry* **2015**, *13*, 646-654.

[135] F. Cuminet, S. Caillol, É. Dantras, É. Leclerc, V. Ladmiral, "Exploring How Vitrimer-like Properties Can Be Achieved from Dissociative Exchange in Anilinium Salts", *Macromolecules* **2021**, *54*, 3927-3961.

[136] A. Liguori, M. Hakkarainen, "A. Liguori, M. Hakkarainen, Macromol Rapid Commun 2022, 43, e2100816.", *Macromolecular Rapid Communications* **2022**, *43*, e2100816.

[137] M. Ciaccia, R. Cacciapaglia, P. Mencarelli, L. Mandolini, S. Di Stefano, "Fast transimination in organic solvents in the absence of proton and metal catalysts. A key to imine metathesis catalyzed by primary amines under mild conditions", *Chemical Science* **2013**, *4*, 2253.

[138] R. F. Abdulla, T. L. Emmick, H. M. Taylor, "A New Synthetic Approach to 4(1H)-Pyridone Derivatives. I. 1-Alkyl-3,5-diaryl-4(1H)-pyridones", *Synthetic Communications* **1977**, *7*, 305-312.

[139] A. Sanchez-Sanchez, D. A. Fulton, J. A. Pomposo, "pH-responsive single-chain polymer nanoparticles utilising dynamic covalent enamine bonds", *Chemical Communications* **2014**, *50*, 1871-1874.

[140] J. Witzeman, W. D. Nottingham, "Transacetoacetylation with tert-butyl acetoacetate: synthetic applications", *Journal of Organic Chemistry* **1991**, *56*, 1713-1718.

[141] Robert J. Clemens, J. A. Hyatt, "Acetoacetylation with 2,2,6-trimethyl-4H-1,3-dioxin-4-one: a convenient alternative to diketene", *Journal of Organic Chemistry* **1985**, *50*, 2433-2435.

[142] P. Haida, G. Signorato, V. Abetz, "Blended vinylogous urethane/urea vitrimers derived from aromatic alcohols", *Polymer Chemistry* **2022**, *13*, 946-958.
[143] M. Guerre, C. Taplan, R. Nicolay, J. M. Winne, F. E. Du Prez, "Fluorinated Vitrimer Elastomers with a Dual Temperature Response ", *Journal of Applied Polymer Science* **2018**, *140*, 13272-13284.
[144] Y. Spiesschaert, C. Taplan, L. Stricker, M. Guerre, J. M. Winne, F. E. Du Prez, Influence of the polymer matrix on the viscoelastic behaviour of vitrimers", *Polymer Chemistry* **2020**, *11*, 5377-5385.
[145] P. Haida, V. Abetz, "Acid-Mediated Autocatalysis in Vinylogous Urethane Vitrimers", *Macromolecular Rapid Communications* 2020, *41*, e2000273.
[146] Y. Spiesschaert, M. Guerre, L. Imbernon, J. M. Winne, F. Du Prez, "Filler reinforced polydimethylsiloxane-based vitrimers", *Polymer* **2019**, *172*, 239-246.
[147] B. Marco-Dufort, M. W. Tibbitt, "Design of moldable hydrogels for biomedical applications using dynamic covalent boronic esters", *Materials Today Chemistry* **2019**, *12*, 16-33.
[148] N. Fujita, S. Shinkai, T. D. James, "Boronic Acids in Molecular Self-Assembly", *Chemistry - An Asian Journal* **2008**, *3*, 1076-1091.
[149] R. Bernardini, A. Oliva, A. Paganelli, E. Menta, M. Grugni, S. D. Munari, L. Goldoni, "Stability of Boronic Esters to Hydrolysis: A Comparative Study ", *Chemistry Letters* **2009**, *38*, 750-751.
[150] W. L. Brooks, B. S. Sumerlin, "Synthesis and Applications of Boronic Acid-Containing Polymers: From Materials to Medicine", *Chemical Reviews* **2016**, *116*, 1375-1397.
[151] S. Cho, S. Y. Hwang, D. X. Oh, J. Park, "Recent progress in self-healing polymers and hydrogels based on reversible dynamic B–O bonds: boronic/boronate esters, borax, and benzoxaborole", *Journal of Materials Chemistry A* **2021**, *9*, 14630-14655.
[152] Y. Dong, W. Wang, O. Veiseh, E. A. Appel, K. Xue, M. J. Webber, B. C. Tang, X. W. Yang, G. C. Weir, R. Langer, D. G. Anderson, "Injectable and Glucose-Responsive Hydrogels Based on Boronic Acid-Glucose Complexation.", *Langmuir* **2016**, *32*, 8743-8747.
[153] A. Pettignano, S. Grijalvo, M. Haring, R. Eritja, N. Tanchoux, F. Quignard, D. Diaz Diaz, "Boronic acid-modified alginate enables direct formation of injectable, self-healing and multistimuli-responsive hydrogels", *Chemical Communications* **2017**, *53*, 3350-3353.
[154] J. J. Cash, T. Kubo, D. J. Dobbins, B. S. Sumerlin, "Maximizing the symbiosis of static and dynamic bonds in self-healing boronic ester networks", *Polymer Chemistry* **2018**, *9*, 2011-2020.
[155] S. H. Hong, S. Kim, J. P. Park, M. Shin, K. Kim, J. H. Ryu, H. Lee, "Dynamic Bonds between Boronic Acid and Alginate: Hydrogels with Stretchable, Self-Healing, Stimuli-Responsive, Remoldable, and Adhesive Properties", *Biomacromolecules* **2018**, *19*, 2053-2061.
[156] D. Roy, J. N. Cambre, B. S. Sumerlin, "Triply-responsive boronic acidblock copolymers: solution self-assembly induced by changes in temperature, pH, or sugar concentration" *Chemical Communications* **2009**, 2106-2108.
[157] X. Zhang, Y. Zhao, S. Wang, X. Jing, "Cross-linked polymers based on B–O bonds: synthesis, structure and properties", *Materials Chemistry Frontiers* **2021**, *5*, 5534-5548.

[158] A. P. Bapat, B. S. Sumerlin, A. Sutti, “Bulk network polymers with dynamic B–O bonds: healable and reprocessable materials“, *Materials Horizons* 2020, 7, 694-714.

[159] C. C. Deng, W. L. A. Brooks, K. A. Abboud, B. S. Sumerlin, “Boronic Acid-Based Hydrogels Undergo Self-Healing at Neutral and Acidic pH“, ACS Macro Letters, **2015**, *4*, 220-224.

[160] M. Röttger, T. Domenech, R. van der Weegen, A. Breuillac, Renaud Nicolaÿ, Ludwik Leibler, “High-performance vitrimers from commodity thermoplastics through dioxaborolane metathesis“, *Science* **2017**, *356*, 62-65.

[161] J. D. Currey, “Mechanical properties of mother of pearl in tension”, *Proceedings of the Royal Society B* **1977**, *196*, 443-463.

[162] A.P. Jackson, J. F. V. Vincent, R. M. Turner, “The mechanical design of nacre”, *Proceedings of the Royal Society B* **1988**, *234*, 415-440.

[163] W. J. Landis, “The strength of a calcified tissue depends in part on the molecular structure and organization of its constituent mineral crystals in their organic matrix “, *Bone* **1995**, *16*, 533-544.

[164] A. V. Steve Weiner, Elia Beniash, Talmon Arad, Jerry W. Dillon, Boris Sabsay, Farida Siddiqui, “Peritubular Dentin Formation: Crystal Organization and the Macromolecular Constituents in Human Teeth”, *Journal of Structural Biology* **1999**, *126*, 27-41.

[165] R. C. Pettersen, “The chemistry of solid wood”, *Advances in Chemistry* **1984**, *207*, 57-126.

[166] X. S. S. Kamat, R. Ballarini, A. H. Heuer, ”Structural basis for the fracture toughness of the shell of the conch Strombus gigas“, *Nature* **2000**, *405*, 1036-1040.

[167] P. Fratzl, R. Weinkamer, “Nature’s hierarchical materials”, *Progress in Materials Science* **2007**, *52*, 1263-1334.

[168] B. Ji, H. Gao, “Local buckling analysis of biological nanocomposites based on a beam-spring model”, *Annual Review of Materials Research* **2010**, *40*, 77-100.

[169] H. Gao, “Application of Fracture Mechanics Concepts to Hierarchical Biomechanics of Bone and Bone-like Materials”, *International Journal of Fracture* **2006**, *138*, 101-137.

[170] F. J. Martin-Martinez, K. Jin, D. Lopez Barreiro, M. J. Buehler, “The Rise of Hierarchical Nanostructured Materials from Renewable Sources: Learning from Nature”, *ACS Nano* **2018**, *12*, 7425-7433.

[171] Z. Liu, Z. Zhang, R. O. Ritchie, ”On the Materials Science of Nature's Arms Race”, *Advanced Materials* **2018**, 30, e1705220.

[172] H. Gao, B. Ji, I. L. Jäger, “Materials become insensitive to flaws at nanoscale: Lessons from nature”; *Proceedings of the National Academy of Sciences* **2003**, *100*, 5597-5600.

[173] G. Signorato, L. R. Klauke, P. Haida, T. Vossmeyer, V. Abetz, “Superparamagnetic iron oxide nanoparticle – vitrimer nanocomposites: Reprocessable and multi-responsive materials”, *Polymer* **2025**, *318*, 127968.

[174] P. Schütz, S. Weerathaworn, C. Jürgensen, B. Hankiewicz, V. Abetz, ”Nanocomposites from Au-Doped Vinylogous Urethane Vitrimers Based on Different Block Copolymers and Their Recyclability in Combination with Plasmonic Heating“ *Macromolecular Rapid Communications* **2025**, 2401027.

[175] H. Zhao, Z. Yang, L. Guo, "Nacre-inspired composites with different macroscopic dimensions: strategies for improved mechanical performance and applications", *NPG Asia Materials* **2018**, *10*, 1-22.

[176] F. Lossada, D. Jiao, D. Hoenders, A. Walther, "Recyclable and Light-Adaptive Vitrimer-Based Nacre-Mimetic Nanocomposites", *ACS Nano* **2021**, *15*, 5043-5055.

[177] A. Dreyer, A. Feld, A. Kornowski, E. D. Yilmaz, H. Noei, A. Meyer, T. Krekeler, C. Jiao, A. Stierle, V. Abetz, H. Weller, G. A. Schneider, "Organically linked iron oxide nanoparticle supercrystals with exceptional isotropic mechanical properties", *Nature Materials* **2016**, *15*, 522-528.

[178] A. Plunkett, K. Temiz, C. Warren, V. Wisniewski, K. P. Furlan, J. Garay, D. Giutini, B. Domenech, G. A. Schneider, " Bridging nanocrystals to robust, multifunctional, bulk materials through nature-inspired, hierarchical design", ChemRxiv **2022**, 10.26434/chemrxiv-22022-mxtm26434.

[179] B. F. Winhard, P. Haida, A. Plunkett, J. Katz, B. Domènech, V. Abetz, K. P. Furlan, G. A. Schneider, "4D-printing of smart, nacre-inspired, organic-ceramic composites", *Additive Manufacturing* **2023**, *77*, 103776.

[180] L. H. Sperling, in "*Interpenetrating Polymer Networks*", Advances in Chemistry, American Chemical Society, Washington DC, **1994**.

[181] L. H. Sperling, R. Hu, in "*Polymer Blends Handbook*", Kluwer Academic Publishers, **2003**, 417-447.

[182] Y. You, W. L. Peng, P. Xie, M. Z. Rong, M. Q. Zhang, D. Liu, "Topological rearrangement-derived homogeneous polymer networks capable of reversibly interlocking: From phantom to reality and beyond", *Materials Today* **2020**, *33*, 45-55.

[183] Z. Wang, Y. Gu, M. Ma, Y. Liu, M. Chen, "Strengthening Polyethylene Thermoplastics through a Dynamic Covalent Networking Additive Based on Alkylboron Chemistry", *Macromolecules* **2021**, *54*, 1760-1766.

[184] Y. Lei, A. Zhang, Y. Lin, "Interpenetrating covalent adaptable networks with enhanced mechanical properties and facile reprocessability and recyclability", *Polymer Chemistry* **2021**, *12*, 4052-4062.

[185] M. R. Monteiro, C. L. Kugelmeier, R. S. Pinheiro, M. O. Batalha, A. da Silva César, "Glycerol from biodiesel production: Technological paths for sustainability", *Renewable Sustainable Energy Reviews* **2018**, *88*, 109-122.

[186] U. I. Nda-Umar, I. Ramli, Y. H. Taufiq-Yap, E. N. Muhamad, "Optimization and Characterization of Mesoporous Sulfonated Carbon Catalyst and Its Application in Modeling and Optimization of Acetin Production", *Catalysts* **2018**, *9*, 5221.

[187] P. Haida, Dissertation, "*Advances in Vitrimer Design and their Application as Matrix Materials in Composites*", Universität Hamburg, **2023**.

[188] D. Berne, S. Lemouzy, P. Guiffrey, S. Caillol, V. Ladmiral, E. Manoury, R. Poli, E. Leclerc, "Catalyst-Free Thia-Michael Addition to alpha-Trifluoromethylacrylates for 3D Network Synthesis", *Chemistry – A European Journal* **2023**, *29*, 202203712.

[189] J. W. Chan, C. E. Hoyle, A. B. Lowe, M. Bowman, "Nucleophile-Initiated Thiol-Michael Reactions: Effect of Organocatalyst, Thiol, and Ene", *Macromolecules* **2010**, *43*, 6381-6388.

[190] Y. Li, L. Yang, Y. Zeng, Y. Wu, Y. Wei, L. Tao, "Boronate Ester Hydrogels for Biomedical Applications: Challenges and Opportunities", *Chemistry of Materials* **2019**, *31*, 5576-5583.

[191] J. Zheng, X. Y. Oh, E. Ye, W. H. Chooi, Q. Zhu, X. J. Loh, Z. Li, "Self-healing polymer design from dynamic B–O bonds to their emerging applications ", *Materials Chemistry Frontiers* **2023**, *7*, 381-404.

[192] S. Ren, Z. Li, W. Zhou, J. Zhu, Y. Zhao, C. Liu, H. Fang, Y. Ding, "Simultaneous robustness, reprocessing and self-healing of castor oil-based polyurethane vitrimers enabled by supramolecular nitrogen-coordinated dynamic covalent boronic ester", *Industrial Crops and Products* **2023**, *206*, 117738.

[193] B. D. Mather, K. Viswanathan, K. M. Miller, T. E. Long, "Michael addition reactions in macromolecular design for emerging technologies", *Progress in Polymer Science* **2006**, *31*, 487-531.

[194] L. H. Sperling, "Interpenetrating polymer networks and related materials", *Journal of Polymer Science* **1977**, *12*, 141-180.

[195] O. Konuray, X. Fernandez-Francos, X. Ramis, A. Serra, "State of the Art in Dual-Curing Acrylate Systems", *Polymers* **2018**, *10*, 178.

[196] O. Konuray, X. Fernandez-Francos, X. Ramis, A. Serra, "Acetoacetate Based Thermosets Prepared by Dual-Michael Addition Reactions ", *Polymers* **2019**, *11*, 1408.

[197] A. O. Konuray, A. Ruiz, J. M. Morancho, J. M. Salla, X. Fernández-Francos, À. Serra, X. Ramis, "Sequential dual curing by selective Michael addition and free radical polymerization of acetoacetate-acrylate-methacrylate mixtures", *European Polymer Journal* **2018**, *98*, 39-46.

[198] A. O. Konuray, F. Liendo, X. Fernández-Francos, À. Serra, M. Sangermano, X. Ramis, "Sequential curing of thiol-acetoacetate-acrylate thermosets by latent Michael addition reactions", *Polymer* **2017**, *113*, 193-199.

[199] N. Suresh Kumar, R. Padma Suvarna, K. Chandra Babu Naidu, P. Banerjee, A. Ratnamala, H. Manjunatha, "A review on biological and biomimetic materials and their applications", *Applied Physics A* **2020**, *126*, 445.

[200] J. Sun, B. Bhushan, "Hierarchical structure and mechanical properties of nacre: a review", *RSC Advances* **2012**, *2*, 7617-7632.

[201] K. Cerdan, C. Moya, P. Van Puyvelde, G. Bruylants, J. Brancart, "Magnetic Self-Healing Composites: Synthesis and Applications", *Molecules* **2022**, *27*, 3796.

[202] L. Klauke, Dissertation, "*Oberflächenmodifizierte Eisenoxid-Nanokristalle als Bausteine für neuartige Nanokomposite*", Universität Hamburg, **2025**.

[203] M. Kampferbeck, L. R. Klauke, H. Weller, T. Vossmeyer, "Little Adjustments Significantly Simplify the Gram-Scale Synthesis of High-Quality Iron Oxide Nanocubes", *Langmuir* **2021**, *37*, 9851-9857.

[204] S. Schäfer, G. Kickelbick, "Double Reversible Networks: Improvement of Self-Healing in Hybrid Materials via Combination of Diels–Alder Cross-Linking and Hydrogen Bonds", *Macromolecules* **2018**, *51*, 6099-6110.

[205] S. He, G. Kickelbick, "Reversible Diels–Alder Reactions with a Fluorescent Dye on the Surface of Magnetite Nanoparticles", *Molecules* **2021**, *26*, 877.

[206] R. Sauer, P. Froimowicz, K. Scholler, J. M. Cramer, S. Ritz, V. Mailander, K. Landfester, "Design, Synthesis, and Miniemulsion Polymerization of New Phosphonate Surfmers and Application Studies of the Resulting Nanoparticles as Model Systems for Biomimetic Mineralization and Cellular Uptake", *Chemistry – A European Journal* **2012**, *18*, 5201-5212.

[207] M. Beljaars, H. J. Heeres, A. A. Broekhuis, F. Picchioni, "Bio-Based Aromatic Polyesters Reversibly Cross-linked via the Diels–Alder Reaction", *Applied Sciences* **2022**, *12*, 2461.

[208] F. Van Lijsebetten, Y. Spiesschaert, J. M. Winne, F. E. Du Prez, "Reprocessing of Covalent Adaptable Polyamide Networks through Internal Catalysis and Ring-Size Effects", *Journal of the American Chemical Society* **2021**, *143*, 15834-15844.

[209] H. Q. Pham, M. J. Marks, "*Epoxy Resins*" in "*Encyclopedia of Polymer Science and Technology*", Dow Chemical, Freeport, **2005**.

[210] F.-L. Jin, X. Li, S.-J. Park, "Synthesis and application of epoxy resins: A review", *Journal of Industrial and Engineering Chemistry* **2015**, *29*, 1-11.

[211] J. Zhang, Z. Zhang, R. Huang, L. Tan, "Advances in Toughening Modification Methods for Epoxy Resins: A Comprehensive Review", *Polymers* **2025**, *17*, 1288.

[212] T. Kouser, F. Nur, A. Aliyu, F. Altaf, H. Zulfiqar, L. M. Alhems, "Applications of Epoxy Resins as a Coating Technology in Fluid Systems", *ChemBioEng Reviews* **2025**, *12*, e70000.

[213] L.-Y. Zhan, P. Li, Y.-D. Li, Y. Ran, J.-B. Zeng, "Fully bio-based epoxy vitrimer from resorcinol diglyceryl ether, vanillin, and 1,10-diaminodecane", *European Polymer Journal* **2025**, *227*, 113749.

[214] P. Markouti, E. Tzouma, A. S. Paipetis, N. M. Barkoula, "Conventional Thermoset Composites and Their Sustainable Alternatives with Vitrimer Matrix—Waste Management/Recycling Options with Focus on Carbon Fiber Reinforced Epoxy Resin Composites", *Materials* **2025**, *18*, 351.

[215] F. Ferretti, G. Damonte, F. Cantamessa, R. Arrigo, A. Athanassiou, A. Zych, A. Fina, O. Monticelli, "On a Bio-based Epoxy Vitrimer from a Cardanol Derivative Prepared by a Simple Thiol–Epoxy "Click" Reaction", *ACS Omega* **2024**, *9*, 1242-1250.

[216] T. Liu, C. Hao, S. Zhang, X. Yang, L. Wang, J. Han, Y. Li, J. Xin, J. Zhang, "A Self-Healable High Glass Transition Temperature Bioepoxy Material Based on Vitrimer Chemistry", *Macromolecules* **2018**, *51*, 5577-5585.

[217] B. Xue, R. Tang, D. Xue, Y. Guan, Y. Sun, W. Zhao, J. Tan, X. Li, "Sustainable alternative for bisphenol A epoxy resin high-performance and recyclable lignin-based epoxy vitrimers", *Industrial Crops and Products* **2021**, *168*, 113583.

[218] R. Yang, W. Li, R. Mo, X. Zhang, "Recyclable and Degradable Vinylogous Urethane Epoxy Thermosets with Tunable Mechanical Properties from Isosorbide and Vanillic Acid", *ACS Applied Polymer Materials* **2023**, *5*, 2553-2561.

[219] H. Xu, H. Wang, Y. Zhang, J. Wu, "Vinylogous Urethane Based Epoxy Vitrimers with Closed-Loop and Multiple Recycling Routes", *Industrial & Engineering Chemistry Research* **2022**, *61*, 17524-17533.

[220] Y. Spiesschaert, M. Guerre, I. De Baere, W. Van Paepegem, J. M. Winne, F. E. Du Prez, ”Dynamic Curing Agents for Amine-Hardened Epoxy Vitrimers with Short (Re)processing Times“, *Macromolecules* **2020**, *53*, 2485-2495.

[221] F. Van Lijsebetten, S. Engelen, E. Bauters, W. Van Vooren, M. M. J. Smulders, F. E. Du Prez, ”Recyclable vitrimer epoxy coatings for durable protection”, *European Polymer Journal* **2022**, *176*, 111426.

[222] N. Van Herck, D. Maes, K. Unal, M. Guerre, J. M. Winne, F. E. Du Prez, “Covalent Adaptable Networks with Tunable Exchange Rates Based on Reversible Thiol–yne Cross-Linking”, *Angewandte Chemie International Edition* **2020**, *59*, 3609-3617.

[223] Y. Spiesschaert, J. Danneels, N. Van Herck, M. Guerre, G. Acke, J. Winne, F. Du Prez, ”Polyaddition Synthesis Using Alkyne Esters for the Design of Vinylogous Urethane Vitrimers”, *Macromolecules* **2021**, *54*, 7931-7942.

[224] A. Roig, P. Hidalgo, X. Ramis, S. De la Flor, À. Serra, “Vitrimeric Epoxy-Amine Polyimine Networks Based on a Renewable Vanillin Derivative”, *ACS Applied Polymer Materials* **2022**, *4*, 9341-9350.

[225] T. Türel, Ž. Tomović, “Chemically Recyclable and Upcyclable Epoxy Resins Derived from Vanillin”, *ACS Sustainable Chemistry & Engineering* **2023**, *11*, 8308-8316.

[226] S. Kumar, S. Krishnan, K. Prabakaran, “Renewable Resource-Based Epoxy Vitrimer Composites for Future Application: A Comprehensive Review”, *ACS Sustainable Resource Management* **2024**, *1*, 2086-2107.

9 Appendix

9.1 Author contributions to the Publications

Reprocessable Vanillin-based Polyschiff Vitrimer Networks: Tuning Mechanical and Thermomechanical Properties by Network Design

Florian C. Klein, Malte Vogt, and Volker Abetz
Macromol. Mater. Eng., **2024**, *309*, 2300187. (doi.org/10.1002/mame.202300187)

F.C.K., V.A.: conceptualization; F.C.K.: methodology, investigation, data curation, formal analysis, validation, and performing the experiments together with M.V.; V.A.: supervision and resources; F.C.K.: writing – the original draft; F.C.K., V.A.: writing – review and editing. All authors have read and agreed to the published version of the manuscript.

Bio-Based Vinylogous Urethane Vitrimers from Waste-Wood Lignosulfonate and Enzymatic Lignin: Explorations in Stress Relaxation Behavior and Mechanical Strength

Florian C. Klein, Nils Sobania, and Volker Abetz
J. Mater. Chem. A, **2025**, *13*, 29120. (doi.org/10.1039/D5TA02533H)

F. C. K. and N. S. contributed equally to this work. F. C. K., N. S., and V. A.: conceptualization; F. C. K. and N. S.: methodology, investigation, data curation, formal analysis, validation, visualization, and experiments; V. A.: supervision and resources; F.C. K. and N. S.: writing – the original draft; F. C. K., N. S., and V.A.: writing – review and editing. All authors have read and agreed to the published version of the manuscript.

Transparent Boronic Acid Acrylate Vitrimers Through One-Pot Click Reaction with Superior Strength as Matrix Material for Titania Nanoplates

Florian C. Klein, Jana Struck, Tobias Vossmeyer, and Volker Abetz
Macromol. Chem. Phys., **2025**, *226*, 0:e00276. (doi.org/10.1002/macp.202500276)

F.C.K.: writing – review and editing, writing – the original draft, conceptualization, methodology, investigation, data curation, formal analysis, validation, and performing the experiments; J.S.: writing – review and editing, writing – original draft, investigation, formal analysis, synthesis and characterization of the nanoparticles, T.V.: writing – review and editing, writing – original draft, supervision, resources, and funding acquisition; V.A.: writing – review and editing, writing – original draft, conceptualization, supervision, resources, and funding acquisition.

9.2 Publication 1 – Supporting Information

The publication is reprinted with permission from F.C. Klein, M. Vogt, and V. Abetz, *Macromol. Mater. Eng.*, **2024**, *309*, 2300187 – published by Wiley.

Macromolecular Materials and Engineering
Open Access

Supporting Information

for *Macromol. Mater. Eng.*, DOI 10.1002/mame.202300187

Reprocessable Vanillin-Based Schiff Base Vitrimers: Tuning Mechanical and Thermomechanical Properties by Network Design

*Florian C. Klein, Malte Vogt and Volker Abetz**

Supporting Information

Reprocessable Vanillin-based Schiff Base Vitrimers: Tuning Mechanical and Thermomechanical Properties by Network Design

*Florian C. Klein, Malte Vogt and Volker Abetz**

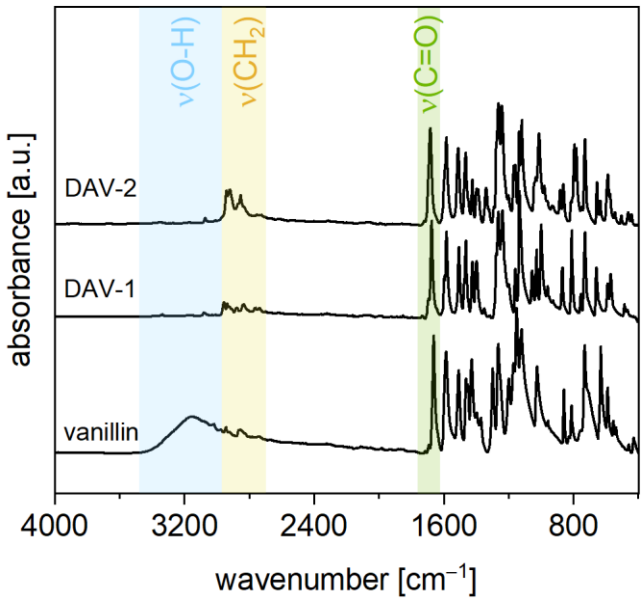

Figure S1. ATR-FT-IR spectra of the vanillin-based dialdehyde monomers DAV-1 and DAV-2 as well as vanillin showing the disappearance of the O-H stretching vibration (3500 – 2970 cm^{-1}), and the appearance of the characteristic CH_2, CH (2970 – 2670 cm^{-1}), and the C=O (1770 – 1620 cm^{-1}) aldehyde stretching vibrations.

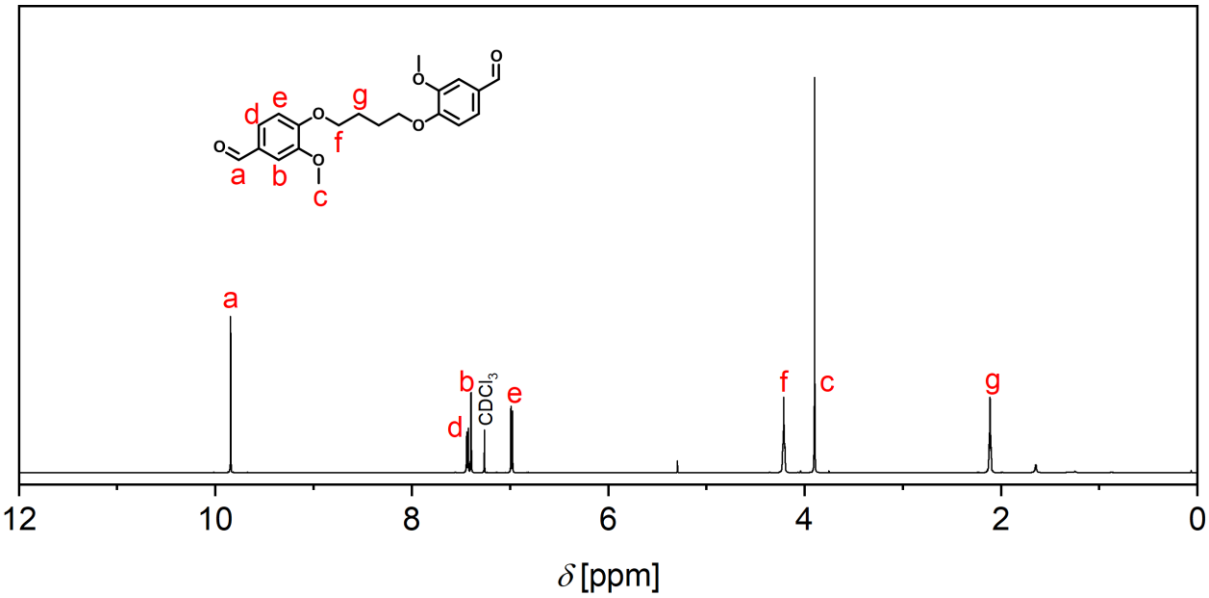

Figure S2. ^{1}H NMR (500 MHz, $CDCl_3$, 298 K) spectrum of dialdehyde monomer 4,4'-(butane-1,4-diylbis(oxy))bis(3-methoxybenzaldehyde) (DAV-1), showing the characteristic signals and intensities. ^{1}H NMR (500 MHz, $CDCl_3$, δ): 9.84 (s, 2H, CHO), 7.43 (dd, ^{3}J = 8.2 Hz, ^{4}J = 1.9 Hz, 2H; Ar H), 7.40 (d, ^{3}J = 8.2 Hz, ^{4}J = 1.9 Hz, 2H; Ar H), 6.98 (d, ^{3}J = 8.1 Hz, 2H; Ar H), 4.21 (t, ^{3}J = 5.8 Hz, 4H; CH_2), 3.90 (s, 6H; CH_3), 2.15-2.06 (m, 4H; CH_2).

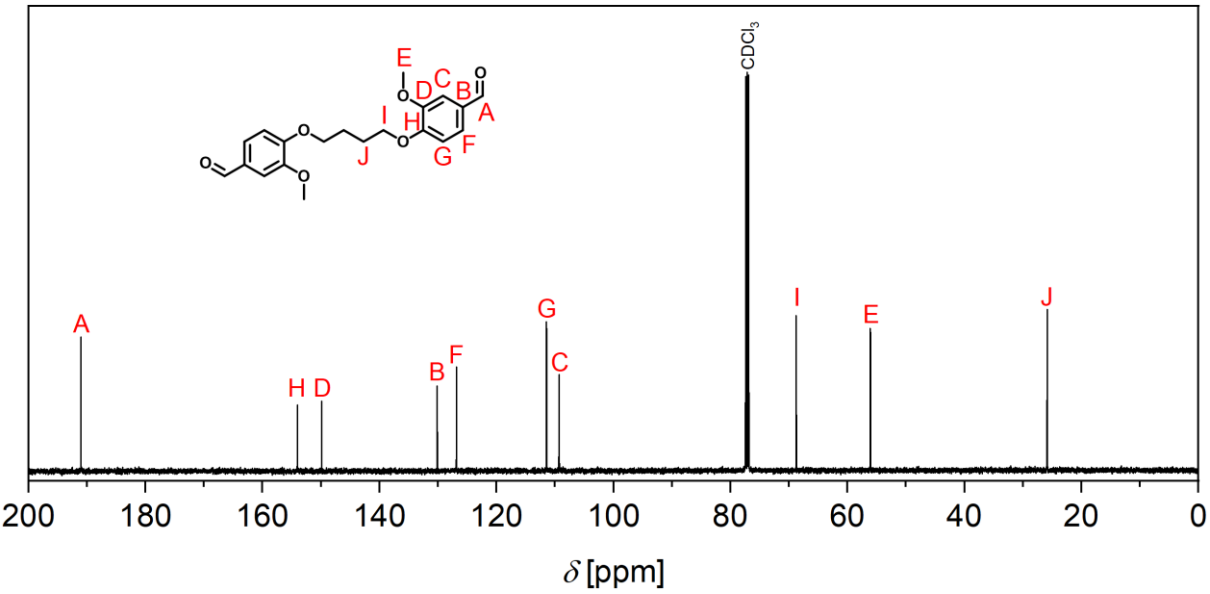

Figure S3. ^{13}C NMR (126 MHz, $CDCl_3$, 298 K) spectrum of dialdehyde monomer 4,4'-(butane-1,4-diylbis(oxy))bis(3-methoxybenzaldehyde) (DAV-1), showing the characteristic signals and intensities. ^{13}C NMR (126 MHz, $CDCl_3$, δ): 191.1 (C=O), 154.0 (C4), 149.9 (C4), 130.1 (C4), 126.9 (Ar), 111.5 (Ar), 109.3 (Ar), 68.8 (CH_2), 56.1 (CH_3), 25.9 (CH_2).

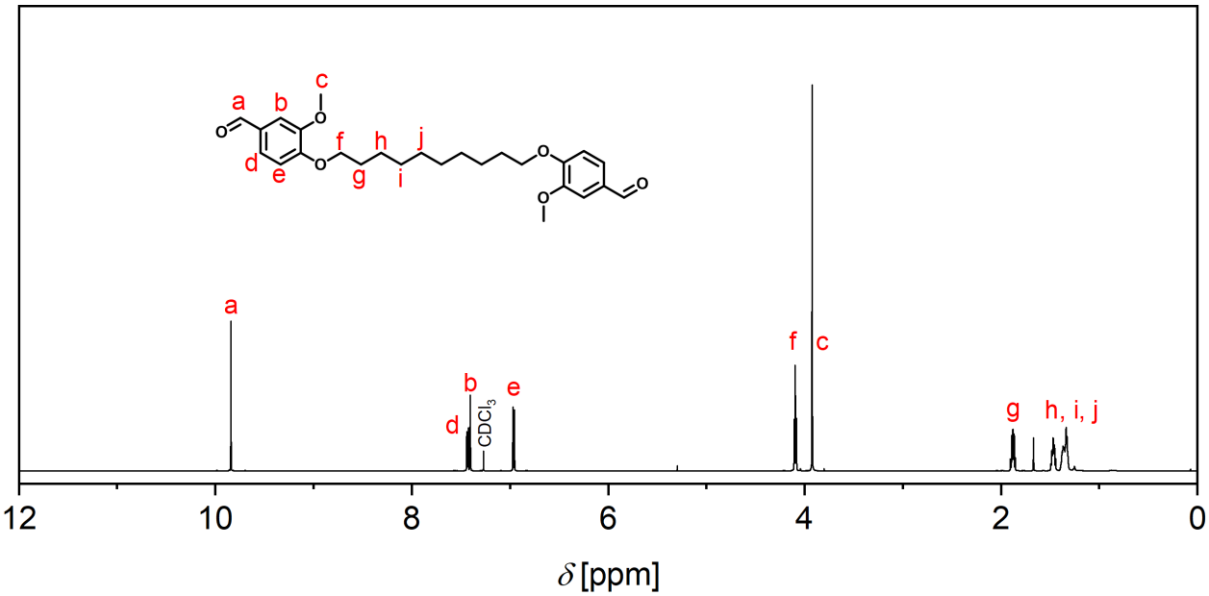

Figure S4. ^{1}H NMR (600 MHz, $CDCl_3$, 298 K) spectrum of dialdehyde monomer 4,4'-(decane-1,10-diylbis(oxy))bis(3-methoxybenzaldehyde) (DAV-2), showing the characteristic signals and intensities. ^{1}H NMR (600 MHz, $CDCl_3$, δ): 9.84 (s, 2H, CHO), 7.44 (dd, ^{3}J = 8.1 Hz, ^{4}J = 1.9 Hz, 2H; Ar H), 7.41 (d, ^{4}J = 1.9 Hz, 2H; Ar H), 6.96 (d, ^{3}J = 8.2 Hz, 1H; Ar H), 4.09 (t, ^{3}J = 6.8 Hz, 2H; CH_2), 3.92 (s, 6H; CH_3), 1.88 (m, 4H; CH2), 1.47 (m, 4H; CH_2), 1.34 (m, 8H; CH_2).

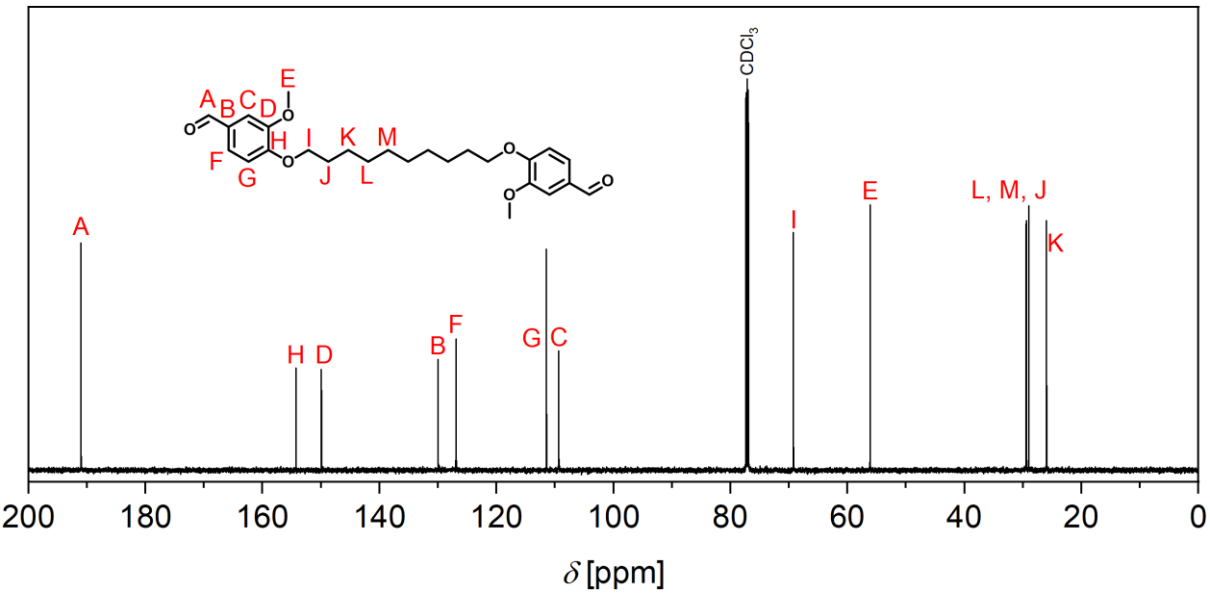

Figure S5. ^{13}C NMR (151 MHz, $CDCl_3$, 298 K) spectrum of dialdehyde monomer 4,4'-(butane-1,4-diylbis(oxy))bis(3-methoxybenzaldehyde) (DAV-1), showing the characteristic signals and intensities. ^{13}C NMR (151 MHz, $CDCl_3$, δ): 191.0 (C=O), 154.0 (C4), 150.0 (C4), 130.0 (C4), 126.9 (Ar), 111.5 (Ar), 109.4 (Ar), 69.3 (CH_2), 56.2 (CH_3), 29.52 (CH_2), 29.42 (CH_2), 29.02 (CH_2), 25.99 (CH_2).

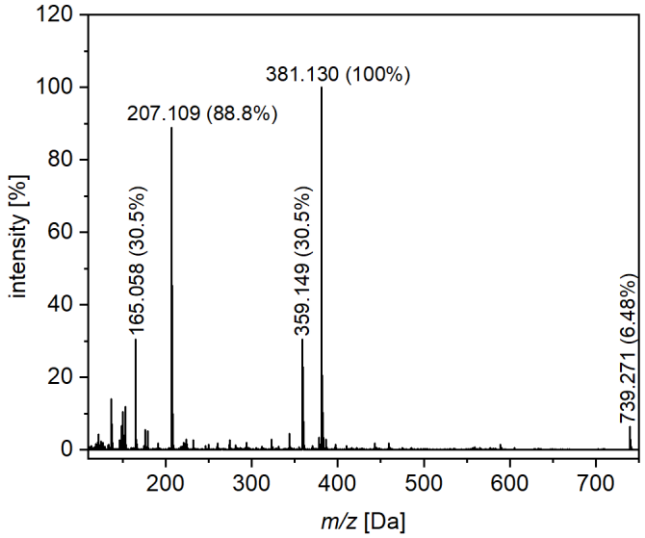

Figure S6. ESI-MS (+) spectrum of dialdehyde monomer 4,4'-(butane-1,4-diylbis(oxy))bis(3-methoxybenzaldehyde) (DAV-1) showing the characteristic peak of M^{Na+} with *m*/z = 381.130.

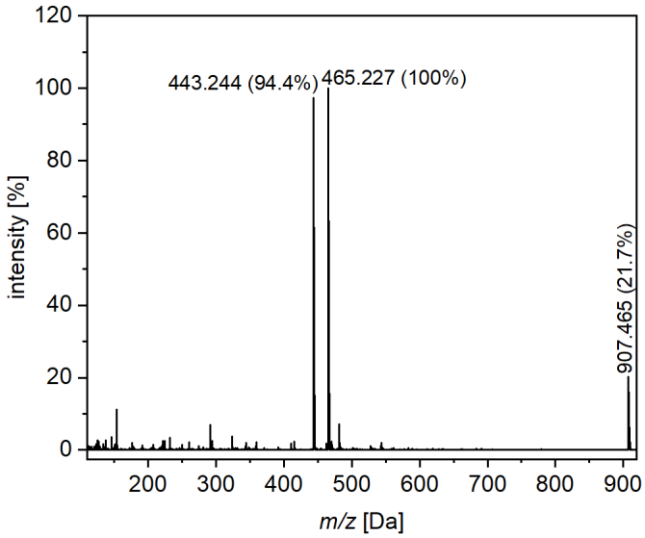

Figure S7. ESI-MS (+) spectrum of 4,4'-(decane-1,10-diylbis(oxy))bis(3-methoxybenzaldehyde) (DAV-2) showing the characteristic peak of M^{Na+} with *m*/z = 465.227.

Table S1. Formulations of the Schiff base vitrimer films prepared in this work with the molar contents of the DAV building block used and the contents of the di- and triamines as well as the respective *R*-values of the films.

Schiff base vitrimer film[a)]	DAV [mmol]	Diamine [mmol]	Triamine [mmol]	*R*-value[b)] [a.u.]
DAV-1/$DETA_{0.3}TREN_{0.7}$	2.79	0.84	1.30	1.0
DAV-2/$DETA_{0.3}TREN_{0.7}$	2.26	0.67	1.06	1.0
DAV-1/$JD_{0.1}JT_{0.9}$	2.79	0.28	1.67	1.0
DAV-2/$JD_{0.1}JT_{0.9}$	2.26	0.23	1.36	1.0
DAV-1/$JD_{0.3}JT_{0.7}$	2.79	0.84	1.30	1.0
DAV-1/$CAD_{0.3}JT_{0.7}$	2.79	0.84	1.30	1.0
DAV-1/$CAD_{0.5}JT_{0.5}$	2.79	1.40	0.93	1.0
DAV-2/$CAD_{0.5}JT_{0.5}$	2.26	1.13	0.75	1.0
DAV-1.2/$CAD_{0.5}JT_{0.5}$	1.40	1.40	0.93	1.0
DAV-1/$CAD_{0.7}JT_{0.7}$	2.79	1.96	1.30	0.71
DAV-2/$CAD_{0.7}JT_{0.7}$	2.26	1.58	1.05	0.71

a) The Schiff base vitrimer films were abbreviated following this nomenclature: First, the DAV building block is introduced, then, the amine amount (Equation S1) of the di- and then of the trifunctional amine is abbreviated. An example is given by DAV-1/$DETA_{0.3}TREN_{0.7}$.
b) The *R*-value is determined by the ratio of the aldehyde groups to the amino functions.

Equation S1.

$$\text{amine amount} = \frac{n_a \cdot f_a}{n_{DAV} \cdot f_{DAV}} \quad \text{(S1)}$$

The amine amount of the different di- and triamines in the Schiff base vitrimer films was calculated according to Equation S1. The abbreviations n_a and f_a describe the molar amount of amine and the functionality of amine, respectively. Accordingly, the abbreviations n_{DAV} and f_{DAV} describe the amount and the functionality of dialdehyde building block, respectively. Hence, the Schiff base vitrimer films were abbreviated following this nomenclature: First, the DAV building block is introduced, then, the amine amount of the di- and then of the trifunctional amine is abbreviated (as subscript). An example is given by DAV-1/$DETA_{0.3}TREN_{0.7}$ with an *R*-value of 1.0.

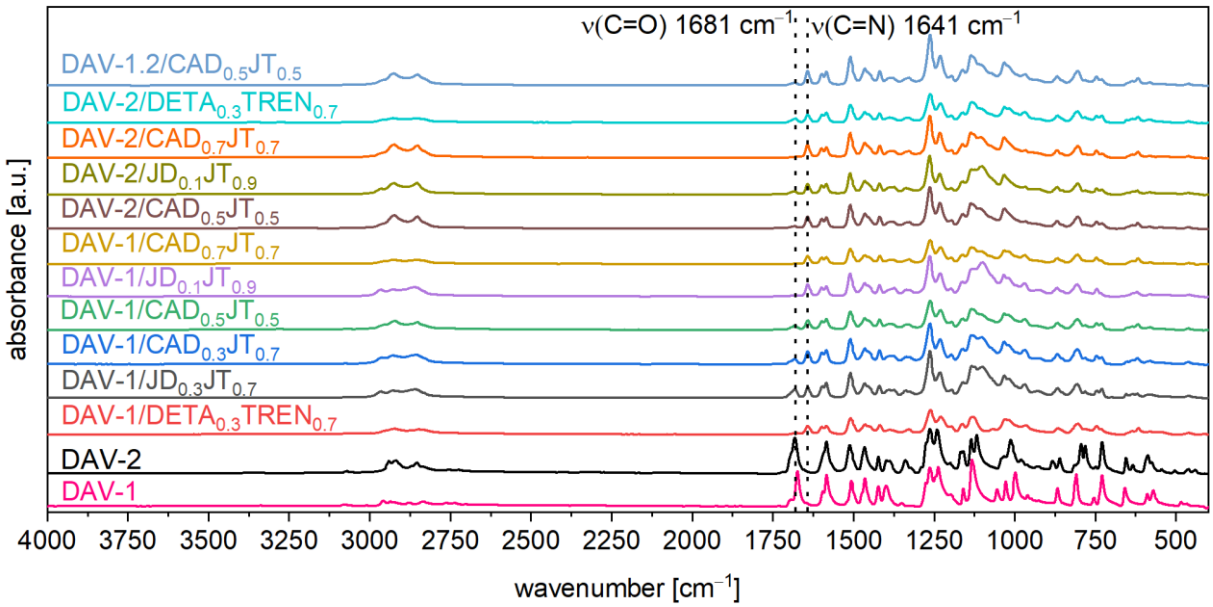

Figure S8. Full ATR-FT-IR spectra of the dialdehyde monomers DAV-1 and DAV-2 as well as the prepared Schiff base vitrimer films with different DAV, di- and triamine contents, showing the disappearance of the characteristic aldehyde stretching vibration (1681 cm^{-1}) and the formation of imine bond stretching vibration (1681 cm^{-1}).

Table S2. Overview of the synthesized Schiff base vitrimers and their soluble fractions (SFs) in the different solvents in tetrahydrofuran (THF), methanol (MeOH), dimethylformamide (DMF), and water.

Schiff base vitrimer film	THF	MeOH	DMF	H_2O[a)]
	SF [wt.%]	SF [wt.%]	SF [wt.%]	SF [wt.%]
DAV-1/$DETA_{0.3}TREN_{0.7}$	0.5	2.8	0.3	-
DAV-2/$DETA_{0.3}TREN_{0.7}$	100	0.5	87	-
DAV-1/$JD_{0.1}JT_{0.9}$	69	3.2	5.3	-
DAV-2/$JD_{0.1}JT_{0.9}$	58	2.1	16	-
DAV-1/$JD_{0.3}JT_{0.7}$	100	0.3	13	-
DAV-1/$CAD_{0.3}JT_{0.7}$	100	9.1	100	-
DAV-1/$CAD_{0.5}JT_{0.5}$	7.7	3.2	13	-
DAV-2/$CAD_{0.5}JT_{0.5}$	100	0.3	6.6	-
DAV-1.2/$CAD_{0.5}JT_{0.5}$	100	0.5	5.3	-
DAV-1/$CAD_{0.7}JT_{0.7}$	42	1.5	0.2	-
DAV-2/$CAD_{0.7}JT_{0.7}$	55	2.4	4.8	-

a) Soluble fractions were not detectable after immersion in deionized water for 24 h.

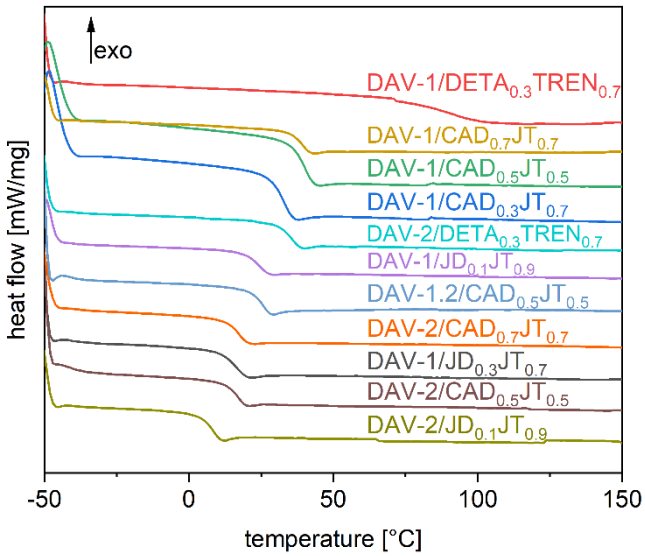

Figure S9. DSC-heating curves (−50 °C to 150 °C, 10 K min^{-1}, N_2 atmosphere) of the Schiff base vitrimer films using different DAV, di-, and triamine building blocks. Glass transition temperatures of 7 °C to 91 °C were measured.

Table S3. Overview of the synthesized Schiff base vitrimers and their characteristic properties measured by DSC, DMA, TGA, and tensile tests.

Schiff base vitrimer film	$T_{g,DSC}$ [a] [°C]	$T_{g,DMA}$ [b] [°C]	$T_{5\%}$ [c] [°C]	$G'_{10°C}$ [b] [GPa]	$G'_{110°C}$ [b] [MPa]	$E_{t,Ø,r.t.}$ [d] [MPa]	$\sigma_{y,Ø,r.t.}$ [e] [MPa]	$\sigma_{b,Ø,r.t.}$ [e] [MPa]	$\varepsilon_{b,Ø,r.t.}$ [e] [%]	$\tau_{130°C}$ [f] [s]	E_a [g] [kJ mol^{-1}]
DAV-1/DETA$_{0.3}$TREN$_{0.7}$	91	99	290	0.34	9.11	1574 ± 138	76.6 ± 11.6	73.2 ± 17.4	7.4 ± 0.5	6.2	89.3 ± 0.35
DAV-2/DETA$_{0.3}$TREN$_{0.7}$	34	43	325	0.20	0.14	1412 ± 178	41.6 ± 6.15	41.6 ± 6.15	3.7 ± 0.2	8.2	61.6 ± 1.8
DAV-1/JD$_{0.1}$JT$_{0.9}$	23	26	317	0.30	0.18	580 ± 138	17.1 ± 1.74	19.4 ± 4.43	193 ± 42	9.7	83.6 ± 1.6
DAV-2/JD$_{0.1}$JT$_{0.9}$	7	10	325	0.014	0.35	2.97 ± 1.80	0.20 ± 0.05	2.58 ± 0.51	311 ± 3.2	214	126 ± 7.7
DAV-1/JD$_{0.3}$JT$_{0.7}$	15	22	315	0.012	0.27	1.55 ± 1.09	0.46 ± 0.17	3.49 ± 1.23	400 ± 34	6.3	63.4 ± 0.55
DAV-1/CAD$_{0.3}$JT$_{0.7}$	29	34	318	0.87	0.18	1193 ±25.3	38.5 ± 3.56	15.2 ± 6.11	19.1 ± 12	11.5	83.4 ± 0.43
DAV-1/CAD$_{0.5}$JT$_{0.5}$	36	38	330	0.58	1.01	1364 ± 158	50.5 ± 7.42	39.0 ± 5.86	169 ± 22	6.0	75.5 ± 0.46
DAV-2/CAD$_{0.5}$JT$_{0.5}$	16	17	332	0.18	0.35	3.66 ± 2.68	7.53 ± 2.51	7.12 ± 2.58	375 ± 55	13	73.9 ± 1.4
DAV-1.2/CAD$_{0.5}$JT$_{0.5}$	24	28	332	0.35	1.15	389 ± 98.8	13.3 ± 1.09	36.6 ± 1.88	315 ± 21	7.1	80.8 ± 0.64
DAV-1/CAD$_{0.7}$JT$_{0.7}$	38	42	325	0.33	1.71	1279 ± 49.2	55.6 ± 2.59	56.1 ± 7.77	188 ± 33	0.65	58.2 ± 3.2
DAV-2/CAD$_{0.7}$JT$_{0.7}$	16	21	327	0.37	1.66	4.65 ± 2.45	19.55 ± 7.68	14.7 ± 2.92	347 ± 80	0.58	47.6 ± 1.2

a) The $T_{g,DSC}$ was determined using the mid-point of the step in the DSC-curves. b) The $T_{g,DMA}$ was determined by the maximum of the tan δ curve of the temperature-sweep measurements, which were also used to determine the values of G' (ω = 62.8 rad s^{-1}, γ = 0.1%, T = 150 – 0 °C). c) The temperature of 5% mass loss was determined by TGA-measurements (T = 25 – 600 °C, 10 K min^{-1}). d) The elastic modulus was determined at the start of the stress strain measurement (1 mm min^{-1}, ε = 0.05% – 0.25%, 23 °C). e) The stress, strain, and elongation values were determined in a stress-strain measurement (1 mm min^{-1} between 0.05% and 0.25% elongation and the rest of the test was carried out at 10 mm min^{-1}, T = 23 °C). f) The stress-relaxation time at 130 °C was determined by stress-relaxation measurements (γ = 1%). g) The activation energy was determined by linearization of the characteristic stress-relaxation times τ at 37% normalized stress-relaxation (γ = 1%, T = 150 – 90 °C).

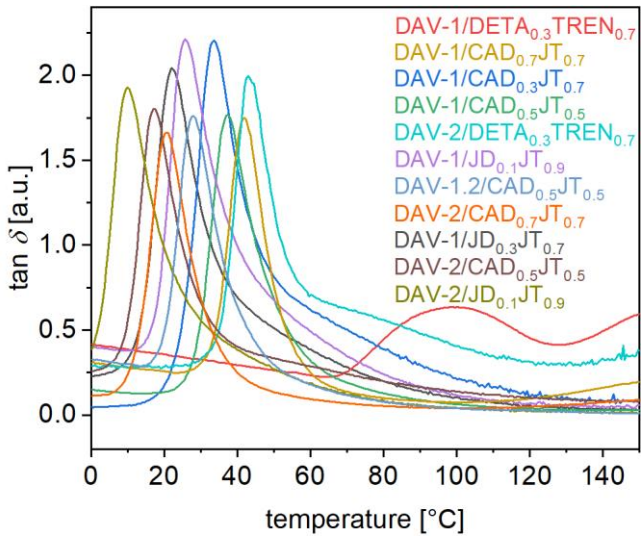

Figure S10. Tan δ of temperature-dependent DMA measurements of the Schiff base vitrimer films with different DAV and di- and triamine building blocks carried out in the range of 150 °C to 0 °C (ω = 62.8 rad s^{-1} and γ = 0.1%), showing cross-linked materials and the glass transition temperature of the materials as the maximum of the tan δ curves.

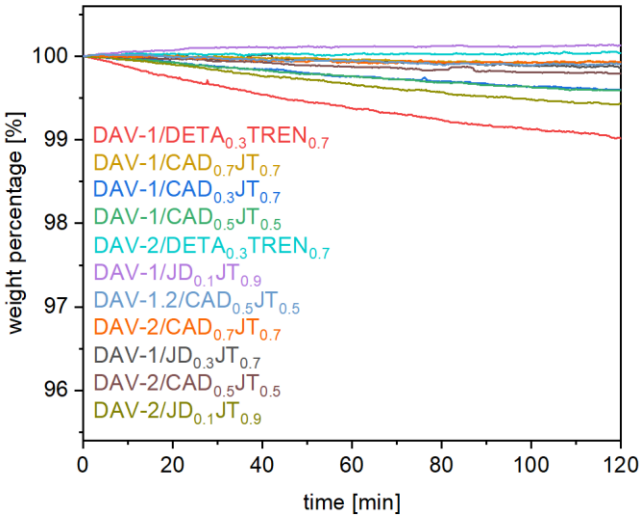

Figure S11. Isothermal thermogravimetric analysis measurements under oxygen atmosphere of the Schiff base vitrimer films with different DAV and di- and triamine building blocks carried out at a temperature of 150 °C for 2 h, showing no thermal degradation.

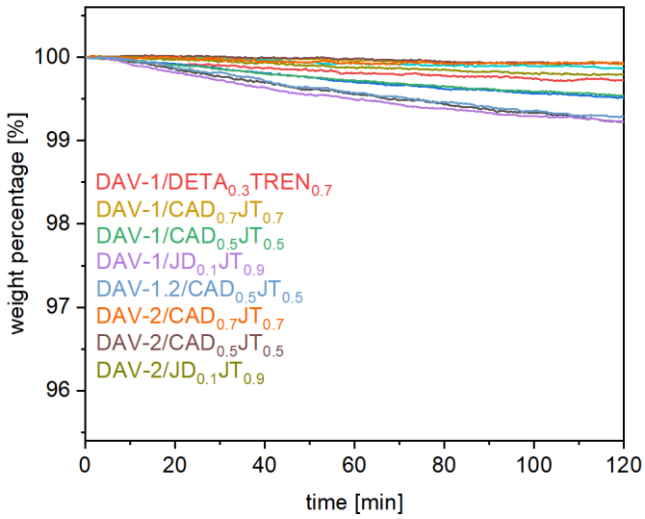

Figure S12. Isothermal thermogravimetric analysis measurements under nitrogen atmosphere of the Schiff base vitrimer films with different DAV and di- and triamine building blocks carried out at a temperature of 150 °C for 2 h, showing no thermal degradation.

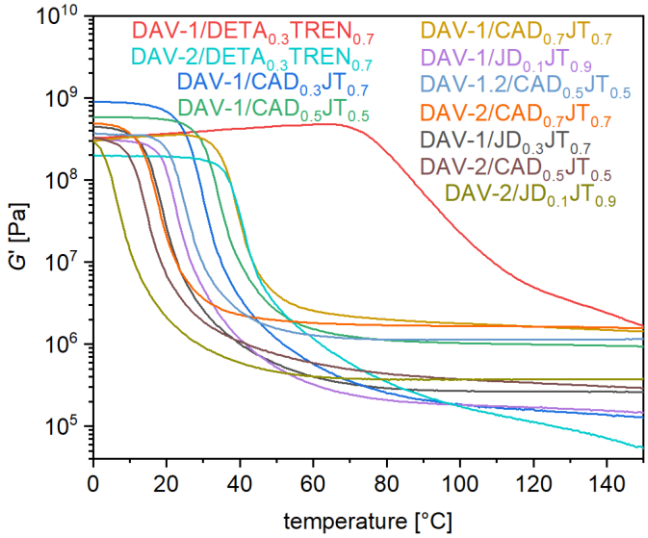

Figure S13. Temperature-dependent DMA measurements of the Schiff base vitrimer films displaying the storage modulus *G′* with different DAV and di- and triamine building blocks carried out in the range of 150 °C to 0 °C (ω = 62.8 rad s^{-1} and γ = 0.1%).

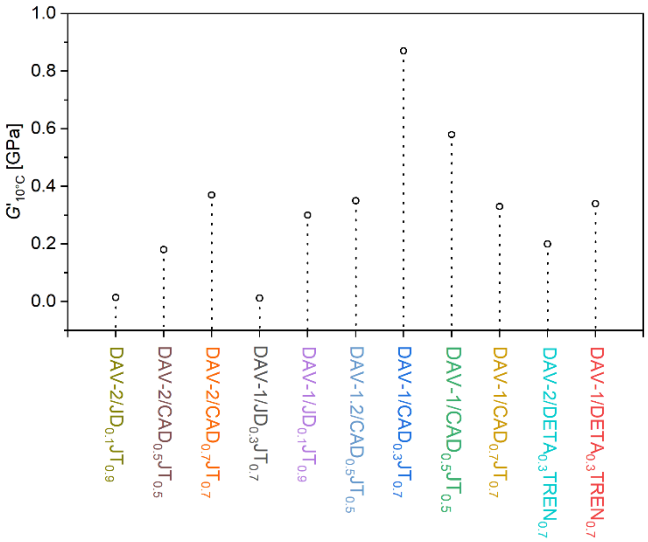

Figure S14. *G′* values at 10 °C for the Schiff base vitrimers measured via temperature-dependent DMA measurements of the Schiff base vitrimer films (ω = 62.8 rad s^{-1} and γ = 0.1%).

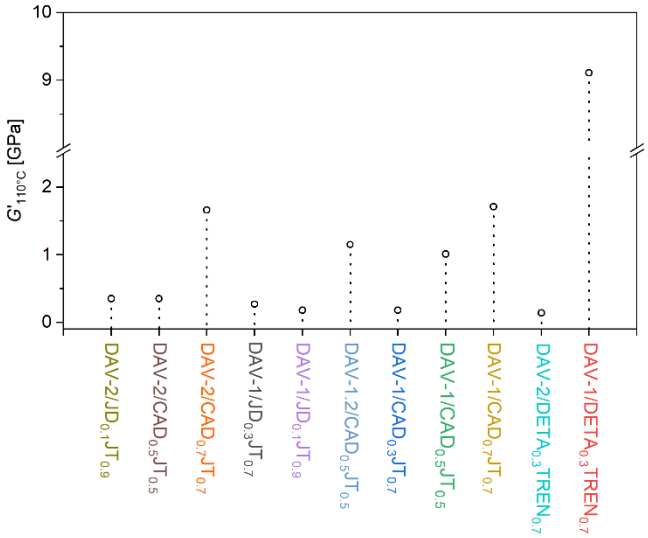

Figure S15. *G′* values at 110 °C for the Schiff base vitrimers measured via temperature-dependent DMA measurements of the Schiff base vitrimer films (ω = 62.8 rad s^{-1} and γ = 0.1%).

Equation S2.

$$\tau(T) = \tau_0 \cdot e^{\frac{E_a}{R \cdot T}} \quad \text{(S2)}$$

The stress relaxation time as a function of temperature can be calculated according to the Arrhenius law in Equation S2, where the relaxation time τ is recorded when the relaxation modulus $G(t)$ decreased to $G(1/e)$ following the Maxwell model for viscoelastic fluids as a function of temperature. τ_0 is the characteristic relaxation time, E_a is the experimental activation energy, R is the molar gas constant and T is the temperature. The activation energy E_a was calculated by plotting ln τ versus 1000/T.

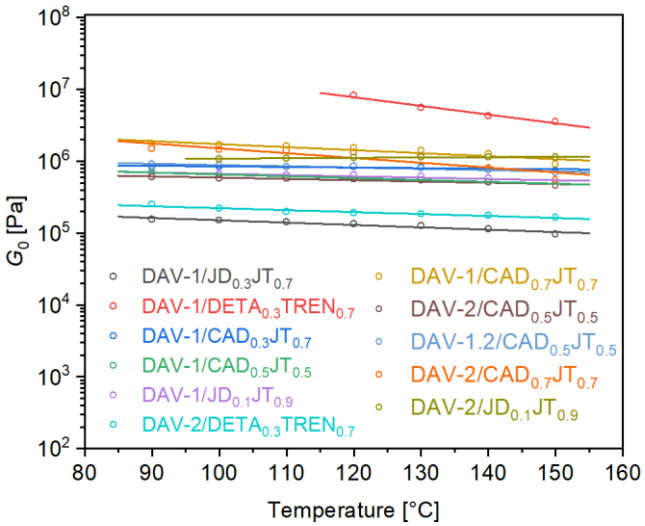

Figure S16. Initial relaxation moduli G_0 of the Schiff base vitrimers produced in this work as a function of temperature.

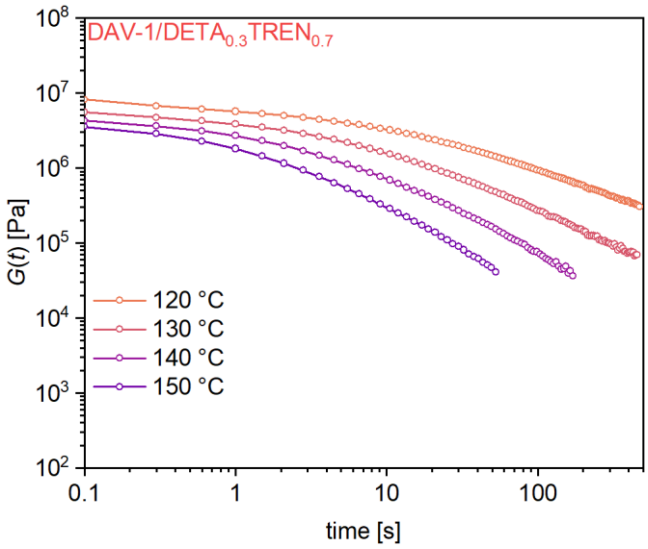

Figure S17. Stress-relaxation measurement of Schiff base vitrimer film DAV-1/DETA$_{0.3}$TREN$_{0.7}$ plotting the non-normalized stress-relaxation modulus $G(t)$ versus the stress-relaxation time measured at temperatures in the range of 150 to 120 °C while applying a shear strain of 1%.

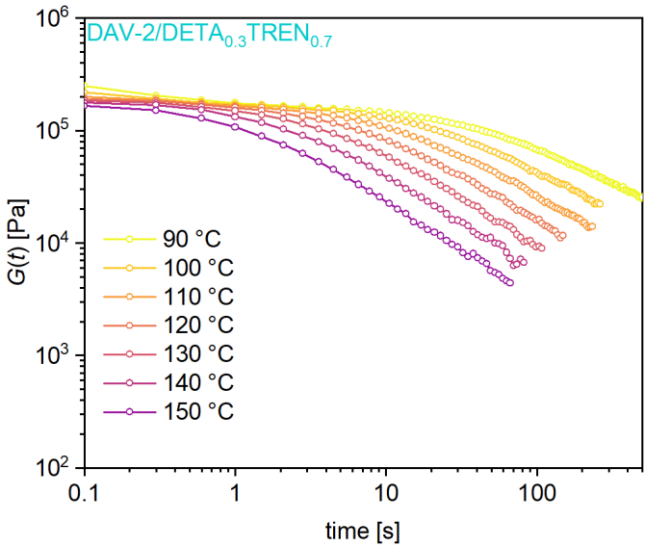

Figure S18. Stress-relaxation measurement of Schiff base vitrimer film DAV-2/DETA$_{0.3}$TREN$_{0.7}$ plotting the non-normalized stress-relaxation modulus $G(t)$ versus the stress-relaxation time measured at temperatures in the range of 150 to 90 °C while applying a shear strain of 1%.

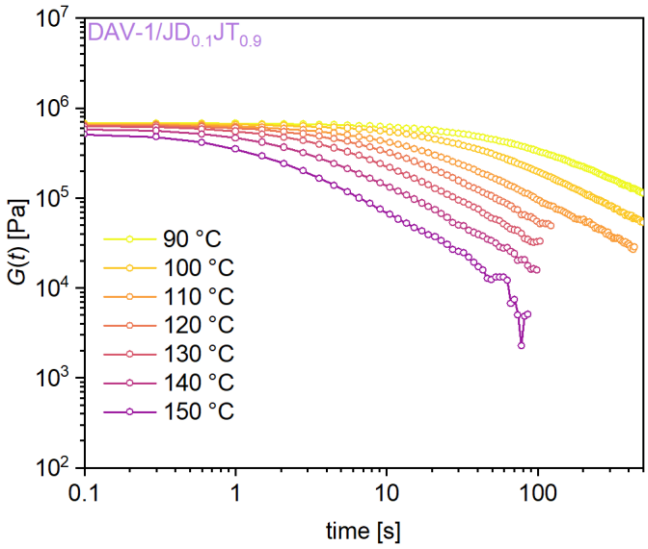

Figure S19. Stress-relaxation measurement of Schiff base vitrimer film DAV-1/$JD_{0.1}JT_{0.9}$ plotting the non-normalized stress-relaxation modulus $G(t)$ versus the stress-relaxation time measured at temperatures in the range of 150 to 90 °C while applying a shear strain of 1%.

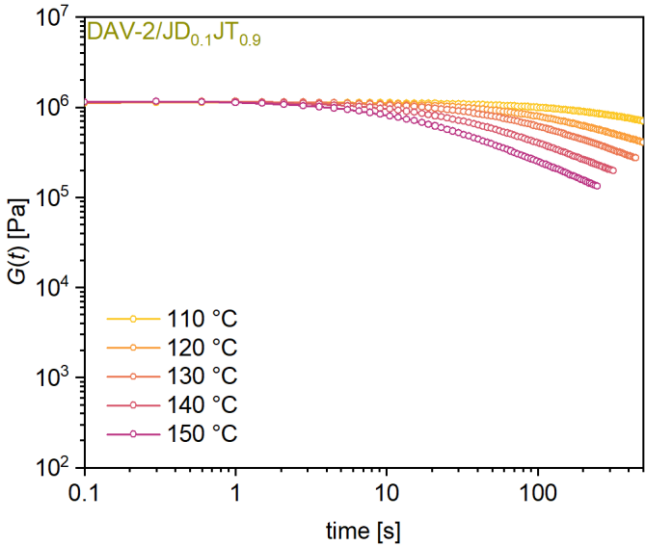

Figure S20. Stress-relaxation measurement of Schiff base vitrimer film DAV-2/$JD_{0.1}JT_{0.9}$ plotting the non-normalized stress-relaxation modulus $G(t)$ versus the stress-relaxation time measured at temperatures in the range of 150 to 110 °C while applying a shear strain of 1%.

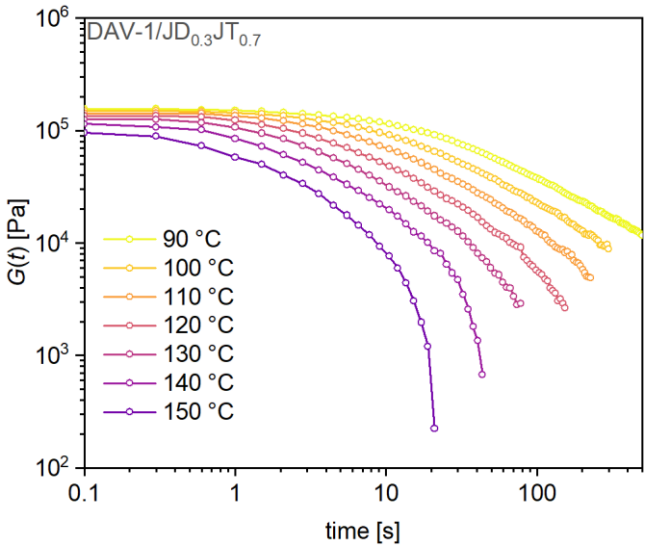

Figure S21. Stress-relaxation measurement of Schiff base vitrimer film DAV-1/$JD_{0.3}JT_{0.7}$ plotting the non-normalized stress-relaxation modulus $G(t)$ versus the stress-relaxation time measured at temperatures in the range of 150 to 110 °C while applying a shear strain of 1%.

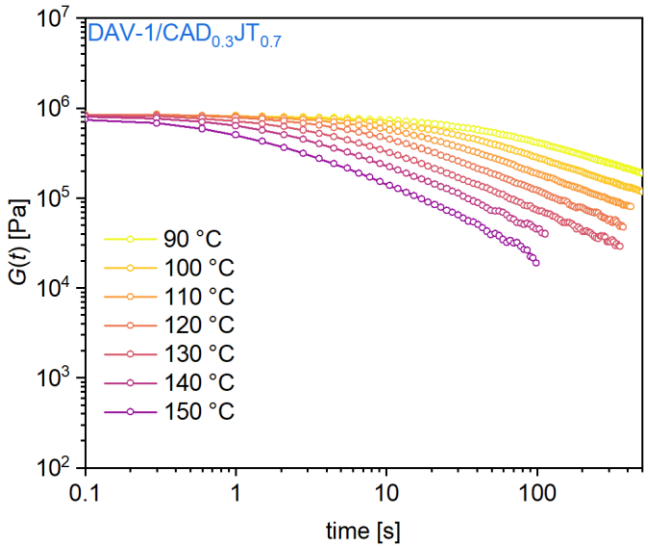

Figure S22. Stress-relaxation measurement of Schiff base vitrimer film DAV-1/$CAD_{0.3}JT_{0.7}$ plotting the non-normalized stress-relaxation modulus $G(t)$ versus the stress-relaxation time measured at temperatures in the range of 150 to 110 °C while applying a shear strain of 1%.

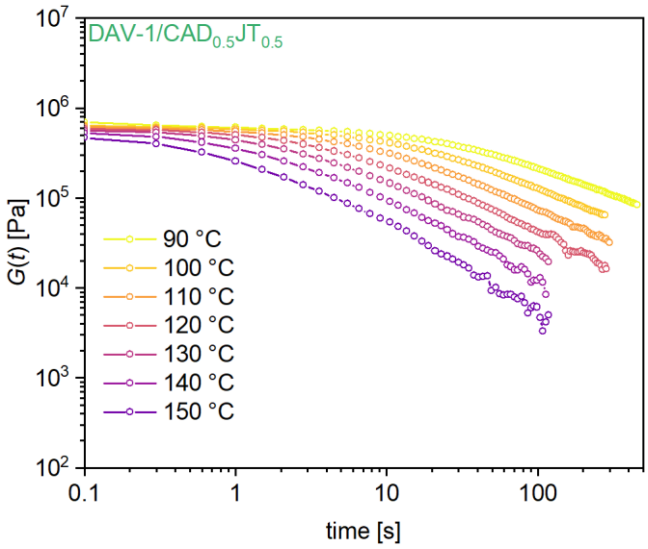

Figure S23. Stress-relaxation measurement of Schiff base vitrimer film DAV-1/$CAD_{0.5}JT_{0.5}$ plotting the non-normalized stress-relaxation modulus $G(t)$ versus the stress-relaxation time measured at temperatures in the range of 150 to 90 °C while applying a shear strain of 1%.

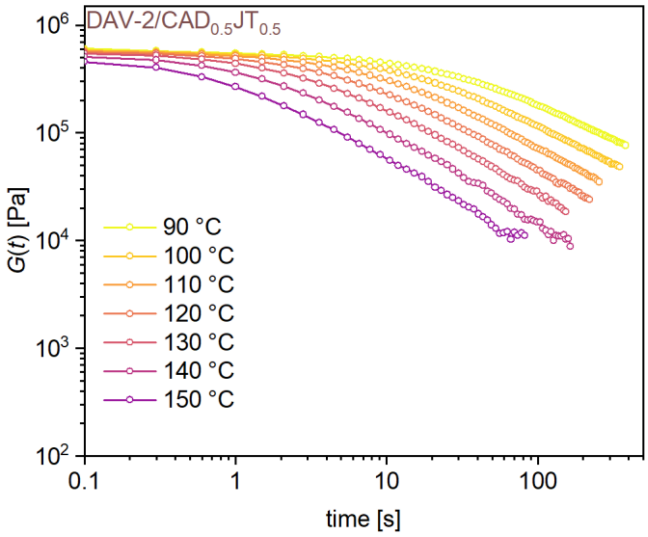

Figure S24. Stress-relaxation measurement of Schiff base vitrimer film DAV-2/$CAD_{0.5}JT_{0.5}$ plotting the non-normalized stress-relaxation modulus $G(t)$ versus the stress-relaxation time measured at temperatures in the range of 150 to 90 °C while applying a shear strain of 1%.

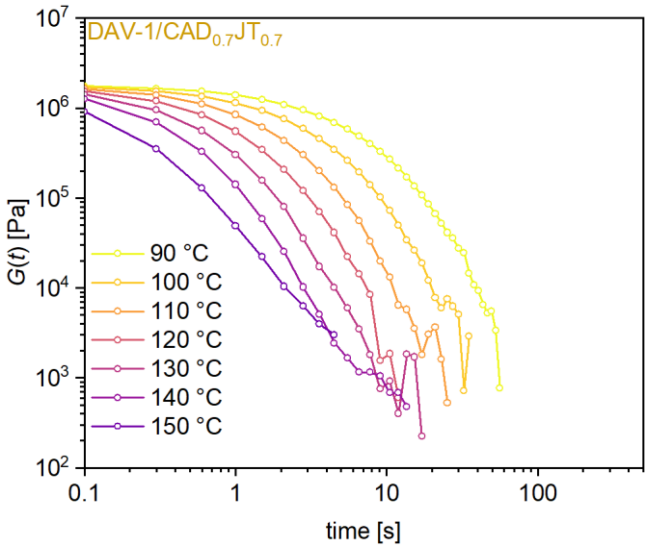

Figure S25. Stress-relaxation measurement of Schiff base vitrimer film DAV-1/$CAD_{0.7}JT_{0.7}$ plotting the non-normalized stress-relaxation modulus $G(t)$ versus the stress-relaxation time measured at temperatures in the range of 150 to 90 °C while applying a shear strain of 1%.

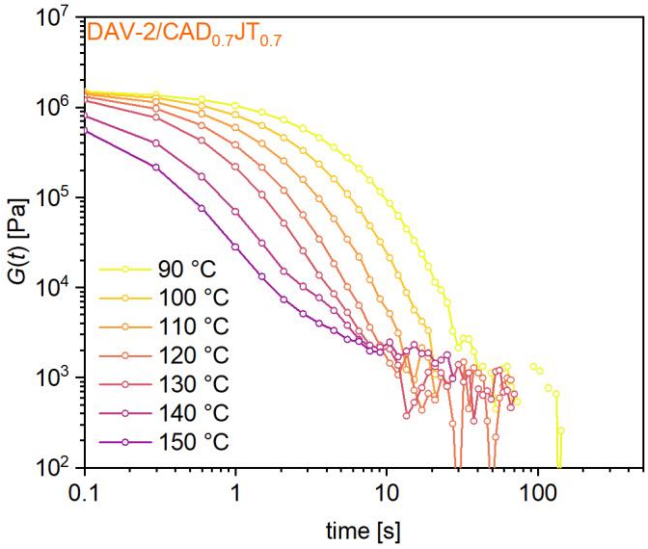

Figure S26. Stress-relaxation measurement of Schiff base vitrimer film DAV-2/$CAD_{0.7}JT_{0.7}$ plotting the non-normalized stress-relaxation modulus $G(t)$ versus the stress-relaxation time measured at temperatures in the range of 150 to 90 °C while applying a shear strain of 1%.

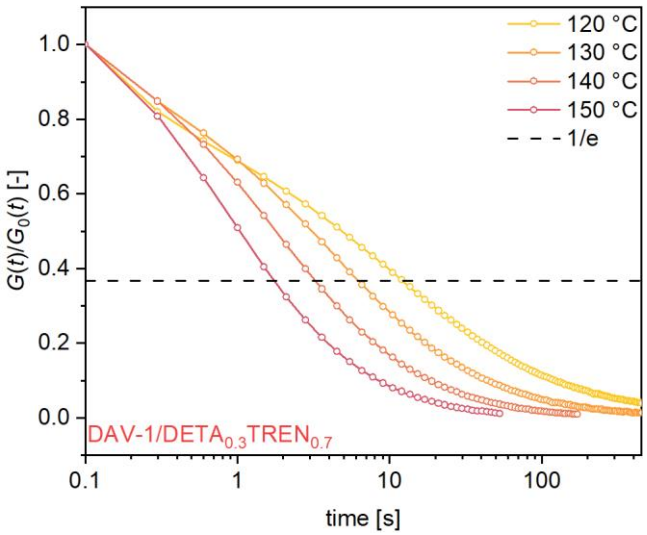

Figure S27. Stress-relaxation measurement of Schiff base vitrimer film DAV-1/DETA$_{0.3}$TREN$_{0.7}$ plotting the normalized stress-relaxation modulus $G(t)$ versus the stress-relaxation time measured at temperatures in the range of 150 to 120 °C while applying a shear strain of 1%. The dashed line indicates 37% of the normalized stress relaxation.

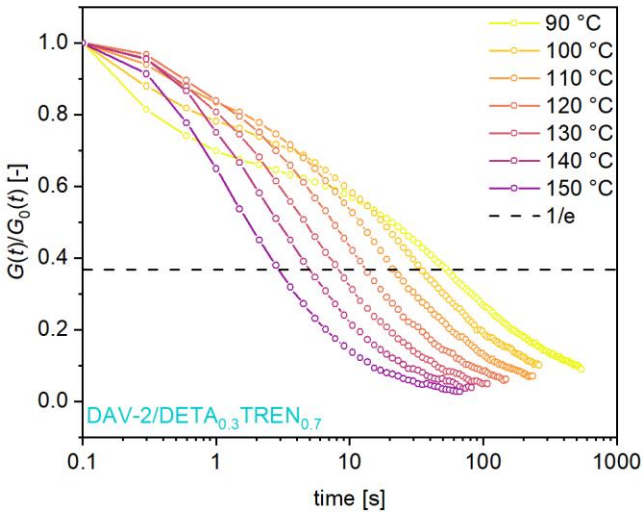

Figure S28. Stress-relaxation measurement of Schiff base vitrimer film DAV-2/DETA$_{0.3}$TREN$_{0.7}$ plotting the normalized stress-relaxation modulus $G(t)$ versus the stress-relaxation time measured at temperatures in the range of 150 to 90 °C while applying a shear strain of 1%. The dashed line indicates 37% of the normalized stress relaxation.

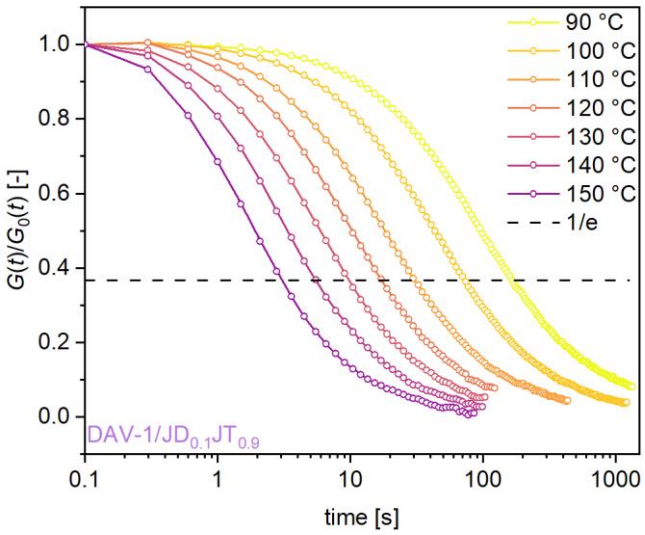

Figure S29. Stress-relaxation measurement of Schiff base vitrimer film DAV-1/$JD_{0.1}JT_{0.9}$ plotting the normalized stress-relaxation modulus $G(t)$ versus the stress-relaxation time measured at temperatures in the range of 150 to 90 °C while applying a shear strain of 1%. The dashed line indicates 37% of the normalized stress relaxation.

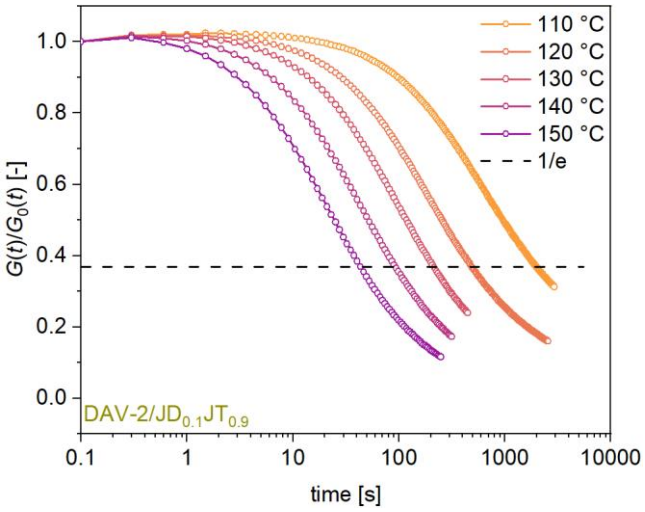

Figure S30. Stress-relaxation measurement of Schiff base vitrimer film DAV-2/$JD_{0.1}JT_{0.9}$ plotting the normalized stress-relaxation modulus $G(t)$ versus the stress-relaxation time measured at temperatures in the range of 150 to 110 °C while applying a shear strain of 1%. The dashed line indicates 37% of the normalized stress relaxation.

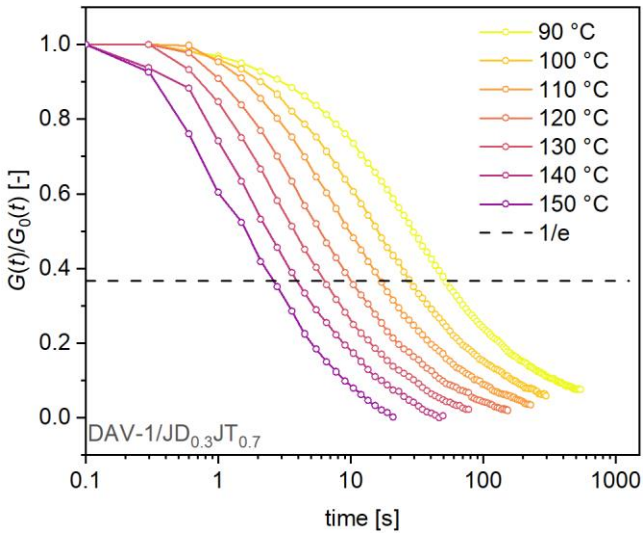

Figure S31. Stress-relaxation measurement of Schiff base vitrimer film DAV-1/$JD_{0.3}JT_{0.7}$ plotting the normalized stress-relaxation modulus $G(t)$ versus the stress-relaxation time measured at temperatures in the range of 150 to 90 °C while applying a shear strain of 1%. The dashed line indicates 37% of the normalized stress relaxation.

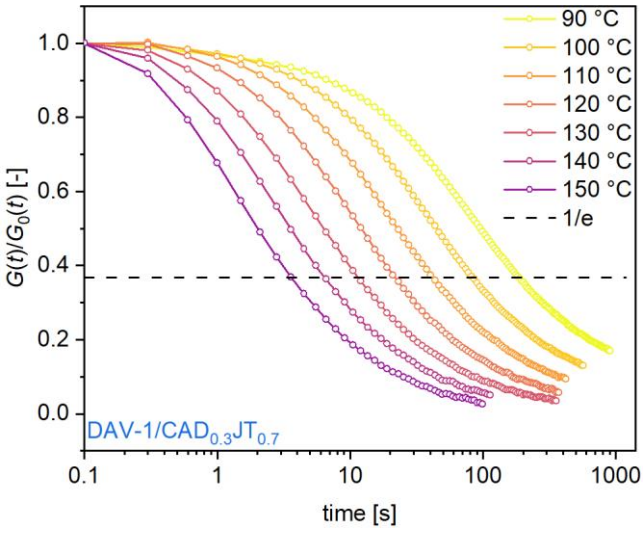

Figure S32. Stress-relaxation measurement of Schiff base vitrimer film DAV-1/$CAD_{0.3}JT_{0.7}$ plotting the normalized stress-relaxation modulus $G(t)$ versus the stress-relaxation time measured at temperatures in the range of 150 to 90 °C while applying a shear strain of 1%. The dashed line indicates 37% of the normalized stress relaxation.

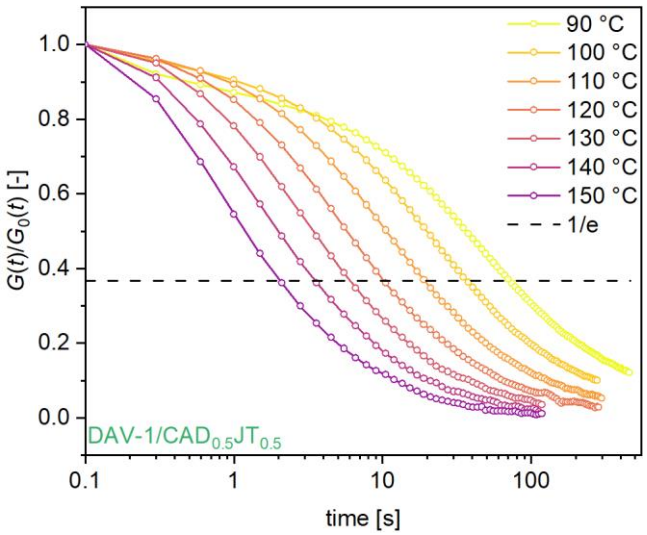

Figure S33. Stress-relaxation measurement of Schiff base vitrimer film DAV-1/$CAD_{0.5}JT_{0.5}$ plotting the normalized stress-relaxation modulus $G(t)$ versus the stress-relaxation time measured at temperatures in the range of 150 to 90 °C while applying a shear strain of 1%. The dashed line indicates 37% of the normalized stress relaxation.

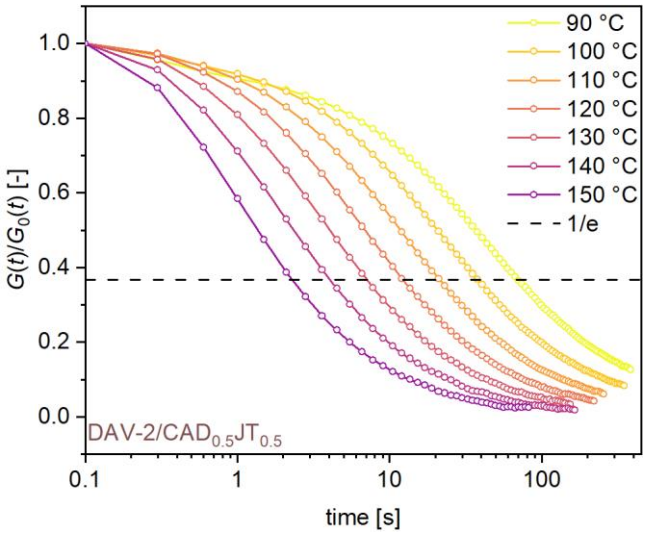

Figure S34. Stress-relaxation measurement of Schiff base vitrimer film DAV-2/$CAD_{0.5}JT_{0.5}$ plotting the normalized stress-relaxation modulus $G(t)$ versus the stress-relaxation time measured at temperatures in the range of 150 to 90 °C while applying a shear strain of 1%. The dashed line indicates 37% of the normalized stress relaxation.

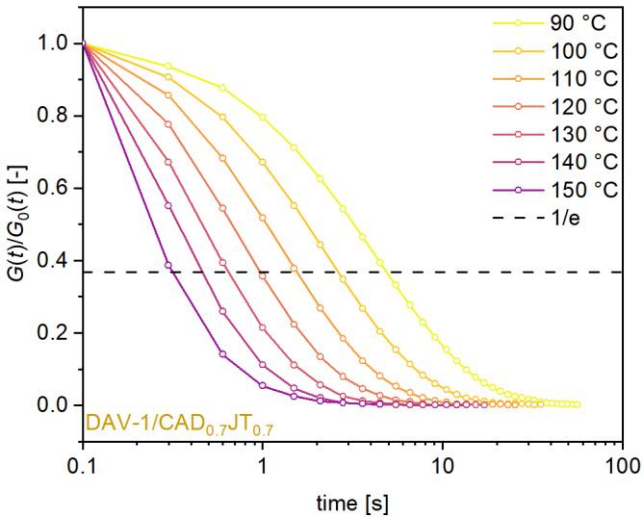

Figure S35. Stress-relaxation measurement of Schiff base vitrimer film DAV-1/$CAD_{0.7}JT_{0.7}$ plotting the normalized stress-relaxation modulus $G(t)$ versus the stress-relaxation time measured at temperatures in the range of 150 to 90 °C while applying a shear strain of 1%. The dashed line indicates 37% of the normalized stress relaxation.

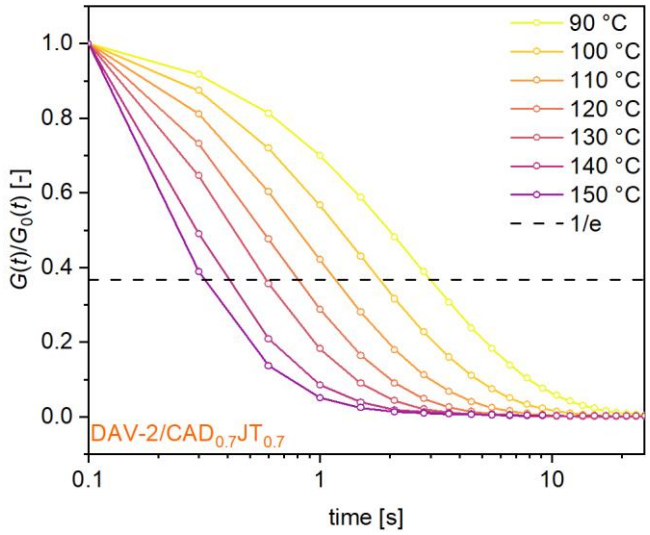

Figure S36. Stress-relaxation measurement of Schiff base vitrimer film DAV-2/$CAD_{0.7}JT_{0.7}$ plotting the normalized stress-relaxation modulus $G(t)$ versus the stress-relaxation time measured at temperatures in the range of 150 to 90 °C while applying a shear strain of 1%. The dashed line indicates 37% of the normalized stress relaxation.

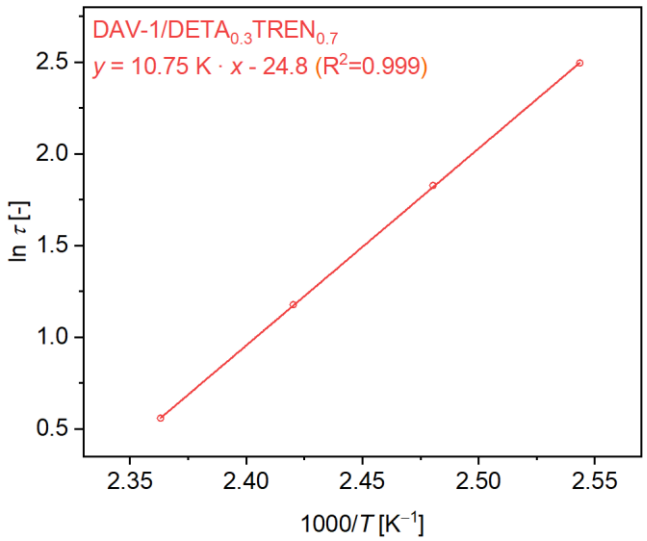

Figure S37. Plot of ln τ versus 1000/T to calculate the activation energies from the slope of the linear fit of the measured τ values for Schiff base vitrimer DAV-1/DETA$_{0.3}$TREN$_{0.7}$ in the temperature range of 150 °C to 120 °C.

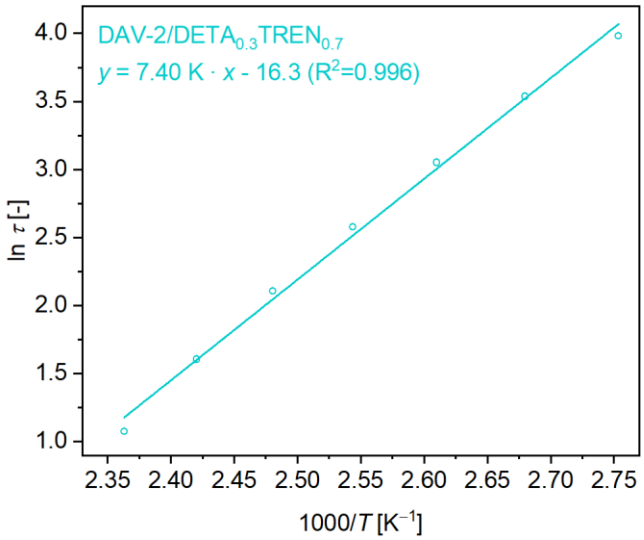

Figure S38. Plot of ln τ versus 1000/T to calculate the activation energies from the slope of the linear fit of the measured τ values for Schiff base vitrimer DAV-2/DETA$_{0.3}$TREN$_{0.7}$ in the temperature range of 150 °C to 90 °C.

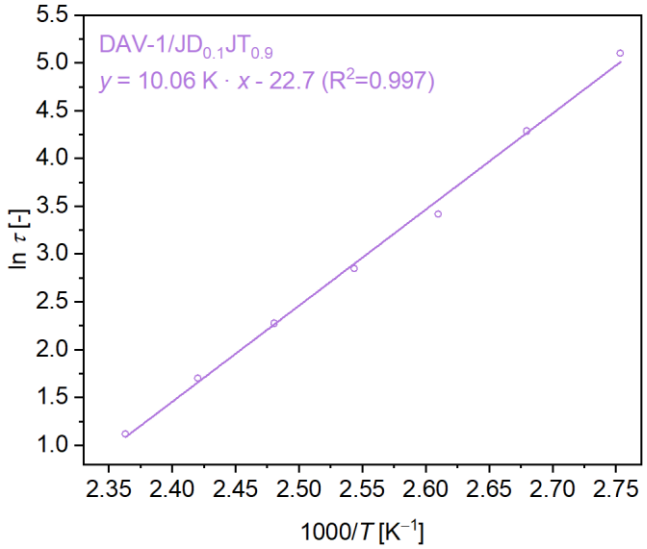

Figure S39. Plot of ln τ versus 1000/T to calculate the activation energies from the slope of the linear fit of the measured τ values for Schiff base vitrimer DAV-1/$JD_{0.1}JT_{0.9}$ in the temperature range of 150 °C to 90 °C.

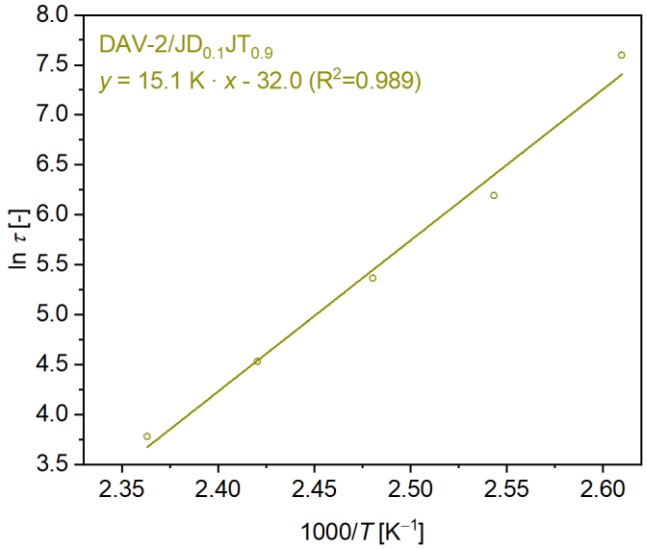

Figure S40. Plot of ln τ versus 1000/T to calculate the activation energies from the slope of the linear fit of the measured τ values for Schiff base vitrimer DAV-2/$JD_{0.1}JT_{0.9}$ in the temperature range of 150 °C to 110 °C.

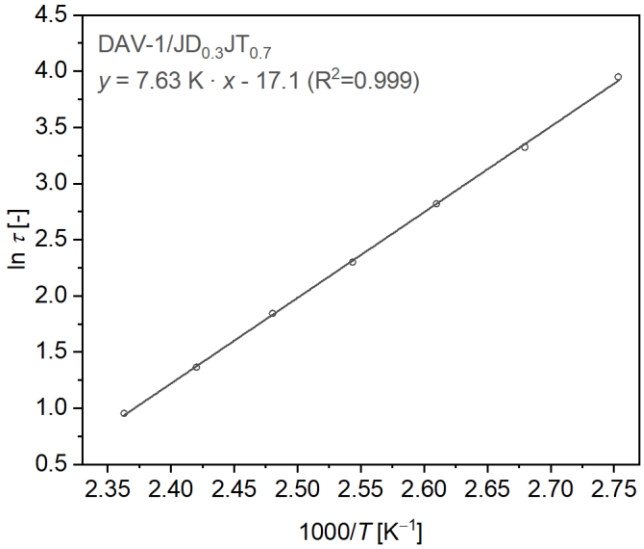

Figure S41. Plot of ln τ versus 1000/T to calculate the activation energies from the slope of the linear fit of the measured τ values for Schiff base vitrimer DAV-1/$JD_{0.3}JT_{0.7}$ in the temperature range of 150 °C to 90 °C.

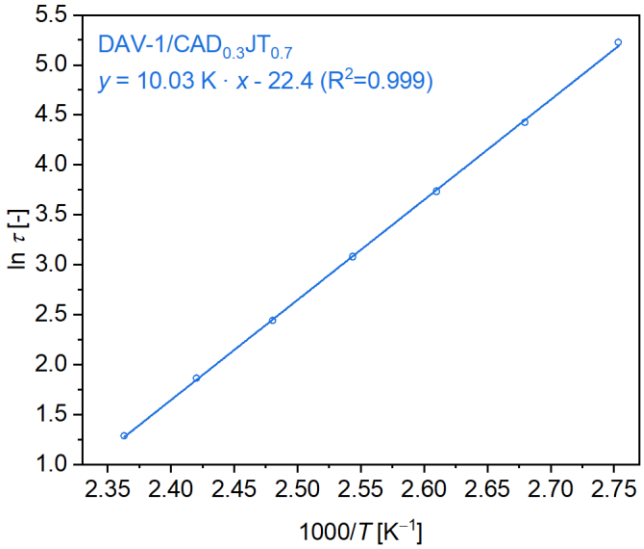

Figure S42. Plot of ln τ versus 1000/T to calculate the activation energies from the slope of the linear fit of the measured τ values for Schiff base vitrimer DAV-1/$CAD_{0.3}JT_{0.7}$ in the temperature range of 150 °C to 90 °C.

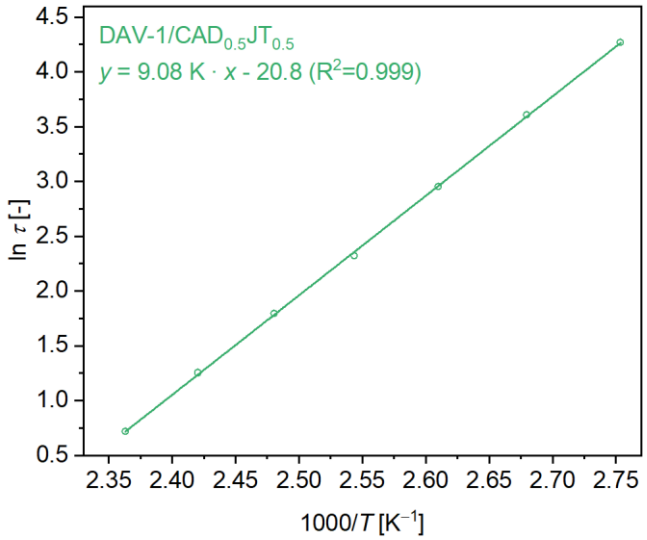

Figure S43. Plot of ln τ versus 1000/T to calculate the activation energies from the slope of the linear fit of the measured τ values for Schiff base vitrimer DAV-1/$CAD_{0.5}JT_{0.5}$ in the temperature range of 150 °C to 90 °C.

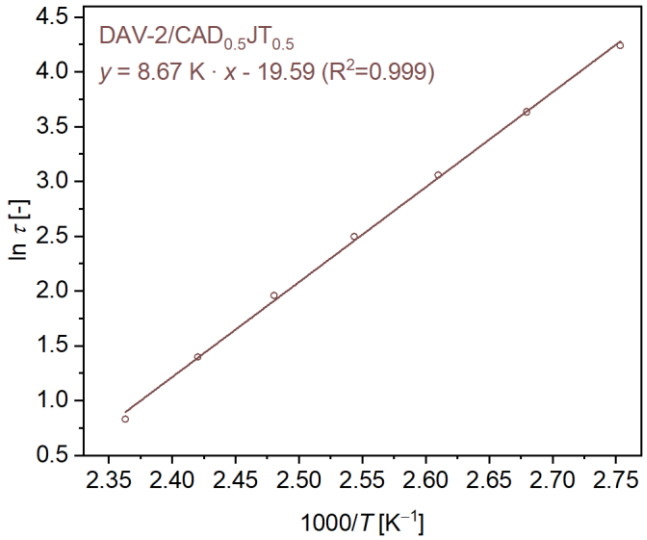

Figure S44. Plot of ln τ versus 1000/T to calculate the activation energies from the slope of the linear fit of the measured τ values for Schiff base vitrimer DAV-2/$CAD_{0.5}JT_{0.5}$ in the temperature range of 150 °C to 90 °C.

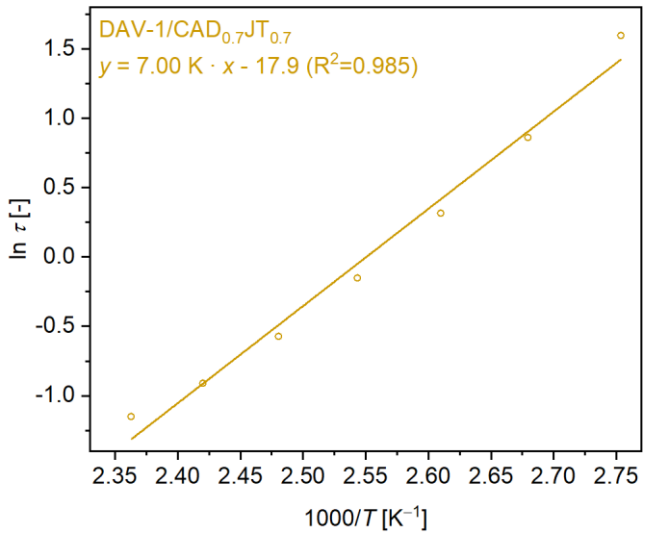

Figure S45. Plot of ln τ versus 1000/T to calculate the activation energies from the slope of the linear fit of the measured τ values for Schiff base vitrimer DAV-1/$CAD_{0.7}JT_{0.7}$ in the temperature range of 150 °C to 90 °C.

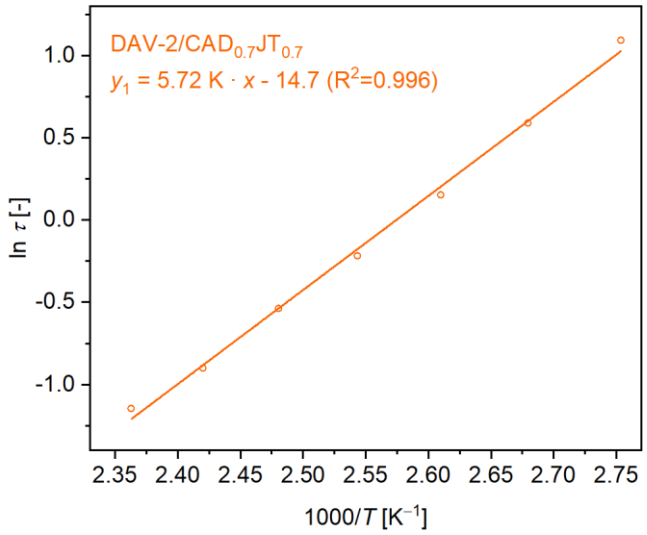

Figure S46. Plot of ln τ versus 1000/T to calculate the activation energies from the slope of the linear fit of the measured τ values for Schiff base vitrimer DAV-2/$CAD_{0.7}JT_{0.7}$ in the temperature range of 150 °C to 90 °C.

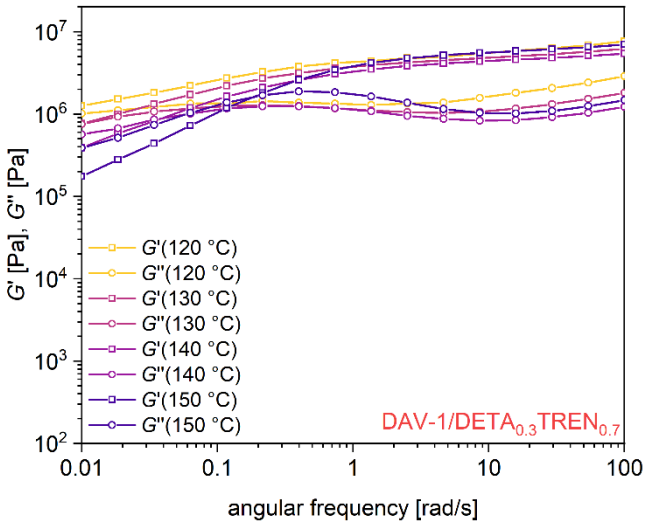

Figure S47. Frequency sweep measurement of Schiff base vitrimer DAV-1/DETA$_{0.3}$TREN$_{0.7}$ in the temperature range of 150 °C to 120 °C and the frequency range of 100 rad s^{-1} to 0.01 rad s^{-1}.

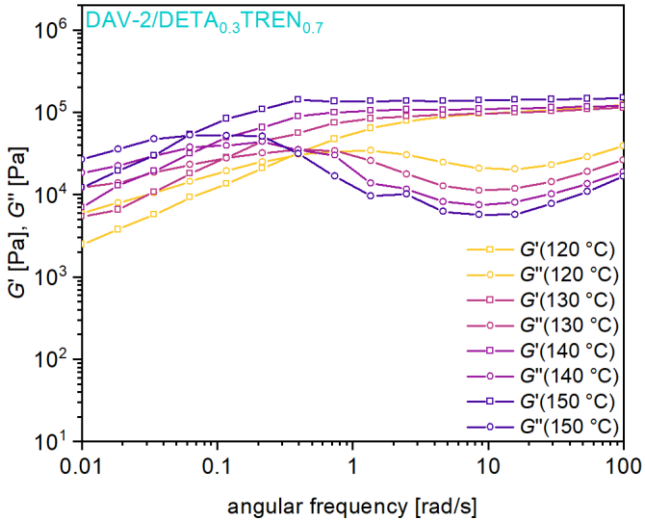

Figure S48. Frequency sweep measurement of Schiff base vitrimer DAV-2/DETA$_{0.3}$TREN$_{0.7}$ in the temperature range of 150 °C to 120 °C and the frequency range of 100 rad s^{-1} to 0.01 rad s^{-1}.

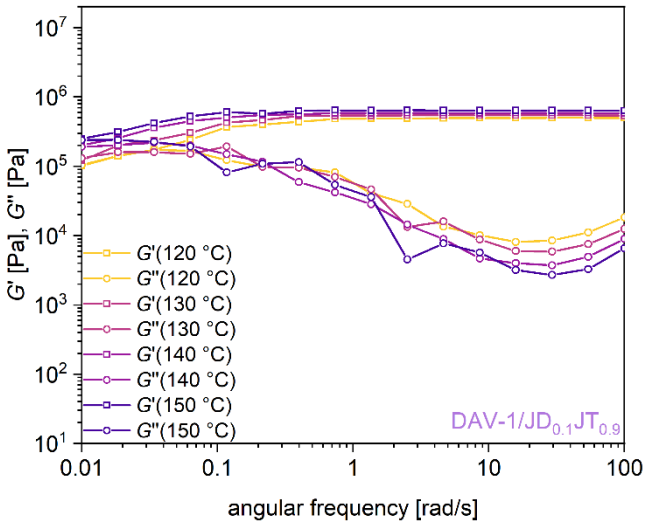

Figure S49. Frequency sweep measurement of Schiff base vitrimer DAV-1/$JD_{0.1}JT_{0.9}$ in the temperature range of 150 °C to 120 °C and the frequency range of 100 rad s^{-1} to 0.01 rad s^{-1}.

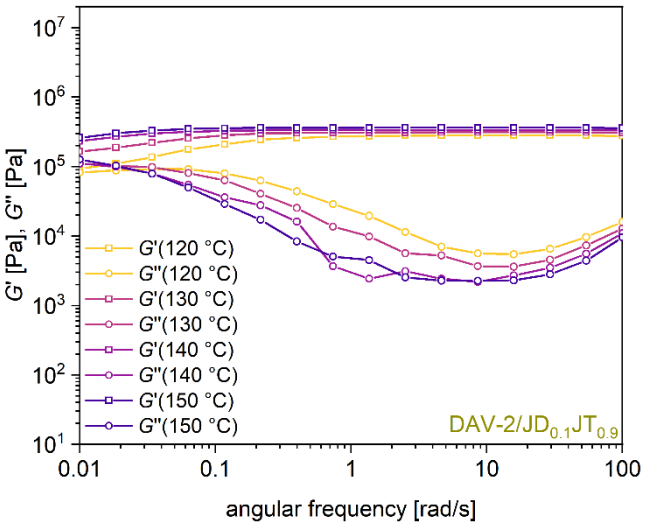

Figure S50. Frequency sweep measurement of Schiff base vitrimer DAV-2/$JD_{0.1}JT_{0.9}$ in the temperature range of 150 °C to 120 °C and the frequency range of 100 rad s^{-1} to 0.01 rad s^{-1}.

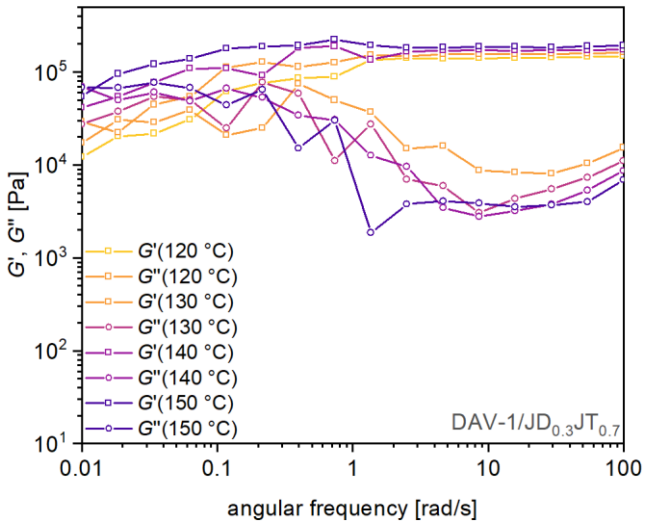

Figure S51. Frequency sweep measurement of Schiff base vitrimer DAV-1/$JD_{0.3}JT_{0.7}$ in the temperature range of 150 °C to 120 °C and the frequency range of 100 rad s^{-1} to 0.01 rad s^{-1}.

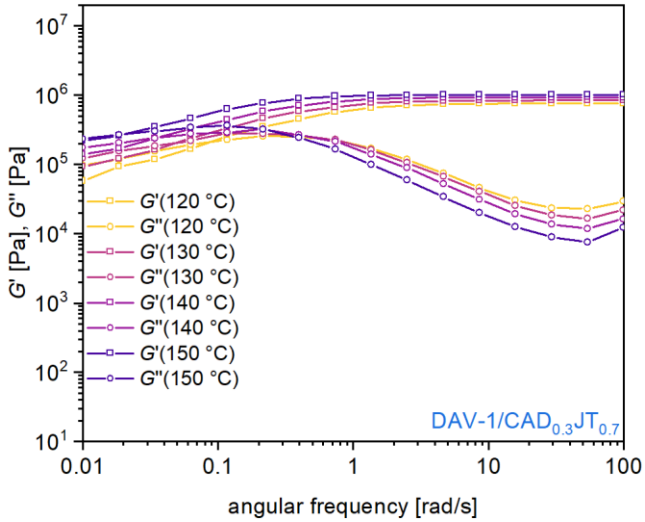

Figure S52. Frequency sweep measurement of Schiff base vitrimer DAV-1/$CAD_{0.3}JT_{0.7}$ in the temperature range of 150 °C to 120 °C and the frequency range of 100 rad s^{-1} to 0.01 rad s^{-1}.

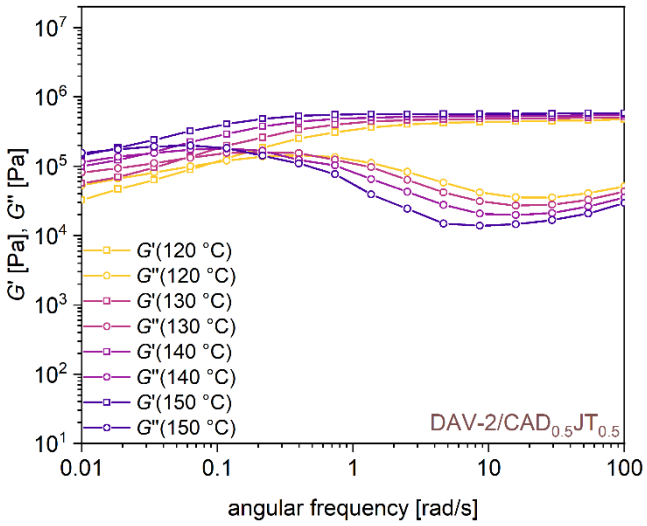

Figure S53. Frequency sweep measurement of Schiff base vitrimer DAV-2/$CAD_{0.5}JT_{0.5}$ in the temperature range of 150 °C to 120 °C and the frequency range of 100 rad s^{-1} to 0.01 rad s^{-1}.

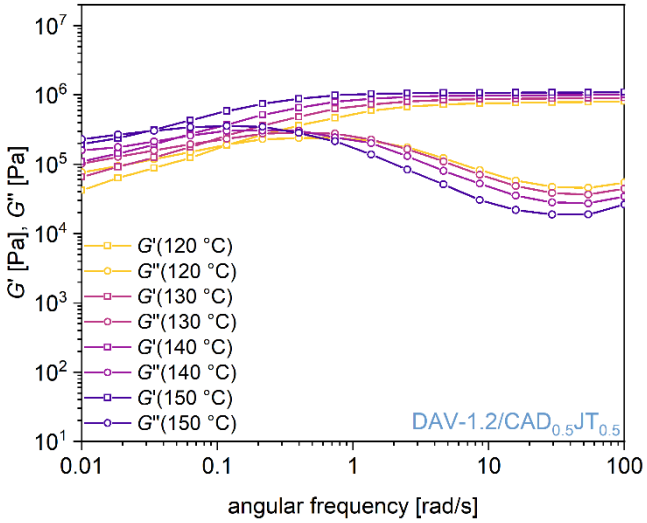

Figure S54. Frequency sweep measurement of Schiff base vitrimer DAV-1.2/$CAD_{0.5}JT_{0.5}$ in the temperature range of 150 °C to 120 °C and the frequency range of 100 rad s^{-1} to 0.01 rad s^{-1}.

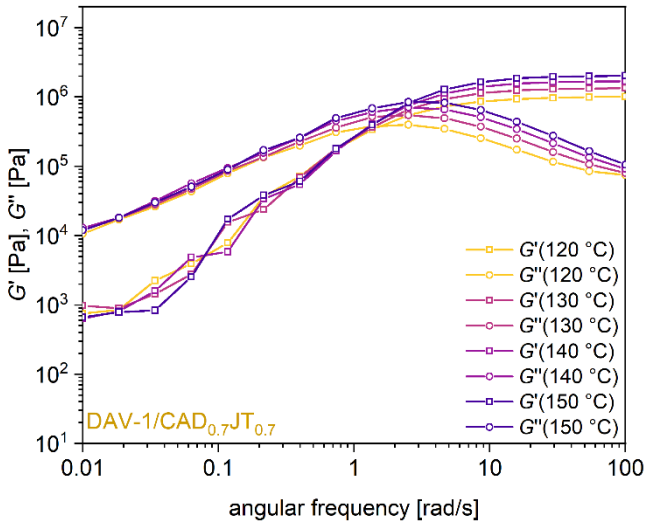

Figure S55. Frequency sweep measurement of Schiff base vitrimer DAV-1/$CAD_{0.7}JT_{0.7}$ in the temperature range of 150 °C to 120 °C and the frequency range of 100 rad s^{-1} to 0.01 rad s^{-1}.

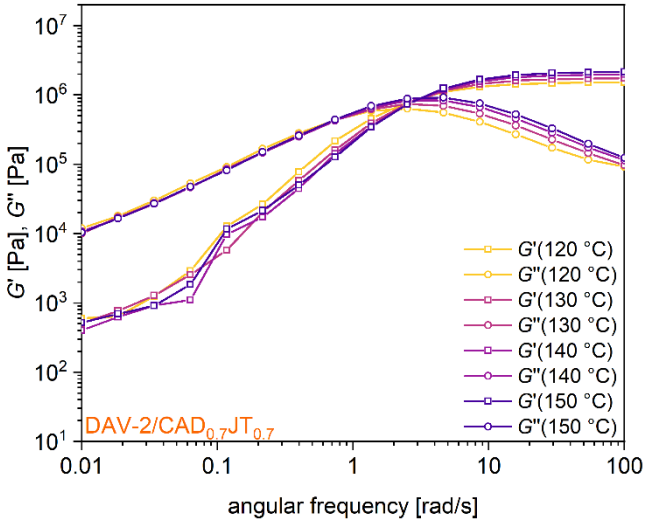

Figure S56. Frequency sweep measurement of Schiff base vitrimer DAV-2/$CAD_{0.7}JT_{0.7}$ in the temperature range of 150 °C to 120 °C and the frequency range of 100 rad s^{-1} to 0.01 rad s^{-1}.

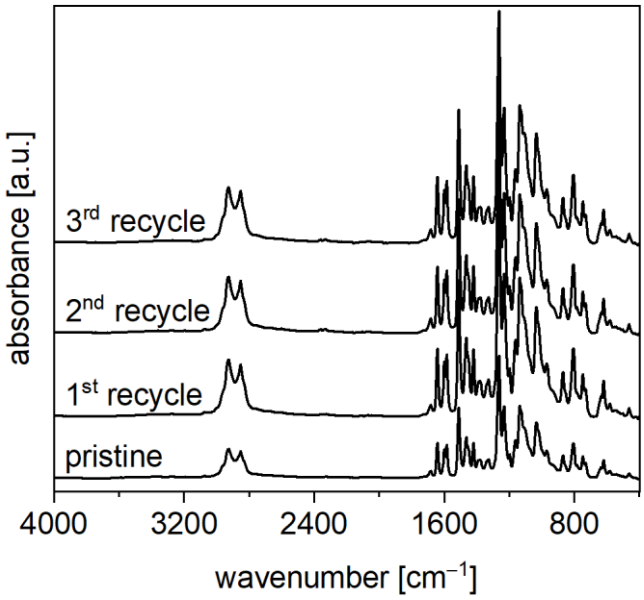

Figure S57. Demonstration of reprocessing of the Schiff base vitrimer films by consecutive grinding and heat compression molding (150 °C, 30 min, 10 kN), generating homogeneous, bubble-free recycled films. ATR-FT-IR spectra of the exemplary reprocessing cycles display the identity of the recycled material and the pristine material DAV-1.2/$CAD_{0.5}JT_{0.5}$.

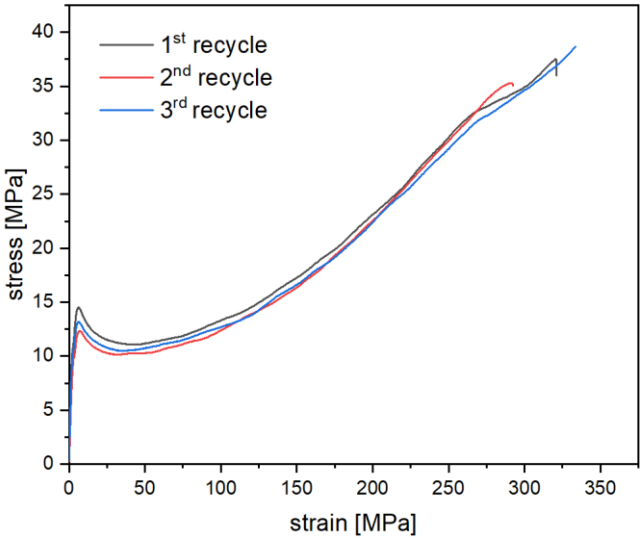

Figure S58. Demonstration of reprocessing of the Schiff base vitrimer films by consecutive grinding and heat compression molding (150 °C, 30 min, 10 kN), generating homogeneous, bubble-free recycled films. Repetitive stress-strain measurements of the recycled material and the pristine material DAV-1.2/$CAD_{0.5}JT_{0.5}$ show stable values of stress and strain behavior.

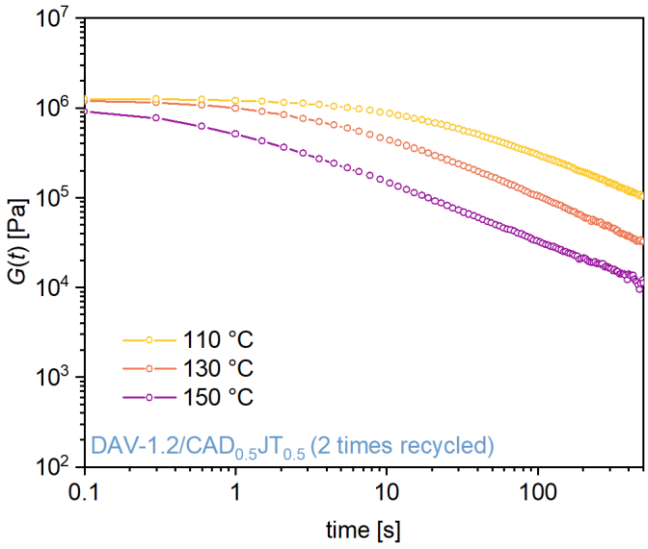

Figure S59. Stress-relaxation measurement of Schiff base vitrimer film DAV-1.2/$CAD_{0.5}JT_{0.5}$ after two consecutive recycling cycles plotting the non-normalized stress-relaxation modulus $G(t)$ versus the stress-relaxation time measured at 110 °C, 130 °C, and 150 °C while applying a shear strain of 1%.

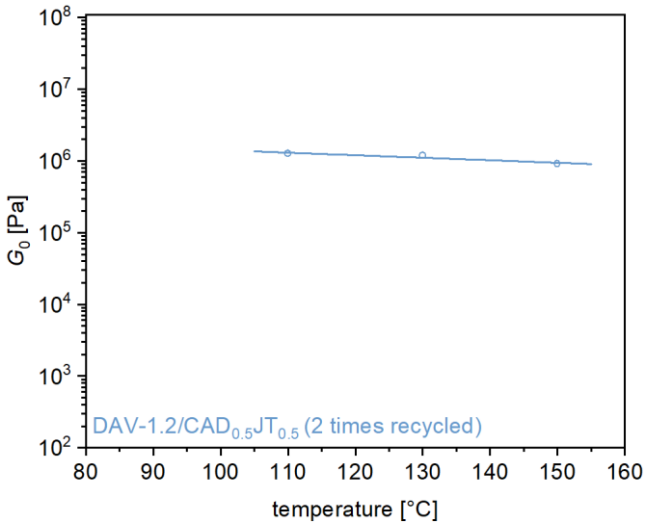

Figure S60. Initial relaxation moduli G_0 of the Schiff base vitrimer DAV-1.2/$CAD_{0.5}JT_{0.5}$ after two consecutive recycling cycles as a function of temperature.

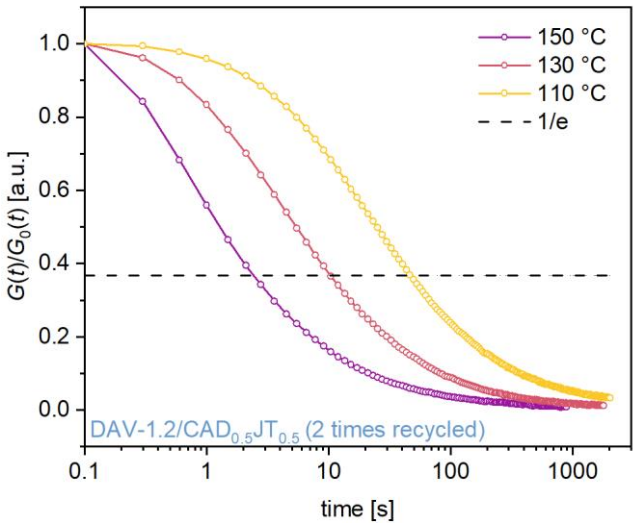

Figure S61. Stress-relaxation measurement of Schiff base vitrimer film DAV-1.2/$CAD_{0.5}JT_{0.5}$ after two consecutive recycling cycles plotting the normalized stress-relaxation modulus $G(t)$ versus the stress-relaxation time measured at 110 °C, 130 °C, and 150 °C while applying a shear strain of 1%. The dashed line indicates 37% of the normalized stress relaxation.

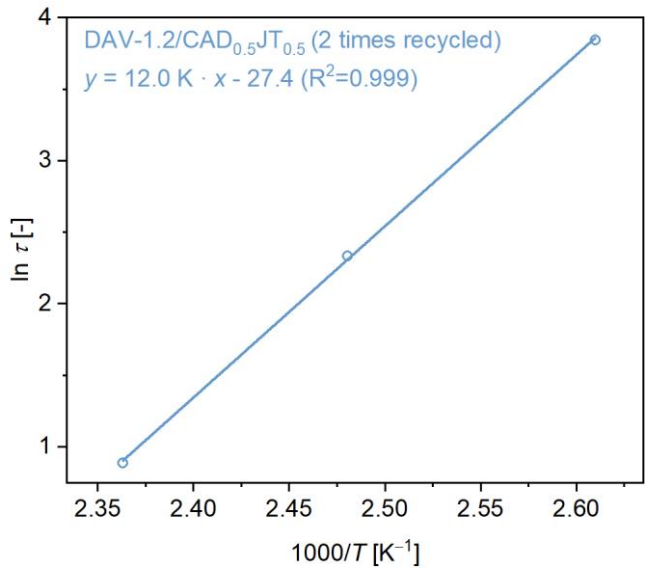

Figure S62. Plot of ln τ versus 1000/T to calculate the activation energies from the slope of the linear fit of the τ values for Schiff base vitrimer DAV-1.2/$CAD_{0.5}JT_{0.5}$ after two consecutive recycling cycles measured at 110 °C, 130 °C, and 150 °C.

Table S4. Soluble fractions (SFs) of Schiff base vitrimer DAV-1.2/$CAD_{0.5}JT_{0.5}$ after two consecutive recycling cycles in the different solvents in tetrahydrofuran (THF), methanol (MeOH), dimethylformamide (DMF), and water (H_2O).

Schiff base vitrimer film	THF	MeOH	DMF	H_2O[a)]
	SF [wt.%]	SF [wt.%]	SF [wt.%]	SF [wt.%]
DAV-1.2/$CAD_{0.5}JT_{0.5}$	100	0.7	2.3	-

a) Soluble fractions were not detectable after immersion in deionized water for 24 h.

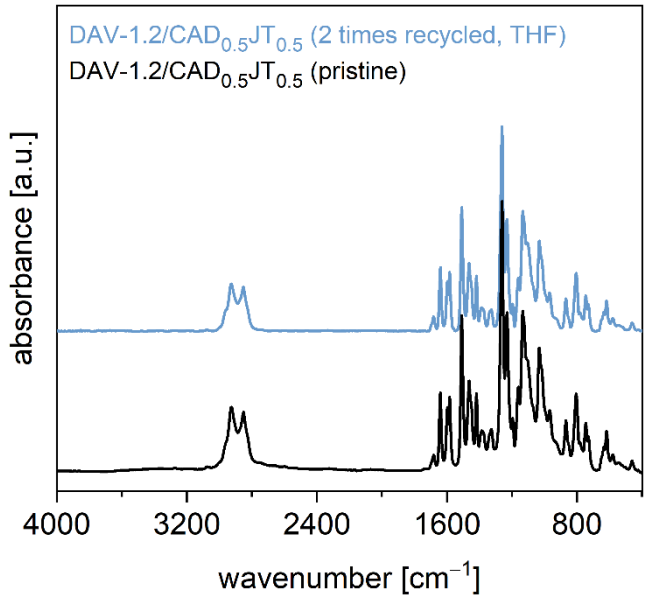

Figure S63. Demonstration of reformation of a polymeric Schiff base vitrimer film DAV-1.2/$CAD_{0.5}JT_{0.5}$. ATR-FT-IR spectra displays the comparability of the recycled material DAV-1.2/$CAD_{0.5}JT_{0.5}$ after two consecutive recycling cycles, immersion in THF, and subsequent drying, and the pristine material DAV-1.2/$CAD_{0.5}JT_{0.5}$.

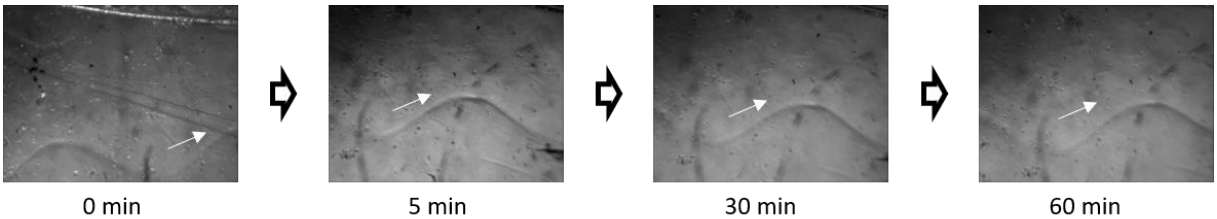

Figure S64. Optical microscopy images of scratched (position of scratch is indicated with a white arrow on every picture) Schiff base vitrimer DAV-1/$CAD_{0.5}JT_{0.5}$ after different times of storage at 120 °C. After 60 min self-healing of the Schiff base vitrimers was successfully demonstrated. The texture is due to the teflon sheets used.

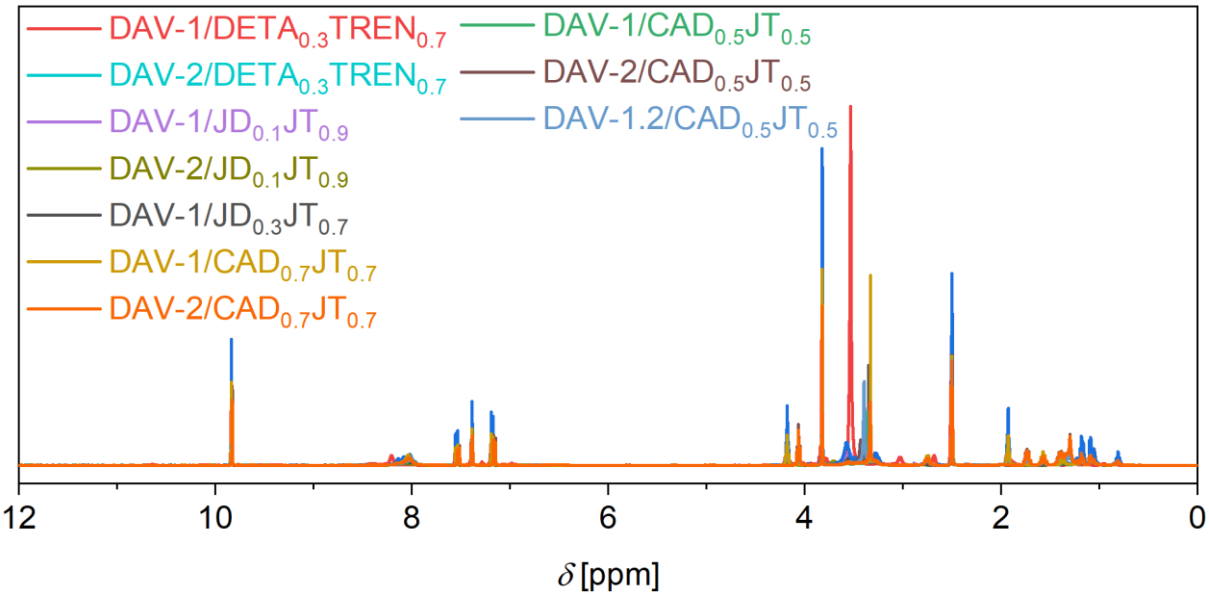

Figure S65. ^{1}H NMR (500 MHz, DMSO-D_6, 298 K) spectra of the white residue of the degradation experiment of the Schiff base vitrimer films. The samples showed decross-linking, fragmentation and white residues after exposition to mild acidic solution (0.1 M HCl) for 16 hours at room temperature, which can be observed by aldehyde peaks (9.8 ppm) of the aromatic DAV building blocks (7.56 ppm – 7 ppm), and free amines (1 ppm – 2 ppm). The region between 0.8 ppm and 4.3 ppm comprises the residual peaks of the amine building blocks and the DAV-dialdehydes. Signals in the region of 8.3 ppm – 8 ppm indicate imine bonds, indicating that some covalent bonds are still intact after the degradation. Longer degradation times or stirring at the degradation process could improve the chemical recycling performance.

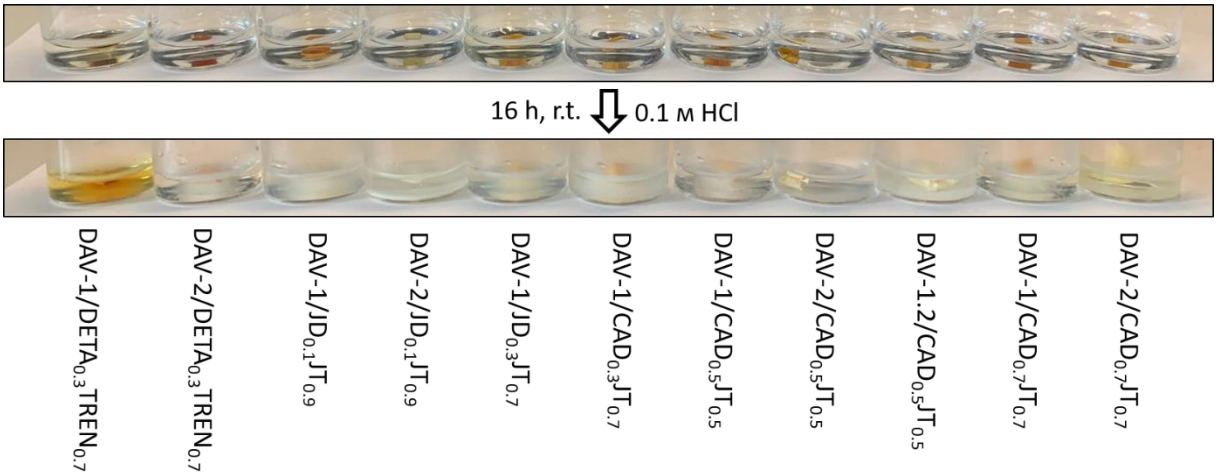

Figure S66. Degradation experiment of the Schiff base vitrimer films. The samples showed decross-linking, fragmentation and white residues after exposition to mild acidic solution (0.1 M HCl) for 16 hours at room temperature.

9.3 Publication 2 – Supporting Information

The publication is reprinted with permission from F. Klein, N. Sobania, and V. Abetz, *J. Mater. Chem. A*, **2025**, *13*, 29120–29137, with permission from the Royal Society of Chemistry.

Supplementary Information (SI) for Journal of Materials Chemistry A.

Supporting Information

Bio-Based Vinylogous Urethane Vitrimers from Waste-Wood Lignosulfonate and Enzymatic Lignin: Explorations in Stress Relaxation Behavior and Mechanical Strength

*Florian C. Klein, Nils Sobania, and Volker Abetz**

Table S1: Summary of the masses of the educts, the grinding, and the heat compression conditions of the lignin vitrimer samples.

Sample[a)]	**Acetoacetylated Lignin** Species Mass	**APPD** Mass	**Priamine™ 1073** Mass	**Grinding** Condition Frequency Duration	**Heat compression** Temperature Duration Pressure
VU-(ALs-Pri)$_{0.4}$	ALs 1.333 g	-	1.588 g	Cryogenic 20 Hz 60 s	160 °C 30 min 1.9 MPa
VU-(ALs-Pri)$_{0.5}$	ALs 1.467 g	-	1.482 g	Cryogenic 20 Hz 60 s	150 °C 30 min 1.9 MPa
VU-(ALs-Pri)$_{0.6}$	ALs 1.586 g	-	1.361 g	Cryogenic 20 Hz 60 s	150 °C 30 min 1.9 MPa
VU-(ALs/APPD$_5$-Pri)$_{0.6}$	ALs 1.549 g	0.153 g	1.327 g	Ambient 20 Hz 60 s	180 °C 30 min 1.9 MPa
VU-(ALs/APPD$_{10}$-Pri)$_{0.6}$	ALs 1.388 g	0.304 g	1.319 g	Cryogenic 20 Hz 60 s	180 °C 30 min 1.9 MPa
VU-(ALs/APPD$_{15}$-Pri)$_{0.6}$	ALs 1.223 g	0.459 g	1.321 g	Cryogenic 20 Hz 60 s	180 °C 30 min 1.9 MPa
VU-(ALnC-Pri)$_{0.7}$	ALnC 1.505 g	-	1.494 g	Ambient 30 Hz 60 s	180 °C 30 min 2.5 MPa
VU-(ALnC-Pri)$_{0.8}$	ALnC 1.608 g	-	1.408 g	Ambient 30 Hz 60 s	180 °C 30 min 2.5 MPa
VU-(ALnC-Pri)$_{0.9}$	ALnC 1.699 g	-	1.309 g	Ambient 30 Hz 60 s	180 °C 30 min 2.5 MPa
VU-(ALnP-Pri)$_{0.7}$	ALnP 1.665 g	-	1.331 g	Ambient 30 Hz 60 s	180 °C 30 min 2.5 MPa
VU-(ALnP-Pri)$_{0.8}$	ALnP 1.764 g	-	1.231 g	Ambient 30 Hz 60 s	180 °C 30 min 2.5 MPa
VU-(ALnP-Pri)$_{0.9}$	ALnP 1.848 g	-	1.150 g	Ambient 30 Hz 60 s	180 °C 30 min 2.5 MPa

a) The lignin vitrimers were abbreviated following this nomenclature: First, the vinylogous urethane chemistry is introduced (VU), then, the lignin source (ALs/ALnC/ALnP) and the Priamine™ 1073 (Pri) are abbreviated, and the *R*-value (acetoacetate/amine ratio) is displayed in the index.

Figure S1: A heat compression mold with a diameter of 5 cm was used for the reprocessing of the vitrimers.

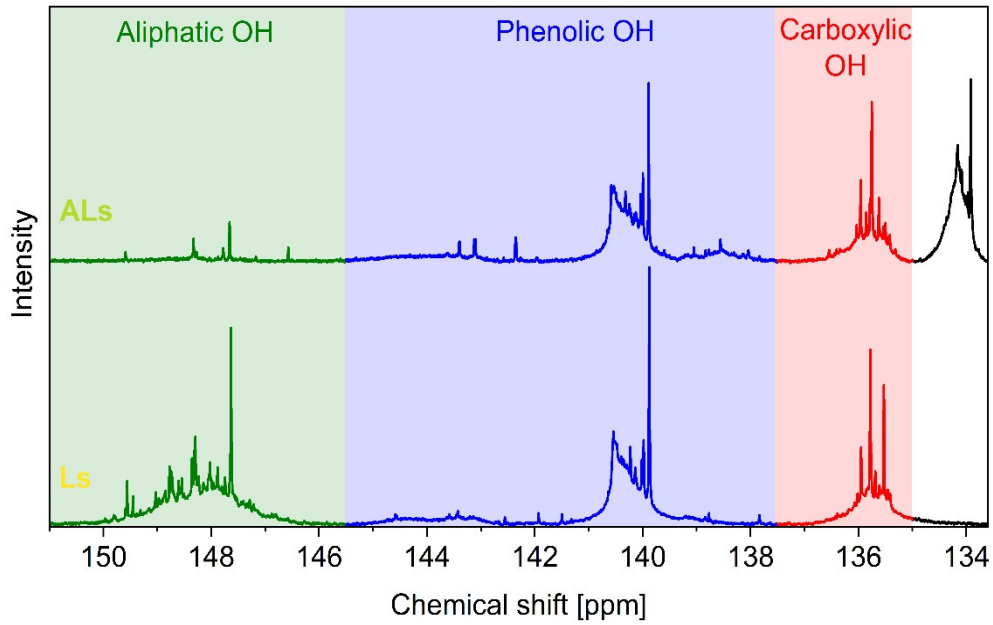

Figure S2: ^{31}P NMR spectra of lignosulfonate (bottom) and acetoacetylated lignosulfonate (top). The regions corresponding to aliphatic (green), phenolic (blue), and carboxylic (red) hydroxy groups are indicated. Notably, the intensity of the aliphatic hydroxy groups is decreased in the corresponding acetoacetylated species. A broad range of signals around 134 ppm appears as a result of the enolization of the acetoacetate moieties. ^{31}P NMR (243 MHz, DMF-d_7/DMF/pyridine, 298 K). Preparations and measurements were carried out according to the procedure outlined in the experimental section, using DMF as the solvent.

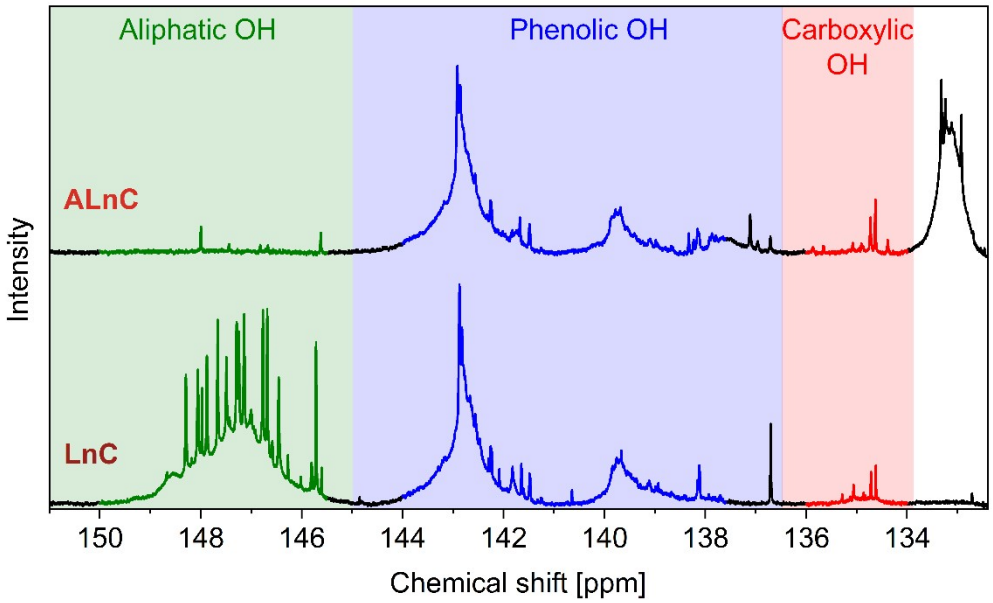

Figure S3: ^{31}P NMR spectra of Lignova™ Crude (bottom) and acetoacetylated Lignova™ Crude (top). The regions corresponding to aliphatic (green), phenolic (blue), and carboxylic (red) hydroxy groups are indicated. Notably, the intensity of the aliphatic hydroxy groups is decreased in the corresponding acetoacetylated species. A broad range of signals around 133 ppm is observed as a result of the enolization of the acetoacetate moieties.^{31}P NMR (243 MHz, $CDCl_3$/pyridine, 298 K). Preparations and measurements were conducted following the procedure outlined in the experimental section, using $CDCl_3$ as the solvent.

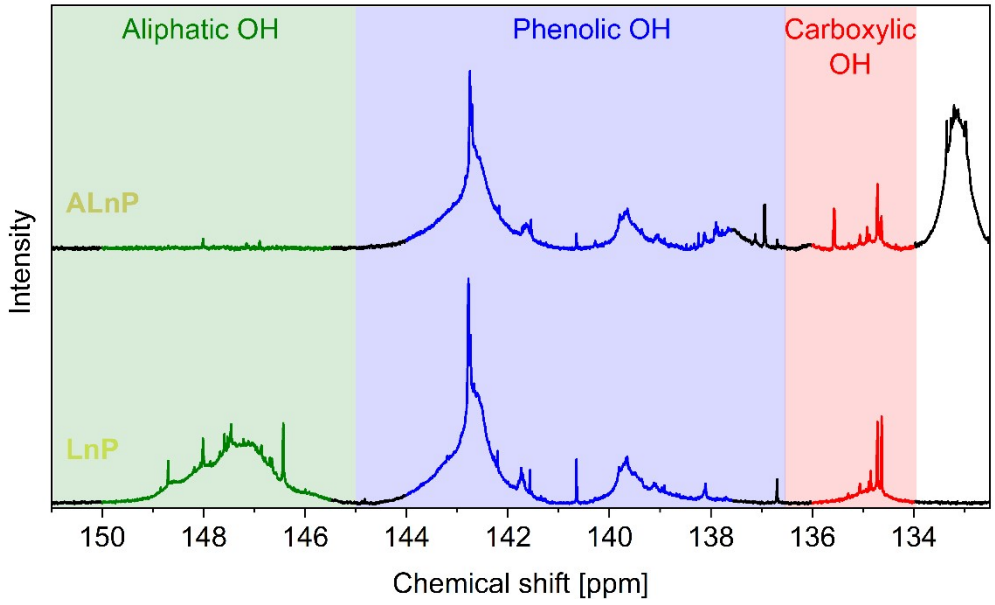

Figure S4: ^{31}P NMR spectra of Lignova™ Pure (bottom) and acetoacetylated Lignova™ Pure (top). The regions corresponding to aliphatic (green), phenolic (blue), and carboxylic (red) hydroxy groups are indicated. Notably, the intensity of the aliphatic hydroxy groups is decreased in the corresponding acetoacetylated species. A broad array of signals around 133 ppm appears as a result of the enolization of the acetoacetate moieties.^{31}P NMR (243 MHz, $CDCl_3$/pyridine, 298 K). Preparation and measurements were conducted in accordance with the procedure described in the experimental section, using $CDCl_3$ as the solvent.

Equation S1

$$\text{OH group moieties [mmol/g]} = \frac{n_{OH}}{m_{Lignin}} = \frac{I_{OH}}{I_{NHND}} \cdot \frac{n_{NHND,NMR}}{m_{Lignin,NMR}}$$

n_{OH} : Amount of hydroxy groups [mmol]
m_{Lignin} : Mass of lignin [g]
I_{OH} : Integral of spectral region of OH moieties [-]
I_{NHND} : Integral of NHND region [-]
$n_{NHND,NMR}$: Amount of NHND in the NMR sample [mmol]
$m_{Lignin,NMR}$: Mass of lignin in the NMR sample [g]

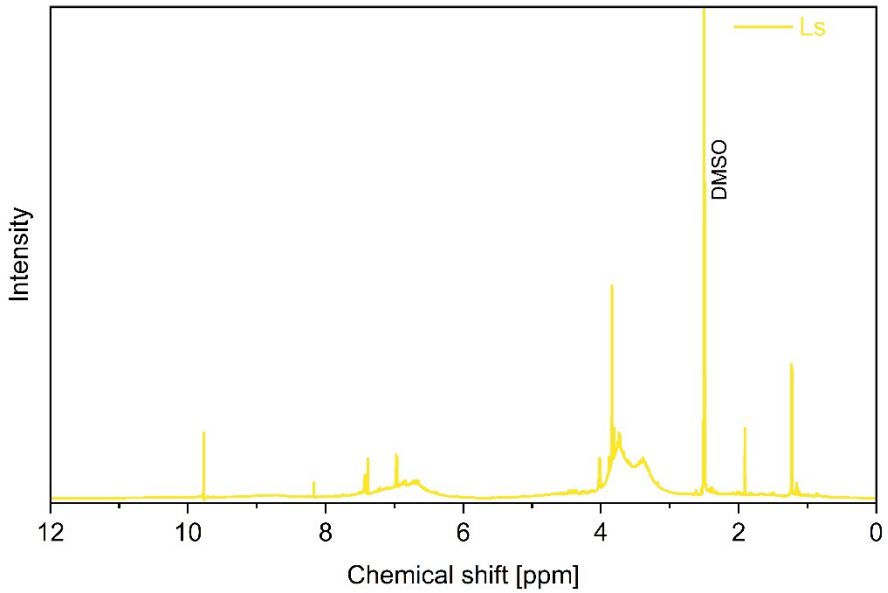

Figure S5: The ^{1}H NMR spectrum of lignosulfonate displays the characteristic signals and intensities associated with the lignin backbone. ^{1}H NMR (400 MHz, DMSO-d_6, 298 K)

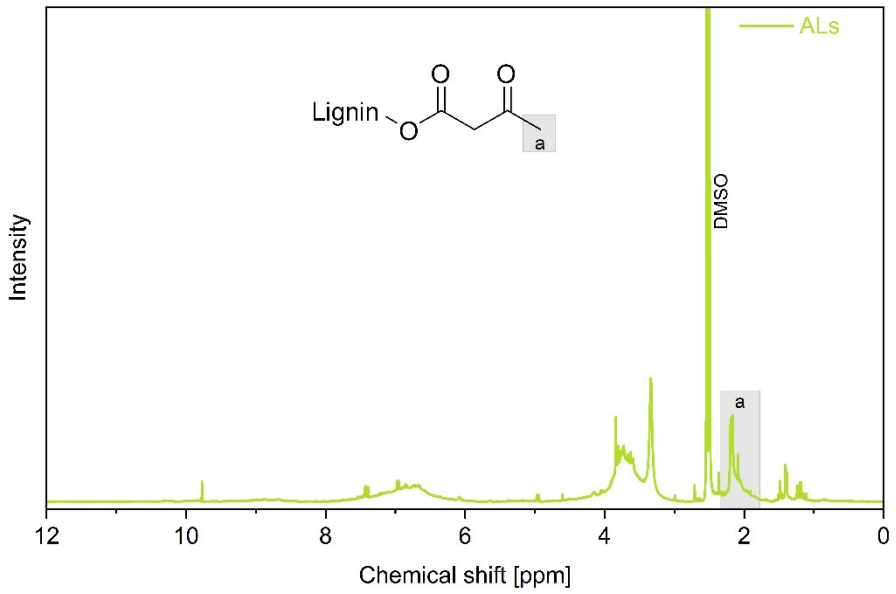

Figure S6: The ^{1}H NMR spectrum of acetoacetylated lignosulfonate shows the methyl group of the acetoacetate moieties, along with the characteristic signals and intensities of the lignin backbone. The signal corresponding to the methyl group of the acetoacetate moieties is indicated in gray.^{1}H NMR (600 MHz, DMSO-d_6, 298 K)

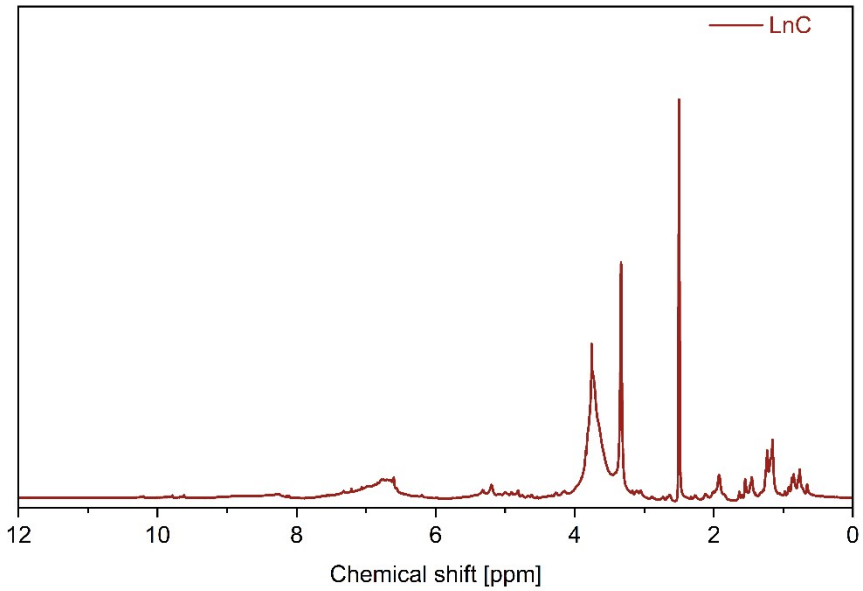

Figure S7: The ^{1}H NMR spectrum of Lignova™ Crude displays the characteristic signals and intensities associated with the lignin backbone. ^{1}H NMR (400 MHz, DMSO-d_6, 298 K).

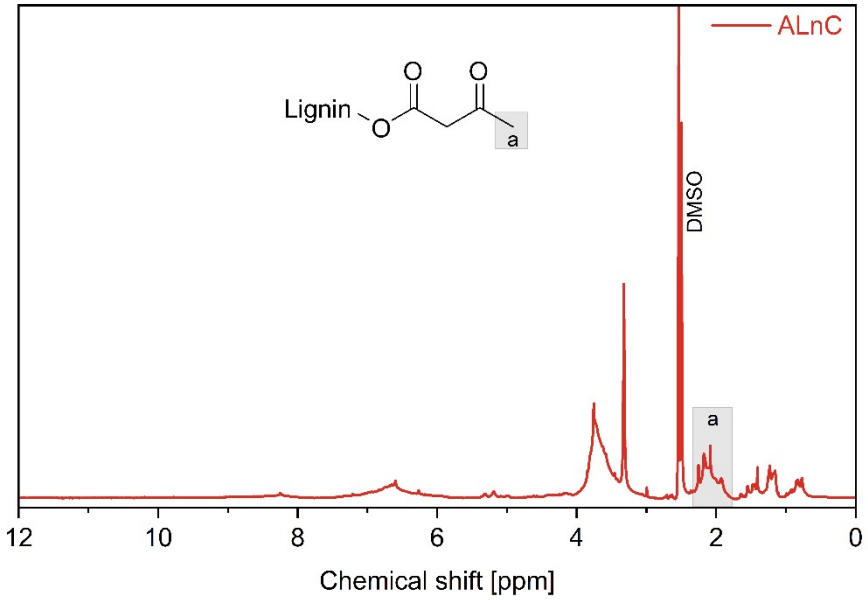

Figure S8: The ^{1}H NMR spectrum of acetoacetylated Lignova™ Crude shows the characteristic signals and intensities of the lignin backbone. The signal corresponding to the methyl group of the acetoacetate moieties is indicated in grey. ^{1}H NMR (400 MHz, DMSO-d_6, 298 K).

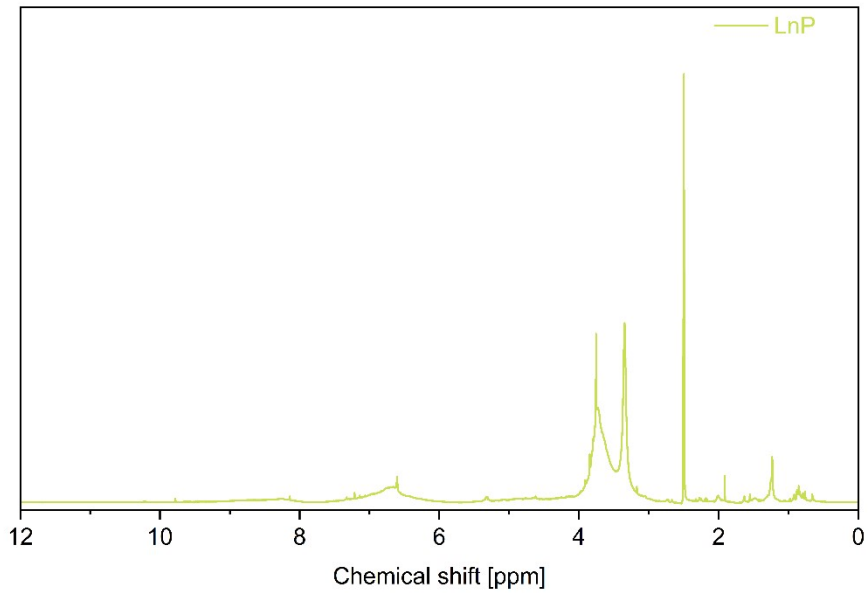

Figure S9: ^{1}H NMR spectrum of Lignova^{TM} Crude displays the characteristic signals and intensities associated with the lignin backbone. ^{1}H NMR (400 MHz, DMSO-d_6, 298 K).

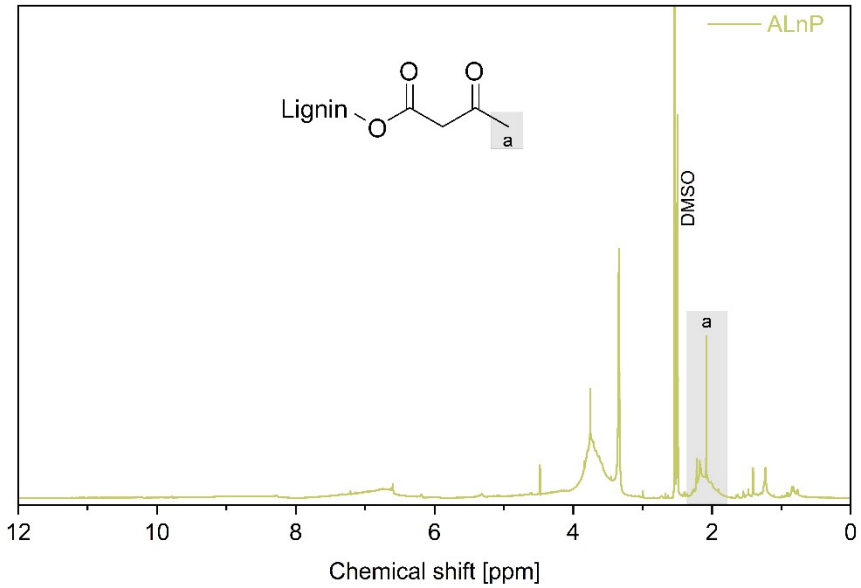

Figure S10: ^{1}H NMR spectrum of acetoacetylated Lignova^{TM} Pure displays the characteristic signals and intensities associated with the lignin backbone. The signal corresponding to the methyl group of the acetoacetate moieties is indicated in grey. ^{1}H NMR (400 MHz, DMSO-d_6, 298 K).

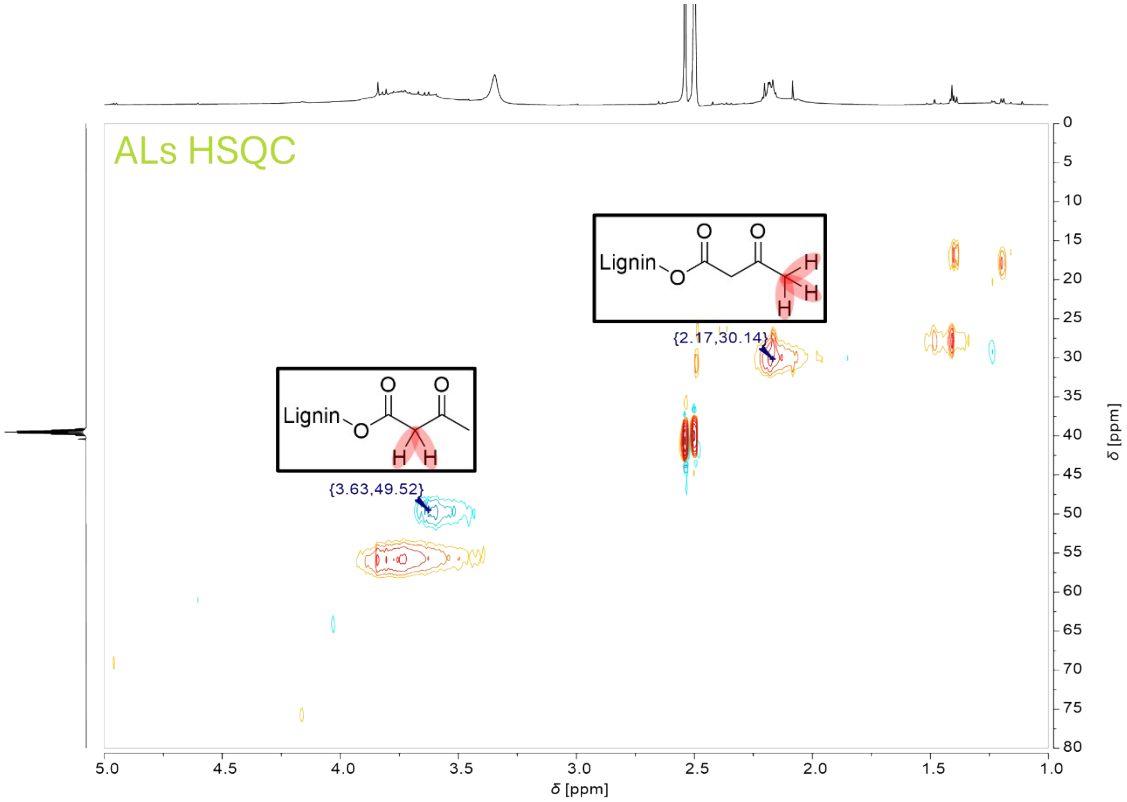

Figure S11: HSQC spectrum of Als. The ^{1}J couplings of the terminal methyl group and the ^{1}J of the methylene group of the acetoacetate functionalities are presented. Measured with an AVIII600 600 MHz spectrometer in DMSO-d_6.

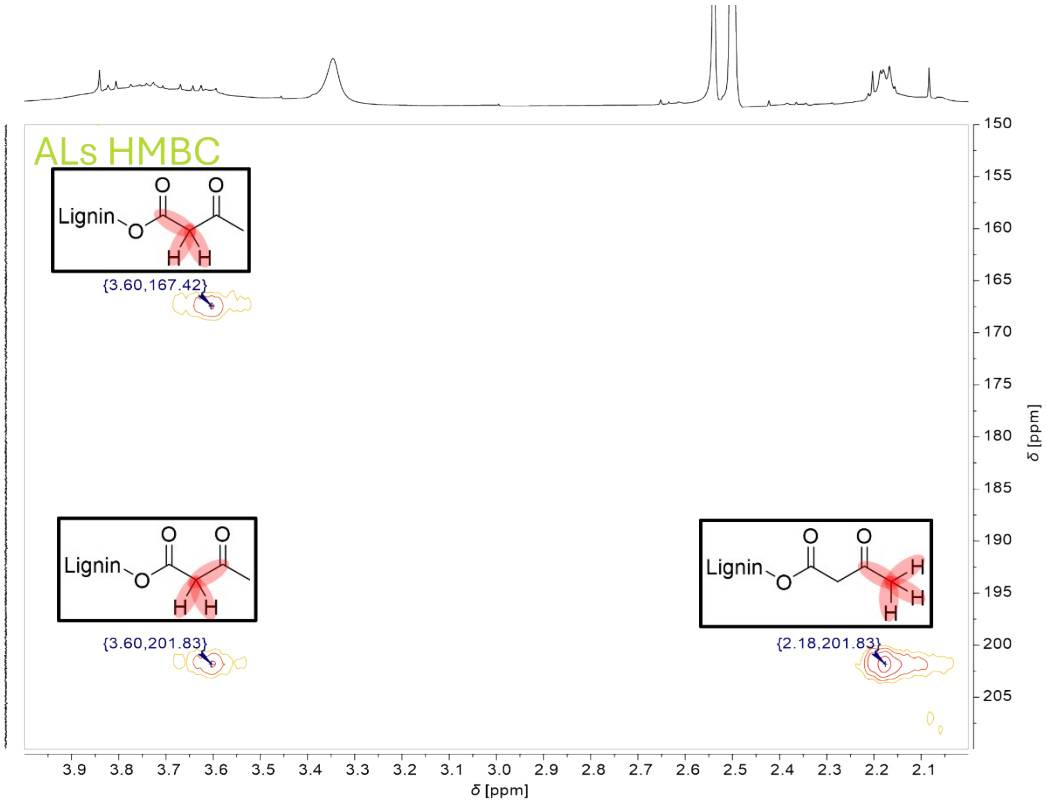

Figure S12: HMBC spectrum of ALs. The respective ^{2}J couplings of acetoacetate moieties indicated in the structure above respective signals are presented. Measured with an AVIII600 600 MHz spectrometer in DMSO-d_6.

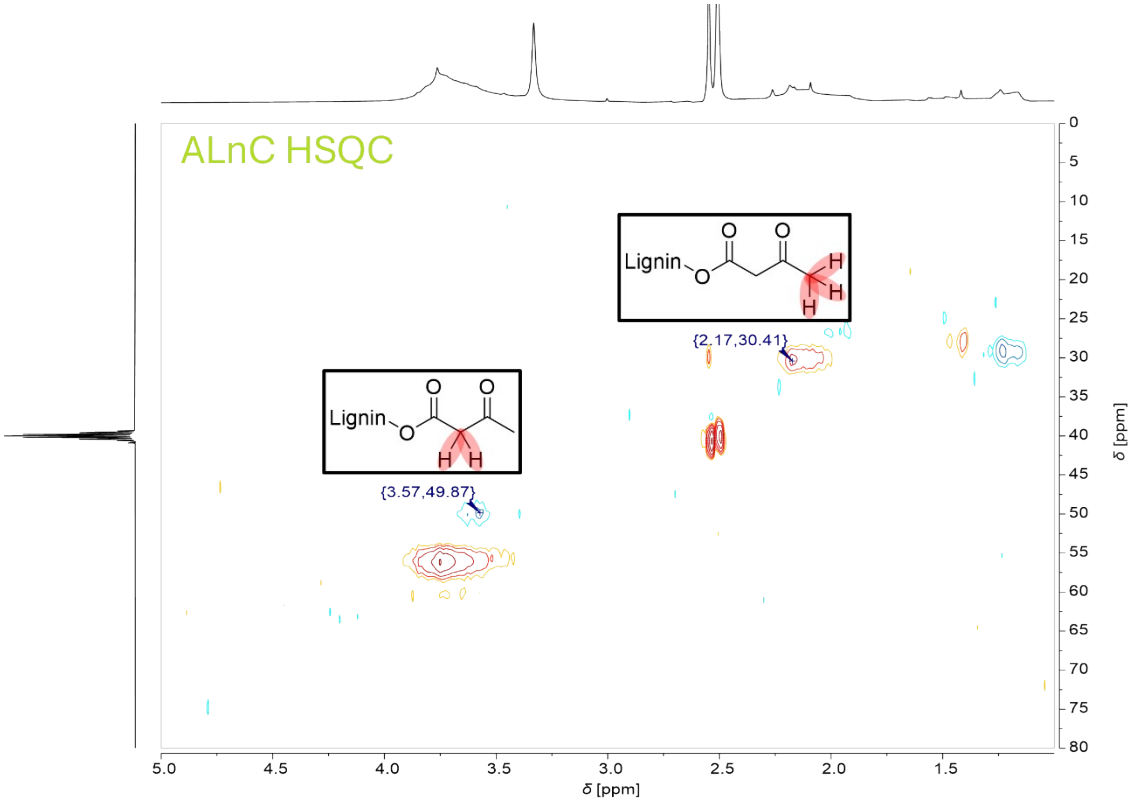

Figure S13: HSQC spectrum of ALnC. The ^{1}J couplings of the terminal methyl group and the ^{1}J of the methylene group of the acetoacetate functionalities are presented. Measured with an AVIII 400 MHz NMR spectrometer in DMSO-d_6.

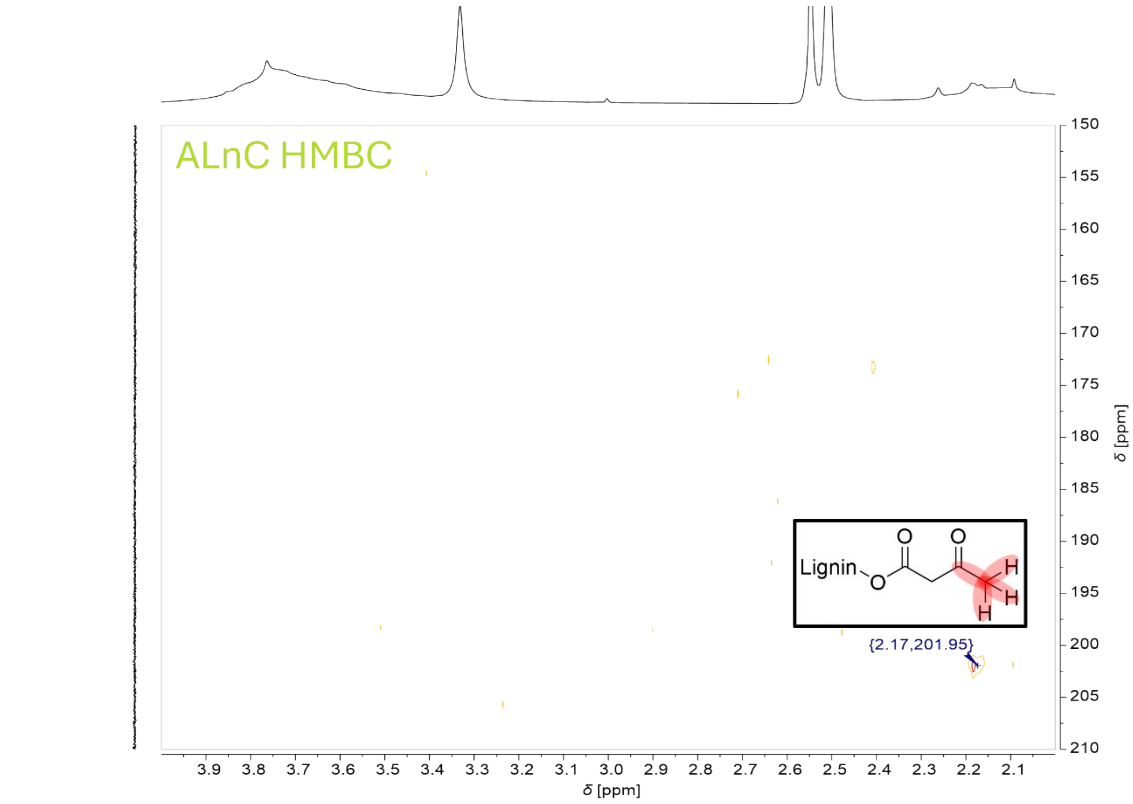

Figure S14: HMBC spectrum of ALnC. The corresponding ^{2}J coupling of the acetoacetate moieties is indicated in the structure above the respective signal. Measured with an AVIII 400 MHz NMR spectrometer in DMSO-d_6.

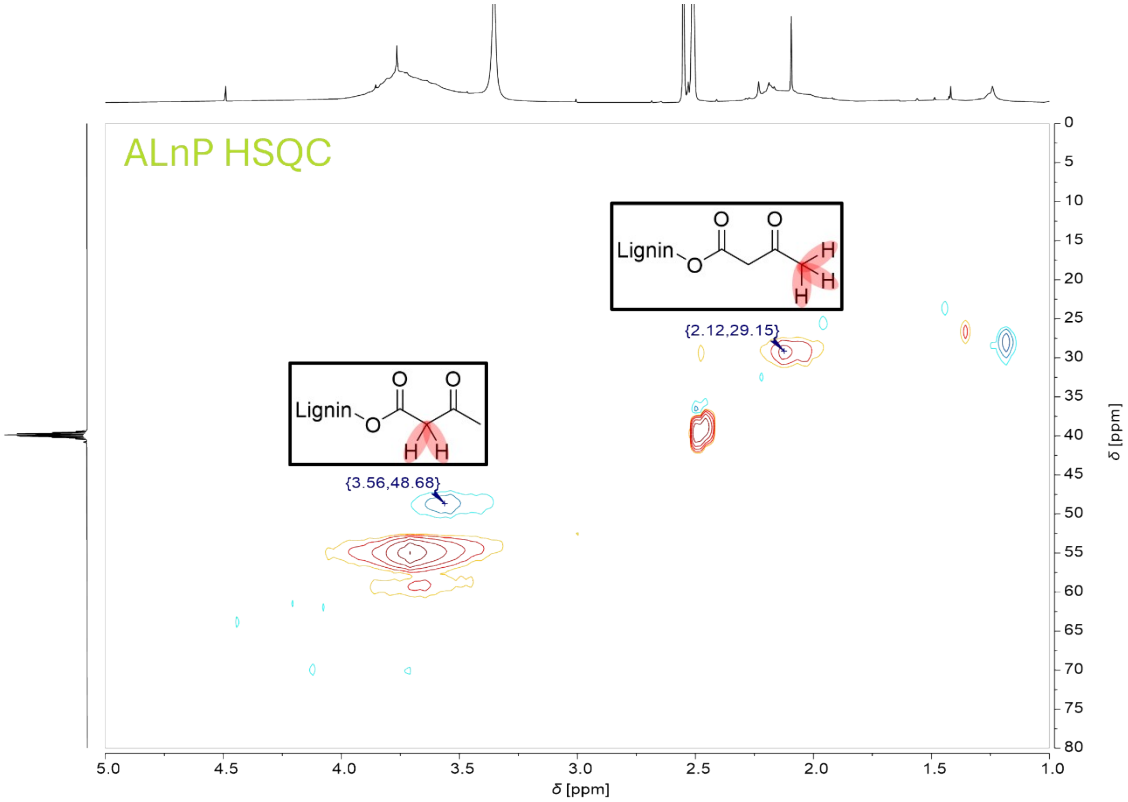

Figure S15: HSQC spectrum of ALnP. The ^{1}J couplings of the terminal methyl group and the ^{1}J of the methylene group of the acetoacetate functionalities are presented. Measured with an AV500 NMR spectrometer at 500 MHz in DMSO-d_6.

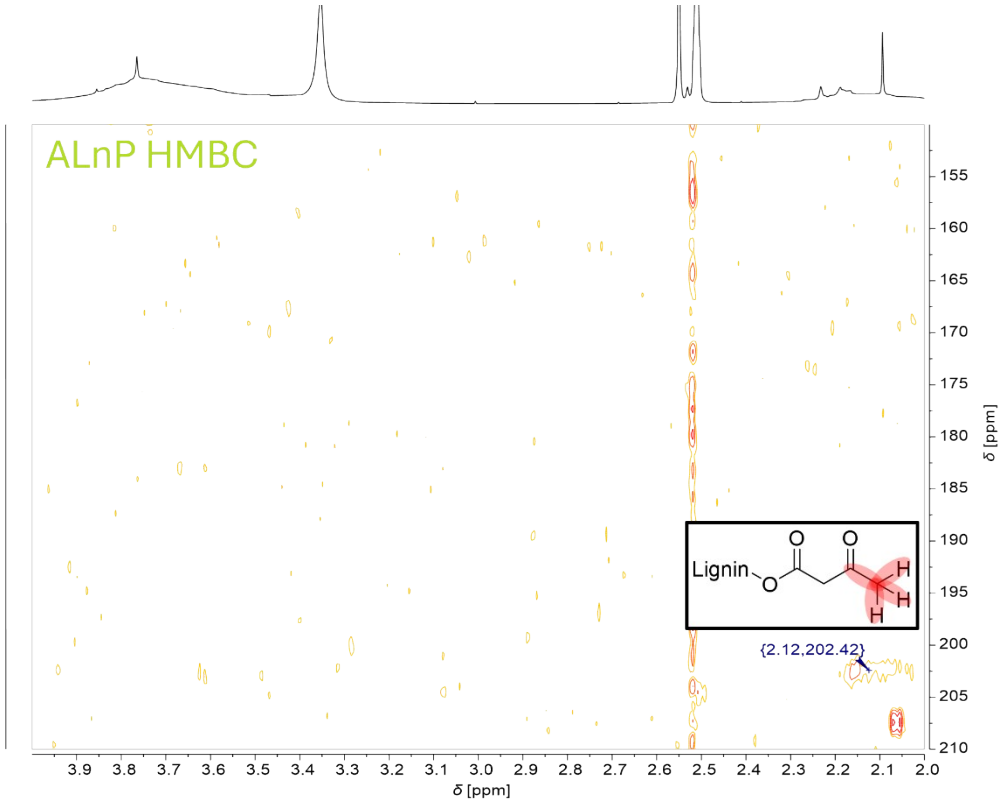

Figure S16: HMBC spectrum of ALnP. The corresponding ^{2}J coupling of the acetoacetate moieties is indicated in the structure above the respective signal. Measured with an AV500 NMR spectrometer at 500 MHz in DMSO-d_6.

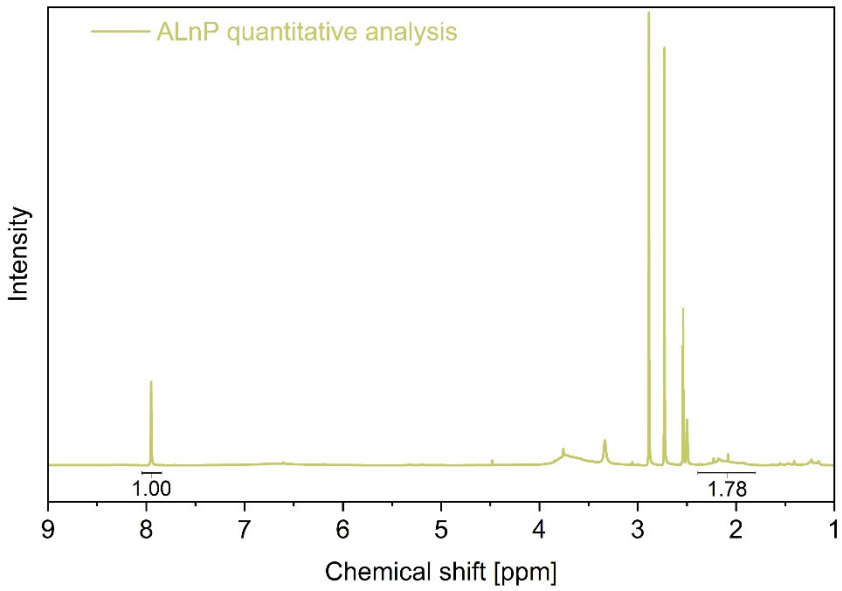

Figure S17: Quantitative determination of the acetoacetate moieties of ALnP by ^{1}H NMR spectroscopy with DMF as an internal standard in DMSO-d_6. Integrals of the amide proton of DMF (8.5 mg) at 7.95 ppm and the methyl group of acetoacetate moieties of ALnP (30.2 mg) at 2.4 – 1.8 ppm are shown below the respective signal. Calculations result in a content of 2.28 mmol/g of acetoacetate functionalities in ALnP.

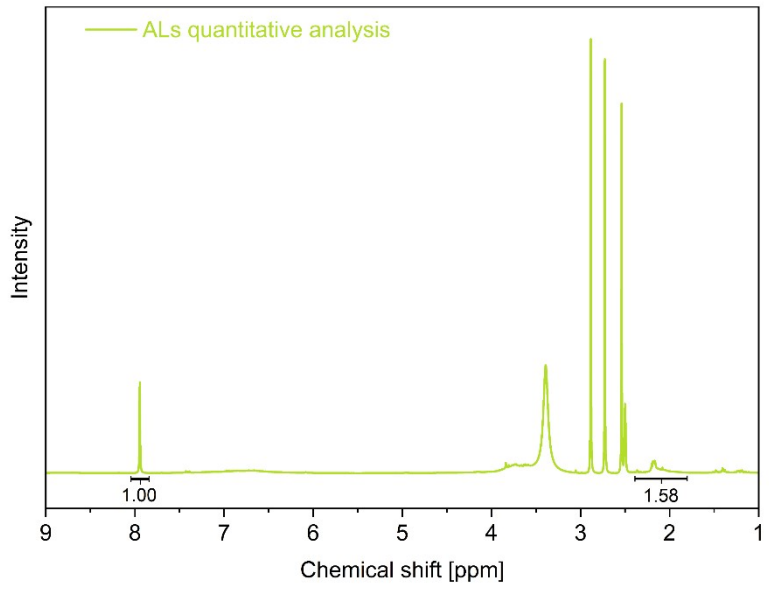

Figure S18: Quantitative determination of the acetoacetate moieties of ALs by ^{1}H NMR spectroscopy with DMF as an internal standard in DMSO-d_6. Integrals of the amide proton of DMF (6.8 mg) at 7.95 ppm and the methyl group of acetoacetate moieties of ALs (30.1 mg) at 2.4 – 1.8 ppm are shown below the respective signal. Calculations result in a content of 1.63 mmol/g of acetoacetate functionalities in ALs.

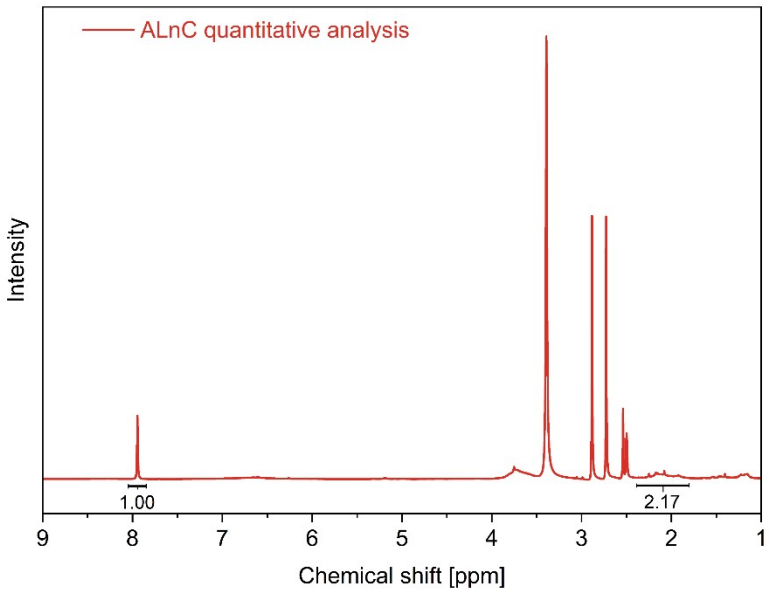

Figure S19: Quantitative determination of the acetoacetate moieties of ALnC by ^{1}H NMR spectroscopy with DMF as an internal standard in DMSO-d_6. Integrals of the amide proton of DMF (7.4 mg) at 7.95 ppm and the methyl group of acetoacetate moieties of ALnC (28.6 mg) at 2.4 – 1.8 ppm are shown below the respective signal. Calculations result in a content of 2.57 mmol/g of acetoacetate functionalities in ALnC.

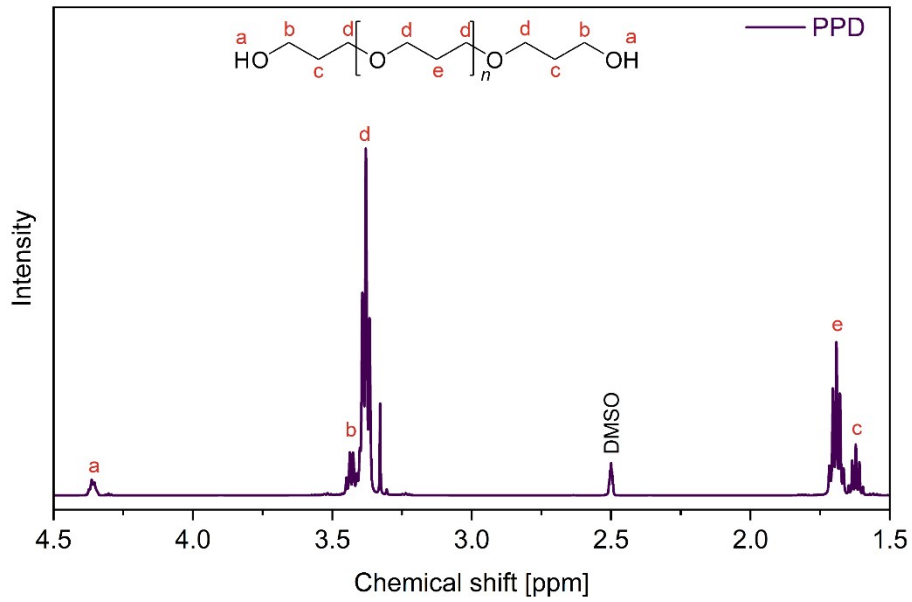

Figure S20: The ^{1}H NMR spectrum of Poly(oxy-1,3-propanediyl) displays the characteristic signals and intensities. ^{1}H NMR (400 MHz, DMSO-d_6, 298 K): 4.36 (2H, m, OH), 3.50 – 3.34 (42H, m, CH_2), 1.77 – 1.53 (22H, m, CH_2).

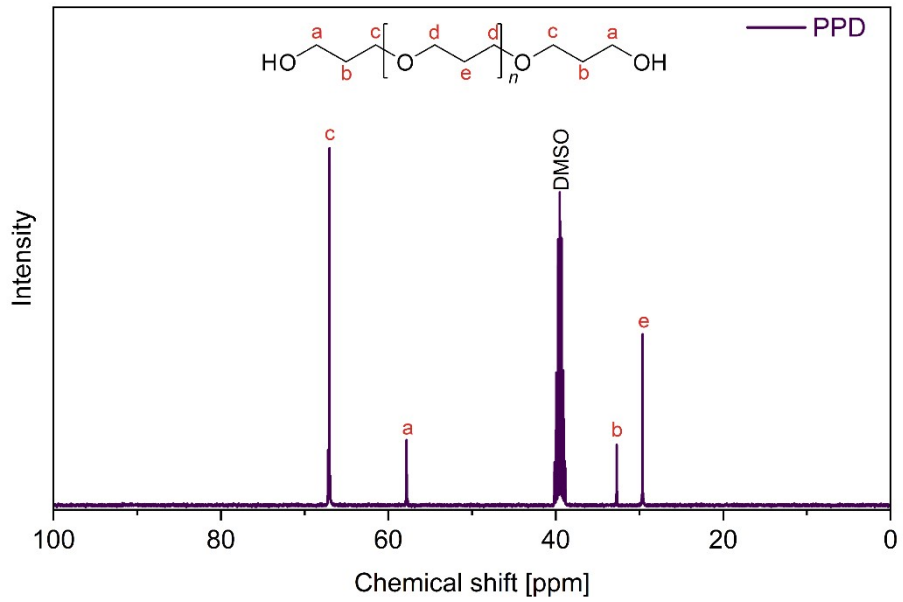

Figure S21: The ^{13}C NMR spectrum of Poly(oxy-1,3-propanediyl) displays the characteristic signals and intensities. ^{13}C NMR (100 MHz, DMSO-d_6, 298 K): 67.3 – 66.9 (m, CH_2), 58.0 – 57.6 (m, CH_2), 32.8 – 32.6 (m, CH_3), 30.0 – 29.3 (m, CH_3).

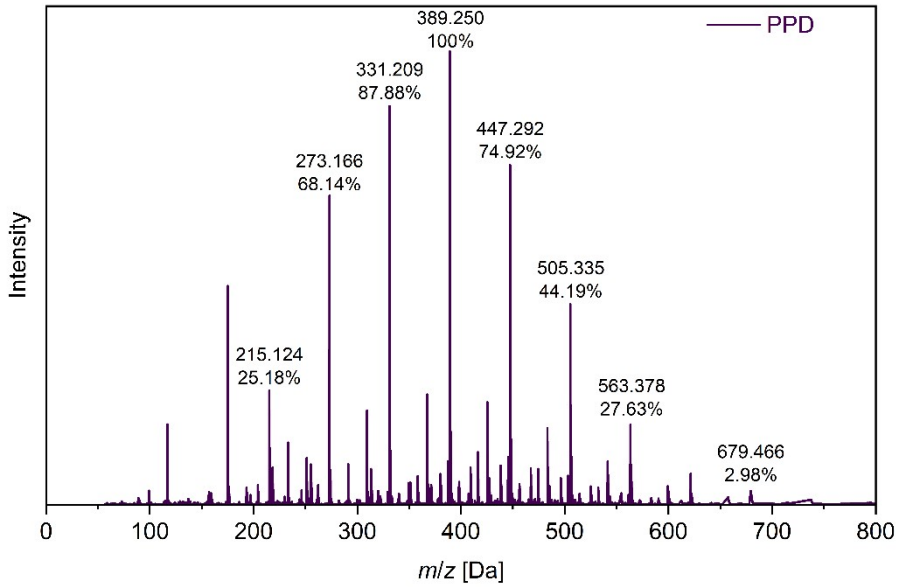

Figure S22: The ESI-MS (+) spectrum displays the characteristic peaks of $[M+Na]^+$ of Poly(oxy-1,3-propanediyl) with 3, 4, 5, 6, 7, 8, 9, and 11 repeating units (*m/z*: 215.124, 273.166, 33.209, 389.250, 447.292, 505.335, 563.378, 679.466, respectively).

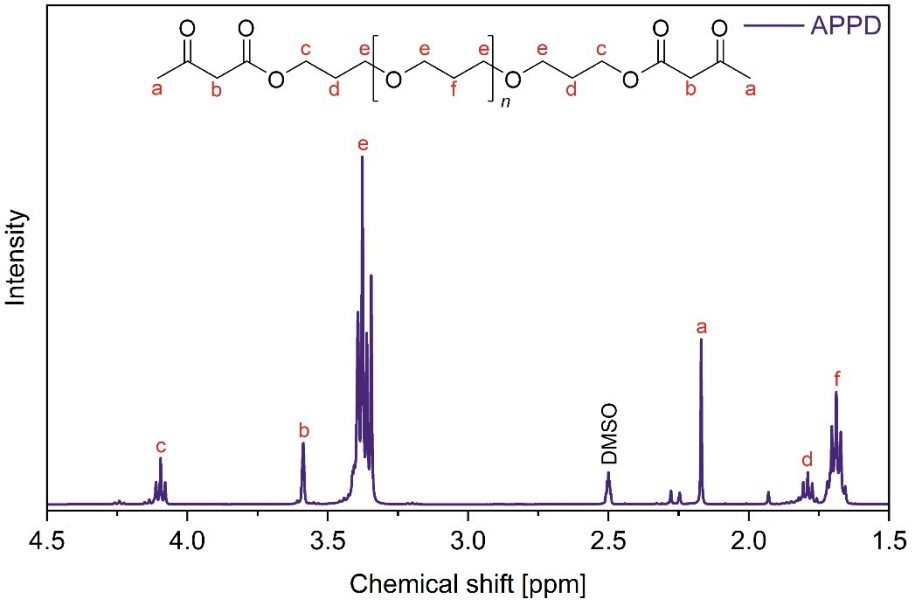

Figure S23: The ^{1}H NMR spectrum of acetoacetylated Poly(oxy-1,3-propanediyl) displays the characteristic signals and intensities. ^{1}H NMR (400 MHz, DMSO-d_6, 298 K): 4.10 (4H, t, CH_2), 3.59 (4H, s, CH_2), 3.50 – 3.34 (41H, m, CH_2), 2.17 (6H, s, CH_3), 1.90 – 1.61 (23H, m, CH_2).

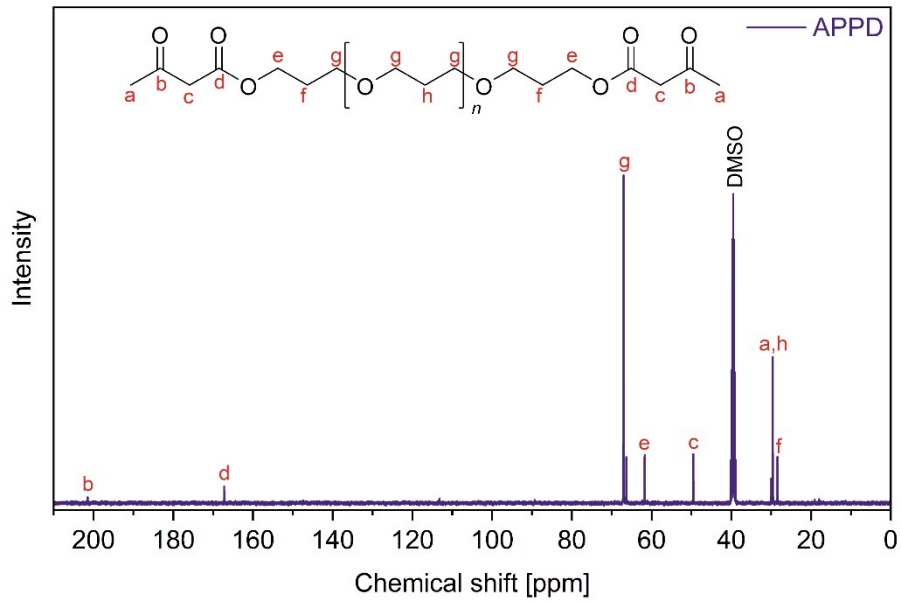

Figure S24: The ^{13}C NMR spectrum of acetoacetylated Poly(oxy-1,3-propanediyl) displays the characteristic signals and intensities. ^{13}C NMR (100 MHz, DMSO-d_6, 298 K): 201.4 (s, $C_{arbonyl}$), 167.2 (s, $C_{arboxyl}$), 67.2 – 66.7 (m, CH_2), 66.4 (s, CH_2), 61.7 (s, CH_2), 49.5 (s, CH_2), 30.1 – 29.5 (m, CH_3, CH_2), 28.4 (s, CH_2).

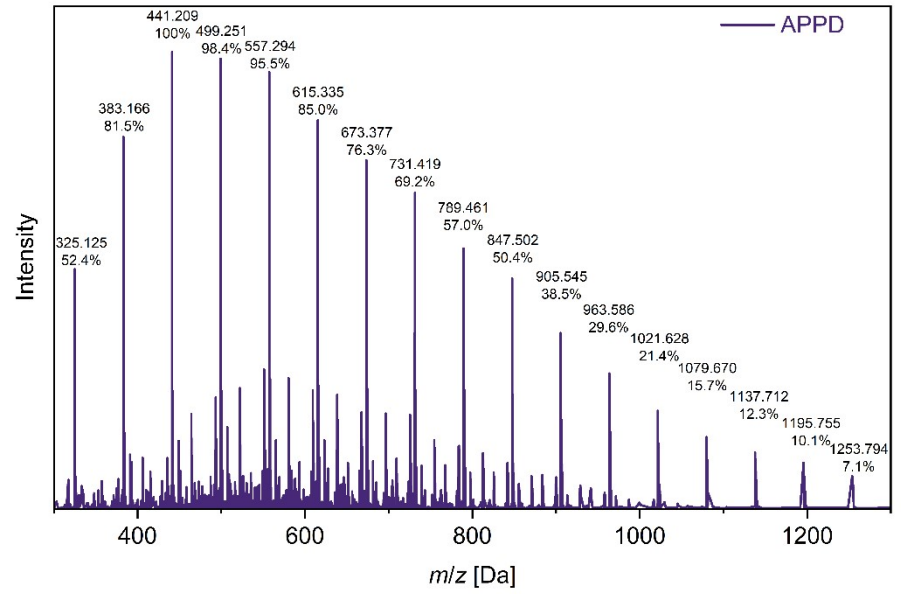

Figure S25: The ESI-MS (+) spectrum showing displays the characteristic peaks of $[M+Na]^+$ of acetoacetylated Poly(oxy-1,3-propanediyl) with 2, 3, 4, 5, 6, 7, 8, 9, 10, 11, 12, 13, 14, 15, 16, 17, and 18 repeating units (*m*/*z*: 325.125, 383.166, 441.209, 499.251, 557.294, 615.335, 673.377, 731.419, 789.461, 847.502, 905.545, 963.586, 1021.628, 1079.670, 1137.712, 1195.755, and 1253.794, respectively).

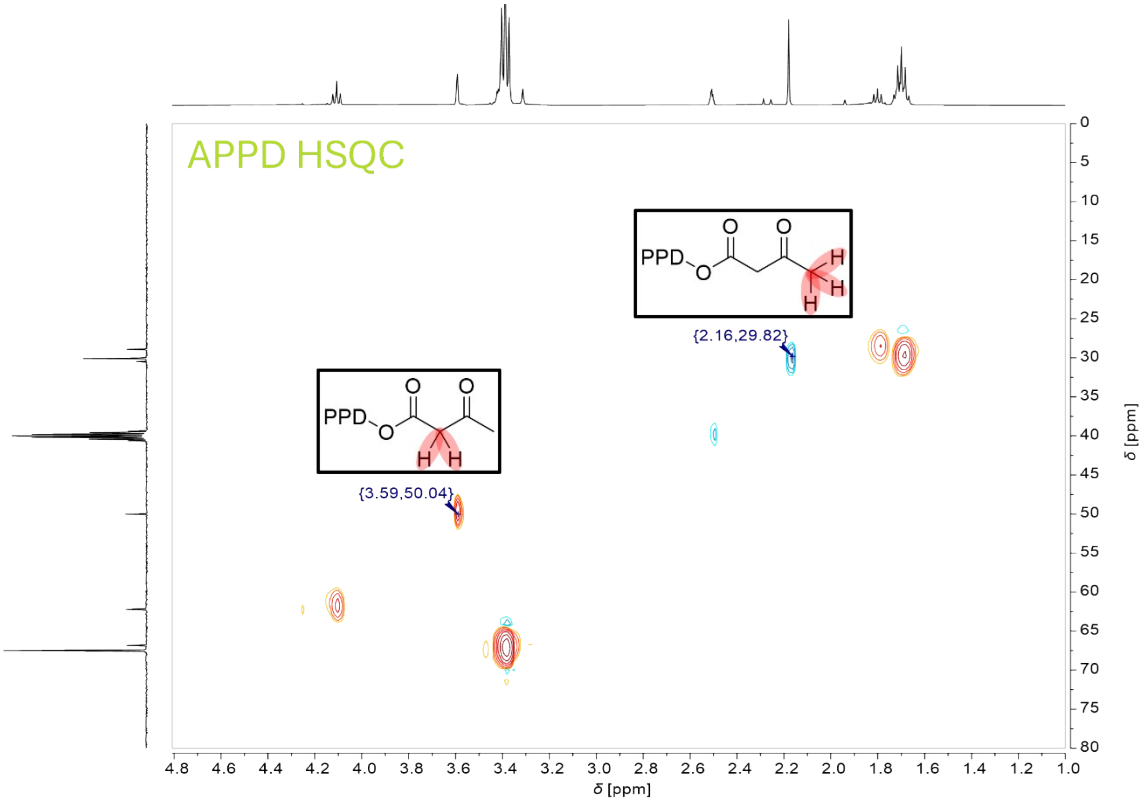

Figure S26: HSQC spectrum of APPD. The ^{1}J couplings of the terminal methyl group and the ^{1}J of the methylene group of the acetoacetate functionalities are presented. Measured with an AVIII 400 MHz NMR spectrometer in DMSO-d_6.

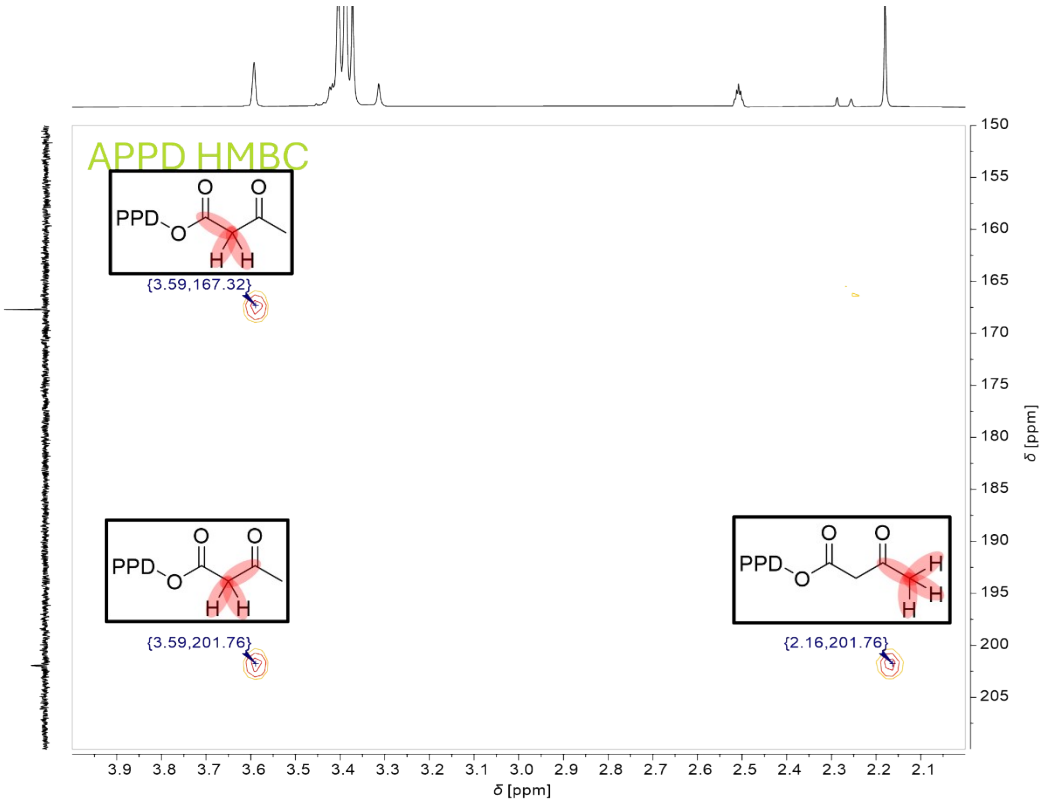

Figure S27: HMBC spectrum of APPD. The corresponding ^{2}J coupling of the acetoacetate moieties is indicated in the structure above the respective signal. Measured with an AVIII 400 MHz NMR spectrometer in DMSO-d_6.

Figure S28: ESI-MS (+) spectrum showing the characteristic peaks of $[M+Na]^+$ of acetoacetylated Poly(oxy-1,3-propanediyl) with 2, 3, 4, 5, 6, 7, 8, 9, 10, 11, 12, 13, 14, 15, 16, 17, and 18 repeating units (*m*/*z*: 325.125, 383.166, 441.209, 499.251, 557.294, 615.335, 673.377, 731.419, 789.461, 847.502, 905.545, 963.586, 1021.628, 1079.670, 1137.712, 1195.755, and 1253.794 respectively).

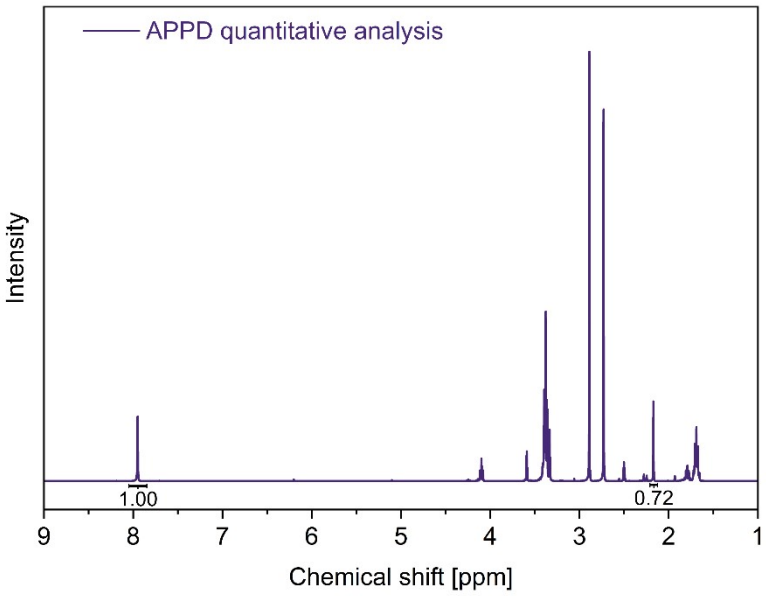

Figure S29: Quantitative determination of the acetoacetate moieties of APPD by ^{1}H NMR spectroscopy with DMF as an internal standard in DMSO-d_6. Integrals of the amide proton of DMF (19.4 mg) at 7.95 ppm and the methyl group of acetoacetate moieties of APPD (25.5 mg) at 2.17 ppm are shown below the respective signal. Calculations result in a content of 2.49 mmol/g of acetoacetate functionalities in APPD.

Figure S30: Lignosulfonate-based vinylogous urethane vitrimer crosslinked with Priamine™ 1073. Weight ratio of lignosulfonate exceeds 55 wt.% and therefore the inhomogeneous sample is too brittle to be processed. Cutting out the samples for tensile testing and DMA only led to the shattering of the film into smaller pieces.

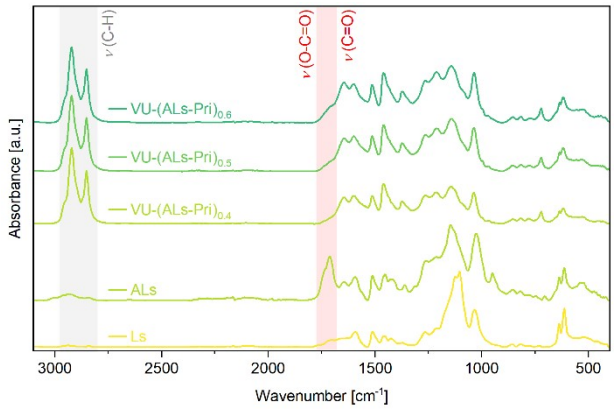

Figure S31: ATR-FT-IR spectra of the lignosulfonate-based (Ls) lignin vitrimers, showing the acetoacetylated ALs with the characteristic acetoacetate bands of the ester (1740 cm^{-1}) and ketone stretching vibrations (1711 cm^{-1}). After the conversion with Priamine™ 1073, the characteristic acetoacetate bands disappear, while the conjugated C=C (1593 cm^{-1}) and C=O ester (1644 cm^{-1}) display the stretching vibration bands of the vinylogous urethanes.

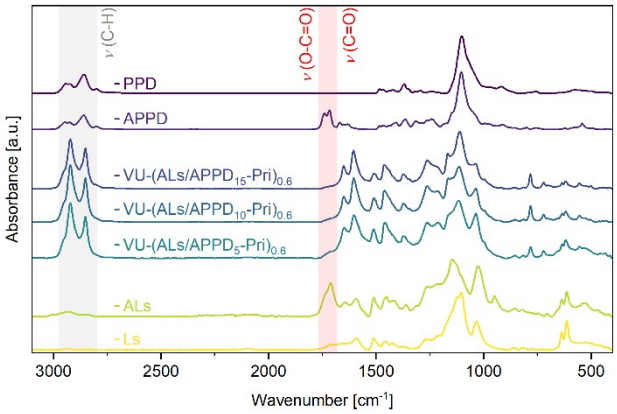

Figure S32: ATR-FT-IR spectra of the lignosulfonate-based (Ls) lignin vitrimers combined with poly(oxypropane-1,3-diyl) (PPD), showing the acetoacetylated ALs and APPD with the characteristic acetoacetate bands of the ester (1740 cm^{-1}) and ketone stretching vibrations (1711 cm^{-1}). After the conversion with Priamine™ 1073, the characteristic acetoacetate bands disappear, while the conjugated C=C (1593 cm^{-1}) and C=O ester (1644 cm^{-1}) display the stretching vibration bands of the vinylogous urethanes.

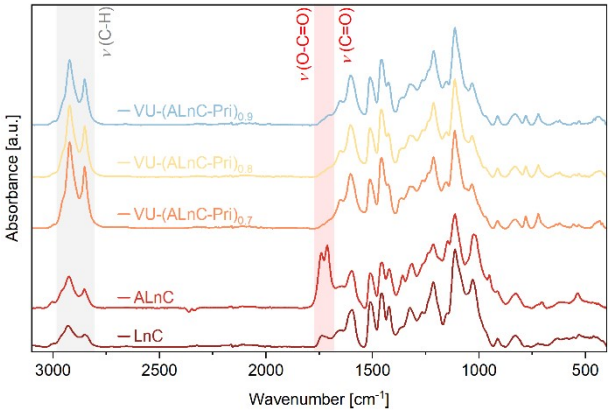

Figure S33: ATR-FT-IR spectra of the Lignova Crude™-based (LnC) lignin vitrimers, showing the acetoacetylated ALnC with the characteristic acetoacetate bands of the ester (1740 cm^{-1}) and ketone stretching vibrations (1711 cm^{-1}). After the conversion with Priamine™ 1073, the characteristic acetoacetate bands disappear, while the conjugated C=C (1593 cm^{-1}) and C=O ester (1644 cm^{-1}) display the stretching vibration bands of the vinylogous urethanes.

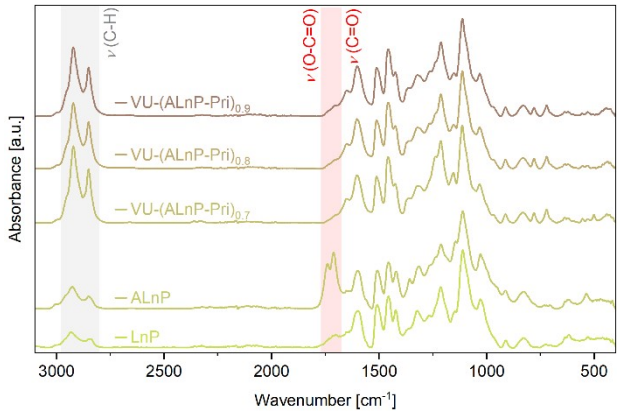

Figure S34: ATR-FT-IR spectra of the Lignova Pure™-based (LnP) lignin vitrimers, showing the acetoacetylated ALnP with the characteristic acetoacetate bands of the ester (1740 cm^{-1}) and ketone stretching vibrations (1711 cm^{-1}). After the conversion with Priamine™ 1073, the characteristic acetoacetate bands disappear, while the conjugated C=C (1593 cm^{-1}) and C=O ester (1644 cm^{-1}) display the stretching vibration bands of the vinylogous urethanes.

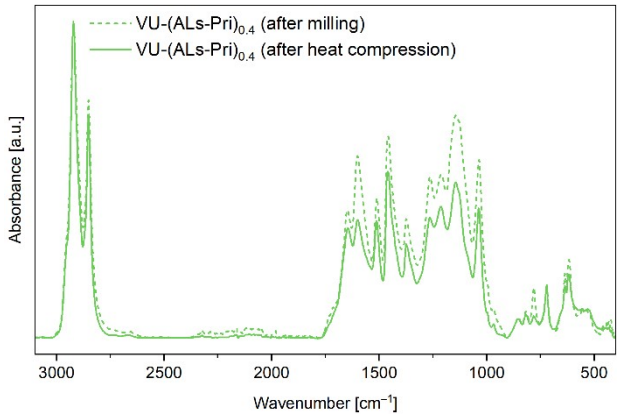

Figure S35: ATR-FT-IR spectra of the lignosulfonate-based lignin vitrimer VU-(ALs-Pri)$_{0.4}$ after ball milling and after the film formation by heat compression, showing a similar absorption pattern. The conjugated C=C (1593 cm^{-1}) band and the C=O ester (1644 cm^{-1}) band display the stretching vibration bands of the vinylogous urethanes.

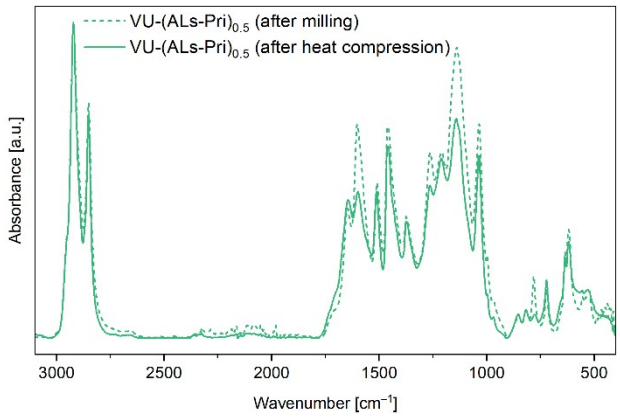

Figure S36: ATR-FT-IR spectra of the lignosulfonate-based lignin vitrimer VU-(ALs-Pri)$_{0.5}$ after ball milling and after the film formation by heat compression, showing a similar absorption pattern. The conjugated C=C (1593 cm^{-1}) band and the C=O ester (1644 cm^{-1}) band display the stretching vibration bands of the vinylogous urethanes.

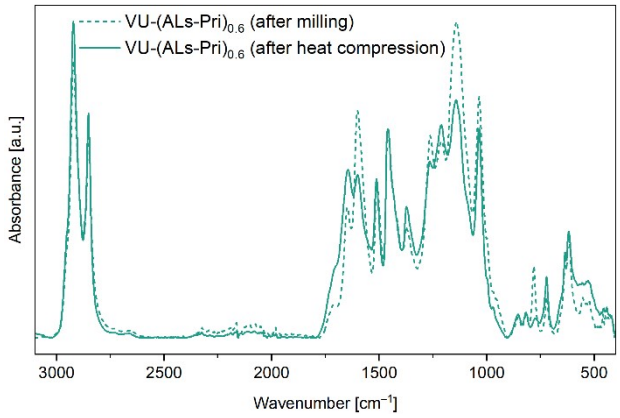

Figure S37: ATR-FT-IR spectra of the lignosulfonate-based lignin vitrimer VU-(ALs-Pri)$_{0.6}$ after ball milling and after the film formation by heat compression, showing a similar absorption pattern. The conjugated C=C (1593 cm^{-1}) band and the C=O ester (1644 cm^{-1}) band display the stretching vibration bands of the vinylogous urethanes.

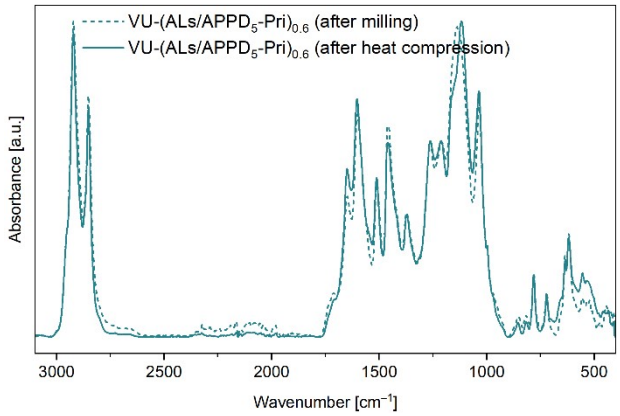

Figure S38: ATR-FT-IR spectra of the lignosulfonate-based lignin vitrimer VU-(ALs/APPD$_5$-Pri)$_{0.6}$ after ball milling and after the film formation by heat compression, showing a similar absorption pattern. The conjugated C=C (1593 cm^{-1}) band and the C=O ester (1644 cm^{-1}) band display the stretching vibration bands of the vinylogous urethanes.

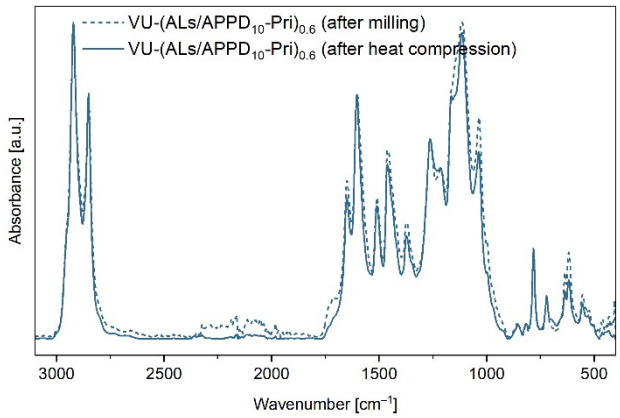

Figure S39: ATR-FT-IR spectra of the lignosulfonate-based lignin vitrimer VU-(ALs/APPD$_{10}$-Pri)$_{0.6}$ after ball milling and after the film formation by heat compression, showing a similar absorption pattern. The conjugated C=C (1593 cm^{-1}) band and the C=O ester (1644 cm^{-1}) band display the stretching vibration bands of the vinylogous urethanes.

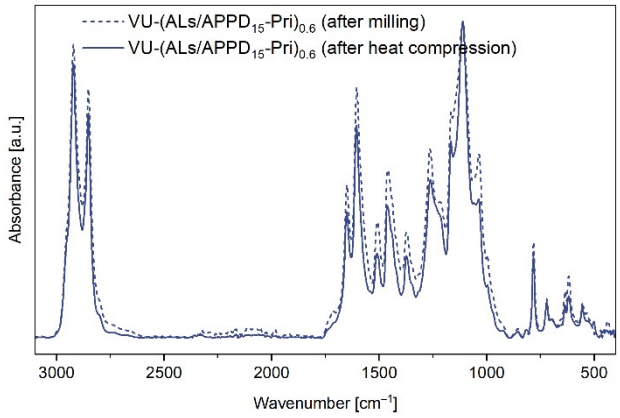

Figure S40: ATR-FT-IR spectra of the lignosulfonate-based lignin vitrimer VU-(ALs/$APPD_{15}$-Pri)$_{0.6}$ after ball milling and after the film formation by heat compression, showing a similar absorption pattern. The conjugated C=C (1593 cm^{-1}) band and the C=O ester (1644 cm^{-1}) band display the stretching vibration bands of the vinylogous urethanes.

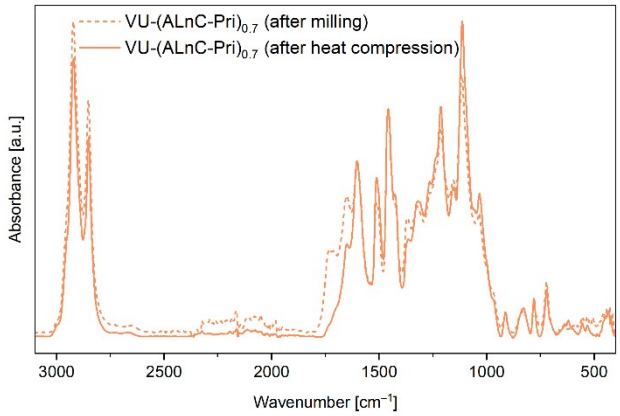

Figure S41: ATR-FT-IR spectra of the enzymatic-based lignin vitrimer VU-(ALnC-Pri)$_{0.7}$ after ball milling and after the film formation by heat compression. After the heat compression, the characteristic acetoacetate bands disappear completely, while the conjugated C=C (1593 cm^{-1}) and C=O ester (1644 cm^{-1}) display the stretching vibration bands of the vinylogous urethanes.

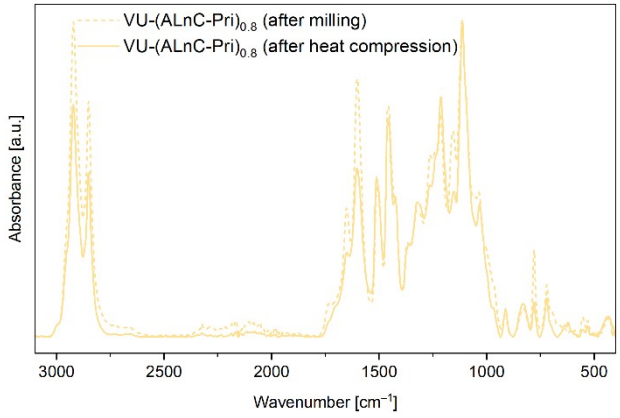

Figure S42: ATR-FT-IR spectra of the enzymatic-based lignin vitrimer VU-(ALnC-Pri)$_{0.8}$ after ball milling and after the film formation by heat compression. After the heat compression, the characteristic acetoacetate bands disappear completely, while the conjugated C=C (1593 cm^{-1}) and C=O ester (1644 cm^{-1}) display the stretching vibration bands of the vinylogous urethanes.

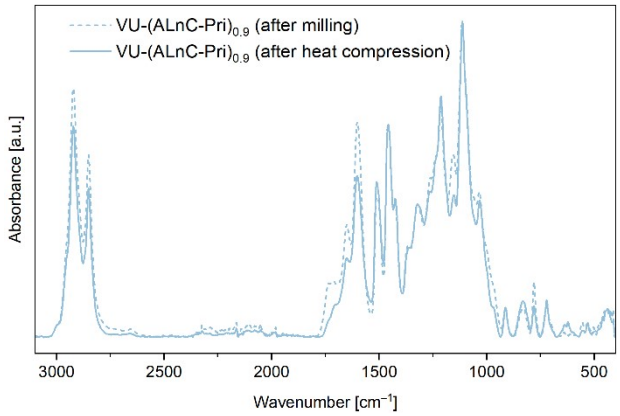

Figure S43: ATR-FT-IR spectra of the enzymatic-based lignin vitrimer VU-(ALnC-Pri)$_{0.9}$ after ball milling and after the film formation by heat compression. After the heat compression, the characteristic acetoacetate bands disappear completely, while the conjugated C=C (1593 cm^{-1}) and C=O ester (1644 cm^{-1}) display the stretching vibration bands of the vinylogous urethanes.

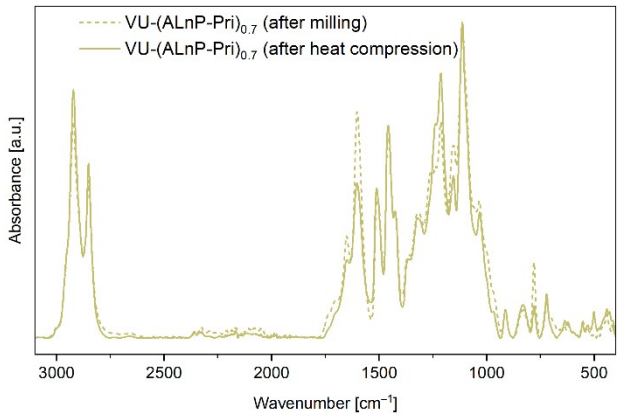

Figure S44: ATR-FT-IR spectra of the enzymatic-based lignin vitrimer VU-(ALnP-Pri)$_{0.7}$ after ball milling and after the film formation by heat compression, showing a similar absorption pattern. The conjugated C=C (1593 cm^{-1}) band and the C=O ester (1644 cm^{-1}) band display the stretching vibration bands of the vinylogous urethanes.

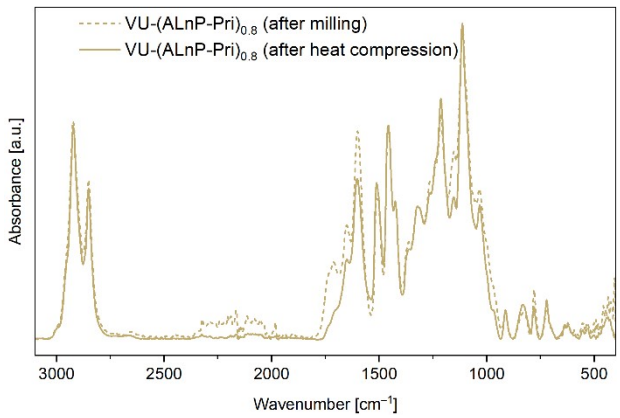

Figure S45: ATR-FT-IR spectra of the enzymatic-based lignin vitrimer VU-(ALnP-Pri)$_{0.8}$ after ball milling and after the film formation by heat compression. After the heat compression, the characteristic acetoacetate bands disappear completely, while the conjugated C=C (1593 cm^{-1}) and C=O ester (1644 cm^{-1}) display the stretching vibration bands of the vinylogous urethanes.

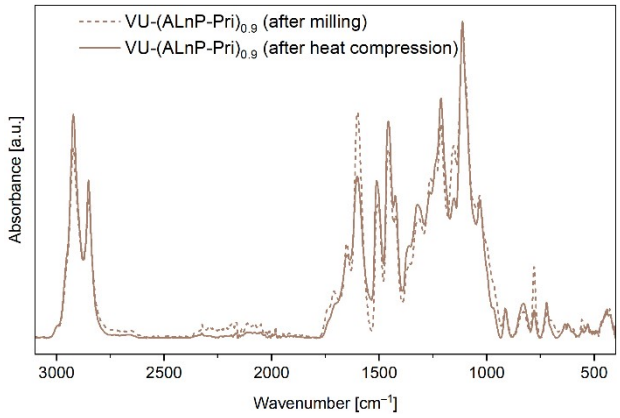

Figure S46: ATR-FT-IR spectra of the enzymatic-based lignin vitrimer VU-(ALnP-Pri)$_{0.9}$ after ball milling and after the film formation by heat compression. After the heat compression, the characteristic acetoacetate bands disappear completely, while the conjugated C=C (1593 cm^{-1}) and C=O ester (1644 cm^{-1}) display the stretching vibration bands of the vinylogous urethanes.

Equation S2

$$S = \frac{m_1 - m_0}{m_0} \cdot 100$$

S : Swelling ratio [%]
m_0 : Weight of the sample before swelling [g]
m_1 : Weight of the sample after swelling [g]

Equation S3

$$SF = \frac{m_0 - m_2}{m_0} \cdot 100$$

SF : Soluble fraction [%]
m_0 : Weight of the sample before swelling [g]
m_2 : Weight of the sample after drying [g]

Table S2: Results of the swelling tests performed by addition of 1 mL of solvent (deionized water, acetone) to approximately 50 mg (m_0) of the respective sample. The vials were subsequently sealed and stored for 24 h at 25 °C. Afterwards, the supernatant was decanted, and the sample was weighed (m_1) and stored at 80 °C under vacuum for at least 24 h until a constant mass was measured (m_2).The swelling ratio was calculated via (m_1–m_0)/m_0; the soluble fraction was calculated via (m_0–m_2)/m_0.

Sample	H_2O		Acetone	
	S **[wt.%]**	***SF*** **[wt.%]**	***S*** **[wt.%]**	***SF*** **[wt.%]**
VU-(ALs-Pri)$_{0.4}$	15	1.6	24	3.7
VU-(ALs-Pri)$_{0.5}$	19	2.7	25	1.8
VU-(ALs-Pri)$_{0.6}$	28	2.8	30	4.7
VU-(ALs/APPD$_5$-Pri)$_{0.6}$	39	4.4	29	5.9
VU-(ALs/APPD$_{10}$-Pri)$_{0.6}$	24	2.8	30	5.9
VU-(ALs/APPD$_{15}$-Pri)$_{0.6}$	25	1.9	34	9.0
VU-(ALnC-Pri)$_{0.7}$	2.5	0.3	31	6.3
VU-(ALnC-Pri)$_{0.8}$	5.1	0	30	7.2
VU-(ALnC-Pri)$_{0.9}$	1.6	0.2	34	7.0
VU-(ALnP-Pri)$_{0.7}$	3.6	0	41	6.1
VU-(ALnP-Pri)$_{0.8}$	2.4	0	36	9.6
VU-(ALnP-Pri)$_{0.9}$	3.1	0	34	12

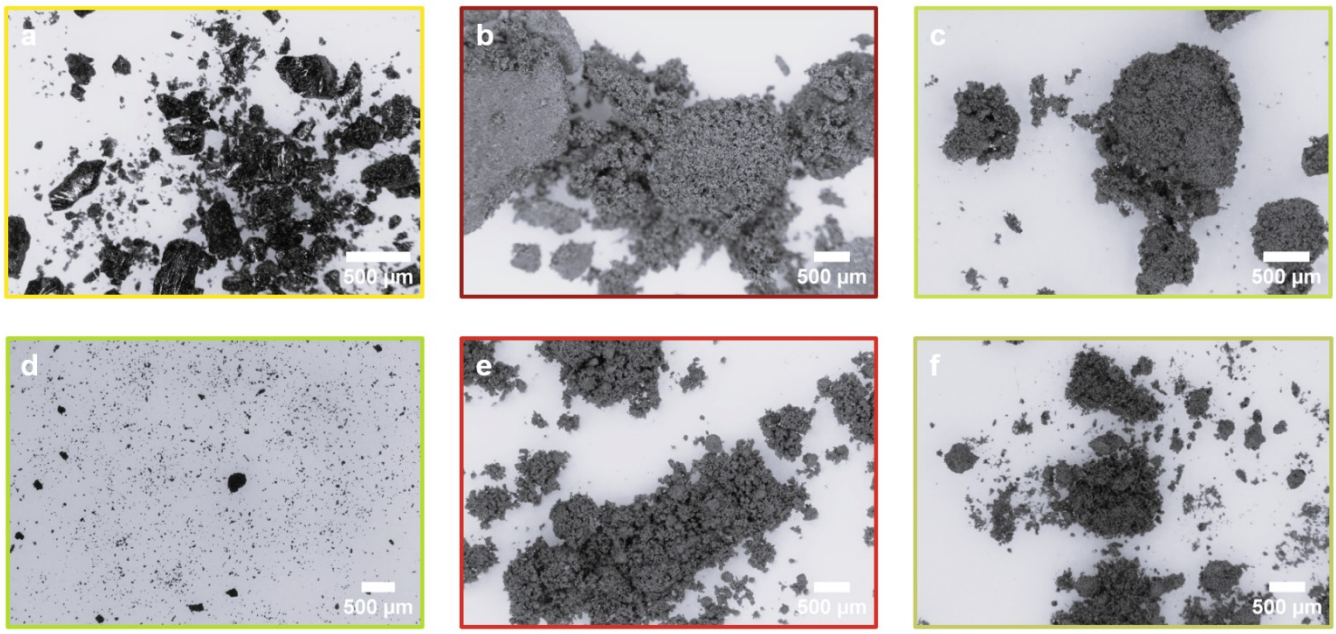

Figure S47**:** OM images of the different lignin sources Ls (a), LnC (b), and LnP c), and the acetoacetylated lignin sources ALs d), ALnC e), and ALnP f), showing similar powders with granules and agglomerates in all images.

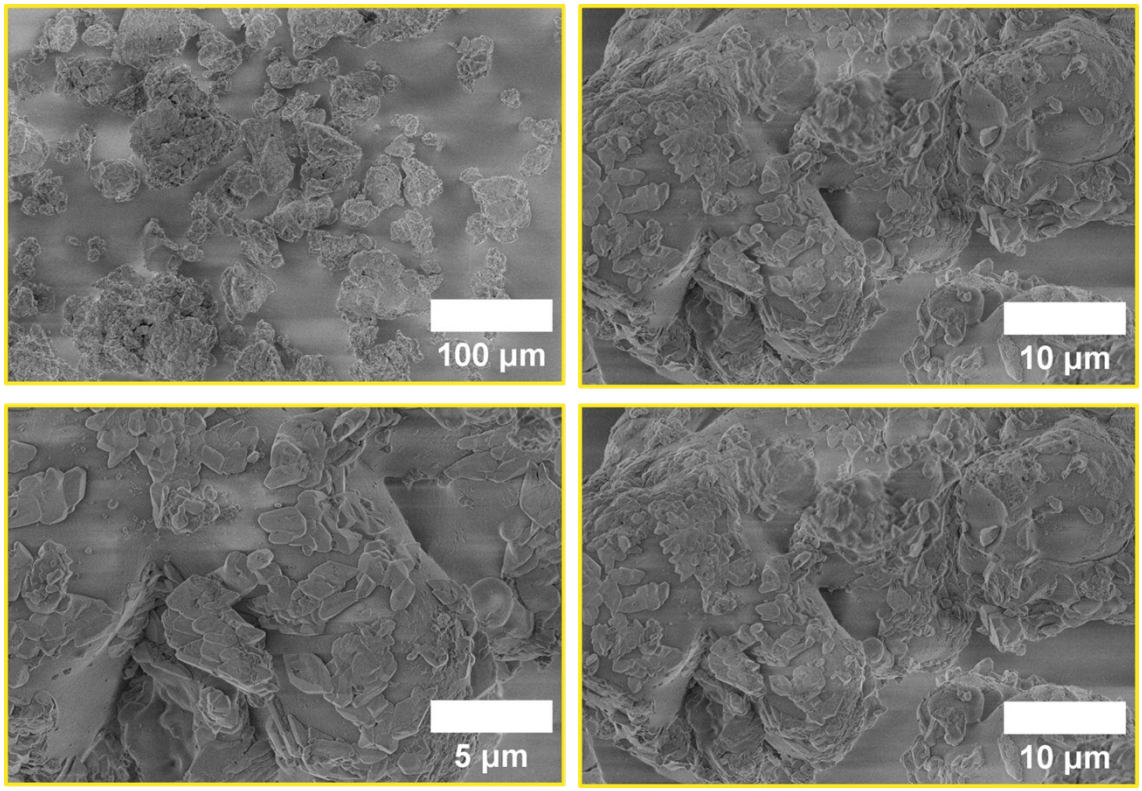

Figure S48: SEM images of the raw lignosulfonate Ls with different magnifications.

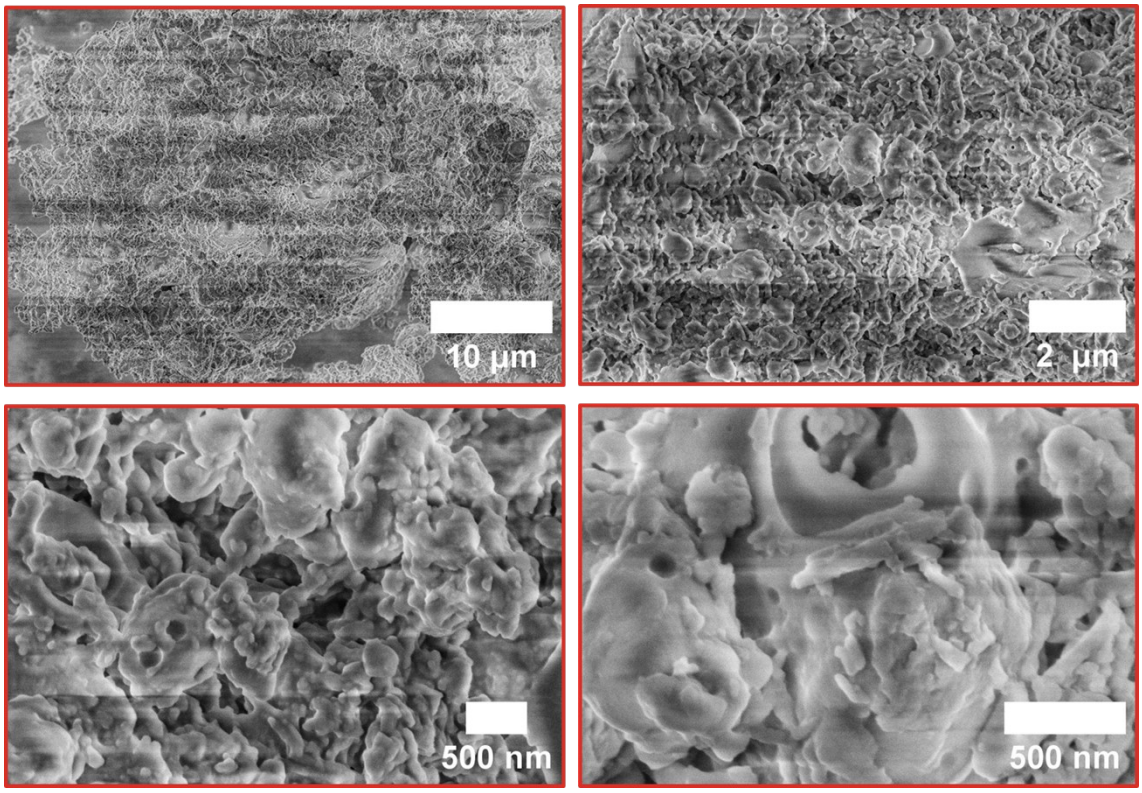

Figure S49: SEM images of the raw enzymatic LnC with different magnifications.

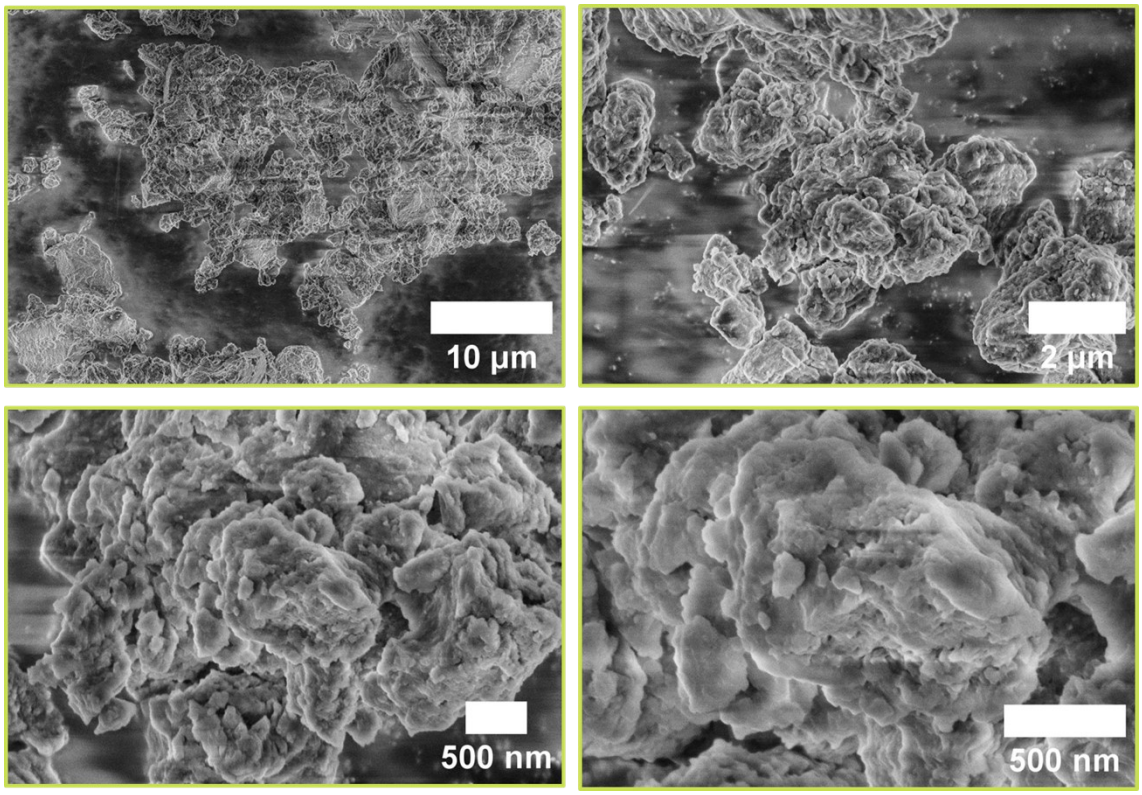

Figure S50: SEM images of the raw enzymatic LnP with different magnifications.

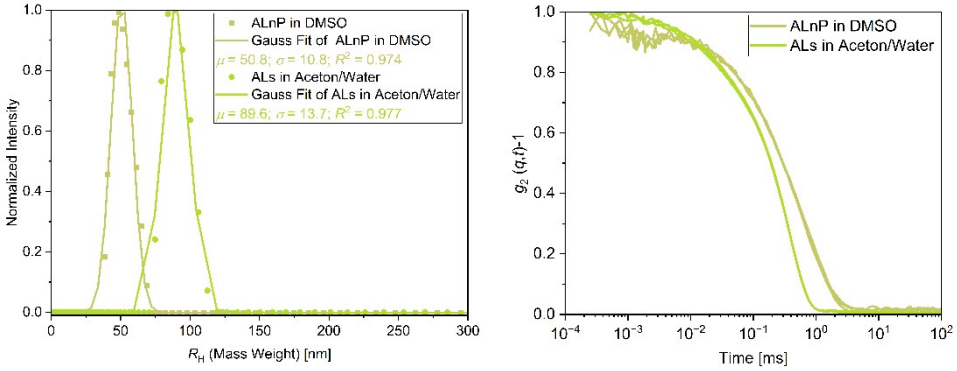

Figure S51: DLS measurements of Als and ALnP. Shown are the distributions of the hydrodynamic radii of the particles (left) and the correlation curves of respective samples (right). A Gaussian fit was used to determine the expected value and standard deviation of the distributions. Measured at a temperature of 30 °C and an angle of 90°.

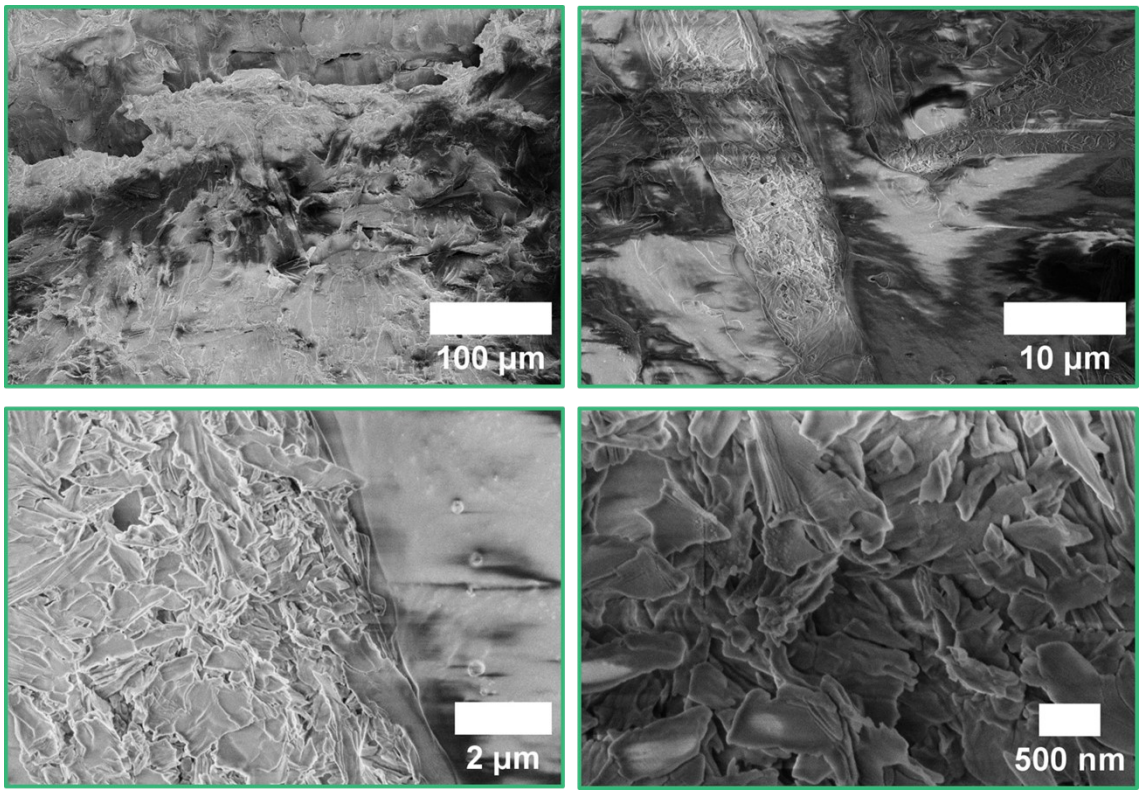

Figure S52: SEM images of VU-(AIs-Pri)$_{0.5}$ with different magnifications.

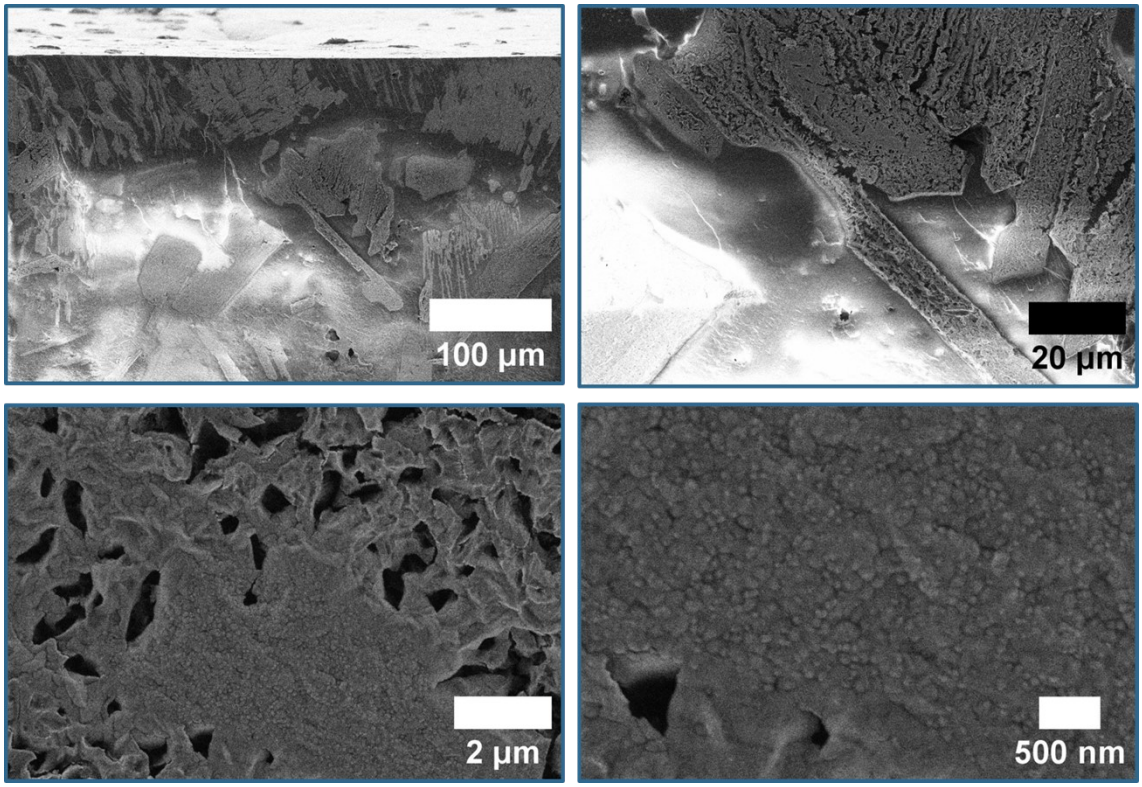

Figure S53: SEM images of VU-(Als/APPD$_{10}$-Pri)$_{0.6}$ with different magnifications.

Table S3: EDX-measurements of VU-(ALs-Pri)$_{0.5}$, showing the irradiated area (left), the EDX spectra (middle) and a table with the relative intensity of respective elements in % (right).

VU-(ALs-Pri)$_{0.5}$

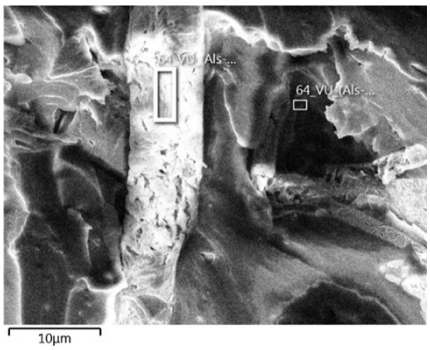

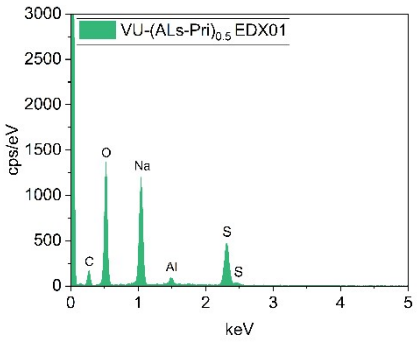

Element	Atom%
C	25.44
N	-
O	42.32
Na	19.84
Al	1.25
S	11.15

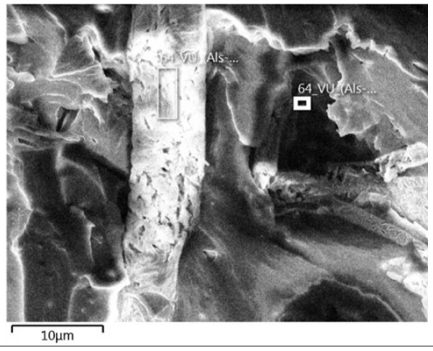

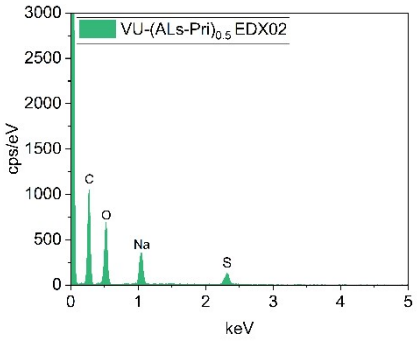

Element	Atom%
C	67.10
N	-
O	24.99
Na	5.47
Al	-
S	2.45

Table S4: EDX-measurements of VU-(ALs/APPD$_{10}$-Pri)$_{0.}$, showing the irradiated area (left), the EDX spectra (middle) and a table with the relative intensity of respective elements in % (right).

VU-(ALs/APPD$_{10}$-Pri)$_{0.6}$

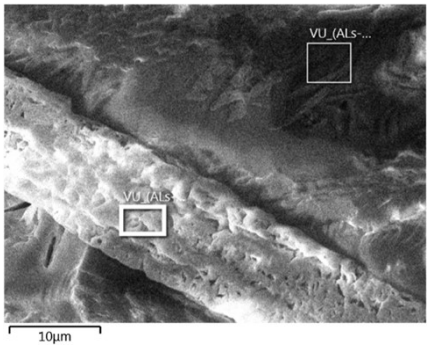

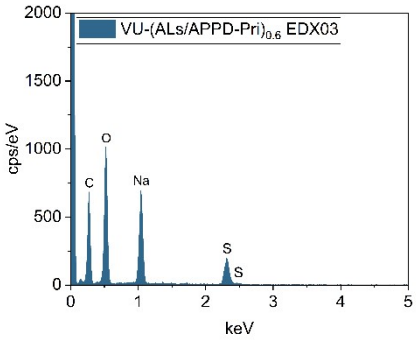

Element	Atom%
C	53.73
N	-
O	31.90
Na	10.35
Al	-
S	4.03

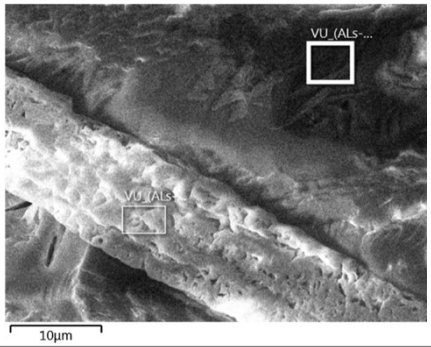

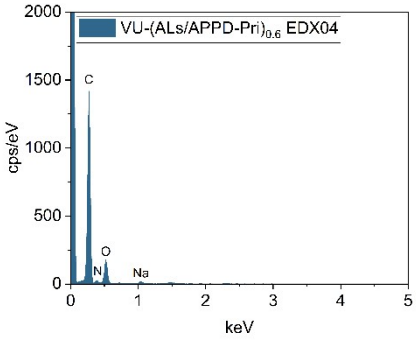

Element	Atom%
C	76.58
N	8.56
O	14.49
Na	0.37
Al	-
S	-

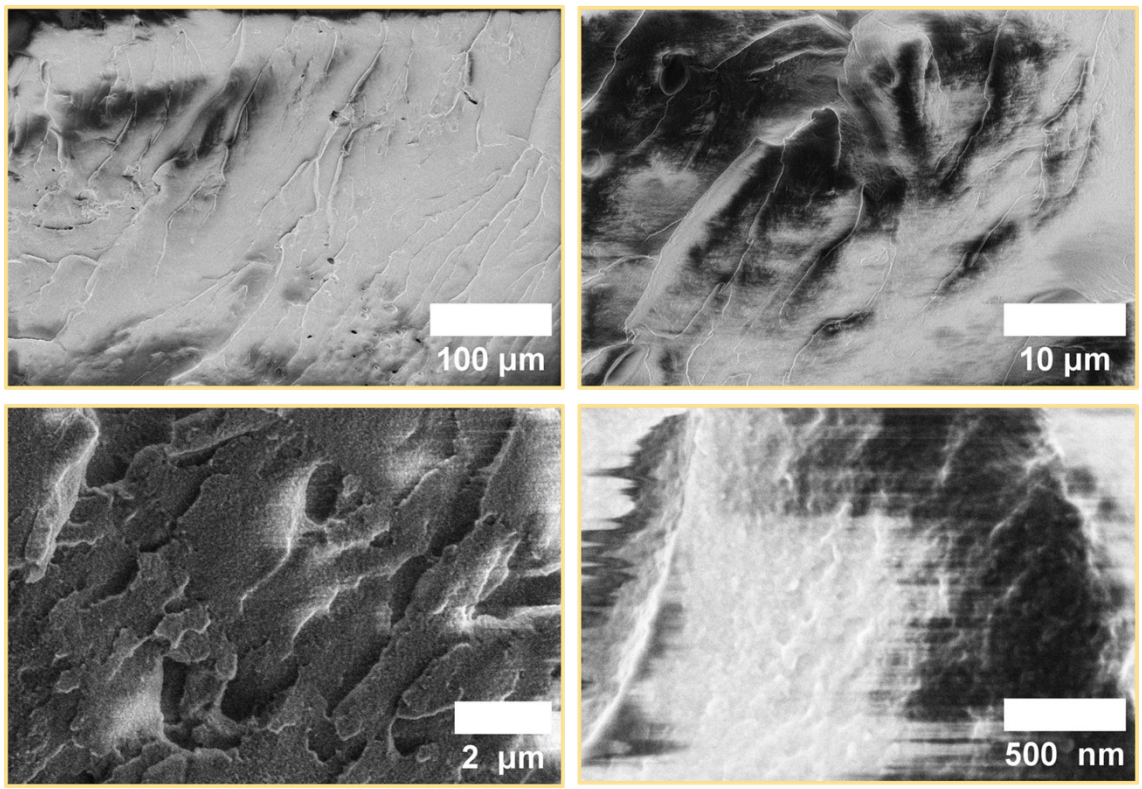

Figure S54: SEM images of VU-(AlnC-Pri)$_{0.8}$ with different magnifications.

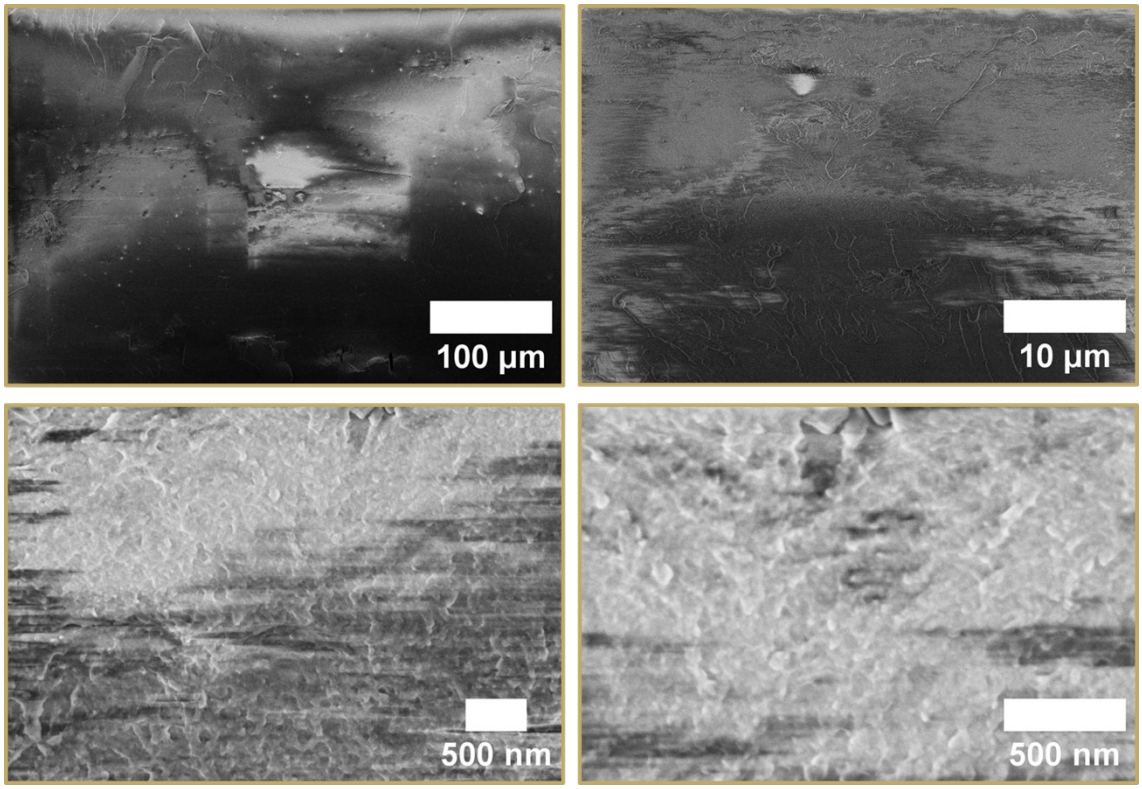

Figure S55: SEM images of VU-(AlnP-Pri)$_{0.8}$ with different magnifications.

Table S5: EDX-measurements of VU-(ALnC-Pri)$_{0.8}$,, showing the irradiated area (left), the EDX spectra (middle) and a table with the relative intensity of respective elements in % (right).

VU-(ALnC-Pri)$_{0.8}$

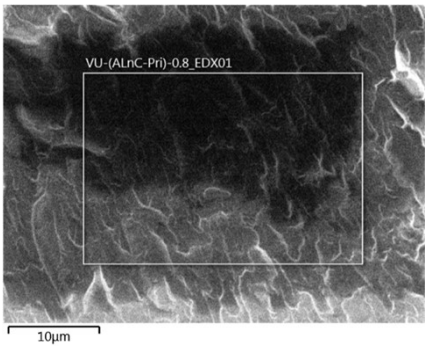

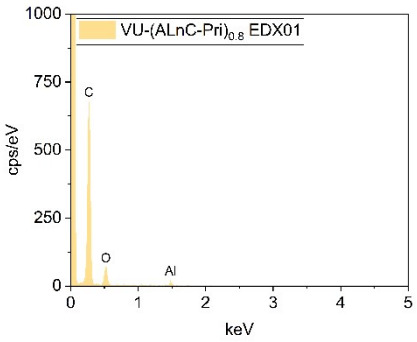

Element	Atom%
C	86.06
N	-
O	13.22
Na	-
Al	0.72
S	-

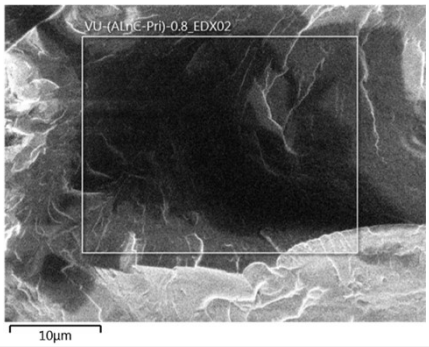

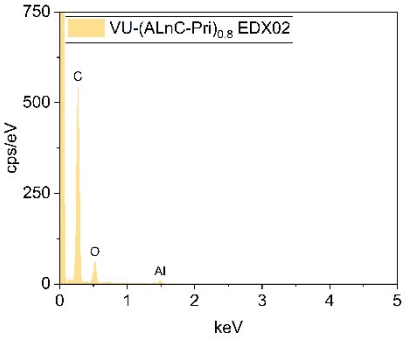

Element	Atom%
C	84.69
N	-
O	14.72
Na	-
Al	0.60
S	-

Table S6: EDX-measurements of VU-(ALnP-Pri)$_{0.8}$, showing the irradiated area (left), the EDX spectra (middle) and a table with the relative intensity of respective elements in % (right).

VU-(ALnP-Pri)$_{0.8}$

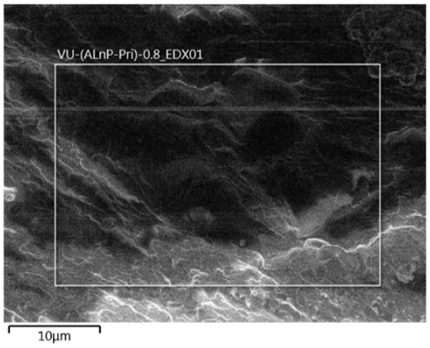

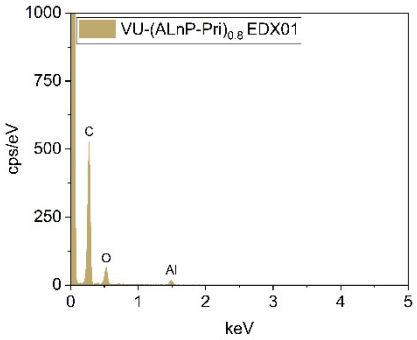

Element	Atom%
C	84.69
N	-
O	14.17
Na	-
Al	1.14
S	-

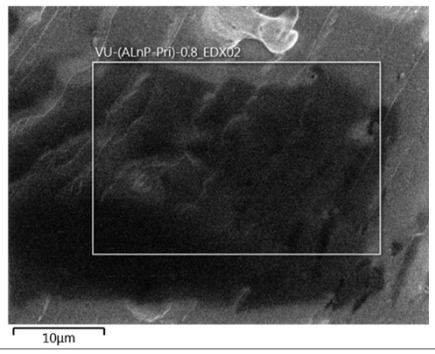

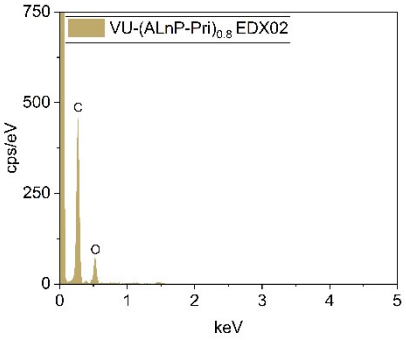

Element	Atom%
C	80.86
N	-
O	19.14
Na	-
Al	-
S	-

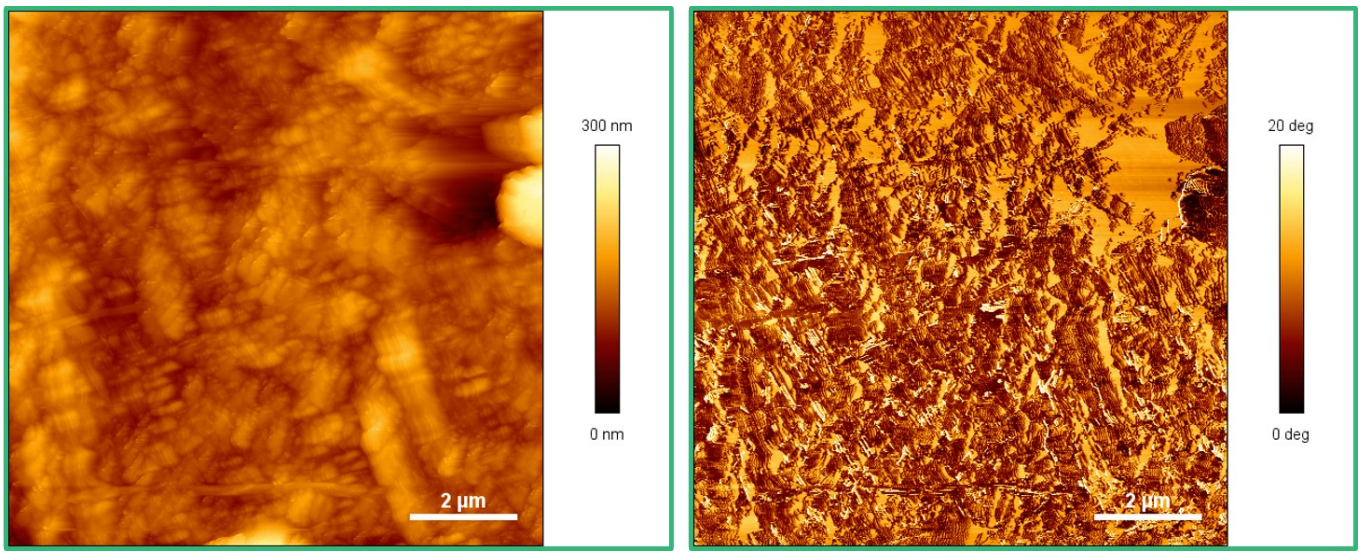

Figure S56: AFM image of VU-(ALs-Pri)$_{0.5}$ showing the height plot (left) and the phase plot (right).

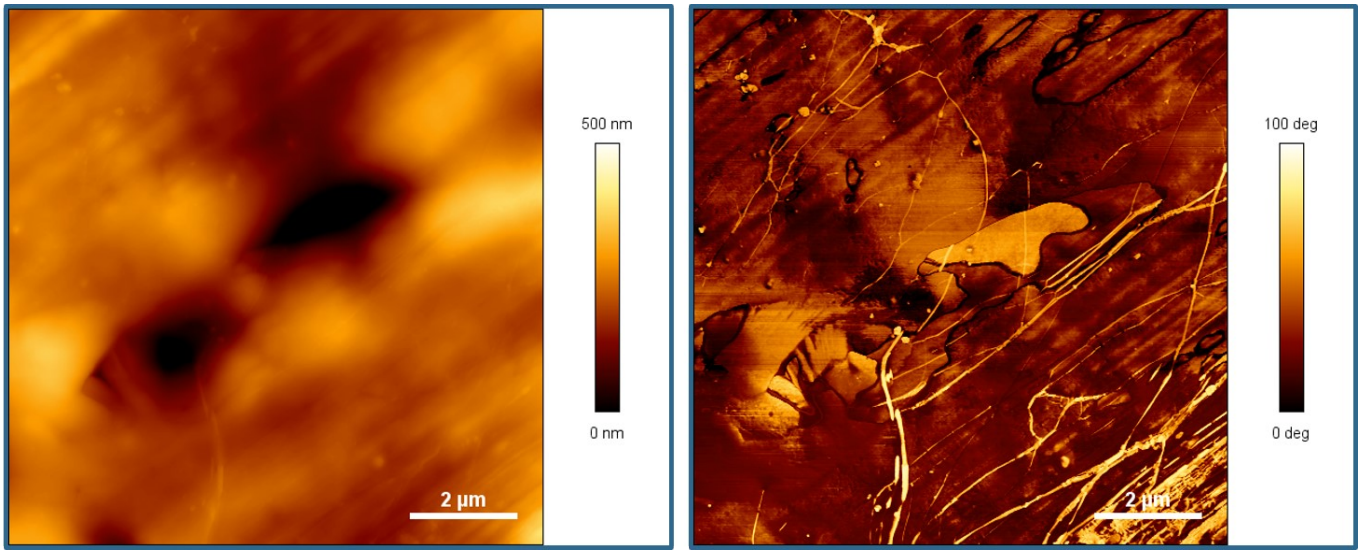

Figure S57: AFM image of VU-(ALs/APPD$_{10}$-Pri)$_{0.5}$ showing the height plot (left) and the phase plot (right).

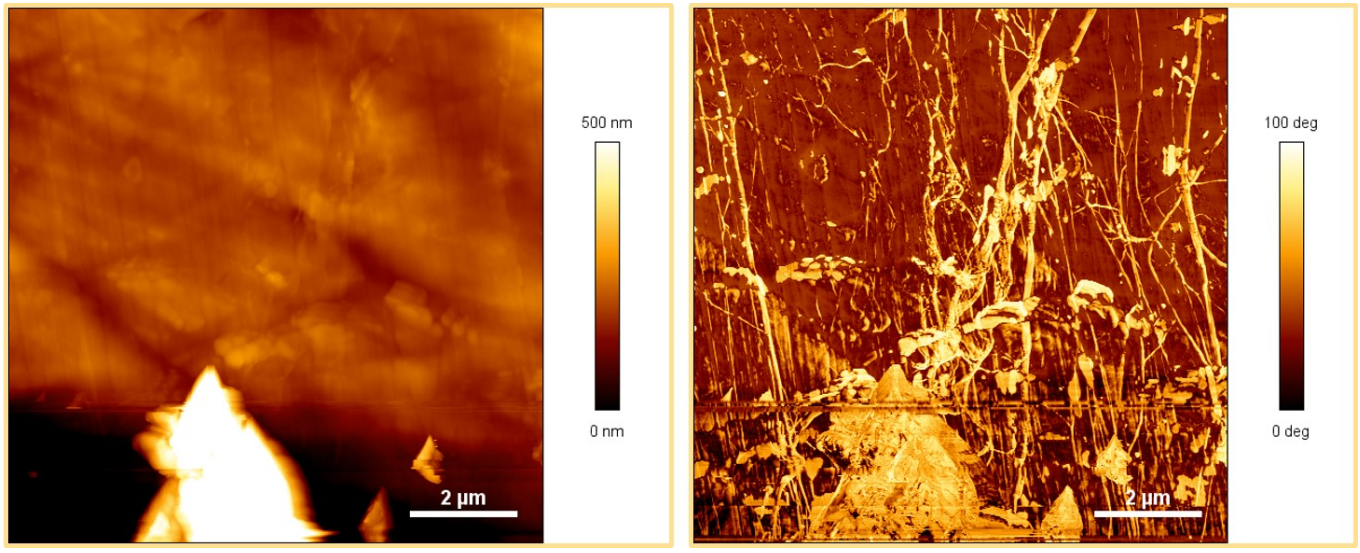

Figure S58: AFM image of VU-(ALnC-Pri)$_{0.8}$ showing the height plot (left) and the phase plot (right).

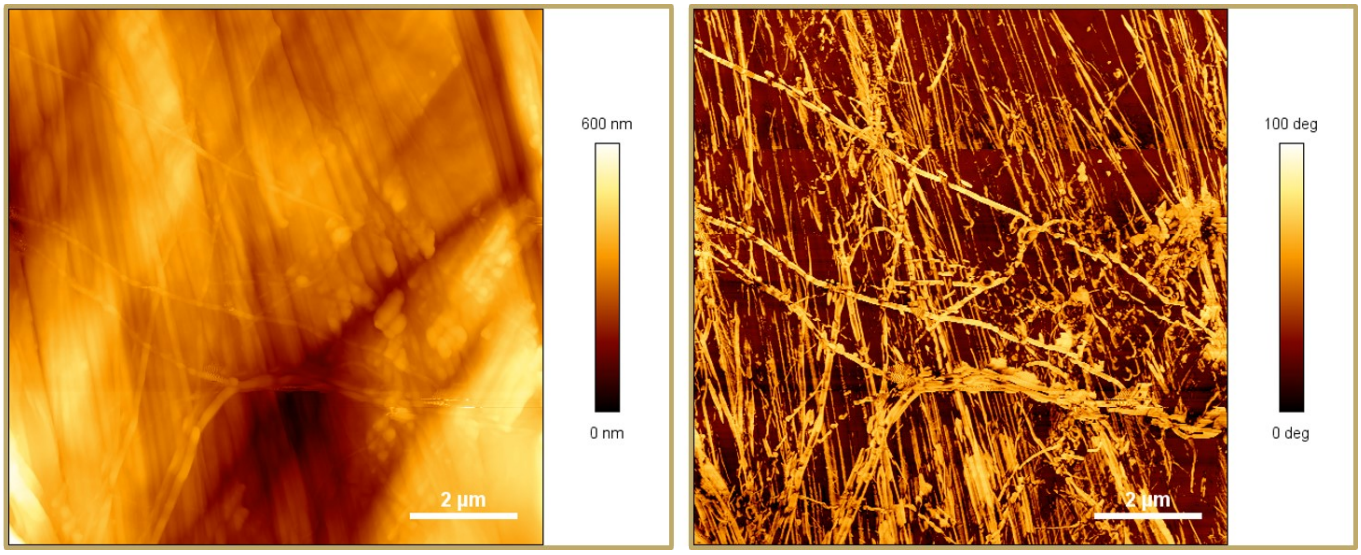

Figure S59: AFM image of VU-(ALnP-Pri)$_{0.8}$ showing the height plot (left) and the phase plot (right).

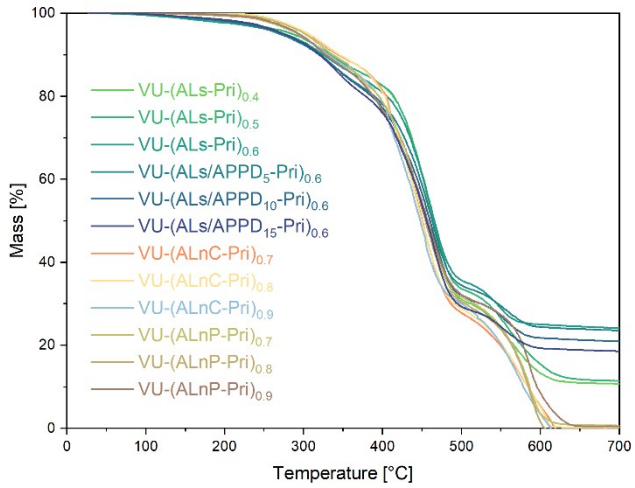

Figure S60: Thermogravimetric analysis measurements of the lignin vitrimers carried out in the range of 25 °C to 800 °C (10 K min^{-1}) under ambient (oxygen) atmosphere, showing thermal degradation temperatures $T_{5\%}$ of 272 °C to 307 °C.

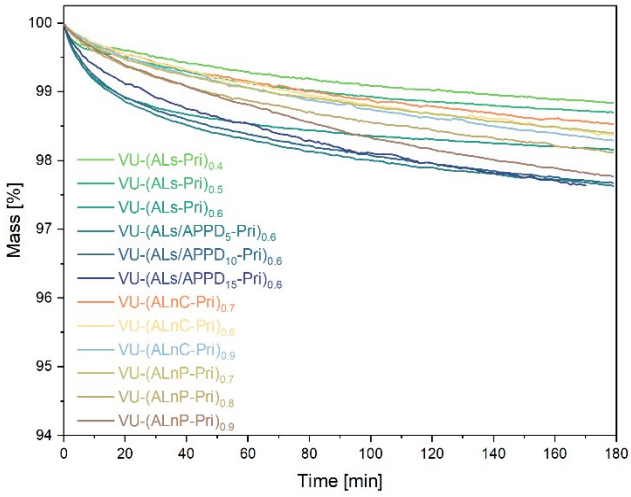

Figure S61: Isothermal thermogravimetric analysis measurements under oxygen atmosphere of the lignin vitrimers carried out at a temperature of 180 °C for 3 h, showing no thermal degradation.

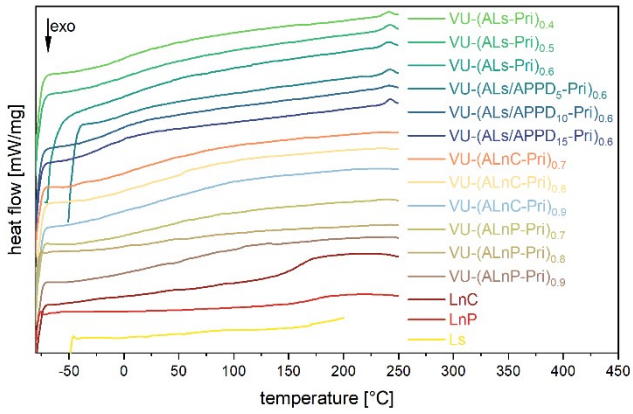

Figure S62: DSC-heating curves (−50 °C to 250 °C, 10 K min^{-1}, N_2 atmosphere, second heating cycle) of the lignin vitrimers.

Table S7: Overview of the synthesized Lignin vitrimers and their characteristic properties measured by DSC, DMA, TGA, and tensile testing.

Sample	$T_{g,DSC}$[a] [°C]	$T_{g,DMA}$[b] [°C]	$T_{5\%}$[c] [°C]	$G'_{20°C}$[d] [MPa]	$G'_{110°C}$[e] [MPa]	$E_{t,Ø,r.t.}$[f] [MPa]	$\sigma_{m,Ø,r.t.}$[g] [MPa]	$\varepsilon_{m,Ø,r.t.}$[h] [%]	E_a[i] [kJ mol^{-1}]
VU-(ALs-Pri)$_{0.4}$	-	35	287	144.3	3.91	255 ± 19	13.5 ± 0.2	13.3 ± 2.0	61.4 ± 1.7
VU-(ALs-Pri)$_{0.5}$	-	40	287	173.7	6.61	383 ± 20	17.5 ± 1.3	8.3 ± 0.4	63.8 ± 3.1
VU-(ALs-Pri)$_{0.6}$	-	45	272	192.7	11.5	489 ± 8.8	10.6 ± 1.6	2.1 ± 0.3	123 ± 3.6
VU-(ALs/APPD$_5$-Pri)$_{0.6}$	-	-	271	253.2	16.5	360 ± 19	11.5 ± 2.8	3.7 ± 1.1	81.3 ± 3.0
VU-(ALs/APPD$_{10}$-Pri)$_{0.6}$	-	-	274	100.0	6.86	230 ± 6.0	13.0 ± 0.3	20.1 ± 1.7	64.1 ± 1.9
VU-(ALs/APPD$_{15}$-Pri)$_{0.6}$	-	-	275	85.2	8.75	108 ± 12	6.0 ± 1.8	11.5 ± 4.4	79.3 ± 1.8
VU-(ALnC-Pri)$_{0.7}$	-	85	305	340.8	5.1	479 ± 53	24.3 ± 3.0	10.6 ± 1.5	*219 ± 11*[j]
VU-(ALnC-Pri)$_{0.8}$	-	95	307	347.1	6.5	594 ± 14	29.4 ± 1.1	8.9 ± 1.0	*170 ± 4.5*[j]
VU-(ALnC-Pri)$_{0.9}$	-	110	295	440.7	10.3	672 ± 25	30.3 ± 1.0	6.8 ± 1.2	*290 ± 16*[j]
VU-(ALnP-Pri)$_{0.7}$	-	115	302	487.1	12.1	704 ± 17	24.5 ± 1.0	3.7 ± 0.2	*312 ± 6.4*[j]
VU-(ALnP-Pri)$_{0.8}$	-	125	294	370.9	18.5	798 ± 27	21.0 ± 0.6	2.7 ± 0.1	*465 ± 2.3*[j]
VU-(ALnP-Pri)$_{0.9}$	-	135	295	430.2	25.9	837 ± 114	17.1 ± 6.5	2.1 ± 0.5	*773 ± 53*[j]

a) The $T_{g,DSC}$ was determined using the mid-point of the step in the DSC-curves of the second heating cycle. b) The $T_{g,DMA}$ was determined by the maximum of the tan δ curve of the temperature-sweep measurements, if applicable, which were also used to determine the values of G' (ω = 6.28 rad s^{-1}, γ = 0.01%, T = 150 – 0 °C) at 20 °C d) and 110 °C. c) The temperature of 5% mass loss was determined by TGA-measurements (T = 25 – 700 °C, 10 K min^{-1}). f) The elastic modulus was determined at the start of the stress strain measurement (1 mm min^{-1}, ε = 0.05% – 0.25%, 23 °C). g,h) The stress, strain, and elongation values were determined in a stress-strain measurement (1 mm min^{-1} between 0.05% and 0.25% elongation and the rest of the test was carried out at 10 mm min^{-1}, T = 23 °C) i) The activation energy was determined by linearization of the characteristic averaged stress-relaxation times from KWW-fitted stress-relaxation modulus data (γ = 1%, T = 180 – 110 °C). j) The calculated values are strongly influenced by the T_g of the lignin source, thereby leading to significant error, showing influence of segmental relaxation and movement.

Table S8: Overview of vinylogous urethane lignin vitrimers from the literature and their characteristic properties measured by DSC, DMA, TGA, and tensile stress.

Sample	Lignin	Lignin [wt.%]	E (MPa)	σ (MPa)	ε (%)	T_g (°C)	$T_{5\%}$ (°C)	E_a [kJ mol^{-1}]
Ph-VU-600[1]	OOSL	46	2.4 ± 0.10	1.0 ± 0.05	115 ± 4	- 10	266	68 ± 5
VU-50-300[2]	OSL	50	420 ± 30	17.2 ± 0.7	22 ± 3	18	270	72
Vitrimer-1[3]	WSL	39.8	184 ± 7.1	15.1 ± 1.5	34.5 ± 7.6	87	309	134

1) L. Sougrati, A. Duval and L. Avérous, *Chem. Eng. J.*, **2025**, 511. 2) L. Sougrati, A. Duval and L. Averous, *ChemSusChem*, **2023**, 16, e202300792. 3) J. Liu, A. Pich and K. V. Bernaerts, *Green Chem*., **2024**, 26, 1414-1429.

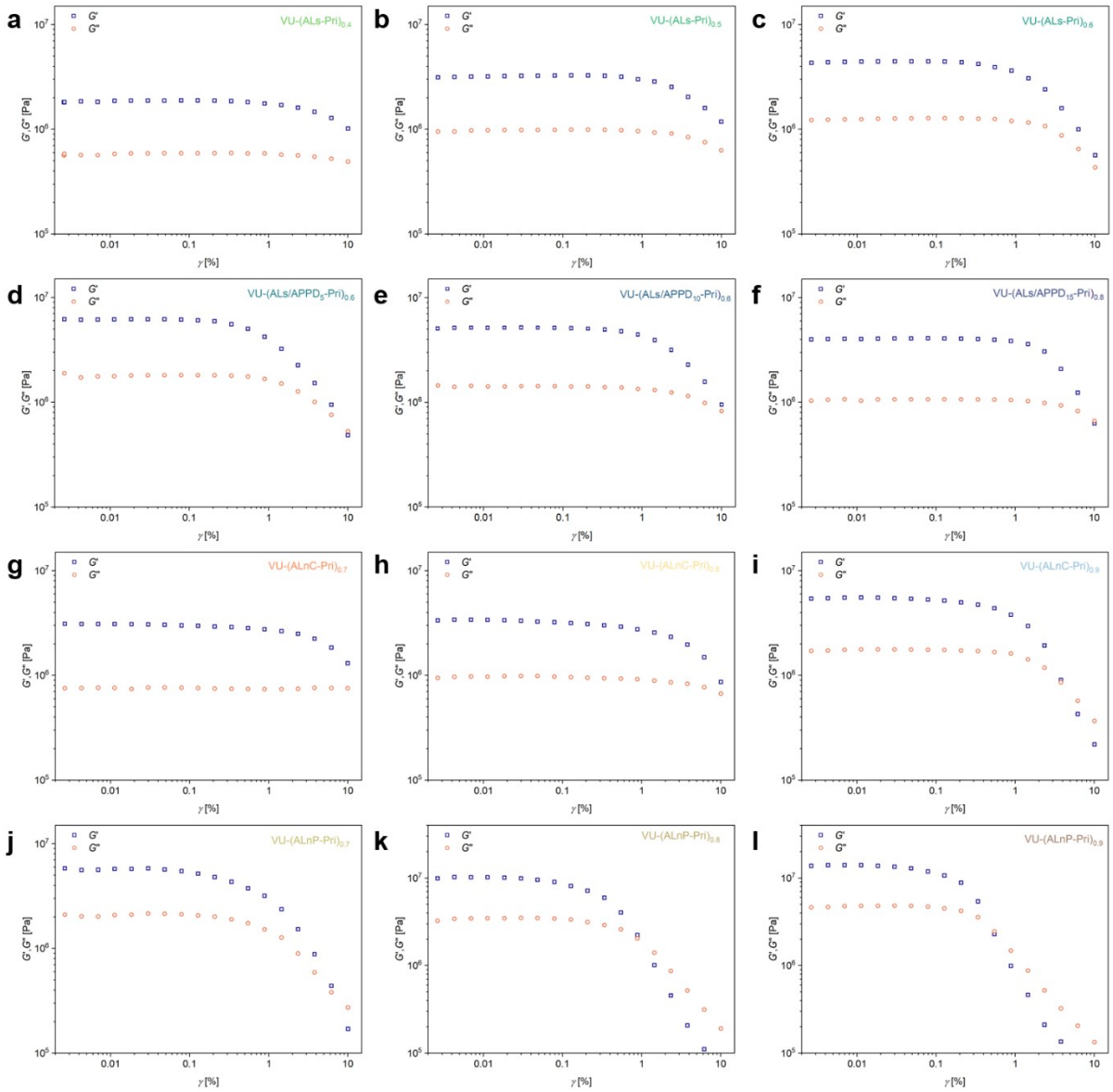

Figure S63: Amplitude sweep measurements of the produced lignin vitrimers between 0.001% and 10% shear strain *γ* performed at a constant angular frequency of 6.28 rad s^{-1}.

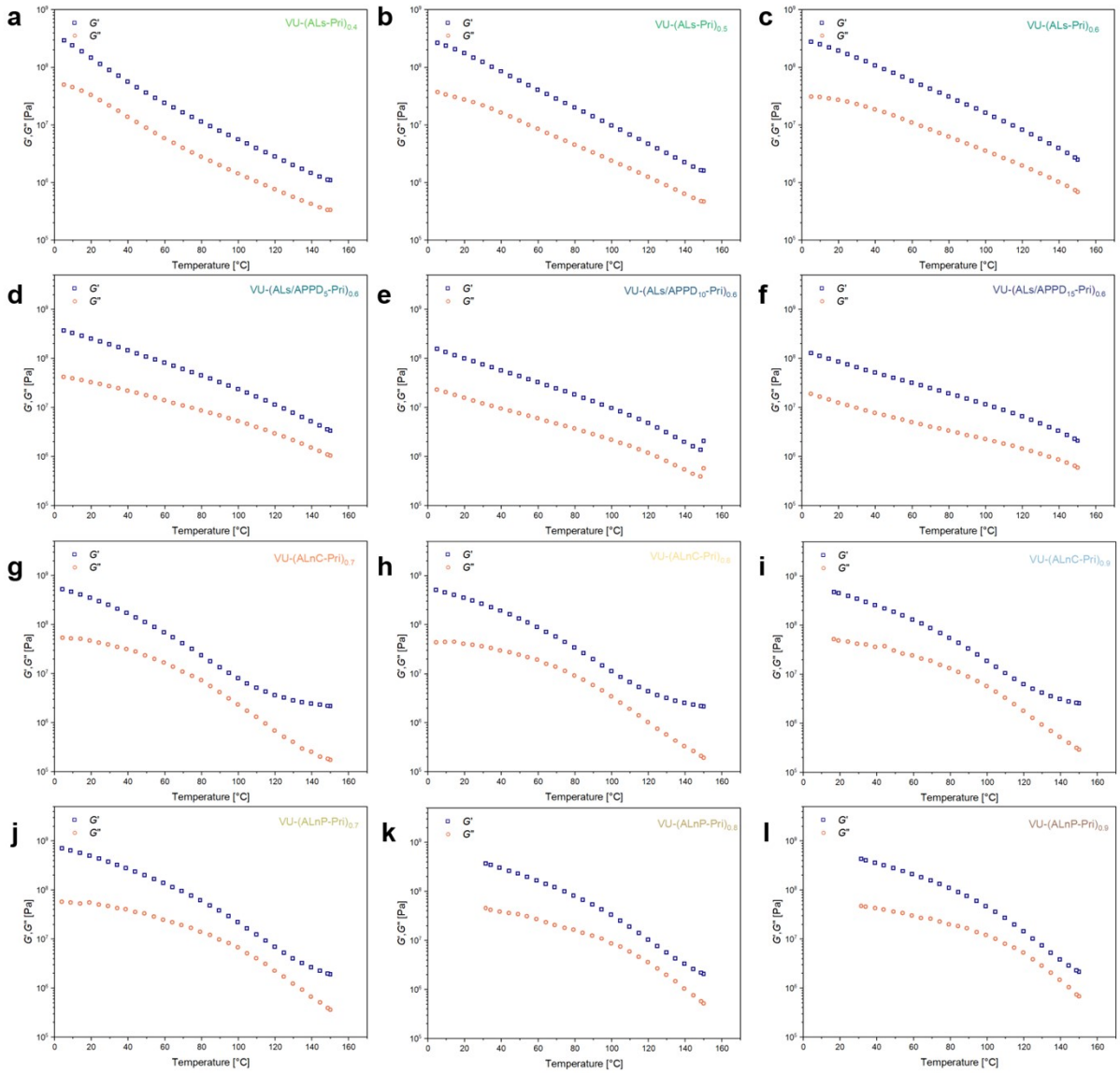

Figure S64: Temperature sweep measurements of the produced lignin vitrimers in the temperature range of 150 °C – 0 °C performed at a constant angular frequency of 6.28 rad s^{-1} and a constant shear strain amplitude of 0.01%.

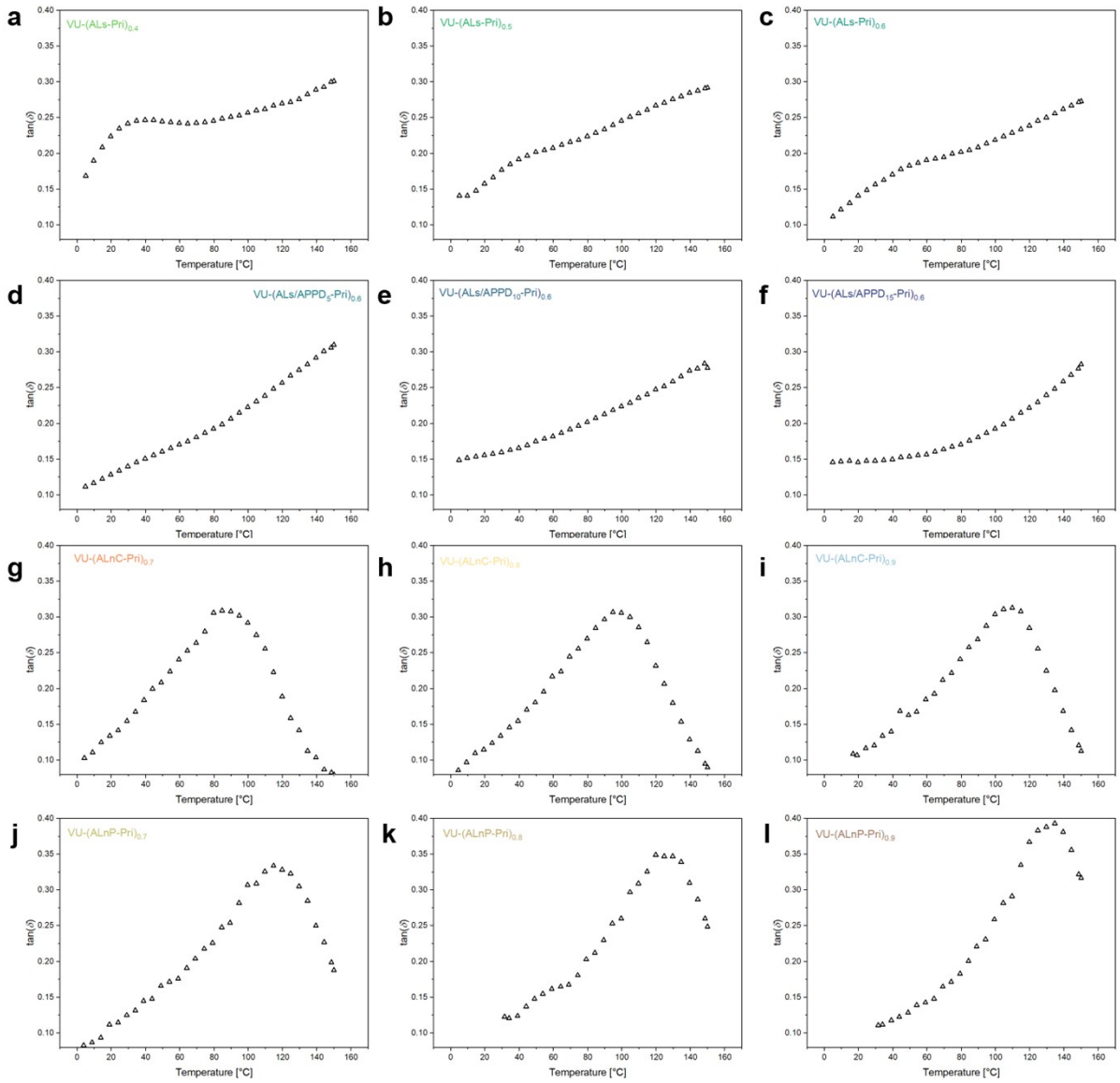

Figure S65: Tan(δ) values calculated from the storage and loss moduli of the temperature sweep measurements of the produced lignin vitrimer materials in the temperature range of 150 °C – 0 °C performed at a constant angular frequency of 6.28 rad s^{-1} and a shear strain amplitude of 0.01%.

Equation S4

$$G(t) = G_0 \, e^{\left(\frac{-t}{\tau_r}\right)^{\beta}}$$

$G(t)$: stress modulus at relaxation time [Pa]
G_0 : initial stress modulus [Pa]
t : time [s]
τ_r : characteristic relaxation time [s]
β : stretch parameter ($0 \leq \beta \leq 1$) [-]

Equation S5

$$\langle \tau_r \rangle = \frac{\tau_r \, \Gamma\left(\frac{1}{\beta}\right)}{\beta}$$

$\langle \tau_r \rangle$: average stress relaxation time [s]

Γ : gamma function [-]

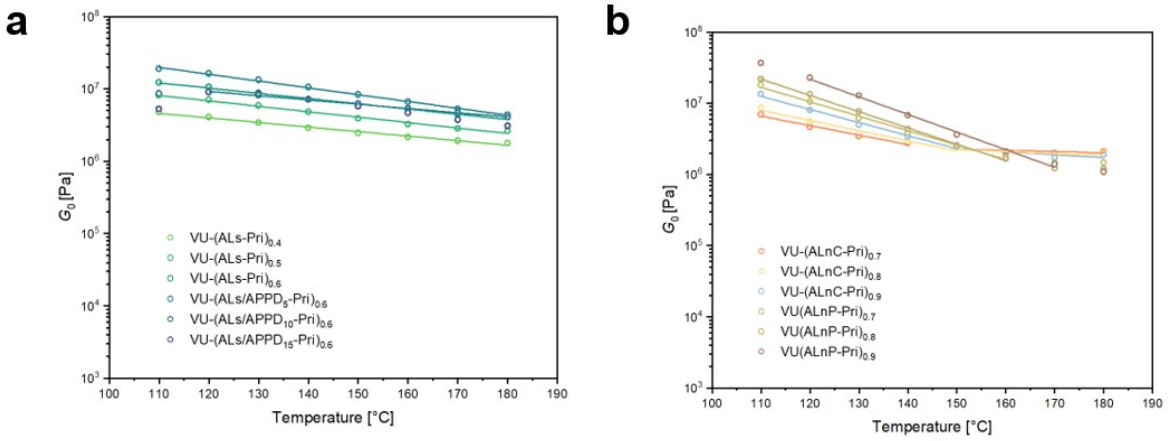

Figure S66: Initial relaxation moduli G_0 of the lignin vitrimers VU-(ALs-Pri) and VU-(ALs/APPD-Pri) (a) and the vitimers VU-(ALnC-Pri) and VU-(ALnP-Pri) (b) as a function of temperature from the stress-relaxation measurement (γ = 1%, F_N = 1N) between 110 °C and 180 °C. The straight lines connecting the dots serve as an orientation guide for the eye. The materials VU-(ALnC-Pri) and VU-(ALnP-Pri) (b) show two different slopes of these straight lines above and under 160 °C.

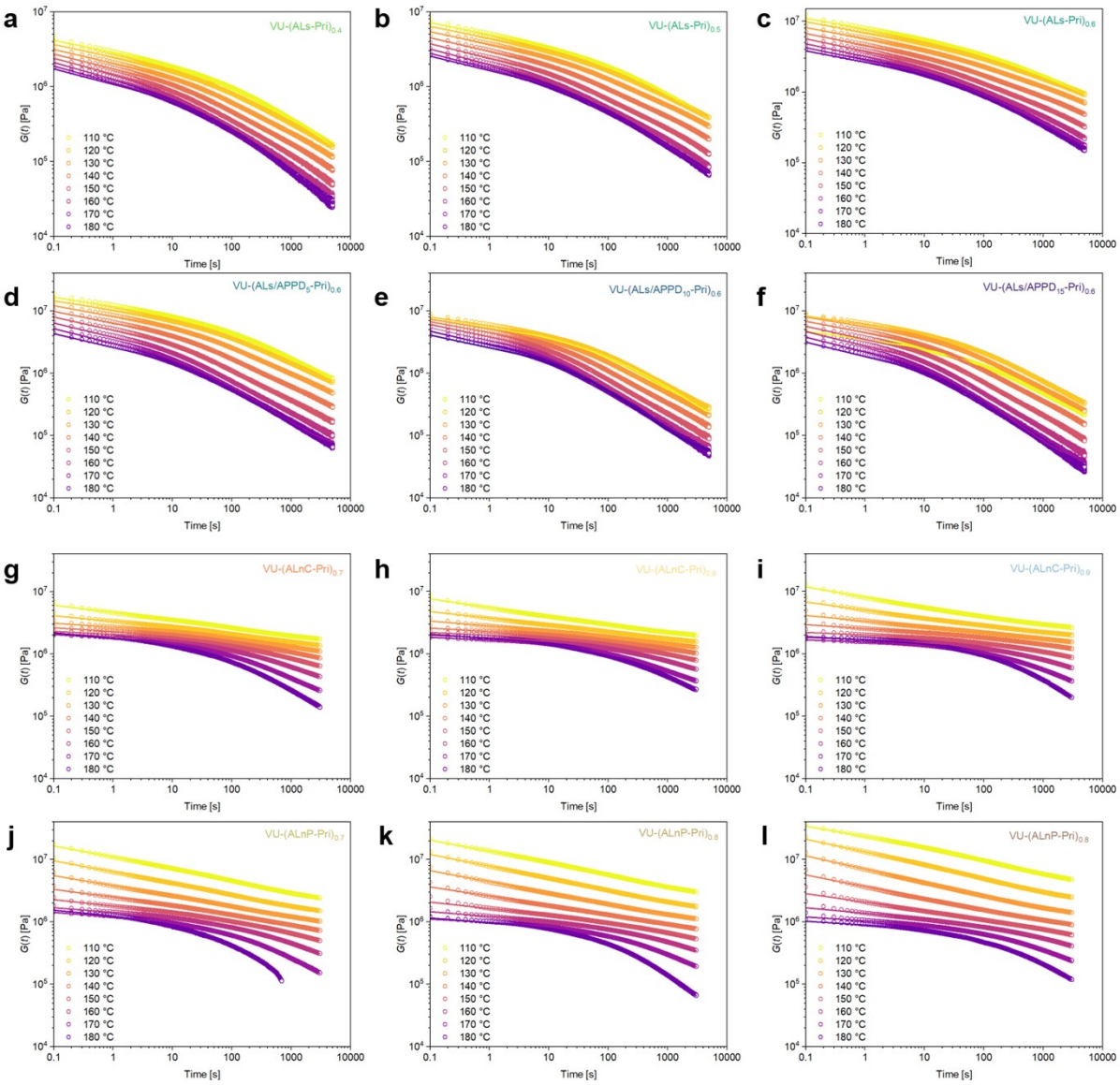

Figure S67: Stress-relaxation measurement of the lignin vitrimers, plotting the stress-relaxation modulus $G(t)$ versus the stress-relaxation time measured at temperatures in the range of 110 to 180 °C while applying a shear strain of 1%. The lines display the stretched exponential fit functions for the respective temperatures, calculated from the stress-relaxation data.

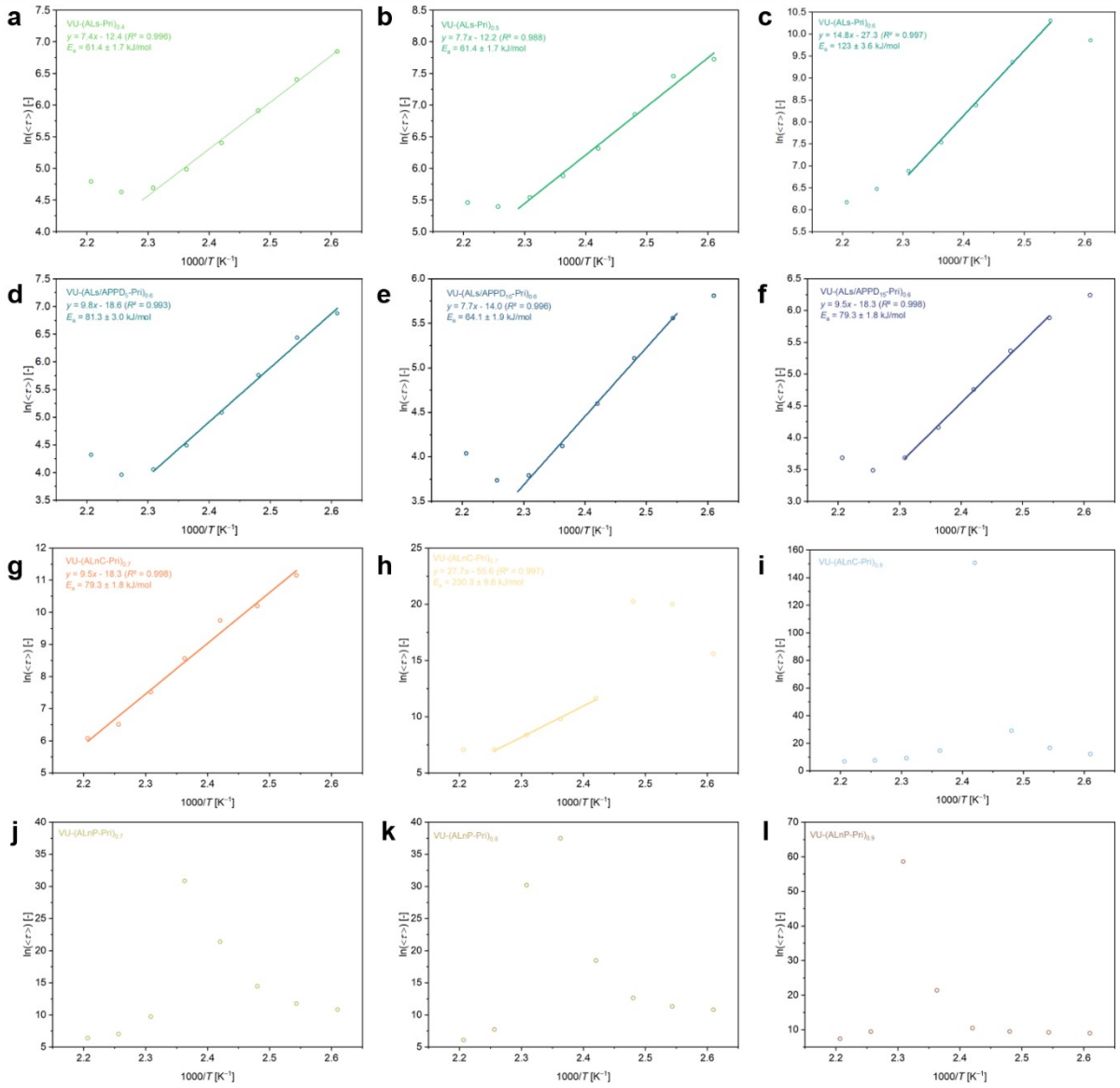

Figure S68: Plot of ln <τ> versus 1000/T of the lignin vitrimers to calculate the activation energies (a – h) from the slope of the linear fit of the calculated <τ> values from the stretched exponential fit in the temperature range of the stress-relaxation measurements (γ = 1%, F_N = 1N) between 110 °C and 180 °C of the lignin vitrimers. The stress relaxation times of the materials VU-(ALnC-Pri)$_{0.8}$, VU-(ALnC-Pri)$_{0.9}$, VU-(ALnC-Pri)$_{0.7}$, VU-(ALnC-Pri)$_{0.8}$, and VU-(ALnC-Pri)$_{0.9}$ are influenced by the T_g of the lignin particles and show deviations from the expected values, and the diagrams cannot be used to calculate the activation energy of the transamination reaction under 160 °C.

Table S9: Summary of the values of the stretch factor β and the calculated average values of the characteristic stress relaxation time <τ> for the KWW fit of the stress-relaxation measurements (γ = 1%, F_N = 1N) between 110 °C and 180 °C of the lignin vitrimers. The orange markings are used to highlight the relaxation times, which are influenced by the T_g of the respective materials (VU-(ALnC-Pri) and VU-(ALnP-Pri)) and show deviations from the expected values.

Sample	$\beta_{110°C}$ [-]	$\beta_{120°C}$ [-]	$\beta_{130°C}$ [-]	$\beta_{140°C}$ [-]	$\beta_{150°C}$ [-]	$\beta_{160°C}$ [-]	$\beta_{170°C}$ [-]	$\beta_{180°C}$ [-]	$\langle\tau\rangle_{110°C}$ [s]	$\langle\tau\rangle_{120°C}$ [s]	$\langle\tau\rangle_{130°C}$ [s]	$\langle\tau\rangle_{140°C}$ [s]	$\langle\tau\rangle_{150°C}$ [s]	$\langle\tau\rangle_{160°C}$ [s]	$\langle\tau\rangle_{170°C}$ [s]	$\langle\tau\rangle_{180°C}$ [s]
VU-(ALs-Pri)$_{0.4}$	0.151	0.156	0.157	0.159	0.158	0.160	0.160	0.174	940	603	369	221	146	109	102	120
VU-(ALs-Pri)$_{0.5}$	0.138	0.140	0.144	0.146	0.145	0.146	0.151	0.167	2263	1729	945	552	358	254	221	235
VU-(ALs-Pri)$_{0.6}$	0.111	0.103	0.108	0.116	0.126	0.136	0.150	0.176	19130	29962	11618	4363	1871	980	651	480
VU-(ALs/APPD$_{5}$-Pri)$_{0.6}$	0.170	0.175	0.180	0.181	0.182	0.182	0.179	0.179	966	623	317	161	89	57	52	75
VU-(ALs/APPD$_{10}$-Pri)$_{0.6}$	0.218	0.227	0.227	0.226	0.225	0.224	0.223	0.222	333	259	165	99	62	44	42	57
VU-(ALs/APPD$_{15}$-Pri)$_{0.6}$	0.209	0.217	0.211	0.208	0.207	0.210	0.210	0.208	513	359	213	116	64	40	33	40
VU-(ALnC-Pri)$_{0.7}$	0.069	0.120	0.165	0.201	0.248	0.287	0.315	0.281	$2.5{\cdot}10^{6}$	$6.9{\cdot}10^{4}$	$2.7{\cdot}10^{4}$	$1.7{\cdot}10^{4}$	5216	1837	673	435
VU-(ALnC-Pri)$_{0.8}$	0.051	0.053	0.166	0.229	0.286	0.229	0.324	0.280	$5.9{\cdot}10^{6}$	$4.8{\cdot}10^{8}$	$6.2{\cdot}10^{8}$	$1.1{\cdot}10^{5}$	$1.8{\cdot}10^{4}$	4264	1164	1167
VU-(ALnC-Pri)$_{0.9}$	0.052	0.048	0.043	0.022	0.172	0.287	0.344	0.360	$1.7{\cdot}10^{5}$	$1.7{\cdot}10^{7}$	$4.1{\cdot}10^{12}$	$2.7{\cdot}10^{65}$	$2.0{\cdot}10^{6}$	9185	1990	819
VU-(ALnP-Pri)$_{0.7}$	0.067	0.060	0.056	0.053	0.055	0.194	0.277	0.244	$5.1{\cdot}10^{4}$	$1.3{\cdot}10^{5}$	$1.9{\cdot}10^{6}$	$1.9{\cdot}10^{9}$	$2.5{\cdot}10^{13}$	$1.7{\cdot}10^{4}$	1128	597
VU-(ALnP-Pri)$_{0.8}$	0.068	0.056	0.051	0.047	0.041	0.079	0.289	0.328	$4.9{\cdot}10^{4}$	$8.3{\cdot}10^{4}$	$3.1{\cdot}10^{5}$	$1.1{\cdot}10^{8}$	$1.9{\cdot}10^{16}$	$1.3{\cdot}10^{13}$	2273	443
VU-(ALnP-Pri)$_{0.9}$	0.092	0.067	0.054	0.056	0.045	0.038	0.223	0.278	7922	$1.1{\cdot}10^{4}$	$1.3{\cdot}10^{4}$	$3.5{\cdot}10^{4}$	$1.9{\cdot}10^{9}$	$2.8{\cdot}10^{25}$	$1.3{\cdot}10^{4}$	1630

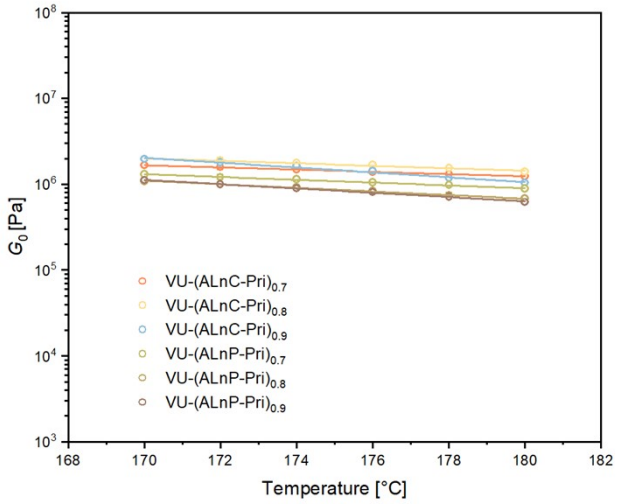

Figure S69: Initial relaxation moduli G_0 of the lignin vitrimers VU-(ALnC-Pri) and VU-(ALnP-Pri) as a function of temperature of the stress-relaxation measurements (γ = 1%, F_N = 1N) between 170 °C and 180 °C of the indicated lignin vitrimers. The straight lines connecting the dots serve as an orientation guide for the eye.

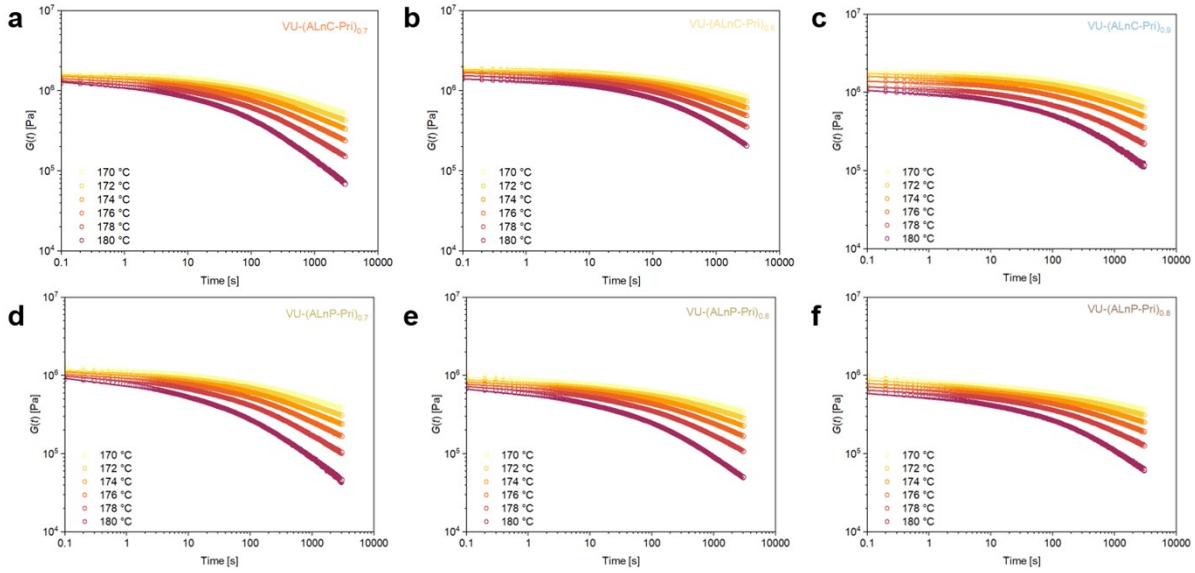

Figure S70: Stress-relaxation measurement of the lignin vitrimers VU-(ALnC-Pri) and VU-(ALnP-Pri), plotting the stress-relaxation modulus $G(t)$ versus the stress-relaxation time measured at temperatures in the range of 170 to 180 °C while applying a shear strain of 1%. The lines display the stretched exponential fit functions for the respective temperatures, calculated from the stress-relaxation data.

Table S10: Summary of the β $<\tau>$ values for the KWW fit of the stress-relaxation measurements of the lignin vitrimer materials VU-(ALnC-Pri) and VU-(ALnP-Pri)in the temperature range of 170 °C to 180 °C while applying a shear strain of 1%.

Sample	$\beta_{170°C}$ [-]	$\beta_{172°C}$ [-]	$\beta_{174°C}$ [-]	$\beta_{176°C}$ [-]	$\beta_{178°C}$ [-]	$\beta_{180°C}$ [-]	$<\tau>_{170°C}$ [s]	$<\tau>_{172°C}$ [s]	$<\tau>_{174°C}$ [s]	$<\tau>_{176°C}$ [s]	$<\tau>_{178°C}$ [s]	$<\tau>_{180°C}$ [s]
VU-(ALnC-Pri)$_{0.7}$	0.363	0.364	0.364	0.357	0.347	0.334	1668	1325	1032	809	570	289
VU-(ALnC-Pri)$_{0.8}$	0.373	0.383	0.389	0.394	0.391	0.396	2939	2350	1956	1543	1303	923
VU-(ALnC-Pri)$_{0.9}$	0.347	0.361	0.368	0.381	0.363	0.344	5331	3439	2531	1667	1341	790
VU-(ALnP-Pri)$_{0.7}$	0.305	0.312	0.320	0.316	0.300	0.275	3053	2163	1448	1029	678	312
VU-(ALnP-Pri)$_{0.8}$	0.202	0.262	0.290	0.299	0.294	0.279	149858	10062	4094	2336	1353	597
VU-(ALnP-Pri)$_{0.9}$	0.163	0.174	0.183	0.192	0.204	0.237	30662	20130	13835	9751	6599	3230

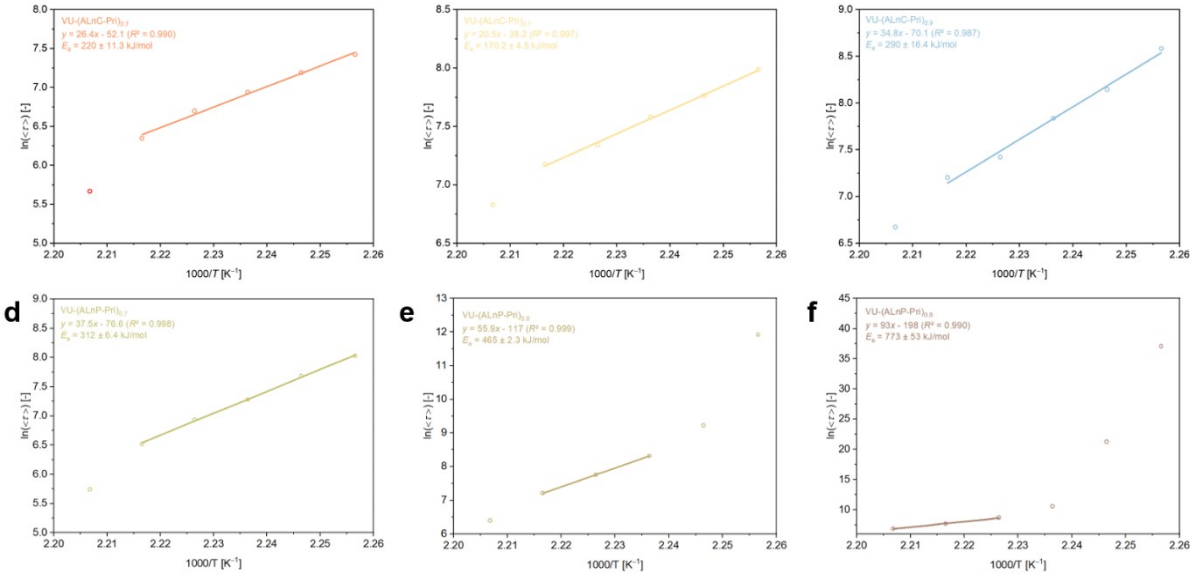

Figure S71: Plot of ln <τ> versus 1000/T of the lignin vitrimers VU-(ALnC-Pri) and VU-(ALnP-Pri) in the range of 170 to 180 °C while applying a shear strain of 1% to calculate the activation energies (a – f) from the slope of the linear fit of the calculated <τ> values from the stretched exponential fit. The stress relaxation times of the materials are still influenced by the T_g of the lignin particles and show high relaxation activation energies, which cannot be assigned solely to the transamination reaction of vinylogous urethanes but also involve other relaxation effects.

Table S11: Overview of the recycled lignin vitrimers and their characteristic properties measured by DSC, DMA, TGA, and tensile stress.

Sample	$T_{g,DMA}$ [a)] [°C]	$G'_{20°C}$ [b)] [MPa]	$G'_{110°C}$ [c)] [MPa]	$E_{t,Ø,r.t.}$ [d)] [MPa]	$\sigma_{m,Ø,r.t.}$ [e)] [MPa]	$\varepsilon_{m,Ø,r.t.}$ [f)] [%]	E_a [i)] [kJ mol^{-1}]
VU-(ALs-Pri)$_{0.5}$ (5 recycles)	45	11.2	2.78	415 ± 26	18.3 ± 1.0	8.3 ± 0.4	-
VU-(ALs/APPD$_{10}$-Pri)$_{0.6}$ (5 recycles)	35	31.8	4.36	133 ± 4.9	12.0 ± 0.8	19.3 ± 0.5	1171 ± 182 [j)]
VU-(ALnC-Pri)$_{0.8}$ (5 recycles)	95	43.4	1.15	598 ± 17	21.6 ± 2.6	4.0 ± 0.8	1797 ± 484.5 [j)]
VU-(ALnP-Pri)$_{0.8}$ (5 recycles)	140	95.8	3.45	418 ± 7.4	18.8 ± 1.3	5.1 ± 0.5	13902 ± 469 [j)]

a) The $T_{g,DMA}$ was determined by the maximum of the tan δ curve of the temperature-sweep measurements, which were also used to determine the values of G' (ω = 6.28 rad s^{-1}, γ = 0.01%, T = 150 – 0 °C) at 20 °C b) and 110 °C c). The closest available data point to the respective temperature is listed. d) The elastic modulus was determined at the start of the stress strain measurement (1 mm min^{-1}, ε = 0.05% – 0.25%, 23 °C). e,f) The stress, strain, and elongation values were determined in a stress-strain measurement (1 mm min^{-1} between 0.05% and 0.25% elongation and the rest of the test was carried out at 10 mm min^{-1}, T = 23 °C) i) The activation energy was determined by linearization of the characteristic averaged stress-relaxation times from KWW-fitted stress-relaxation modulus data (γ = 1%, T = 180 – 110 °C) j) The calculated values are strongly influenced by the T_g of the lignin resource, thereby leading to significant error, showing influence of segmental relaxation and movement.

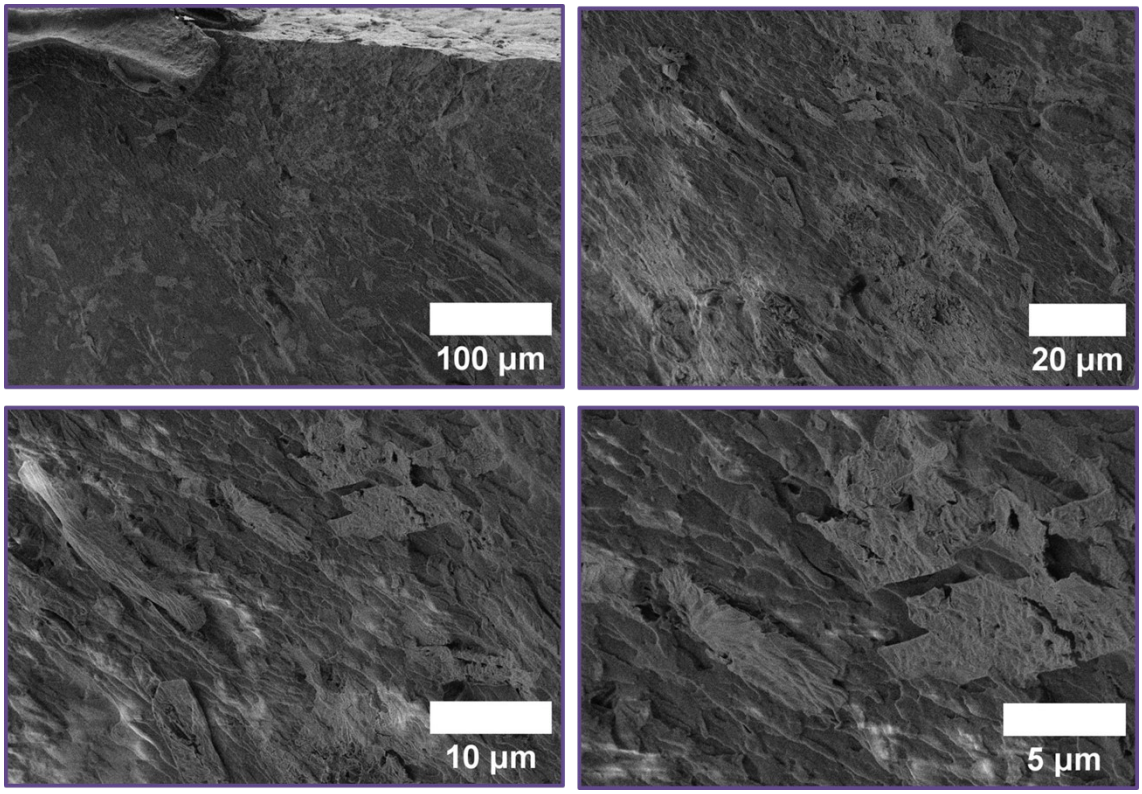

Figure S72: SEM images of recycled VU-(Als-Pri)$_{0.5}$ with different magnifications.

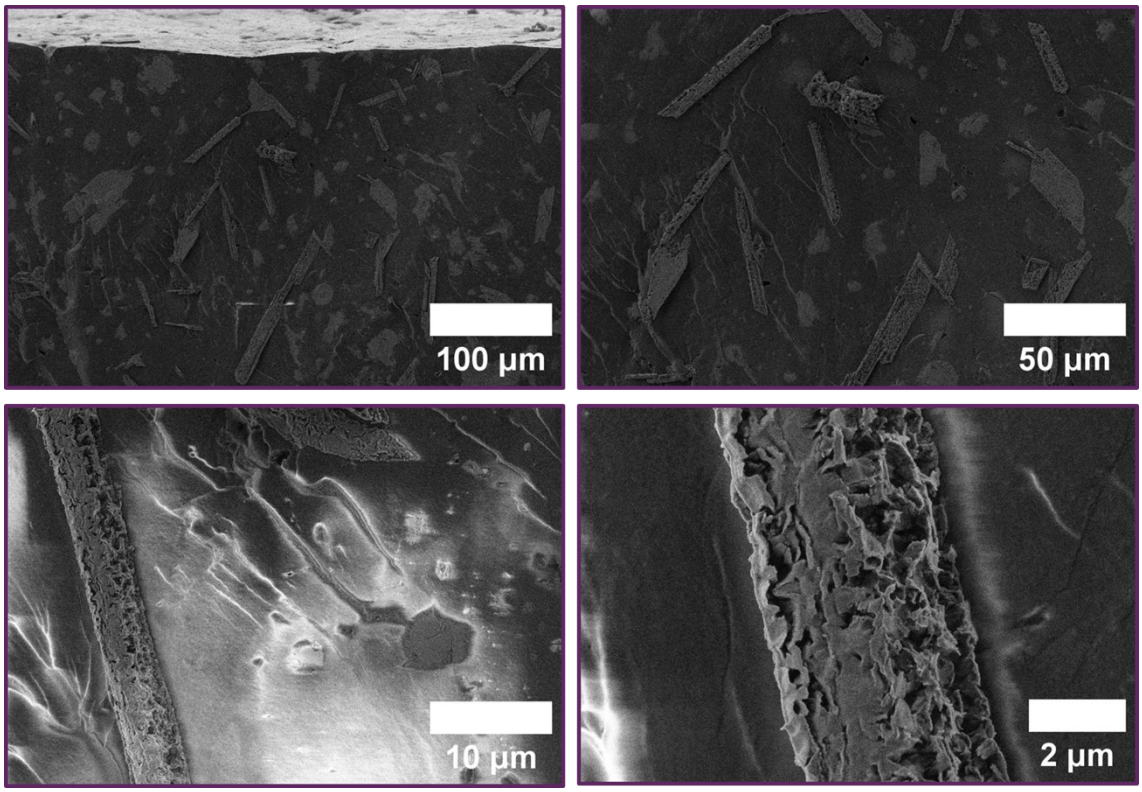

Figure S73: SEM images of recycled VU-(Als/APPD$_{10}$-Pri)$_{0.6}$ with different magnifications.

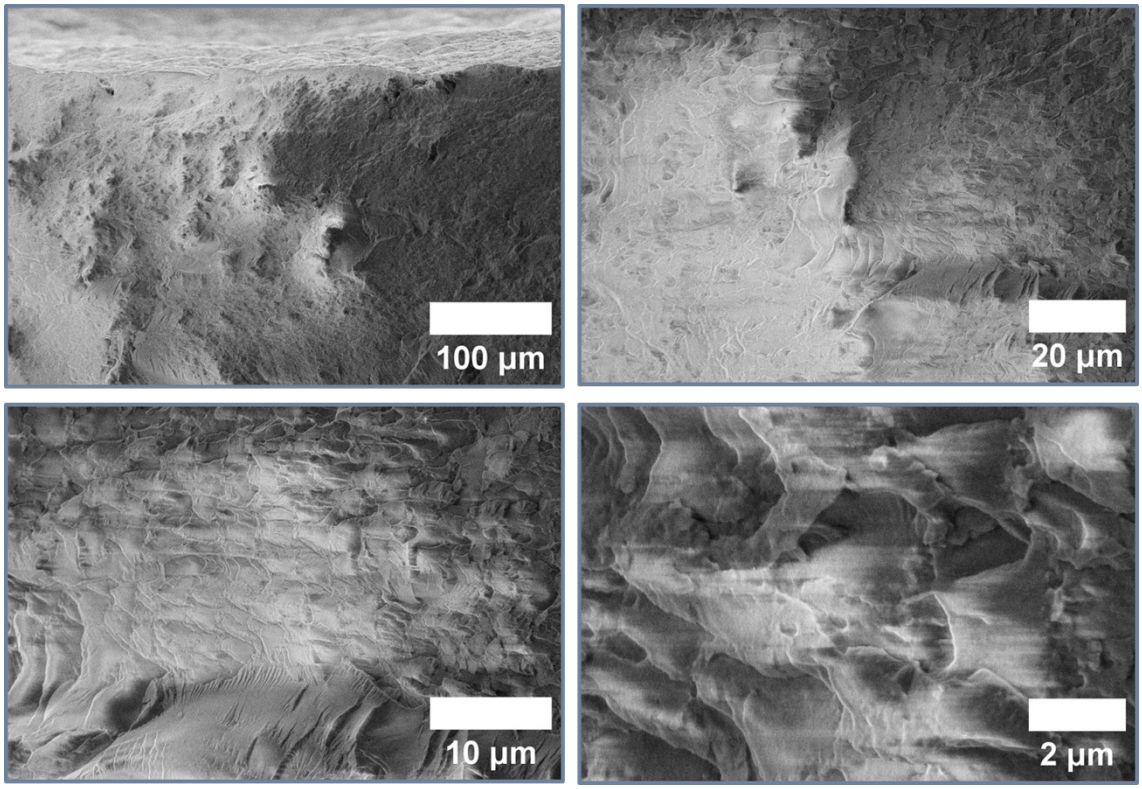

Figure S74: SEM images of recycled VU-(AlnC-Pri)$_{0.8}$ with different magnifications.

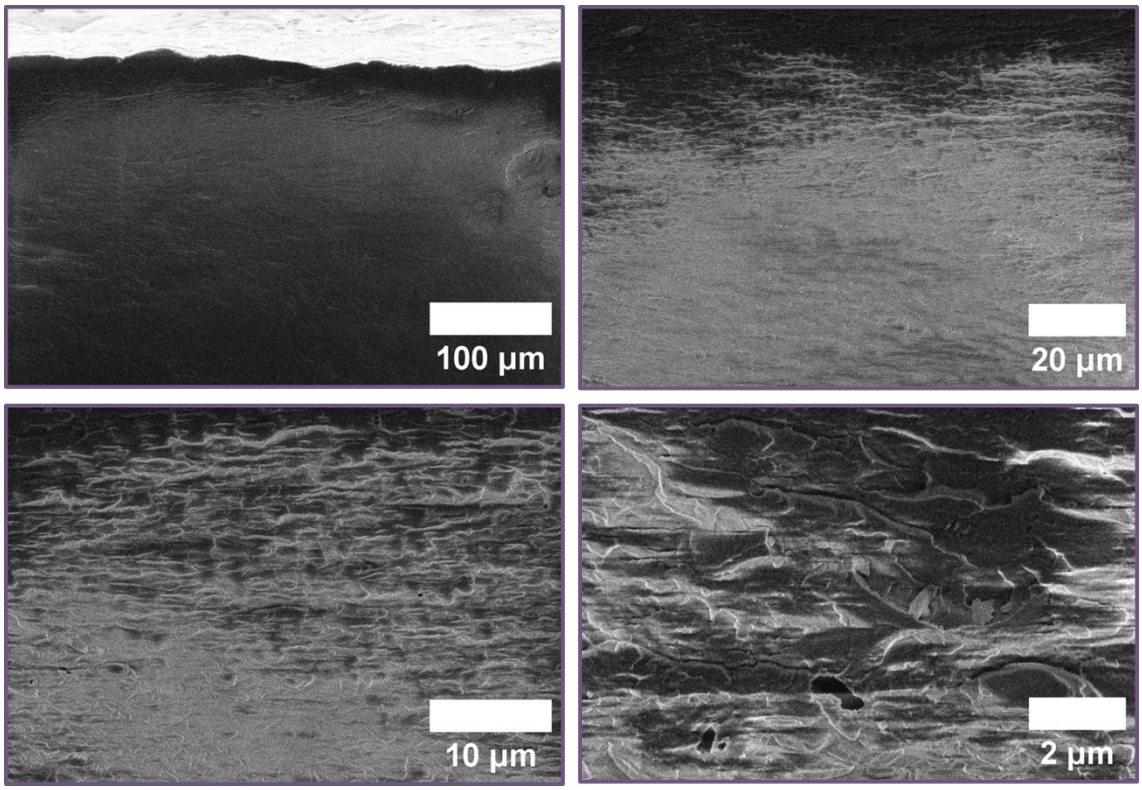

Figure S75: SEM images of recycled VU-(AlnP-Pri)$_{0.8}$ with different magnifications.

Table S12: EDX-measurements of VU-(ALs-Pri)$_{0.5}$ after recycling, showing the irradiated area (left), the EDX spectra (middle) and a table with the relative intensity of respective elements in % (right).

VU-(ALs-Pri)$_{0.5}$ recycled

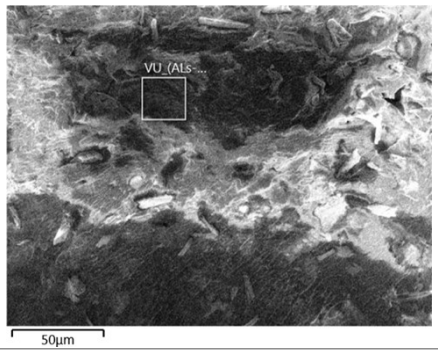

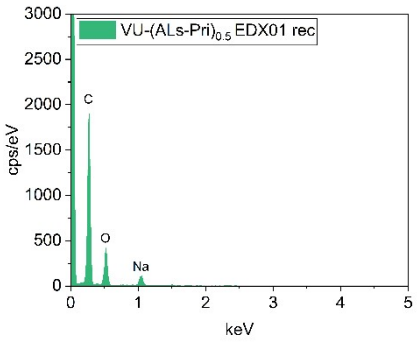

Element	Atom%
C	77.78
N	-
O	19.91
Na	1.89
Al	0.18
S	0.25

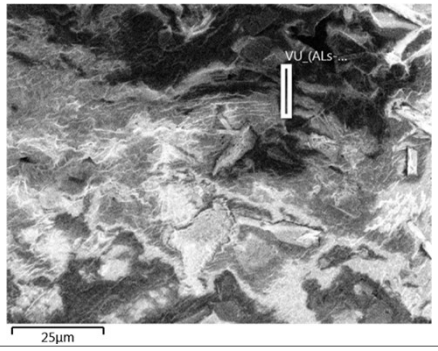

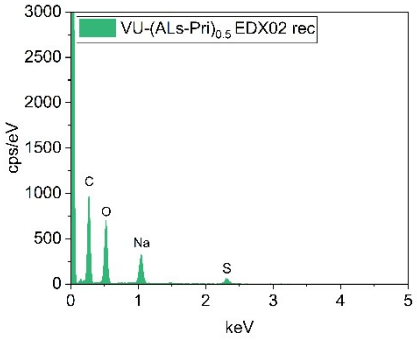

Element	Atom%
C	62.99
N	-
O	29.76
Na	5.88
Al	-
S	1.37

Table S13: EDX-measurements of VU-(ALs/APPD$_{10}$-Pri)$_{0.6}$ after recycling, showing the irradiated area (left), the EDX spectra (middle) and a table with the relative intensity of respective elements in % (right).

VU-(ALs/APPD$_{10}$-Pri)$_{0.6}$ recycled

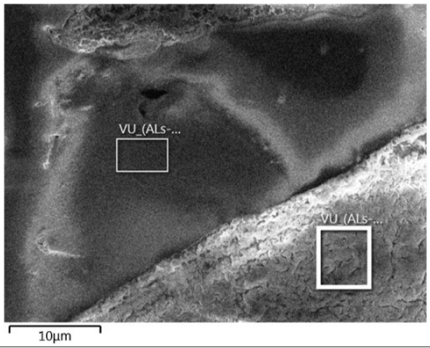

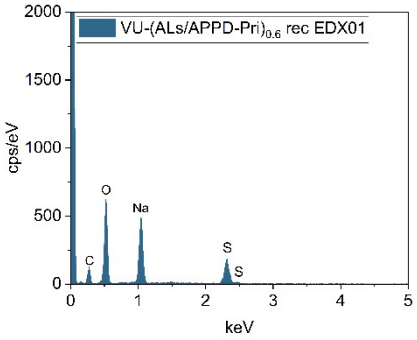

Element	Atom%
C	32.11
N	-
O	41.37
Na	17.76
Al	-
S	8.76

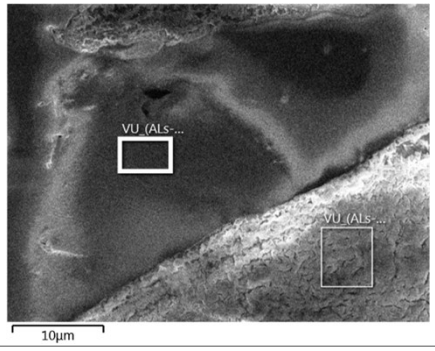

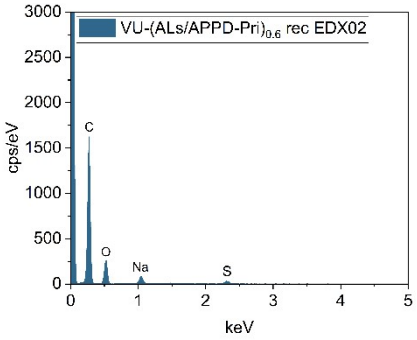

Element	Atom%
C	81.73
N	-
O	15.88
Na	1.60
Al	-
S	0.78

Table S14: EDX-measurements of VU-(ALnC-Pri)$_{0.8}$ after recycling, showing the irradiated area (left), the EDX spectra (middle) and a table with the relative intensity of respective elements in % (right).

VU-(ALnC-Pri)$_{0.8}$ recycled

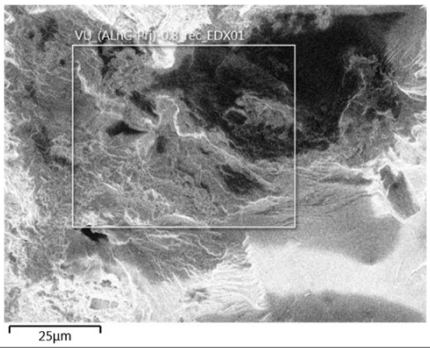

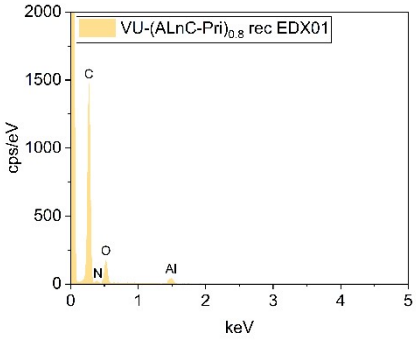

Element	Atom%
C	79.45
N	6.50
O	13.13
Na	-
Al	0.92
S	-

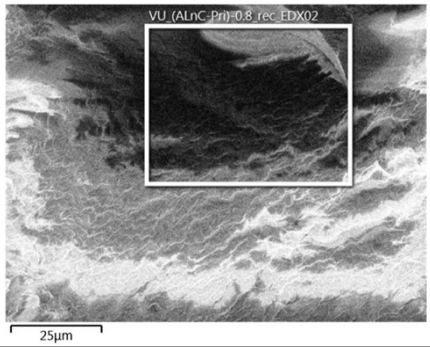

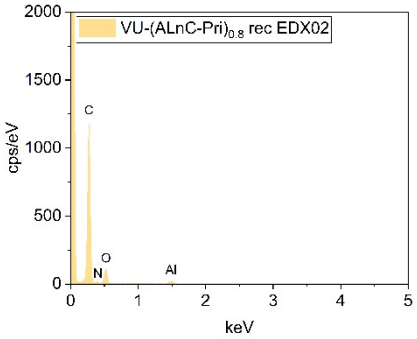

Element	Atom%
C	80.81
N	7.19
O	11.25
Na	-
Al	0.75
S	-

Table S15: EDX-measurements of VU-(ALnP-Pri)$_{0.8}$ after recycling, showing the irradiated area (left), the EDX spectra (middle) and a table with the relative intensity of respective elements in % (right).

VU-(ALnP-Pri)$_{0.8}$ recycled

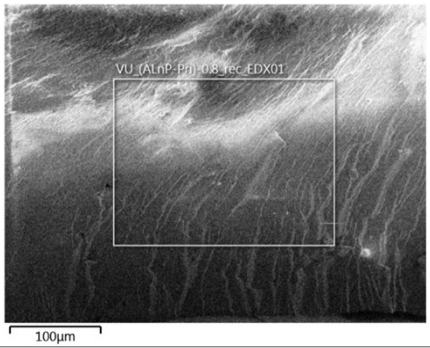

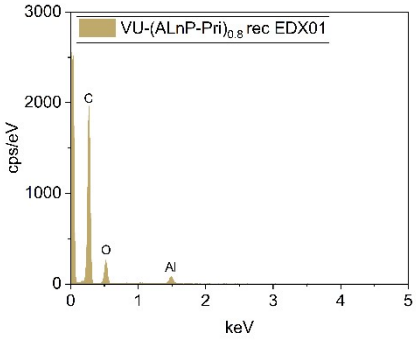

Element	Atom%
C	83.50
N	-
O	15.12
Na	-
Al	1.39
S	-

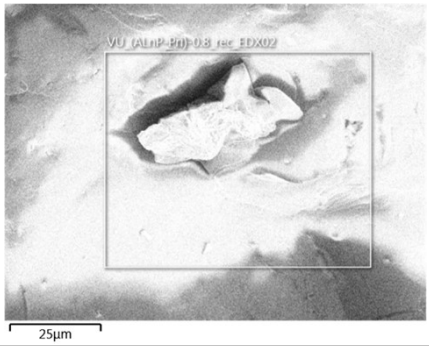

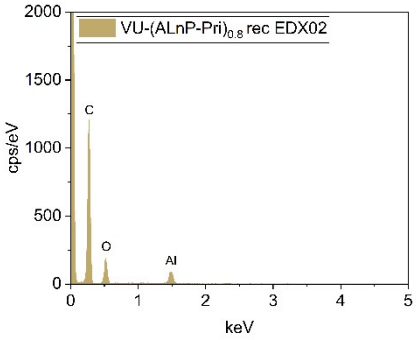

Element	Atom%
C	82.27
N	-
O	15.37
Na	-
Al	2.36
S	-

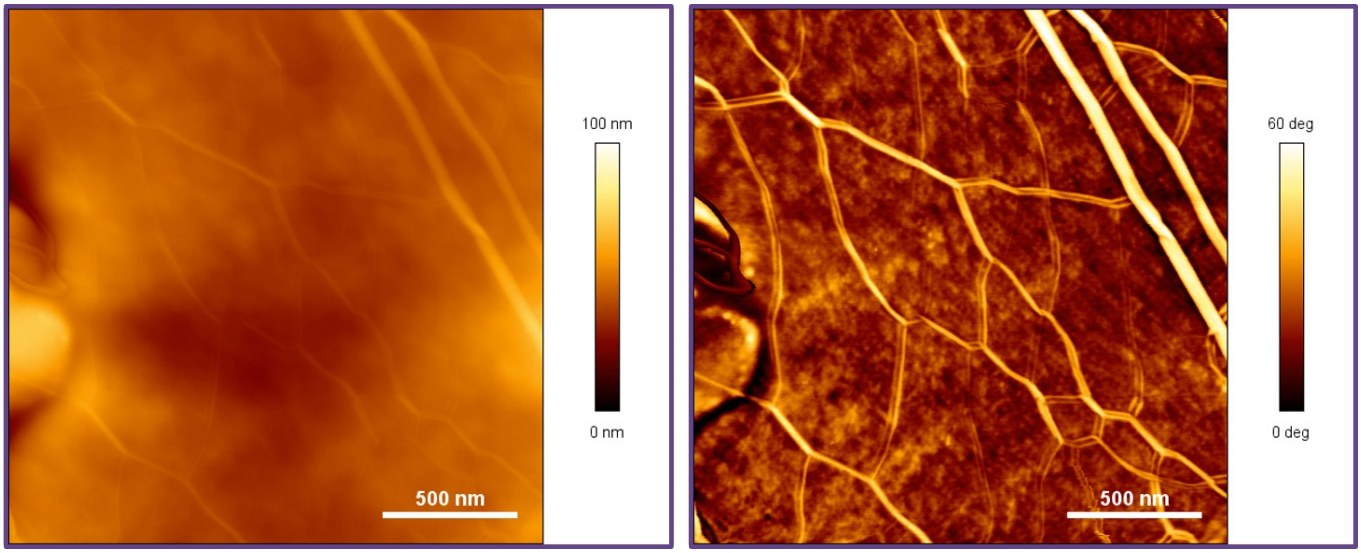

Figure S76: AFM image of recycled VU-(Als-Pri)$_{0.5}$ showing the height plot (left) and the phase plot (right).

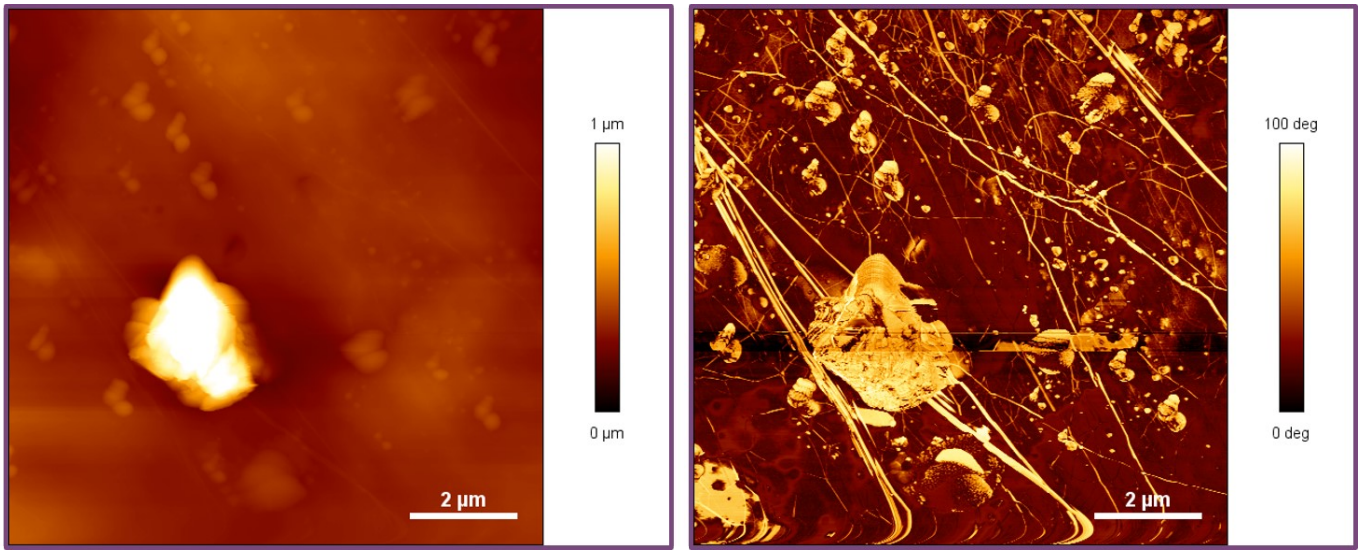

Figure S77: AFM image of recycled VU-(AIs/APPD$_{10}$-Pri)$_{0.6}$ showing the height plot (left) and the phase plot (right).

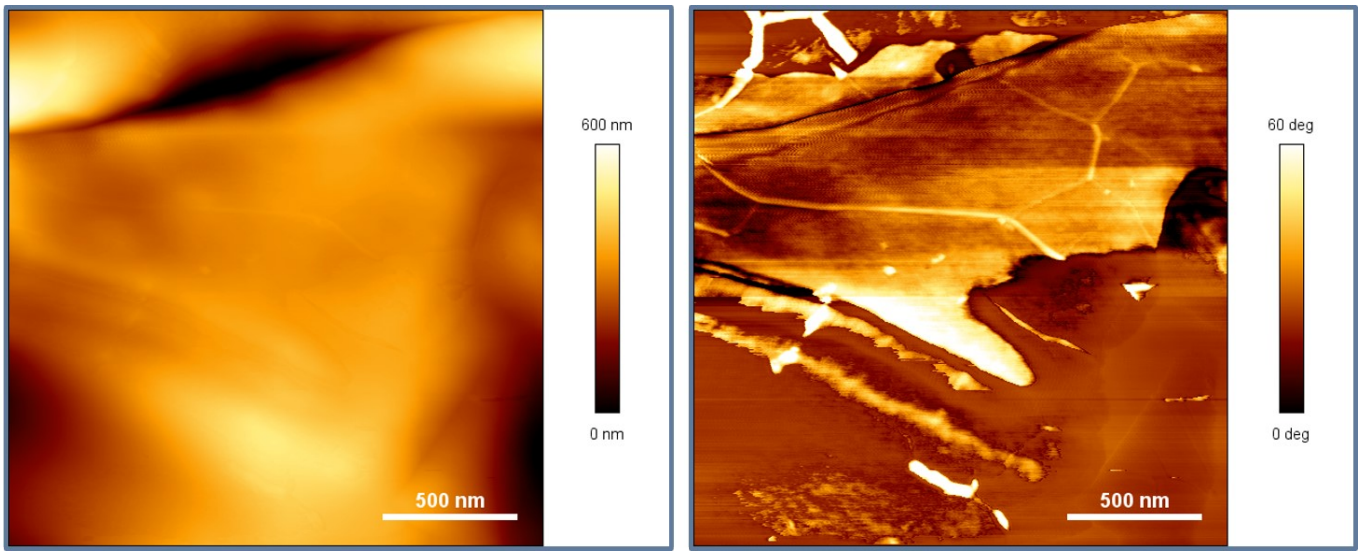

Figure S78: AFM image of recycled VU-(AlnC-Pri)$_{0.8}$ showing the height plot (left) and the phase plot (right).

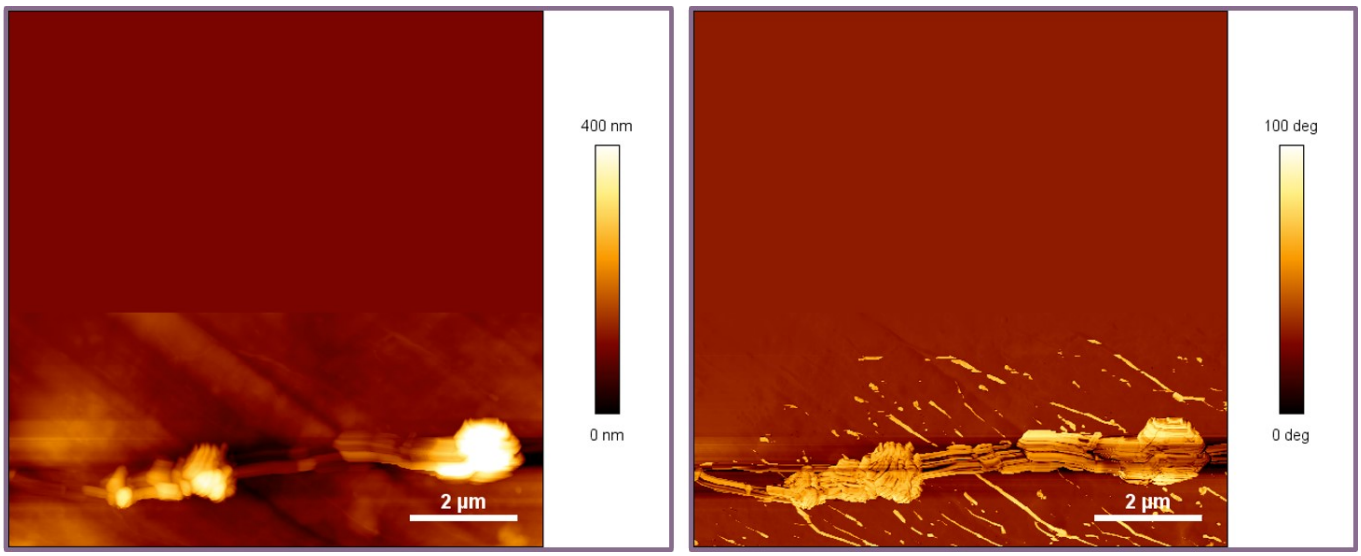

Figure S79: AFM image of recycled VU-(AlnP-Pri)$_{0.8}$ showing the height plot (left) and the phase plot (right).

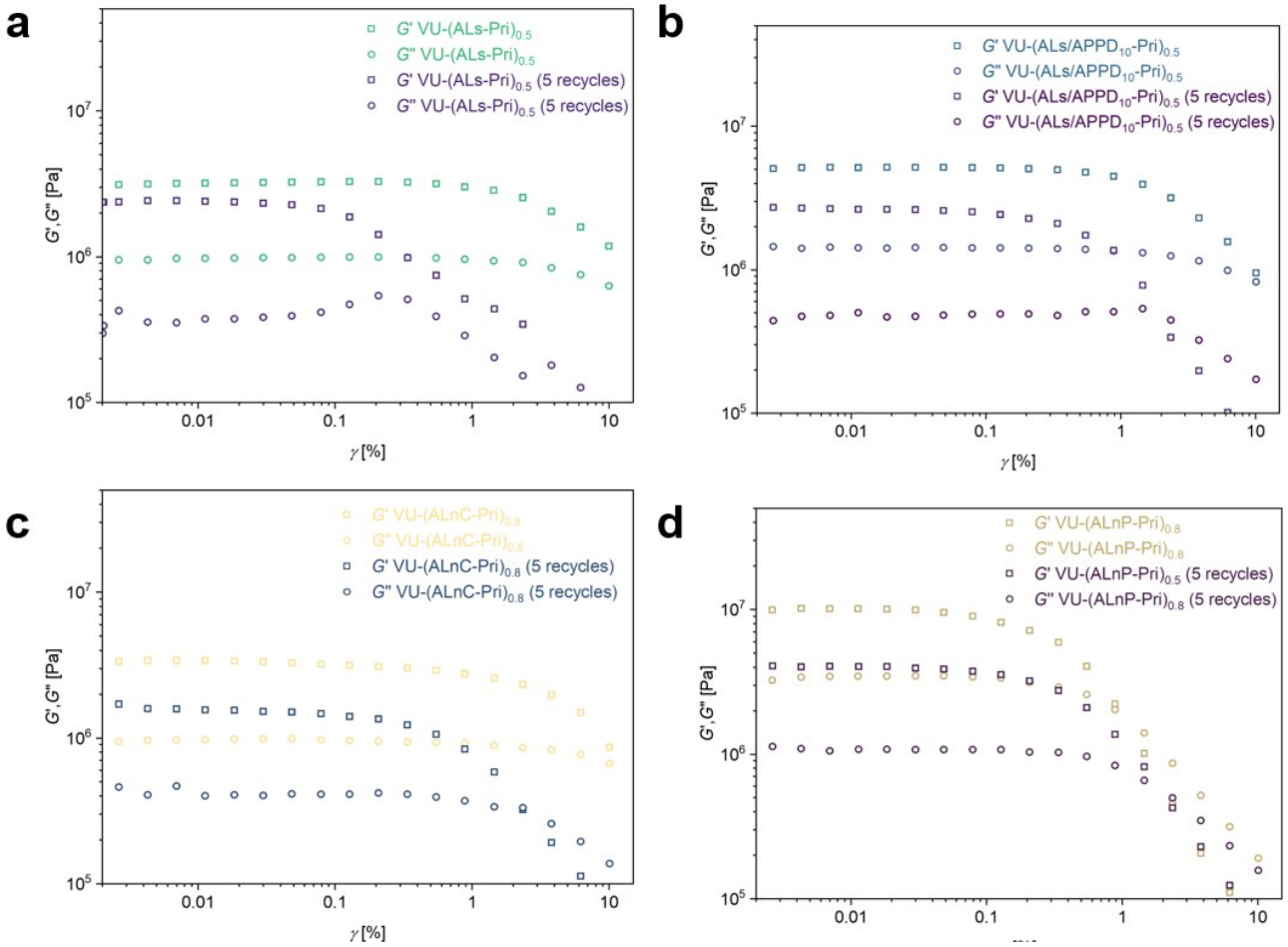

Figure S80: Amplitude sweep measurements of the recycled lignin vitrimer materials between 0.001% and 10% shear strain γ performed at a constant angular frequency of 6.28 rad s^{-1} of selected vitrimer materials VU-(ALs-Pri)$_{0.5}$ (a), VU-(ALs/APPD10-Pri)$_{0.6}$ (b), VU-(ALnC-Pri)$_{0.8}$ (c) and VU-(ALnP-Pri)$_{0.8}$ (d) in comparison of the pristine and five times reprocessed materials.

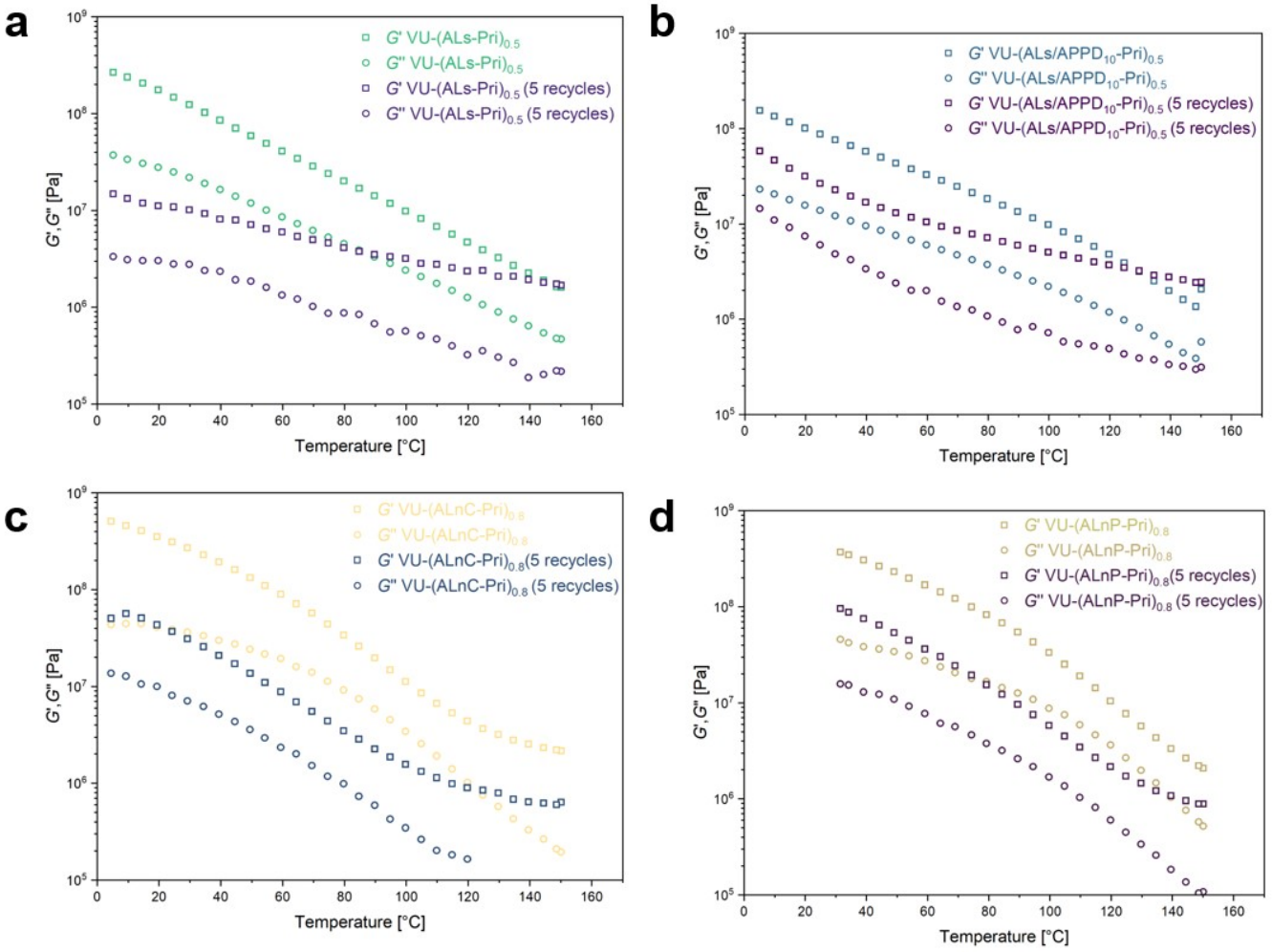

Figure S81: Temperature sweep measurements of the recycled lignin vitrimers in the temperature range of 150 °C – 0 °C performed at a constant angular frequency of 6.28 rad s^{-1} and a constant shear strain amplitude of 0.01% of selected vitrimers VU-(ALs-Pri)$_{0.5}$ (a), VU-(ALs/APPD10-Pri)$_{0.6}$ (b), VU-(ALnC-Pri)$_{0.8}$ (c) and VU-(ALnP-Pri)$_{0.8}$ (d) in comparison of the pristine and five times reprocessed materials.

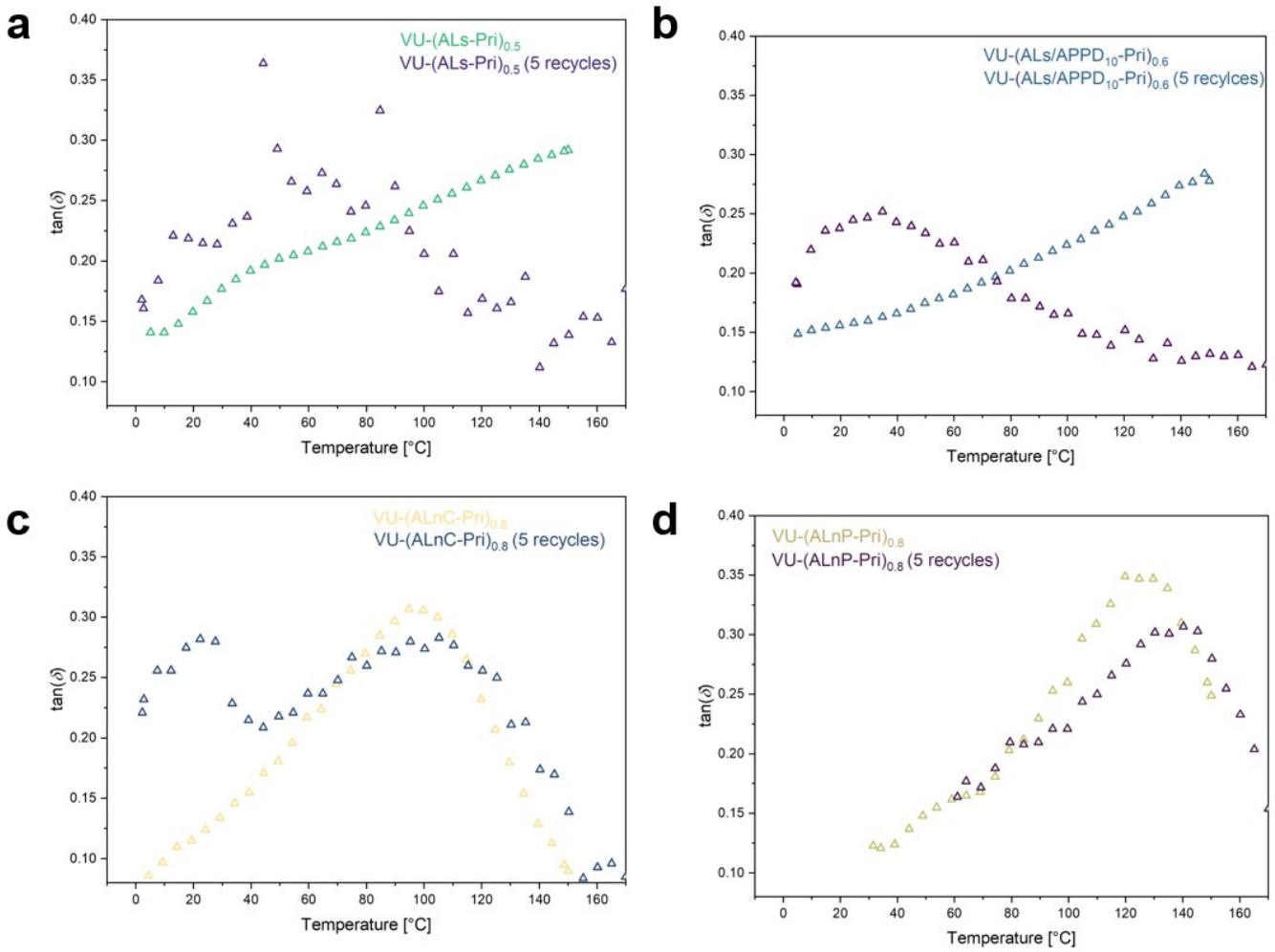

Figure S82: Tan(δ) values calculated from the storage and loss moduli of the temperature sweep measurements of the recycled lignin vitrimers in the temperature range of 150 °C – 0 °C performed at a constant angular frequency of 6.28 rad s^{-1} and a constant shear strain amplitude of 0.01% of selected vitrimers VU-(ALs-Pri)$_{0.5}$ (a), VU-(ALs/APPD10-Pri)$_{0.6}$ (b), VU-(ALnC-Pri)$_{0.8}$ (c) and VU-(ALnP-Pri)$_{0.8}$ (d) in comparison of the pristine and five times reprocessed materials.

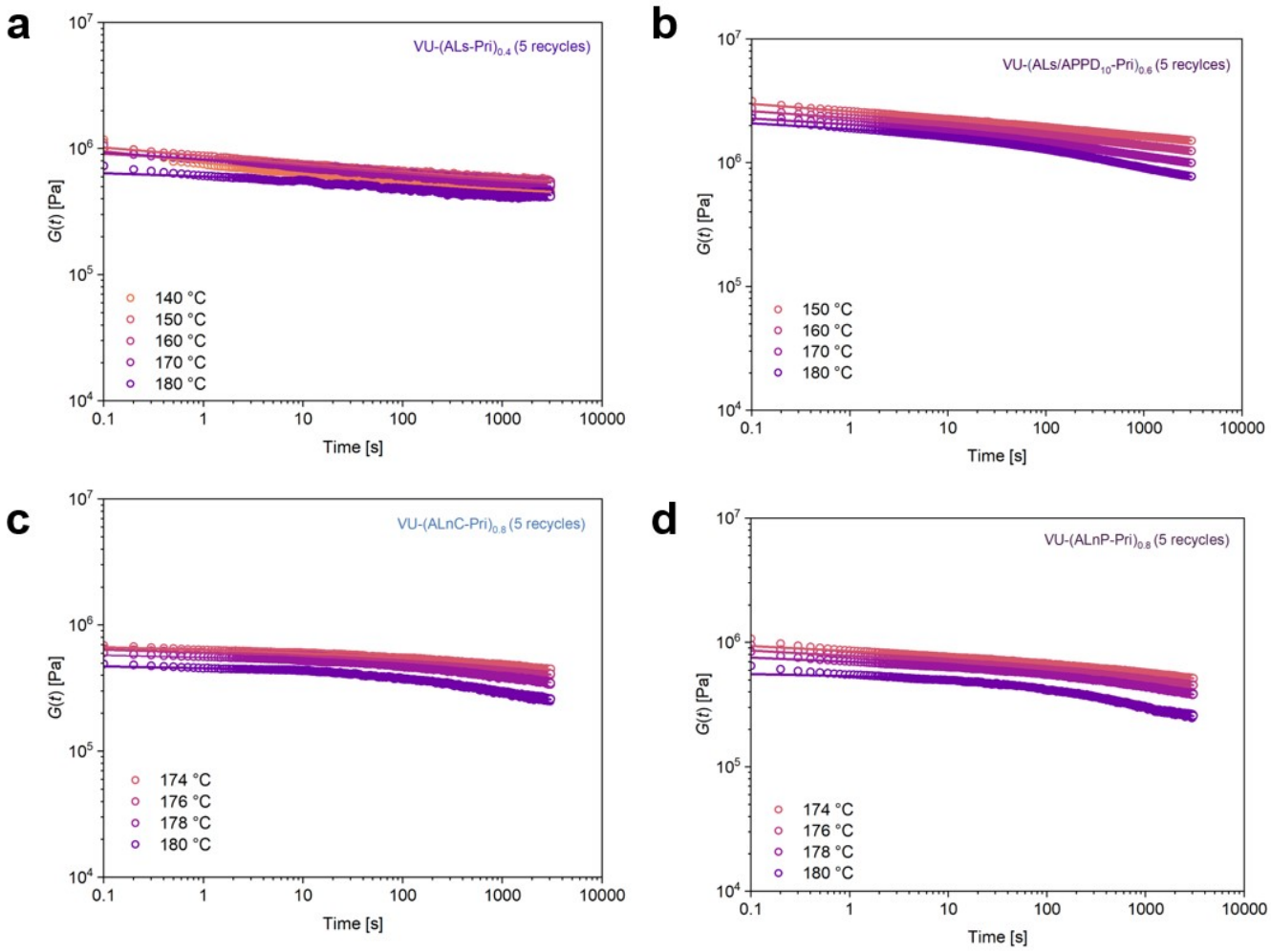

Figure S 83: Stress-relaxation measurement of selected vitrimers VU-(ALs-Pri)$_{0.5}$ (a), VU-(ALs/APPD10-Pri)$_{0.6}$ (b), VU-(ALnC-Pri)$_{0.8}$ (c) and VU-(ALnP-Pri)$_{0.8}$ (d) in after five reprocessing cycles, plotting the stress-relaxation modulus $G(t)$ versus the stress-relaxation time while applying a shear strain of 1%. The lines display the stretched exponential fit functions for the respective temperatures, calculated from the stress-relaxation data.

Table S16: Summary of the β and $<\tau>$ values for the KWW fit of the stress-relaxation measurements of the lignin vitrimers VU-(ALs-Pri)$_{0.5}$ and VU-(ALs/APPD-Pri)$_{0.6}$ after five recycling steps in the temperature range of 140 °C to 180 °C while applying a shear strain of 1%.

Sample	$\beta_{150°C}$ [-]	$\beta_{160°C}$ [-]	$\beta_{170°C}$ [-]	$\beta_{180°C}$ [-]	$<\tau>_{150°C}$ [s]	$<\tau>_{160°C}$ [s]	$<\tau>_{170°C}$ [s]	$<\tau>_{180°C}$ [s]
VU-(ALs-Pri)$_{0.5}$ (5x recycled)	0.052	0.188	0.097	0.380	$5.9 \cdot 10^{9}$	2250	$4.3 \cdot 10^{5}$	122
VU-(ALs/APPD$_{10}$-Pri)$_{0.6}$ (5x recycled)	0.056	0.091	0.178	0.248	$5.5 \cdot 10^{12}$	$4.8 \cdot 10^{8}$	$3.40 \cdot 10^{4}$	3310

Table S17: Summary of the β $<\tau>$ values for the KWW fit of the stress-relaxation measurements of the lignin vitrimers VU-(ALnC-Pri)$_{0.8}$ and VU-(ALnP-Pri)$_{0.8}$ after being 5 recycling steps in the temperature range of 170 °C to 180 °C while applying a shear strain of 1%.

Sample	$\beta_{174°C}$ [-]	$\beta_{176°C}$ [-]	$\beta_{178°C}$ [-]	$\beta_{180°C}$ [-]	$<\tau>_{174°C}$ [s]	$<\tau>_{176°C}$ [s]	$<\tau>_{178°C}$ [s]	$<\tau>_{180°C}$ [s]
VU-(ALnC-Pri)$_{0.8}$	0.141	0.221	0.321	0.408	$1.81 \cdot 10^{11}$	$1.14 \cdot 10^{5}$	4997	1629
VU-(ALnP-Pri)$_{0.8}$	0.057	0.072	0.136	0.407	$1.8 \cdot 10^{24}$	$4.1 \cdot 10^{17}$	$2.65 \cdot 10^{9}$	1200

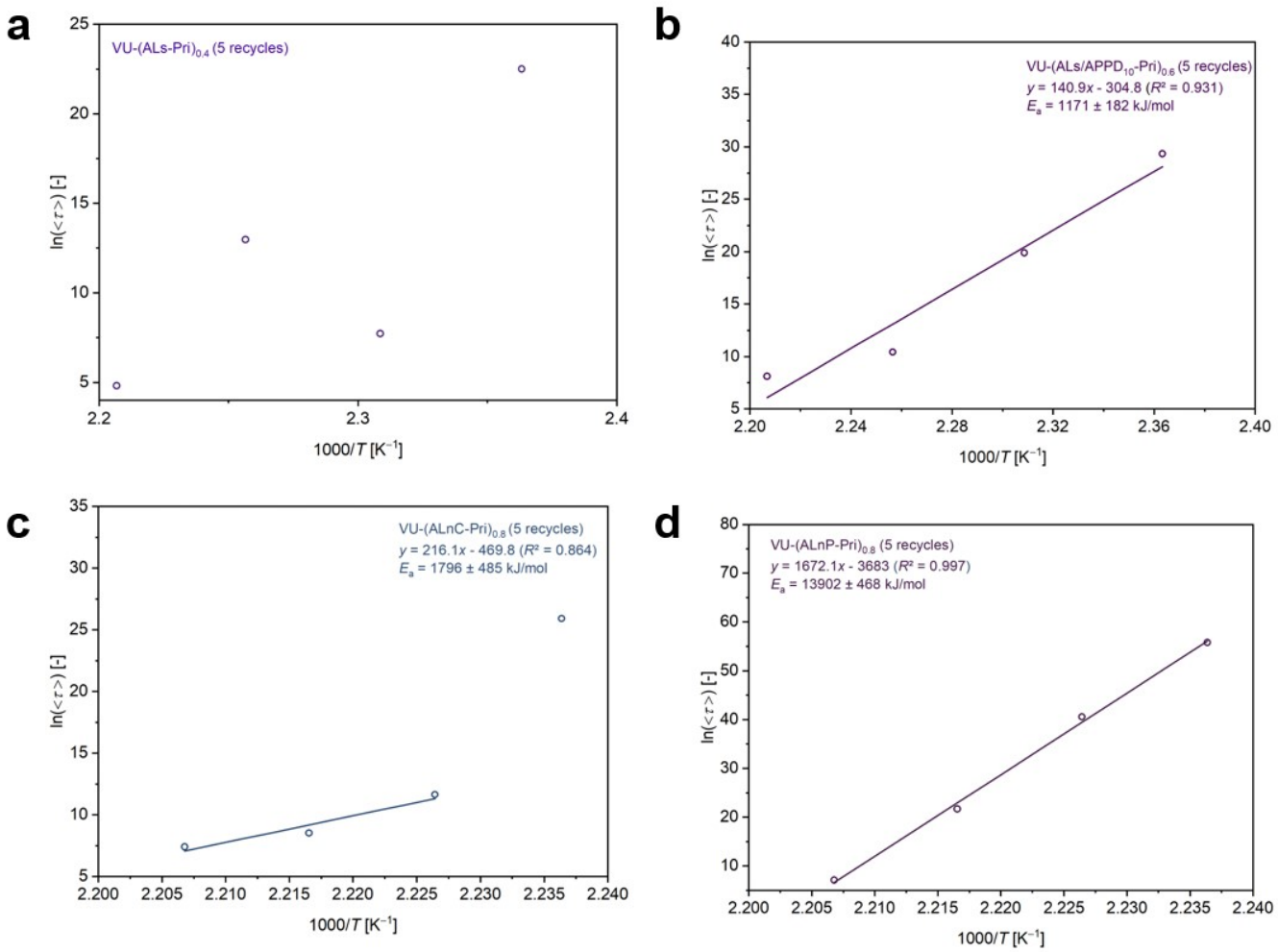

Figure S84: Plot of ln <τ> versus 1000/*T* of selected vitrimers VU-(ALs-Pri)$_{0.5}$ (a), VU-(ALs/APPD10-Pri)$_{0.6}$ (b), VU-(ALnC-Pri)$_{0.8}$ (c) and VU-(ALnP-Pri)$_{0.8}$ (d) in after five reprocessing cycles while applying a shear strain of 1% to show potential stress relaxation behavior of the materials.

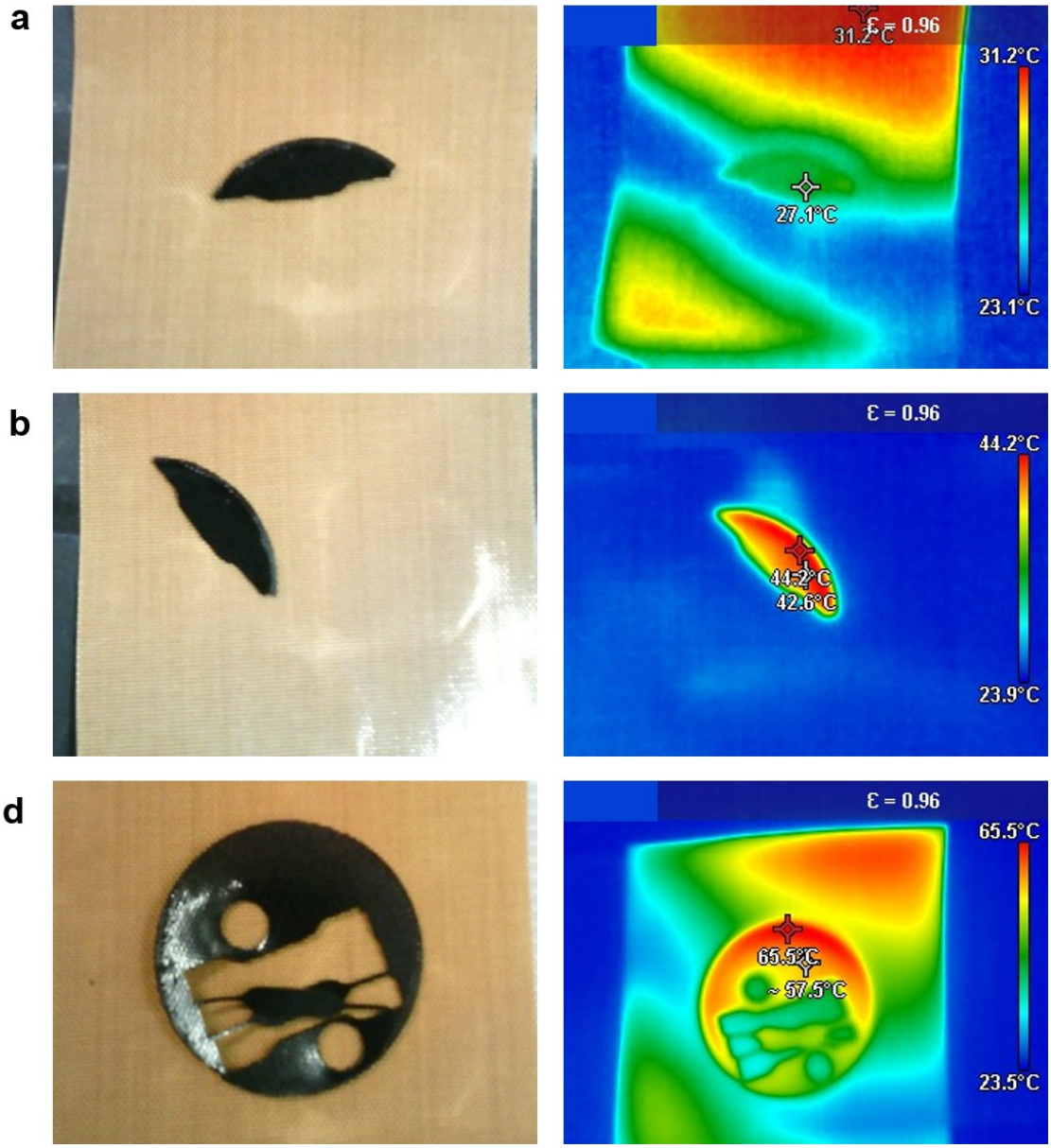

Figure S85: Pictures of the heating experiment by UV-light absorption. The setup included irradiation via an UV-light source (OmniCure 460) with a wavelength of 365 nm and an irradiation intensity of 69 mW cm^{-2}. Pictures were taken after three irradiation times. (a) Irradiation experiment with a duration of 10 s, yielding a surface temperature of 27.1 °C. (b) Irradiation experiment with a duration of 60 s, yielding a surface temperature of 44.2 °C. (c) Irradiation experiment with a duration of 10 s, yielding a surface temperature of 65.5 °C. As the sheet holding the sample also heated, no significant UV-light-induced heating effect was observed.

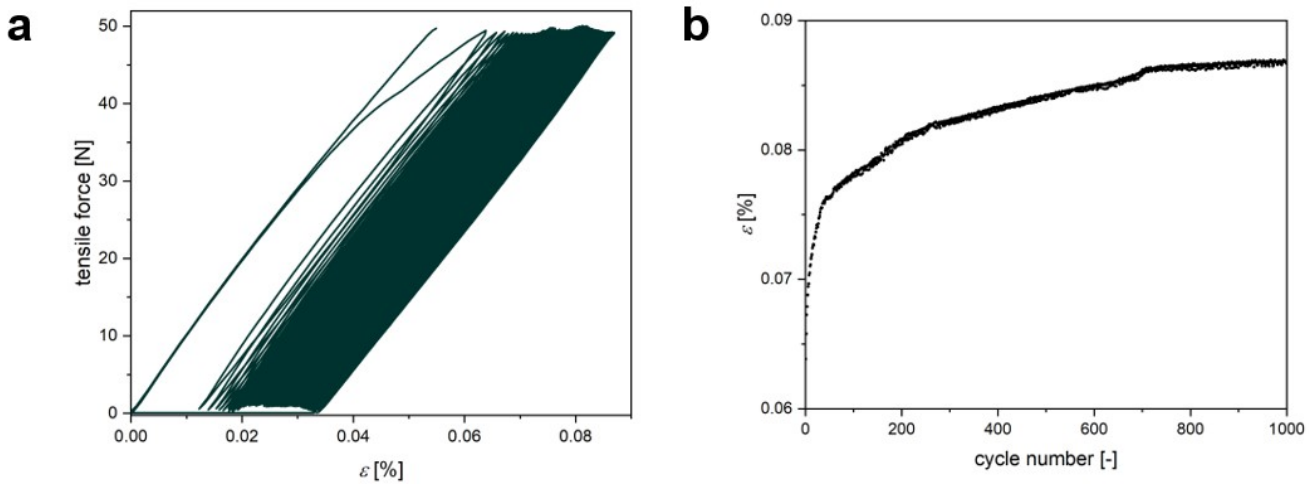

Figure S86: Durability and fatigue testing of a test sheet in a cyclic deformation test setup, displaying the tensile force plotted against the elongation (a) for 1000 cycles of repeated loading with a force of 50 N. (b) Plot of the elongation versus the cycle number, showing increasing elongation with a plateau after 700 cycles.

9.4 Publication 3 – Supporting Information

The publication is reprinted with permission from F.C. Klein, J. Struck, T. Vossmeyer, and V. Abetz, *Macromol. Chem. Phys.*, **2025**, *226*, 0:e00276 – published by Wiley.

Supporting Information

Transparent Dioxaborolane Acrylate-Based Vitrimers Through One-Pot Click Reaction with Superior Strength as Matrix Material for Carbon Fibers and TiO_2 Nanoplates

*Florian C. Klein, Jana Struck, Tobias Vossmeyer and Volker Abetz**

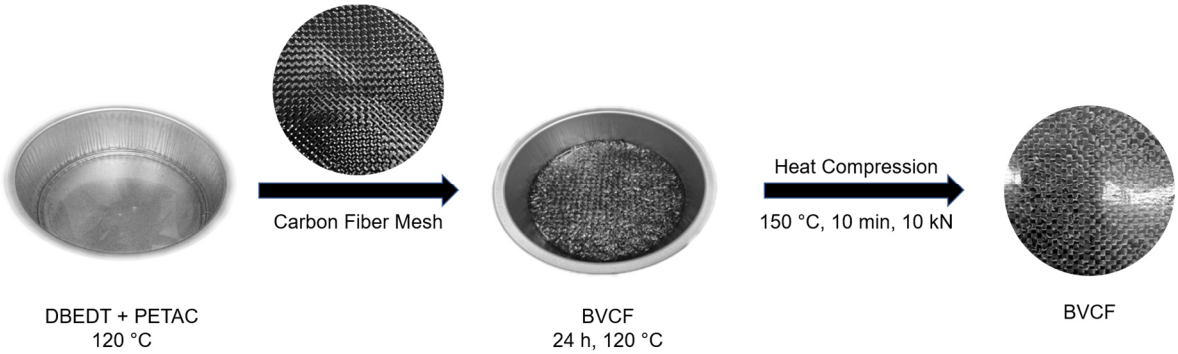

Figure S1: Schematic representation of the production process of dioxaborolane acrylate vitrimer carbon fiber reinforced (BVCF) composites including the mixture of the monomers 2,2-(1,4-phenylene)-bis[4-mercaptan-1,3,2-dioxaborolane] (DBEDT) and 2,2-bis([(1-oxoallyl)oxy]methyl)1,3-propandiyl diacrylate (PETAC) at 120 °C, addition of the carbon fiber mesh (CF), and subsequent gelation to give BVCF. The composite was stored at 120 °C for 24 h and afterwards pressed using heat compression into the composite vitrimer film BVCF.

Table S1: Overview of the used reaction parameters for the titania nanoplates (TNPs) synthesis. The abbreviations OLAM, OLAC and ODE represent oleyl amine, oleic acid and 1-octadecene, respectively. The added precursor volume for the seed formation is represented by V_{seeds} and the added volume for the nanoparticle growth is V_{growth}.

TNP batch	Reaction Solution OLAM/OLAC/ODE [mmol/mmol/mL]	V_{seeds} [mL]	V_{growth} [mL]	Addition Rate [mL/h]
TNP-2	18/3.6/60	1	18	9
TNP-10	18/3.6/60	0.5	18	9
TNP-11	18/3.6/60	0.5	18	9
TNP-13	18/3.6/60	0.5	18	9

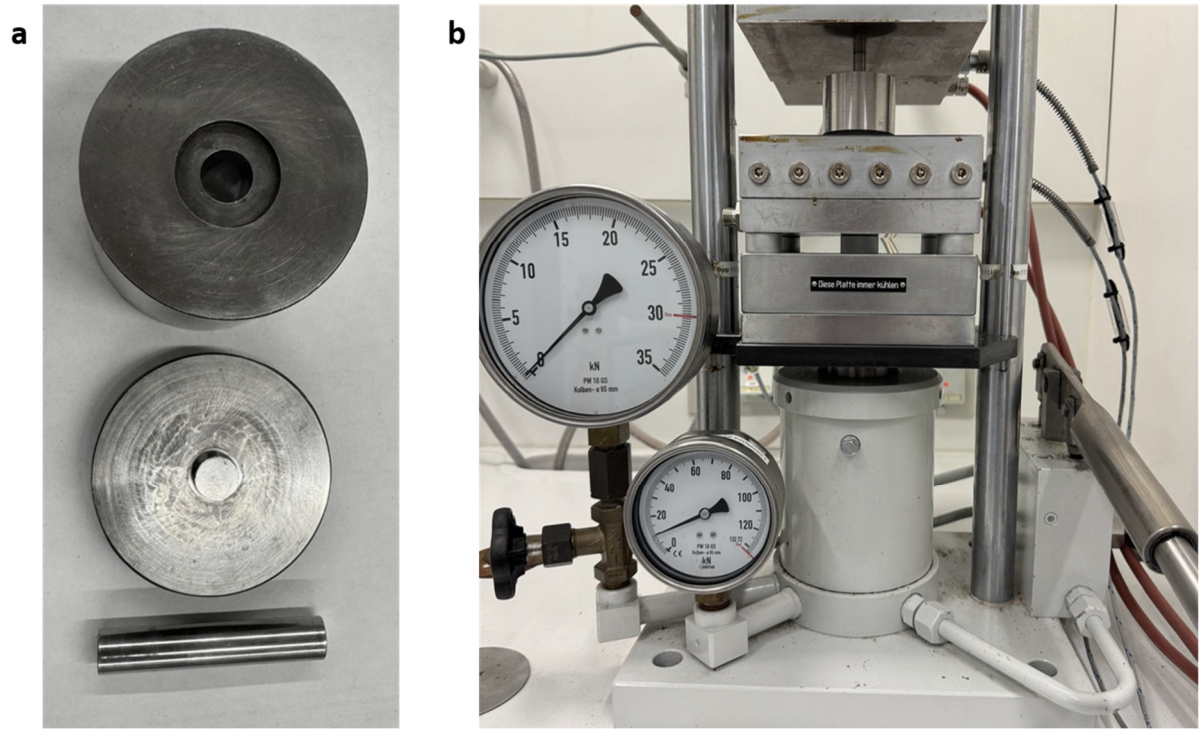

Figure S2: a) Custom-made stainless-steel mold for the formation of vitrimer nanocomposites containing titanium dioxide nanoplates (BVS-TNP). b) Heat compression PW 10 H (Paul-Otto Weber GmbH, Remshalden, Germany) using the custom-made stainless-steel mold for the formation of vitrimer nanocomposites.

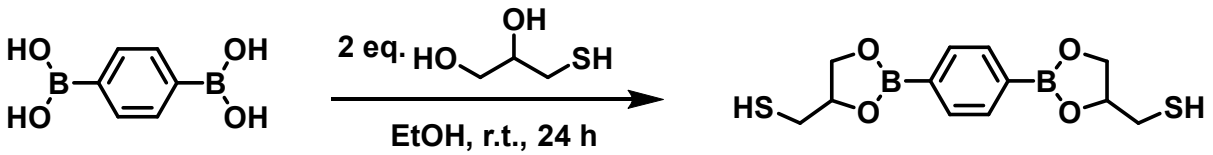

Figure S3: Synthetic route of 2,2-(1,4-phenylene)-bis[4-mercaptan-1,3,2-dioxaborolane] (DBEDT) via an environmentally friendly synthesis using ethanol and stirring at room temperature.[1,2]

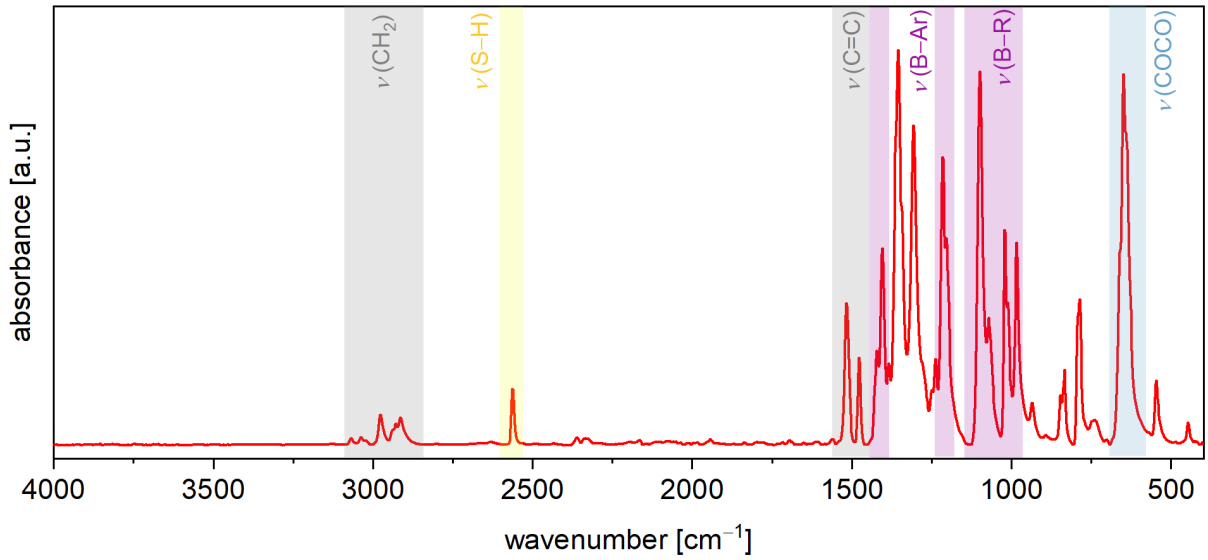

Figure S4: ATR-FT-IR spectrum of 2,2-(1,4-phenylene)-bis[4-mercaptan-1,3,2-dioxaborolane] (DBEDT) showing the characteristic S-H (2563 cm^{-1}, yellow) stretching vibrations, the dioxaborolane bands (1423 – 1403 cm^{-1}, 1216-1203 cm^{-1}, 1099 – 983 cm^{-1}, purple), the bands of the boronic ester's oxygen and carbon atoms (649 cm^{-1}, blue), and the vibrations of the methylene groups of the carbon backbone (3087 – 2850 cm^{-1}, grey) and the aromatic backbone (1577 – 1477 cm^{-1}, grey).

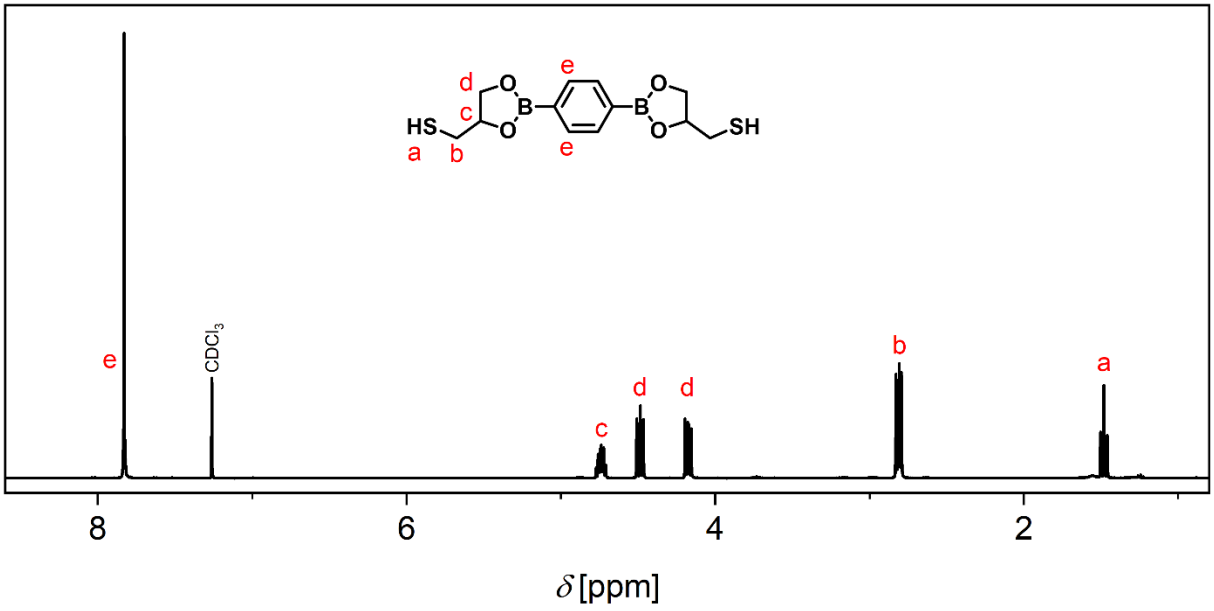

Figure S5: ^{1}H NMR spectrum of 2,2-(1,4-phenylene)-bis[4-mercaptan-1,3,2-dioxaborolane] (DBEDT). ^{1}H NMR (400 MHz, $CDCl_3$, δ): 7.83 (s, 4H, Ar-H), 4.74 (ddt, 2H, CH), 4.48 (dd, 2H, CH_2), 4.17 (dd, 2H, CH_2), 2.81 (dd, 4H, CH_2), 1.48 (2H, SH).

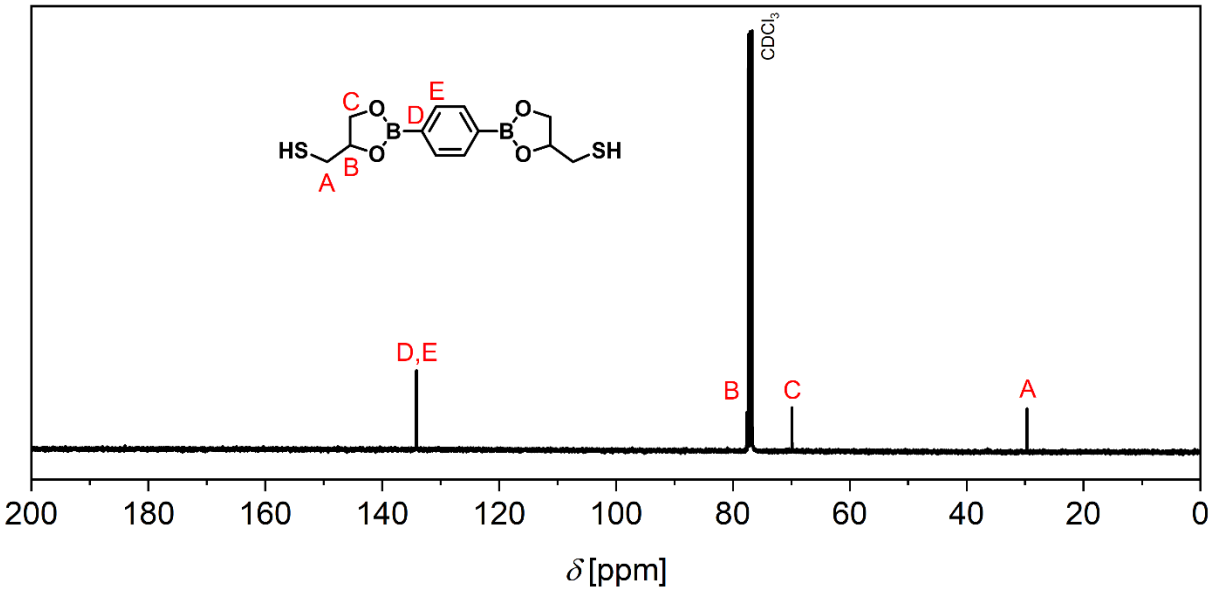

Figure S6: ^{13}C NMR spectrum of 2,2-(1,4-phenylene)-bis[4-mercaptan-1,3,2-dioxaborolane] (DBEDT). ^{13}C NMR (101 MHz, $CDCl_3$, δ): 134.3 (Ar), 77.7 (CH), 70.0 (CH_2), 29.8 (CH_2).

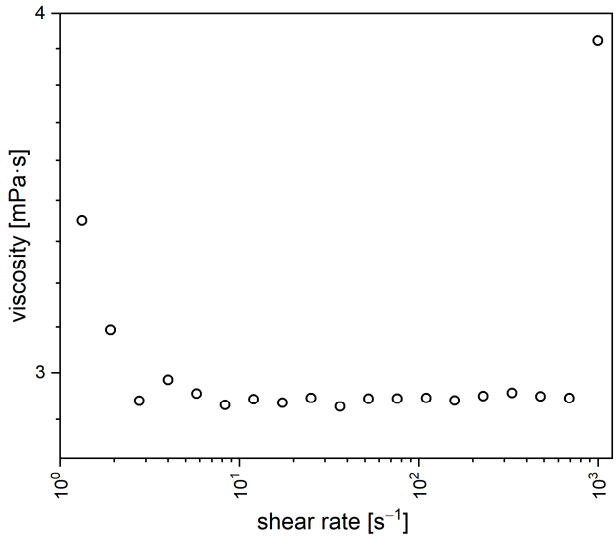

Figure S7: Viscosity measurement of DBEDT at 120 °C while increasing the shear rate from 1 s^{-1} up to 1000 s^{-1}.

Equation S1

$$S = \frac{m_1 - m_0}{m_0} \cdot 100$$

In Equation S1 are:

S = Swelling ratio [wt.%]
m_0 = Weight of the sample before swelling [g]
m_1 = Weight of the sample after swelling [g]

Equation S2

$$SF = \frac{m_0 - m_2}{m_0} \cdot 100$$

In Equation S2 are:
SF = Soluble fraction [wt.%]
m_0 = Weight of the sample before swelling [g]
m_2 = Weight of the sample after drying [g]

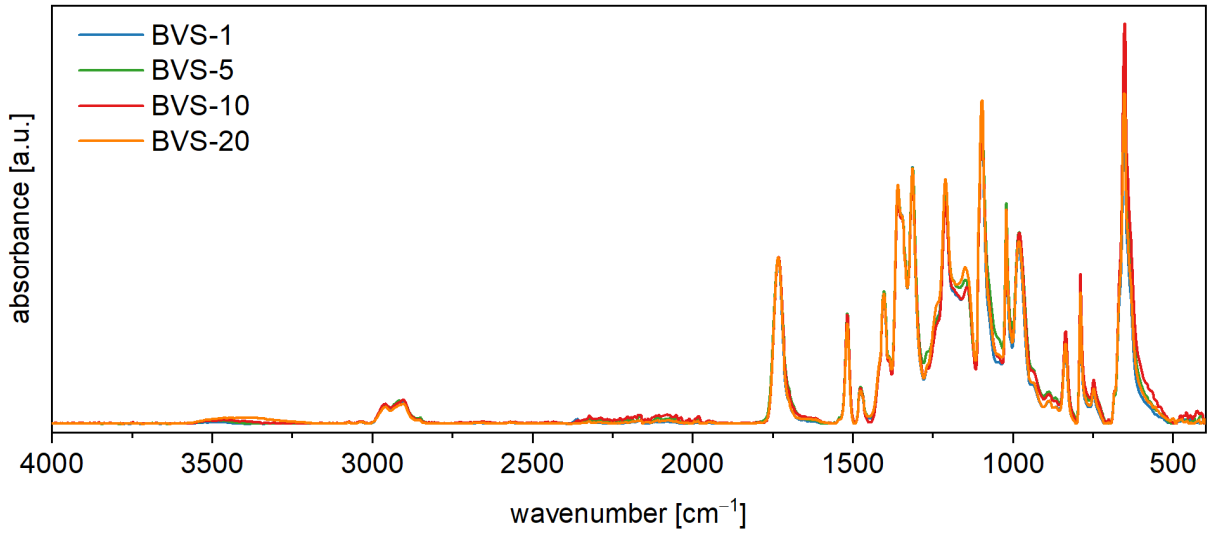

Figure S8: ATR-FT-IR spectra of the BVS materials after different stages of reprocessing.

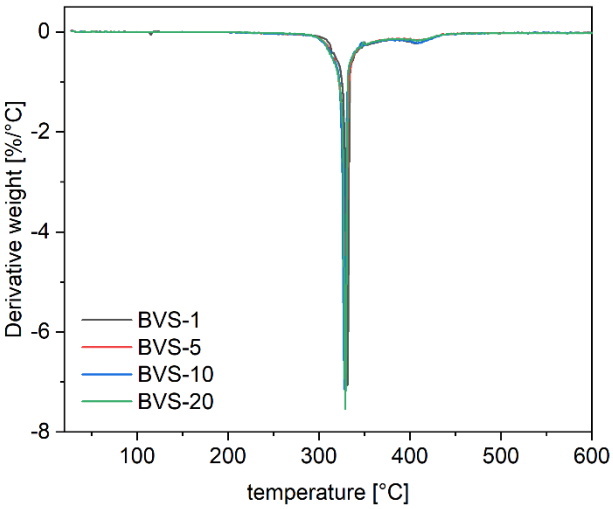

Figure S9: First derivative curves for the TGA of the BVS materials over the temperature range of 25 – 600 °C at a heating rate of 10 K min^{-1} under ambient (oxygen) atmosphere, revealing a thermal degradation step at 328 °C.

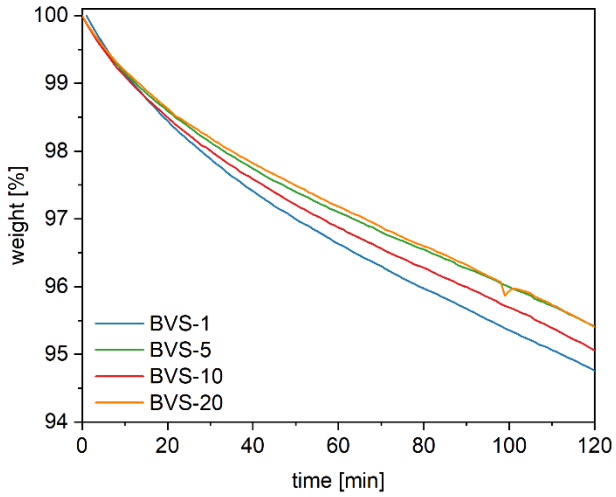

Figure S10: Isothermal TGA measurements under ambient (oxygen) atmosphere of the BVS materials carried out at a temperature of 220 °C for 2 h, showing thermal degradation of 4 – 5%.

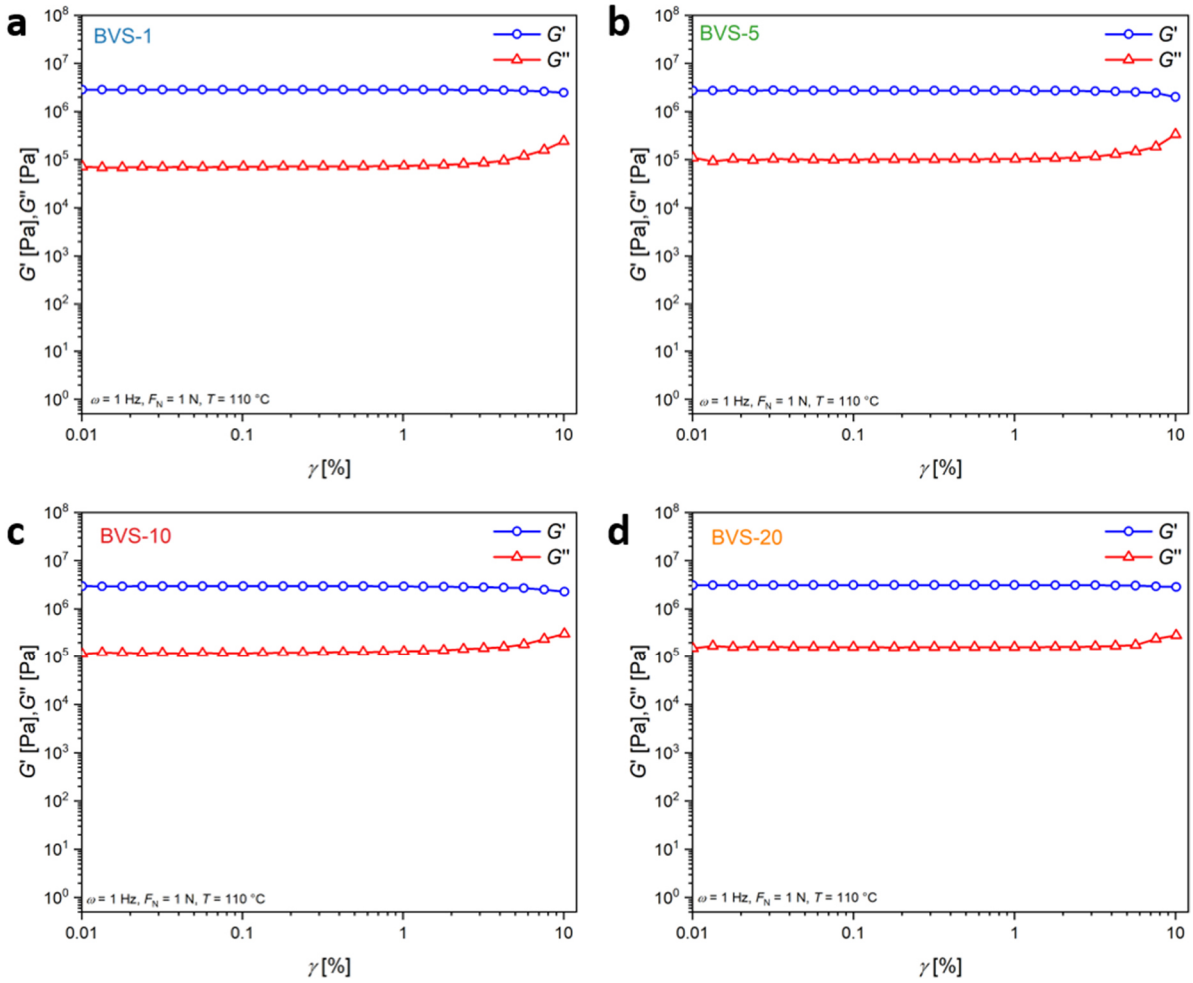

Figure S11: Amplitude sweep measurements of the produced dioxaborolane vitrimer materials between 0.01 – 10% shear strain γ, performed at a constant angular frequency of 6.28 rad s^{-1}, a temperature of 110 °C, and a normal force F_N of 1 N.

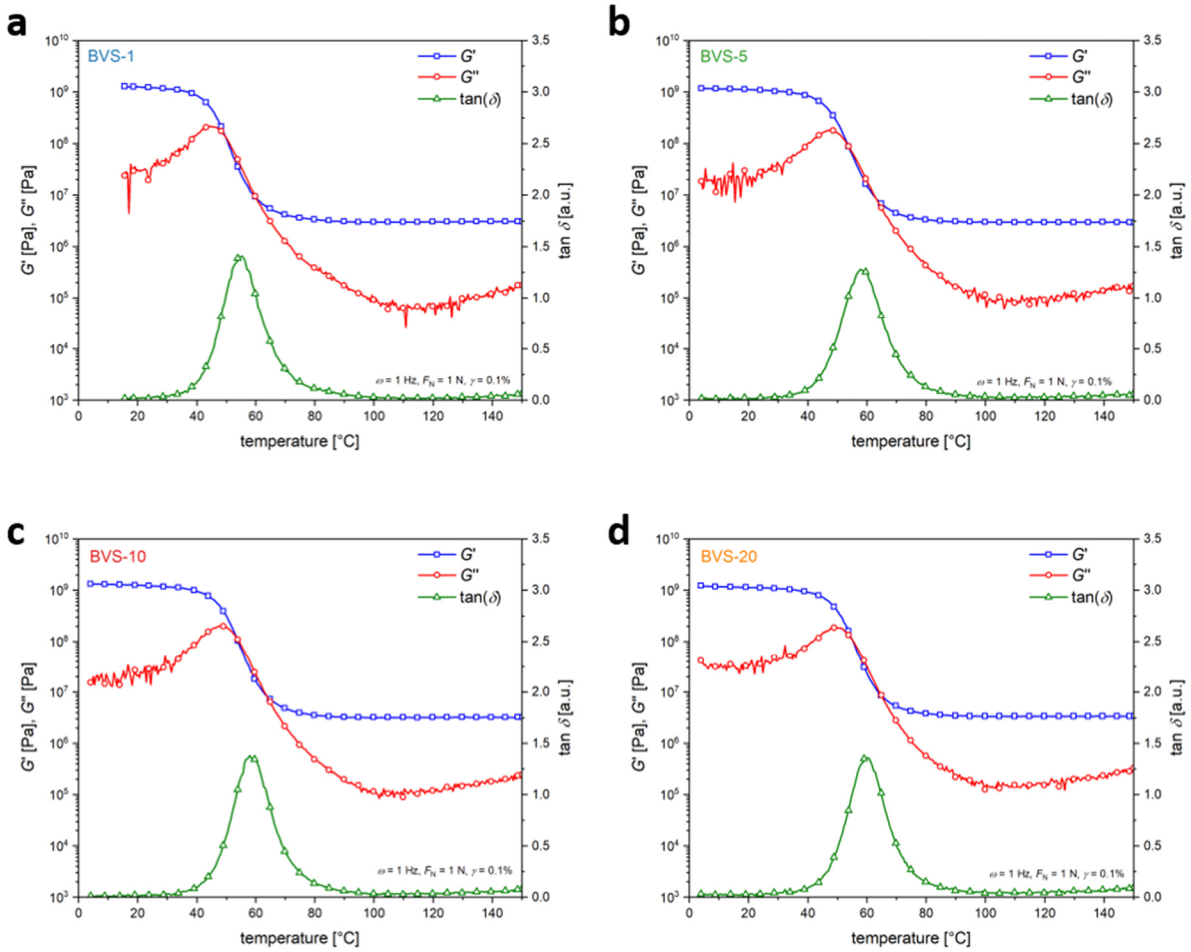

Figure S12: Temperature sweep measurements of the dioxaborolane vitrimer materials in the temperature range of 0 – 150 °C performed at a constant angular frequency of 6.28 rad s^{-1}, a constant shear strain of 0.1%, and a normal force F_N of 1 N.

Equation S3

$$G(t) = G_0 \, e^{\left(\frac{-t}{\tau_r}\right)^{\beta}}$$

In Equation S3 are:

$G(t)$ = Stress modulus at relaxation time [Pa]
G_0 = Initial stress modulus [Pa]
t = Time [s]
τ_r = Characteristic relaxation time [s]
β = Stretch parameter ($0 < \beta \leq 1$) [-]

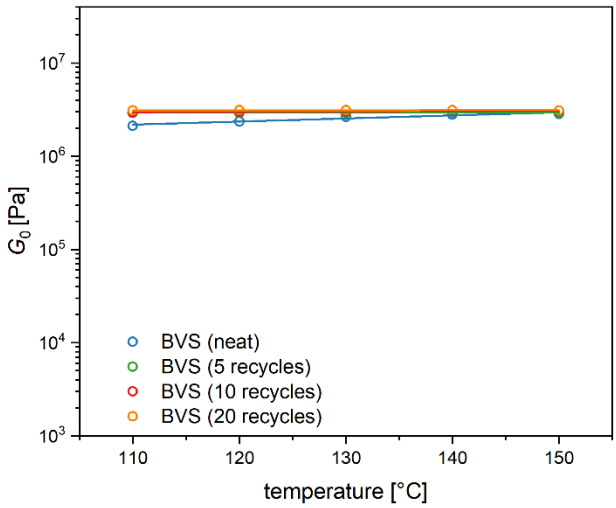

Figure S13: Initial relaxation moduli G_0 of the dioxaborolane material after different stages of reprocessing as a function of temperature from the stress-relaxation measurement (γ = 1%, F_N = 1 N). the straight lines connecting the dots serve as an orientation guide to the eye.

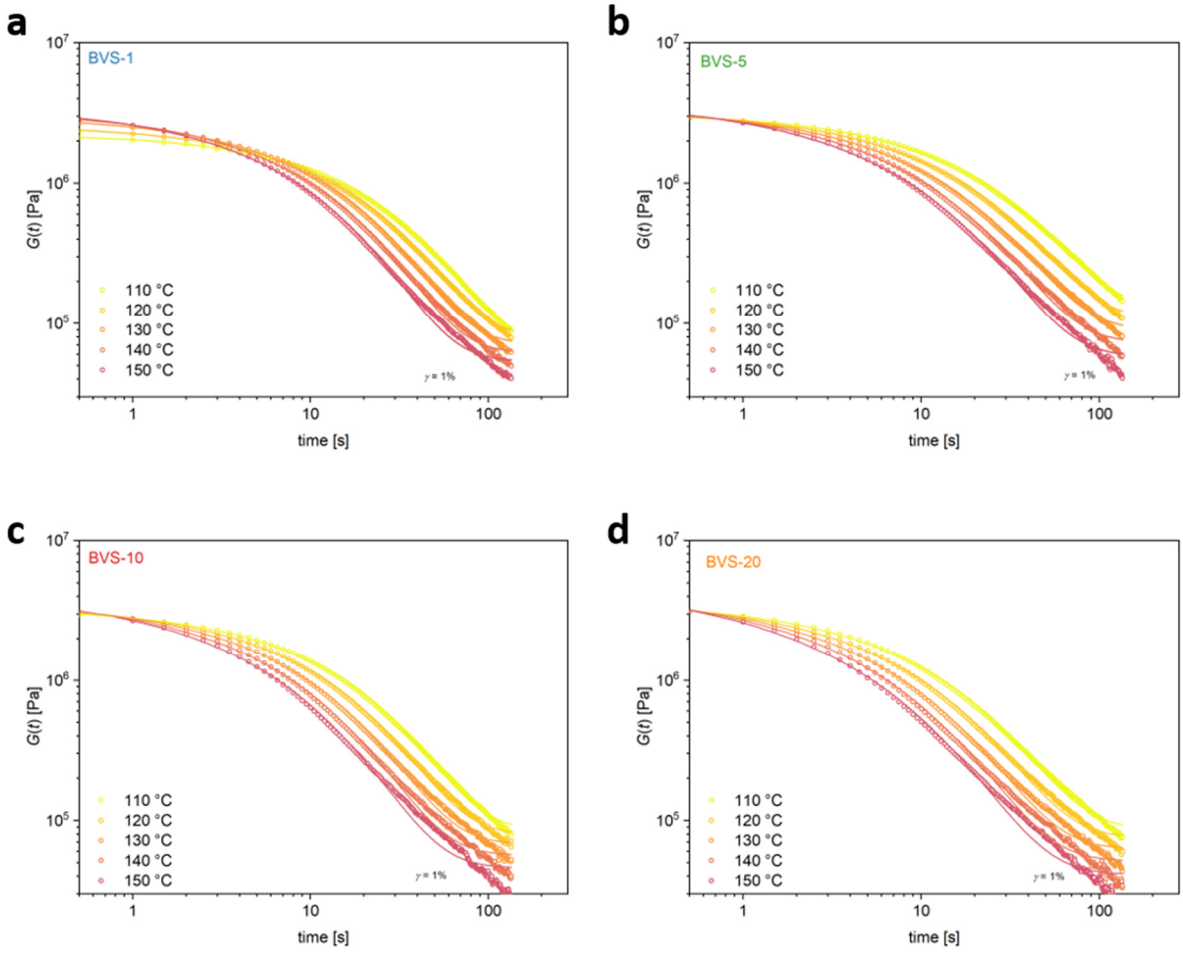

Figure S14: Stress-relaxation measurements of the dioxaborolane vitrimer materials, plotting the stress-relaxation modulus $G(t)$ versus the stress-relaxation time measured at temperatures in the range of 110 to 150 °C while applying a shear strain of 1%. The lines display the stretched exponential fit functions for the respective temperatures, calculated from the stress-relaxation data.

Table S2: Summary of the values of the stretch factor β and the calculated average values of the characteristic stress-relaxation time $\langle\tau\rangle$ for the KWW fit of the stress-relaxation measurements (γ = 1%, F_N = 1 N) between 110 – 150 °C of the dioxaborolane vitrimers.

Sample	$\beta_{110°C}$ [-]	$\beta_{120°C}$ [-]	$\beta_{130°C}$ [-]	$\beta_{140°C}$ [-]	$\beta_{150°C}$ [-]	$\langle\tau\rangle_{110°C}$ [s]	$\langle\tau\rangle_{120°C}$ [s]	$\langle\tau\rangle_{130°C}$ [s]	$\langle\tau\rangle_{140°C}$ [s]	$\langle\tau\rangle_{150°C}$ [s]
BVS-1	0.779	0.762	0.736	0.703	0.675	18.0	13.3	9.7	7.4	5.7
BVS-5	0.730	0.704	0.676	0.648	0.618	16.5	12.1	8.9	6.7	5.0
BVS-10	0.730	0.700	0.671	0.641	0.608	11.2	8.1	6.0	4.5	3.4
BVS-20	0.667	0.637	0.610	0.577	0.539	8.2	5.7	4.1	2.9	2.1

Equation S4

$$\langle\tau_r\rangle = \frac{\tau_r\,\Gamma\left(\frac{1}{\beta}\right)}{\beta}$$

In Equation S4 are:

$\langle\tau_r\rangle$ = Average stress-relaxation time [s]
Γ = Gamma function [-]

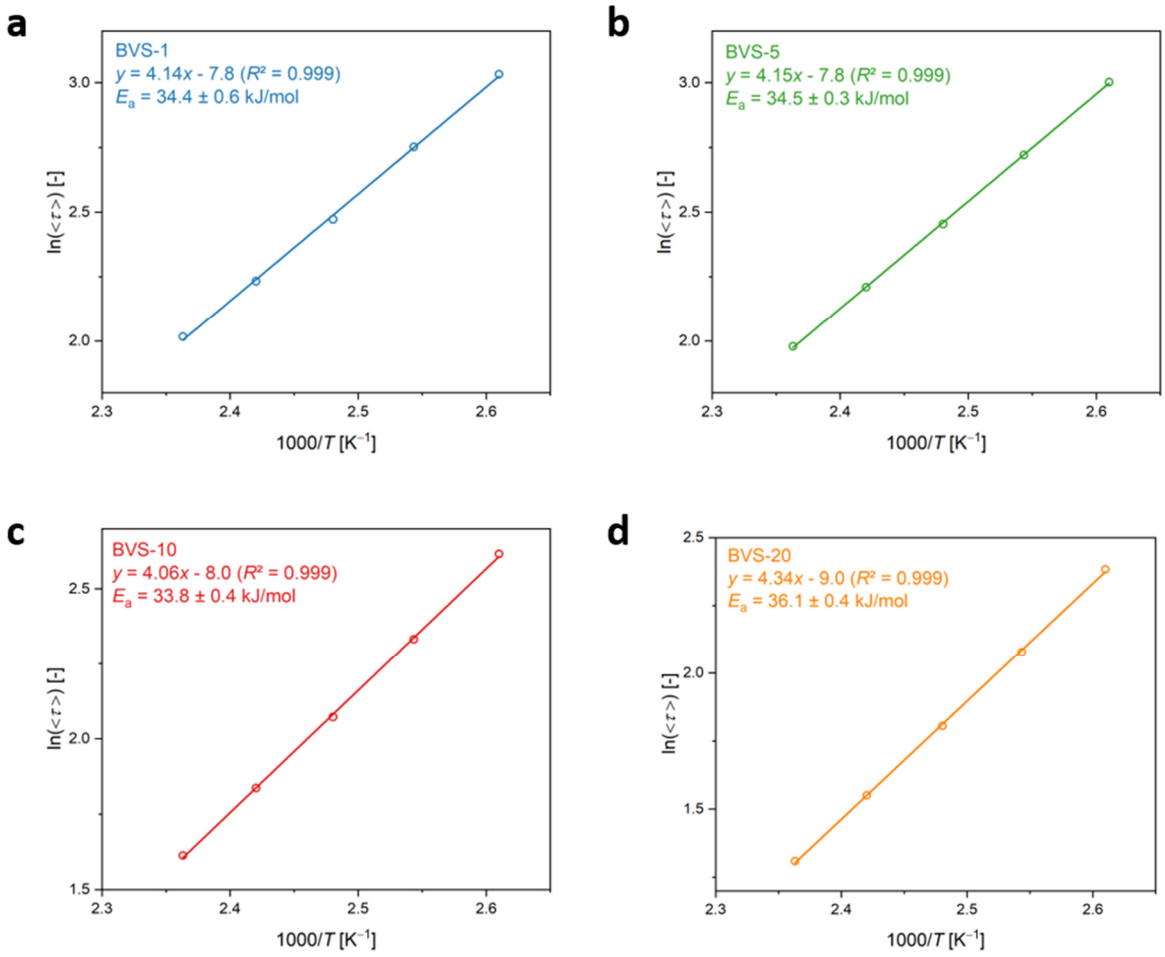

Figure S15: Plots of ln $\langle\tau\rangle$ versus 1000/T of the dioxaborolane vitrimer materials after different stages of reprocessing to calculate the activation energies (a – d) from the slope of the linear fit of the calculated $\langle\tau\rangle$ values from the stretched exponential fit in the temperature range of the stress-relaxation measurements (γ = 1%, F_N = 1 N) between 110 – 150 °C.

Equation S5

$$p = 2 \cdot (1 - \mathrm{TCDF}(|t|,df)$$

In Equation S5 are:

TCDF = *t*-distribution cumulative distribution function [-]
df = degrees of freedom [-]

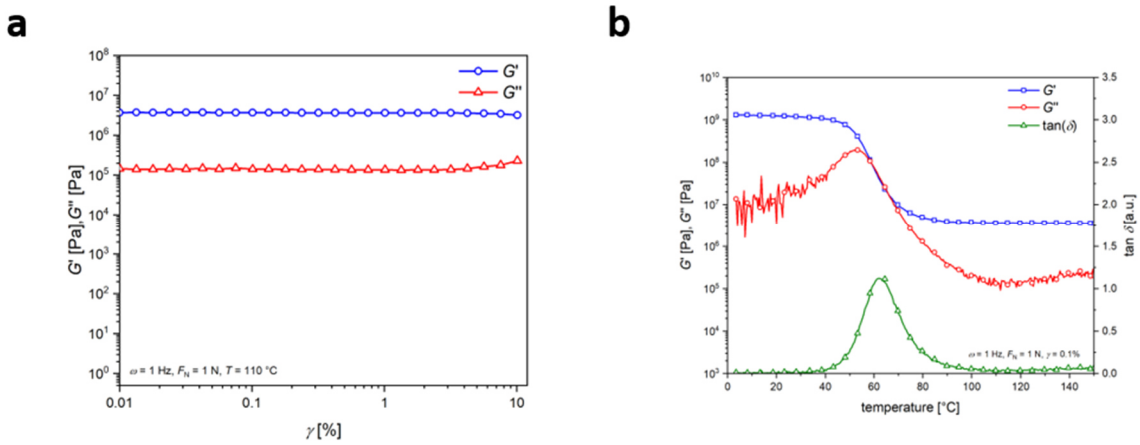

Figure S16: (a) Amplitude sweep measurements of the annealed dioxaborolane vitrimer material BVS-20A between 0.01 – 10% shear strain γ, performed at a constant angular frequency of 6.28 rad s^{-1}, a temperature of 110 °C, and a normal force F_N of 1 N. (b) Temperature sweep measurements of the annealed dioxaborolane vitrimer material BVS-20A in the temperature range of 0 – 150 °C performed at a constant angular frequency of 6.28 rad s^{-1}, a constant shear strain of 0.1%, and a normal force F_N of 1 N.

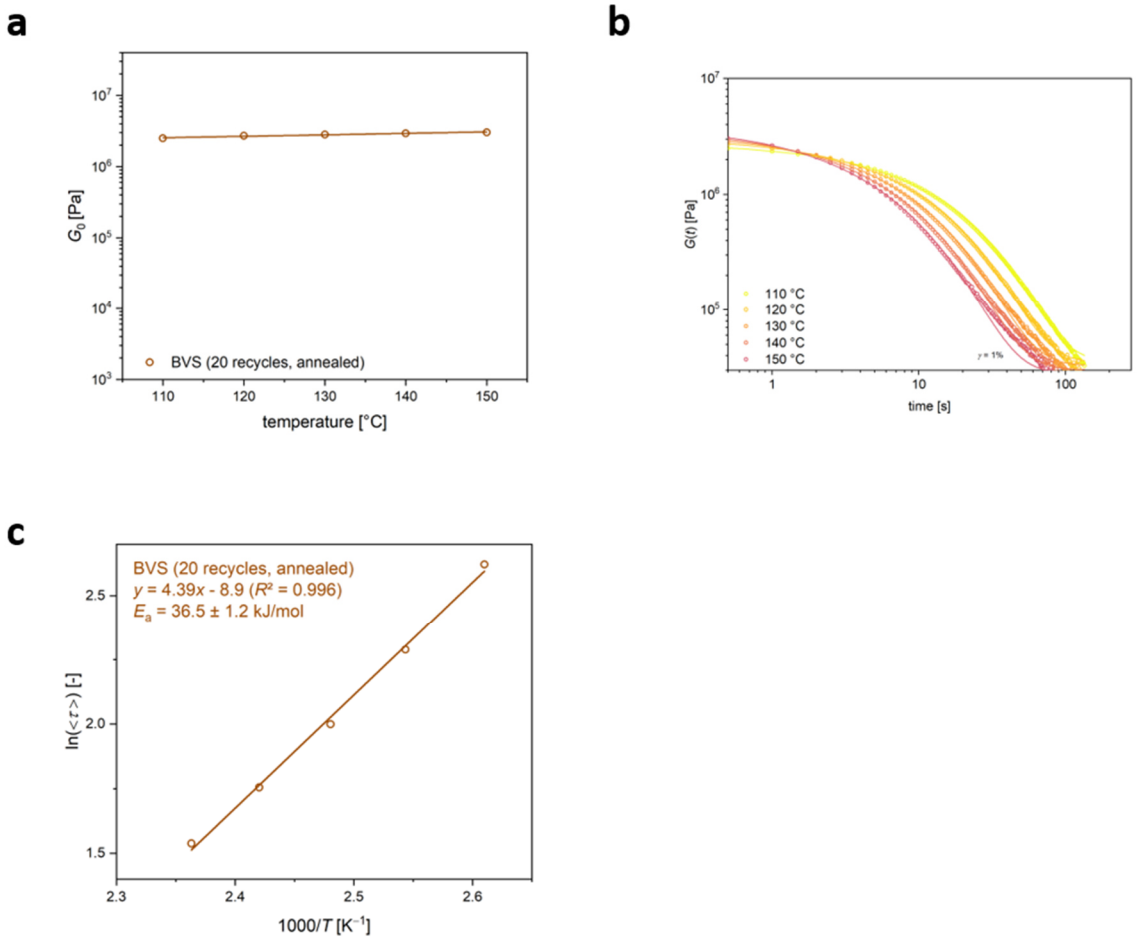

Figure S17: (a) Initial relaxation moduli G_0 of the annealed dioxaborolane vitrimer material BVS-20A as a function of temperature from the stress-relaxation measurement (γ = 1%, F_N = 1 N). The straight lines connecting the dots serve as an orientation guide to the eye. (b) Stress-relaxation measurements of the annealed dioxaborolane vitrimer material BVS-20A, plotting the stress-relaxation modulus $G(t)$ versus the stress-relaxation time measured at temperatures in the range of 110 to 150 °C while applying a shear strain of 1%. The lines display the stretched exponential fit functions for the respective temperatures, calculated from the stress-relaxation data. (c) Plot of ln $\langle\tau\rangle$ versus 1000/T of the annealed dioxaborolane vitrimer material BVS-20A to calculate the activation energy from the slope of the linear fit of the calculated $\langle\tau\rangle$ values from the stretched exponential fit in the temperature range of the stress-relaxation measurements (γ = 1%, F_N = 1 N) between 110 – 150 °C.

Table S3: Summary of the values of the stretch factor β and the calculated average values of the characteristic stress-relaxation time $\langle\tau\rangle$ for the KWW fit of the stress-relaxation measurements (γ = 1%, F_N = 1 N) between 110 – 150 °C of the annealed dioxaborolane vitrimer BVS-20A.

Sample	$\beta_{110°C}$ [-]	$\beta_{120°C}$ [-]	$\beta_{130°C}$ [-]	$\beta_{140°C}$ [-]	$\beta_{150°C}$ [-]	$\langle\tau\rangle_{110°C}$ [s]	$\langle\tau\rangle_{120°C}$ [s]	$\langle\tau\rangle_{130°C}$ [s]	$\langle\tau\rangle_{140°C}$ [s]	$\langle\tau\rangle_{150°C}$ [s]
BVS-20A	0.759	0.742	0.721	0.699	0.676	14.0	9.8	7.3	5.8	4.7

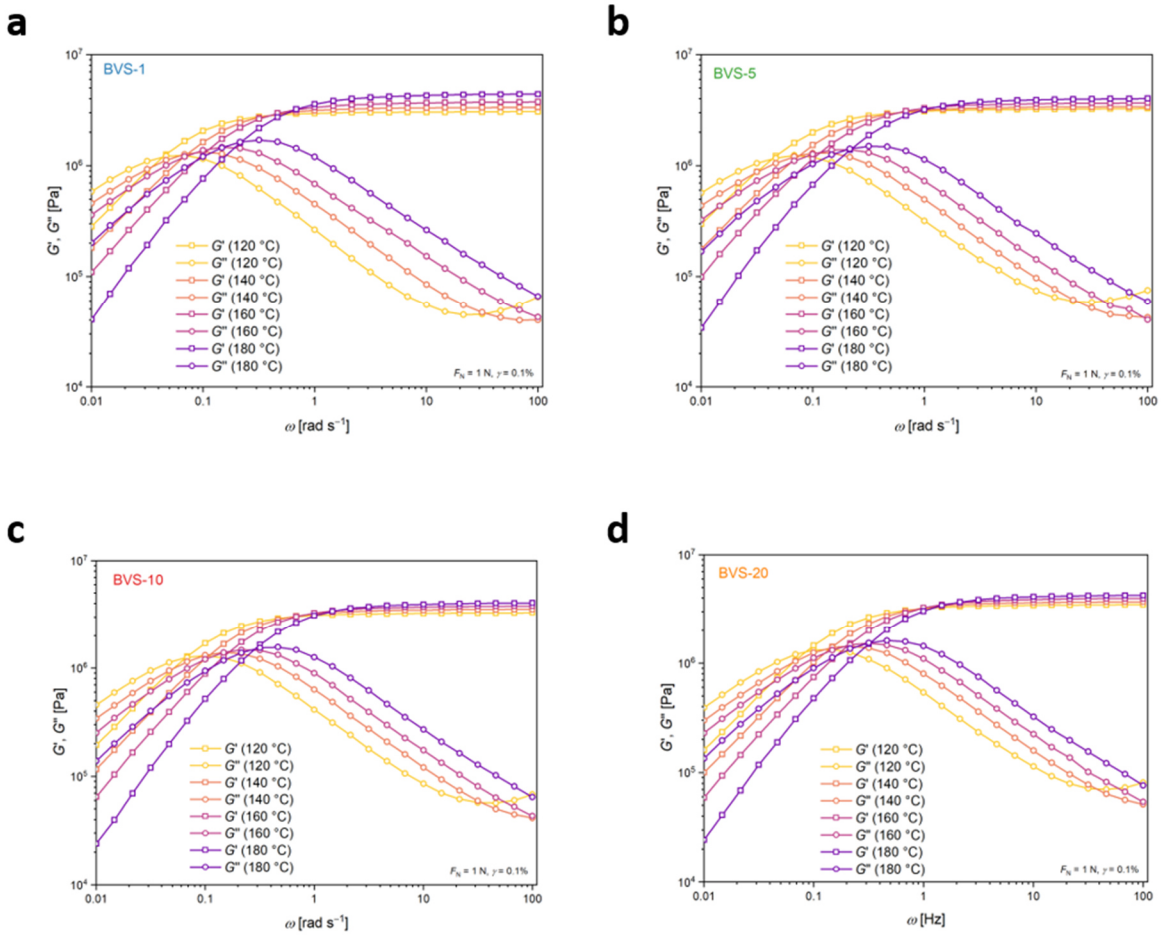

Figure S18: Frequency sweep measurements of the dioxaborolane vitrimer materials at temperatures in the range of 120 – 180 °C performed in the frequency range of 100 – 0.01 rad s^{-1} at a constant shear strain of 0.1% and a normal force F_N of 1 N.

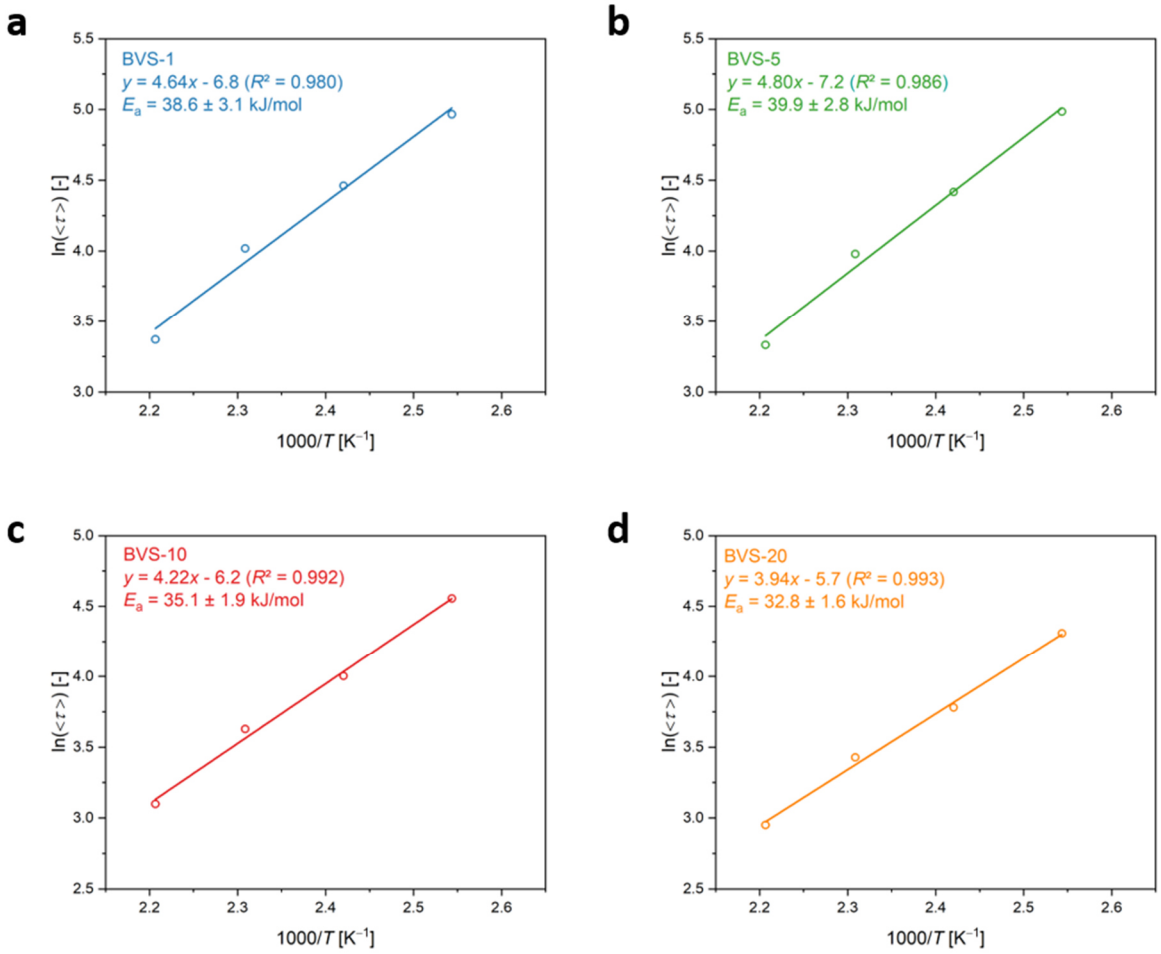

Figure S19: Plots of τ versus $1000/T$ of the dioxaborolane vitrimer materials after different stages of reprocessing to calculate the activation energies (a – d) from the slope of the linear fit of the τ values determined from the crossover points in the temperature range of 120 – 180 °C of the frequency sweep measurements in the frequency range of 100 – 0.01 rad s^{-1} at a constant shear strain of 0.1% and a normal force F_N of 1 N.

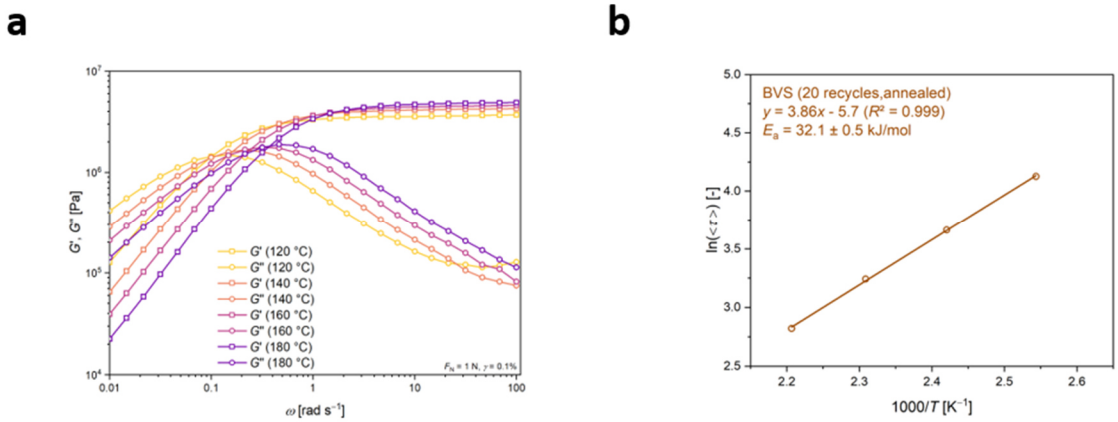

Figure S20: (a) Frequency sweep measurements of the annealed dioxaborolane vitrimer material BVS-20A at temperatures in the range of 120 – 180 °C performed in the frequency range of 100 – 0.01 rad s^{-1} at a constant shear strain of 0.1% and a normal force F_N of 1 N. (b) Plot of τ versus $1000/T$ of the annealed dioxaborolane vitrimer material BVS-20A to calculate the activation energy from the slope of the linear fit of the τ values determined from the crossover points in the temperature range of 120 – 180 °C of the frequency sweep measurements in the frequency range of 100 – 0.01 rad s^{-1} at a constant shear strain of 0.1% and a normal force F_N of 1 N.

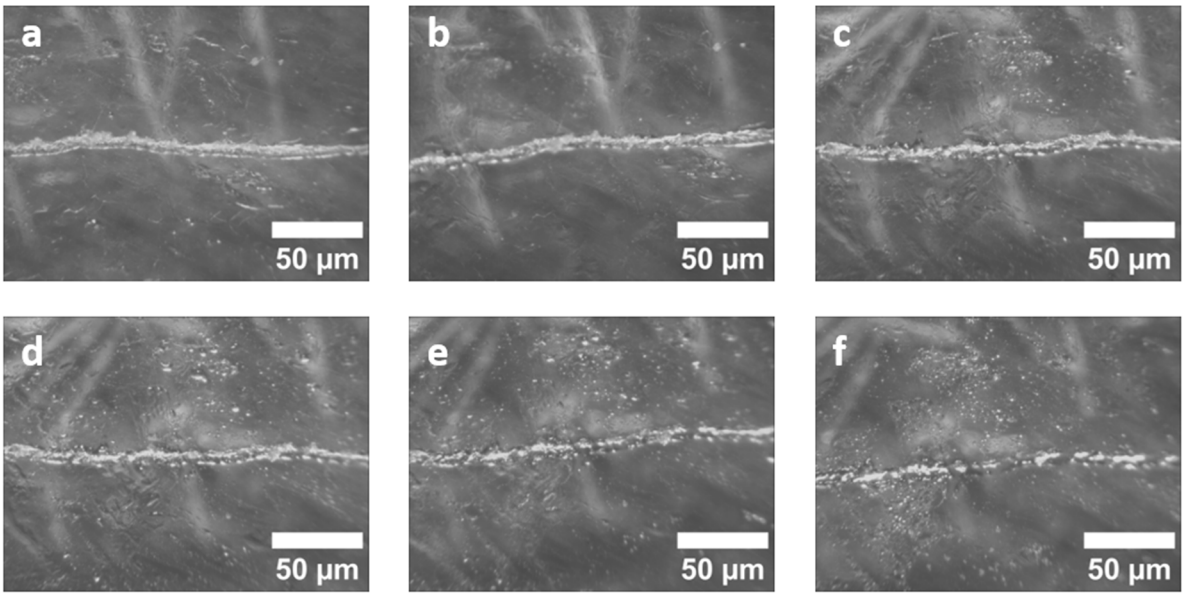

Figure S21: Optical microscopy images of a scratched sample BVS-1 after 0 min (a), 5 min (b), 30 min (c), 60 min (d), 120 min (e), and 180 min (f) of storage at 150 °C.

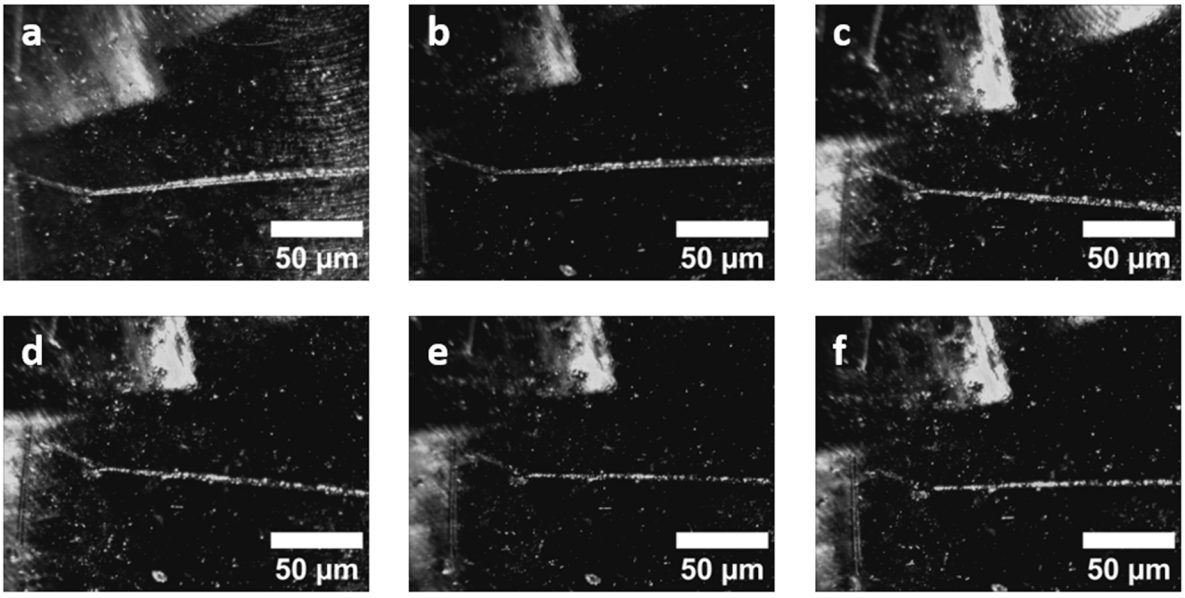

Figure S22: Optical microscopy images of a scratched sample BVCF after 0 min (a), 5 min (b), 30 min (c), 60 min (d), 120 min (e), and 180 min (f) of storage at 150 °C.

Table S4: Overview of the properties (edge length, thickness, crystal phase and organic fraction) of the various TNP batches that were combined for the studies shown in section 3.7.

TNP batch	Edge Length [nm]	Thickness [nm]	Crystal Phase	Organic Fraction [%]
TNP-2	24.5±3.7	-	anatase	23.5
TNP-10	24.8±4.7	5.3±0.7	anatase	26.0
TNP-11	25.5±3.8	5.4±0.7	anatase	22.4
TNP-13	24.9±4.1	6.8±1.1	anatase	19.6

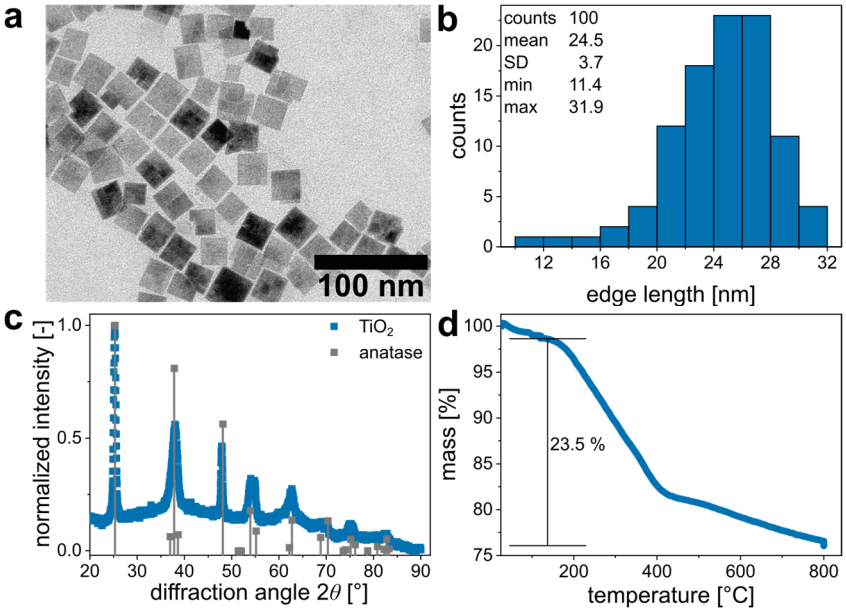

Figure S23: (a) Representative TEM image of TNPs from batch TNP-2. (b) Size-distribution of the edge length of the TNPs, obtained from the evaluation of 100 particles from various TEM images at different positions of the sample. (c) Normalized XRD diffractogram referenced to the anatase crystal phase.[3] (d) TGA graph showing the thermal decomposition of the organic fraction of the dried TNP-2 sample.

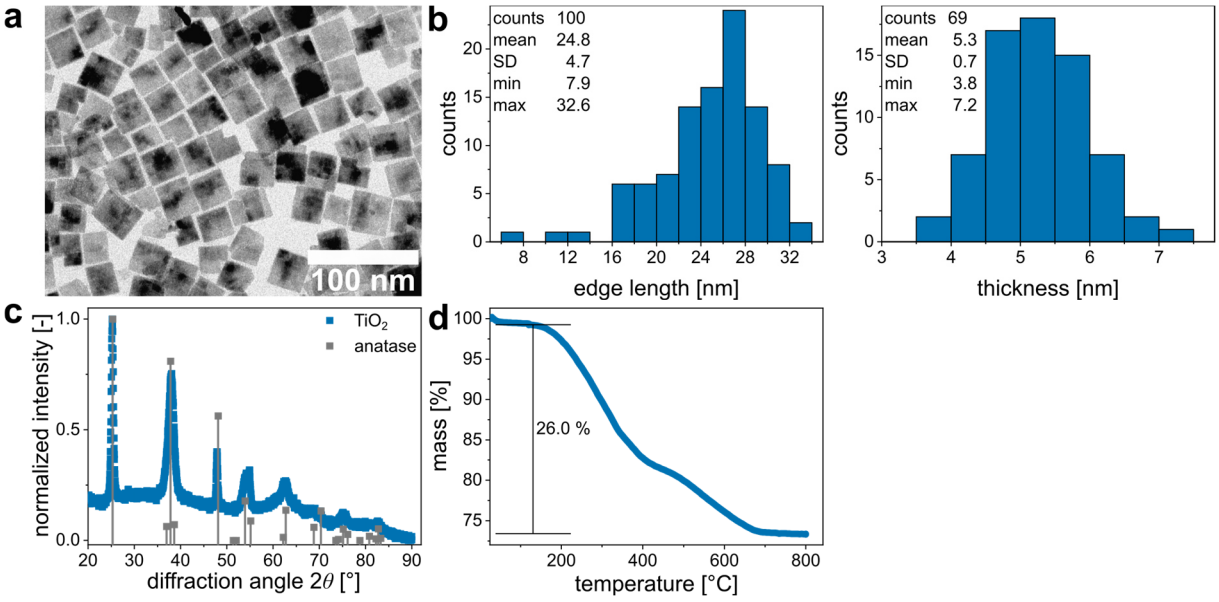

Figure S24: (a) Representative TEM image of TNPs from batch TNP-10. (b) Size-distribution of the edge length (left) and of the thickness (right) of the TNPs, obtained from the evaluation of 100 particles from various TEM images at different positions of the sample. (c) Normalized XRD diffractogram referenced to the anatase crystal phase.[3] (d) TGA graph showing the thermal decomposition of the organic fraction of the dried TNP-10 sample.

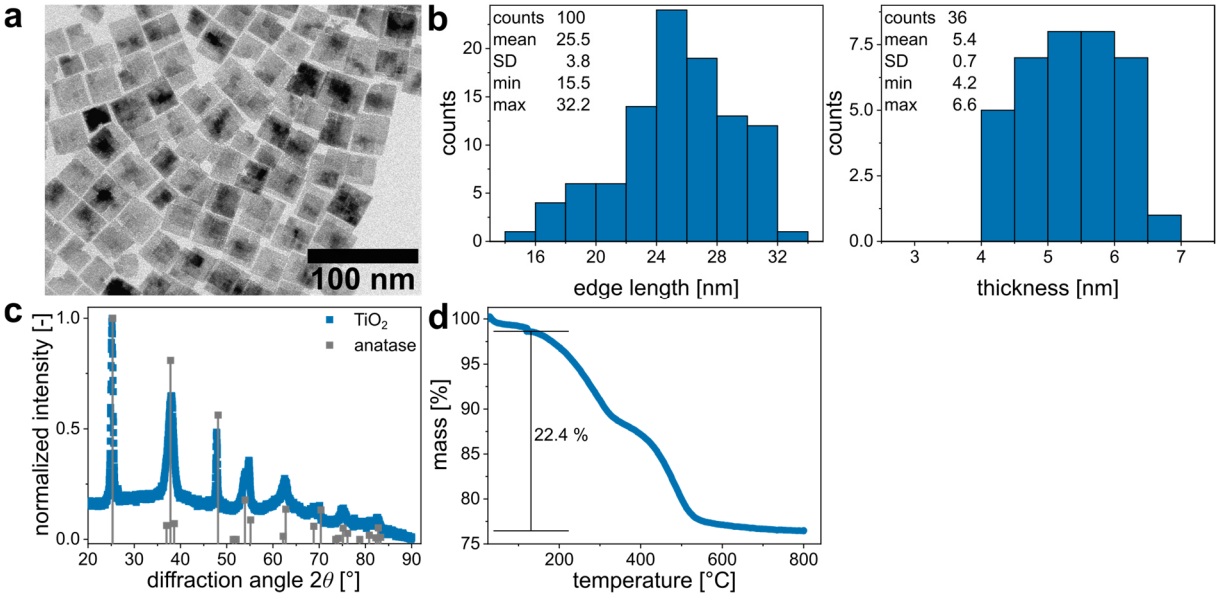

Figure S25: (a) Representative TEM image of TNPs from batch TNP-11. (b) Size-distribution of the edge length (left) and of the thickness (right) of the TNPs, obtained from the evaluation of 100 particles from various TEM images at different positions of the sample. (c) Normalized XRD diffractogram referenced to the anatase crystal phase.[3] (d) TGA graph showing the thermal decomposition of the organic fraction of the dried TNP-11 sample.

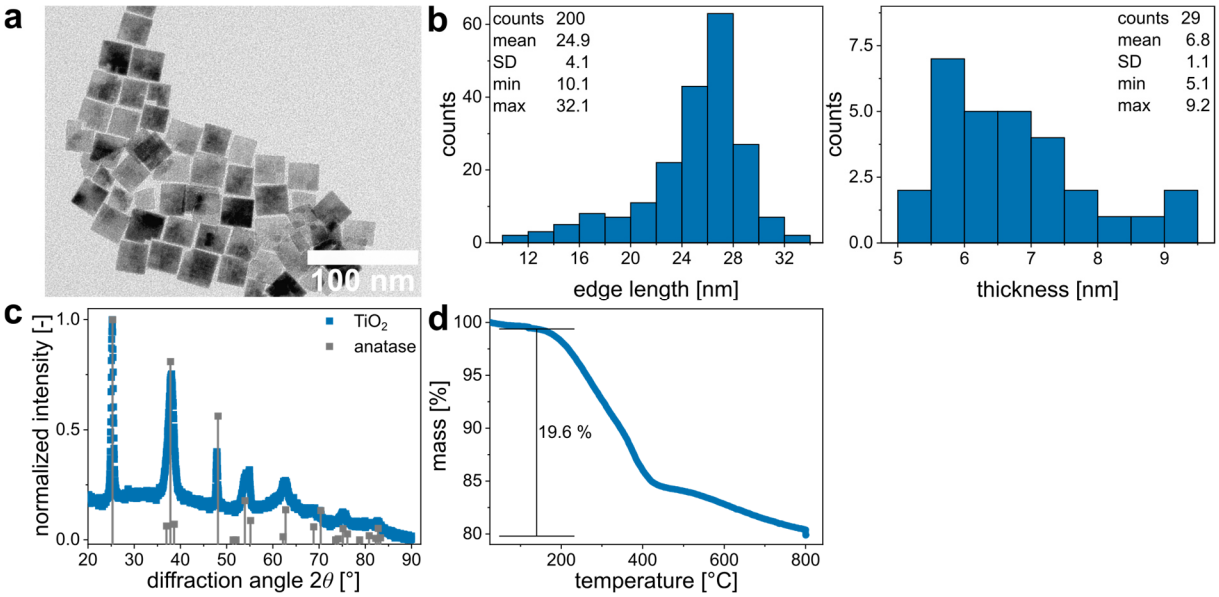

Figure S26: (a) Representative TEM image of TNPs from batch TNP-13. (b) Size-distribution of the edge length (left) and of the thickness (right) of the TNPs, obtained from the evaluation of 100 particles from various TEM images at different positions of the sample. (c) Normalized XRD diffractogram referenced to the anatase crystal phase.[3] (d) TGA graph showing the thermal decomposition of the organic fraction of the dried TNP-13 sample.

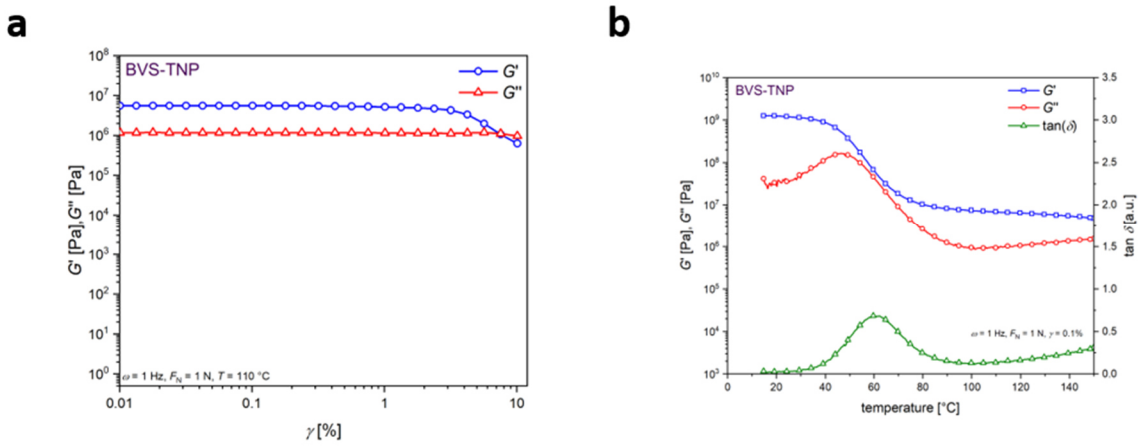

Figure S27: (a) Amplitude sweep measurements of BVS-TNP between 0.01 – 10% shear strain γ, performed at a constant angular frequency of 6.28 rad s^{-1}, a temperature of 110 °C, and a normal force F_N of 1 N. (b) Temperature sweep measurements of BVS-TNP in the temperature range of 0 – 150 °C performed at a constant angular frequency of 6.28 rad s^{-1}, a constant shear strain of 0.1%, and a normal force F_N of 1 N.

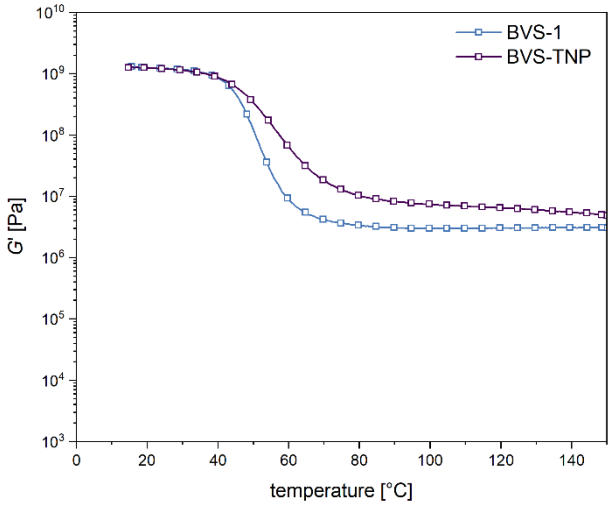

Figure S28: Comparison of the storage modulus G' of the temperature sweep measurements of BVS-1 and the nanocomposite BVS-TNP in the temperature range of 0 – 150 °C performed at a constant angular frequency of 6.28 rad s^{-1}, a constant shear strain of 0.1%, and a normal force F_N of 1 N.

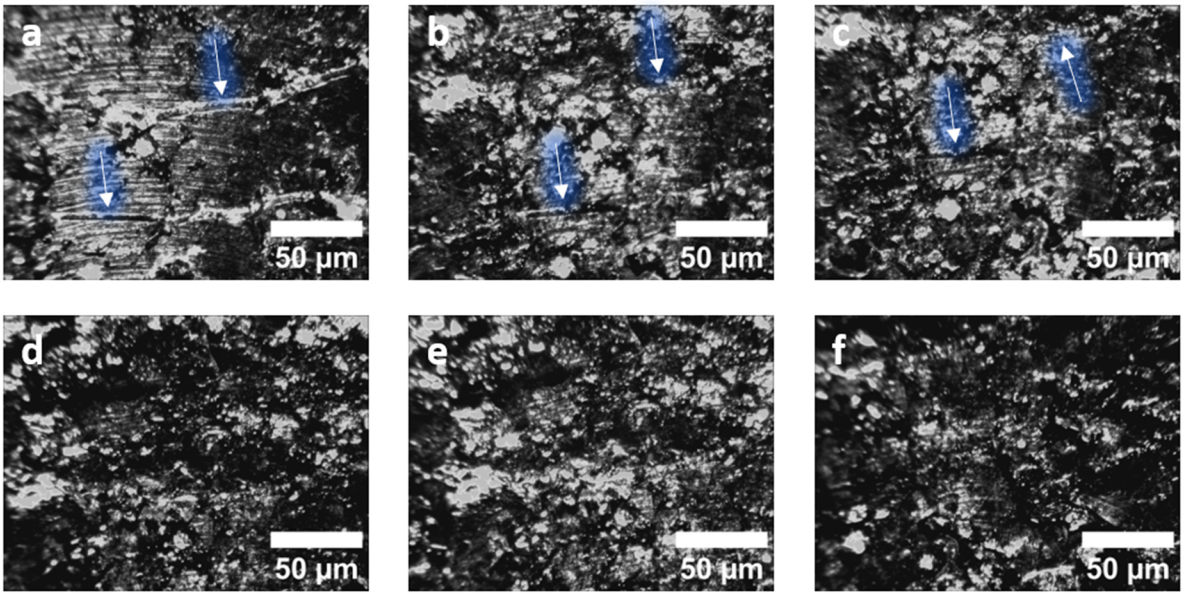

Figure S29: Optical microscopy images of a scratched sample BVS-TNP after 0 min (a), 5 min (b), 30 min (c), 60 min (d), 120 min (e), and 180 min (f) of storage at 150 °C. Optical self-healing could not be determined, due to the morphology changes of the surface.

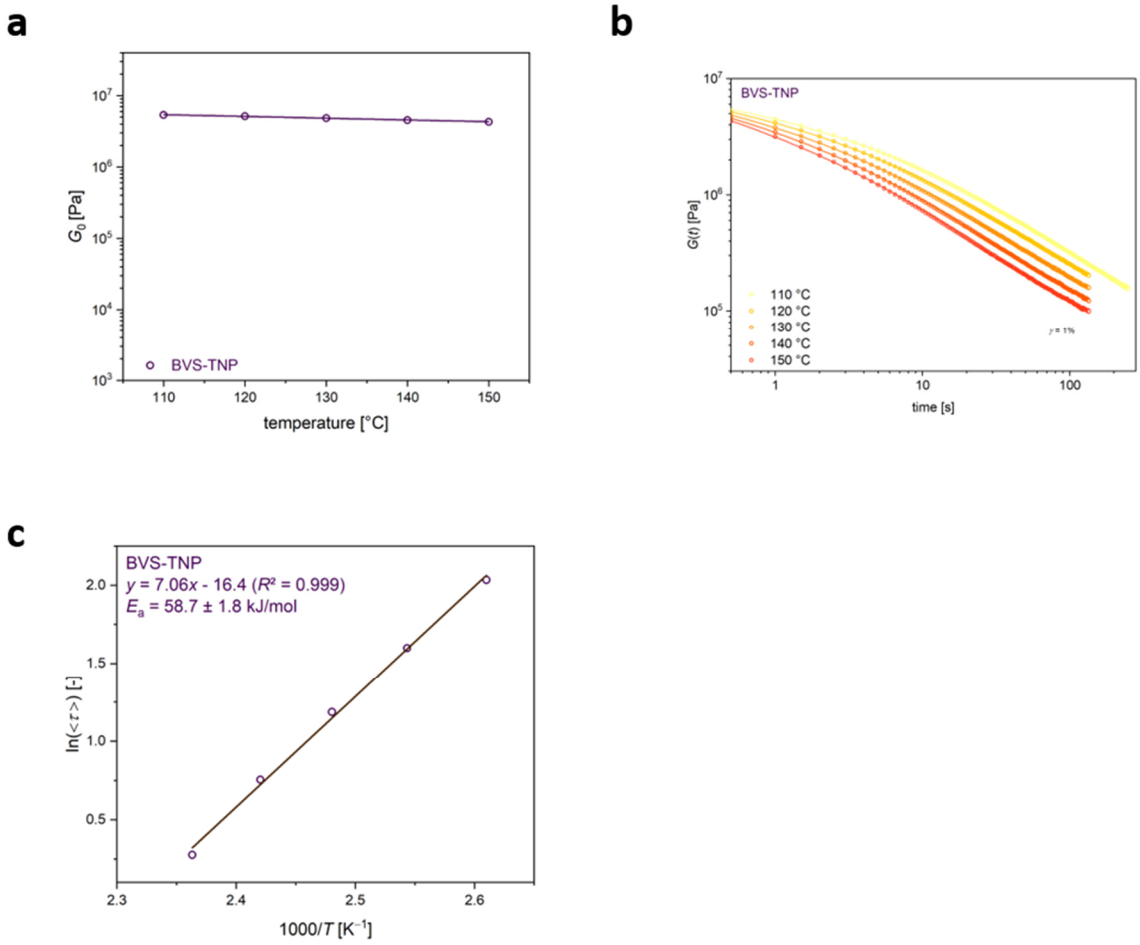

Figure S30: (a) Initial relaxation moduli G_0 of BVS-TNP as a function of temperature from the stress-relaxation measurement (γ = 1%, F_N = 1 N). The straight lines connecting the dots serve as an orientation guide to the eye. (b) Stress-relaxation measurements of BVS-TNP, plotting the stress-relaxation modulus $G(t)$ versus the stress-relaxation time measured at temperatures in the range of 110 to 150 °C while applying a shear strain of 1%. The lines display the stretched exponential fit functions for the respective temperatures, calculated from the stress-relaxation data. (c) Plot of ln $<\tau>$ versus 1000/T of BVS-TNP to calculate the activation energy from the slope of the linear fit of the calculated $<\tau>$ values from the stretched exponential fit in the temperature range of the stress-relaxation measurements (γ = 1%, F_N = 1 N) between 110 – 150 °C.

Table S5: Summary of the values of the stretch factor β and the calculated average values of the characteristic stress-relaxation time $<\tau>$ for the KWW fit of the stress-relaxation measurements (γ = 1%, F_N = 1 N) between 110 – 150 °C of the annealed dioxaborolane vitrimer BVS-TNP.

Sample	$\beta_{110°C}$ [-]	$\beta_{120°C}$ [-]	$\beta_{130°C}$ [-]	$\beta_{140°C}$ [-]	$\beta_{150°C}$ [-]	$<\tau>_{110°C}$ [s]	$<\tau>_{120°C}$ [s]	$<\tau>_{130°C}$ [s]	$<\tau>_{140°C}$ [s]	$<\tau>_{150°C}$ [s]
BVS-TNP	0.286	0.288	0.266	0.246	0.226	0.66	0.44	0.19	0.08	0.03

References

[1] A. Zych, J. Tellers, L. Bertolacci, L. Ceseracciu, L. Marini, G. Mancini, A. Athanassiou, "Biobased, Biodegradable, Self-Healing Boronic Ester Vitrimers from Epoxidized Soybean Oil Acrylate," *ACS Applied Polymer Materials*, **2020**, *3*, 1135-1144, https://doi.org/10.1021/acsapm.0c01335.

[2] X. Wang, S. Zhang, Y. He, W. Guo, Z. Lu, "Reprocessable Polybenzoxazine Thermosets with High T_gs and Mechanical Strength Retentions Using Boronic Ester Bonds as Crosslinkages," *Polymers*, **2022**, *14*, 2234 (1-11), https://doi.org/10.3390/polym14112234.

[3] C. F. S. M. Horn, E. P. Meagher, "Refinement of the structure of anatase at several temperatures," *Zeitschrift für Kristallographie*, **1972**, *136*, 273-281, https://doi.org/10.1524/zkri.1972.136.16.273.

9.5 Unpublished Results – Supporting Information

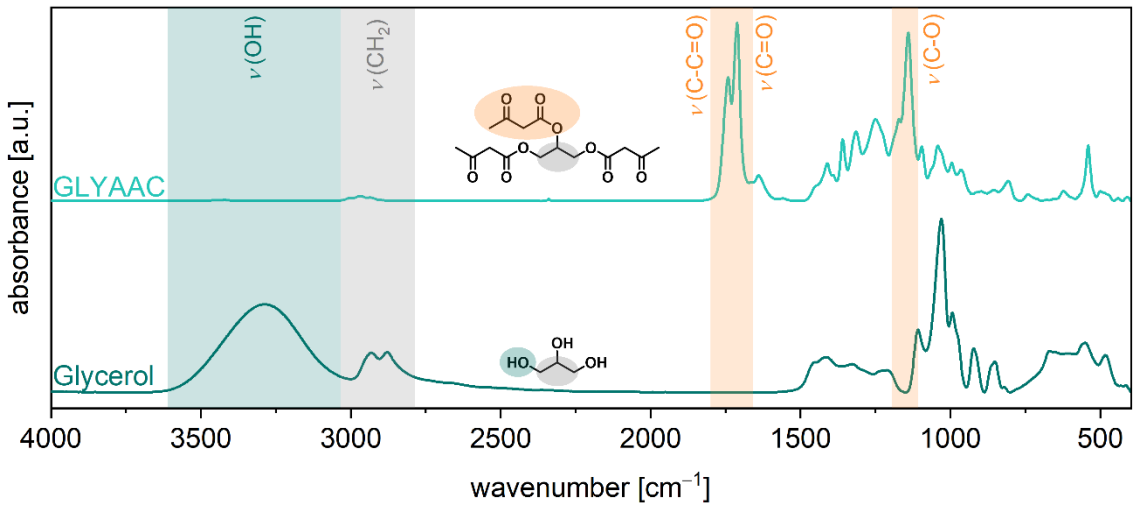

Figure A1: ATR-FT-IR spectra of the acetoacetylated propane-1,2,3-triyl tris(3-oxobutanoate) (GLYAAC) and glycerol showing the characteristic OH-stretching vibrations (green) before the acetoacetylation and the acetoacetate stretching vibrations (orange) after the acetoacetylation.

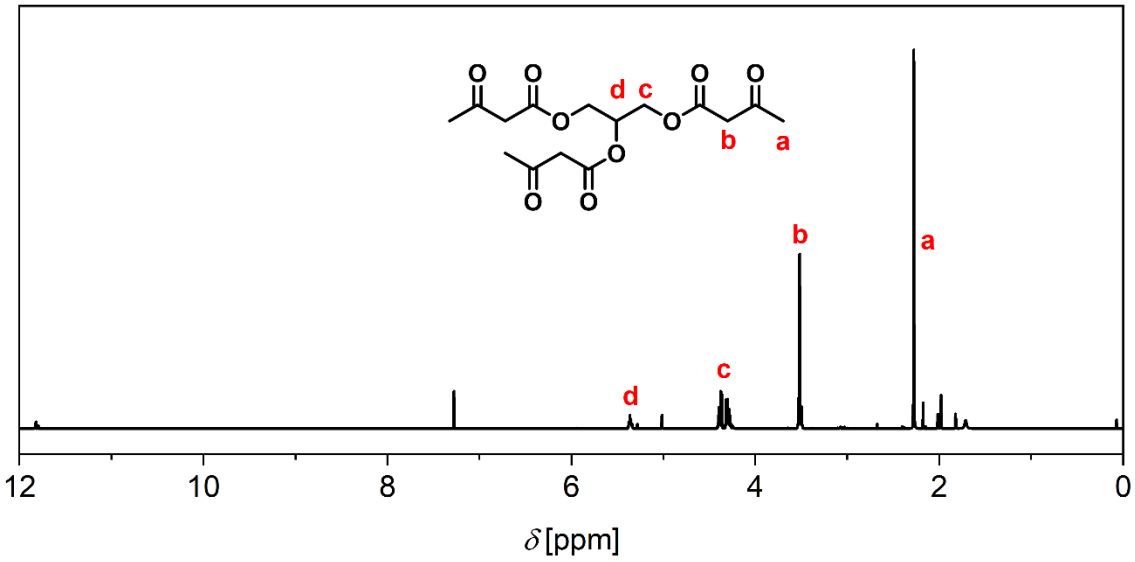

Figure A2: ^{1}H NMR spectrum of propane-1,2,3-triyl tris(3-oxobutanoate) (GLYAAC), showing the characteristic signals and intensities. ^{1}H NMR (500 MHz, $CDCl_3$, 296 K) [ppm]: 5.36 (1H, tt, CH), 4.37 - 4.30 (4H, m, CH_2), 3.52 (6H, m, CH_2), 2.27 (9H, s, CH_3).

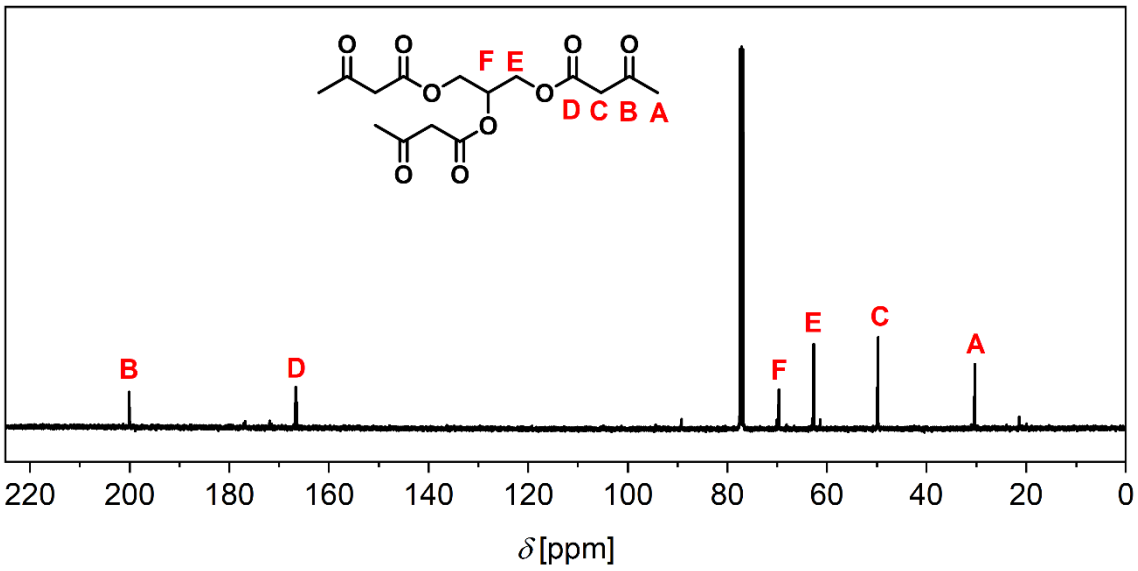

Figure A3: ^{13}C NMR spectrum of propane-1,2,3-triyl tris(3-oxobutanoate) (GLYAAC), showing the characteristic signals and intensities. ^{13}C NMR (100 MHz, $CDCl_3$, 300 K) [ppm]: 200.2 (C=O), 166.7 (C=O), 69.7 (CH), 62.7 (CH_2), 49.9 (CH_2), 30.3 (CH_3).

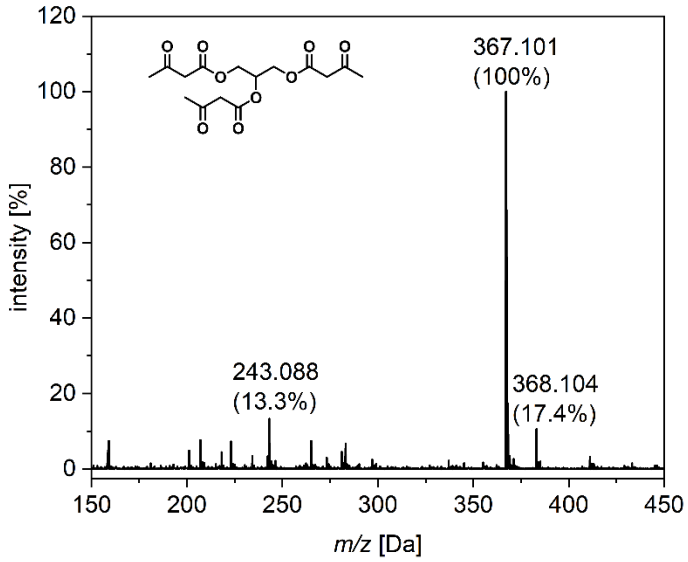

Figure A4: ESI-MS (+) spectrum, showing the characteristic peak of propane-1,2,3-triyl tris(3-oxobutanoate) (GLYAAC) with m/z = 367.101.

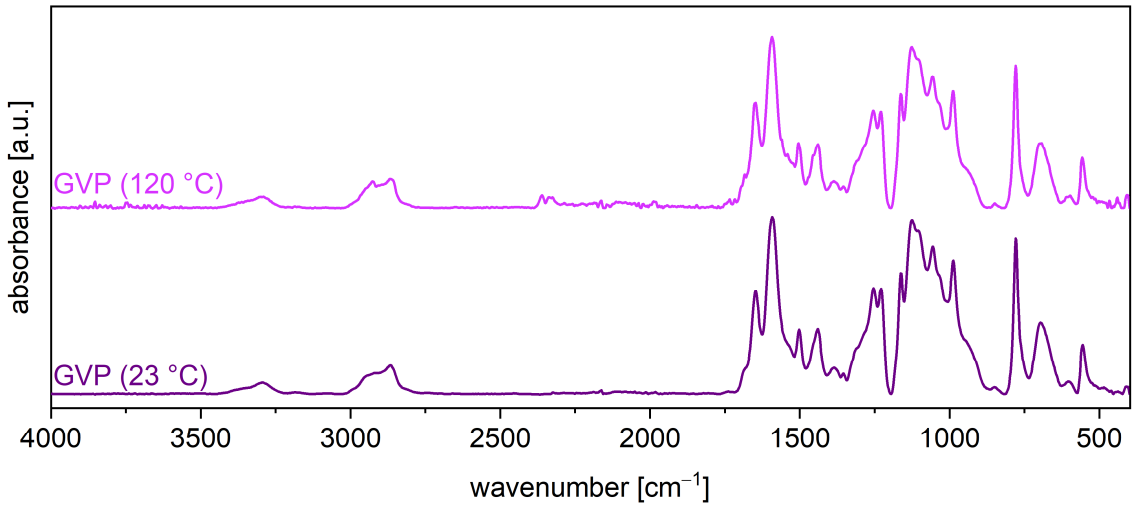

Figure A5: Comparison of the ATR-FT-IR spectra of GVP, formed at 23 °C and 120 °C, after heat compression. There are no differences between the bands in the two spectra.

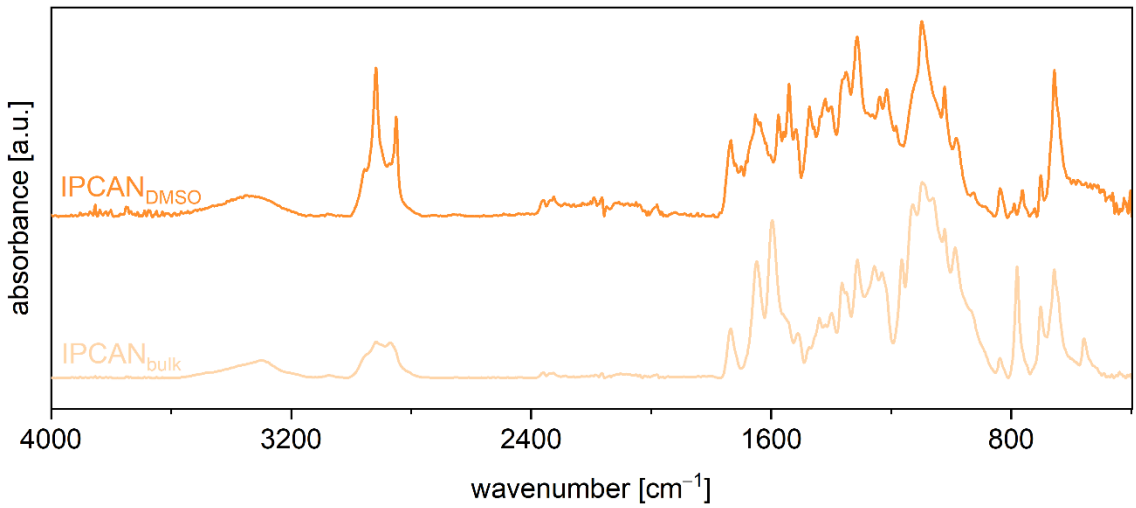

Figure A6: Comparison of the ATR-FT-IR spectra of IPCAN from BVS and GVP, formed in bulk and solvent-mediated in DMSO, after heat compression.

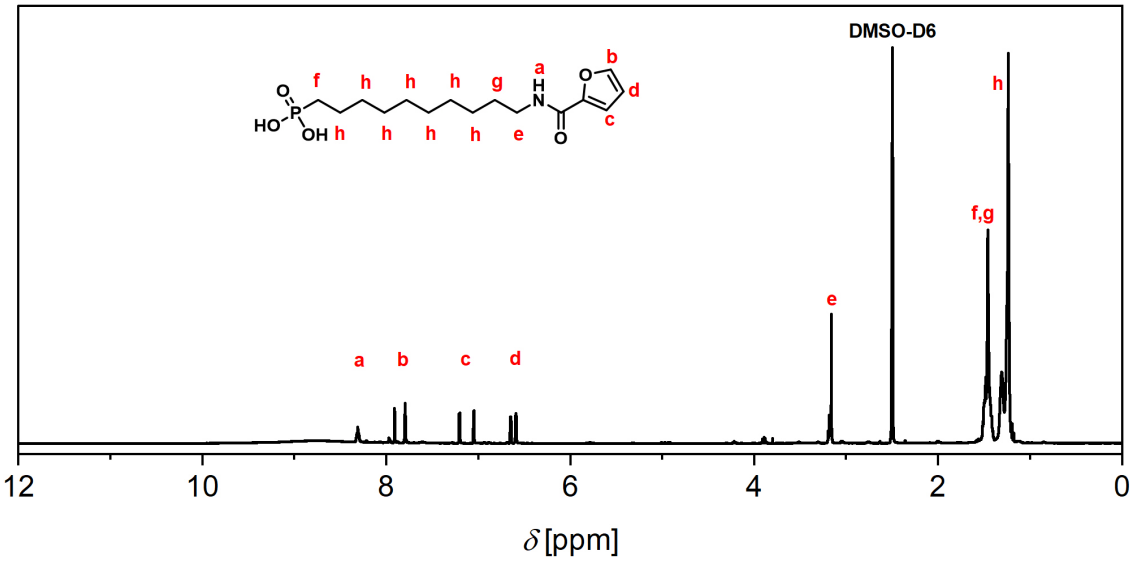

Figure A7: ^{1}H NMR spectrum of (10-(furan-2-carboxamido)decyl)phosphonic acid (FDPA), showing the characteristic signals and intensities. ^{1}H NMR (500 MHz, DMSO-d_6, 296 K) [ppm]: 8.31 (1H, NH), 7.91-7.81 (1H, CH), 7.20-7.06 (1H, CH), 6.66-6.59 (1H, CH), 3.18 (2H, CH_2), 1.48 (6H, CH_2), 1.24 (12H, CH_2).

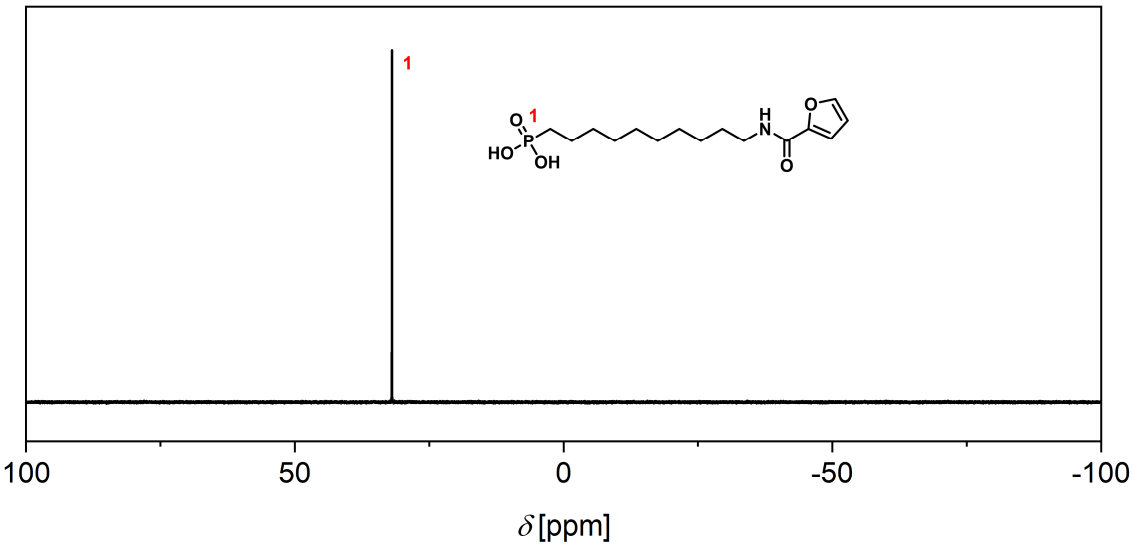

Figure A8: ^{31}P NMR spectrum of (10-(furan-2-carboxamido)decyl)phosphonic acid (FDPA), showing the characteristic signal. ^{31}P NMR (162 MHz, DMSO-d_6, 300 K) [ppm]: 31.95.

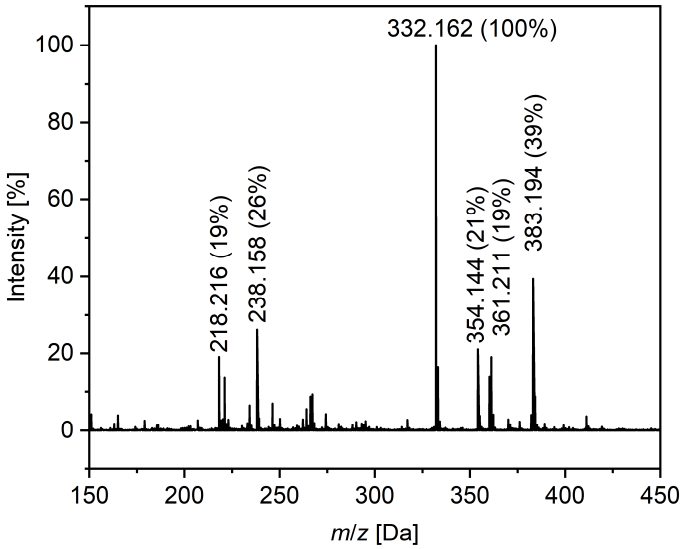

Figure A9: ESI-MS (+) spectrum, showing the characteristic peak of (10-(furan-2-carboxamido)decyl)phosphonic acid (FDPA) with m/z = 332.162.

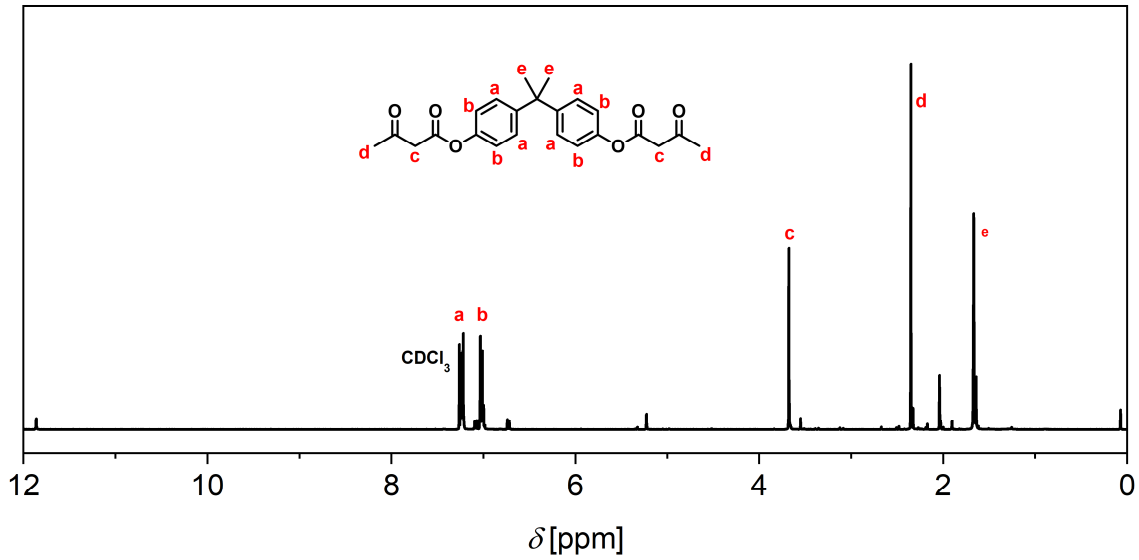

Figure A10: ^{1}H NMR spectrum of propane-2,2-diylbis(4,1-phenylene) bis(3-oxobutanoate) (BPAAC), showing the characteristic signals and intensities. ^{1}H NMR (500 MHz, $CDCl_3$, 296 K) [ppm]: 7.22 (4H, d, CH), 7.02 (4H, d, CH), 3.68 (4H, s, CH_2), 2.35 (6H, s, CH_3), 1.67 (6H, d, CH_3).

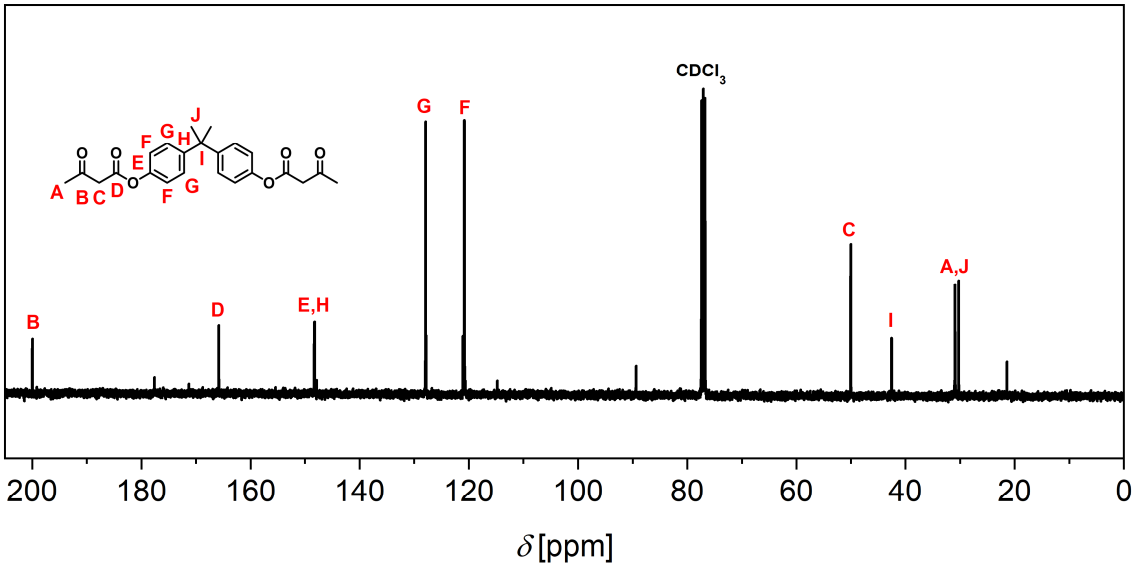

Figure A11: ^{13}C NMR spectrum of propane-2,2-diylbis(4,1-phenylene) bis(3-oxobutanoate) (BPAAC), showing the characteristic signals and intensities. ^{13}C NMR (100 MHz, $CDCl_3$, 300 K) [ppm]: 200.0 (C=O), 165.8 (C=O), 148.3 (C) 127.9 (CH), 120.8 (CH), 50.0 (CH_2), 42.6 (C), 30.9 (CH_3), 30.3 (CH_3).

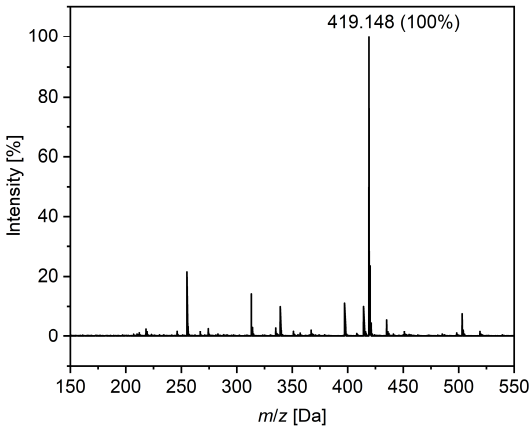

Figure A12: ESI-MS (+) spectrum, showing the characteristic peak of propane-2,2-diylbis(4,1-phenylene) bis(3-oxobutanoate) (BPAAC) with m/z = 419.148.

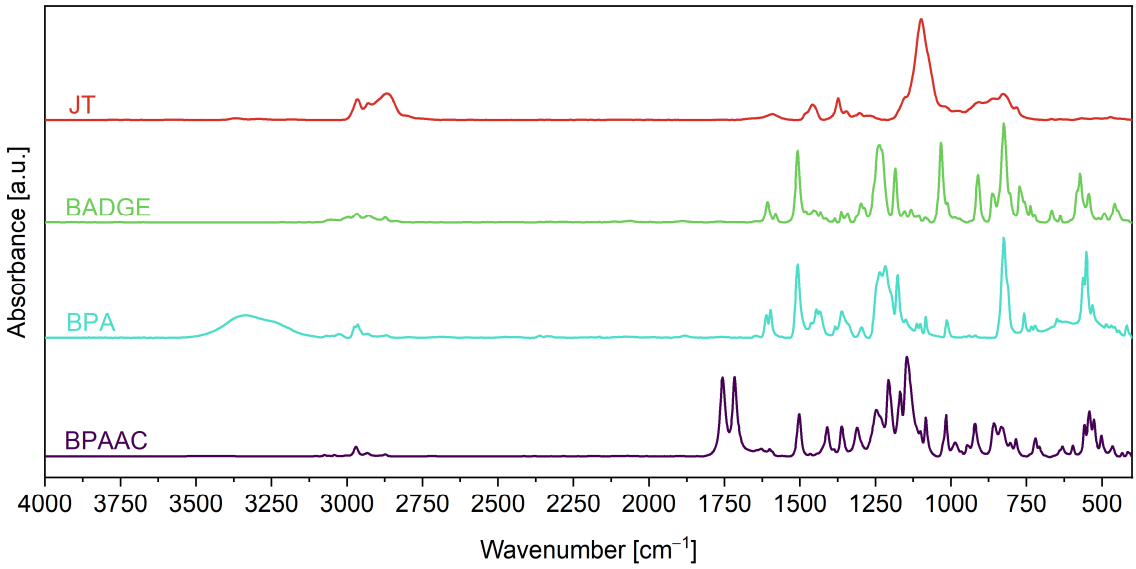

Figure A13: ATR-FT-IR spectra of JT, BADGE, BPA, and BPAAC, which were used to form VIPOXY materials.

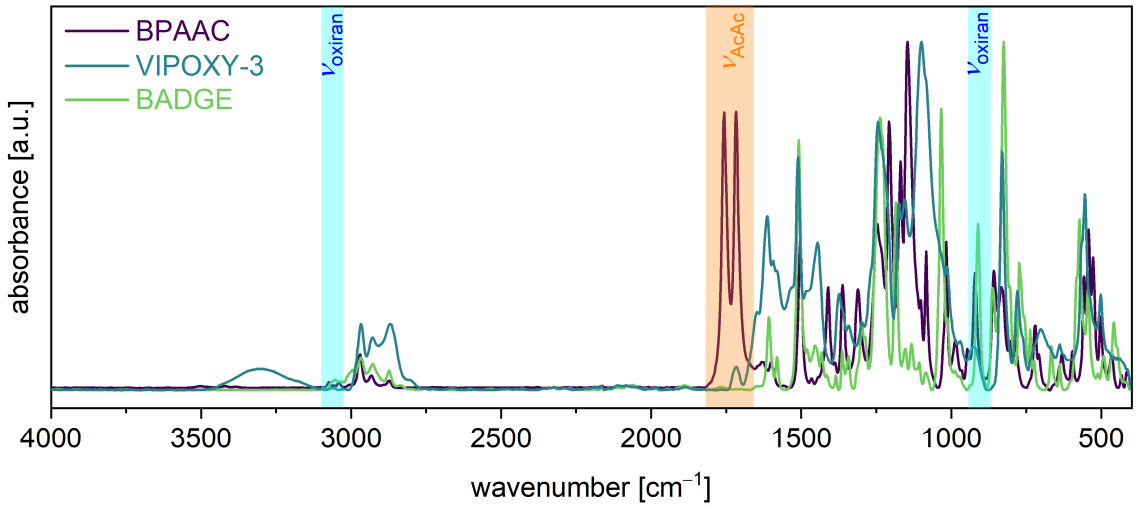

Figure A14: ATR-FT-IR spectra of BPAAC, VIPOXY-3, and BADGE with the vanishing oxirane bands marked in blue.

9.6 Safety and Disposal

The chemicals that were used in this work are listed in Table 5 together with their GHS-Pictograms, Hazard- and Precautionary-Statements, as well as indications for disposal. Carcinogenic, mutagenic substances, and substances toxic for reproduction are listed in Table 6.

Table 5: Used chemicals, their Hazard- and Precautionary-Statements, plus indications for disposal.

Substance	Symbol	Hazard-State-ments	Precautionary-State-ments	Disposal
1,10-Dibromodec-ane	*Not a hazardous substance or mixture according to Regulation (EC) No 1272/2008.*			(2)
1,1'-Carbonyldiim-idazole		302, 314	260, 270, 280, 301+312, 303+361+353, 303+361+353, 305+351+338	(2)
1,4-Dibromobutane		315, 319	264, 280, 302+ 352, 305+351+ 338, 332+313, 337+313	(2)
10-(furan-2-car-boxamido)-decylphosphonic acid	*Not yet classified according to Regulation (EC) No 1272/2008.*			(1)
1-Thioglycerol		311, 317	261, 280	(2)
2,2,6-Trimethyl-4*H*-1,3-dioxin-4-one		225, 319	210, 305+351+338	(1)
2,2-Bis[[(1-oxo-2-propenyl)oxy]me-thyl]-1,3-pro-panediyl ester		315, 317, 319	261, 264, 272, 280, 302+352, 305+351+338	(1)
2-Methyltetrahy-drofuran		225, 302, 315, 318	210, 233, 301+312, 303+361+353, 305+351+338 EUH019	(1)
Acetone		225, 319, 336	210, 305+351+338, 370+378, 403+235	(1)
Acetonitrile		225, 302, 312, 319, 332	210, 280, 305+351+338	(1)
Benzene-1,4-dibo-ronic acid		302	264, 270, 301+312	(1)
Bio-based poly(oxy-1,3-pro-panediyl)	*Not a hazardous substance or mixture according to Regulation (EC) No 1272/2008.*			(1)

Substance	Symbol	Hazard-State-ments	Precautionary-State-ments	Disposal
5,5-Dimethyl-3,7-dioxa-1,9(2)-bis(oxirana)-4,6(2,4)-diben-zenanonaphane		315, 317, 319	280, 305+351+338	(1)
4,4′-(Propane-2,2-diyl)diphenol		317, 318, 335, 360F, 410	202, 273, 280, 302+352, 305+351+338, 308+313	(2)
Calcium chloride		319	305+351+338	(3)
Calcium hydride		260, 315, 319	223, 231+232, 264, 280, 302+352, 305+351+338	(3)
Carbon fiber	*Not a hazardous substance or mixture according to Regulation (EC) No 1272/2008.*			(3)
Chloroform		302, 331, 315, 319, 351, 361d, 336, 372, 412	201, 273, 301+312+330, 302+352, 304+340+311, 308+313	(2)
1,8-Diamino-3,6-dioxaoctan		302, 314, 317, 334	261, 280, 301+312, 303+363+353, 304+340+310, 305+351+338	(1)
Deuterated chloro-form		302, 315, 319, 331, 336, 351, 361, 372, 373	201, 202, 260, 261, 264, 270, 271, 280, 281, 301+312, 302+352, 304+340, 305+351+338, 308+313, 311, 312, 314, 321, 330, 332+313, 337+313, 362, 403+233, 405, 501	(2)
Deuterated dime-thyl sulfoxide	*Not a hazardous substance or mixture according to Regulation (EC) No 1272/2008.*			(1)
Dichloromethane		315, 319, 336, 351	201, 302+352, 305+351+338, 308+313	(2)
Diethyl ether		224, 302, 336, EUH019, EUH066	210, 233, 240, 241, 301+312, 403+233	(1)
Diethyl phospho-nate		317, 318	261, 280, 302+352, 305+351+338	(4)
Diethylenetriamine		330, 302, 312, 314, 317, 335	260, 280, 301+312, 303+361+353, 304+340+310, 305+351+338	(2)
Dimethyl sulfoxide	*Not a hazardous substance or mixture according to Regulation (EC) No 1272/2008.*			(1)

Substance	Symbol	Hazard-State-ments	Precautionary-State-ments	Disposal
endo-N-Hydroxy-5-norbonene-2,3-dicarboxylic acid imide	*Not a hazardous substance or mixture according to Regulation (EC) No 1272/2008.*			(1)
Ethanol		225, 319	210, 233, 305+351+338	(1)
Ethyl acetate		225, 319, 336	210, 233, 240, 305+351+338, 403+235	(1)
Furancarboxylic acid		315, 319, 335	261, 305+351+338	(1)
Glycerol	*Not a hazardous substance or mixture according to Regulation (EC) No 1272/2008.*			(1)
Hydrazine mono-hydrate		226, 301+311, 330, 314, 317, 350, 410	201,260, 273, 280, 304+340+310, 305+351+338	(2)
Hydrochloric acid (37%)		290, 314, 335	280, 303+361+353, 304+340, 305+351+338, 312	(5)
Jeffamine® D-400		302, 312, 314, 412	273, 280, 303+361+353, 305+351+338, 310	(1)
Jeffamine® T-430		302, 312, 318, 411	273, 280, 305+351+338, 310	(1)
Lignosulfonate	*Not a hazardous substance or mixture according to Regulation (EC) No 1272/2008.*			(3)
Lignova™ Crude	*Not a hazardous substance or mixture according to Regulation (EC) No 1272/2008.*			(3)
Lignova™ Pure	*Not a hazardous substance or mixture according to Regulation (EC) No 1272/2008.*			(3)
Magnesium sulfate	*Not a hazardous substance or mixture according to Regulation (EC) No 1272/2008.*			(3)
Methanol		225, 301+311+331, 370	210, 270, 280, 303+361+353, 304+340, 308+311	(2)
N-(10-ami-nodecyl)diethyl phosphonate	*Not yet classified according to Regulation (EC) No 1272/2008.*			(1)
N-(10-bromo-decyl)phthalimide	*Not yet classified according to Regulation (EC) No 1272/2008.*			(1)

Substance	Symbol	Hazard-State-ments	Precautionary-State-ments	Disposal
N-(10-phthalimidoal-kyl)diethyl phosphonate	*Not yet classified according to Regulation (EC) No 1272/2008.*			(1)
N,*N*-Dimethylfor-mamide		226, 312, 319, 332, 360	280, 305+351+338, 308+313	(2)
N,*N*-Dimethylfor-mamide-d7		226, 332, 312, 319, 360D	210, 280, 303+361+353, 304+340+312, 305+351+338, 308+313	(2)
n-Hexane		225, 304, 361f, 373, 315, 336, 411	210, 240, 273, 301+310, 331, 302+352,403+235	(2)
n-Pentane		225, 304, 336, 411, EUH066	210, 233, 240, 273, 301+310-331	(1)
Oleic acid	*Not a hazardous substance or mixture according to Regulation (EC) No 1272/2008.*			(1)
Oleyl amine		302, 304, 314, 335, 373, 410	273, 280, 301+330+331, 303+361+353, 304+340+310, 305+351+338	(2)
Phosphorus trichlo-ride		300+330, 373, 314, EUH014, EUH029	280, 301+330+331, 305+351+338-304+340, 310, 402+404	(6)
Potassium car-bonate		315, 319, 335	280, 302+352, 305+351+338, 337+313	(3)
Potassium phthali-mide		315, 319	264, 280, 302+352, 305+351+338, 332+313, 337+313	(3)
Priamine™ 1073		302, 312, 314, 411	273, 280, 303+361+353, 305+351+338, 310	(1)
Propane-2,2-diylbis(4,1-pheny-lene)bis(3-oxobu-tanoate)	*Not yet classified according to Regulation (EC) No 1272/2008.*			(1)

Substance	Symbol	Hazard-State-ments	Precautionary-State-ments	Disposal
Pyridine		225, 302+312+332, 315, 319	210, 280, 301+312, 303+361+353, 304+340+312, 305+351+338	(1)
Sodium chloride	*Not a hazardous substance or mixture according to Regulation (EC) No 1272/2008.*			(3)
Sodium hydroxide		290, 314	280, 303+361+353, 305+351+338, 310	(7)
SPIONs	*Not yet classified according to Regulation (EC) No 1272/2008.*			(3)
tert-Butyl acetoacetate	*Not a hazardous substance or mixture according to Regulation (EC) No 1272/2008.*			(1)
Tetrahydrofuran (THF)		225, 302, 319, 335, 351	210, 280, 301+312+330, 305+351+338, 370+378, 403+235	(1)
Titanium dioxide	*Not a hazardous substance or mixture according to Regulation (EC) No 1272/2008.*			(3)
Triethyl phosphite		226, 302, 317, 412	210, 233, 273, 280, 301+312,303+361+353	(4)
Triethylamine		225, 301+311+331, 314, 335	210, 280, 301+312, 303+361+353, 304+340+310, 305+351+338+310	(1)
Trimethylsilyl bromide		226, 314, 335, 410 EU014	210, 233, 273, 280, 303+361+353, 305+351+338	(6)
Tris(2-aminoethyl)amine		302, 312, 314, 332, 335	261, 264, 270, 280, 301+312, 304+340, 305+351+338	(1)
Tris(acetylacetonato)chromium(III)		315, 319	280, 302+352, 332+313, 337+313	(3)
Vanillin		319	280, 305+351+338, 337+313	(1)
Xylene		226, 304, 312+332, 315, 319, 335, 373	210, 260, 280, 301+310, 303+361, 305+351+338	(1)

Substance	Symbol	Hazard-State-ments	Precautionary-State-ments	Disposal
Toluene		225, 304, 315, 336, 361d, 373	210, 240, 301+310, 302+352, 308+313, 314, 403+233	(2)

Table 6: Used carcinogenic, mutagenic substances and substances toxic for reproduction.

Substance	Hazard-Statements	CMR-Classification	Amount
Bisphenol A	360F	R1B	120 g
Chloroform	351, 361d	K2, R2	500 mL
Deuterated chloroform	351, 361	K2, M2, R2	550 x 0.7 mL
Dichloromethane	351	K2	300 mL
Hydrazine monohydrate	350	K1B	2 g
N,*N*-Dimethylforma-mide	360	R1B	100 mL
N,*N*-Dimethylforma-mide-d7	360D	R1B	5 mL
n-Hexane	361f	R2	3 L
Tetrahydrofuran	351	K2	4 L
Toluene	361d	R2	1.5 L

Disposal:

(1) Liquid is disposed in the container for halogen free, organic solvents. Solid is dissolved in an appropriate solvent and the solution is disposed in the container for halogen free, organic solvents.

(2) Liquid is disposed in the container for halogen containing, toxic organic solvents and carcinogenic substances. Solid is dissolved and the solution is disposed in the container for halogen containing, toxic organic solvents and carcinogenic substances.

(3) Solid is disposed in container for contaminated resources.

(4) Residues can be oxidized under nitrogen atmosphere and stirring at 0 °C using a sodium hypochlorite solution (5%) with some mL of a NaOH solution (50%). Phosphates can be precipitated using calcium hydroxide, the solid residues can be discarded in the container for contaminated resources.

(5) Residues can be neutralized after being dropped in water at 0 °C and addition of NaOH solution. After a pH of 6 – 8 is reached, the solution can be disposed in the container for chlorine-containing acids.

(6) Residues can be dropped carefully in a NaOH solution (10%) at 0 °C. After a pH of 6 – 8 is reached, the solution can be disposed in the container for chlorine-containing acids.

(7) Residues can be neutralized after being dropped in water at 0 °C and addition of HCl solution. After a pH of 6 – 8 is reached, the solution can be disposed in the container for bases.

10 Acknowledgment

Für eine lehrreiche und vor allem sehr schöne Zeit möchte ich mich bei denen bedanken, die mich in den vergangenen Jahren unterstützt haben. Ein besonderer Dank gilt dabei meinem Doktorvater Professor Dr. Volker Abetz, der mich während meiner Promotion betreut hat und dabei immer unterstützend und fördernd war. Für die Möglichkeit, eine Doktorarbeit auf dem interessanten und herausfordernden Thema von Vitrimeren und thermoresponsiven Polymernetzwerken zu forschen, bin ich sehr dankbar und habe es sehr genossen, der Kreativität und meinen Ideen auch mal freien Lauf zu lassen und immer wieder Neues zu entdecken. Für die inspirierenden thematischen Gespräche, das offene Ohr in schlechten Zeiten - auch privat - bin ich besonders dankbar. Die Möglichkeiten zu Konferenzen zu fahren, meine Forschung zu präsentieren und zu publizieren sowie das angenehme Arbeitsklima haben mich geprägt und der vergnügliche Humor werden mich auch in Zukunft immer mit einem Lächeln an die Zeit zurückerinnern. Ich möchte außerdem Birgit danken, dafür dass du immer ein offenes Ohr hattest und immer bereit warst, mit deiner ruhigen und überlegten Art Struktur in den bewegten Doktorandenalltag zu bringen. Gerne denke ich an die jährlichen Grillabende und AK-Ausflüge zurück.
Vielen Dank, Herr Priv.-Doz. Dr. Christoph Wutz, für die Übernahme des Zweitgutachtens dieser Dissertation.
Lieber AK Abetz, danke für die schöne Zeit! Angefangen von stets brühwarmem Kaffee, den vielen Schnackereien, einer angenehmen Arbeitsatmosphäre und dem angenehmen Beisammensein denke ich an viele unvergessliche Abende, Events und lustige Momente, die die letzten Jahre kurzweilig erscheinen lassen. Ich danke Tilman für die Begleitung meiner ersten Schritte in der Arbeitsgruppe und unsere abgespacten Unterhaltungen von Sport bis Musik – mittlerweile flimmert auch bei mir Tennis über die Mattscheibe. Danke an Philipp, mit dir habe ich richtig gerne im Büro gesessen, über Reisen, Festivals und Forschung philosophiert und freue mich schon auf neue Updates vom Strand oder der Skipiste. Meinen Kolleginnen aus Büro 363, Gloria und Sabrina, danke ich für das Ertragen (und Gießen) meiner pflanzlichen Mitbewohnis, die tollen Unterhaltungen und das nette Beisammensein im Büro. Nils, LigMa wird uns wohl immer begleiten, ich danke dir für die gute Zeit, das zielgerichtete gemeinsame Forschen und das Anstoßen nach mindestens zwei Loopings und drei Plings. Ein großes Danke an Gloria und Nils für das Korrekturlesen dieser Arbeit.
Meinen Student:innen Ira, Malte, Paul, Jannik, Moritz, Hanh, Nils und Claire möchte ich für eure Zeit und eure Hingabe zu unseren gemeinsamen Forschungsprojekten danken. Mit euch wusste ich immer, dass im Labor für gute Laune und klasse Ergebnisse gesorgt ist. Egal ob auf den Sommerfesten, Halloweenpartys, in der Katze oder auf Konzerten – ich danke euch für die gemeinsamen Erlebnisse auch abseits unserer Laborschichten.
Danke an Siraphat und Gloria für die gemeinsame Zeit im Graduiertenkolleg und zwei unvergessliche Reisen nach Spanien und Italien. Mit euch wurden die Konferenzen kurzweilig und das Besuchen der Städte hat richtig Spaß gemacht.

Ich denke immer wieder gerne an italienische Weinkeller und 40 Kilometer atemberaubende Fußmärsche in Madrids malerischen Gassen.
Siraphat, Gloria und Philipp sowie allen Mitgliedern des SFB-986 danke ich für die angenehme Zeit, anregende Diskussionen, aufregende Kanufahrten, Konferenzen und Summer Schools. Danke an Clemens und Layla für das Leiten und Organisieren des Graduiertenkollegs und die gute Versorgung mit Kaffee und veganen Snacks.
Bedanken möchte ich mich bei Maria, Patrick, Amrei, Larissa, Marvin und Samar, mit euch wurde es im AK nie langweilig und das gemeinsame Beisammensein im Sozialraum, im Labor oder auf einem der vielen Festivitäten habe ich sehr genossen. Vegan oder Nicht-Sein, das war hier immer die Frage. Martin, danke für deine lustige und aufgeschlossene Art, deine Hilfsbereitschaft und das Messen meiner unzähligen Proben an der DSC und TGA. Unsere Geschichten und Erlebnisse beim gemeinsamen Mittagessen zu hören und zu besprechen werde ich vermissen. Melle danke ich für die kurzweiligen Gespräche im, über und rund um das PCP. Gerne denke ich an das Besprechen der neuesten Ergebnisse rund um unseren braun-weißen Fußballverein. Andreas danke ich für das offene Ohr für meine Praktikumsideen, das Erklären und Nutzen von SAXS und AFM und den wahrscheinlich meistzitiertesten XP-Rechner des AKs am Mikroskop.
Ich danke meinen Kooperationspartner:innen an der Universität Hamburg und der Technischen Universität Hamburg. Lea, Jana und Tobias, ich möchte euch für die reichhaltige Versorgung mit Nanoteilchen danken und die vielen guten Diskussionen und die tollen Ergebnisse. Ich habe viel über die Wunderteilchen gelernt und danke euch für das Vertrauen, sie auch mal abseits der stabilisierten Lösung in meine Komposite einzubetten.
Auch außerhalb der akademischen Welt gibt es einige Personen, die mich auf meinem Weg unterstützt haben. Danke an Susanne, Christian, Oliver und Manon für eure immerwährende Unterstützung und die vielen aufmunternden Momente. Can, Lennard und Marcie danke ich für die beste wöchentliche Selektion Schabernack und immer so viel Spaß bei jeder Bandprobe seit über 16 Jahren. Danke für gemeinsame Alben, Touren, Feedback-Alarm, Mona, Günther III. und eure Passion für ProgRock. Bastian, Lukas, Jonas, Leo, Marie und Hildegard danke ich für das gemeinsame Musikmachen auf den Spuren der Hamburger Schule – wir sitzen so vorm Molotow! Unsere Stunden im Proberaum, im Studio, im WoZi, in Berlin und auf den Konzerten haben mich immer mit neuer Motivation versorgt. Danke an das Pegasus, mit euch haben sich das Veranstalten im Kulturbereich, die großen Festivals und unsere gemeinsamen Unternehmungen immer wie Urlaub vom Forschungstrubel angefühlt.
Danke an meine Freunde und Familie, ohne eure Unterstützung wäre ich auf dieser Reise nicht am Ziel angekommen.

11 Declaration of Academic Integrity

Eidesstattliche Versicherung:
Hiermit versichere ich an Eides statt, die vorliegende Dissertationsschrift selbst verfasst und keine anderen als die angegebenen Hilfsmittel und Quellen benutzt zu haben. Sofern im Zuge der Erstellung der vorliegenden Dissertationsschrift generative Künstliche Intelligenz (gKI) basierte elektronische Hilfsmittel verwendet wurden, versichere ich, dass meine eigene Leistung im Vordergrund stand und dass eine vollständige Dokumentation aller verwendeten Hilfsmittel gemäß der Guten wissenschaftlichen Praxis vorliegt. Ich trage die Verantwortung für eventuell durch die gKI generierte fehlerhafte oder verzerrte Inhalte, fehlerhafte Referenzen, Verstöße gegen das Datenschutz- und Urheberrecht oder Plagiate.

Hamburg, 18.12.2025 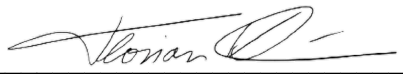

Ort, Datum, Unterschrift

Affidavit:
I hereby declare and affirm that this doctoral dissertation is my own work and that I have not used any aids and sources other than those indicated. If electronic resources based on generative artificial intelligence (gAI) were used in the course of writing this dissertation, I confirm that my own work was the main and value-adding contribution and that complete documentation of all resources used is available in accordance with good scientific practice. I am responsible for any erroneous or distorted content, incorrect references, violations of data protection and copyright law or plagiarism that may have been generated by the gAI.

Hamburg, 18.12.2025 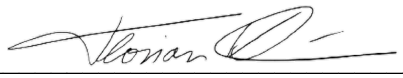

City, Date, Signature